The Flow Dynamics and Buttressing of Ice Shelves

MARTIN G. WEARING

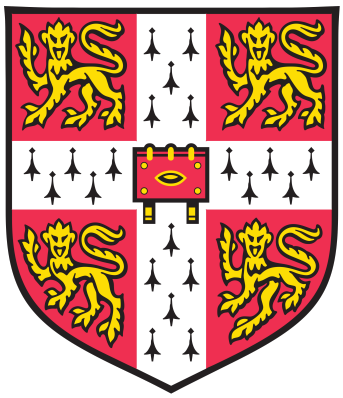

Downing College
University of Cambridge

July 2016

This dissertation is submitted for the degree of Doctor of Philosophy

Acknowledgements

This work was supported by a British Antarctic Survey stundentship funded by the Natural Environment Research Council, grant No. NE/K50094X/1

I would like to thank my supervisors Prof. M. G. Worster, Dr. R. C. A. Hindmarsh and Dr. R. J. Arthern for their support and guidance throughout my PhD.

I am grateful for the support and assistance of Prof. S. B. Dalziel, Dr. J. L. Partridge, Dr. M. A. Hallworth and the technicians in the G.K. Batchelor Lab in the set up of laboratory experiments.

I would like to thank fellow PhD students and Postdocs in the Department of Applied Mathematics and Theoretical Physics, and the British Antarctic Survey who have made my time as a PhD student in Cambridge very enjoyable.

Thank you to my parents for their endless love and encouragement.

Declaration

This dissertation is the result of my own work carried out under the supervision of Prof. M. G. Worster, Dr. R. C. A. Hindmarsh and Dr. R. J. Arthern.

Chapter 4 forms the basis of a paper authored by myself, M. G. Worster and R. C. A. Hindmarsh and published in the Journal of Glaciology.

No part of this dissertation has already been submitted, or, is being concurrently submitted for any degree, diploma or other qualification at any institution.

Martin G. Wearing
July 2016

The Flow Dynamics and Buttressing of Ice Shelves

MARTIN G. WEARING

In this thesis, I explore the flow dynamics associated with ice shelves confined within channels and the buttressing they provide to grounded ice. Ice shelves are the floating extensions of ice sheets and act as the interface between the ice sheet and the ocean. They form when ice flows out from the interior of the ice sheet towards the coast and begins to float as the ice thins. Ice shelves are often found within a channel or pinned in place by stationary bedrock outcrops. The interest in their dynamics is motivated by the buttressing effect they provide to the grounded ice, which strongly controls the rate of ice discharge and thereby the contribution to sea-level rise. I use a combination of mathematical modeling, fluid-mechanical laboratory experiments and geophysical data analysis to develop an improved understanding of ice-shelf flow dynamics.

Initially, geophysical data in the form of Antarctic ice-surface velocity data is analysed, producing maps of strain rate, shear rate and strain orientation for Antarctic ice shelves. This allows the geophysical setting and flow processes to be explored, particularly by identifying areas where resistance to ice flow is generated and regions of the shelf that make no contribution to buttressing. Using the geophysical data, I find good agreement between a theoretical scaling relationship for ice flow at the ice-shelf calving front and data from Antarctic ice shelves.

I proceed to develop an idealized mathematical model of an ice shelf confined to flow in a channel. By assuming shear-dominated dynamics within the shelf, analytical solutions are obtained for steady-state ice-shelf thickness profiles in parallel and diverging channels. This model is developed further to include both shear and extensional stresses, from which numerical solutions for steady-state shelves are calculated. The results from these two models are then compared. It is found that shear stresses dominate the dynamics throughout the majority of the shelf, with adjustment regions at the upstream and downstream boundaries where extensional dynamics become important. Output from these models is also compared with geophysical data and it is observed that there is good agreement between several features of the thickness profiles and velocity fields.

In addition to the geophysical data, comparisons are made with fluid-mechanical laboratory experiments designed to simulate the flow of an ice shelf in a channel. The advantage of performing experiments of this kind is that parameters such as the fluid rheology can be varied, allowing for direct comparison with a range of parameters in the mathematical models. From these experiments, surface velocity fields and thickness profiles are collected, which are used to make comparisons with the models. Clear differences are observed in the velocity and strain-rate fields produced using fluids with different rheologies, for which there is qualitative agreement with the output from the mathematical models.

Contents

Chapter 1

Introduction

Ice sheets are continental-sized glacial ice masses, such as those which presently cover Greenland and Antarctica. They form due to the accumulation of snow and ice at high altitude, and usually high latitude, which then spreads under gravity and flows towards the edge of the continent. They can either terminate before reaching the coast because of melting, or flow out over the ocean to form a floating ice shelf. These ice shelves can melt from below if they are in contact with warm ocean waters, and/or sections can break off at the front of the shelf to form icebergs in a process known as calving.

During the Last Glacial Maximum (LGM), around 21,000 years ago, in addition to the ice sheets of Greenland and Antarctica, the Laurentide and Fennoscandian ice sheets covered much of North America and Northern Europe respectively. The formation, advance/retreat and disappearance of ice sheets plays a key role in the climate system, not only as a store of freshwater but also affecting: surface albedo (the proportion of solar radiation reflected by a surface); ocean salinity; atmospheric and oceanic circulation. The change in mass of these ice sheets has a direct impact on global sea level. Ice sheets also provide a surface loading, which deforms the underlying and surrounding lithosphere and has wider implications for regional sea-level rise. For example, when an ice sheet melts and retreats from a location, the lithosphere there rebounds due to the removal of loading. This rebound causes a lowering of local sea level despite the volume of water in the ocean increasing. There is also an effect owing to the gravitational attraction of the ocean water towards the ice sheet. As mass is lost from the ice sheet, this attraction is reduced and the local sea level is lowered. In turn, a more pronounced sea-level rise is observed elsewhere, far from the ice sheet, where there has been no change in surface loading.

At present, sea-level rise is a threat to many lower-lying communities throughout the world, with IPCC AR5 projections estimating a global mean sea-level rise of 0.45 - 0.82 m by 2081 - 2100 relative to a mean sea level from 1986 - 2005 (Church et al., 2013).

This projection is under Representative Concentration Pathways (RCP) scenario 8.5, in which there is a long term high energy demand and greenhouse gas emissions in absence of climate change policies (Riahi et al., 2011). There are many factors inducing changes in sea level, such as the thermal expansion of the ocean water and changes in groundwater storage. However, projections concerning the contribution from ice sheets remain the most uncertain owing to a lack of understanding and observations (Church et al., 2013). It is estimated that between 1992 and 2011, the ice sheets of Greenland and Antarctica contributed 11.2 ± 3.8 mm to sea-level rise (Shepherd et al., 2012). This is a significant amount and accounts for approximately 20% of the sea level rise observed in this period (Church et al., 2013).

The mass loss from the Greenland Ice Sheet is due to a combination of sublimation, runoff of surface melting and ice flow to the coast. When ice reaches the coast it is then lost by direct melting of tidewater glaciers in contact with the ocean water, or the collapse of the ice front, which leads to the formation of icebergs. Different dynamics dominate the mass balance of the Antarctic Ice Sheet, where atmospheric and ocean temperatures are on average colder than those in Greenland. The term Equilibrium Line Altitude (ELA) is used to describe the zone in which there is a transition from an area that has net accumulation of snow and ice throughout the year, to an area that has net ablation throughout the year. For Greenland the ELA is found at approximately 1500 m above sea level (depending on location) (Oerlemans and van der Veen, 1984), however in Antarctica the ELA is located approximately at sea level. As a result, in Antarctica there is very little surface melting (which often refreezes within the ice if melt does occur) and once the ice reaches the coast it is able to form a floating ice shelf rather than a semi-grounded tidewater glacier, as is the case in many areas around the coast of Greenland. This means that mass loss from the Antarctic Ice Sheet is mainly due to the flow of ice off the continent into the floating ice shelves. Once the ice crosses the grounding line, the line at which the ice transitions from being grounded to floating, the ice has made its contribution to sea level as it displaces the equivalent volume of water. The extent of the ice shelves is regulated by the viscous deformation of the shelf along with the processes of submarine melting and iceberg calving at the ice-shelf front.

The two largest ice shelves in Antarctica, the Ross and Ronne Ice Shelves are found in West Antarctica. Here, large sections of the ice sheet are grounded on bedrock below sea level. This configuration is referred to as a marine ice sheet. The extent to which this section of the ice sheet is grounded below sea level can be seen in Figure 1.1a, a map of bedrock bathymetry. As this region of the ice sheet is below sea level, grounding-line retreat would expose more ice to ocean waters, which may act to melt the ice. This process has the potential to be influenced by changes in ocean heat con-

tent and circulation. Furthermore, much of the ice sheet in this section of Antarctica is located on a retrograde slope, meaning the bedrock slopes down in the upstream direction, which is thought to be fundamentally unstable to grounding line retreat for a one-dimensional flow line approximation of the system. This 'marine ice sheet instability' was first proposed by Weertman (1974) and clarified more recently by the work of Schoof (2007). These two mechanisms for ice-sheet retreat are significant as the west section of the Antarctic Ice Sheet has the potential to raise sea level by 7m (Fretwell et al., 2013).

Ice shelves around the coast of Antarctica are fed by fast flowing sections of the ice sheet known as ice streams. Ice in these ice streams flows at up to 1000 m yr^{-1}, while ice flow in the surrounding areas is less than 50 m yr^{-1} and typically on the order of 5 m yr^{-1}. This channelized tributary structure of ice flow can be seen in a map of ice surface velocity as shown in Figure 3.1, taken from Rignot et al. (2011a). These ice streams act to channel and transport 90% of the ice discharged from the Antarctic continent into the floating ice shelves (Bamber et al., 2000). This rate of ice discharge is controlled by a number of characteristics.

One factor controlling discharge is the basal conditions of the ice streams, which determines whether the ice slips along a well lubricated bed, or whether the base of the ice stream is frozen in place and flow is solely due to the deformation of the overlying ice. These differences may stem from the properties of the materials found at the ice-bed interface, be it rock or till. In Greenland there is evidence to suggest that there are seasonal changes in the basal conditions due to surface melt water reaching the bed and helping to lubricate the interface (Bartholomew et al., 2010). This may lead to the formation of a subglacial drainage system in the form of distributed cavities or interlinking channels (Hewitt, 2011, 2013), which may evolve during the seasonal cycle depending on the volume of water and driving pressures. In Antarctica, there are locations where water is present at the base of the ice streams (Blankenship et al., 1986) but this most likely forms as a result of frictional shear heating at the ice-bed interface or due to geothermal heat warming the ice from below rather than input at the surface as in Greenland, where annual temperatures are greater.

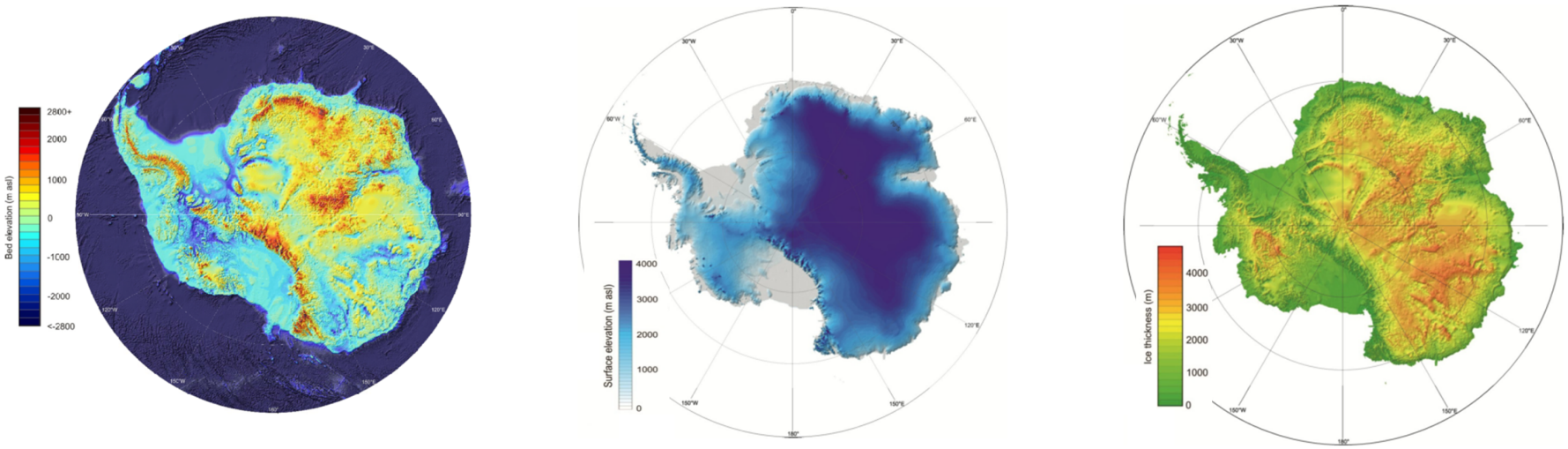

(a) (b) (c)

Figure 1.1: Figures adapted from Fretwell et al. (2013) showing the Bedmap2 dataset: (a) bed elevation; (b) surface elevation; (c) ice thickness.

When considering the relevant length-scales and timescales for ice-sheet dynamics: 100 m - 100 km length-scales; and 10 - 1000 year timescales, ice flows like a viscous fluid. However, glacial ice has shear-thinning Non-Newtonian characteristics and is widely modelled using Glen's Flow Law (Cuffey and Paterson, 2010). This empirically derived model for ice rheology is based on a power-law rheological model, where the effective viscosity of the fluid is proportional to a simple power of the rate of strain. Within the Glen's-Flow-Law model there are two parameters, a rate factor or consistency index and the power-law exponent. These values are empirically derived and may depend on ice temperature and the deformation history. Further explanation of Glen's Flow Law and other rheological approximations for ice are given in later sections.

In Antarctica, most ice streams feed into a floating ice shelf. These ice shelves are often found in a channel or embayment with bedrock outcrops located along the edges or within the embayments. These outcrops act to restrict the flow of the shelf. In turn the shelf exerts a backstress on the grounded ice due to the resistance generated by the deformation of the ice shelf. This buttressing effect acts to reduce the rate of ice discharge from the ice streams. Evidence of this effect can be seen in the speed up and thinning of glaciers and ice streams following the collapse of an ice shelf downstream. Examples include the collapse of the Larsen A (Rott et al., 2002) and Larsen B (Scambos et al., 2004; Rignot et al., 2004) Ice Shelves, in 1995 and 2002 respectively. In the case of the Larsen B collapse, some glaciers that were former tributaries to the ice shelf sped up significantly, with one temporarily reaching speeds up to 8 times pre-collapse flow speed, from approximately 250 m yr^{-1} to approximately 2000 m yr^{-1} (Rignot et al., 2004). Ice-shelf thinning due to atmospheric and ocean melt has also been linked to dynamic thinning of tributary ice streams (Pritchard et al., 2012), suggesting that small changes in buttressing can have substantial impacts on discharge.

Therefore, these ice shelves and the buttressing effect they have on the grounded ice are an important aspect of ice-sheet dynamics and is one factor controlling the rate of ice discharge and as a consequence the rate of sea-level change. Increasing atmospheric and ocean temperatures are likely to have an impact on the extent and strength of ice shelves. The Antarctic Peninsula is an area of particularly rapid warming, warming at a rate of 3.7 ± 1.6°C per century (from measurements between 1904 and 2001) (Vaughan et al., 2003). This warming may lead to the retreat or collapse of ice shelves along the Antarctic Peninsula, such as the Larsen A and B ice shelves, with empirical relations suggesting that ice shelves can not withstand average annual temperatures greater than -5° (Vaughan and Doake, 1996).

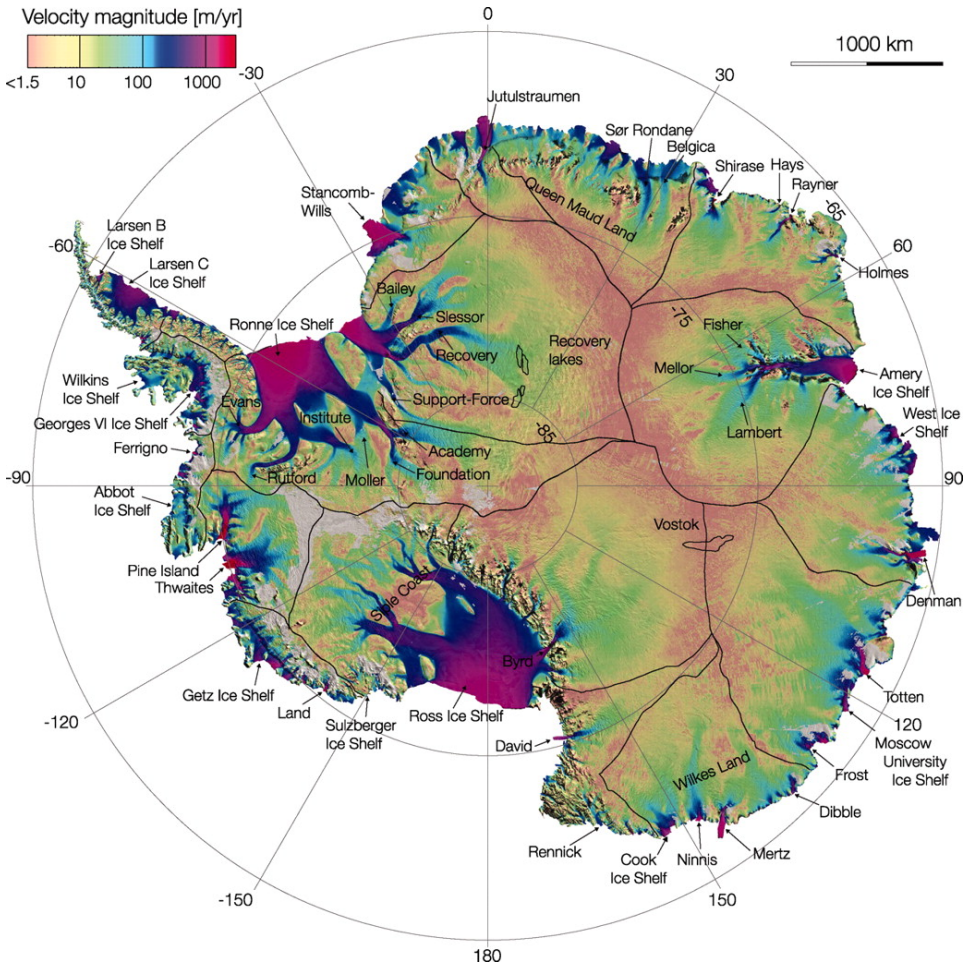

Figure 1.2: Antarctic ice-surface speed, figure taken from Rignot et al. (2011a)

Many ice-sheet models are based on a two-dimensional flow-line geometry that considers one horizontal dimensional along the flow of the ice sheet and one vertical dimension in which the ice-sheet thickness varies. In these models, the buttressing effect of the ice shelves is not inherently included but some parameterization of the effect can be included in an attempt to capture the dynamics. However, this overlooks the interesting and often complex dynamics that occur in the shelf. By including an additional horizontal dimension, the flow within the shelf can be studied and the mechanisms contributing to buttressing can be investigated. For instance, when the dynamics of an ice shelf are considered in a model with two horizontal dimensions, it has been shown by Gudmundsson (2013) that the presence of an ice shelf can help to stabilize a marine ice sheet with a grounding line situated on a retrograde slope.

This thesis aims to further elucidate the flow dynamics of ice shelves and the mechanisms by which they buttress the grounded ice. Simple equations governing the ice flow are first introduced, with particular attention paid to the ways in which buttressing can be generated by the shelf and the rheological properties of ice. Geophysical data from Antarctic ice shelves are then analysed in Chapter 3, in order to develop an understanding of the geophysical setting as well as the qualitative and quantitative features present. An Antarctic-wide velocity dataset is used to investigate the flow dynamics found in ice shelves, with analysis of the induced deformation. Areas of the ice shelf are identified that contribute to the buttressing of the grounded ice. In Chapter 4 a simple relationship is derived for the flow of ice at the front of a ice shelf, which is then compared with geophysical data. This comparison identifies ice shelves that conform to the scaling relationship and those that flow faster than expected, owing to weak ice in the shear margins or an absence of lateral pinning-points.

A set of idealized models for the flow of an ice shelf in a channel are then developed in Chapter 5, with the aim of developing a fundamental understanding of the controls on the flow dynamics of the shelf. From these models, analytical and numerical solutions are obtained for the ice-shelf thickness profile and velocity field. These model results are then compared with the geophysical data, clarifying the controls on the large-scale dynamics observed throughout the shelf. In addition to the comparisons with the geophysical data, a set of fluid mechanical laboratory experiments are performed to simulate the flow of an ice shelf confined to a channel. These experiments are described and the results presented in the penultimate chapter. Both Newtonian and shear-thinning fluids are used to simulate an ice shelf, with thickness profiles and velocity fields obtained. Clear differences are observed between the dynamics in each case, and similarities are identified with the geophysical examples and idealized models.

Chapter 2

Fundamental Equations for the Flow of Ice Shelves

2.1 Introduction

In this chapter, I introduce the equations for the Shallow-Shelf Approximation, which govern the flow of an ice shelf when ice flow is uniform in the vertical. I then use these equations to outline how resistance to flow or buttressing can be generated for simple ice-shelf flows. These ideas will be applied to the analysis of geophysical data in Chapter 3.

2.2 Fundamental Equations

An ice shelf spreading under gravity can be modelled using the incompressible Stokes equations for flows with low Reynolds number. For a typical ice shelf, ice-flow speeds are of the order of 500 m yr^{-1}, varying over a length scale of approximately 100 km. The dynamic viscosity is approximately 2×10^{14} Pa s, which leads to a typical Reynolds number of $\mathrm{Re} \sim 10^{-11}$. For the flow of an ice shelf, deformation occurs over long timescales. However, if the ice is forced over a short time period there is an elastic response, such as when an ice shelf oscillates with tidal forcing (Anandakrishnan and Alley, 1997; Sayag and Worster, 2013a). The elastic and viscous response of an ice shelf to tidal forcing have been investigated by Reeh et al. (2003); Gudmundsson (2011) amongst others. Reeh et al. (2003) saw good agreement between data for tidal displacement of an ice shelf and results from a viscoelastic beam model. The rheological model used in this work captured the instantaneous elastic response, delayed elastic response and viscous response. Using this viscoelastic model and the parameter values listed in the paper (Reeh et al., 2003) it is apparent that the instantaneous and delayed elastic effects dominate within the two weeks of an imposed constant loading, with the viscous effects dominating thereafter.

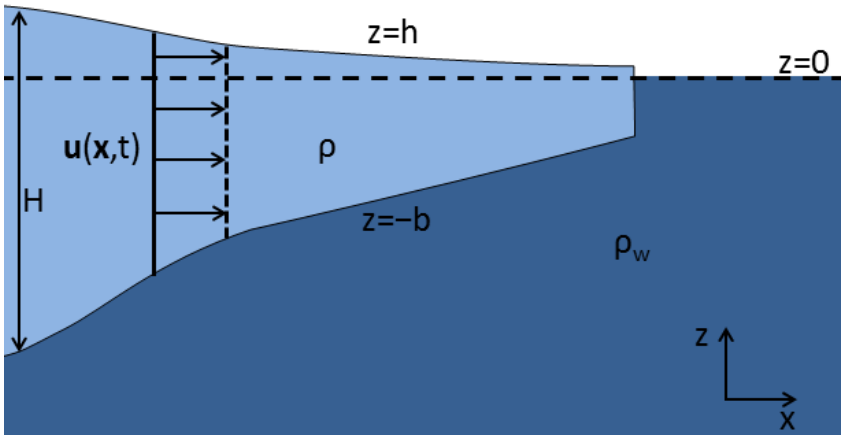

Figure 2.1: Diagram depicting a floating ice shelf flowing over a dense and inviscid ocean.

The viscoelastic rheological model and parameter values can be found in the Appendix (Section A) along with a plot of the evolution of the three components of strain and the total strain rate for this constant imposed stress, Figure A.1.

In this work I focus on the long timescale viscous deformation of an ice shelf over years to thousands of years and neglect the short-time elastic behaviour.

I now outline the equations for the vertically integrated flow of an ice shelf, as derived by Pegler (2012) and previously by Di Pietro and Cox (1979) and MacAyeal (1989). Amongst glaciologists, these equations are known as the Shallow-Shelf Approximation (SSA).

Consider an ice shelf of density ρ, floating in a dense ocean ($\rho_w > \rho$), as shown in the schematic in Figure 2.1. The force-balance equation for the shelf balances the divergence of the stress tensor with the gravitational body force and we consider the ice to be an incompressible fluid,

$$\nabla.\boldsymbol{\sigma} = \nabla.\left(-P\mathbf{I} + 2\mu\mathbf{e}\right) = \rho g\hat{\mathbf{z}}, \tag{2.1}$$

$$\nabla.\mathbf{u} = 0. \tag{2.2}$$

Here $\boldsymbol{\sigma}$ denotes the (Cauchy) stress tensor, P is the isotropic pressure, $\mathbf{I}$ the 3D identity matrix, μ is the effective (dynamic) viscosity, ρ the ice density, g the acceleration due to gravity, $\hat{\mathbf{z}}$ the vertically aligned unit vector, $\mathbf{u}$ the velocity and $\mathbf{e} = \frac{1}{2}\left[\nabla\mathbf{u} + (\nabla\mathbf{u})^T\right]$ is the rate-of-strain tensor. The derivation below assumes that ice behaves like a generalised Newtonian fluid, with the effective viscosity μ dependent on strain rate. In later

sections, a Newtonian model and non-Newtonian model will be developed, with the non-Newtonian model capturing the shear-thinning properties of ice.

Consider the horizontal component of the force balance from the Stokes equation (2.1),

$$\tilde{\nabla}.\tilde{\boldsymbol{\sigma}} + \frac{\partial}{\partial z}(\hat{\mathbf{z}}.\tilde{\boldsymbol{\sigma}}) = 0, \tag{2.3}$$

where all the terms with a tilde ($\sim$) refer to the horizontal component of that term, such that

$$\tilde{\nabla} \equiv \begin{pmatrix} \frac{\partial}{\partial x} \\ \frac{\partial}{\partial y} \\ 0 \end{pmatrix}, \tag{2.4}$$

$$\tilde{\boldsymbol{\sigma}} \equiv \begin{pmatrix} \sigma_{xx} & \sigma_{xy} & \sigma_{xz} \\ \sigma_{yx} & \sigma_{yy} & \sigma_{yz} \end{pmatrix}. \tag{2.5}$$

The full force-balance equation is subject to the boundary conditions

$$\boldsymbol{\sigma}.\mathbf{n} = \mathbf{0} \qquad (z = h), \tag{2.6}$$

$$\begin{aligned} \boldsymbol{\sigma}.\mathbf{n} &= \rho_w g z \mathbf{n} \qquad (z = -b), \\ &= \rho_w g(-b)\mathbf{n}, \end{aligned} \tag{2.7}$$

where h is the position of the upper surface of the shelf in contact with the atmosphere and b is the thickness of the shelf below sea level, denoted by $z = 0$. The vector $\mathbf{n}$ is the outward-pointing unit vector normal to each surface (pointing out from the ice). The first condition states that there are no stresses acting normal to the surface on the top surface of the ice shelf, while the second condition gives the normal stress acting on the lower surface of the ice shelf as a result of the pressure of the ocean water beneath the ice shelf, with ρ_w denoting the density of the ocean. It is assumed that there are no tangential stresses acting on the upper or lower ice interfaces.

Here we assume that the horizontal extent of the shelf is much larger than the shelf thickness H, so that gradients in thickness (∇H) are small. (A typical ice shelf may be 100 - 500 km long, thinning from up to 1000 m at the grounding line to approximately 200 m at the calving front.) The horizontal component of these boundary conditions can then be rewritten to leading order in ∇H, where $\nabla H \ll 1$. Here the surface gradients are small such that the normal vectors to the surface and the surface gradient vectors can be approximated as aligned in the vertical $\mathbf{z}$-direction. The surface and base of the shelf can be given in terms of the shelf thickness; $h = (1-\rho/\rho_w)H$ and $b = (\rho/\rho_w)H$, assuming from Archimedes Principle that the shelf is subject to an upward body force equal to the

weight of the fluid displaced. The horizontal component of the first boundary condition, (2.6), gives

$$\begin{aligned} &\tilde{\boldsymbol{\sigma}}.\tilde{\mathbf{n}} = 0 && (z = h), \qquad (2.8)\\ &\Rightarrow \tilde{\boldsymbol{\sigma}}.\hat{\mathbf{z}} \approx \tilde{\boldsymbol{\sigma}}.\tilde{\nabla} h \approx 0,\\ &\Rightarrow \begin{pmatrix} \sigma_{xz} \\ \sigma_{yz} \end{pmatrix} \approx \left(1 - \frac{\rho}{\rho_w}\right) \begin{pmatrix} H_x\sigma_{xx} + H_y\sigma_{xy} \\ H_x\sigma_{yx} + H_y\sigma_{yy} \end{pmatrix} \approx 0, \end{aligned}$$

while the horizontal component of the second boundary condition (2.7) gives

$$\begin{aligned} &\tilde{\boldsymbol{\sigma}}.\tilde{\mathbf{n}} = \rho_w g(-b)\tilde{\mathbf{n}}, && (z = -b), \qquad (2.9)\\ &\Rightarrow \tilde{\boldsymbol{\sigma}}.\hat{\mathbf{z}} \approx \tilde{\boldsymbol{\sigma}}.\tilde{\nabla}(-b) \approx \rho_w g(-b)\tilde{\nabla}(-b),\\ &\begin{pmatrix} \sigma_{xz} \\ \sigma_{yz} \end{pmatrix} \approx -\frac{\rho}{\rho_w} \begin{pmatrix} H_x\sigma_{xx} + H_y\sigma_{xy} \\ H_x\sigma_{yx} + H_y\sigma_{yy} \end{pmatrix} \approx -\frac{\rho^2 g}{\rho_w} H \begin{pmatrix} H_x \\ H_y \end{pmatrix}. \end{aligned}$$

This implies that vertical shear stresses (σ_{iz} with $i = x, y$) are much smaller, by a factor of ∇H, than stresses due to horizontal velocity variations (σ_{ij} with $i, j = x, y$).

In addition to this, for an ice shelf there are no tangential stresses acting on the top surface with the atmosphere or the bottom surface with the ocean. (These tangential stresses are sometimes referred to as tractions.) This implies that the vertical-shear stresses are negligible in the z-component of the Stokes equation (2.1). The vertical component of the Stokes equation therefore reduces to

$$\frac{\partial \sigma_{zz}}{\partial z} = \rho g. \qquad (2.10)$$

This equation has boundary conditions determined by the vertical stresses acting on the top and bottom surfaces of the ice shelf. As earlier, under the assumption that the thickness gradient (∇H) is small, the top and bottom surfaces of the shelf can therefore be approximated as horizontal surfaces

$$\sigma_{zz} = 0 \qquad (z = h), \qquad (2.11)$$

$$\sigma_{zz} = -\rho g(h + b) \qquad (z = -b). \qquad (2.12)$$

Atmospheric pressure has been set to zero, so there is no normal stress acting on the upper surface, while the normal stress acting on the lower surface of the shelf is a result of the hydrostatic pressure of the ice above it. These boundary conditions can be used

to solve for σ_{zz} in (2.1) and produce an equation for the pressure in the ice shelf,

$$\sigma_{zz} = \rho g(z-h) = -P + 2\mu\frac{\partial w}{\partial z}, \tag{2.13}$$

$$\Rightarrow P = 2\mu\frac{\partial w}{\partial z} - \rho g(z-h). \tag{2.14}$$

Returning to the horizontal component of the Stokes equation (2.3) and integrating across the depth of the flow,

$$\int_{-b}^{h} \tilde{\nabla}.\tilde{\boldsymbol{\sigma}}dz + [\hat{\mathbf{z}}.\tilde{\boldsymbol{\sigma}}]_{-b}^{h} = 0. \tag{2.15}$$

Using the boundary conditions (2.8) and (2.9), we obtain

$$\int_{-b}^{h} \tilde{\nabla}.\tilde{\boldsymbol{\sigma}}dz + \tilde{\boldsymbol{\sigma}}.\tilde{\nabla}h - \tilde{\boldsymbol{\sigma}}.\tilde{\nabla}(-b) = -\frac{\rho^2 g}{\rho_w}H\tilde{\nabla}H, \tag{2.16}$$

$$\Rightarrow \tilde{\nabla}.\int_{-b}^{h} \tilde{\boldsymbol{\sigma}}dz = -\frac{\rho^2 g}{\rho_w}H\tilde{\nabla}H, \tag{2.17}$$

using Leibniz's rule. Here the term on the right of equation (2.17) corresponds to the hydrostatic pressure of the ocean acting on the bottom of the ice shelf, while the term on the left-hand side is the divergence of the depth-integrated horizontal stress. It is now possible to produce an equation for the depth integrated horizontal stress,

$$\int_{-b}^{h} \tilde{\boldsymbol{\sigma}}dz = \int_{-b}^{h} \left(-P\tilde{\mathbf{I}} + 2\mu\tilde{\mathbf{e}}\right)dz, \tag{2.18}$$

$$= \int_{-b}^{h} \left[\left(-2\mu\frac{\partial w}{\partial z} + \rho g(z-h)\right)\tilde{\mathbf{I}} + 2\mu\tilde{\mathbf{e}}\right]dz, \tag{2.19}$$

$$= -\frac{1}{2}\rho g(h+b)^2\tilde{\mathbf{I}} + 2\mu(h+b)\left[(\tilde{\nabla}.\tilde{\mathbf{u}})\tilde{\mathbf{I}} + \tilde{\mathbf{e}}\right], \tag{2.20}$$

$$= -\frac{1}{2}\rho g H^2\tilde{\mathbf{I}} + 2\mu H\left[(\tilde{\nabla}.\tilde{\mathbf{u}})\tilde{\mathbf{I}} + \tilde{\mathbf{e}}\right]. \tag{2.21}$$

The incompressibility condition, equation (2.2), has been used to substitute $-\frac{\partial w}{\partial z}$ with the horizontal divergence of the horizontal velocity $\tilde{\nabla}.\tilde{\mathbf{u}}$. Now taking the divergence of the depth-integrated horizontal stress,

$$\tilde{\nabla}.\left(-\frac{1}{2}\rho g H^2\tilde{\mathbf{I}} + 2\mu H\left[(\tilde{\nabla}.\tilde{\mathbf{u}})\tilde{\mathbf{I}} + \tilde{\mathbf{e}}\right]\right) = -\frac{\rho^2 g}{\rho_w}H\tilde{\nabla}H, \tag{2.22}$$

$$-\rho g H\tilde{\nabla}H + 2\tilde{\nabla}\mu H(\tilde{\nabla}.\tilde{\mathbf{u}}) + 2\tilde{\nabla}.(\mu H\tilde{\mathbf{e}}) = -\frac{\rho^2 g}{\rho_w}H\tilde{\nabla}H, \tag{2.23}$$

$$\tilde{\nabla}\mu H(\tilde{\nabla}.\tilde{\mathbf{u}}) + \tilde{\nabla}.(\mu H\tilde{\mathbf{e}}) = \frac{\rho g'}{2}H\tilde{\nabla}H. \tag{2.24}$$

This is the depth-integrated horizontal force balance for the ice shelf, with a generalised

Newtonian rheology (i.e. μ has not been specified). Here g' is the reduced gravity given by

$$g' = \left(\frac{\rho_w - \rho}{\rho_w}\right) g. \tag{2.25}$$

The depth-integrated horizontal force balance determines the flow within the ice shelf. The ice shelf thickness then evolves subject to the continuity equation

$$\frac{\partial H}{\partial t} + \nabla.(H\mathbf{u}) = a. \tag{2.26}$$

The variable a accounts for accumulation or ablation of ice on the surface or base of the shelf. This may be due to: snowfall; surface or basal melting; or the freeze-on of ocean water. For the theoretical models developed later in this thesis, I neglect these effects and focus on the deformation due to flow and therefore set $a = 0$.

I now briefly consider some of the dynamics for three types of ice flow: purely extensional flow; shear flow; and radial spreading. This will give an insight into the basic dynamics before investigating/analysing the ice-shelf flow field from some geophysical examples in the following chapter. Of particular interest is the variety of dynamics that may act to provide resistance to the flow of the ice shelf and therefore contribute to the buttressing of the grounded ice.

2.3 Cartesian Coordinates

In Cartesian coordinates the force-balance equation (2.24) takes the form of a system of equations,

$$4\frac{\partial}{\partial x}\left(\mu H\frac{\partial u}{\partial x}\right) + 2\frac{\partial}{\partial x}\left(\mu H\frac{\partial v}{\partial y}\right) + \frac{\partial}{\partial y}\left(\mu H\frac{\partial u}{\partial y}\right) + \frac{\partial}{\partial y}\left(\mu H\frac{\partial v}{\partial x}\right) = \rho g' H\frac{\partial H}{\partial x}, \tag{2.27}$$

$$4\frac{\partial}{\partial y}\left(\mu H\frac{\partial v}{\partial y}\right) + 2\frac{\partial}{\partial y}\left(\mu H\frac{\partial u}{\partial x}\right) + \frac{\partial}{\partial x}\left(\mu H\frac{\partial u}{\partial y}\right) + \frac{\partial}{\partial x}\left(\mu H\frac{\partial v}{\partial x}\right) = \rho g' H\frac{\partial H}{\partial y}, \tag{2.28}$$

representing the x and y components of the force-balance equation, with u the velocity component aligned in the x-direction and v the velocity component in the y-direction.

2.3.1 1D Flowline Ice Shelf - Extension Only

Consider a one-dimensional flow-line model for an ice shelf with horizontal flow in the x-direction only ($\mathbf{u} = (u(x), 0)$) and a thickness profile that varies in the x-direction only, such that $H \equiv H(x, t)$. The force-balance equation then reduces to

$$4\frac{\partial}{\partial x}\left(\mu H\frac{\partial u}{\partial x}\right) = \rho g' H\frac{\partial H}{\partial x}. \tag{2.29}$$

This can be integrated in the along-flow, x-direction to give

$$\mu \frac{\partial u}{\partial x} = \frac{\rho g'}{8} H. \tag{2.30}$$

Here the term on the left-hand side represents the extensional stresses within the shelf, while the term on the right denotes the hydrostatic driving pressure. This is the simplest example of ice-shelf flow, where the hydrostatic driving stress is balanced by only the extensional stresses within the shelf. In this case I consider there to be no resistance to the flow of the shelf and therefore no buttressing. This state will be used to compare whether the dynamics within a shelf provide resistance to flow and therefore make a contribution to buttressing.

Here it is assumed that the shelf thins in the along-flow direction and $\partial H/\partial x < 0$. However, if there is an area of compression, such as when a pinning point blocks the flow of an ice shelf, then this will lead to thickening of the shelf upstream of the pinning point, and therefore changing the sign of the partial derivative in H. This compression leads to a reduction in the extensional stress and hence buttressing.

2.3.2 Flow in a Channel - Shear Stresses

Consider the flow of an ice shelf in a long and narrow parallel channel of width W. The flow of the ice shelf is assumed to be in the along-channel, x-direction only and the shelf has a uniform cross-channel thickness profile. The magnitude of the velocity can vary across the width of the channel and the horizontal velocity is given by $\mathbf{u} = (u(x, y), 0)$, with the thickness profile taking the form $H \equiv H(x, t)$. Along the channel walls at $y = 0$ and $y = W$, we can prescribe boundary conditions such as no-slip ($u = 0$) or some form of Coulomb friction: $\partial u/\partial y = \kappa u/\mu$, where $\kappa = \infty$ signifies no-slip along the channel walls and $\kappa = 0$ signifies free-slip. For this system, the along-channel component of the force-balance equation reduces to

$$4\frac{\partial}{\partial x}\left(\mu H \frac{\partial u}{\partial x}\right) + \frac{\partial}{\partial y}\left(\mu H \frac{\partial u}{\partial y}\right) = \rho g' H \frac{\partial H}{\partial x}. \tag{2.31}$$

Here the two terms on the left hand side are partial derivatives of the depth-integrated extensional stress and the shear stress, which balance the along-channel derivative of the depth-integrated hydrostatic driving stress, given on the right. Here there are two resisting stresses balancing the driving hydrostatic pressure gradient. When compared with the previous flowline case, which considered only extensional stresses, we see that there is now additional resistance to flow from this shear stress term (a source of buttressing).

2.4 Radial Flow - Hoop Stresses

Now consider a flow that is unconfined by lateral walls, the simplest case being an axisymmetric, radially spreading ice shelf. In cylindrical coordinates with radial flow denoted by u and azimuthal flow by v, the horizontal strain-rate tensor $\mathbf{e}$ has components

$$e_{rr} = \frac{\partial u}{\partial r}, \tag{2.32}$$

$$e_{\theta\theta} = \frac{1}{r}\frac{\partial v}{\partial \theta} + \frac{u}{r}, \tag{2.33}$$

$$e_{r\theta} = \frac{1}{r}\frac{\partial u}{\partial \theta} - \frac{v}{r} + \frac{\partial v}{\partial r}. \tag{2.34}$$

The radial component of the force-balance equation (2.24) then becomes

$$\frac{\partial}{\partial r}\left[\mu H\left(\frac{u}{r} + 2e_{rr}\right)\right] + \frac{1}{r}\frac{\partial}{\partial \theta}\left(\mu H e_{\theta\theta}\right) + \frac{\mu H}{r}\left(e_{rr} - e_{\theta\theta}\right) = \frac{\rho g'}{2} H \frac{\partial H}{\partial r}. \tag{2.35}$$

If we consider an idealized theoretical case with axisymmetric flow in the radial direction, as considered by Pegler and Worster (2012), then terms involving partial derivatives in the θ-direction are set to zero and the radial force balance becomes

$$\frac{\partial}{\partial r}\left(\mu H\left(2\frac{\partial u}{\partial r} + \frac{u}{r}\right)\right) + \mu H \frac{\partial}{\partial r}\left(\frac{u}{r}\right) = \frac{\rho g'}{2} H \frac{\partial H}{\partial r}. \tag{2.36}$$

Here the first term on the left-hand side of the equation represents the radial extension of the shelf, in a similar manner to the along-flow extension found in the force-balance equation for the 1D flowline ice shelf in a simple Cartesian system, as considered in the previous section. In the Cartesian 1-D flowline system, this was balanced by the hydrostatic driving pressure only, which is the term on the right hand side of (2.36). This has a negative value due to the decrease in the shelf thickness (H) with radial (along-flow) distance r. However, for this radial flow there is an additional term on the left-hand side, which must balance the hydrostatic driving pressure. This additional term is the hoop stress, which is due to the azimuthal extension of the shelf as the current spreads radially.

$$\mu H \frac{\partial}{\partial r}\left(\frac{u}{r}\right). \tag{2.37}$$

If the hoop-stress term is negative it reduces the influence of the hydrostatic driving pressure on the extensional stress and effectively acts to resist the flow of the shelf. Therefore a negative hoop-stress term acts as a source of buttressing. Conversely, if it is positive then it acts to increase the radial extension.

Physically, positive hoop stress can be thought of as the extensional resistance generated by azimuthal spreading. A driving pressure is required to induce this spread and

therefore this reduces the magnitude of the along-flow extension and hence produces resistance to flow.

From these simple examples of ice flow, it is clear that flow in the shelf is induced primarily by the hydrostatic driving pressure, which in the simplest case (uni-directional flow with no transverse gradient) is then balanced by the extensional stress in the shelf. In addition to this, resistance to flow or buttressing can be generated due to the presence of shear or hoop stresses. The shear and hoop stresses act to reduce the extensional strain rate in comparison to the extension-only case.

In the following chapters when analysing shelf velocities I use the term 'resistance to flow' to describe when the extensional stress at a point is less than the extensional stress expected in the case of basic extensional flow, as described by a 2D flow-line model, with no buttressing parameterization. This resistance and the reduction in the extensional stress then make a positive contribution to buttressing.

2.5 Ice Rheology - Glen's Flow Law

One fundamental parameter that controls the flow of an ice shelf is the ice rheology, and for ice shelves and glaciers this rheology can often be complex. For the case of ice-shelf flow, where deformation occurs on relatively long timescales (weeks - 100 years), the elasticity component of the ice rheology can be neglected and the deformation can be accurately modelled as purely viscous. In the theoretical and experimental investigations in this thesis, I use a selection of fluids with different rheologies to assess the effects of rheology on the dynamics. Basic models use a Newtonian rheology, for which the viscosity is constant. This approximation allows the underlying physical balances to be understood without complications from temporal or spatial variations in viscosity or feedbacks between dynamics and viscosity.

However, ice is known to be a shear-thinning fluid, with increased strain rates leading to a decrease in the effective viscosity. This implies that there is a nonlinear relationship between the strain rate and stress. Figure 2.2a shows a plot of strain rate versus shear stress for three different rheologies (Newtonian ($n = 1$), shear-thinning power-law ($n = 3$), and perfectly plastic (yield stress =100 kPa)). Here the difference between the Newtonian and shear-thinning behaviour is clear. There is a linear relationship between shear stress and strain rate in the case of the Newtonian fluid. However, for the shear-thinning fluid, an increase in the strain rate leads to a nonlinear increase in the shear stress, with the increase in shear stress reduced for larger strain rates.

Ice rheology is often modelled using a power-law model, known as Glen's Flow Law. The effective viscosity under this theory takes the form

$$\mu = \frac{1}{2} B e_{II}^{(1-n)/n}, \tag{2.38}$$

with B the rate factor, n the flow-law exponent and e_{II} the second invariant of the strain-rate tensor $\mathbf{e}$. The second invariant of the strain-rate tensor is a measure of the rate of deformation of the ice and is given by

$$e_{II} = \frac{1}{2}\mathbf{e} : \mathbf{e} = \left[\frac{1}{2}\left(e_{xx}^2 + e_{yy}^2 + e_{zz}^2\right) + e_{xy}^2 + e_{xz}^2 + e_{yz}^2\right]^{1/2}. \tag{2.39}$$

Alternatively, the deviatoric stress experienced by the fluid can also be expressed as a function of the strain rate,

$$\tau_{ij} = B e_{II}^{(1-n)/n} e_{ij}. \tag{2.40}$$

The flow exponent n has been determined from multiple sets of field data and is thought to take a value between 1.5 and 4.2 (Cuffey and Paterson, 2010). As the value of n is increased, the effective viscosity is reduced more for the same strain rate. In most modelling studies it is assumed that $n \approx 3$ (Cuffey and Paterson, 2010) and in this thesis I use a power-law rheology with $n = 3$ to capture the shear-thinning nature of ice. Some field data from a range of ice shelves used to derive a value of n can be seen in Figure 2.2b.

The rate factor (or consistency index) B encapsulates all dependencies other than the strain rate. The most important of these is temperature dependence, as the ice softens with increasing temperature. The two ice temperatures considered in this work are 0°C and -10°C. For these two values the rate factor is $B = 7.47 \times 10^7$ $\mathrm{s}^{1/3}$ Pa for ice at 0°C, and $B = 1.42 \times 10^8$ $\mathrm{s}^{1/3}$ Pa for ice at -10°C (Cuffey and Paterson, 2010). Other characteristics which may affect the value of B are: the water content of the ice; the deformation history and presence of damage, such as fractures or crevasses; the crystal structure and crystal orientation; ice grain size; and the concentration of impurities. Therefore the version of Glens Flow Law used in this work, with constant rate factor B, is most likely to break down in areas with large temperature variations or large-scale damage in the form of fractures.

In the following chapter, I assess the flow field for Antarctic ice shelves. The ice rheology becomes particularly important in the margins of the shelves where there are high rates of deformation.

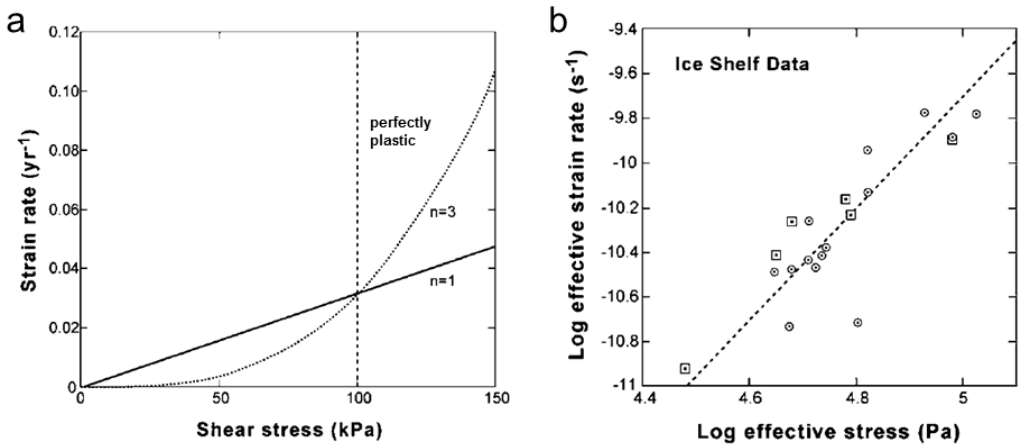

Figure 2.2: Figures adapted from Cuffey and Paterson (2010). (a) Plot of strain rate against shear stress for three rheological models: Newtonian, $n = 1$; shear-thinning, $n = 3$; and perfectly plastic, yield stress 100 kPa. (b) Ice-shelf field data showing strain rate against stress in log-log space. Circles denote data from the Ross Ice Shelf, and squares data from five other shelves. Dashed line represents best fit with slope $n = 2.5$.

Chapter 3

Ice-Surface Velocity Data for Antarctic Ice Shelves

3.1 Introduction

Along many parts of the Antarctic coast, ice shelves form the interface between the continental ice sheet and the ocean. The flow of ice from the interior of the continent towards the coast occurs mainly in fast flowing ice streams, which feed into the floating ice shelves. Understanding the flow of ice within an ice shelf is important in order to determine the scale and spatial distribution of the viscous deformation that is occurring. The viscous deformation of the shelf generates resistance to ice flow and can be transferred back upstream towards the grounded ice. This leads to buttressing from the ice shelf that can act to reduce the rate of ice discharge. In this chapter I use geophysical data, mainly ice-surface velocity data, to investigate the flow dynamics present in Antarctic ice shelves. I concentrate on the large-scale ice dynamics, such as processes that lead to the buttressing of the grounded ice or lead to the advance of the ice front. In addition, I consider the flow dynamics associated with fracturing and crevasse formation.

From analysis of the velocity field for a selection of Antarctic ice shelves, I can develop an understanding of the geophysical system and determine characteristic properties that will be used in later sections of this thesis to develop idealized models. These models will provide further insight into the flow dynamics of an ice shelf. One such property is the geometry of the ice-shelf embayment, and the location and type of pinning points about which buttressing is generated. From the analysis of the velocity data I am able to identify the locations of pinning points that are generating local resistance to flow and thereby may contribute to buttressing. In addition to this, the uniformity of ice rheology and viscosity can be assessed, with the presence of damaged ice and weak-ice zones potentially having significant impact on the flow.

3.2 Ice-surface velocity data

Figure 3.1 shows a map of ice-surface speed for the whole of Antarctica (Rignot et al., 2011a). It is clear that most of the ice on the continent flows slowly, less than 20 m yr^{-1}, with fast flow in the ice streams and ice shelves at the coast reaching speeds of over 1000 m yr^{-1}. This velocity data is collected from satellites using a technique known as Interferometric Synthetic Aperture Radar (InSAR). This method uses radar to identify features within the ice and uses the displacement of these features between repeat satellite passes, and also the displacement of features when observed on different independent satellite paths, in order to determine a surface velocity. The ice velocity is assumed to be parallel to the ice surface (Rignot et al., 2011a). The dataset displayed in Figure 3.1, from Rignot et al. (2011a), gives ice-surface velocity at a 900 m grid resolution for the entire Antarctic continent. For the following analysis I used the updated 450 m grid resolution dataset (Rignot et al., 2011b).

The surface-velocity dataset from Rignot et al. (2011b) is a compilation of data from multiple satellites and was mainly collected between 2007 and 2009, although the complete dataset contains data from 1996 to 2011. In addition to the surface velocity, this data product also contains an estimate of the error associated with the velocity field. There are a number of ways errors can enter the data, which have been accounted for in this error estimation (Rignot et al., 2011b): errors in analysis of displacements; errors from ionospheric perturbations (affecting radar signal from satellite to target and target to satellite); errors from averaging over multiple velocity measurements in each location; errors from weighting of different instruments/satellites in the compilation. A plot of this error can be seen in Figure 3.2. It is clear that the pattern produced by this error plot corresponds to the satellite swath coverage across the continent. For locations in Eastern Antarctica, where there is slow ice-flow, the error in velocity is equivalent to 50-100% of the ice-surface speed, while in the fast-flowing ice streams and ice shelves, the error is of a similar magnitude but amounts to a relative error of less than 10%.

When using this dataset to analyse the flow and dynamics of ice in Antarctica, it is important to bear in mind that this dataset contains data from different instruments collected at different times and has been averaged to provide a continent-wide data product. When assessing this data I will take derivatives of the velocity field in order to identify areas where the flow is changing spatially. Spurious results are likely to be obtained where derivatives are taken across satellite swath patches. (An example of this is given below for the case of Amery Ice Shelf.) I therefore apply a Gaussian low-pass filter to the data in order to remove small-scale noise but retain the large-scale dynamics.

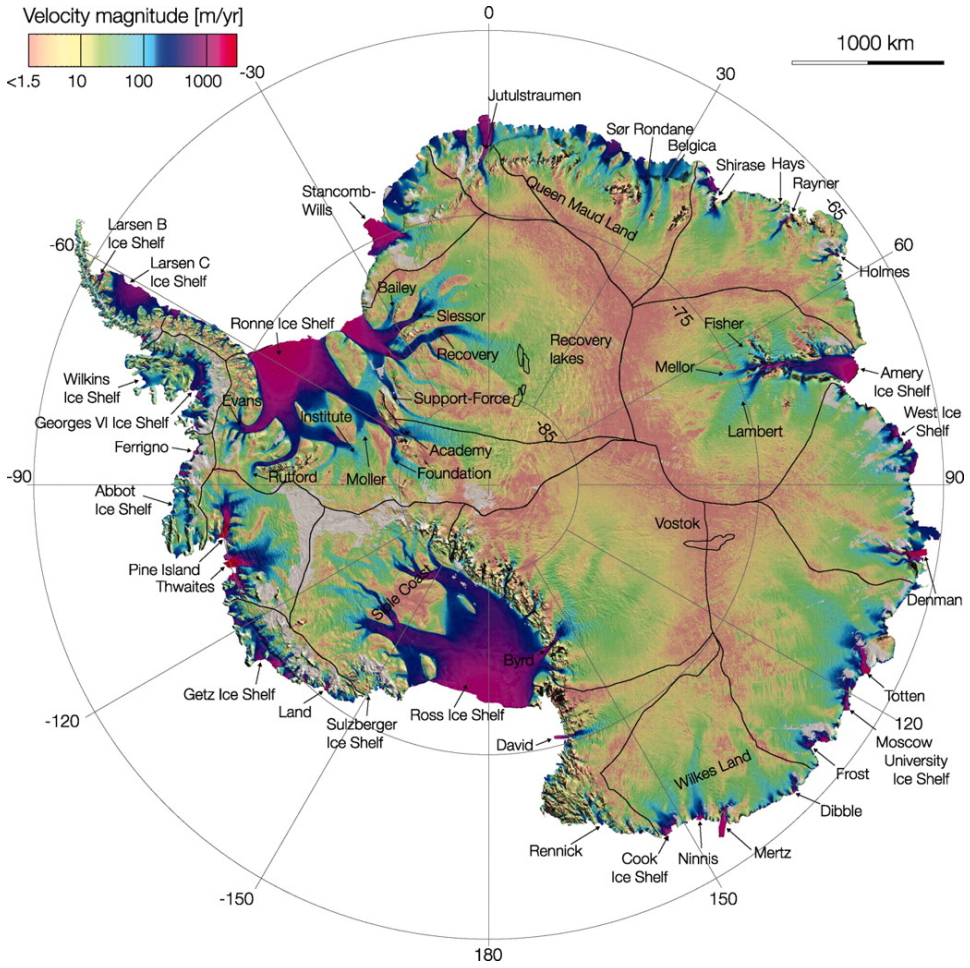

Figure 3.1: Antarctic ice-surface speed, figure taken from Rignot et al. (2011a). Data is complied from multiple datasets of Interferometric Synthetic Aperture Radar (InSAR) data, mostly collected between 2007 and 2009.

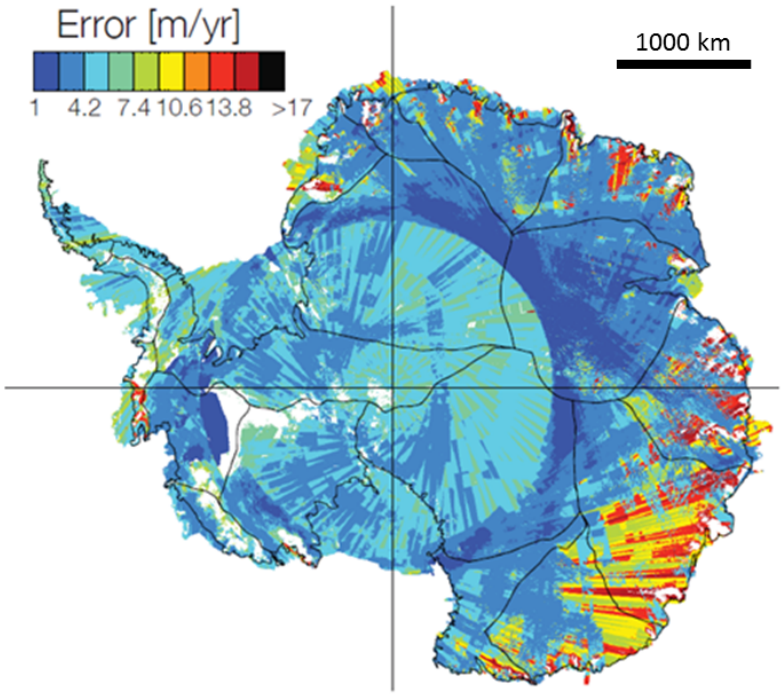

Figure 3.2: Estimated error in Antarctic ice-surface velocity-field. Figure taken from Rignot et al. (2011a).

This ice-surface velocity data with a 450 m grid-resolution is processed using the computer program MATLAB and the low-pass Gaussian filtering is performed using the MATLAB function *imfilter*, with the Gaussian filter option. The suitability of the Gaussian filter and the choice of parameter values is assessed using the flow field from Amery Ice Shelf. Figure 3.3 shows a map of surface speed for the ice shelf (Fig. 3.3a) along with the associated error from the published data (Fig. 3.3b). Here the error in ice-surface velocity is estimated to be approximately 1% of the surface speed.

Amery Ice Shelf has a long and narrow geometry and is located in East Antarctica. In Figure 3.3a, the ice can be seen flowing from inland (left) towards the ocean (right), bounded on either side by slow-flowing ice. The shelf widens as it approaches the ocean and protrudes approximately 50 km out into the ocean at the downstream end. The maximum velocity is found at the centre of the calving front where the ice is flowing at approximately 1.5 km yr^{-1}. From the error plot (Fig. 3.3b) it is clear that there are a number of bands running diagonally across the shelf that may contribute to false values when derivatives are taken.

In a later section of this chapter I will determine the along-flow strain rate for a number of ice shelves. This is a measure of the component of the strain-rate tensor aligned in the direction of ice flow at each grid point, and is given in vector notation as $\hat{\mathbf{u}}.\mathbf{e}.\hat{\mathbf{u}}$. Here

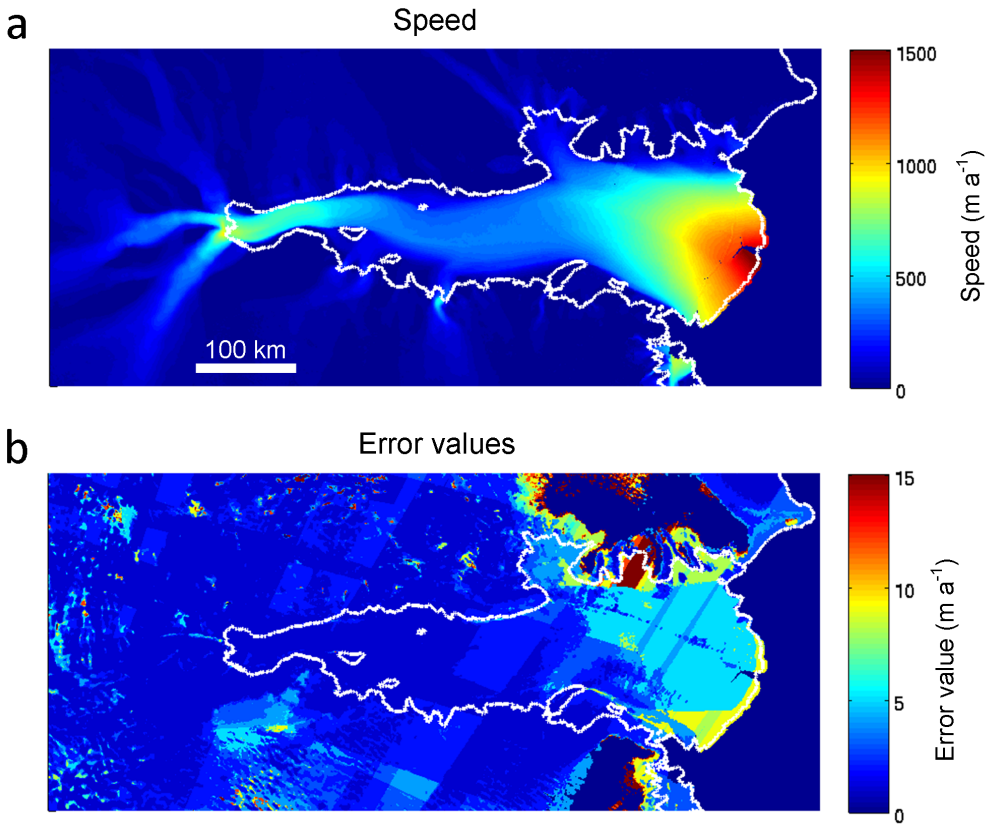

Figure 3.3: Amery Ice Shelf; (a) Ice-surface speed and (b) Estimated error value in ice-surface velocity, taken from Rignot et al. (2011b). Grounding line and boundary with the ocean is indicated by a white line.

$\hat{\mathbf{u}}$ is the unit vector in the flow direction and $\mathbf{e}$ is the horizontal strain-rate tensor,

$$\mathbf{e} = \begin{pmatrix} e_{xx} & e_{xy} \\ e_{xy} & e_{yy} \end{pmatrix} = \begin{pmatrix} \frac{\partial u}{\partial x} & \frac{1}{2}\left(\frac{\partial v}{\partial x} + \frac{\partial u}{\partial y}\right) \\ \frac{1}{2}\left(\frac{\partial v}{\partial x} + \frac{\partial u}{\partial y}\right) & \frac{\partial v}{\partial y} \end{pmatrix}, \tag{3.1}$$

where u is the velocity component in the x-direction and v is the component in the y-direction.

Before calculating this strain rate, a Gaussian low-pass filter is applied to the velocity field data. I tested different values for the filter's range and standard deviation in an effort to obtain the best results. The quality of the results is dependent on removing small-scale noise, whilst retaining the large-scale dynamics that I am interested in assessing. The strain-rate fields for the range of values used in the Gaussian filter are given in Figure 3.4. Here the range of the Gaussian filter is 9 km, 18 km or 36 km, while the standard deviation is 0.9 km, 1.8 km or 3.6 km respectively. The range indicates the size of the filtering area centred on the target cell. (i.e. a range of 9 km corresponds to a 9 km $\times$ 9 km square, with the target cell at the centre.)

The along-flow strain-rate field obtained without using any filtering of the velocity field is shown in Figure 3.4a. Here it is clear that the final third of the channel is an area of mainly positive strain rate, but there are many small-scale strain-rate features throughout the shelf and surrounding ice. It is apparent that there are some coherent high strain-rate features that run linearly across the width of the shelf and are aligned parallel to each other. They have the same orientation as bands that run across the shelf in the error plot, Figure 3.3b. This suggests that these features are artificial and possibly result from the boundaries between satellite swath patches, or the boundaries between areas where multiple datasets have been averaged.

Figure 3.4b gives the along-flow strain-rate field when a low-pass Gaussian filter is applied to the data with a range of 9 km and standard deviation of 0.9 km. In comparison to the non-filtered strain rate there are far fewer small-scale features but the linear features running across the width of the channel are still prominent. There is a clear curve of negative strain-rate at the boundary between the ocean and the ice that traces the ice front. This is an artefact of the low-pass Gaussian filter, which samples the zero ice velocities in the ocean. We have chosen to retain these features rather than masking them so that the effects of the Gaussian filtering can be seen.

The range of the low-pass Gaussian filter and the size of the standard deviation are increased to 18 km and 1.8 km respectively in Figure 3.4c. Here the linear features are

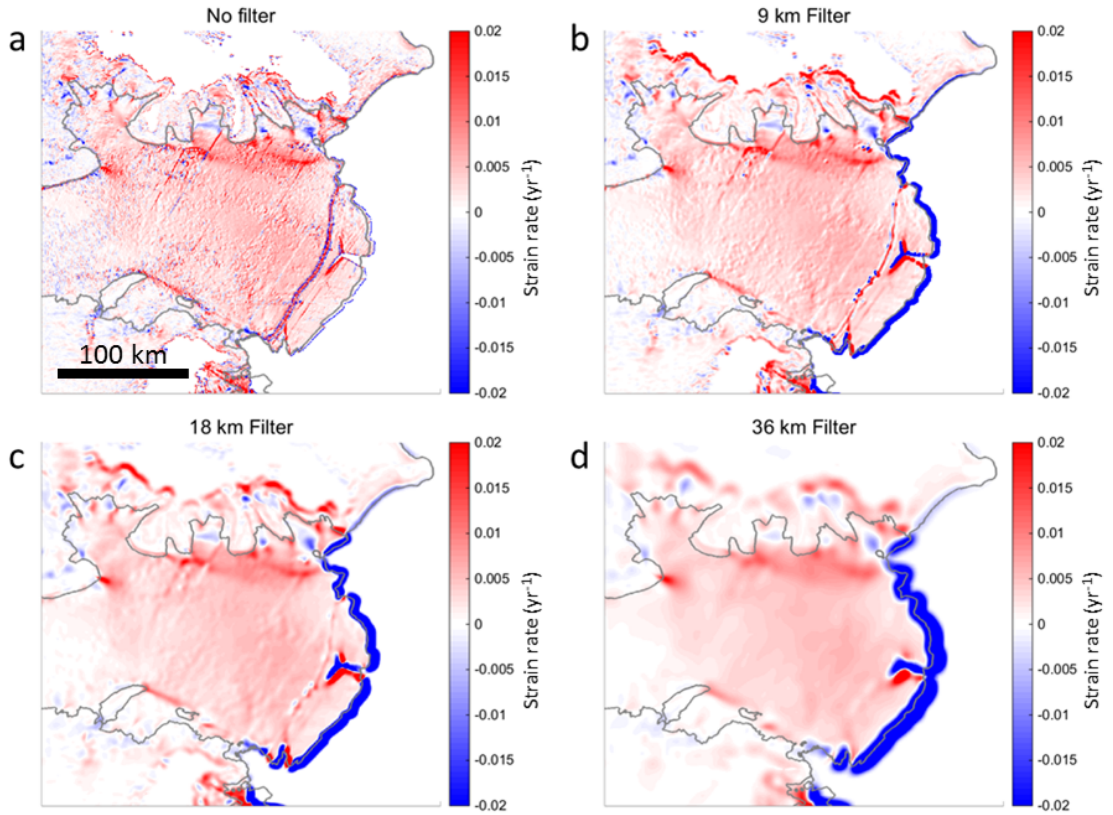

Figure 3.4: Along-flow strain-rate for the final half of Amery Ice Shelf, with different Gaussian filtering variables applied to the velocity field prior to calculating the strain rate. (a) No filtering of the velocity field. (b), (c) and (d) Gaussian low-pass filters applied with ranges of 9 km, 18 km and 36 km and standard deviations of 0.9 km, 1.8 km and 3.6 km respectively. The grounding line and ocean boundary is indicated by grey curve (Haran et al., 2005).

no longer as prominent, but importantly dynamical features are still clearly visible, such as the high positive strain-rate found after the ice flows past an island on the right side of the shelf (facing downstream towards the ocean).

In Figure 3.4d the range of the Gaussian filter has been increased to 36 km and the standard deviation to 3.6 km. Here, there is no clear evidence of features that derive from errors in the velocity field. The field is very similar to the previous filter values (range 18 km and standard deviation 1.8 km) however some (small-scale) features within the shelf have been blurred out.

I therefore chose to use the second set of parameter values (range 18 km and standard deviation 1.8 km) as these provide good smoothing of the data to avoid small-scale noise but retain the larger-scale dynamics.

3.3 Analysing Ice-Shelf Flow Dynamics

I calculate a strain-rate tensor at each point on the grid, which is used to analyse the large-scale flow dynamics. The strain-rate tensor is calculated using a shifted grid, which is aligned halfway between the original grid-points in both horizontal directions (x and y) and is shown in Figure 3.5. The velocity values at the shifted-grid points are determined by averaging across the four surrounding points. It is then possible to calculate a strain-rate tensor at each point in the original grid by taking appropriate derivatives across the grid point. This two-dimensional strain-rate tensor is

$$\mathbf{e} = \begin{pmatrix} e_{xx} & e_{xy} \\ e_{xy} & e_{yy} \end{pmatrix}, \tag{3.2}$$

where

$$e_{xx} = \frac{(u_B - u_A) + (u_C - u_D)}{2\Delta x}, \tag{3.3}$$

$$e_{yy} = \frac{(v_A - v_D) + (v_B - v_C)}{2\Delta x}, \tag{3.4}$$

$$e_{xy} = \frac{1}{2}\left(\frac{(v_B - v_A) + (v_C - v_D)}{2\Delta x} + \frac{(u_A - u_D) + (u_B - u_C)}{2\Delta x}\right). \tag{3.5}$$

Here subscripts correspond to the positions on the shifted grid as shown in Figure 3.5, and Δx denotes the spacing between grid points, which is 450 m for this data set.

This shifted grid provides a further smoothing to the velocity data, and is used to determine a strain-rate tensor that is most representative of the dynamics about the original grid point.

3.3.1 Making comparisons with other geophysical datasets

When analysing the ice-surface velocity data, it is useful to compare features observed in the velocity field with ice-surface features, such as crevasses or fractures. In addition to this, the ice-shelf thickness and thickness gradients are used to assess the features of the flow dynamics as it is the hydrostatic pressure gradient induced by the ice-shelf thickness that induces the flow of the ice shelf.

The visual ice-surface data used to make comparisons with the velocity data from Rignot et al. (2011b) is from the Moderate Resolution Imaging Spectroradiometer (MODIS) and provides visual data at a resolution of 125 m (Haran et al., 2005). The version used here was collected between 2003-2004. This data is used to analyse features that arise on the surface of the ice, and comparisons are made with patterns of flow identified through

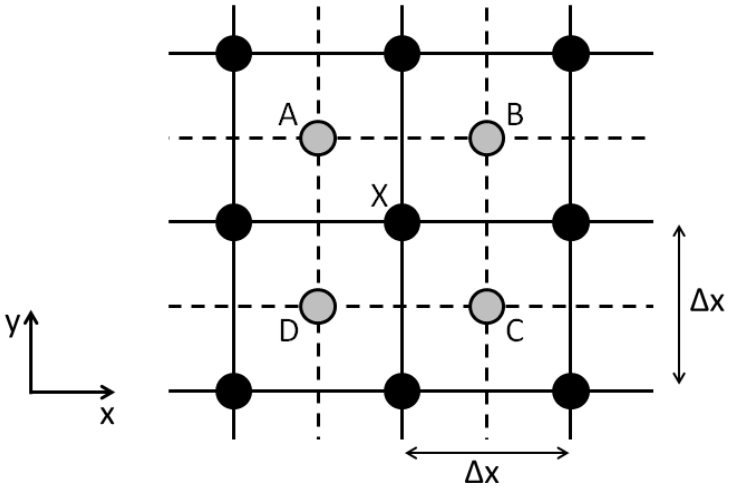

Figure 3.5: Schematic for calculation of strain-rate tensor. Grid and data points for the original 450 m (Δx) velocity dataset are shown as solid lines and points. The shifted grid used to calculate the strain rate at point X is depicted using dashed lines and grey points. Velocities are calculated at points A, B, C and D from the mean of 4 surrounding original data points. The strain rate at X is determined by averaging appropriate velocity differences between points A, B, C and D, as shown in equations (3.3) - (3.5) .

analysis of the ice-surface velocity field in the following sections.

Ice-thickness data is available for Antarctica from the Bedmap2 dataset (Fretwell et al., 2013). This a compilation of all ice-thickness datasets available before 2012 and provides data gridded at a uniform resolution of 1 km over the entire continent. This dataset contains data for ice-surface elevation, ice thickness and subglacial and sea-floor bed elevation. For the floating ice shelves I chose to use the ice-thickness data only. The original Bedmap2 dataset used mainly surface altimetry data to infer an ice-shelf thickness using the hydrostatic approximation, with an approximation made for firn density and thickness (Fretwell et al., 2013). This data was then supplemented by direct radar measurements of ice thickness. This dataset is provided on a 1 km grid. Any direct calculations using the velocity field and ice thickness are performed on the ice-thickness grid, with surface velocities calculated by averaging across the surrounding data points to match to the ice-thickness grid.

These two datasets were not collected at the same time as the velocity field data, but it is expected that these datasets will be representative of the state of the ice shelf and the large-scale flow dynamics. We expect the large-scale processes in this system to evolve slowly and be relatively unchanged over a 10 year period, barring any sudden changes, such as the collapse of the Larsen B Ice Shelf.

However, there are some ice shelves that have undergone substantial change over the past few decades. Pritchard et al. (2012) published an Antarctic-wide dataset detailing the thickness change of ice shelves between 2003 - 2008. Figure 3.6a shows a plot of the rate of thickness change in this time interval. It is clear that throughout the majority of the continent there are only small changes in the thickness of most ice shelves. However, there are considerable thickness changes for the ice shelves in the Amundsen and Bellingshausen Sea areas in Western Antarctica (identified by Fig.3 box in Figure 3.6a and shown in detail in Figure 3.6b), including Pine Island Glacier (PIG) Ice Shelf (-0.53 m yr^{-1} surface height change) and Getz Ice Shelf (-0.18 m yr^{-1} surface height change). Thickness changes for ice shelves in other areas of Antarctica are much less: Amery (-0.06 m yr^{-1} surface height change); Fimbul (0.00 m yr^{-1} surface height change); Ross (0.01 m yr^{-1} surface height change); Ronne (0.02 m yr^{-1} surface height change) (data has a spatially averaged error across Antarctica of 0.007 m yr^{-1}).

These significant changes in ice thickness for PIG are thought to be caused by the increased presence of warm ocean water at the base of the ice shelf, which has induced increased melting (Pritchard et al., 2012; Jacobs et al., 2011; Jenkins et al., 2010). This thinning of the ice shelf is linked to the acceleration and increased ice discharge rate of PIG, due to the decrease in buttressing and retreat of the grounding line (Rignot, 2008; Joughin et al., 2010; Shepherd et al., 2004). The increase in velocity of the ice stream and ice shelf has been documented by Joughin et al. (2003); Rignot (2008); Joughin et al. (2010). Plots demonstrating this can be seen in Figures B.1, B.2 and B.3 in the Appendix.

Despite these rapid and substantial changes for PIG, it can be inferred from the thickness-change data (Pritchard et al., 2012) that, with the exception of a few ice shelves in the Amundsen and Bellingshausen Sea areas, most ice shelves in Antarctica are changing slowly and therefore considering their large-scale flow dynamics to be in steady-state over the period between the datasets used in this work is a valid assumption.

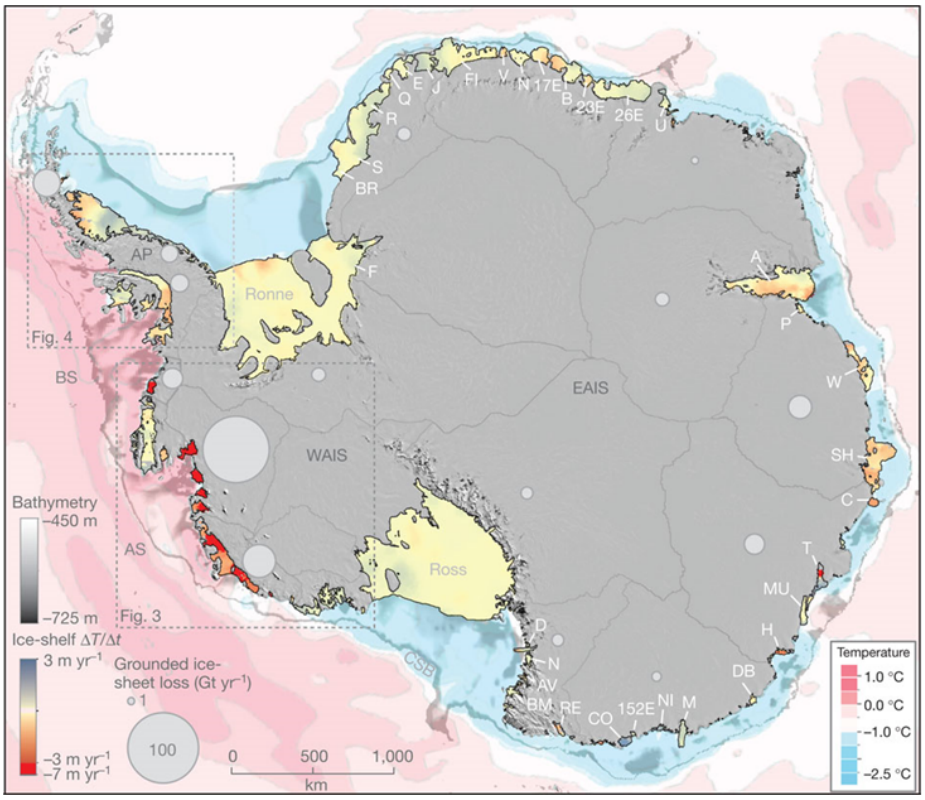

(a)

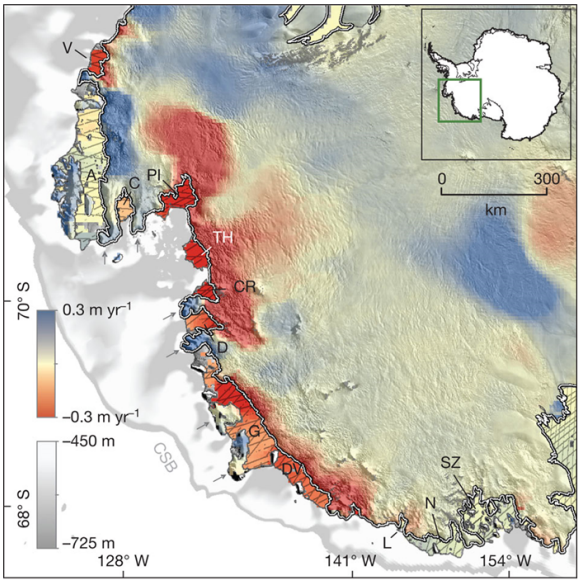

(b)

Figure 3.6: Figures adapted from Pritchard et al. (2012). (a) Rate of Antarctic ice-shelf thickness change 2003 - 2008, with estimated average sea-floor potential temperatures around coast. (b) Surface height change for ice shelves and grounded ice in the Amundsen and Bellingshausen Sea area, 2003 - 2008.

3.4 Divergence

From this two-dimensional surface velocity field it is possible to calculate the divergence of the flow at each point to determine whether the surface flow is diverging or converging. This is determined at each grid point by

$$\nabla.\mathbf{u} = \frac{\partial u}{\partial x} + \frac{\partial v}{\partial y}, \tag{3.6}$$

where ∇ is the horizontal component of the divergence and $\mathbf{u}$ is the horizontal surface velocity field. We expect the flow within the ice shelves to be mainly divergent, with $\nabla.\mathbf{u} > 0$. This is because the ice is stretched out by the hydrostatic pressure gradient, which drives the flow within the ice shelf away from the grounding line. There is also often lateral spreading of the ice as it flows out from a narrow ice stream into a wider ice shelf. However, there may be some areas where the flow is converging with $\nabla.\mathbf{u} < 0$, such as upstream of pinning points, where the ice is being compressed against a stationary region of ice, or in areas where there are high shear rates. The effects of basal processes such as melting and freeze-on may also affect the ice flow, so we should bear this in mind when analysing the divergence fields. These basal processes will be investigated further in the following section.

3.4.1 Divergence field for Antarctic Ice Shelves

The ice-surface velocity divergence for Amery Ice Shelf can be seen in Figure 3.7a. Here convergence of the flow is observed in the narrow upstream section of the shelf, where there are high shear values and the potential for submarine melting of the thick ice shelf near the grounding line ($\sim$1500 m). However, as the shelf moves downstream and the channel becomes wider there is a transition to divergence, with the final 100 km of the shelf having strong divergence. This is due to the spreading of the ice shelf in the along-flow and lateral directions.

The divergence field for Getz Ice Shelf can be seen in Figure 3.7b. The upstream section of the shelf is an area of mainly convergent flow, where there are several large islands restricting the flow of ice. As the ice reaches the calving front the flow-field is divergent, with the greatest divergence found at the centre of the calving front.

For Larsen C and Fimbul Ice Shelves, Figures 3.7c and 3.7d, there are mainly divergent flow fields. This may be because these ice shelves flow in relatively wide embayments and can therefore spread both laterally and along-flow. In the case of Fimbul Ice Shelf, there

are two areas of convergence on either side of the main inflow as ice flows into the main section of the ice shelf. This may be because the ice is slowing and being compressed as it meets more slow flowing ice in the shelf.

Figure 3.8 gives the ice-surface velocity divergence for Pine Island Glacier (PIG) Ice Shelf. Here values of convergence and divergence are large relative to the values observed in the other shelves shown here (Figs. 3.7 & 3.9), with a 2.5 - 5 fold increase in magnitude. For PIG ice shelf there is large divergence at the grounding line and divergent flow throughout the majority of the shelf. There are some locations in both margins where the flow is convergent, suggesting there is resistance to flow in these regions from the stationary ice in the margins. However, PIG has been identified as a region where rapid change is occurring, with high levels of melting and thinning of the shelf and acceleration of the flow, as identified by Pritchard et al. (2012) (melting and thinning) and Rignot (2008); Joughin et al. (2010) (acceleration).

For both the Ronne and Ross Ice Shelves, as shown in Figure 3.9, there is mainly divergent flow throughout the shelf. This divergence is particularly prominent downstream of ice rises and islands. There are also prominent linear high-divergence features, which are identified in the following section and are associated with fractures. Here the presence of fractures may lead to the weakening of the ice, and in turn it can be deformed more readily. Where Byrd Glacier meets the Ross Ice Shelf there is high divergence in the trunk of the inflow area, followed by convergence in the margins as it meets the slower flowing ice in the shelf and is compressed in the horizontal plane.

The patterns of divergence and convergence here may be the result of the flow dynamics within the shelf, but they may also be strongly influenced by the interaction between the ice-shelf base and the ocean, where there may be melting of the ice shelf, thereby reducing its thickness. Alternatively, the thickness may be increased when ocean water freezes to the ice-shelf base or there is surface accumulation from snow fall. We investigate this in the following section.

3.4.2 Detecting the net accumulation and ablation of ice shelves

If we assume a steady-state thickness for an ice shelf, it is possible to infer the net rate of surface (accumulation/melt) and basal (melt/freeze-on) processes. We use the steady-state version of the continuity equation with a net accumulation/ablation term to do this. The general continuity equation is

$$\frac{\partial H}{\partial t} + \nabla.\,(H\mathbf{u}) = a, \tag{3.7}$$

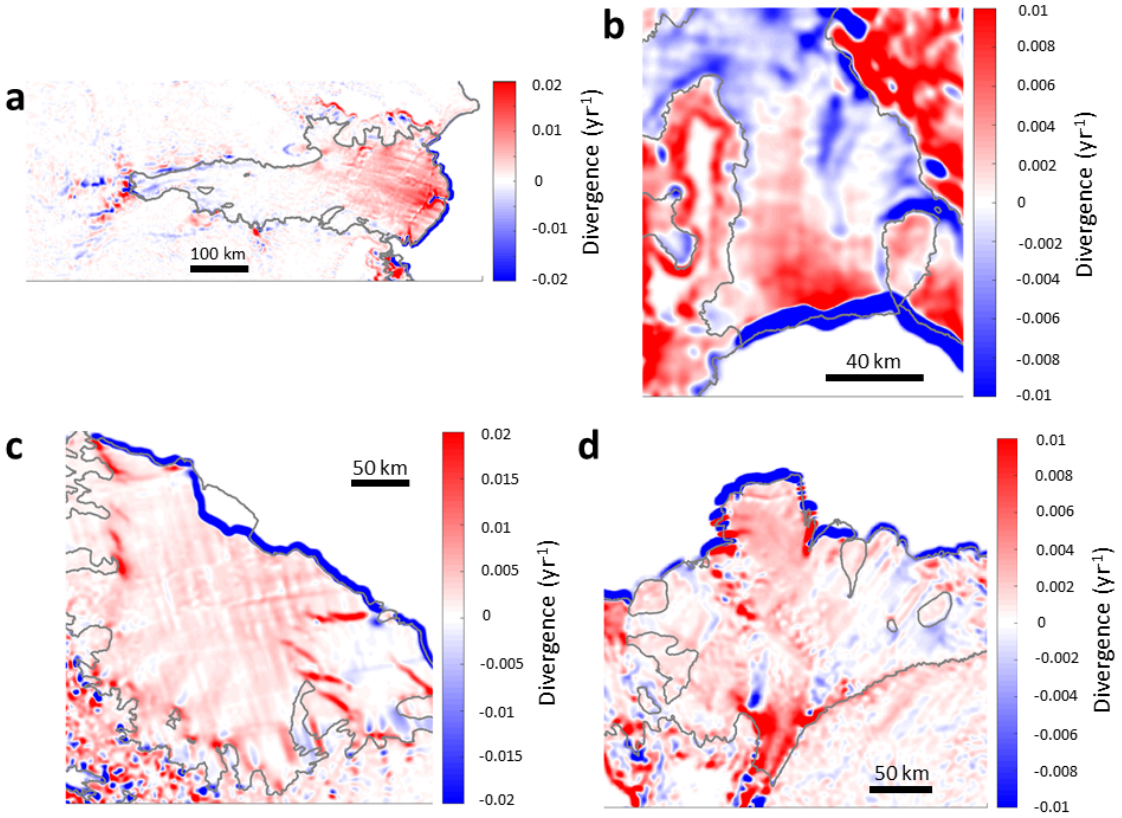

Figure 3.7: Maps of ice-surface velocity divergence for; (a) Amery, (b) Getz, (c) Larsen C and (d) Fimbul Ice Shelves.

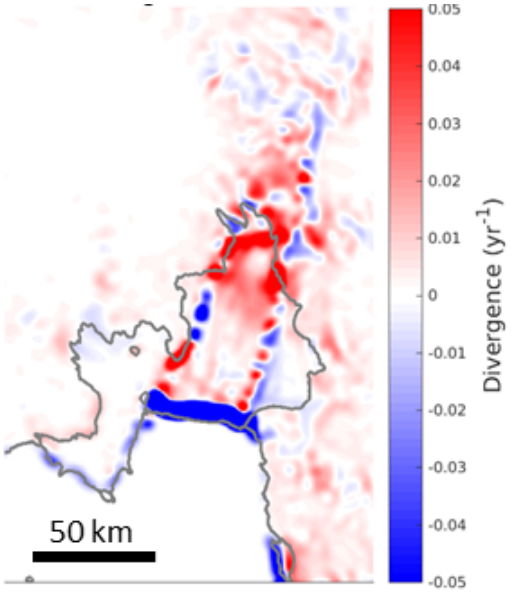

Figure 3.8: Map of ice-surface velocity divergence for Pine Island Glacier Ice Shelf.

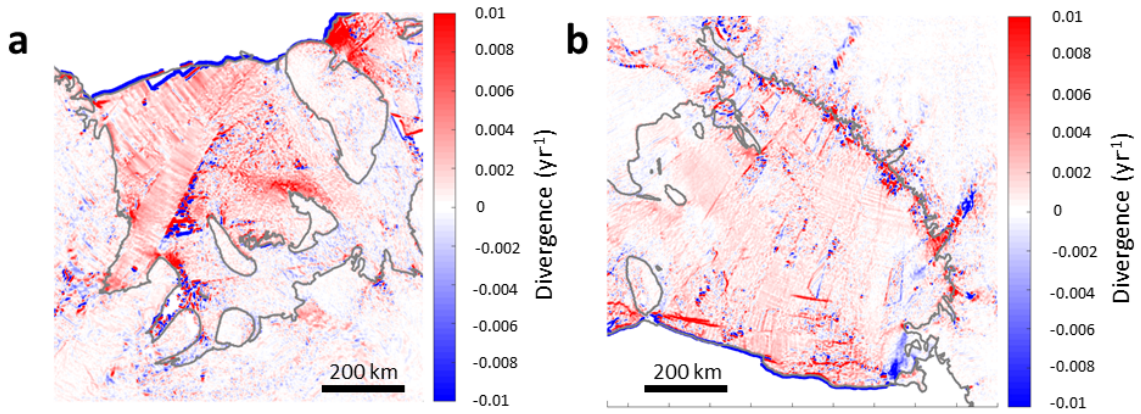

Figure 3.9: Maps of ice-surface velocity divergence for; (a) Ronne and (b) Ross Ice Shelves

so in steady state we set $\partial H/\partial t = 0$ and have

$$(\nabla H)\,.\mathbf{u} + H\,(\nabla.\mathbf{u}) = a, \tag{3.8}$$

where, H is the ice-shelf thickness, $\mathbf{u}$ is the ice-flow velocity and a the net accumulation/ablation. Negative a represents net ablation (melting), while positive a is indicative of net accumulation (marine-ice forming on the ice-shelf base or surface accumulation of snow). In the examples below, the ice thickness is taken from the Bedmap2 dataset (Fretwell et al., 2013), while the velocity field is determined from the Rignot et al. (2011b) dataset, but interpolated to the Bedmap2 grid. We have made the assumption that the system is in steady state. However, there are likely to be some transient dynamics resulting from inter-annual and seasonal variation, and occasional events such as large iceberg calving. In addition, these datasets were not collected during the same time period. Here we have assumed a steady-state ice thickness between datasets, however some small improvements could be made if we used measured thickness changes such as those from Pritchard et al. (2012). Therefore, we can only expect to detect large-scale and persistent net accumulation/ablation patterns at points in the shelf, which are descriptive of the parameter a. The resolution of the dataset is also quite coarse, so small-scale features such as incised basal melt channels will be hard to detect. Instead this analysis is most relevant for broad-scale features that may effect the large-scale flow of the shelves.

Geophysical Examples

The inferred net accumulation/ablation pattern for Amery Ice Shelf can be seen in Figure 3.10a. Here it is clear that there is a large amount of small-scale noise within the data,

possibly arising from the coarse spatial resolution of the data and the fact that the ice-thickness dataset and the ice-surface velocity dataset were not collected simultaneously. However, on the large scale, there appears to be prominent ablation in the upstream section of the shelf, within approximately 100 km of the grounding line, exceeding 5 m yr^{-1}. This is most likely because of basal melt, as the shelf is very thick in this region (+1000 m) and exposed to relatively warm water at depth. Conversely at the downstream end of the channel, there is net accumulation covering an area from the left (west) margin of the shelf, where there is inflow from the Charybdis Glacier, diagonally across the shelf towards the calving front. Here the rate of accumulation is approximately 2.5 m yr^{-1}. Both these values of net accumulation/ablation, as well as the approximate size and location of the areas, agree well with the findings of independent studies focused on the basal processes (melting and freeze-on) for Amery Ice Shelf; Rignot et al. (2013) using data, and Wen et al. (2010) using modeling results. Plots from both of these papers can be found in the Appendix (Figures B.4 andB.5).

This pattern of basal melting upstream, where the shelf is thick, and freeze-on downstream, where the shelf is thinner, can partially be explained by the ice-pump mechanism, as proposed by Robin (1979). Here melt of the ice shelf occurs at depth, where the melting temperature is reduced due to the increase in pressure with depth. This melting produces 'ice-shelf water' (ISW) that is fresh and buoyant relative to the surrounding ocean water so rises along the sloping ice-shelf base. As the cold ISW rises the freezing temperature is reduced and this cold water freezes, producing salty and dense 'High Salinity Shelf Water' (HSSW) in the process. The newly formed ice can then collect on the base of the ice shelf, while the HSSW sinks and initiates further melting at depth.

Figure 3.10b shows the inferred net accumulation/ablation for Getz Ice Shelf. Here, net ablation is observed in the upstream sections and the highest ablation values are found at the grounding line. Accumulation is seen in the more downstream locations. The pattern observed here is very similar to that observed for the flow-divergence field (Fig. 3.7b), suggesting that the flow dynamics of this shelf are strongly influenced by the basal and surface processes that affect the shelf thickness.

For Larsen C Ice Shelf (Fig. 3.10c) there appear to be low levels of net accumulation across the majority of the shelf. However, over the central section of the shelf the mean rate of accumulation is 0.5 m yr^{-1}, with a standard deviation of 1 m yr^{-1}, suggesting that this apparent result may stem from high levels of noise, rather than a true accumulation signal. Large values of net accumulation and ablation are found at the northern and southern margins of the shelf, which correspond to heavily fractured areas. This suggests that there are alternating bands of melt and freezing. However, it is most likely

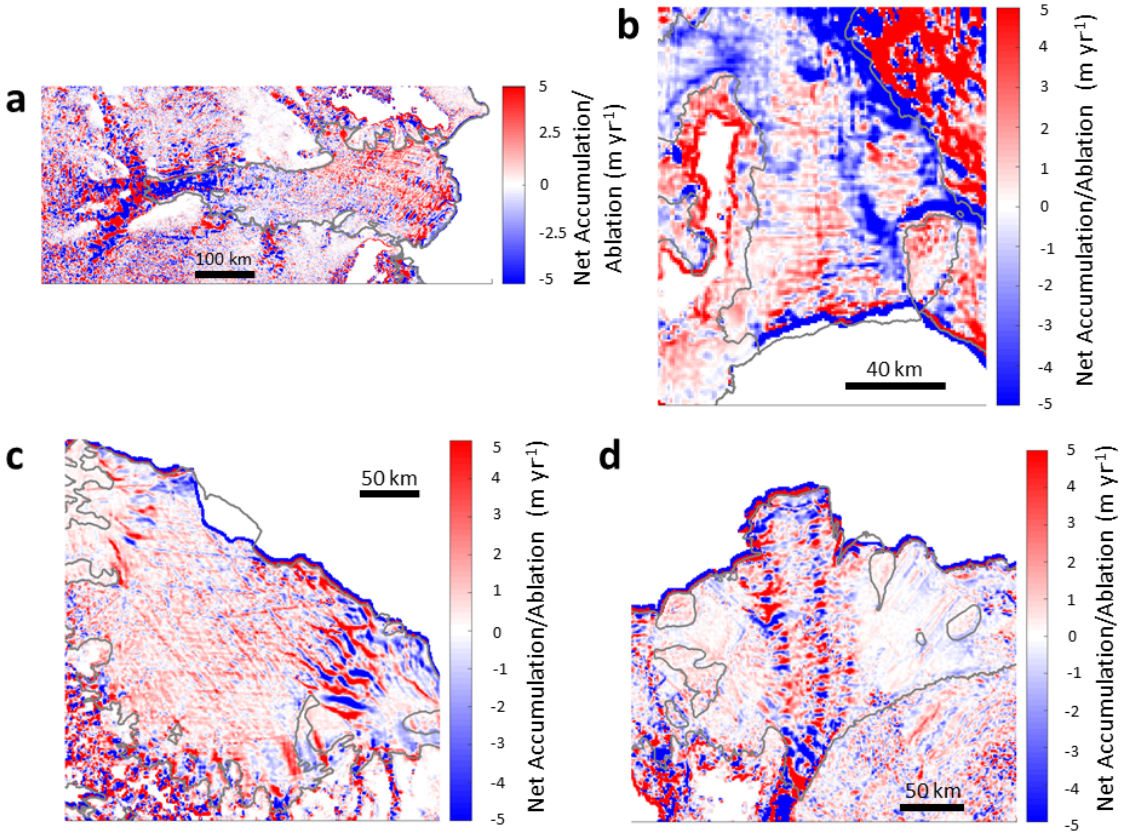

Figure 3.10: Maps of inferred net accumulation/ablation for; (a) Amery, (b) Getz, (c) Larsen C and (d) Fimbul Ice Shelves.

that this is due to errors from using two datasets, which poorly sample the area and are not concurrent. This is especially important in these fractured areas where there are rapidly changing ice thicknesses and flow speeds, both spatial and temporally.

From Figure 3.10d, the inferred net accumulation/ablation for Fimbul Ice Shelf, there appears to be no coherent signal. An exception to this may be near the grounding line where the fast and concentrated ice-flow enters the larger shelf; here there is possibly some melting of the ice-shelf base. When comparisons are made with the divergence field, Figure 3.7d, there are very few similar patterns between the plots, suggesting that the divergence field is a result of the ice-flow and is not impacted greatly by the effects of melting or freeze-on/surface accumulation.

In contrast to the lack of coherence between the net accumulation/ablation field and divergence field for Fimbul Ice Shelf, clear comparisons can be made between the net accumulation/ablation inferred for PIG Ice Shelf (Fig. 3.11) and the divergence field (Fig. 3.8). In Figure 3.11 high ablation rates are observed at the grounding line of PIG, where values exceed 30 m yr^{-1}, with high values also found across the rest of the shelf. However, PIG is experiencing rapid change as highlighted earlier and hence the

steady-state assumption is not appropriate for this location.

Figure 3.12a, presents the inferred net accumulation/ablation for Ronne Ice Shelf. Net ablation is observed at the grounding line where the tributary ice streams (Evans and Rutford particularly) flow out into the shelf. High levels of ablation, most probably basal melting, are also found across the calving front and approximately 50 km back, peaking to the east of the calving-front centre where net ablation reaches approximately 5 m yr^{-1}. These results agree well with the observational results of melting and freeze-on from Joughin and Padman (2003) and Rignot et al. (2013) (Figures B.4 and B.6 in Appendix). While ablation is prominent in those regions, there is an area in the centre of the shelf where there is inferred accumulation (basal freeze-on), downstream of the Henry Ice Rise and at the confluence of the inflow from the Evans and Rutford Ice Streams. Again these regions are also identified in the previous work of Joughin and Padman (2003) and Rignot et al. (2013) as freeze-on areas. However, our analysis does not identify clearly the lower values of accumulation around these locations as detected previously. (The previous work was focused on detecting melting and freezing patterns rather than their impact on flow dynamics, which is our focus.) When compared with the flow-divergence field in Figure 3.9a, we see that the flow is divergent throughout the majority of the shelf, while there are spatial transitions between areas of net accumulation and ablation. Therefore, it is clear that the flow of the ice shelf is not dominated by the processes at the surface or base. As with Amery Ice Shelf, the distribution of melt and freeze-on beneath Ronne Ice Shelf may be a consequence of the ice-pump mechanism.

For the inferred net accumulation/ablation of the Ross Ice Shelf (Fig. 3.12b), there are few areas with large values. At the eastern end of the calving front there is a region of ablation, which coincides with convergent flow, as seen in Figure 3.9b. This suggests that the basal melting of the shelf in this area leads to the formation of a thin section of ice, which induces a hydrostatic pressure gradient and thereby ice flow into this region.

3.4.3 Summary: Flow Divergence and Ice-Shelf Net Accumulation/Ablation

In the first half of this section the divergence of the ice-flow field was analysed, identifying regions of convergence and divergence. It was observed that for many ice shelves divergence was present at the grounding line, where a narrow ice stream fed into a wider shelf. Divergence was also present at the downstream end of the shelf, where the ice nears the calving front. Here there is a reduction in the lateral resistance from pinning

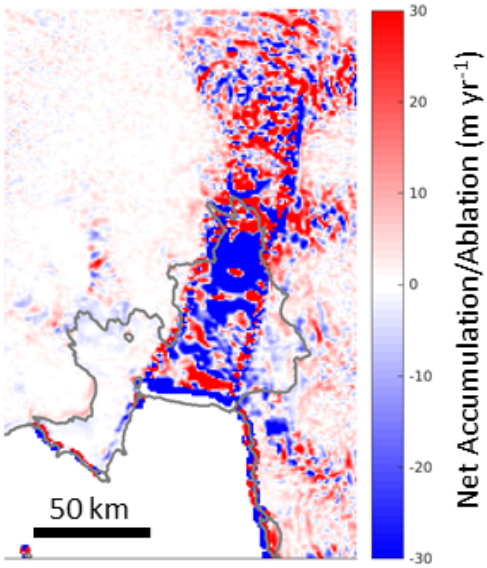

Figure 3.11: Map of inferred net accumulation/ablation for Pine Island Glacier Ice Shelf.

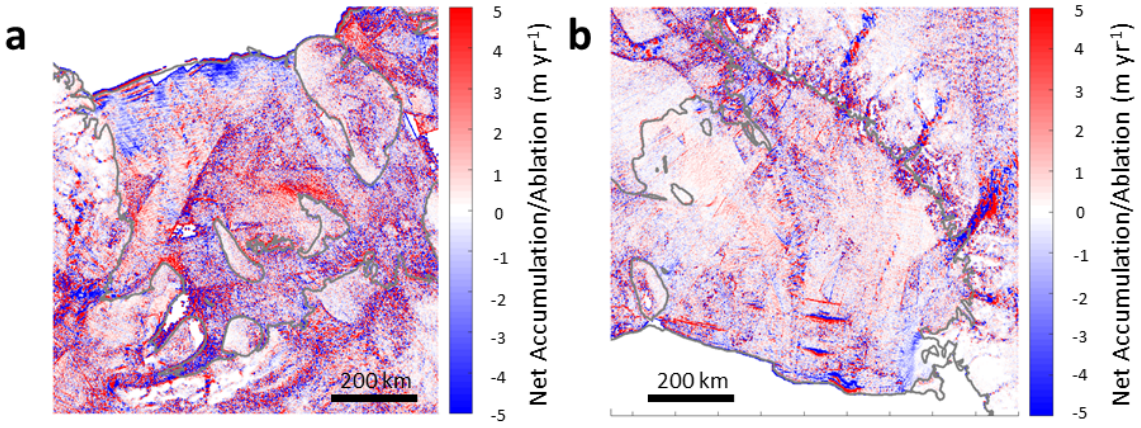

Figure 3.12: Maps of inferred net accumulation/ablation for; (a) Ronne and (b) Ross Ice Shelves (label Evans and Rutford, and Henry Ice Rise)

points and the shelf begins to spread both laterally and in the along-flow direction.

These patterns of divergence and convergence may result from the flow of the ice shelf interacting with the changing geometry of an embayment or the resistance from pinning points. However, these dynamics can also be induced by melting and freeze-on/accumulation at the ice shelf surface or base, which acts to thin or thicken the shelf and produces a gradient in hydrostatic pressure. Using the steady-state continuity equation, this net accumulation/ablation could be inferred. In all cases considered here, melting of the ice shelf was identified at the grounding line. This melting at the grounding line is due to the reduction of the melting temperature of ice with depth. For some of the shelves, such as Amery and Ronne, freeze-on of marine ice was observed midway along the shelf, this is most likely due to the ice-pump mechanism. The extent of melting and freeze-on varies between shelves as each is affected by different oceanographic forcing, which will depend on: location; ocean currents;/ sea-floor bathymetry; sub-glacial melt and run-off; grounding line depth; basal slope of the shelf and the spatial extent of the shelf.

Using the Bedmap2 ice thickness dataset (Fretwell et al., 2013) and the velocity field from Rignot et al. (2011b), we have been able to infer the same large-scale basal processes as those in more targeted studies on large ice shelves (Amery and Ronne ice shelves (Rignot et al., 2013; Wen et al., 2010; Joughin and Padman, 2003)). This suggests that this technique provides valid information about the broad-scale thinning (melting) and thickening (freeze-on/accumulation) processes.

By making comparisons between the ice-surface flow divergence and the inferred net accumulation/ablation, it is possible to determine those shelves with flow dynamics affected by these processes. For example the low values of convergence in the upstream section of Amery Ice Shelf correspond to melting of the ice shelf base, in an area where the shelf should be accelerating and diverging into a widening channel, with reduced resistance. Getz Ice Shelf appears to be strongly influenced by sub-ice-shelf processes, with the divergence field and net accumulation/ablation field having similar structure. However, it is also clear that in some cases the flow-dynamics within the shelf are not strongly influenced by accumulation/ablation processes, for example Fimbul, Ross and Ronne Ice Shelves.

3.5 Strain Rate and Shear Rate

3.5.1 Strain Rate in Direction of Flow

The rate of extension or compression in the along-flow direction inferred from the surface velocity is given by

$$f_1 = \hat{\mathbf{u}}.\mathbf{e}.\hat{\mathbf{u}}. \tag{3.9}$$

This measure of deformation aligned in the direction of ice flow is particularly relevant near the calving front of ice shelves, where the flow is often aligned perpendicular to the ice front. Therefore, this strain rate may be descriptive of the extension of the ice in this region and the possible advance of the calving front position. Alternatively, high strain rates may lead to the formation of fractures or crevasses. This is a significant process throughout the entire shelf, but very important near the calving front where it may be a strong control on the formation of icebergs.

Further upstream towards the grounding line, the flow is often aligned perpendicular to the grounding line position. Therefore the value of the strain rate in the flow direction will be informative of the buttressing from the ice shelf, which is transferred across the grounding line to the grounded ice.

3.5.2 Shear Rate Transverse to Flow

As the ice shelf flows towards the ocean it deforms as it flows past stationary or slow flowing ice in the shelf margins or near pinning points. A measure of this type of deformation can be determined using the shear-rate transverse to the flow direction, which is defined as

$$f_2 = \hat{\mathbf{n}}.\mathbf{e}.\hat{\mathbf{u}}, \tag{3.10}$$

where $\hat{\mathbf{n}}$ is the unit vector perpendicular to the flow direction. This lateral shearing is important in the ice-shelf margins and may be informative about damaged areas of ice, or the temperature dependent viscosity. The resistance to flow generated by viscous deformation of the ice as it is sheared past side walls and pinning points acts to buttress the grounded ice and is therefore important for ice-discharge rates.

Within some of the larger ice shelves there are multiple areas of faster flow, which are fed by multiple ice streams. These sections of ice from different sources meet within the ice shelf and merge to flow towards the calving front. The dynamics at this confluence and the associated deformation can be identified by assessing the transverse-shear rate.

3.5.3 Geophysical Examples: Strain Rate in Flow-Direction and Shear Rate Transverse-to-Flow

Using the strain rate in the direction of flow and the absolute value of the transverse-shear rate, I investigate the flow dynamics present in Antarctic ice shelves.

Amery Ice Shelf

The strain rate in the flow direction can be seen for the case of Amery Ice Shelf in Figure 3.13c. Here there is positive strain rate in the tributary ice streams before the ice crosses the grounding line at the southern end of the shelf. Once the ice flows over the grounding line and begins to float, the strain-rate value becomes negative. In this narrow section of the channel, there is resistance to flow from the channel side-walls and the channel diverges slowly, which may act to slow the flow as the ice spreads laterally to fill the channel and is resisted by stationary ice in the margins. This is an area where there is known to be high levels of melting at the base of the ice shelf (as seen in the previous section and the work of Rignot et al. (2013) and Wen et al. (2010)). This may act to alter the dynamics and reduce the driving hydrostatic pressure gradient.

As the channel begins to widen, about 150 km from the grounding line, there are two islands located in the margins of the shelf on either side of the channel. Upstream of these islands there are prominent negative strain-rate features corresponding to the compression of the ice as it approaches these stationary pinning-points. Downstream of these points there is a positive strain-rate region, where the ice accelerates after passing these stationary ice areas.

Once the shelf widens there is low strain rate in the middle section of the shelf, which may be a consequence of the reduced resistance from side walls in this wider section of the channel. In the final third of the channel the shelf accelerates towards the exit, which is represented by the large area of positive strain rate. This may be a result of the shelf widening as it approaches the channel exit and also the absence of strong buttressing downstream as the shelf leaves the confinement of the channel. In addition to these processes, there is also an extra inflow in this final third from the Charybis Glacier on the western side of the main shelf. This addition of ice may help to accelerate the flow.

Figure 3.13d shows the absolute transverse shear-rate field for Amery Ice Shelf. It is clear that the most prominent shear rates are found in the upstream section of the shelf, where there is fast flow confined within a narrow channel. The shear rate decays as the shelf flows downstream. For the remainder of the shelf the shear rates are low, with slightly larger values found in the shelf margins as expected. Greater shear-rate values

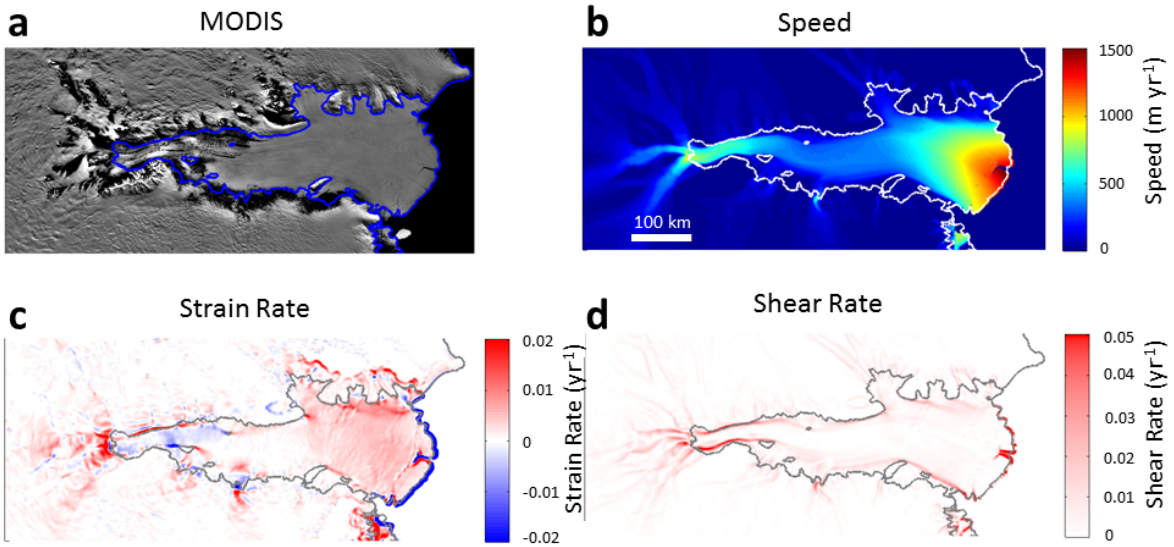

Figure 3.13: MODIS image (a), speed map (b), strain rate in direction of flow (c) and absolute shear-rate transverse to flow (d) for Amery Ice Shelf.

are found on the eastern (lower) margin of the shelf near the channel exit. This corresponds to a heavily crevassed region (that is analysed more closely in the following section (3.6)) and visible in the MODIS imagery. This suggests that the crevassing in this region has weakened the ice allowing the ice to deform more easily and large shear rates to be achieved.

Fimbul Ice Shelf

The strain rate in the flow direction for Fimbul Ice Shelf is plotted in Figure 3.14c. For the main section of the flow, which can be identified in the speed map (Fig. 3.14b), there are low strain rates with a small negative strain-rate signal after the ice crosses the grounding line and begins to spread into the much wider shelf. In both margins of the main flow the strain rates are high. This is especially so in the left (west) margin where the high strain rates correspond to the presence of crevasses and fractures as shown in the MODIS image (Fig. 3.14a). These types of feature are less visible in the right (east) margin where there are slightly lower strain rates. In the right (east) margin there is evidence of compression upstream of the island located near the ice front. This gives a clear demonstration of how pinning points act to modify the flow.

The transverse shear-rate can be seen in Figure 3.14d. Here the margins of the main section of the flow are highlighted by high shear rates. In particular, there are especially high shear rates in the upstream section of the shelf where the ice crosses the grounding line and leaves the initial confinement. These high shear rates suggest that the ice is damaged or severely deformed in this area. As these bands of ice, which have experi-

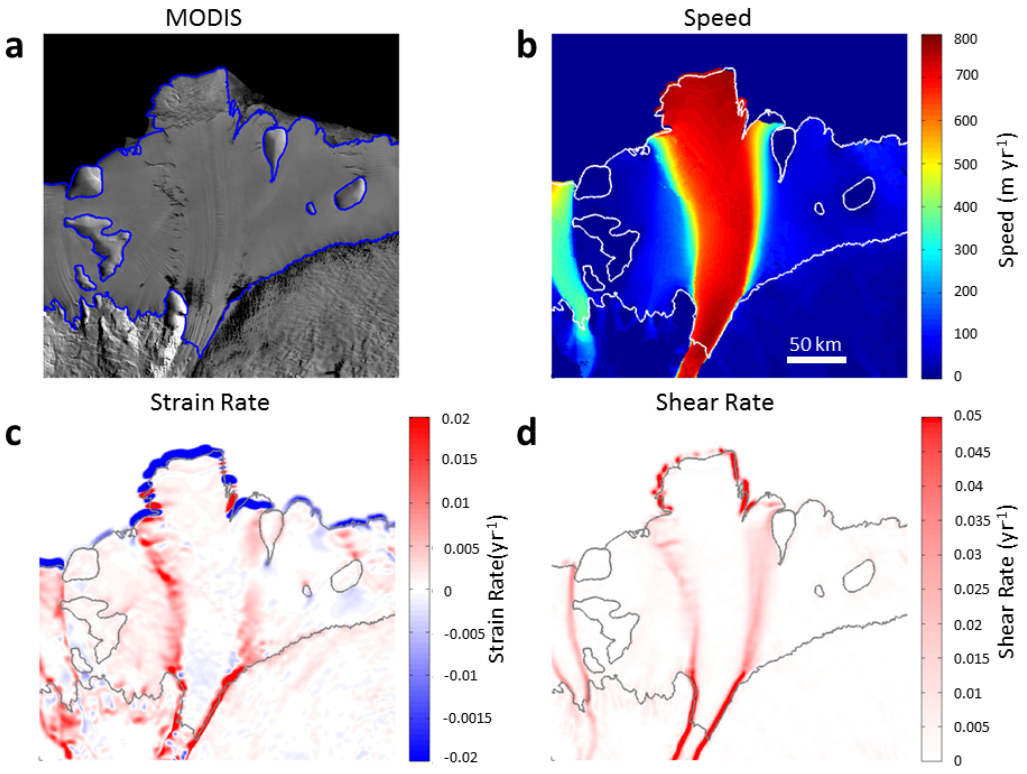

Figure 3.14: MODIS image (a), speed map (b), strain rate in direction of flow (c) and absolute shear-rate transverse to flow (d) for Fimbul Ice Shelf.

enced high shear rates, are advected into the shelf, the high levels of damage may allow the high shear and strain rates to be attained in the margins of the main flow and aid the formation of crevasses in the margins.

Getz Ice Shelf

The Getz Ice Shelf is approximately 60 km wide at the calving front and is fed by two ice streams. The surface flow speed of these ice streams and the ice shelf can be seen in Figure 3.15b. The shelf is mainly an area of positive strain rate as can be seen in Figure 3.15c. There is an area of negative along-flow strain rates in the upstream section of the shelf and upstream of an island located on the right (west) of the shelf. Here the ice is being compressed against pinning points. We see that there are negative along-flow strain rates as the ice crosses the grounding line. This suggests that this ice is providing buttressing to the grounded ice. The along-flow strain rate increases in the along-flow direction with a peak in strain rate seen at the centre of the calving front.

The transverse shear-rate plot identifies the margins of the main flow (Fig. 3.15d), as well as the boundary between the input from the two ice streams. In comparison to the shear rates achieved on Fimbul Ice Shelf, the shear rates for Getz are relatively low

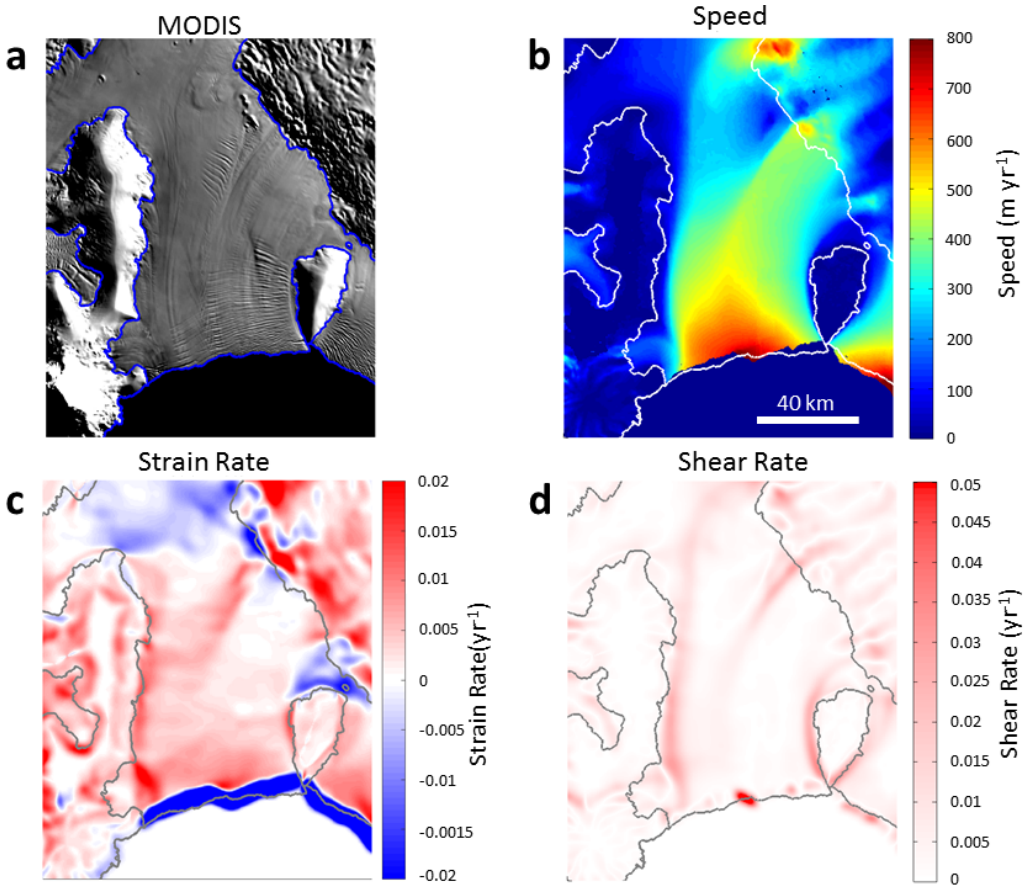

Figure 3.15: MODIS image (a), speed map (b), strain rate in direction of flow (c) and absolute shear-rate transverse to flow (d) for Getz Ice Shelf.

and uniformly distributed along the margins, suggesting there is little damage to the ice, which may therefore be able to provide considerable resistance to the flow upstream.

Larsen C Ice Shelf

For the Larsen C Ice Shelf the location of fractures in the ice shelf correspond well to areas where high along-flow strain rates are found. For example, towards the southern edge of the shelf there is an island (Gipps Ice Rise) that forms a pinning point on the calving front of the ice shelf. From this island running towards the centre of the ice shelf there is a large fracture that can be seen in the MODIS image in Figure 3.16a. A feature of this size and orientation is also seen in the along-flow strain-rate field, suggesting that high strain rates in this area have led to the formation of the fractures, or that the damaged ice has allowed high strain rates to be achieved. Features of this kind are also present along the northern boundary of the shelf, where there are several ridges of grounded ice that protrude from the mainland into the shelf. Here there are a number of large fractures, which correspond with high strain-rate areas.

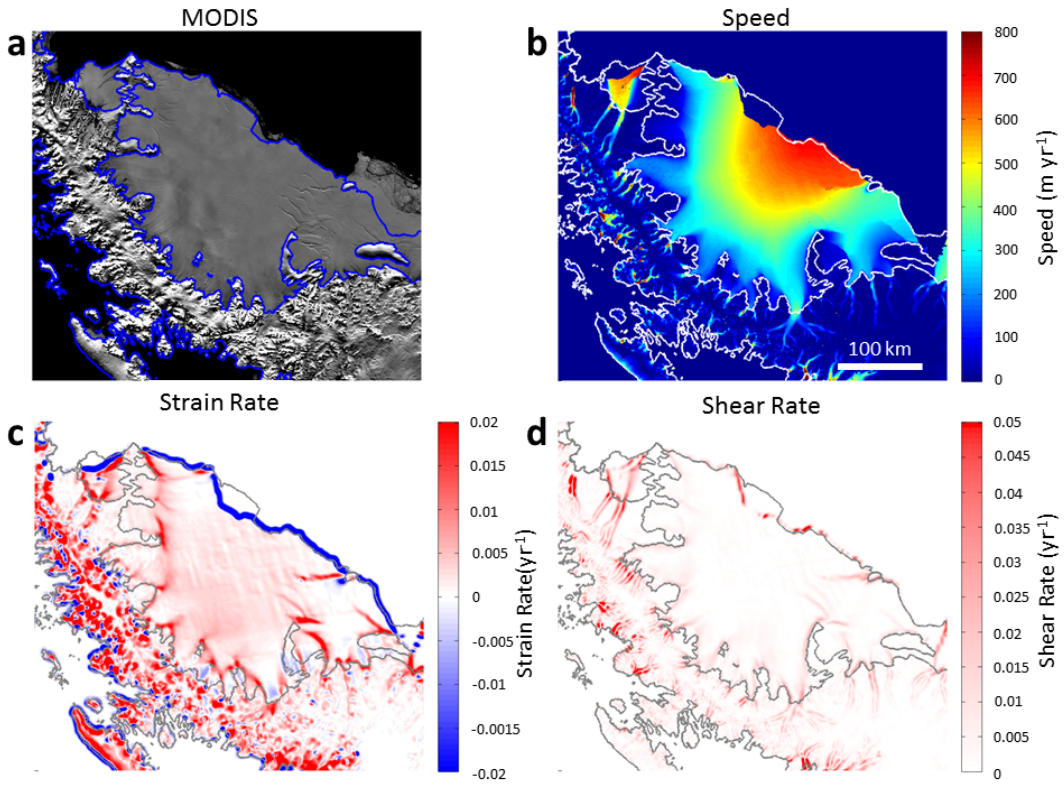

Figure 3.16: MODIS image (a), speed map (b), strain rate in direction of flow (c) and absolute shear-rate transverse to flow (d) for Larsen C Ice Shelf.

PIG Ice Shelf

The Pine Island Glacier (PIG) area is dominated by high along-flow strain rate. This can be seen in Figure 3.17c, where there is high strain rate both in the grounded ice stream and in the margins of the shelf. While the ice is grounded, high strain rates are found across the entire width of the ice stream, with particularly high along-flow strain rates at the grounding line. However, once the ice begins to float, these high strain rates are restricted to the margins of the shelf. This indicates that the flow in the grounded section is accelerating towards the coast, while there is relatively little extensional flow in the floating shelf.

The margins of both the grounded and floating sections of the ice flow are areas of high shear rates, which can be seen in Figure 3.17d. Here high strain and shear rates would lead to low effective viscosity, which in turn would allow higher strain and shear rates to be achieved. In Figure 3.17d the colour scale is saturated at 0.05 yr^{-1}, which corresponds to a shear stress of 135 kPa for ice with a Glen's Flow Law rheology and a rate factor appropriate for ice at 0°C. This sits within the range of critical stresses (90-320 kPa) for crevassing as found in field measurements (Vaughan, 1993). When compared with the MODIS image in Figure 3.17a, it is clear that large areas of damage

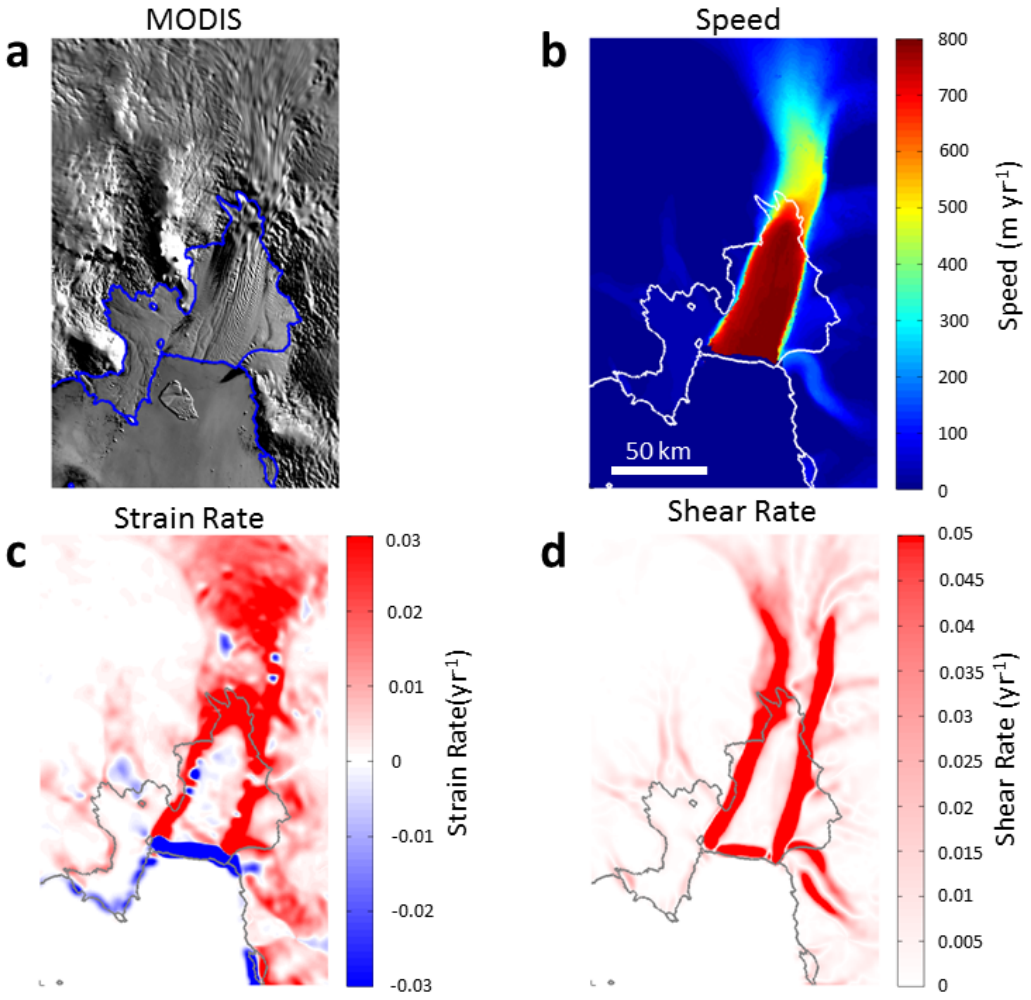

Figure 3.17: MODIS image (a), speed map (b), strain rate in direction of flow (c) and absolute shear-rate transverse to flow (d) for PIG Ice Shelf.

are present on PIG ice shelf.

Throughout the main section of the shelf, the along-flow strain rate is low. However, near the calving front there is a linear feature that runs diagonally across the shelf. It is unclear whether this is an artefact of the InSAR processing or whether this is a feature of the flow. If it is a feature of the flow, it may be formed after the shelf passes the ridge that protrudes into the shelf from the left (west) side of the channel. It is likely that deformation of the shelf past this ridge produces considerable resistance to flow, and once the shelf flows past this point the resistance is reduced.

At the grounding line there is large positive strain rate, with low strain rate further downstream in the shelf. This suggests that the shelf is providing little buttressing to the grounded ice.

Ross Ice Shelf

For the majority of the Ross Ice Shelf there are low positive along-flow strain rates, as is evident in Figure 3.18c. This may be expected; as the shelf flows downstream there is less resistance from ice ahead of it that must be viscously deformed. Therefore the shelf accelerates as it approaches the calving front, which can be seen in Figure 3.18b. Here it is clear that the Ross Ice Shelf is very large and along the approximately 600 km flowline from the grounding line to the calving front there is a increase in speed from approximately 300 m yr^{-1} to 1000 m yr^{-1}. This equates to an average strain rate of 0.0012 yr^{-1} and hence there are only low strain rates observed in the along-flow strain-rate field in Figure 3.18c.

Despite the majority of the shelf containing positive along-flow strain rate, there are some interesting negative along-flow strain rate areas, which give insight into the ice flow at certain locations. The Byrd Glacier feeds the Ross Ice Shelf from the eastern part of the grounding line, and can easily be identified in the speed map (Fig. 3.18b) due to the high ice-surface speed of this inflow. As the ice enters the shelf there is an area of negative along-flow strain rate as the ice spreads and slows, or is resisted by the slow flowing ice already present within the shelf. This may act to buttress the inflow from Byrd Glacier.

Resistance to flow and corresponding negative along-flow strain-rate is also present at the right (east) end of the Ross Ice Shelf calving front. Here there is a pinning point in the form of an island that is approximately 100 km wide. Upstream of this pinning point there is a prominent area of negative along-flow strain rate. From this we can imply that the island is providing a resistance to the flow of the ice shelf and causing the ice to slow and possibly being compressed in this region.

As with the Larsen C Ice Shelf, large positive along-flow strain rates are observed on the Ross Ice Shelf with the same spatial scale and orientation as fractures. From the MODIS image in Figure 3.18a, a number of large fractures can be seen that are roughly 100 km in length, aligned parallel to the calving front and found within 200 km of the calving front. These features correspond to coherent positive strain-rate structures with strain-rate values of over 0.02 yr^{-1}.

There are very few features that can be discerned from the transverse shear-rate plot for the Ross Ice Shelf in Figure 3.18d. One exception is the shear margins that bound the inflow from Byrd Glacier. Here these high shear-rate bands coincide with high strain rates, suggesting a weakened effective viscosity.

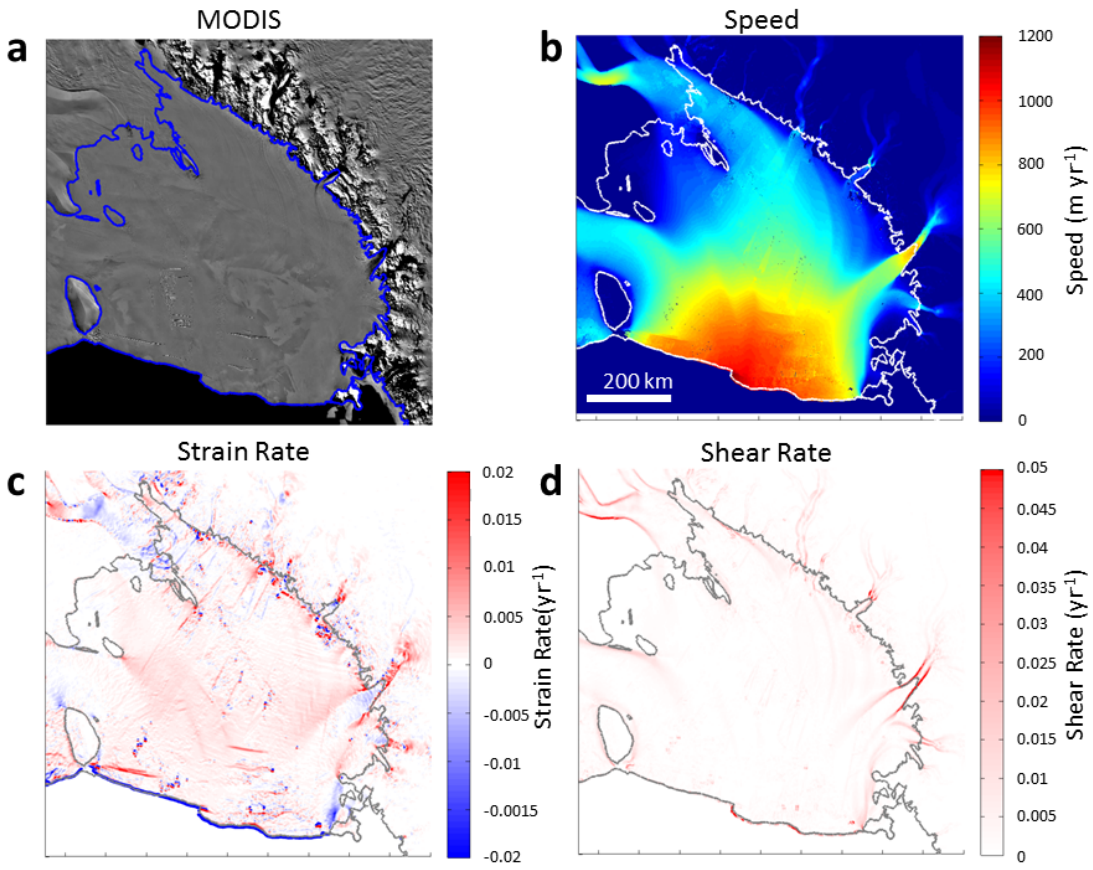

Figure 3.18: MODIS image (a), speed map (b), strain rate in direction of flow (c) and absolute shear-rate transverse to flow (d) for Ross Ice Shelf.

Summary: Strain Rate and Shear Rate

From these geophysical examples using the strain rate in the direction of flow and the shear rate transverse to flow, a number of systematic features appear to be present across most shelves.

Firstly, upstream of the grounding line there is often an area of positive strain rate, as the ice accelerates towards the ice shelf. Here the resistance to flow is reduced as the ice thins and the basal drag is reduced. Once the ice crosses the grounding line, there is often a region of negative strain rate, which may form as the ice spreads to fill (what is often) a wider channel and consequently the ice slows. Alternatively, this negative strain rate may be due to the resistance generated by the stationary/pinned or slow-flowing ice in the shelf. In reality both of these processes are likely to contribute to the negative strain rates after the ice crosses the grounding line. Close to the grounding line there is also likely to be some influence from submarine melting that may act to modify the flow.

From comparison of the along-flow strain-rate field and the MODIS imagery, it is clear

that major fractures within ice shelves can be identified by strips of high strain rate. These fractures are usually aligned perpendicularly to the flow, with the maximum strain rate across them occurring in the flow direction. This suggests that these fractures form due to sections of the ice shelf being stretched in the along-flow direction. The extensional stresses in the ice then exceed some critical value and the fracture is formed. Fractures often form near pinning points, where there is a large gradient in flow speed and therefore high levels of deformation.

Along the margins of tributary ice streams and along the margins of the ice shelves themselves, there are often high transverse-shear and along-flow strain rate values. Here high transverse shear-rate values are obtained due to the large gradient in speed across the margin between the fast and slow flowing ice. This leads to a reduced effective viscosity in these areas due to the shear-thinning nature of glacial ice. The relatively low effective viscosity means higher shear and strain rates are obtained here, which in turn leads to further decreased effective viscosities. High rates of deformation may also lead to the formation of damaged sections of ice that may be unable to withstand the shear and extensional stresses required to resist the ice flow.

3.6 Principal Axes of Strain

The Principal Axes of Strain define the reference frame in which deformation is described with no shear component. This is calculated at each grid point, with the 1$^{\text{st}}$ Principal Axis of Strain aligned in the direction of the maximum absolute Principal Strain Rate. This maximum absolute Principal Strain Rate is defined as the 1$^{\text{st}}$ Principal Strain Rate. Perpendicular to this is the 2$^{\text{nd}}$ Principal Axis of Strain. The 2$^{\text{nd}}$ Principal Strain Rate is aligned in this direction and incorporates all other deformation occurring at this point. Positive Principal Strain Rates correspond to extensional flow, while negative Principal Strain Rates equate to compressive flow. These quantities may be informative for determining the advance of the shelf, processes leading to the formation of crevasses and the calving of icebergs, and in addition the deformation occurring around pinning points.

In the frame of reference of the Principal Axes of Strain, the shear components of the strain-rate tensor are equal to zero. The transformation of the strain-rate tensor into a reference frame orientated at θ to the original frame is given by

$$\begin{pmatrix} e'_{11} & e'_{12} \\ e'_{12} & e'_{22} \end{pmatrix} = \begin{pmatrix} \cos\theta & \sin\theta \\ -\sin\theta & \cos\theta \end{pmatrix} \begin{pmatrix} e_{xx} & e_{xy} \\ e_{xy} & e_{yy} \end{pmatrix} \begin{pmatrix} \cos\theta & -\sin\theta \\ \sin\theta & \cos\theta \end{pmatrix}. \tag{3.11}$$

In the reference frame corresponding to the Principal Axes of Strain $e'_{12} = 0$, therefore we determine the orientation of the Principal Strain Axes θ_P from

$$(e_{yy} - e_{xx}) \sin\theta_P \cos\theta_P + e_{xy} \left(\cos\theta_P{}^2 - \sin\theta_P{}^2\right) = 0, \tag{3.12}$$

$$\Rightarrow \theta_P = \frac{1}{2} \tan^{-1} \left(\frac{2e_{xy}}{e_{xx} - e_{yy}} \right) = \begin{cases} \theta_{Pa} \\ \theta_{Pb} \end{cases}. \tag{3.13}$$

The two Principal Axes are separated by 90°, $\theta_{Pb} = \theta_{Pa} + 90$. I define the 1st Principal Axis of Strain as aligned in the direction of maximum absolute Principal Strain Rate,

$$e'_{11} = \max \begin{cases} e'_{11a} &= \left| e_{xx} \cos^2\theta_{Pa} + e_{yy} \sin^2\theta_{Pa} + e_{xy} \sin\theta_{Pa} \cos\theta_{Pa} \right| \\ e'_{11b} &= \left| e_{xx} \cos^2\theta_{Pb} + e_{yy} \sin^2\theta_{Pb} + e_{xy} \sin\theta_{Pb} \cos\theta_{Pb} \right| \end{cases} \tag{3.14}$$

If e'_{11a} is largest then the 1st Principal Axis of Strain is aligned at an angle θ_{Pa} from the original axes, however if e'_{11b} is largest then the 1st Principal Axis of Strain is aligned at an angle of $\theta_{Pb} = \theta_{Pa} + 90$ from the original axes. We denote this angle as θ_P. Therefore the 1st and 2nd Principal Strain Rates are given by

$$e'_{11} = e_{xx} \cos^2\theta_P + e_{yy} \sin^2\theta_P + e_{xy} \sin\theta_P \cos\theta_P, \tag{3.15}$$

$$e'_{22} = e_{xx} \sin^2\theta_P + e_{yy} \cos^2\theta_P - e_{xy} \sin\theta_P \cos\theta_P. \tag{3.16}$$

In the following subsections the 1st and 2nd Principal Axes of Strain along with the Principal Strain Rates are used to investigate flow features found in a selection of Antarctic ice shelves.

3.6.1 Principal Axes of Strain for Typical Flow Dynamics

In order to develop an understanding of the structure of the Principal Axes of Strain for simple flow dynamics, I have produced a set of basic flow fields with the corresponding Principal Axes of Strain. The Principal Strain Axes have been projected such that their length is proportional to the Principal Strain Rate aligned in that direction. Each axis is also colour coded to give the sign of the strain: red indicates positive 1st Principal Strain Rate; blue - negative 1st Principal Strain Rate; magenta - positive 2nd Principal Strain Rate; and green - negative 2nd Principal Strain Rate.

The first example, given in Figure 3.19, is an example of a simple straining flow, with a fluid source at the centre of the grid, and fluid flowing away from the source in all directions. Here both 1st and 2nd Principal Strain Rates are positive. The flow is given by

$$u = 0.8 * (5 - x) \quad v = (5 - y), \tag{3.17}$$

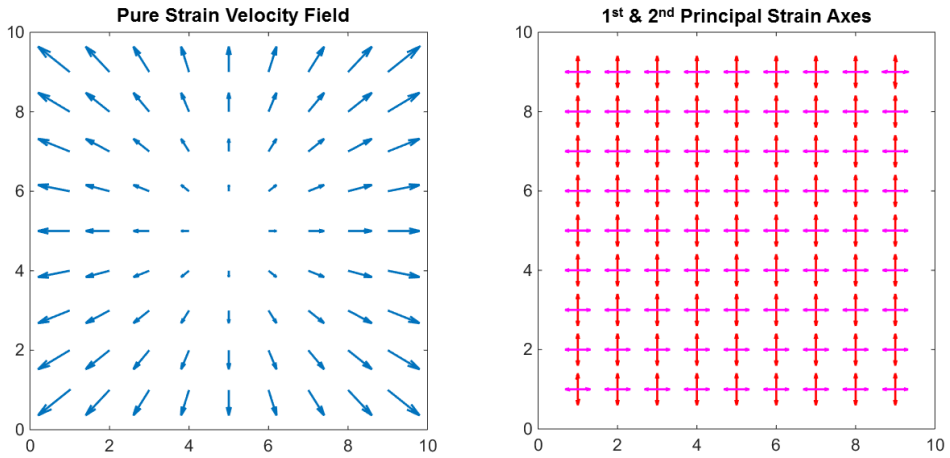

(a) (b)

Figure 3.19: (a) An example of a pure strain velocity field. (b) Principal Axes of Strain: Red axes - positive 1st Principal Strain Rate. Magenta axes positive 2nd Principal Strain Rate.

and hence the 1st Principal Strain Axes are aligned in the y-direction along the largest gradient in the velocity.

Figure 3.20 gives an example of a shear flow, with the y-component of velocity increasing from left to right in a parabolic manner. Due to this parabolic increase in velocity there is a left-to-right gradient in the 1st and 2nd Principal Strain Rates, indicated by the increase in the length of the axes vectors in Figure 3.20b. Here we see that the 1st Principal Strain Rate is positive and the 1st Principal Strain Axis is aligned at 45° to the y-axis, representing extension diagonally across the square. On the other hand, the 2nd Principal Strain Rate is negative, indicating compression, with the 2nd Principal Strain Axis again aligned at 45° to the y-axis, but perpendicular to the 1st Principal Strain Axis.

The velocity fields for the simple strain and shear flow are combined to give the velocity field presented in Figure 3.21a. The corresponding Principal Strain Axes are shown in Figure 3.21b. From this it is clear that the 1st and 2nd Principal Strain Axes are aligned in a similar manner to the shear-only case, with the 1st Principal Strain Rate remaining fairly constant throughout the grid. However, there is variation in the 2nd Principal Strain Rate, which is positive in the left half of the square, where there is extension towards the left margin, and negative to the right of the square, where the largest shearing is found.

Figure 3.22 gives the velocity and Principal Strain Axes for a purely compressional flow, with the y-component of velocity decreasing linearly in the y-direction. This negative

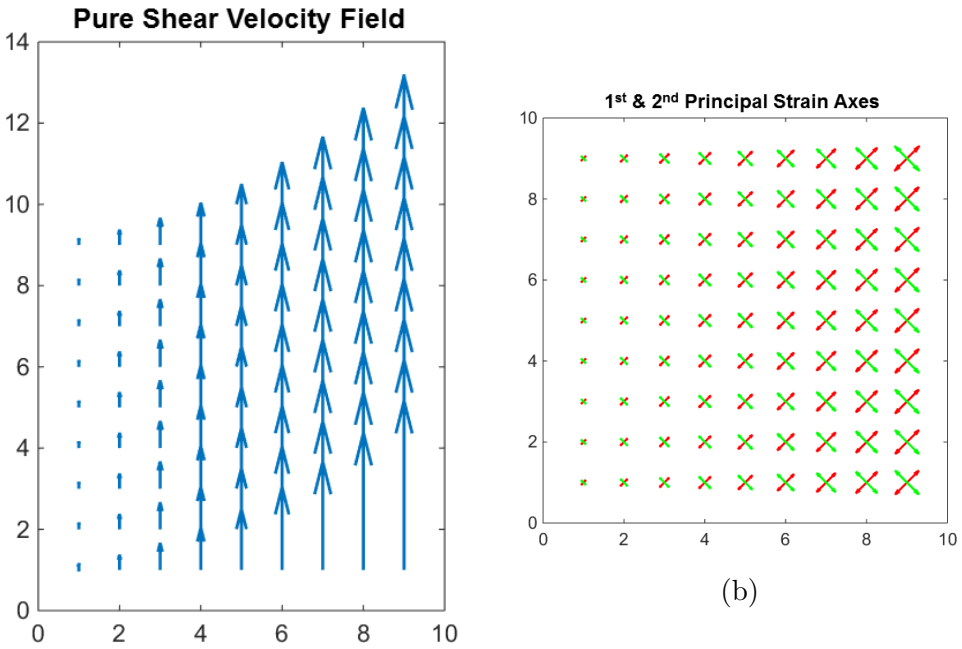

(a) (b)

Figure 3.20: (a) An example of a shear flow velocity field. (b) Principal Axes of Strain: Red axes - positive 1st Principal Strain Rate. Green axes negative 2nd Principal Strain Rate.

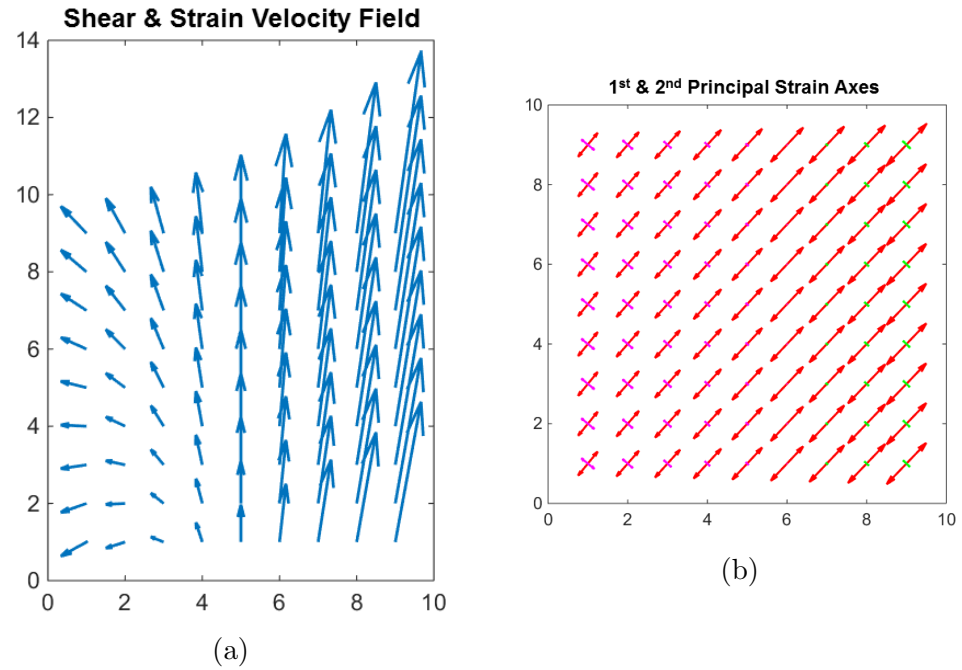

(a) (b)

Figure 3.21: (a) An example of a shearing and straining velocity field. (b) Principal Axes of Strain: Red axes - positive 1st Principal Strain Rate. Magenta axes positive 2nd Principal Strain Rate. Green axes negative 2nd Principal Strain Rate.

linear gradient is represented by a uniform negative 1st Principal Strain Rate, which is aligned with the flow.

The compressional flow is combined with the shearing flow to produce the velocity field shown in Figure 3.23a. The Principal Strain Axes for this flow are presented in Figure 3.23b. It is evident that the 1st Principal Strain Rate is negative, and while the 2nd Principal Strain Rate is positive and increases to the right. This indicates that the dominant dynamics here are compressional, with some extension perpendicular to this resulting from the shear flow.

Here regions of negative Principal Strain Rate suggest resistance to flow is being generated in these areas due to the deformation of the fluid as it moves past slower flowing fluid or is compressed against stationary objects. Negative Principal Strain Rates imply a compressive or shearing flow, which both generate resistance to flow. In the case of an ice shelf, if this resistance generated due to deformation can be transmitted upstream to the grounding line then it will contribute to the buttressing of the grounded ice.

3.6.2 Dynamics associated with the 1st Principal Axis of Strain and 1st Principal Strain Rate

The 1st Principal Axis of Strain is aligned in the direction of the maximum magnitude strain rate in a reference frame oriented to have no shear component. The magnitude of the strain rate in this direction is given by the 1st Principal Strain Rate. Throughout the majority of an ice shelf this is positive and indicates where the ice shelf is being stretched by the driving hydrostatic-pressure gradient. This stretching leads to thinning and flow within the shelf. In turn this causes the shelf to flow and advance towards the ocean. However, ice shelves are known to fracture, leading to the formation of crevasses within the shelf. If this occurs near the ice front this may cause an iceberg to form. I now use plots of the 1st Principal Axis of Strain and 1st Principal Strain Rate to investigate the extensional strain and the link between high strain rates and fracture formation both in terms of the magnitude of the strain and its orientation. I do this on a case-by-case basis examining some individual ice shelves.

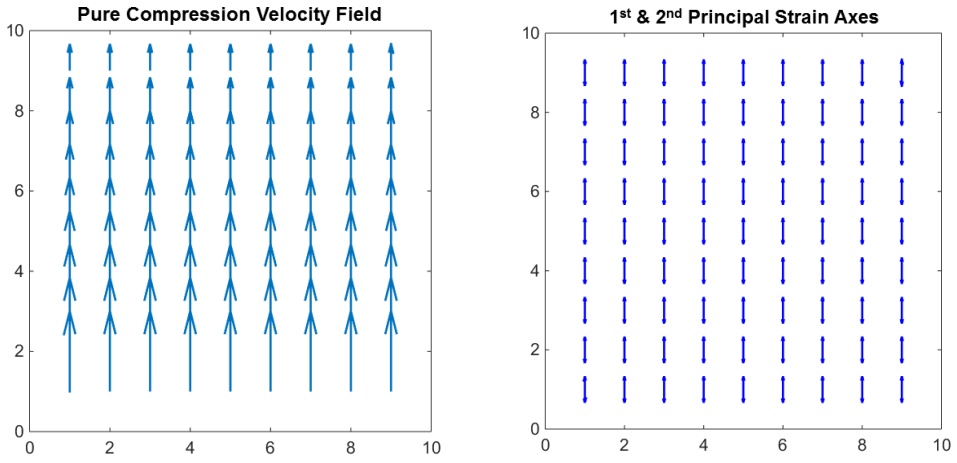

(a) (b)

Figure 3.22: (a) An example of a purely compressional velocity field. (b) Principal Axes of Strain: Blue axes - negative 1st Principal Strain Rate.

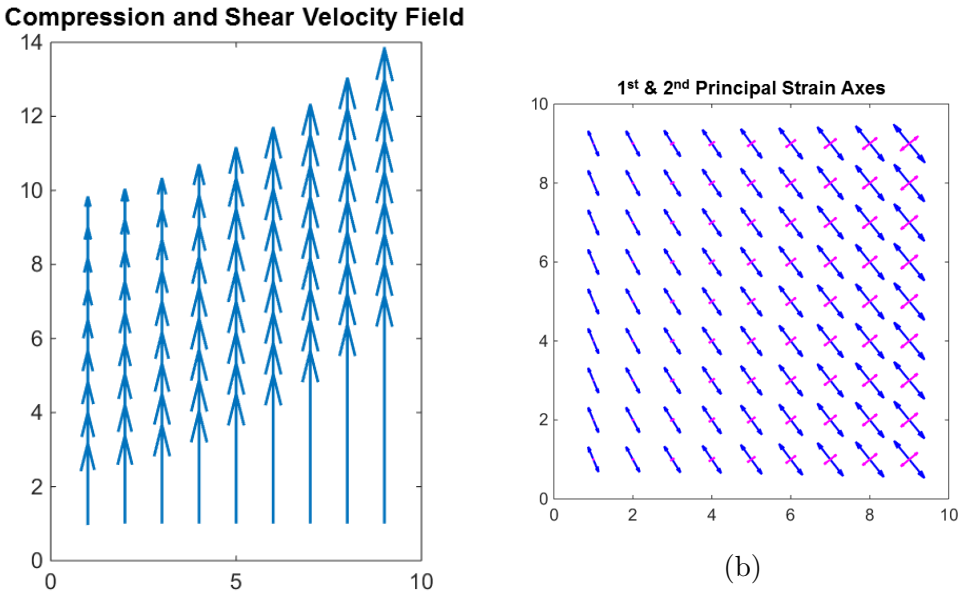

(a) (b)

Figure 3.23: (a) An example of a shearing and compressional velocity field. (b) Principal Axes of Strain: Blue axes - negative 1st Principal Strain Rate. Magenta axes positive 2nd Principal Strain Rate.

Amery Ice Shelf

Figure 3.24 displays plots of ice-surface speed, 1st and 2nd Principal Axes of Strain, Principal Strain Rates and a MODIS image for the final third of Amery Ice Shelf. From the MODIS imagery (Fig. 3.24b) it is evident that there are several areas that are heavily crevassed. One such area is along the eastern boundary of the shelf (lower in plot), where there is flow past an island that protrudes into the main trunk of the shelf (marked as location (1)). When comparing the location of these features with the plot of the 1st Principal Axis of Strain and 1st Principal Strain Rate (Fig. 3.24c) it is clear that this is an area of high strain, though the axes are not orientated perpendicular to the majority of the fractures. I would expect fractures and the 1st Principal Axis of Strain to be aligned at right angles if high strain was resulting in crevasse-formation, or weak ice due to the presence of crevasses was allowing high strain. It appears from the MODIS image (Fig. 3.24b and zoomed in image in Fig. 3.25) that the fractures are initiated as the ice flows past the tip of the protruding island. At this point and in the region towards the centre of the shelf, the crevasses are aligned perpendicular to the 1st Principal Axis of Strain, with positive values of the 1st Principal Strain Rate. This suggests that the fractures are first created in this area, where there is high tensile stress leading to high strain, and then the crevasses are advected with the flow. The presence of these fractures then weakens the ice and allows higher strain rates to occur, which may lead to a lengthening and an increase in the size of the fractures.

At the centre of the ice front there is a large fracture opening at right angles to the calving front (marked as location (2)). This is associated with high positive values for both the 1st and 2nd Principal Strain Rates. It is clear that in this region the 1st Principal Axis is aligned parallel to the calving front and perpendicular to the fracture, which may be causing this fracture to open. Here, at the channel exit, the ice shelf is leaving the lateral confinement of the long channel-like embayment and starting to spread laterally in addition to the along-flow direction. This results in high strain rates perpendicular to the flow direction and the formation of fractures perpendicular to the ice front. This style of fracture is a recurring feature at the calving front of Amery Ice Shelf, with the shape of the calving front in 1962 suggesting an iceberg had broken off following the propagation of a fracture similar to the one observed here (Fricker et al., 2002). Following this, during the Antarctic summer of 1963-64 there was a large calving event that produced an iceberg of 10,000 km^2 (Budd, 1966). Since then the calving front has been advancing to its current position. It has been suggested that the location of these fractures perpendicular to the calving front is linked to the boundaries between ice from different tributaries, which merged hundreds of kilometres upstream (Fricker, 2005). These weak boundaries then form fractures when the ice begins to spread laterally after leaving the

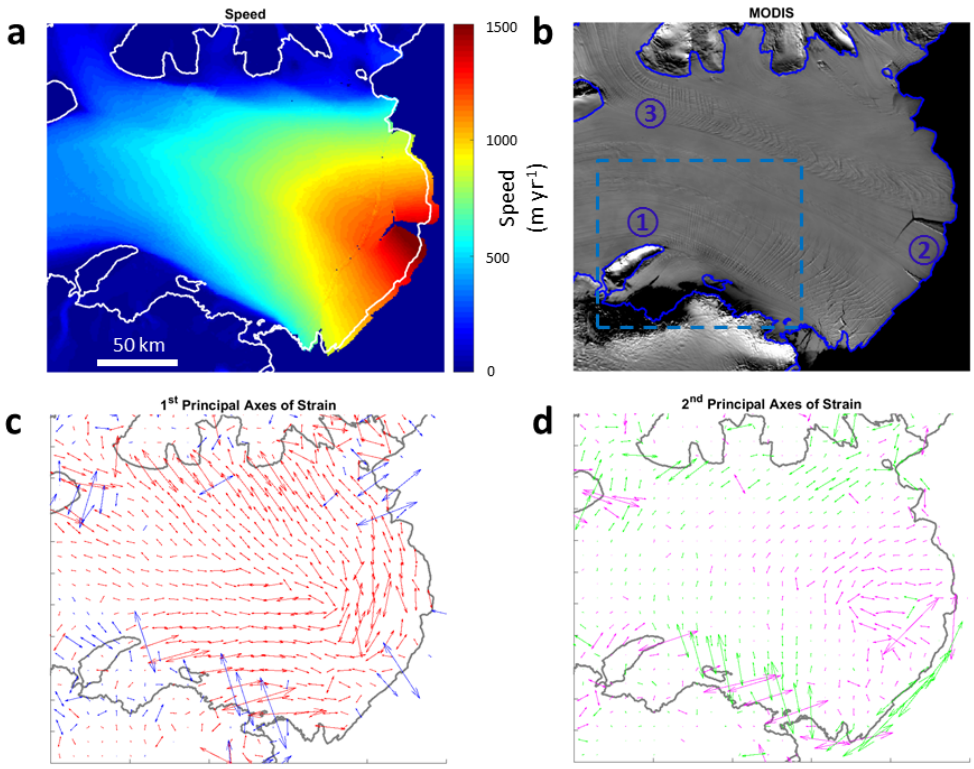

Figure 3.24: Plots showing quantities and details near the ice-shelf calving front of Amery Ice Shelf. (a) Unfiltered ice surface speed. (b) MODIS imagery of shelf surface. (c) The 1st Principal Axis of Strain (red and blue vectors indicate positive and negative 1st Principal Strain Rates respectively). (d) The 2nd Principal Axis of Strain (magenta and green vectors indicate positive and negative 2nd Principal Strain Rates respectively). In each plot the grounding line, location of islands and the ice front are identified. Location (1) identifies the island protruding into the shelf after which crevasses form as the ice is stretched as it flows past this stationary ice area. Location (2) is the fracture that has opened perpendicular to the calving front. Location (3) is positioned where there is an in-flow into the shelf from the Charybdis Glacier and where a set of parallel fractures begin that continue towards the calving front.

confinement of the channel. There is also evidence of several other locations along the calving front where similar but smaller fractures are present (Walker et al., 2015). (See MODIS image Fig. 3.24b.)

On the Western boundary of the ice shelf (upper boundary in Fig. 3.24a, and identified as location (3)), there is ice flow into the shelf from the Charybdis Glacier. As this section of ice merges with the main shelf we see the formation of crevasses perpendicular to the flow, which are advected and deformed further as ice flows towards the calving front. From the plot of ice-surface velocity (Fig. 3.24a), it is clear that the ice from Charybdis Glacier accelerates considerably from approximately 250 m yr^{-1} to over 1000 m yr^{-1} within less than 150 km. In this case, we see that the 1st Principal Axis of Strain

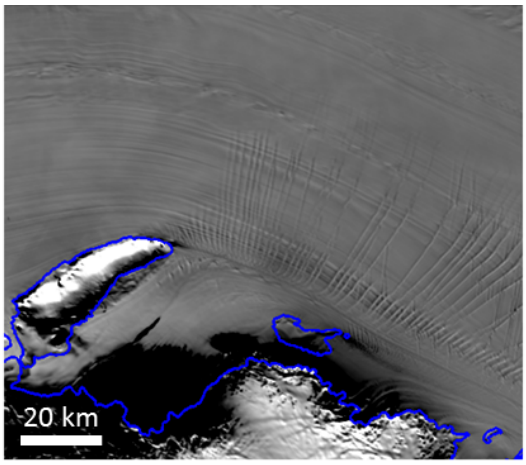

Figure 3.25: MODIS image of crevassing in ice shelf as it flows past an island that protrudes into the main flow. This area is highlighted in Figure 3.24c

is aligned perpendicular to the fractures, suggesting that the fractures are generated by stretching of the ice in the along-flow direction. These fractures are advected toward the calving front by the ice flow. They appear to become more separated as they approach the calving front. This suggests that the surrounding ice is stretched and thinning as it approaches the ice front. Alternatively, there may have been a larger separation between the fractures when they were original formed and the flow has changed slightly over time.

Fimbul Ice Shelf

The 1st Principal Axes of Strain and 1st Principal Strain Rates for Fimbul Ice Shelf are shown in Figure 3.26c. Moving with the ice-shelf flow (from the bottom of the plot), we see that as the ice enters the shelf the 1st Principal Strain Rate is positive and aligned perpendicular to the flow-direction. This indicates the lateral spreading of the ice as it leaves the lateral confinement of the valley in which the main flow is initially found. Here the ice is grounded and relatively thin on both sides of the inflow into the shelf, while the main section of flow into the shelf is thick and fast flowing. There is then a region of negative 1st Principal Strain Rates on both sides of the main flow. Here the ice is decelerating and being compressed as it spreads laterally into the surrounding ice to the sides of the main flow. In this area there is also relatively high positive 2nd Principal Strain Rates indicating that there is still extension occurring in this region. Moving further downstream towards the calving front, we see positive 1st Principal Strain Rates in both margins of the shelf, between the slow-flowing ice that is pinned in place by islands and the main fast-flowing section, as we would expect.

When comparing the 1st Principal Axis of Strain and Principal Strain Rate with the surface features shown in the MODIS plot in Figure 3.26b, we see that surface deformation is mainly localized within the left (west) margin, where there are a series of fractures

aligned perpendicular to the flow. These correspond to areas of high positive 1st Principal Strain Rates. However, in contrast to the right (east) margin, the 1st Principal Axes of Strain don't share the same exact orientation, but are slightly misaligned and have a slightly larger magnitude. The heavily crevassed region in the left margin may explain why the 1st Principal Axes of Strain are misaligned. Where the ice is damaged (fractured) it no longer has a uniform consistency and may be deformed in multiple directions when a stress is applied, whereas an area with less damage is likely to be deformed in a more uniform manner, as is observed in the right margin.

In the centre of the main section of ice flow, the 1st Principal Axes of Strain are mostly aligned perpendicular to the flow direction, suggesting that the main component of strain in this area is the lateral strain due to the lateral spreading of the shelf as the main section of the flow becomes wider. This also suggests that there is only a small along-flow thickness gradient present to drive flow, which may also be inferred from the near-uniform flow observed in the speed plot (Fig. 3.26a).

From Figure 3.27a, a map of ice thickness for Fimbul ice shelf (extracted from the Bedmap2 dataset (Fretwell et al., 2013)), we can see that there is a central band of thicker ice that runs from the tributary ice stream towards the calving front. On either side of this there is thinner ice. This implies that there is a lateral thickness gradient, which may induce a flow transverse to the main flow direction and hence transverse strain. Figure 3.27b, shows the along-flow gradient in ice thickness, given by $\hat{\mathbf{u}}.\nabla H$. From this plot it is clear that there is no coherent pattern to the gradient in ice-thickness in the flow-direction, except near the grounding line, where there is a strong negative signal. This suggests that the main extensional 1st Principal Strain Rate within the shelf results from the shearing between the faster flow in the main section of the shelf and the stationary ice in the margins.

To the left (west) of the main flow, in the upstream section of the shelf, there is a small region of shelf thickening. This can be seen in Figure 3.27b and is identified as location (1). Here there is thin ice south of this region (below in the plot), which may be caused by melting from below, or due to thin grounded ice being transported into the shelf from the peninsula that extends out into the shelf. This section of shelf, at location (1), may then thicken as ice diverges away from the thick central flow and thickens the margins. Alternatively, the flow of the ice in the margin may be towards the central thick region and is pulled towards the front by shearing with the main flow. This ice may then be incorporated into the thicker region downstream.

Throughout both margins of the downstream part of the fast-flowing section of the shelf,

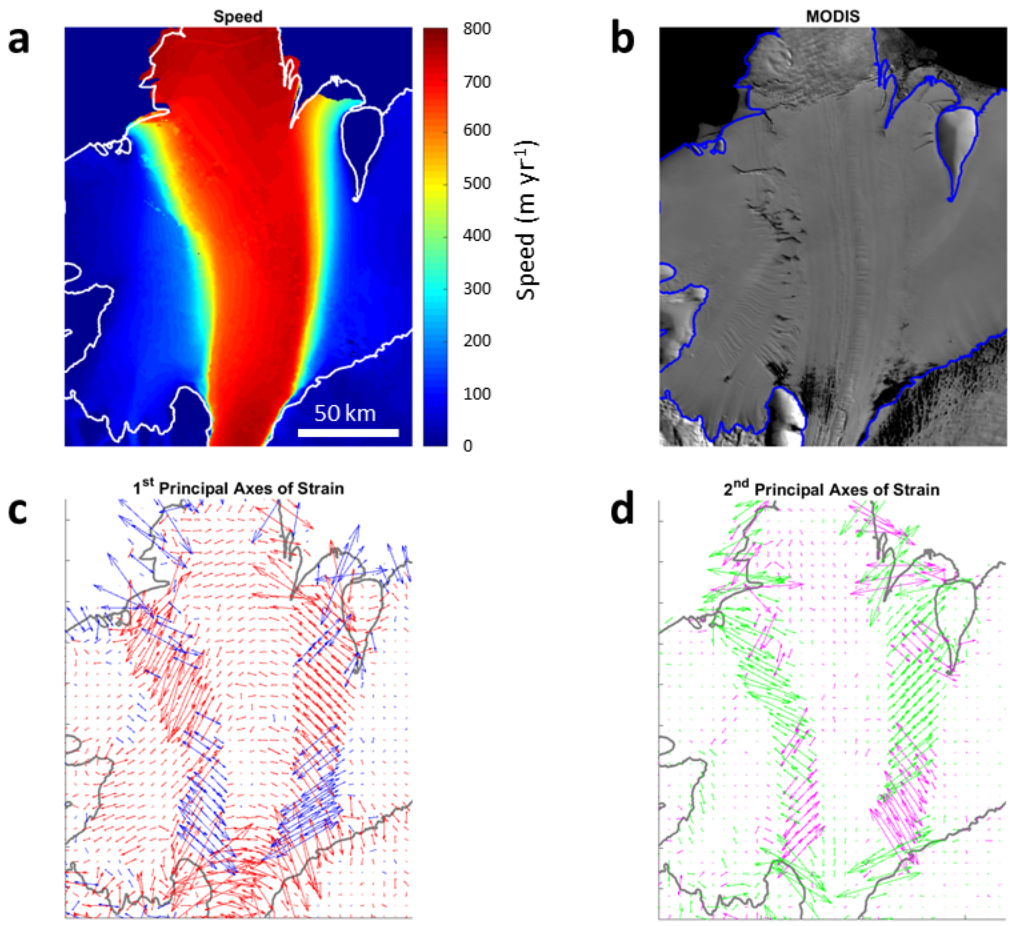

Figure 3.26: Plots showing quantities and details for Fimbul Ice Shelf. (a) Unfiltered ice surface speed. (b) MODIS image with fractures present in the left margin of the main flow in the shelf. (c) The 1st Principal Axis of Strain (red and blue vectors indicate positive and negative 1st Principal Strain Rates respectively). (d) The 2nd Principal Axis of Strain (magenta and green vectors indicate positive and negative 2nd Principal Strain Rates respectively). In each plot the grounding line, location of islands and the ice front are identified.

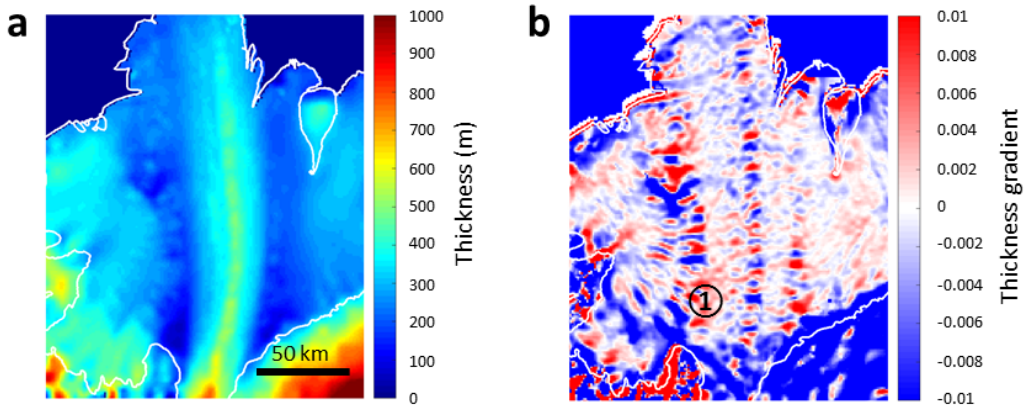

Figure 3.27: (a) Ice thickness and (b) ice-thickness gradient in direction of ice flow both for Fimbul Ice Shelf. Location (1) marks a location of ice thickening.

there are high positive values of the 1st Principal Strain Rate and negative values of the 2nd Principal Strain Rate, with the Principal Axes of Strain aligned at 45° to the main flow. This suggests there is resistance to flow generated in these margins, which is probably a result of the shearing of the ice past pinning points on either side of the main flow located at the shelf front. To the right (east) this takes the form of a single island (approximately 20 km wide at its widest point and 40 km long), while the pinning point to the left (west) is a collection of closely spaced smaller islands, which form a 20 km wide section of stationary ice. Once the shelf passes these pinning points there is no longer this pattern to the Principal Strain Rates suggesting that this section of the shelf does not experience any resistance and therefore makes no contribution to buttressing via shear stresses. Upstream near the grounding line, the 1st Principal Strain Rate is negative in the margins of the flow, and the 2nd Principal Strain Rate is positive, with the Principal Strain Axes again aligned at 45° to the main flow. This suggests that there is high shear and compression in these parts of the shelf margin, which will contribute to resistance of the shelf flow.

Analysis of the velocity-field data such as this can allow the locations of stationary ice or bedrock outcrops to be identified, which are important to ice-shelf buttressing. This may then lead to the discovery of previously uncharted pinning points. A velocity-field from a computational model was implemented by Fürst et al. (2015), where in addition to inverting for the rheological rate factor, locations could be specified as grounded/stationary/pinning in order to best fit observations. In doing so, previously uncharted pinning points (grounded ice) were identified. Similar work has been undertaken by Berger et al. (2016), where an uncharted pinning point was identified from analysis of velocity data and then model simulations run to reproduce the velocity field while varying the spatial extent of the pinning point. In this case (Berger et al., 2016) the closest match to the observed velocity field was obtained with the full extent of the pinning point, with more realistic rate factors also obtained.

Ronne Ice Shelf - Berkner Island Margin

A section of the Ronne Ice Shelf is presented in Figure 3.28. Here Berkner Island is located to the right (east) of the main shelf and forms a large area of stationary grounded ice. Ice flow past this is resisted by the viscous shearing against this pinning point. There is a complex pattern of high positive and negative Principal Strain Rates in the margin of the shelf. Looking at Figure 3.28c, a plot of the 1st Principal Axis of Strain and 1st Principal Strain Rate, we see that for the upstream half of the margin with Berkner Island there is mainly positive strain aligned at approximately 45° to the margin and flow-direction. This suggests an area of high shear and strain. When compared to the MODIS imagery (Fig. 3.28b and zoomed in view in Fig. 3.29) we see that fractures have

formed in this area.

Further downstream, there is a transition to negative 1st Principal Strain Rates and the fractures are no longer present. However, when these two regions are compared using the 2nd Principal Strain Rates (Fig 3.28c), we see the opposite transition has occurred; from negative values to positive as we move downstream. This suggests that the dynamics in this margin change as the shelf nears the ocean. Upstream, extension is most important as the shelf accelerates in the downstream direction. However, compression becomes more important near the front, with lower values of extension observed. This may be because there has been a change in the thickness gradient of the shelf, which is no longer large enough to drive the same flow. Alternatively, the geometry of the embayment may be an important control. As the ice nears the front, the orientation of Berkner Island acts to funnel the ice towards the centre of the front, which may lead to the generation of additional resistance.

The ice thickness in this area is shown in Figure 3.30a. Here we see that the ice thins as it flows downstream; from approximately 800 m at the upstream end of the Berkner margin to 250 m at the calving front. There is a narrow band of thin ice, which runs along the margin of the shelf next to Berkner Island. This narrow band may be the result of a melt channel on the ice-shelf base or where a thin section of ice has entered the shelf upstream. This band of thin ice coincides with the area of crevassing identified above, suggesting that this thinner section is more easily deformed. Looking at the plot of the gradient of ice thickness in the flow-direction, as shown in Figure 3.30b, we see that most of the ice shelf has negative thickness gradient as the ice thins in the along-flow direction. However, in the margin of Berkner Island where the crevassing is found, we see that there is some variation in the thickness gradient. Whether this is a result of the fracturing, the cause of fracturing or due to noise from radar scatter from crevasses is unclear. However, the signal returns to mostly negative downstream where there are no further crevasses. Near the calving front, the thickness gradient in the direction of flow is negative and has a similar value to that observed further upstream. This suggests that the reduction in crevasse formation and the negative 1st Principal Strain Rates is a result of the geometry of the embayment rather than changes in the ice-shelf thickness gradient.

In contrast to the Principal Strain Rates for Fimbul Ice Shelf, here we observe a transition downstream from positive 1st Principal Strain Rate to negative 1st Principal Strain Rate. This suggests that shearing and compression increases downstream and if the ice rheology remains the same this could result in increased resistance to flow locally. This could then be transferred upstream generating buttressing at the grounding line.

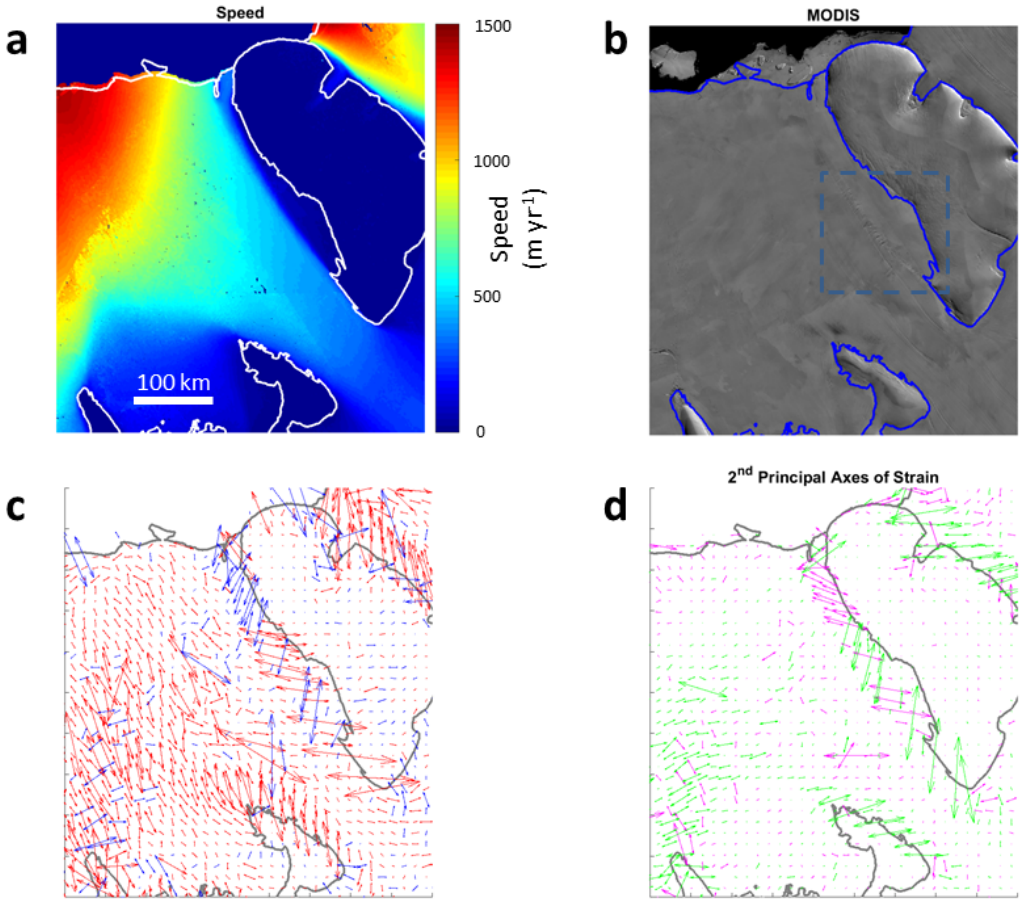

Figure 3.28: Plots showing quantities and details for the Ronne Ice Shelf, along the shelf margin with Berkner Island. (a) Unfiltered ice surface speed. (b) MODIS image with fracture or crevasse features present in the margin with Berkner Island. Blue dashed box shows location of zoomed in MODIS image in Figure 3.29. (c) The 1st Principal Axis of Strain (red and blue vectors indicate positive and negative 1st Principal Strain Rates respectively). (d) The 2nd Principal Axis of Strain (magenta and green vectors indicate positive and negative 2nd Principal Strain Rates respectively). In each plot the grounding line, location of islands and the ice front are identified.

From assessment of Figure 3.28, it is also clear that there is shearing present in the margin next to the ice rise opposite Berkner Island. Along this margin there is a clear shearing pattern in the 1st and 2nd Principal Strain Rates, with Principal Strain Axes aligned at 45° to the flow. Further downstream of the ice rise, the 1st Principal Strain Rate retains similar values but there is a decrease in the 2nd Principal Strain Rate, and the Principal Strain Axes are no longer aligned at 45° to the flow. This indicates that there has been a change in the style of flow in this region, which has become mainly extensional.

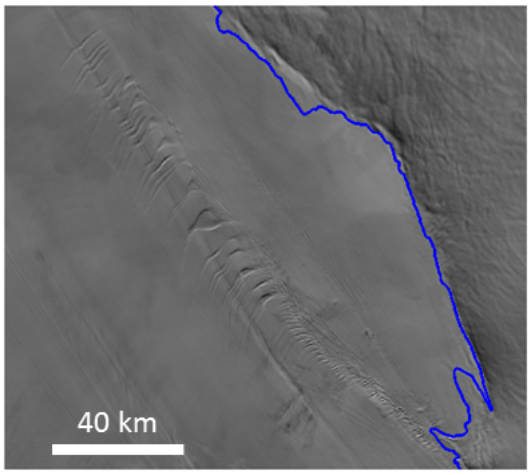

Figure 3.29: MODIS image for the Ronne Ice Shelf, zoomed in on crevassed section in margin with Berkner Island. This section of the shelf is defined in Figure 3.28b.

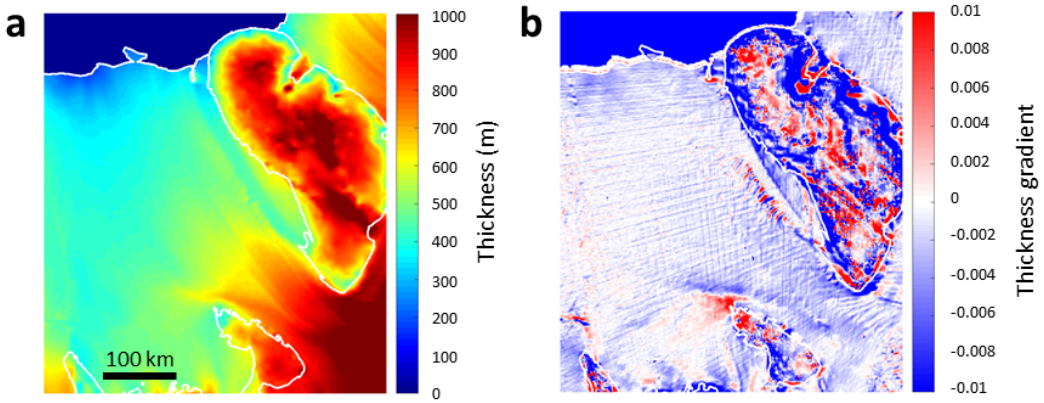

Figure 3.30: (a) Ice thickness and (b) ice-thickness gradient in direction of ice flow both for the section of Ronne Ice Shelf adjacent to Berkner Island.

Ronne Ice Shelf - West Margin

In contrast to the right (east) margin of the Ronne Ice Shelf, the left (west) margin (Figure 3.31) has uniformly positive 1st Principal Strain Rates, with the 1st Principal Axes of Strain aligned at approximately 45° to the flow. This is due to the high shear in the margin and can also be inferred from the 2nd Principal Strain Rates (Fig. 3.31d), which are large and negative within the margin. Here the geometry of the stationary ice in relation to the direction of ice-flow is close to constant along the length of the shelf. Therefore, we wouldn't expect the change in sign of the 1st Principal Strain Rates as observed on the opposite lateral boundary (Berkner), if this feature is generated by the funneling effect of a narrowing channel.

We observe from Figure 3.32b that the western margin is an area of near uniform along-flow ice-thickness gradient, with no features that suggest the presence of crevasses. This corresponds to the near constant values and orientation of the 1st and 2nd Principal Strain Rates and Principal Axes of Strain respectively.

Larsen C Ice Shelf

Large fractures are visible on the southern section of the Larsen C Ice Shelf and can be seen in the MODIS image in Figure 3.33b. They form after the ice shelf has flowed past a bedrock outcrop that protrudes out into the embayment from the mainland (Kenyon Peninsula - location (1)). Large strain rates are associated with the flow at this location and can be seen in Figure 3.33c. These large positive values of strain rate spread in towards the centre of the ice shelf from the bedrock outcrop for approximately 50 km. Here the extent of the damage to the ice shelf is large enough to affect the rheology of the shelf significantly and hence allow such high strain rates to be achieved. In this area there are some negative 2nd Principal Strain Rates (Fig. 3.33d) suggesting that there is some local resistance to flow generated by the island located at the ice front (Gipps Ice Rise - location (2)).

Further crevassing can be seen in the MODIS image following the deformation that occurs as the ice shelf flows past two islands, which can be seen in the lower left corner of Figure 3.33b (location (3)). These features are then advected towards the calving front. Here the 1st Principal Axis of Strain is oriented perpendicular to these crevasses and may act to open them further as they flow downstream.

Ross Ice Shelf

In Figure 3.34b, a MODIS image of a section of the Ross Ice Shelf, a series of roughly parallel fractures can be seen. This array of fractures runs from the middle of the shelf

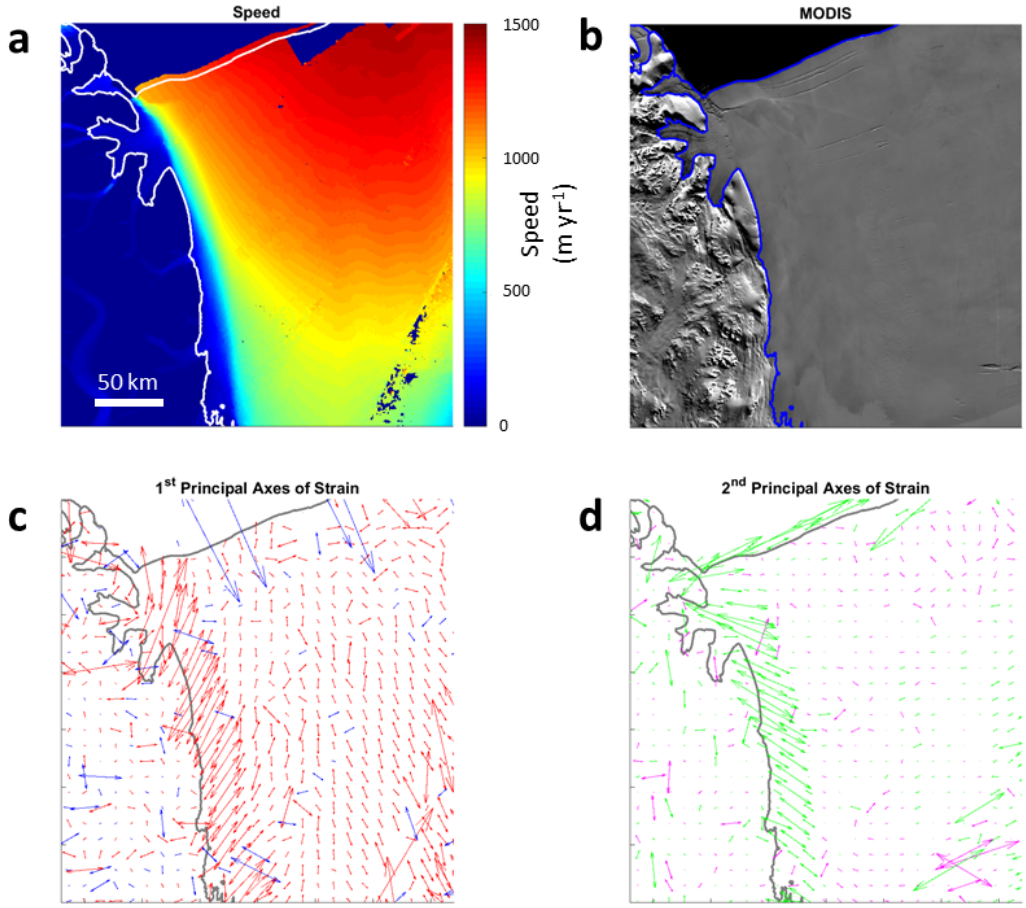

Figure 3.31: Plots showing quantities and details for the Ronne Ice Shelf, along the western shelf margin. (a) Unfiltered ice surface speed. (b) MODIS image. (c) The 1st Principal Axis of Strain (red and blue vectors indicate positive and negative 1st Principal Strain Rates respectively). (d) The 2nd Principal Axis of Strain (magenta and green vectors indicate positive and negative 2nd Principal Strain Rates respectively). In each plot the grounding line, location of islands and the ice front are identified.

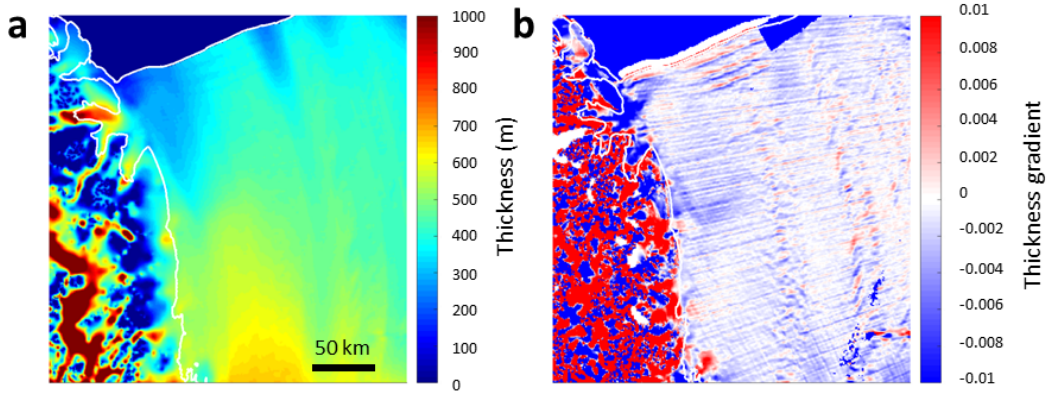

Figure 3.32: (a) Ice thickness and (b) ice-thickness gradient in direction of ice flow both for the western margin of the Ronne Ice Shelf.

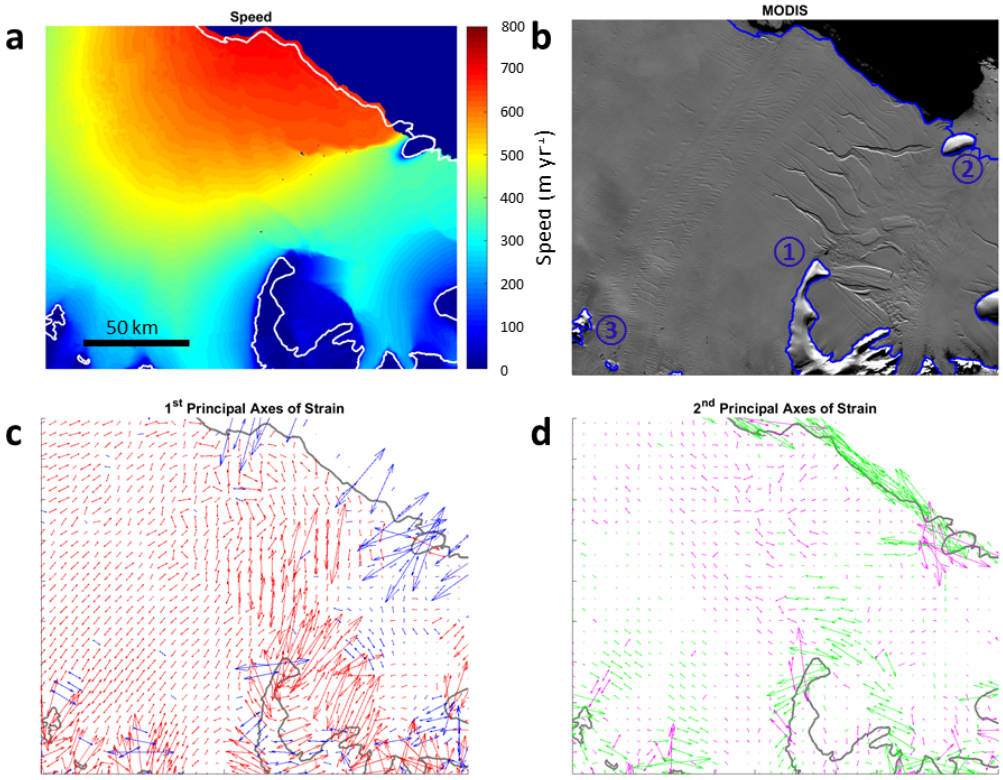

Figure 3.33: Plots showing quantities and details for the southern section of the Larsen C Ice Shelf. (a) Unfiltered ice surface speed. (b) MODIS image. (c) The 1st Principal Axis of Strain (red and blue vectors indicate positive and negative 1st Principal Strain Rates respectively). (d) The 2nd Principal Axis of Strain (magenta and green vectors indicate positive and negative 2nd Principal Strain Rates respectively). In each plot the grounding line, location of islands and the ice front are identified. In the MODIS image (b), large fractures can be seen perpendicular to the flow once the ice has passed the peninsula that protrudes into the shelf, location (1). Buttressing to ice-flow is generated by Gipps Ice Rise, location (2). Crevasses can also be seen in the lower left corner of the MODIS image location (3). They appear to be created as the ice is deformed as it flows past the islands, and are then advected with the flow.

towards the calving front. These fractures appear to form two bands that are aligned with the flow, which can be seen more clearly in the zoomed-in image shown in Figure 3.35. Between these two bands there are some larger fractures that link the bands together. Unlike the fracture features observed in the previous examples, these fractures don't appear to be associated with deformation close to stationary ice or a pinning point, but instead are caused by some deformation within the ice. From the plot of the 1st Principal Axes of Strain and 1st Principal Strain Rates in Figure 3.34c, the crevasses in the upstream half appear to be aligned perpendicular to the 1st Principal Axis of Strain. However, this pattern seems to decay further downstream, where the larger crevasses are present. This suggests that the crevasses are first formed by stretching in the along-flow direction in areas of high extensional stress and strain, they are then advected with the

ice flow. In the upstream half of the plot of 1st Principal Axis of Strain (Fig. 3.34c), to the left (west) of this band of fractures, there is another separate area of high-magnitude 1st Principal Strain Rates (both positive and negative) but it is unclear whether their presence or dynamics in this area have any impact on the formation of crevasses in the adjacent area of ice.

Near the calving front, there are two large fractures aligned parallel to the calving front. From the plot of the 1st Principal Axis of Strain and the 1st Principal Strain Rates it is evident that they are associated with high positive strain-rate values. The bigger of the two fractures may be linked to deformation around Roosevelt Island, which can be seen on the left side of all the plots in Figure 3.34. However, the fracture is disjointed from the comparatively small-scale fracturing occurring in the margin. From the speed map in Figure 3.34a, it is clear that the location and orientation of the crevasse is associated with a step change in ice-flow speed. These two large fractures therefore appear to be the result of stretching within the ice shelf exceeding a critical stress leading to the formation of crevasses. The proximity of these fractures to the calving front suggests that these fractures will allow the formation of large icebergs.

The driving hydrostatic pressure is determined by the ice thickness and thickness gradient. From Figure 3.36a, it is clear that for the Ross Ice Shelf the ice is between 300 and 400 m thick at the calving front, and thins towards the centre of the calving front. This is comparable to the thickness of the ice at the calving front of the Ronne Ice Shelf (Fig. 3.30a and 3.32a). However, the Ross embayment does not narrow towards the calving front, suggesting there is more resistance to flow in the case of the Ronne Ice Shelf and hence large fractures are not found near the calving front. From the plot of the ice-thickness gradient in the flow-direction, the gradient is mainly negative, although there are some positive gradients in the areas that have crevasses, as identified from the MODIS data. This suggests that abrupt changes in along-flow ice-thickness gradients may be associated with the formation of fractures. However, these features in thickness gradient may result from errors/noise in the thickness data in the proximity of fractures.

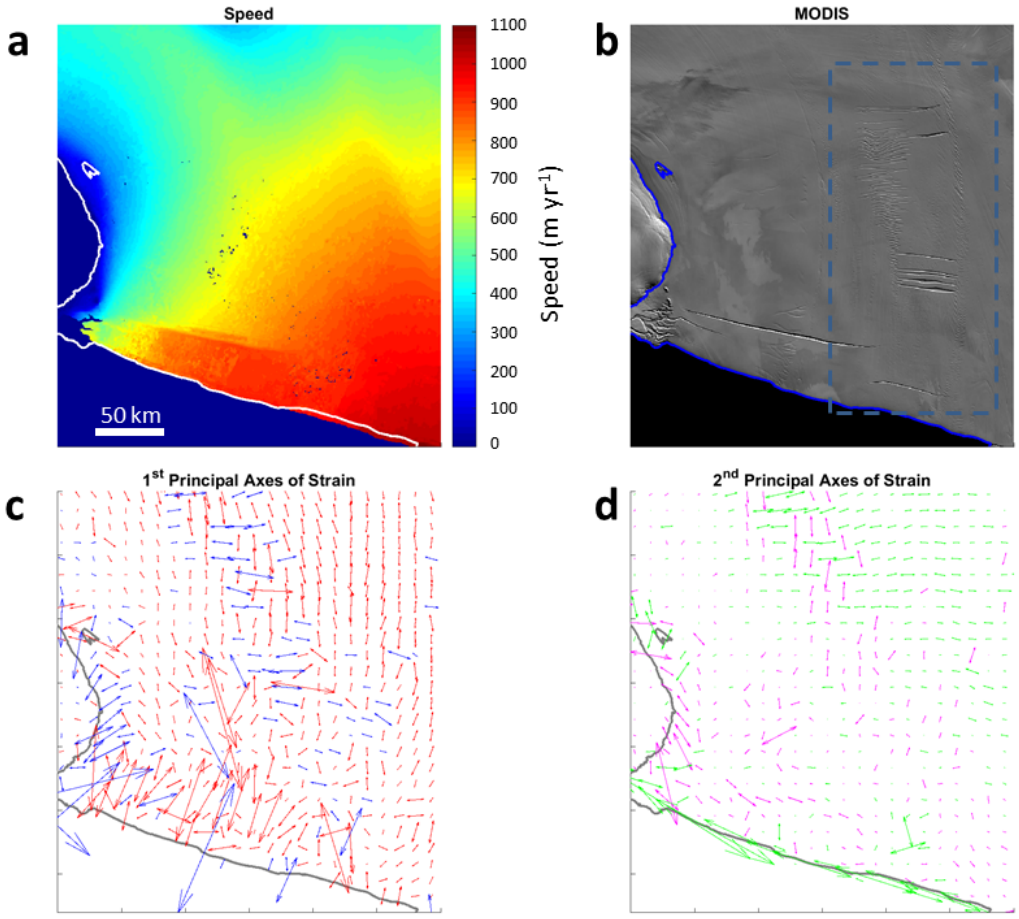

Figure 3.34: Plots showing quantities and details for the western section of the Ross Ice Shelf. (a) Unfiltered ice surface speed. (b) MODIS imagery with fracture or crevasse features present as the ice flows past an island on the lower boundary of the shelf and where inflow from a tributary ice stream merges with the flow near the upper boundary. Blue dashed box shows location of zoomed in MODIS image in Figure 3.35. (c) The 1st Principal Axis of Strain (red and blue vectors indicate positive and negative 1st Principal Strain Rates respectively). (d) The 2nd Principal Axis of Strain (magenta and green vectors indicate positive and negative 2nd Principal Strain Rates respectively). In each plot the grounding line, location of islands and the ice front are identified.

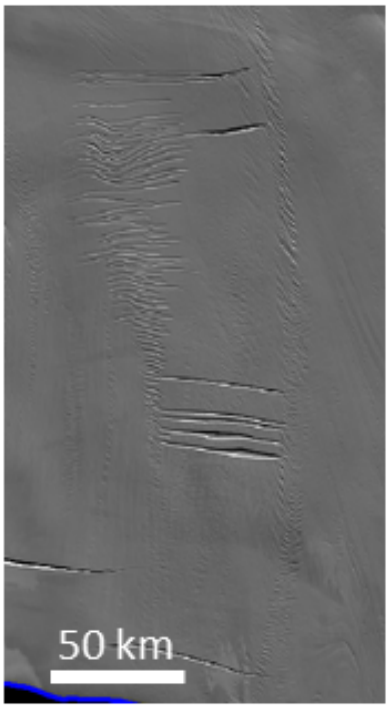

Figure 3.35: MODIS image for the Ross Ice Shelf, zoomed in on location of two along-flow bands of crevasses that are connected in places by larger crevasses. The extent of this image is defined in Figure 3.34b.

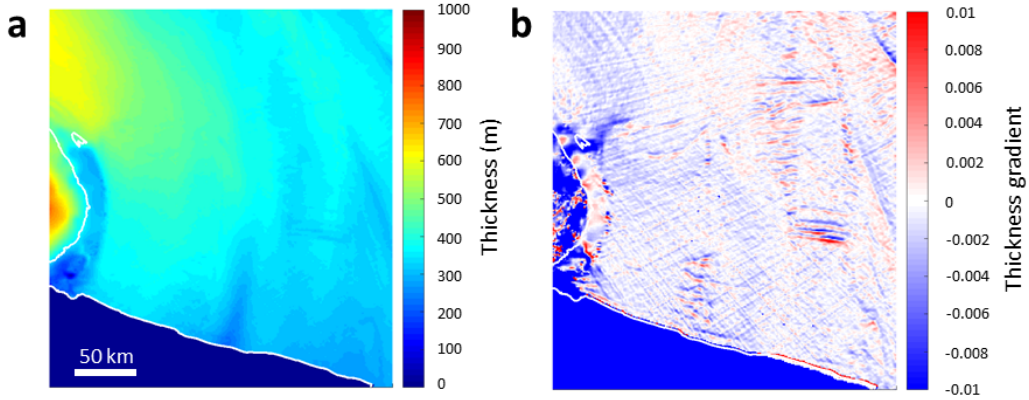

Figure 3.36: (a) Ice thickness and (b) ice-thickness gradient in direction of ice flow both for the western margin of the Ross Ice Shelf.

Summary: Dynamics associated with the 1st Principal Axis of Strain and 1st Principal Axis Strain Rate

From the majority of these examples it appears that often fractures are found in areas of high extensional strain and shear, where there are high rates of deformation, such as near ice-shelf margins or isolated pinning-points within the shelf. It is likely that the crevasses are first formed where there are high values of stress within the ice. Once these fractures are formed, the effective viscosity of the ice is altered and high strain rates can exist in these areas due to the reduced effective viscosity. These fractures are then advected by the ice-shelf flow and are associated with high strain. From the Ronne Ice Shelf margin with Berkner Island, there is evidence that suggests these crevasses can close up if the 1st Principal Strain Rate becomes negative.

As the fractures open and are advected towards the calving front, they form the location of potential iceberg-calving events. It is expected that an iceberg will break off once the stress within the shelf exceeds some critical value. A fracture will form when this critical stress is reached, breaking off a section of the shelf or linking together with other fractures to break off a larger section.

In the case of the Ross Ice Shelf, which is the largest ice shelf in Antarctica, fractures are formed away from areas of deformation past pinning-points and may instead result from convergent flow in the middle of the shelf. Here two sections of ice meet with different velocities, leading to shearing and deformation as they merge and the formation of fractures. Increased stretching and extension can occur near the ice front, where the ice-shelf flow begins to diverge, leading to further fracturing.

From these datasets, there appears to be no direct relation between the formation of crevasses near the calving front and the ice-shelf thickness at these locations. We have seen that for ice shelves with similar thicknesses at the calving front (e.g. Ross and Ronne) large fractures are found in some cases (Ross) but not in others (Ronne). There does however, appear to be a link between the ice-thickness gradient in the flow-direction and the location of crevasses, with ridges of alternating positive and negative thickness-gradient found in crevassed areas. Here it is likely that high extensional stresses have led to the formation of bands of thin ice perpendicular to the flow-direction, as the ice is stretched out in the along-flow direction. In these regions, fractures may then form as the thinner ice is less able to withstand the high strain. This would then lead to a series of parallel crevasses and alternating thickness gradients. In bands of thin and damaged ice, it is likely that further high strain rates will be obtained. It should be noted that care should be taken when assessing these thickness datasets as the presence of fractures

and crevasses may lead to the incorporation of errors and noise into the data. Therefore, before any definite conclusions can be made, thickness data with a higher spatial resolution in the area of these crevasses should be assessed to determine whether thinner ice is linked to crevasse formation.

From this assessment of the Principal Axes of Strain and Principal Strain Rate fields, it is not possible to determine whether the calving front is likely to advance or whether strain rates are likely to exceed a threshold leading to the calving of an iceberg. The rate of advance of the calving front will be considered further with the addition of some theoretical ideas in Chapter 4.

3.6.3 2nd Principal Axis of Strain and 2nd Principal Strain Rates

Throughout the majority of ice shelves, the ice flow is predominantly in one direction and the 1st Principal Strain Rate is positive as the extension and flow of the ice shelf is driven by the hydrostatic pressure gradient between the floating shelf and the ocean, which acts to effectively pull the ice shelf towards the ocean. Although this is broadly the case in the majority of situations, there may be areas where the 1st Principal Strain Rate is negative, such as where an ice shelf is being compressed against a stationary bedrock outcrop or island.

Ice shelves are often confined within embayments or pinned in place by islands or ice-rises. If we consider flow in a parallel-channel geometry, we might expect the flow to be aligned in the along-channel direction only, with slow flow near the channel boundaries and faster flow in the centre of the channel. This would lead to a shearing flow across the width of the channel. As demonstrated earlier for a shear flow, the 1st Principal Strain Rate is positive and the 2nd Principal Strain Rate negative, with the Principal Strain Axes aligned at 45° to the flow. The negative 2nd Principal Strain Rate corresponds to compression, which acts perpendicular to the 1st Principal Strain Rate. This compression is due to the lateral resistance to the flow generated by shear with slow flowing or stationary ice at the edges of the shelf. If there was no frictional resistance from the sides of the channel then a shear profile across the channel would not be established and the flow would be purely extensional with zero 2nd Principal Strain Rate values. Negative 2nd Principal Strain Rate is indicative of compression or shearing and therefore, as discussed in Chapter 2, acts to provide resistance to flow.

At the exit of the confinement there is a transition to positive 2nd Principal Strain Rates as the shelf is able to spread both in the direction of the main flow and transverse to this. This lateral spreading is due to the removal of resistance at the lateral bound-

aries and the presence of a lateral hydrostatic pressure gradient that drives the flow. For a parallel channel some lateral spreading of the shelf is expected just upstream of the exit, as along-flow extension is greatest in the centre of the channel at the exit, which induces thinning in the centre of the shelf and therefore flow in from the lateral boundaries.

Once this transition from negative to positive 2nd Principal Strain Rate occurs (with positive 1st Principal Strain Rate throughout), the shelf is spreading in all directions and no longer experiences shearing against any stationary boundaries such as those that generated resistance to flow while the shelf was confined. Instead resistance to flow may be generated by 'hoop stresses' within the shelf that act to oppose spreading of the shelf perpendicular to the flow direction.

3.7 Identifying Ice That Does Not Contribute to Buttressing

3.7.1 Passive Ice

Fürst et al. (2016) used the term 'passive ice' to define sections of an ice shelf that, if removed, would have no dynamic implications on the remaining ice flow and therefore must have no effect on buttressing. This passive ice was determined by first calculating the effective buttressing at each point in the shelf. This process was performed using a velocity and stress field from a computational model matched to observed velocities, from which internal stresses could be determined. The buttressing at a point within the ice shelf is determined by the difference between the depth-integrated stress exerted on the ice upstream of the point, in the presence of a ice shelf downstream, and the depth-integrated hydrostatic driving pressure at that point (which would be the stress exerted in the absence of a shelf downstream of that point). This difference is then normalized by the depth-integrated hydrostatic driving pressure (Fürst et al., 2016; Gudmundsson, 2013). This buttressing at any point within the shelf is defined to be

$$K = \frac{N_0 - \mathbf{n}.\bar{\boldsymbol{\sigma}}.\mathbf{n}}{N_0}, \tag{3.18}$$

$$\text{where} \quad N_0 = \frac{1}{2}\rho g' H. \tag{3.19}$$

Here $\mathbf{n}$ is the horizontal normal vector pointing in the direction of the buttressing, $\bar{\boldsymbol{\sigma}}$ is the vertically averaged stress tensor $\boldsymbol{\sigma} = -P\boldsymbol{I} + 2\mu\boldsymbol{e}$, as used in the derivation of the fundamental equation of ice flow in Chapter 2. N_0 is the vertically averaged hydrostatic

pressure, with ρ the ice density, ρ_{w} the ocean density, g' the reduced acceleration due to gravity

$$g' = \left(\frac{\rho_w - \rho}{\rho_w}\right) g. \tag{3.20}$$

and H the shelf thickness.

This method considers the stress field in the simple case in which the point being considered is at an imaginary calving front, with planar flow perpendicular to the front and no transverse gradients in thickness, and compares it to the modelled stress field produced with the remaining ice shelf further downstream. Differences between the two stresses are then due to the presence of the ice shelf downstream, which may change if part of the shelf is removed. In a situation with no shelf downstream of the point being considered, and the flow aligned perpendicular to the ice front (in the x-direction) with no shear, then we have no buttressing and the flow would be determined by

$$4\frac{\partial}{\partial x}\left(\mu H \frac{\partial u}{\partial x}\right) = \rho g' H \frac{\partial H}{\partial x}, \tag{3.21}$$

corresponding to the extension-only regime considered in the previous chapter. However, when an ice shelf is present, resistance may be generated by shear or hoop stresses.

The maximum buttressing at a point is obtained when the normal stress is aligned in the direction of the Principal Axis of Strain corresponding to the smallest Principal Strain Rate. This is because K is largest when $\mathbf{n}.\boldsymbol{\sigma}.\mathbf{n}$ is minimised (it can be negative when there is compression in the normal direction).

Fürst et al. (2016) then used contours to split the ice shelf into regions with the same maximum buttressing. If the maximum buttressing is in the direction of the smallest Principal Strain Rate, then contours of maximum buttressing must be aligned along the Principal Strain Axes in the direction of the largest Principal Strain Rate. To test which of these contours denotes the boundary of the passive ice, sections of the ice shelf are removed in the computational model along the maximum buttressing contours. If there is no substantial change in the flow of the ice shelf then the removed section is considered passive. This process is repeated, first removing the smallest area of floating ice, until the boundary of passive ice is found when the ice flow changes considerably after a section is removed.

In this work Fürst et al. (2016) rely on a model output to determine which areas are Passive Ice. However, I hypothesis that given error-free/smooth data of sufficient resolution it should be possible to determine those areas that are contributing to buttressing

and in turn those which provide no contribution to the buttressing.

3.7.2 Compressive Arch

Doake et al. (1998) used the idea of a curve within an ice shelf referred to as a 'compressive arch' to explain the collapse of the Larsen A ice shelf in 1995 and assess the stability of the Larsen B Ice Shelf prior to its subsequent collapse in 2002. The curve, referred to as the compressive arch, identifies the boundary within an ice shelf upstream of which the 2nd Principal Axis of Strain is always negative. Here it is assumed that the 1st Principal Axis of Strain is positive throughout the whole shelf, and hence the 'compressive arch' identifies the curve across which there is a transition from negative (compressive) 2nd Principal Strain Rate to positive 1st and 2nd Principal Strain Rates. Doake et al. (1998) hypothesised that the location of this boundary or 'compressive arch' and the shelf as a whole would be stable to a calving event downstream of the compressive arch. However, if the arch was breached by a calving event then the calving front would undergo irreversible retreat.

This theory was tested by Doake et al. (1998) using model simulations of the Larsen A and B ice shelves to determine the 1st and 2nd Principal Axes of Strain. They observed that in the case of Larsen A, the compressive arch was located closely behind the initial calving front in 1989. After this, subsequent calving events moved the calving front back behind the compressive arch, before the rapid collapse of the ice shelf during 1995. Conversely, in this time period the calving front for Larsen B remained downstream of the compressive arch, despite a retreat of the calving front.

Following this study by Doake et al. (1998), the Larsen B Ice Shelf collapsed rapidly in 2002. It should be noted that there are numerous hypotheses that endeavour to explain the collapse of the Larsen B Ice Shelf, which include both forcing from atmospheric (Scambos et al., 2003; van den Broeke, 2005) and oceanic (Holland et al., 2015) effects in addition to ice-shelf dynamics.

As with the work of Fürst et al. (2016), the analysis of Doake et al. (1998) was undertaken using model output, however it should be possible to make a similar assessment from velocity field data, such as that gathered by Rignot et al. (2011b). I now apply the ideas of passive ice and compressive arches to an analysis of some Antarctic ice shelves, using the data obtained through calculation of the 2nd Principal Axis of Strain value and its orientation.

3.7.3 Analysing Buttressing using Principal Strain Rates

Amery Ice Shelf

The value of the 2nd Principal Strain Rate and the orientation of the 2nd Principal Axis of Strain can be seen in Figures 3.37b and 3.37d for the Amery Ice Shelf. Here we observe that along the ice-shelf margins and upstream the 2nd Principal Strain Rate is mainly negative. However, there is a transition at the exit where the 2nd Principal Strain Rate becomes positive in addition to the positive 1st Principal Strain Rate. This area of positive 2nd Principal Strain Rate occurs mainly once the shelf has left the confines of the embayment in which it is situated. By assessing the orientation of the Principal Axes of Strain, as shown in Figures 3.37c and 3.37d, we see that as the ice approaches the calving front the 2nd Principal Axis of Strain becomes orientated perpendicular to the calving front, aligned in the flow direction, while the 1st Principal Axis of Strain is aligned parallel to the calving front. This indicates that here the lateral spreading of the shelf is the dominant dynamical effect once the shelf leaves the lateral confinement, but there is also extension in the along-channel direction.

Where there are negative 2nd Principal Strain Rates along the channel margins this is due to shearing and the local resistance created by ice flow past stationary grounded ice. This resistance can be transferred upstream to provide buttressing to the flow.

Once there is a transition to both positive 1st and 2nd Principal Strain Rate there is no further resistance generated by shearing. This boundary between negative and positive 2nd Principal Strain Rate identifies the compressive arch proposed by Doake et al. (1998), and is highlighted in the Figure 3.37 by a dashed black curve. Here we can see that this region extends upstream a considerable distance, approximately 75 km. This is a larger region than might have been expected given the slowly diverging geometry of the channel and the distance to the calving front, but indicates that there is lateral spreading of the shelf as the channel slowly widens, and the presence of a region in the centre of the shelf where there is no shearing.

Larsen C Ice Shelf

Figure 3.38 provides plots of the 2nd Principal Axis of Strain and the 2nd Principal Strain Rate for the Larsen C Ice Shelf. This is a large ice shelf fed by multiple glaciers and ice streams around the embayment, and therefore differs from the channel-like geometry previously considered in the case of Amery Ice Shelf. From Figure 3.38b it is clear that between the inflows from the tributary ice streams there are areas of negative 2nd Principal Strain Rate, as the flow is resisted by shearing with slower flow in the surrounding shelf. In the central section of each of these tributaries both the 1st and 2nd Principal

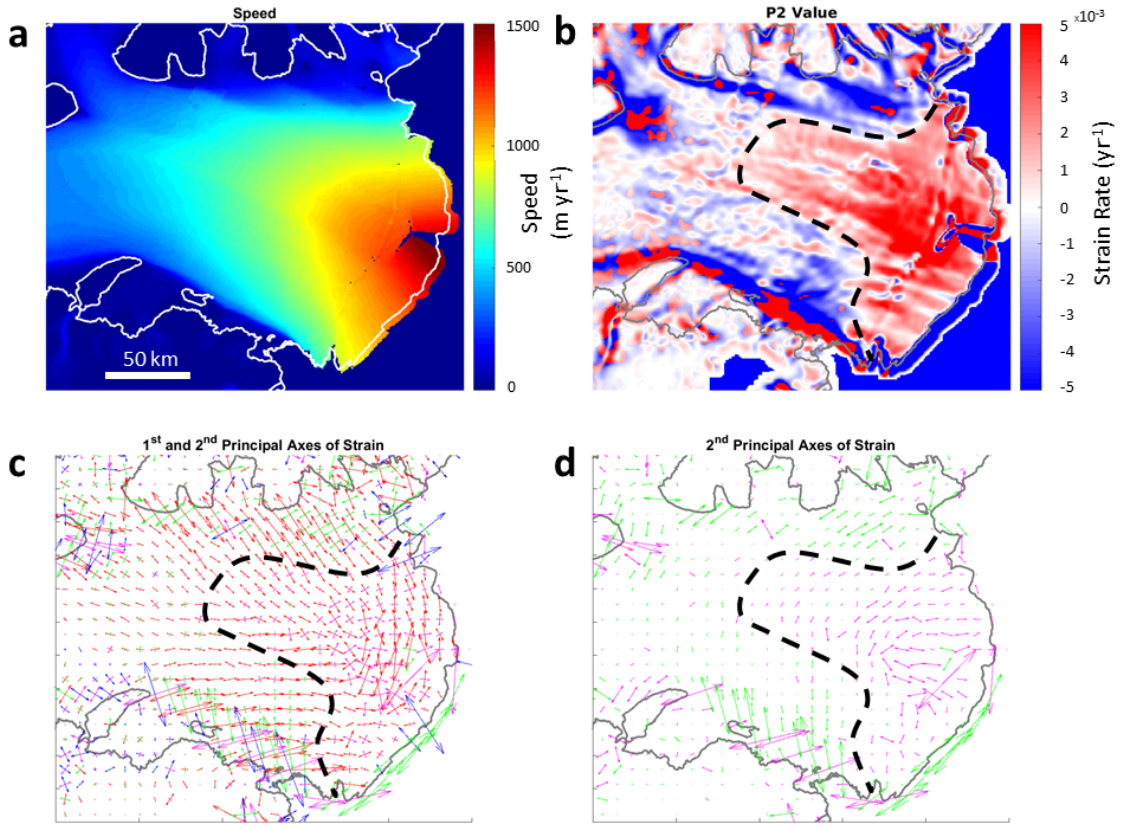

Figure 3.37: Plots showing quantities and details near the ice-shelf calving front of Amery Ice Shelf. (a) Unfiltered ice surface speed. (b) Map showing value of 2nd Principal Strain Rate. (c) The 1st and 2nd Principal Axes of Strain (red and blue vectors indicate positive and negative 1st Principal Strain Rates respectively, while magenta and green vectors indicate positive and negative 2nd Principal Strain Rates respectively). (d) The 2nd Principal Axis of Strain (magenta and green vectors indicate positive and negative 2nd Principal Strain Rates respectively). In each plot the grounding line, location of islands and the ice front are identified. The black dashed curve indicates the approximate position of the compressive arch.

Strain Rate are positive, which suggests that the shelf is spreading in both the along-flow and transverse-to-flow directions.

Both the 1st and 2nd Principal Axes of Strain are shown in Figure 3.38c, with the magnitude of the Principal Strain Rates denoted by the length of the axes. From the magnitude of the vectors it is evident that throughout the majority of the shelf the 1st Principal Strain Rate dominates the flow dynamics. However, there is an area near the centre of the calving front where the 2nd Principal Strain Rate starts to become comparable. This region can be seen more clearly in Figure 3.38d, with high 2nd Principal Strain Rates found near the centre of the calving front. Here the axes appear to have no preferred orientation and indicates that the shelf is spreading both along-flow and laterally as the shelf exits the embayment.

Negative 1st and 2nd Principal Strain Rates are observed close to the island at the southern end of the calving front (Gipps Ice Rise). This suggests that there is compression of material against this pinning point and that it is crucial for providing buttressing to the rest of the shelf.

The approximate location of the compressive arch has been identified by a dashed black line. Here it is evident that there is a large section of the shelf where the ice is spreading in all directions and therefore not providing any resistance to flow via shear stress. The shape of the compressive arch mirrors the shape of the Larsen C embayment and suggests that the interaction between the tributary inflows as they enter the main body of the shelf is crucial for providing resistance to flow.

Ross Ice Shelf

Plots for the large Ross Ice Shelf are given in Figure 3.39. Here there appears to be a complex pattern of positive and negative 2nd Principal Strain Rates (Fig. 3.39b), with lots of relatively small-scale variation.

On the large scale, at the calving front, there appears to be an area of mainly positive 2nd Principal Strain Rate, which spans the width of the shelf and continues upstream for approximately 100 km. This region can be identified in Figures 3.39c and 3.39d, where the orientation of the 2nd Principal Axis of Strain is aligned parallel to the calving front, implying that the shelf is spreading laterally in this area. This may be due to the lack of pinning points downstream of this location. The shelf is effectively unconstrained laterally in the final 100 km as it flows towards the ocean. The positive 1st and 2nd Principal Strain Rates imply that this section of the ice shelf contributes nothing to the buttressing of ice upstream via shearing. The boundary of this spreading region provides

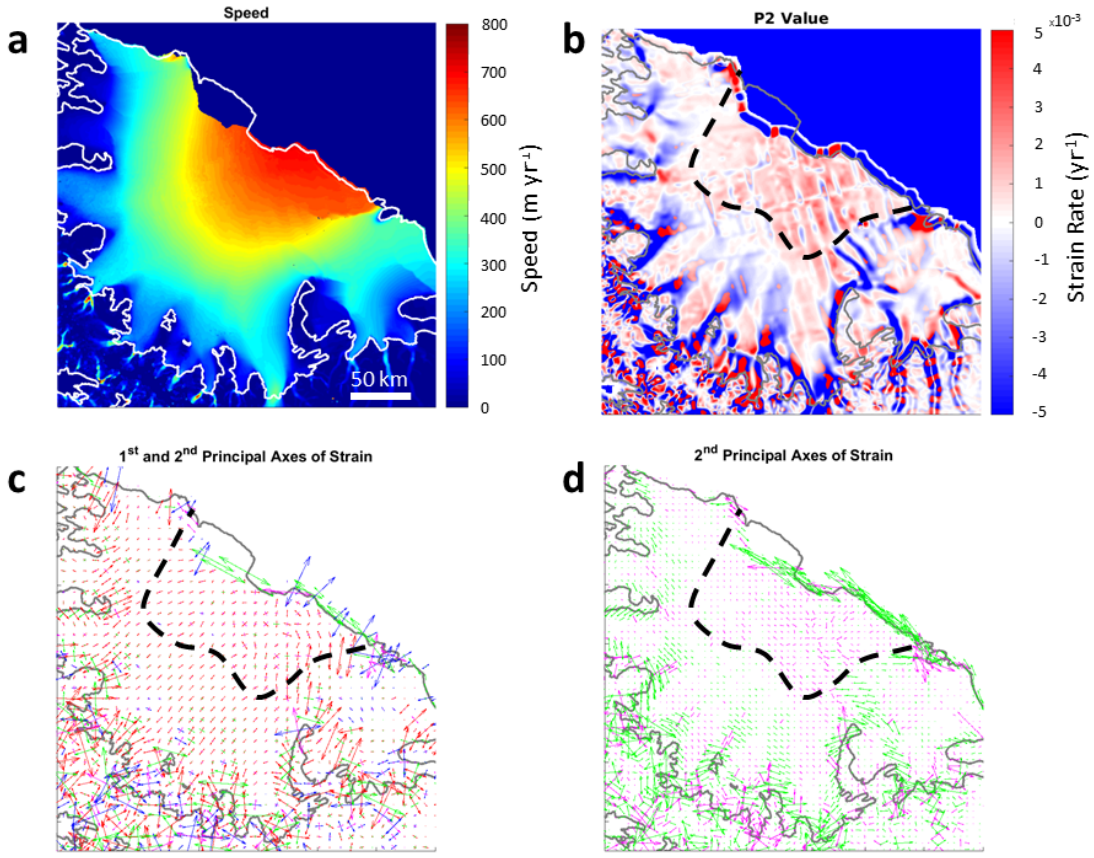

Figure 3.38: Plots showing quantities and details for the Larsen C Ice Shelf. (a) Unfiltered ice surface speed. (b) Map showing value of 2nd Principal Axis of Strain. (c) The 1st and 2nd Principal Axes of Strain (red and blue vectors indicate positive and negative 1st Principal Strain Rates respectively, while magenta and green vectors indicate positive and negative 2nd Principal Strain Rates respectively). (d) The 2nd Principal Axis of Strain (magenta and green vectors indicate positive and negative 2nd Principal Strain Rates respectively). In each plot the grounding line, location of islands and the ice front are identified. The black dashed curve indicates the approximate position of the compressive arch.

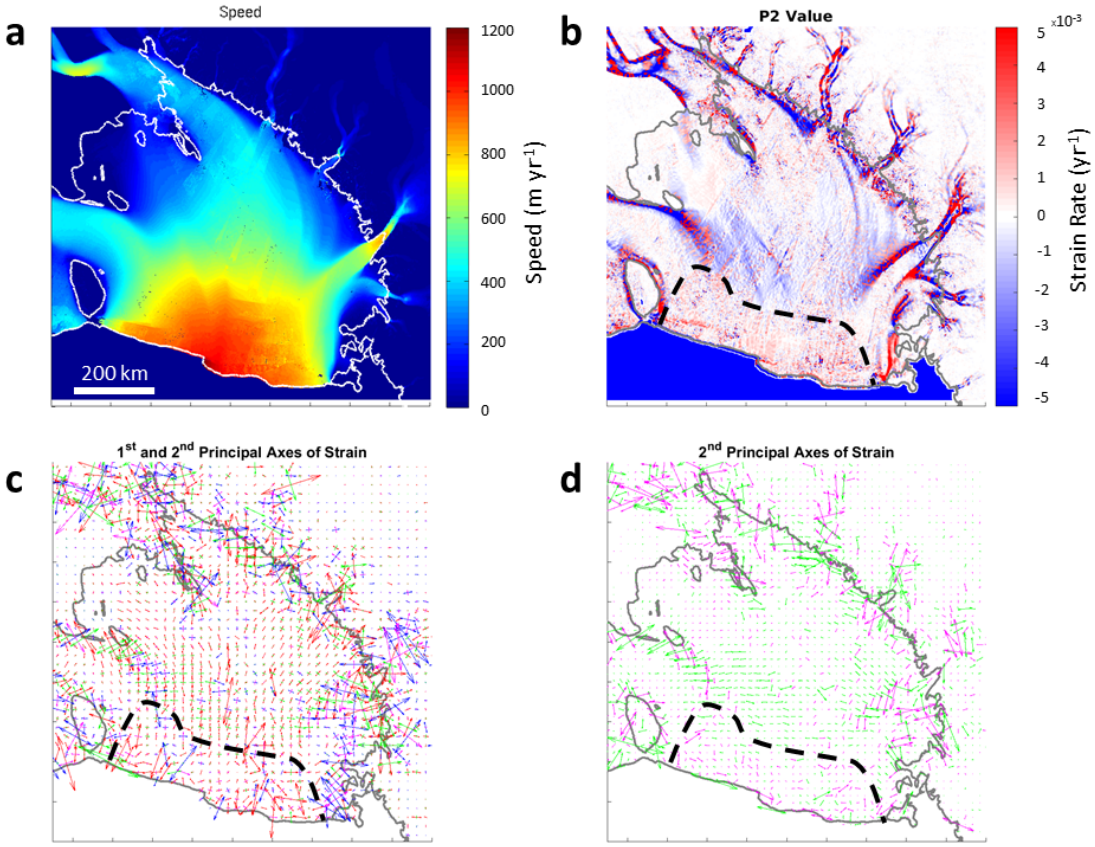

Figure 3.39: Plots showing quantities and details near the ice-shelf for the Ross Ice Shelf. (a) Unfiltered ice surface speed. (b) Map showing value of 2nd Principal Axis of Strain. (c) The 1st and 2nd Principal Axes of Strain (red and blue vectors indicate positive and negative 1st Principal Strain Rates respectively, while magenta and green vectors indicate positive and negative 2nd Principal Strain Rates respectively). (d) The 2nd Principal Axis of Strain (magenta and green vectors indicate positive and negative 2nd Principal Strain Rates respectively). In each plot the grounding line, location of islands and the ice front are identified. The black dashed curve indicates the approximate position of the compressive arch.

the location of the compressive arch. Again due to the abundance of small-scale variations, it is difficult to determine an exact location for the compressive arch. However, it indicates that as the shelf widens near the calving front there is little resistance to flow provided by shear stresses.

Further upstream, the 2nd Principal Strain Rate (plotted in Figure 3.39d), is large and negative with the 2nd Principal Axis of Strain orientated perpendicular to the flow direction. This suggests that this region of ice may provide buttressing for ice further upstream. If this area is assessed in relation to the speed of ice in the area (Fig. 3.39a), it is clear that ice is converging from multiple tributary flows within the shelf. Therefore, as these sections of relatively fast flow meet and are funnelled towards the calving front, there is likely to be some viscous deformation thereby generating resistance to flow.

Ronne Ice Shelf

A similar style of dynamics to the Ross Ice Shelf is observed for the Ronne Ice Shelf in Figure 3.40. Again near the calving front, positive 2nd Principal Strain Rates are present, spanning the width of the shelf and 100 km upstream from the calving front. In this region the shelf is spreading both in the along-flow and transverse-to-flow directions, as illustrated by the 1st and 2nd Principal Axes of Strain and Principal Strain Rates in Figure 3.40c. It is possible to determine an approximate location for the coompressive arch, as shown in Figure 3.40 as a dashed black curve. Again this has a similar structure to the compressive arch that was determined for Ross Ice Shelf, with the compressive arch extending upstream in the direction of the prominent inflow from the Evans Ice Stream (and in the case of Ross the inflow from the tributary to the south of Roosevelt Island).

Along the left (west) margin of the shelf there is an area of pronounced negative 2nd Principal Strain Rate (Fig. 3.40b). This is likely to be due to the high shear rates found in this margin, where fast flowing ice moves past stationary grounded ice. This indicates that there is local resistance to flow generated here. On the left (west) of the plot in Figure 3.40 there is an inflow of ice from the Evans Ice Stream. As this ice flows into the shelf, there are positive 2nd Principal Strain Rates in addition to the positive 1st Principal Strain Rates values, which implies that the ice is spreading both along-flow and laterally as it enters the main body of the shelf.

In the centre of the ice shelf there is an area of negative 2nd Principal Strain Rates, where ice flow from the two sides of the ice shelf converges. In a similar manner to the negative 2nd Principal Strain Rates observed on the Ross Ice Shelf, here the 2nd Principal Axis of Strain is orientated perpendicular to the flow direction, indicating compression and therefore resistance generated between the two sections of the flow.

3.7.4 Hoop Stresses

In Chapter 2, we considered the fundamental equations that govern the flow of an ice shelf with uniform flow in the vertical. Whilst doing so, it was highlighted that resistance to the flow of the shelf can be produced by compression or shearing within the shelf, or hoop stresses when the shelf spreads radially. From consideration of the values of the Principal Strain Rates it is possible to determine whether compression or shear are present in the flow, as detailed above. When both Principal Strain Rates are positive, there is no contribution to buttressing from compression or shear, but there may be a contribution from hoop stresses. The force-balance equation for an axisymmetric radial

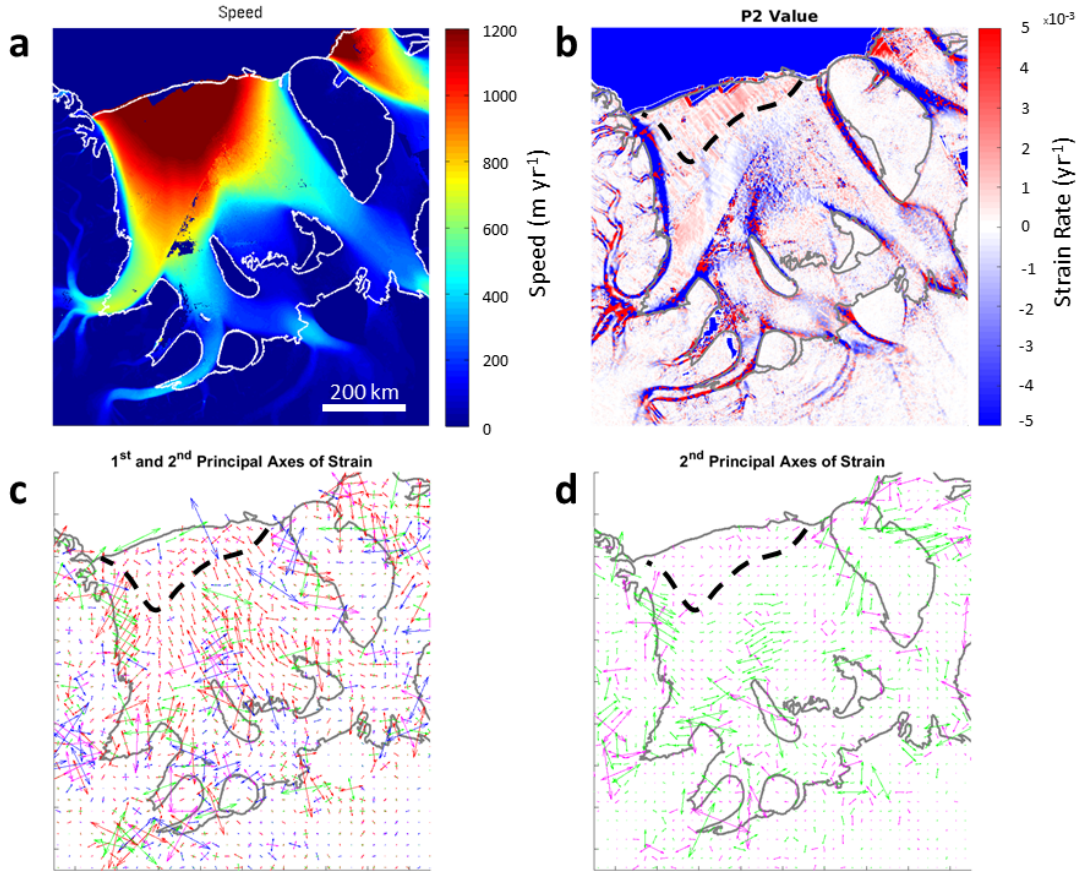

Figure 3.40: Plots showing quantities and details near the ice-shelf for the Ronne Ice Shelf. (a) Unfiltered ice surface speed. (b) Map showing value of 2nd Principal Axis of Strain. (c) The 1st and 2nd Principal Axes of Strain (red and blue vectors indicate positive and negative 1st Principal Strain Rates respectively, while magenta and green vectors indicate positive and negative 2nd Principal Strain Rates respectively). (d) The 2nd Principal Axis of Strain (magenta and green vectors indicate positive and negative 2nd Principal Strain Rates respectively)). In each plot the grounding line, location of islands and the ice front are identified. The black dashed curve indicates the approximate position of the compressive arch.

flow, as shown in equation 2.36 in Chapter 2, takes the form

$$\frac{\partial}{\partial r}\left(\mu H\left(2\frac{\partial u_r}{\partial r}+\frac{u_r}{r}\right)\right)+\mu H\frac{\partial}{\partial r}\left(\frac{u_r}{r}\right)=\frac{\rho g'}{2}H\frac{\partial H}{\partial r}. \tag{3.22}$$

As identified earlier, hoop stresses provide no positive contribution to buttressing in locations where

$$\frac{\partial}{\partial r}\left(\frac{u_r}{r}\right)\geq 0. \tag{3.23}$$

This partial derivative can be split into two parts allowing an insight into the dynamics of the flow

$$\frac{\partial}{\partial r}\left(\frac{u_r}{r}\right)=\frac{1}{r}\left(\frac{\partial u_r}{\partial r}-\frac{u_r}{r}\right), \tag{3.24}$$

where the first term in the brackets is the radial extension and the second term is the azimuthal extension. Therefore, it is clear that a positive contribution to buttressing is achieved when the azimuthal extension is greater than the radial extension.

To determine whether hoop stresses are contributing positively or negatively to buttressing within the shelf I calculate $\partial/\partial r(u_r/r)$ at each point in the domain. However, in order to determine the total contribution to buttressing from hoop stresses, these hoop stress terms should be integrated back to the grounding line. A similar approach was taken by Pegler and Worster (2012) when considering an idealized system with an axisymmetric radially spreading shelf. In that work the hoop stress was integrated from the nose or calving front of the current to the grounding line, giving a total buttressing from hoop stresses. Here I consider only the potential contribution to buttressing at each point and whether it is making a positive or negative contribution. In these geophysical cases, the shelf geometry is complex and therefore this idealized approach needs to be adapted for a Cartesian coordinate system, partly by considering the contribution for hoop stresses at each point within the shelf.

At each point in the velocity field I consider a coordinate system aligned so that the r-coordinate points in the flow direction and denote u_r as the flow in the r-direction, which is given by the flow speed at that point. I define r_c as the radius of curvature at each point. This is calculated from the angle of divergence between neighbouring velocity vectors. At each point in the original grid, angles of divergence are calculated between the velocity vectors in the shifted grid (same shifted grid as presented earlier for calculating strain rates). The largest angle of divergence (calculated from the divergence of the velocity vectors between neighbouring points on the shifted grid) is chosen to represent the divergence at the original grid-point, and corresponds to the shortest possible radius of curvature. Flow throughout most of the shelf is likely to be close to uniform with only small values of divergence. Therefore it is likely that the largest change in

divergence angle will be for those sets of vectors with the largest angles of divergence.

Figure 3.41 shows two diagrams detailing how the angles of divergence and corresponding radius of curvature are calculated, for point X in the original grid. In the first diagram the angle of divergence is calculated between vectors at shifted-grid points B and C. This process is repeated for: A-B, C-D and D-A, with the largest angle being used in the following calculations. The angle of divergence is given by

$$\theta = \left| \arctan\left(\frac{u_i}{v_i}\right) - \arctan\left(\frac{u_j}{v_j}\right) \right|, \tag{3.25}$$

where u and v denote the x and y velocity components respectively (in the Cartesian coordinate system) and subscripts i and j indicate the two grid points being considered (i, j = A, B, C, D). The corresponding radius of curvature is then estimated by

$$r_c \approx \frac{\frac{1}{2}\Delta x}{\sin\left(\frac{\theta}{2}\right)}, \tag{3.26}$$

where $(1/2)\Delta x = 225$ m is half the spacing between the grid points, as shown in the second diagram. As the angles of divergence in the geophysical examples are likely to be small, this approximation for the radius of curvature is likely to provide an accurate estimate. The radius of curvature is then used along with the speed at each location to define the quantity u_r/r_c. Spatial derivatives of this quantity are then taken in the Cartesian coordinate system and projected in the direction of flow at each point to give

$$\frac{\partial}{\partial r}\left(\frac{u_r}{r_c}\right) = \hat{\mathbf{u}}.\nabla\left(\frac{|\mathbf{u}|}{r_c}\right) = \hat{u}\frac{\partial}{\partial x}\left(\frac{|\mathbf{u}|}{r_c}\right) + \hat{v}\frac{\partial}{\partial y}\left(\frac{|\mathbf{u}|}{r_c}\right), \tag{3.27}$$

where $\mathbf{u}$ is the velocity vector in the Cartesian coordinate system. This quantity determines whether there is a positive or negative contribution to buttressing within the shelf: negative $\partial/\partial r(u_r/r_c)$ leads to positive buttressing; positive $\partial/\partial r(u_r/r_c)$ leads to negative buttressing, which acts to pull the ice downstream. In the following section, this methodology is applied to three basic test examples where the flow is divergent. However, when applied to geophysical data, in additional to calculating the sign of the hoop stress, it must also be ensured that the flow is divergent in these locations where a hoop stress is calculated. This is because a positive contribution to buttressing from a hoop stress can only arise when the flow is divergent. For a convergent flow, local resistance to ice flow is generated by compression, which will be identified by negative 1$^{\text{st}}$ and/or 2$^{\text{nd}}$ Principal Strain Rate. Therefore a mask is applied to the hoop-stress buttressing data, with areas of convergent flow represented by zero values of hoop stress.

An analysis of the variation in the flow angle for Antarctic ice flow was undertaken by

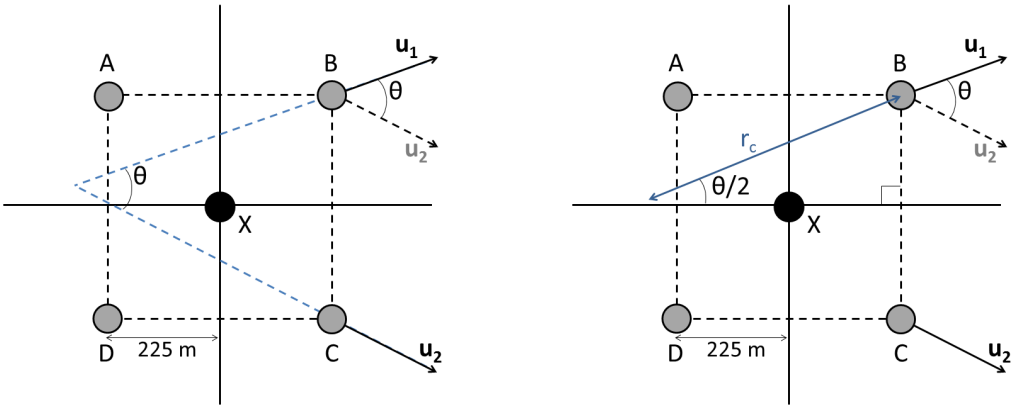

(a) (b)

Figure 3.41: Schematic detailing the methodology for calculating: (a) the angle of divergence, θ; and (b) the radius of curvature, r_c, for two velocity vectors at shifted-grid points B and C. This is applied to the four sets of vectors about the original-grid point X; A-B, B-C, C-D, D-A.

Ng (2015) in which a measure of convergence/divergence was used to investigate the structure of ice flow across the Antarctic Ice Sheet. In this work, regions of different ice flow could be determined by the pattern created when spatial derivatives of the flow angle were taken. This measure of convergence/divergence was denoted by C, with $C = \partial\theta/\partial n$, and θ the flow angle at each grid point. Here n is pointing left-perpendicular to the flow. Regions with relatively slow ice flow (< 20 m yr^{-1}) where said to be 'chaos regions', due to the large variations in C on small spatial scales, of the order of several kilometres or less. Furthermore, the term 'streaming region' identified areas where the value of C varies over much longer distances and the ice flow was greater than 20 m yr^{-1}. For the ice shelves considered in this work, the ice flow is much greater than 20 m yr^{-1} and therefore these areas would be considered streaming regions. The methodology used here to determine the sign of the hoop stress differs from that of Ng (2015), however it is still concerned with the change in flow angle throughout the shelf.

Examples

Below I present some idealized flows, which are used to demonstrate typical flow fields from a point at $x = 0$, $y = 0$ and the sign of the hoop stress that arises from them. Each example is calculated for a 10×10 square region, with unit grid cells. Central differencing is used to calculate the divergence and hence is presented in a 8×8 grid, the angle of divergence and radius of curvature are also calculated on the 8×8 grid. The $\partial/\partial r(u_r/r_c)$ term is calculated (as outlined above) using the radius of curvature and central differences and is therefore given on a 6×6 grid, representing the values in the 6×6 square at the centre of the original 10×10 grid.

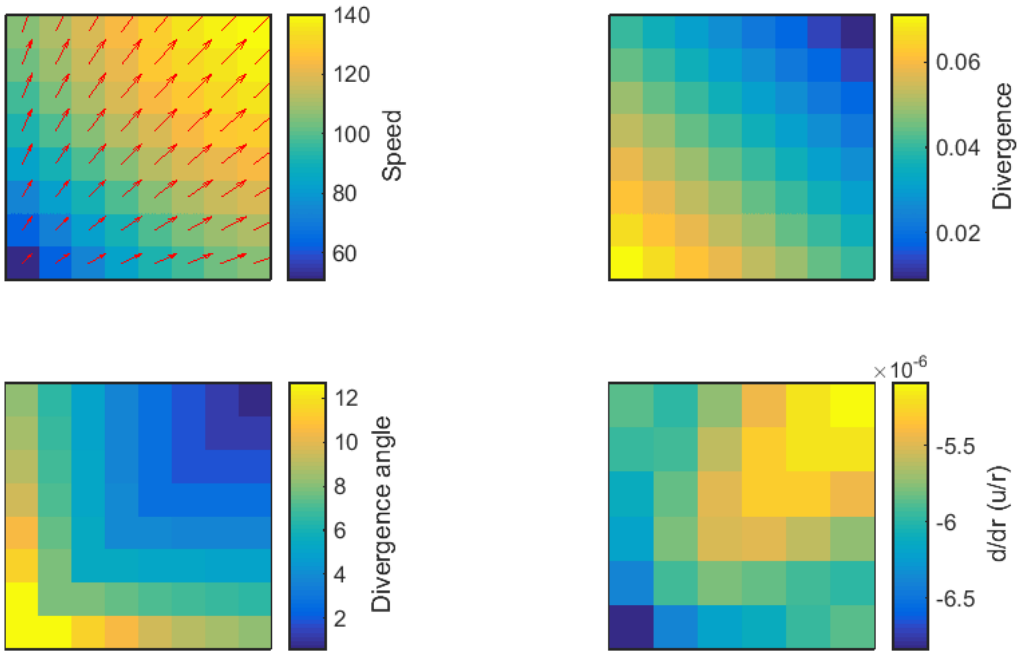

Figure 3.42: Example 1

Example 1

In this case the flow is given by

$$u = 100 - (10 - x)^2, \tag{3.28}$$

$$v = 100 - (10 - y)^2, \tag{3.29}$$

with u the velocity in the x-direction and v the y-direction component. For this flow, the speed, divergence, angle of divergence (θ) and $\partial/\partial r(u_r/r_c)$ are given in Figure 3.42. Here we observe the flow is from the lower left corner predominantly diagonally across the region, accelerating in the flow direction. The divergence and divergence angle are reduced diagonally across the square. This leads to negative values of $\partial/\partial r(u_r/r_c)$ throughout the area and hence a positive contribution to buttressing from the hoop stress.

Example 2

Here the flow is given by

$$u = x^2, \tag{3.30}$$

$$v = y^2. \tag{3.31}$$

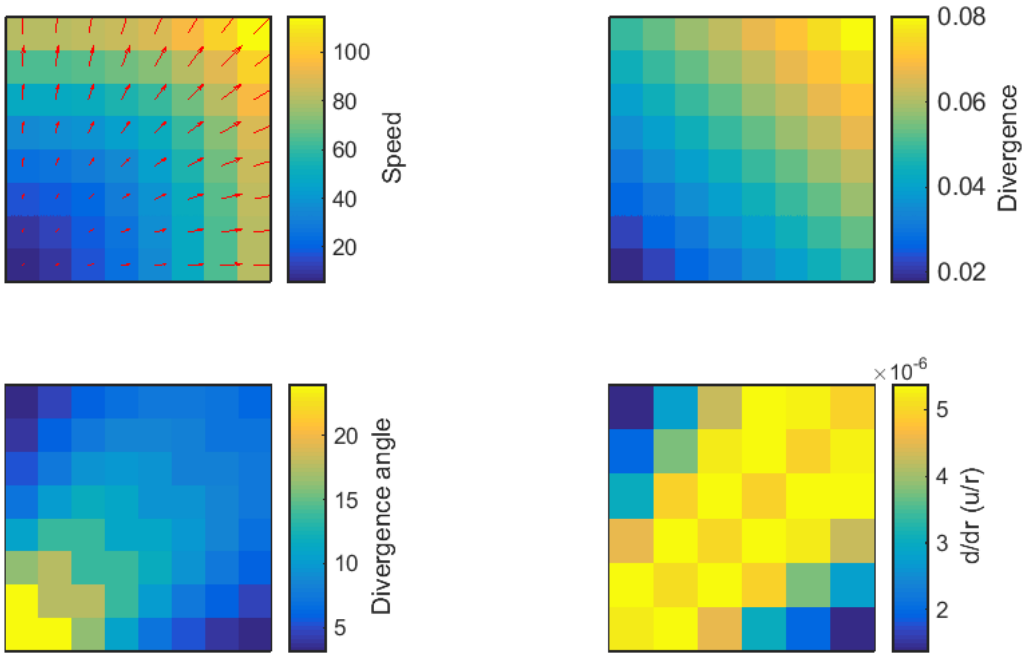

Figure 3.43: Example 2

The corresponding plots for this flow are given in Figure 3.43. In a similar manner to the previous example, the flow is predominantly from the lower left corner diagonally across the square, and accelerating in the flow direction. However, in this case the divergence of the flow is increasing in the flow direction, while the angle of divergence is decreasing, suggesting that the increase in divergence is due to radial extension. This flow leads to positive $\partial/\partial r(u_r/r_c)$ throughout the region, with similar values found along the diagonals. Therefore, the hoop stresses in this region are making a negative contribution to the buttressing and act to pull the fluid in the flow direction.

Example 3

For the third example the flow is

$$u = 200 + (x-5)^3, \tag{3.32}$$

$$v = 200 + (y-5)^3. \tag{3.33}$$

In this case there is a plateau in the velocity field in the centre of the domain, which corresponds to an area of zero divergence and zero divergence angle, as shown in Figure 3.44. This velocity field leads to a varying sign for the hoop stress, initially negative in the lower left corner, corresponding to positive buttressing, and then positive hoop stress in the upper right corner, corresponding to negative buttressing.

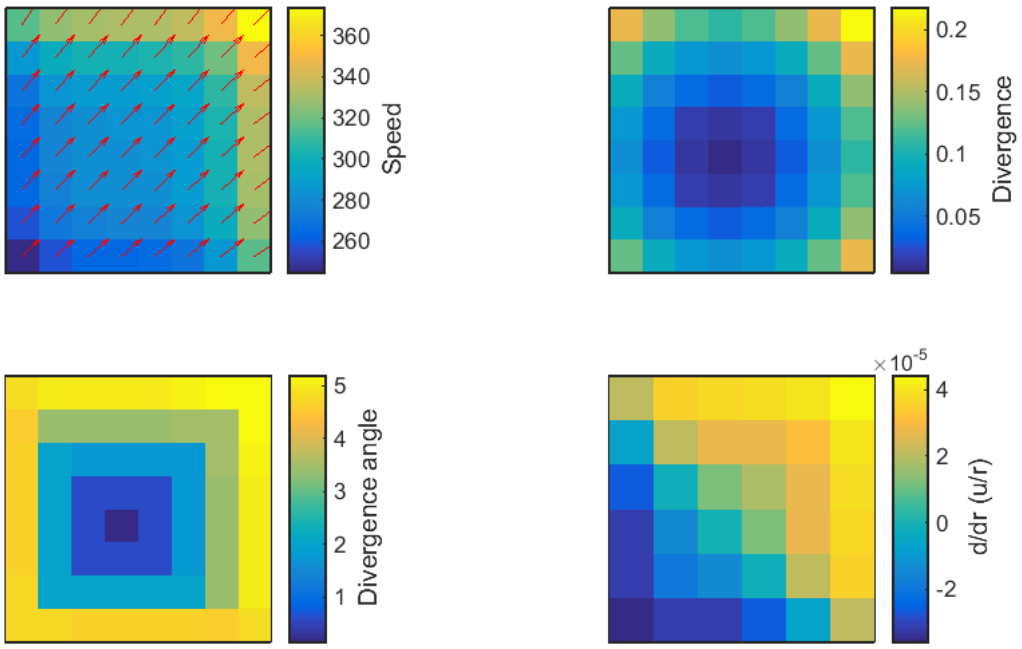

Figure 3.44: Example 3

3.7.5 Geophysical examples: $\partial/\partial r(u_r/r_c)$

The methodology outlined in the previous section was used to assess the sign of the hoop stresses within Antarctic ice shelves, using the ice-surface velocity dataset (Rignot et al., 2011b). As earlier, a low-pass Gaussian filter was applied to the data. However in this case, the range and standard deviation of the filter was increased to 27 km (60 grid points) and 5.4 km (12 grid points) respectively. This was so that the hoop stresses associated with the large-scale dynamics could be assessed, rather than small variations in the velocity field producing a noisy data field with small-scale variation in divergence angle.

Plots showing the value of $\partial/\partial r(u_r/r_c)$ for Amery and Larsen C ice shelves can be seen in Figure 3.45. Here we observe that in both cases the values range between -1×10^{-6} and 1×10^{-6} m^{-1} yr^{-1}. For the final downstream third of Amery Ice Shelf, the ice has a typical thickness of 400 m and a typical viscosity of 2.42×10^{14} Pa s (at -10°C), which implies a maximum hoop stress in this region of 3 kPa. For Larsen C ice shelf, with a typical thickness of 275 m and viscosity 2.02×10^{14} Pa s (at 0°) the maximum hoop stress, corresponding to a $\partial/\partial r(u_r/r_c)$ value of 1×10^{-6} m^{-1} yr^{-1}, is 1.8 kPa. These values of stress are much less than those that are likely to cause fracturing or crevasse-formation, which are of the order 100 kPa (Vaughan, 1993). These hoop stresses may appear to be insignificant, but the integrated hoop stress across the entire shelf may

contribute significantly to the buttressing transferred across the grounding line. In the case of Amery Ice Shelf, if we assume an average value of the partial derivative at every point in the shelf of -1×10^{-8} m^{-1} yr^{-1}, viscosity corresponding to ice -10°C, an average ice thickness of 400 m and an ice-shelf length of 500 km then the total contribution to buttressing from hoop stresses at the grounding line would be of the order 10^{12} kPa. This is probably an overestimation of the total buttressing from hoop stresses as the average value of the partial derivative is likely to be less that -1×10^{-8} m^{-1} yr^{-1}. However, this does highlight the potentially large contribution that could be made by hoop stresses. It also indicates that although the major contribution to buttressing may be from shear stresses, in some areas there may be little shearing and hoop stresses provide a substantial contribution to buttressing.

For Amery Ice Shelf, the upstream section of the shelf contains low values of the partial derivative $\partial/\partial r(u_r/r_c)$, but there are some small-scale features where there is a change in sign of the partial derivative in the along-flow direction. One particularly interesting feature is the change in sign that occurs as the shelf passes an ice rise. This is marked as location (1) in Figure 3.45a. Moving with the ice flow, there is initially a negative value of the partial derivative, implying there is positive buttressing generated from hoop stresses here. However, there is then a transition to positive values, as the ice passes the ice rise and spreads more rapidly. Earlier it was observed that positive buttressing was generated via hoop stresses when the partial derivative was negative, and this occurs when the azimuthal extension is greater than the radial extension. At location (1), it appears that there is initially a slight widening of this section of flow due to the orientation of the ice rise, which leads to increased azimuthal spreading and hence positive buttressing. As the ice reaches the end of the ice rise there is a reduction in the resistance to flow from shear stresses and hence there is an increase in flow speed. This leads to increased extension in the flow-direction (radial-direction) and therefore a transition to negative buttressing.

As the shelf widens rapidly in the final third of the channel downstream of location (2), (from approximately 100 km wide at location 2, to approximately 200 km at the calving front) there are more prominent values of the partial derivative. Upstream of this widening the partial derivative is positive, and positive values span the width of the channel. This may be due to the slight narrowing of the shelf at location (2), which leads to compression in the azimuthal direction and hence a positive value of the partial derivative.

Downstream of location (2), after the onset of divergence, there are negative values of the partial derivative across the entire width of the shelf (Fig. 3.45a). This is also true

for the additional ice entering the shelf from the Charybdis Glacier (location (3)).This is because there is significant lateral spreading of the ice, which is greater than the along-flow extension. As the ice approaches the calving front and begins to become unconfined laterally, the partial derivative becomes positive and therefore this region does not contribute to the positive buttressing of the shelf via hoop stresses. This may be because there is a decrease in resistance from the side walls as the shelf leaves the confines of the channel, and therefore an increase in along-flow (radial) extension, which becomes greater than the azimuthal extension.

As the ice approaches the calving front there is a transition from the dominant component of extension being aligned with the flow, while laterally confined, to a region where the dominant extension is aligned transverse to the flow. These features are identified in the 1st Principal Strain Axes plot in Figure 3.24. At the calving front there is positive buttressing from the hoop stresses ($\partial/\partial r(u_r/r_c) < 0$), as the values of the 1st and 2nd Principal Strain Rates become comparable, but the dominant Strain Rate is transverse to flow. However, this region at the front of the shelf may be disjoint from other sections of the ice shelf further upstream that are contributing to buttressing. Therefore, the hoop stresses in this region may not contribute to the overall buttressing generated by the shelf. The areas of the ice shelf contributing to total buttressing are identified in the next section.

The geometry of the Larsen C Ice Shelf, is very different to that of Amery Ice Shelf and as a consequence the $\partial/\partial r(u_r/r_c)$ plot in Figure 3.45b produces a considerably different pattern and structure. There is significant structure to the field as ice enters the main body of the shelf in the form of tributary ice shelves, which are supplied by ice flow from separate ice streams. As these tributary ice shelves flow out from the confinement of lateral pinning-points and enter the main body of the shelf, they begin to spread laterally. This structure is particularly clear along the northern margin of the shelf, where the locations of inflowing ice have been identified by markers (1), (2) and (3) in Figure 3.45b. (These locations, and the inflow of ice from tributaries can also be seen in the surface speed plot in Figure 3.47 where they are marked with grey numbers.) In these three locations, it is clear that as the ice approaches the final lateral pinning-points and begins to spread laterally, there are positive values of the partial derivative indicating negative buttressing. This is because the along-flow extension is large as the lateral resistance from pinning points is reduced. Once this ice enters the body of the main shelf the partial derivatives become negative, corresponding to positive buttressing, as the lateral (azimuthal) extension is increased and the along-flow extension reduced. These features coincide with an increase and then reduction in the 1st Principal Strain Rate at the tributary ice flows (labelled 1-3 in Figure 3.45b), which can be seen in Figure 3.38.

Throughout the main section of the shelf the 1st and 2nd Principal Strain Rates are low and correspond to low values of $\partial/\partial r(u_r/r_c)$.

From assessment of the plots of $\partial/\partial r(u_r/r_c)$ for Amery and Larsen C ice shelves it is clear that the geometry of the embayment and pinning points leads to a distinctive structure in the sign of the hoop stress. As lateral pinning points are removed or a tributary section of the ice shelf moves past lateral pinning-points into the main section of the shelf, there is initially an area of negative buttressing, represented by positive values of $\partial/\partial r(u_r/r_c)$. This corresponds to the increasing rate of along-flow extension as the lateral resistance is reduced. After this, or in an area where the channel widens, there is then a region of positive buttressing (negative $\partial/\partial r(u_r/r_c)$) as the rate of lateral (azimuthal) spreading becomes larger than the along-flow (radial) extension. These regions span the width of the confinement. In order for the resistance to ice flow generated locally by hoop stresses to contribute to buttressing of the grounded ice, regions where resistance is generated must be linked together and the resistive stresses transferred back to the grounding line. This issue is now addressed by considering the areas of the ice shelf that contribute to buttressing via shear and hoop stresses.

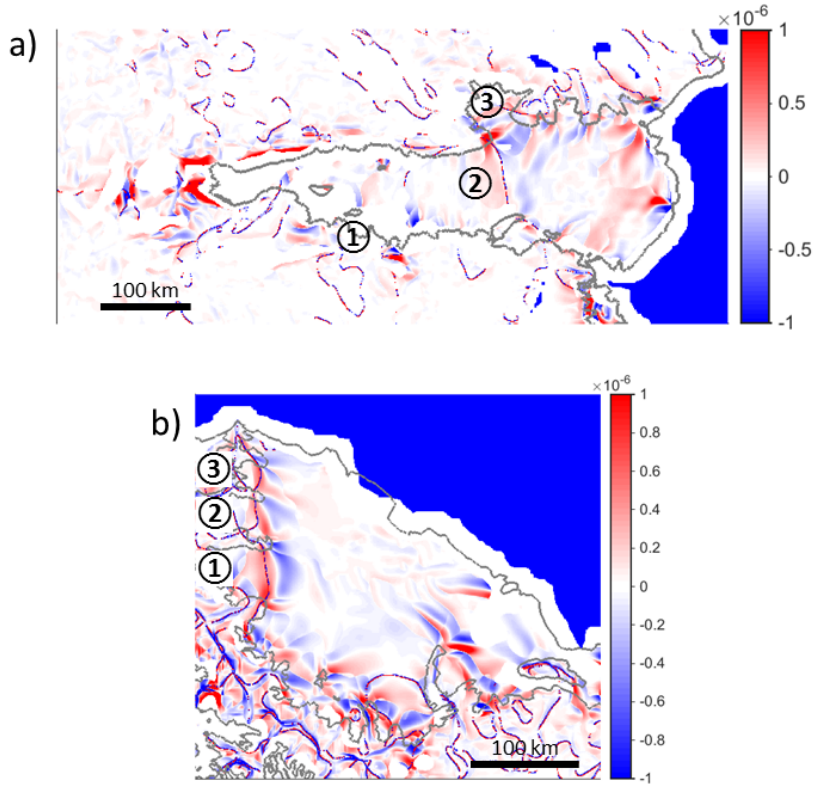

Figure 3.45: Plots showing the value of $\frac{\partial}{\partial r}\left(\frac{u_r}{r_c}\right)$ for: (a) Amery Ice Shelf; (b) Larsen C Ice Shelf. For Amery Ice Shelf: location (1) identifies the position of an ice rise (just above (1)) that initially diverts the flow of the shelf and generates resistance from hoop stresses (blue) and once the ice flows past this point, resistance to flow is reduced and the shelf accelerates making a negative contribution to buttressing; location (2) indicates an area where the channel initially narrows leading to negative hoop stress, this is followed by a positive contribution to buttressing from hoop stresses as the channel widens further downstream; location (3) is positioned where there is an inflow into Amery Ice Shelf from the Charybdis Glacier. For the Larsen C Ice Shelf locations (1), (2) and (3) indicate where there is an inflow into the main body of the shelf from tributary ice flows, ice flowing from left to right at each location. Each inflow is contained within a lateral confinement of pinning points. At the end of these confinements there are positive values of the partial derivative as there is extensional in the radial component of the flow as the resistance to flow is reduced. This is followed by a positive buttressing contribution from buttressing as the dominant compotent of extension is lateral spreading.

3.7.6 Geophysical Examples: Contributions to buttressing

It is clear that resistance to the flow of the ice shelf can be generated locally by compression, shear stresses and hoop stresses. An aim of Fürst et al. (2016) was to identify areas of ice shelves that did not contribute to buttressing of the grounded ice. If these sections of ice broke away, such as during a calving event, then there would be no feedback on the flow of the ice in the remaining shelf and further upstream. This ice was then defined as passive ice. I hypothesise that by identifying areas where there is compression, shear stress and hoop stresses it is possible to determine those sections of the ice shelf that are contributing to the total positive buttressing of the ice shelf. Then as a consequence of this, the remaining sections of the shelf provide no buttressing or contribute negatively to buttressing (acting to pull the shelf downstream).

Areas where there is local resistance to flow due to compression or shear stress can be identified by negative values of the 1^{st} and/or 2^{nd} Principal Strain Rate. Elsewhere, both 1^{st} and 2^{nd} Principal Strain Rates are positive and the ice is spreading in all directions. In these situations additional resistance to flow can be generated by hoop stresses, as detailed above. I therefore identified areas with ice that is potentially contributing to buttressing either by compression, shearing or hoop stresses, which can be seen for the case of Amery Ice Shelf in Figure 3.46. Areas potentially contributing to buttressing are marked in red (1) and areas not contributing, or in the case of the hoop stresses potentially providing negative buttressing, marked in blue (0).

From Figure 3.46b, it is clear to see that shear buttressing is found throughout the narrow upstream section of the shelf, and in the channel margins along the entire length of the shelf, with the buttressing margins being approximately 50 km wide. As the channel becomes wider an area of no-shear-buttressing appears in the centre of the channel, which widens and becomes more pronounced in the downstream direction. In the final third of the shelf, there is a region approximately 100 km wide in the centre of the channel, which widens in the along-flow direction and provides no shear buttressing. At the calving front there is a no-shear-buttressing region spanning the width of the entire front. This region corresponds to that bounded by the compressive arch in the previous section and is marked by a dashed grey curve in Figure 3.46b.

There is a less coherent pattern and structure to the plot for contributions to buttressing from hoop stresses, as shown in Figure 3.46c. Here there are no contributions to buttressing from hoop stresses in the upstream section of the shelf. However, as the shelf becomes wider there are patchy contributions to buttressing from hoop stresses, particularly where the shelf widens two thirds of the way along its length at location (1),

as identified in the previous section and owing to the increased rate of lateral (azimuthal) extension. Comparing the shear-buttressing and hoop-stress-buttressing plots it is clear that the dominant resistance is due to the shear stresses, but hoop stresses are influential near the exit.

The total buttressing plot for Amery Ice Shelf (Fig. 3.46d) shows the combined contributions to buttressing from shear and hoop stresses. From this plot, it is possible to identify areas where the ice is making no contribution to positive buttressing and in turn ice that is providing buttressing. There are some small isolated sections of ice, near the calving front, that appear to make a positive contribution to buttressing. These areas may in fact have little or no impact on the total buttressing as they only counteract the much larger areas upstream that make a negative contribution to buttressing. The total buttressing is found when the contributions to buttressing are integrated back to the grounding line. Near the calving front, these positive buttressing contributions are due to hoop stresses, and the magnitude of the partial derivative ($\partial/\partial r(u_r/r_c)$) is similar throughout the calving front area (although there are regions making positive or negative contributions) and there is an approximately uniform effective viscosity. However, the shelf thickness will decrease in the flow direction, reducing the value of the integrand when the total buttressing from hoop stresses is calculated (see equation (3.22)). Therefore, I consider these regions to have little influence on the total buttressing. On these grounds I estimate the effective extent of non-buttressing ice, as identified by the yellow dashed curve. I hypothesise that this area of the shelf can be removed without a significant reduction in the total buttressing.

An estimate of the area of non-buttressing ice for Amery Ice Shelf has been identified in Figure 3.46d by a dashed yellow curve. Here the region has been determined by visual assessment of the plot showing the contribution to total buttressing, with areas of no or negative buttressing forming a connected region near the calving front. This region forms an arched feature across the front of the shelf that begins near the final lateral pinning-points on both sides of the channel. This can be compared with the region of positive 1st and 2nd Principal Strain Rates, which extends further upstream in the centre of the shelf. This region is marked by a dashed grey curve in Figure 3.46b (and dashed black curve in Fig. 3.37) and corresponds to the compressive arch suggested by Doake et al. (1998). It is clear that the consideration of buttressing from hoop stresses acts to reduce the area of non-buttressing ice in the centre of the shelf, where there is considerable lateral spreading. This suggests that there is ice downstream of the compressive arch that makes a contribution to buttressing and therefore if calved may significantly influence the flow of the ice.

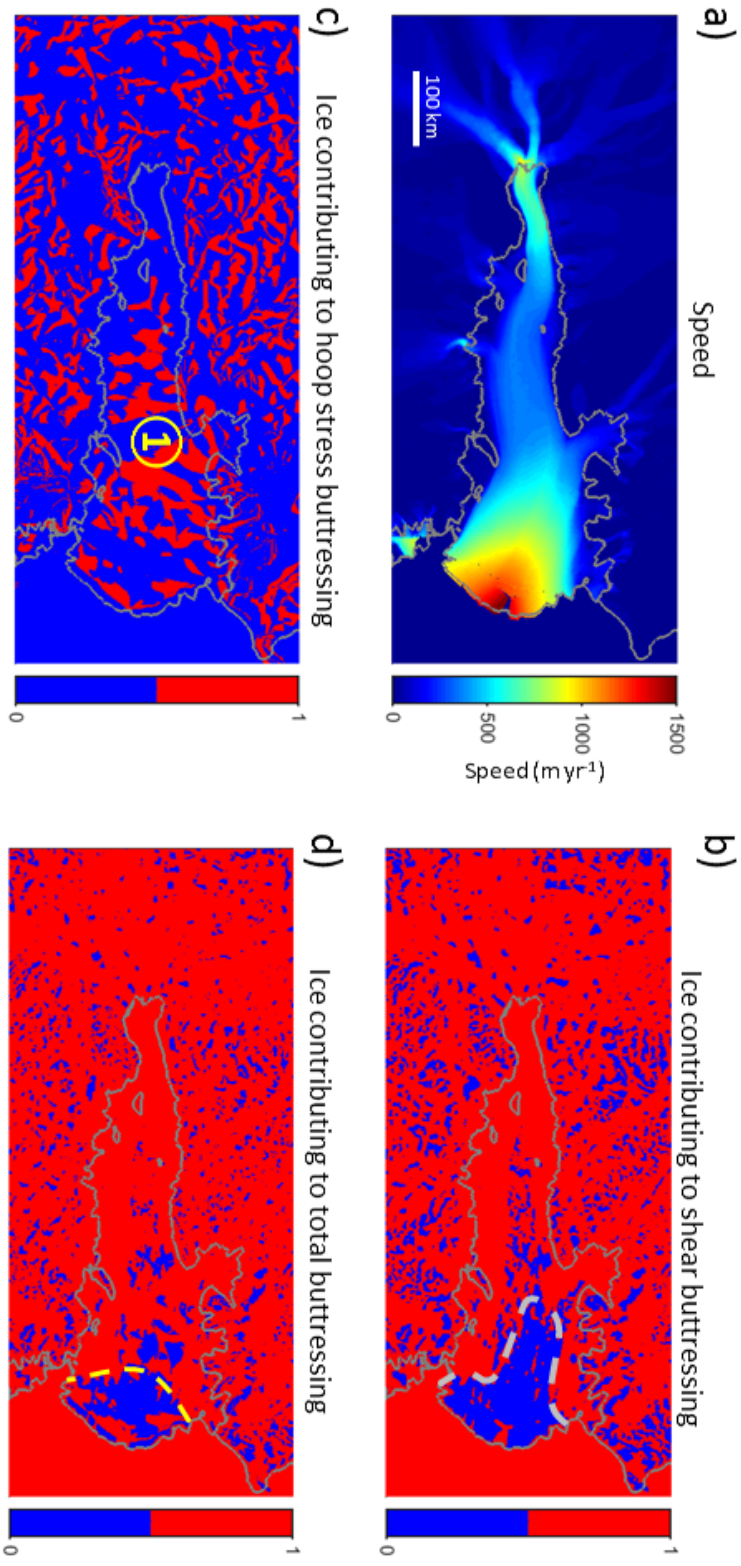

Figure 3.46: Plots for Amery Ice Shelf showing: ice-surface flow speed; areas of ice that contribute to buttressing via shearing; positive buttressing from hoop stresses; and the combined buttressing from shear and hoop stresses. The solid grey curve identifies the boundaries between grounded ice, the shelf and the ocean. Location (1) identifies where the channel begins to diverge. The grey dashed curve highlights the boundary of the area where both Principal Strain Rates are positive - the compressive arch. The dashed yellow curve identifies the approximate extent of the ice that is not contributing to buttressing.

Similar plots for the Larsen C Ice Shelf can be seen in Figure 3.47. As noted earlier the geometry of the embayment and the consequent structure of the flow varies considerably from that of Amery Ice Shelf. This is in evidence in the plot showing the contribution to buttressing from shear stresses, Figure 3.47b. Here bands of shear-buttressing are found in the margins of the flow as ice enters the main body of the shelf while the central sections of these inflows make no contribution. These features are particularly clear at locations (1), (2), (3) and (4), as labelled by yellow numbers in Figure 3.47a and 3.47b. Buttressing from shear stresses is observed along the margins of the lateral pinning-points and into the main body of the shelf as the tributary ice-flows merge. As identified in the previous section, buttressing from hoop stresses is negative in the regions where the tributary ice shelves approach the end of the lateral confinement and along-flow extension is large. After this, there is a region of positive buttressing as can be seen by the red regions in Figure 3.47c. As the shelf approaches the calving front the contribution to positive buttressing from hoop stresses is reduced, particularly away from the centre of the shelf where there is negative or no buttressing. From the plot for total buttressing contributions (Fig 3.47d), it is clear that in the centre of the tributary ice shelves as they enter the main body of the shelf there is no positive contribution to buttressing, due to the absence of shear stresses in this area and the increase in along-flow extension, which leads to negative buttressing from hoop stresses. At the calving front there is a clear concave region that provides no buttressing. This is highlighted by a yellow curve. As with Amery Ice Shelf, this region is smaller than the region that would be identified as passive if we only considered the region where both Principal Strain Rates were positive. This demonstrates that the hoop stresses are an important dynamical process controlling the stability of the ice shelf.

For Fimbul Ice Shelf the main section of the flow forms a fast flowing plug that is bounded by slow flowing ice on either side, with two confining pinning points near the calving front. This flow structure could be inferred from the plot showing the areas contributing to buttressing via shear stresses in Figure 3.48b. Here there is no contribution to buttressing from the ice in the centre of the main flow, identified by blue regions in the plot, while there are approximately 30 km wide margins either side of the main flow, where buttressing is generated. There is a less well defined structure for the plot showing buttressing due to hoop stresses, Figure 3.48c. However, it is clear that there is resistance to flow generated by hoop stresses when the shelf is not confined laterally by pinning points, which can be seen in the centre of the shelf (marked as location (1)) and contrasted with the confined region further downstream, where there is negative or no buttressing from hoop stresses. This is because the transverse (azimuthal) extension of the shelf controls the magnitude of the hoop stress.

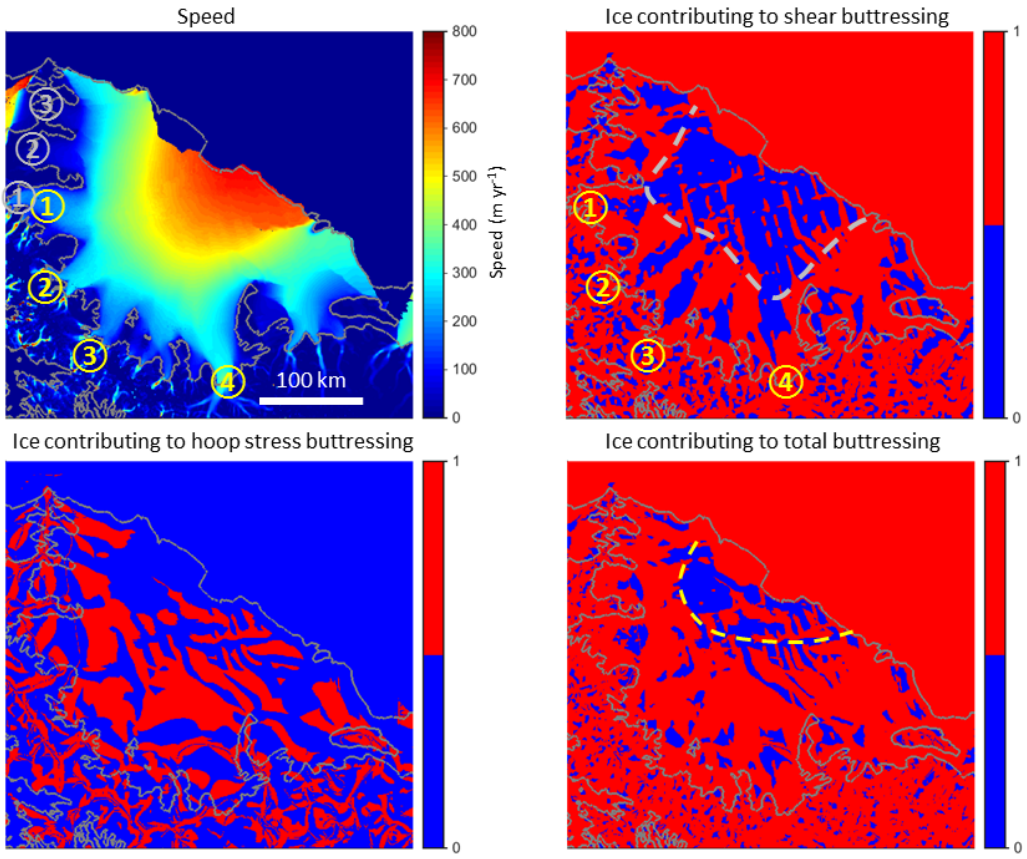

Figure 3.47: Plots for Larsen C Ice Shelf showing: ice-surface flow speed; areas of ice that contribute to buttressing via shearing; positive buttressing from hoop stresses; and the combined buttressing from shear and hoop stresses. The solid grey curve identifies the boundaries between grounded ice, the shelf and the ocean. Yellow locations (1), (2), (3), (4) identify where there is substantial buttressing in the margins of the inflow from shear stresses. Grey locations (1), (2), (3) identify inflow where clear structures in hoop stresses are observed as the inflow spreading into the main body of the shelf. The dashed yellow curve identifies the approximate extent of the ice that is not contributing to buttressing.

The combined contribution to buttressing is given in Figure 3.48d, where it is possible to identify a region of non-positive-buttressing in the centre of the shelf between the two final pinning points. This region is approximately equal in size to the area downstream, which makes a positive contribution to buttressing, therefore counteracting the positive buttressing. The non-buttressing region has been identified by a yellow curve in the plot. This is much smaller than the region of positive Principal Strain Rates, which can be inferred from the shear buttressing plot, and the boundary of which would define the compressive arch. This compressive arch is marked by a grey dashed curve in Figure 3.48b.

The flow of Getz Ice Shelf is funnelled into a parallel channel, which extends approximately 40 km to the calving front. The upstream section of the flow provides buttressing to the grounded ice due to compression and shear stresses, as is evident in Figure 3.49b. In the final section of the shelf, there is a central region where there is no contribution to buttressing from shear stresses, as the shelf spreads both laterally and along-flow. The boundary of this region marks the compressive arch as proposed by Doake et al. (1998) and is marked as a dashed grey curve in Figure 3.49b. Throughout most of the shelf there is no positive contribution to buttressing from hoop stresses. This may be because the channel is either parallel or narrowing and hence the effective radial extension ($\partial u_r/\partial r$) is greater than the azimuthal extension. Near the calving front there is a region of positive buttressing due to hoop stresses, which spans most of the channel width. Here there is some lateral spreading of the shelf as it approaches the calving front. The combined contribution to buttressing can be seen in Figure 3.49d. As expected, this plot is very similar to the plot showing the contributions to buttressing from shear stresses, with some additional buttressing near the calving front due to hoop stresses as the shelf begins to spread laterally. Again a small concave region at the calving front can be identified where the ice is non-positive-buttressing. In these plots (for the relatively small Getz Ice Shelf) the effect of the filtering of the velocity field leaves artefacts along the ice-ocean boundary, and hence in this case there appears to be some artificial buttressing found at the calving front.

Plots for the large Ross Ice Shelf are given in Figure 3.50. As with the previous examples, inflow into the main shelf can be inferred from the plots of ice contributing to buttressing from shear stresses. As ice enters the shelf from locations (1) and (2) there are distinctive shear margins where buttressing is generated, while the central section of the inflow is an area that makes no contribution to buttressing from shearing, as indicated by the blue areas in Figure 3.50b. From the plot of buttressing generated by shear stresses, it is also apparent that there is a large area at the front of the shelf that is non-buttressing. The boundary of this region determines the location of the compressive

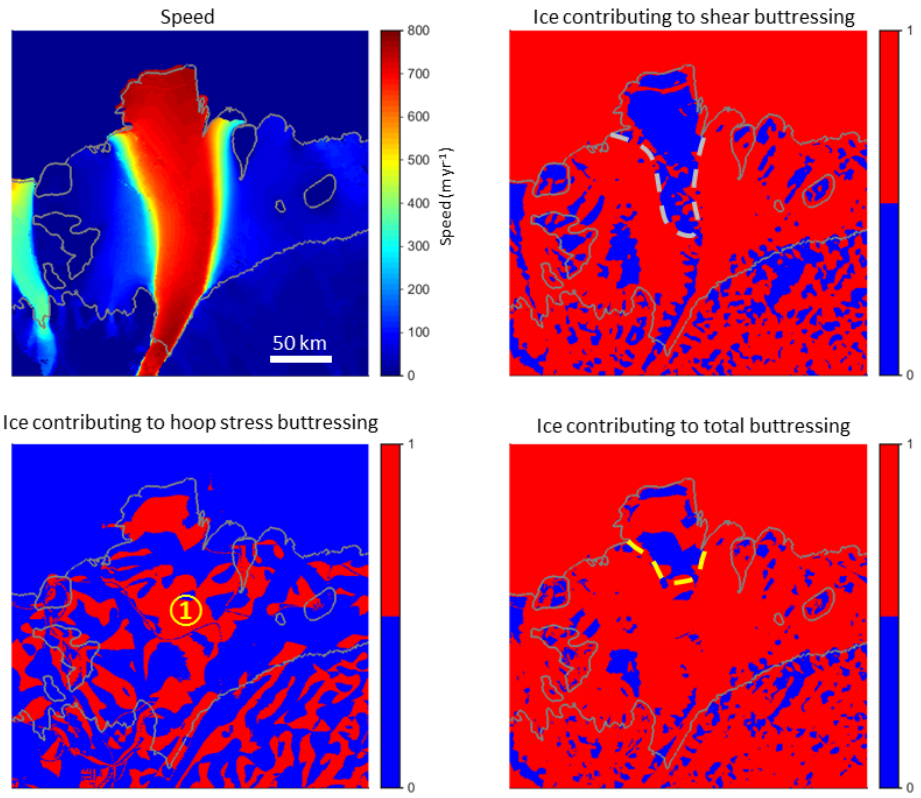

Figure 3.48: Plots for Fimbul Ice Shelf showing: ice-surface flow speed; areas of ice that contribute to buttressing via shearing; positive buttressing from hoop stresses; and the combined buttressing from shear and hoop stresses. The solid grey curve identifies the boundaries between grounded ice, the shelf and the ocean. The dashed yellow curve identifies the approximate extent of the ice that is not contributing to buttressing.

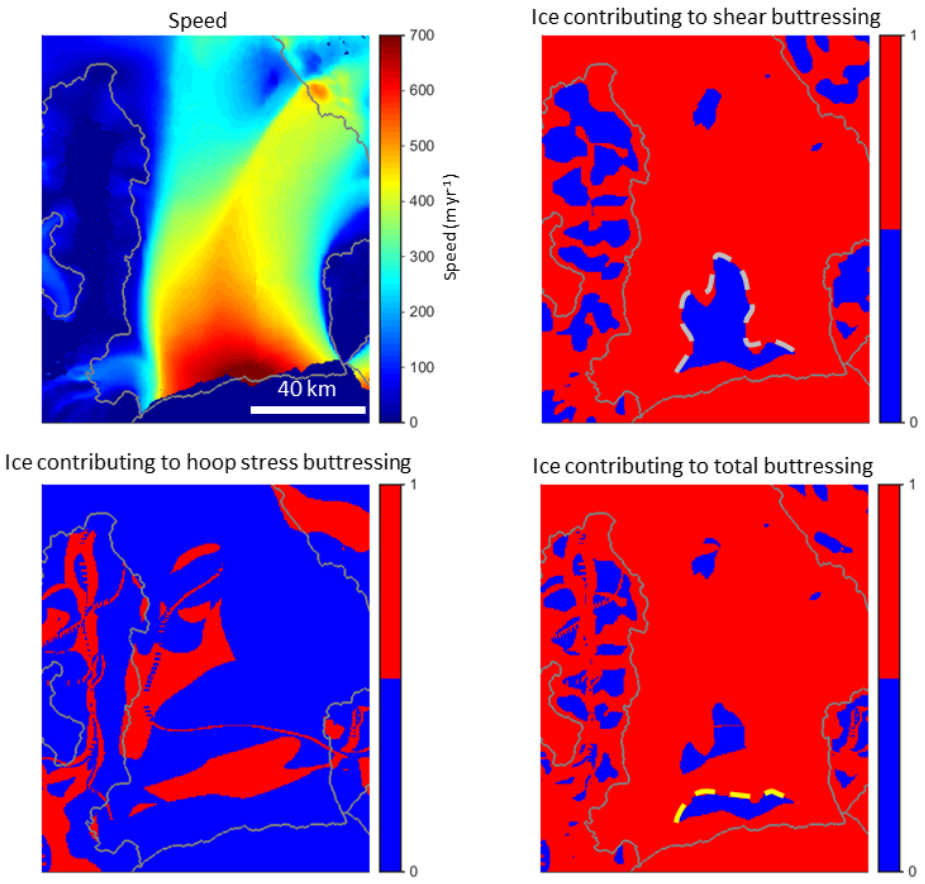

Figure 3.49: Plots for Getz Ice Shelf showing: ice-surface flow speed; areas of ice that contribute to buttressing via shearing; positive buttressing from hoop stresses; and the combined buttressing from shear and hoop stresses. The solid grey curve identifies the boundaries between grounded ice, the shelf and the ocean. The dashed yellow curve identifies the approximate extent of the ice that is not contributing to buttressing.

arch and is marked by a grey dashed curve in Figure 3.50b. However, further resistance is generated by hoop stresses, the distribution of this buttressing can be seen in Figure 3.50c. Here it is clear that there is little large-scale structure to the hoop-stress field, which may be because there is little large-scale divergence of the flow field, as flow is mainly parallel or convergent from tributary ice streams within the shelf. However, the buttressing from hoop stresses does have an influence on the size and shape of the non-positive-buttressing region at the ice-shelf front. Here the region is not clear cut, but is likely to be concave and spanning the width of the calving front, except for a narrow margin near the final lateral pinning point and extends approximately 100 km upstream at the centre of the calving front.

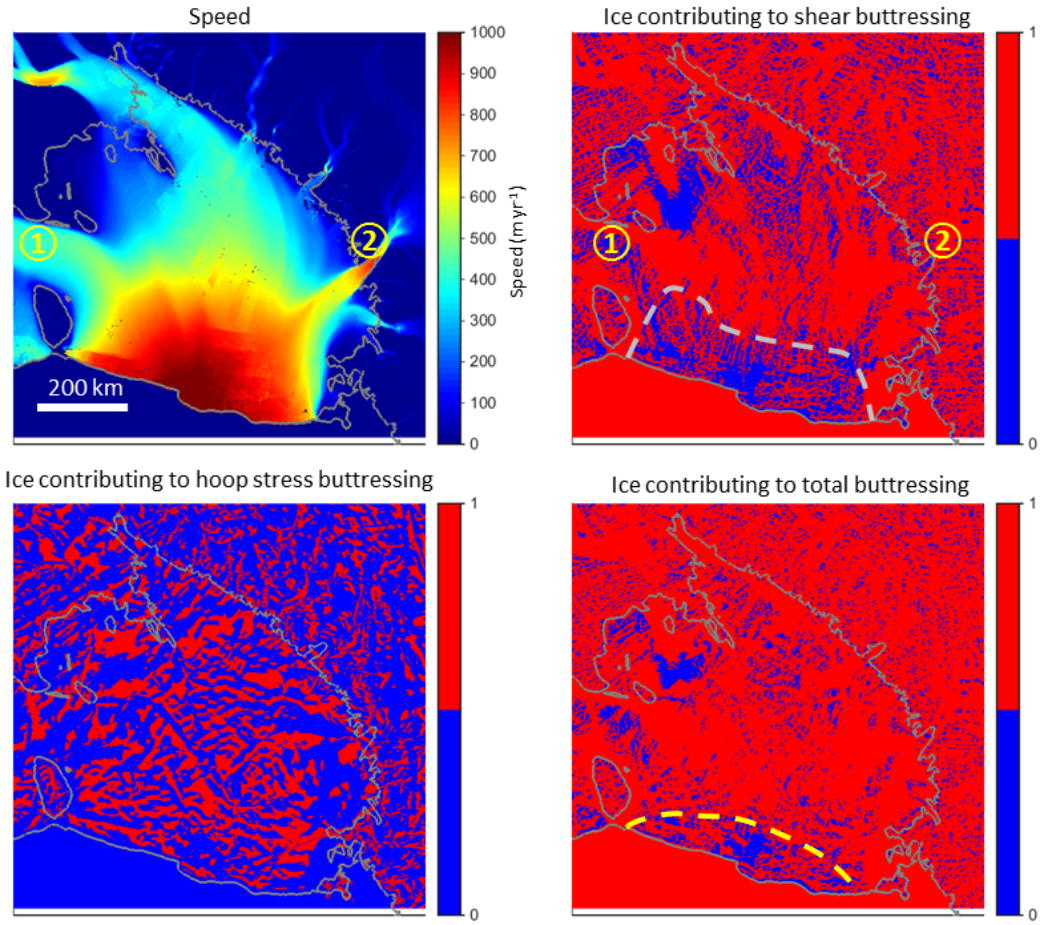

Figure 3.50: Plots for Ross Ice Shelf showing: ice-surface flow speed; areas of ice that contribute to buttressing via shearing; positive buttressing from hoop stresses; and the combined buttressing from shear and hoop stresses. The solid grey curve identifies the boundaries between grounded ice, the shelf and the ocean. Locations (1) and (2) identify regions where there is inflow to the shelf, with shear margins that contribute to buttressing.

3.7.7 Summary: Identifying non-positive-buttressing ice

From this analysis it is clear that buttressing due to shear stresses and compression are the most significant forms of buttressing and there is a clear structure to this type of buttressing, determined by the embayment geometry and flow field. It has been observed that, along channel margins and as ice enters the main body of the ice shelf, there are shear margins which make a positive contribution to buttressing. There is often little shear within the centre of these inflows and as a consequence less buttressing is generated in these regions. These features are observed both when there are a number of tributary ice flows flowing into the main shelf, and also when a section of flow is confined in a channel. Shear margins that contribute to buttressing are also found close to the final lateral pinning-points of ice shelves, which are often located at the calving front. However, across the majority of the calving front the shelf is spreading in all directions and there is no buttressing generated from shear stresses. This leads to the formation of large concave regions at the front of ice shelves, where both Principal Strain Rates are positive. The upstream boundary of this region of positive Principal Strain Rates determines the location of the compressive arch as proposed by Doake et al. (1998).

Hoop stresses make a positive contribution to buttressing when the azimuthal extension is greater than the radial extension and hence this often occurs when there is a widening of the embayment in which the shelf is located. As the ice nears the end of the lateral confinement there is a reduction in resistance to flow from shearing with side walls, and hence the flow accelerates, leading to negative buttressing. Once the shelf leaves the channel, it is able to spread laterally leading to large values of azimuthal extension and hence positive buttressing. This positive buttressing can then be transferred upstream. Positive buttressing from hoop stresses may also occur as multiple tributary ice flows enter the main shelf. Where the ice shelf flows through a narrower section of channel the azimuthal extension may become negative and hence lead to a negative contribution to buttressing, but this may be counteracted by decreasing radial extension and large values of shear stress. When the combined fields of contributions to positive buttressing from shear and hoop stresses are used to identify which regions of the shelf make a positive contribution to buttressing, often a concave region near the front of the shelf is identified that makes no positive contribution to buttressing. Therefore, if this section of shelf were to be removed, then there would not be a rapid acceleration of ice flow as the total positive-buttressing would not have been reduced. Estimates for the extent of these areas have been highlighted in the figures, using the fields of combined buttressing from shear and hoop stresses. These regions are often smaller than those identified by the compressive arch, suggesting that if the compressive arch is used to identify non-buttressing ice, which could be removed with little feedback, then this over-

looks the influence of hoop stresses and will overestimate the area that can be removed.

One aim of Fürst et al. (2016) was to identify areas of 'passive ice', that if removed would have no feedback on the flow upstream. Here I identified similar regions of the ice shelves that are non-positive-buttressing, as can be seen in the comparison plots in Figure 3.51. I hypothesise that if these regions are removed, then there will be no acceleration of the flow. It should be noted, when comparing the non-positive-buttressing regions, that Fürst et al. (2016) used modelled velocity field rather than data, and therefore are able to produce much smoother data fields.

From Figure 3.51 showing the location of the non-positive-buttressing ice and passive ice, as derived by the technique outlined above and by Fürst et al. (2016) respectively, it is clear that there is broadly good agreement between the two methods, with regard to the location and size of the non-buttressing regions. For Amery, Fimbul and Getz there is very good agreement for these shelves that are confined within a narrow embayment. There are some differences in shape for the non-buttressing ice areas on Larsen C and Ross ice shelves, but the size and shape of the regions are similar. This suggests that there is more complex flow in these shelves. Both of these shelves feature ice from multiple sources that merges in the shelf and therefore may be inherit features from deformation upstream, which lead to complex flow and buttressing.

The process detailed above does not distinguish between non-buttressing and negative-buttressing. Therefore, the ice flow upstream may decelerate following the removal of some of these areas of the shelf, if they contain areas of significant negative buttressing. More accurate estimates of the total buttressing contributions could be made if the ice-shelf thickness and effective viscosity were known at a resolution comparable to the InSAR velocity data. Using data of this resolution would mean the magnitude of the buttressing could be calculated along flow lines, and used to determine automatically where there is a transition to non-positive-buttressing ice. An accurate assessment could then be made of the magnitude of the total buttressing and the boundary after which calving events would have a significant impact on the rate of discharge.

This analysis of non-positive-buttressing ice holds so long as there is not a significant rearrangement of the flow after a section of shelf is removed. On first impressions a rearrangement of the flow may be expected if a large section of shelf were removed. However, this analysis of the strain-rate field has shown that if a section ice were removed downstream of the dashed yellow curve (indicating the boundary of non-positive-buttressing ice), then there would be no loss of resistance to flow. The newly formed calving front will continue to flow with dynamics determined by a balance between the hydrostatic

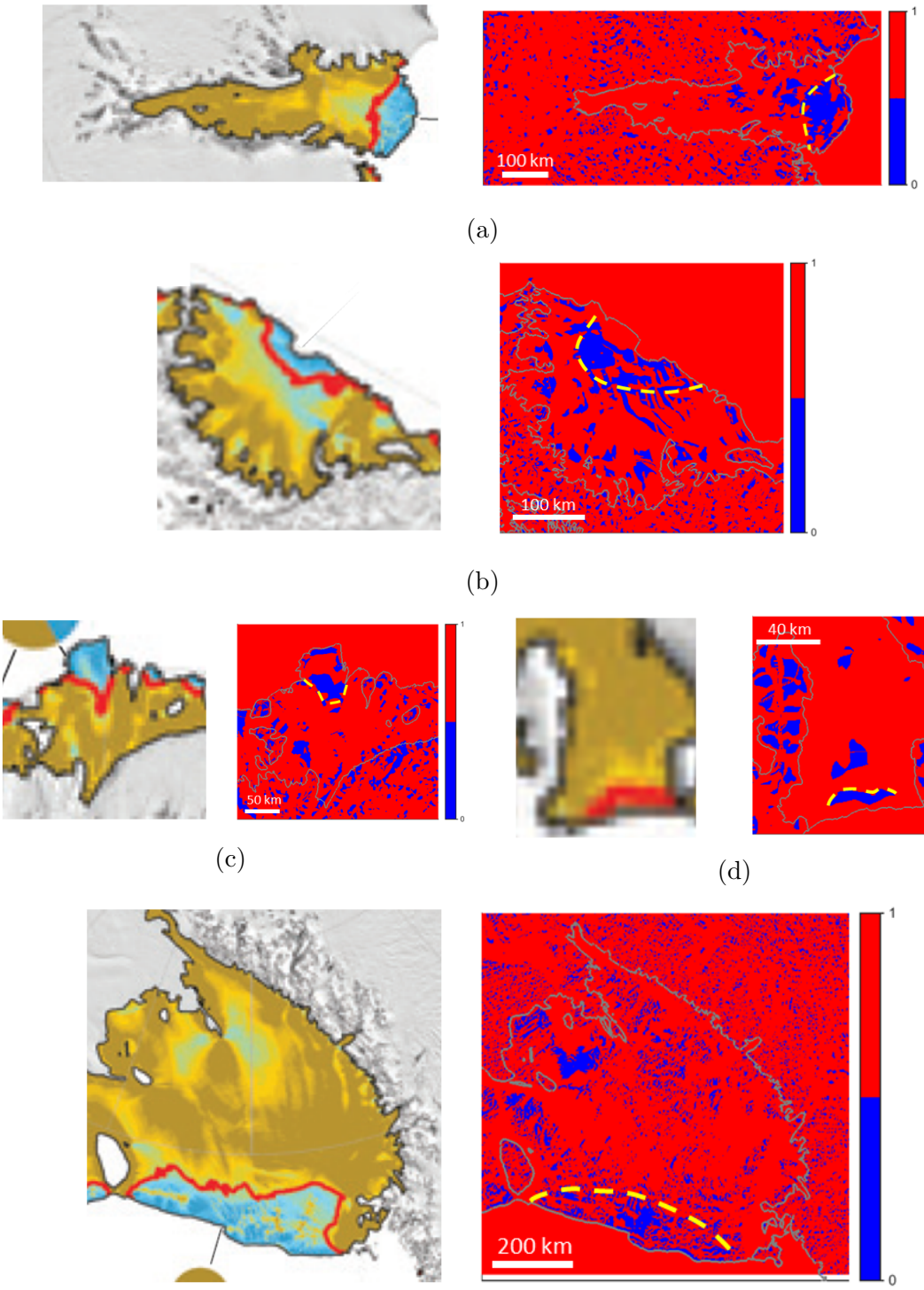

Figure 3.51: Comparison between the passive ice (left) and non-positive-buttressing (right) regions of a selection of ice shelves as determined by Fürst et al. (2016) and the technique outlined in this section. Plots to the left are adapted from Fürst et al. (2016). From top to bottom the ice shelves are: (a) Amery; (b) Larsen C; (c) Fimbul; (d) Getz; (e) Ross.

driving pressure and the extensional resistance within the shelf.

3.8 Conclusion

In this chapter I have used an Antarctic-wide ice-surface velocity dataset to investigate the flow dynamics of ice shelves. Comparisons have been made between flow features present in the velocity data and features present in both visual MODIS imagery and ice-thickness data. It was assumed that most shelves are evolving slowly and despite the approximate 5 year span of the data, large-scale features and dynamics should remain fairly unchanged. Of the example ice shelves analysed, Pine Island Glacier Ice Shelf is an exception, where there are rapid large-scale changes occurring. A low-pass Gaussian filter is applied to the velocity dataset in order to smooth the small-scale noise present due to processing of the original data product, but the filtering preserves the large-scale flow dynamics that are of interest.

From the divergence of the surface velocity, there is a broad pattern present in ice shelves, with convergence in the upstream section and divergence further downstream near the ice front. This can be exampled by the changing geometry of the embayment in which the ice shelf is found and the reduction in resistance as the shelf flows downstream. However, there may also be an influence from surface and basal processes, which lead to accumulation or ablation. The net effect of these processes was determined using the steady-state continuity equation with an accumulation-melting term, along with the ice-surface velocity and ice-thickness datasets. From analysis of the net accumulation/ablation field, it is found that often there is an area of significant melting near the grounding line. As the melting temperature increases with depth, this leads to melting at the base of the shelf and the formation of ocean circulation and melting/freezing processes associated with the ice-pump mechanism. This process causes ice to freeze to the base of the shelf further downstream, where the shelf is thinner. These features are particularly prominent for Amery Ice Shelf. The values and distribution of the accumulation and ablation of the shelves inferred here, agreed well with those from other studies. There are shelves, such as Fimbul Ice Shelf, where it appears that the flow of the shelf has little or no influence from surface or basal processes.

The strain rate in the direction of flow and the shear rate transverse-to-flow, where calculated from the velocity field. From comparison with the MODIS data, it was clear that often fractures and crevasses are linked to areas of high strain rate, and are often aligned perpendicular to the flow direction. Crevasses and fractures often form near pinning points, where there is a large gradient in speed. In the shelf margins there are high strain and shear values, these lead to weak effective viscosity and may be associated

with areas of damaged ice.

Another tool utilized to analysis the ice-shelf flow field and deformation was the Principal Strain Rate and Axes. Here the 1st Principal Strain Axis is aligned in the direction of largest magnitude strain rate and such that there is no shear component in the reference frame aligned with the Principal Strain Axes. For the majority of an ice shelf the 1st Principal Strain Rate is positive as the main component of the flow is due to the hydrostatic pressure gradient within the shelf, which induces flow towards the calving front. From the plots of the 1st Principal Strain Rate and Axes, it is clear that the crevasses are found in areas of high strain rate and are aligned perpendicular to the 1st Principal Strain Axes. They often form near pinning points but may also form when two tributary sections of ice flow merge with different speeds, leading to deformation of the ice.

In the final part of this section I have used the Antarctic-wide velocity data to determine sections of the ice shelf that make a positive contribution to buttressing of the grounded ice. In doing so, the areas making no contribution or a negative contribution have also been identified. These regions can be removed from the shelf and there will not be an acceleration of ice flow within the shelf, or the grounded section. If negatively buttressing ice is removed, this may even lead to a reduction in ice flow.

The most prominent component of buttressing is generated by compression and shear stresses. Areas that contribute to buttressing in this way can be identified by negative values of one or both of the Principal Strain Rates. The boundary between this area and the section of the shelf where both Principal Strain Rates are positive was defined as the compressive arch by Doake et al. (1998) and it was proposed that the compressive arch would be unstable to calving events that breached the arch. However, here I have shown that there may be significant areas of the shelf downstream of the compressive arch, where hoop stresses are important and play a key role in determining the amount of buttressing generated by the ice shelf. A point-wise measure of the hoop stress is calculated, where a positive contribution to buttressing is made when the azimuthal (lateral) extension is greater than the radial (along-flow) extension.

By analysing the ice-shelf velocity fields, calculating Principal Strain Rates and the sign of the hoop stress component, I have been able to determine those areas that contribute to the positive buttressing of the ice upstream. In doing so, I have also made an estimate of the area and location of non-positive-buttressing ice, which could be removed without significant change to the flow of ice upstream. These regions most often form a concave shape at the calving front, which spans the majority of the shelf width, except some narrow regions near the final lateral pinning points. In the case of the larger ice

shelves, such as Ross and Amery, these non-positive buttressing regions can extend 100 km upstream. It has been shown that these areas are usually smaller than those that would be identified by considering the location of the compressive arch only. These estimations agree broadly with those of Fürst et al. (2016), where an ice sheet model was used to determine the location of buttressing ice.

Chapter 4

Assessment of Ice Flow Dynamics in the Zone Close to the Calving Front

4.1 Introduction

If the resistance to flow produced by an ice shelf decreases, such as when an ice shelf breaks up, there can be a dramatic increase in the speed of the glaciers and ice streams flowing into the former shelf. This phenomenon was observed following the collapse of the Larsen A ice shelf (Rott et al., 2002) and also the collapse of the Larsen B ice shelf, where ice streams flowing into the former shelf accelerated up to eight times their previous speed (Rignot et al., 2004) and experienced substantial thinning (Scambos et al., 2004).

There are a number of factors that may determine the magnitude (and mechanics) of the buttressing produced by the floating shelf: the ice-shelf rheology; conditions at the grounding line (such as ice flux and thickness); the geometry of the shelf; and the geometry of the embayment in which it is located.

The ice-shelf geometry is partially determined by the extent of the ice shelf and the calving-front position. This results from a combination of processes causing calving-front retreat, such as iceberg calving, and shelf advance due to the flow of ice at the calving front. While there has been much focus on the dynamics of calving (Alley et al., 2008; Bassis and Jacobs, 2013; Benn et al., 2007), there has been relatively little work on the flow of ice at the calving front.

Alley et al. (2008) proposed an empirically derived calving law, using data from 10 ice shelves known to have near-stationary calving-front positions. This relationship takes

the form

$$c \propto w\epsilon H, \tag{4.1}$$

with c the calving rate, w the shelf width, ϵ the strain-rate normal to calving front and H the ice thickness, with all values measured at the calving front. Given that shelves with stationary calving fronts were considered, the calving rate was inferred from the speed of ice flow at the calving front. Therefore, this data-derived relationship could be interpreted as a way to predict the speed of ice flow at the calving front for ice shelves that retain a near constant front position. If the relationship is written in terms of the flow speed it would take the form $u \propto w\epsilon H$, with u being the flow speed at the calving front.

Alley et al. (2008) interpreted the dependence on the various parameters through consideration of how each parameter would affect the calving rate. For example, one control on calving may be the rate at which fractures open transverse to flow. It is expected that this process is strongly influenced by the rate of extension in the along-flow direction, and hence suggests a proportionality between calving rate and along-flow strain rate. In addition to this, it was observed from the dataset that calving rate was reduced for narrower shelves. Alley et al. (2008) hypothesized that this may be the result of shear with lateral boundaries causing fractures to rotate, such that they are no longer aligned transverse to flow. The rotated fractures may then close up, or prompt the creation of smaller icebergs.

However, if this relationship did provide insight into the calving process it would also suggest an instability in the calving front position: a small retreat would move the calving front into an area of thicker ice, with greater strain rate (once balanced with the hydrostatic pressure of the ocean), which would lead to further retreat. Alternatively, when written in terms of the flow speed at the calving front, a retreat would lead to an increase in flow speed and a re-advance of the calving front.

Figure 4.1, taken from Alley et al. (2008), shows data points corresponding to individual ice-shelf locations and the linear regression used to derive the empirical relationship. The dataset used is made up of 18 data points from 10 ice shelves (the names of which can be found in the caption of Fig. 4.1). A number of shelves have multiple data points corresponding to different locations on the ice shelf. The dataset is a compilation of data from numerous sources, with no apparent systematic methodology for sampling parameter values, especially with regards to along-flow strain rate.

A relationship for the viscous flow of ice at the calving front was derived by Hindmarsh

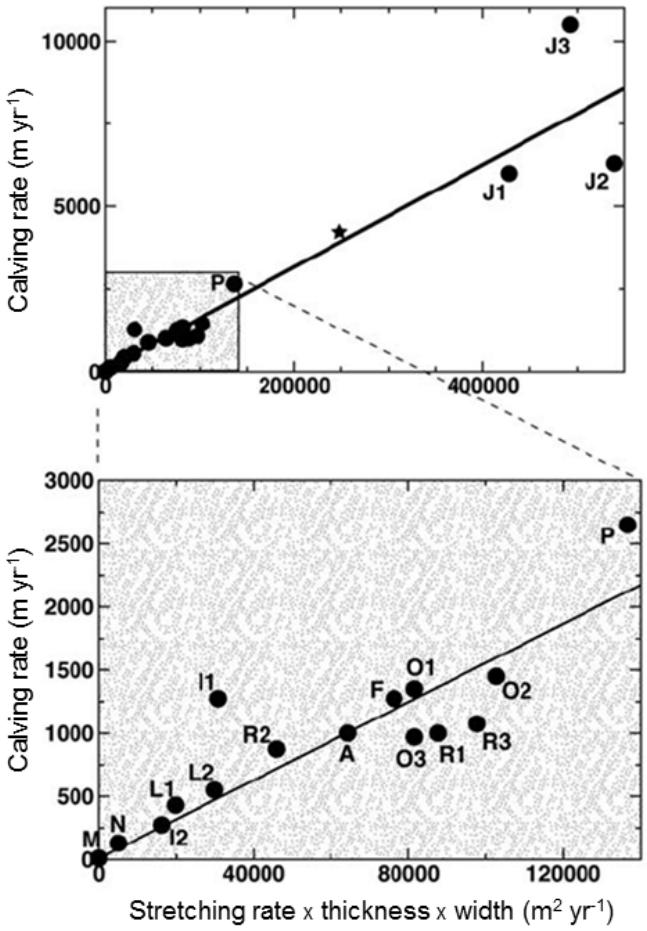

Figure 4.1: Figure adapted from Alley et al. (2008). Reprinted with permission from AAAS. Plot showing ice-shelf velocity at the calving front against the product of shelf width, strain rate and thickness, for 10 ice shelves: Amery (A), Filchner (F), Riiser (I1, I2), Jakobshavn (J1, J2, J3), Larsen B (L1, L2), McMurdo (M), Nivlisen (N), Ronne (O1, O2, O3), Pine Island (P), Ross (R1, R2, R3).

(2012) using a scaling analysis. The relationship takes the form $u \propto w(\epsilon H)^{3/4}$. This scaling analysis is based on the physical balances and scalings that govern the viscous flow of an ice shelf as it approaches the calving front. The ice shelf is assumed to have a uniform shear-thinning rheology given by Glen's Flow Law, with constant flow law parameter B and flow exponent n. The shelf is situated in a parallel channel with a no-slip condition at the lateral boundaries. Ice flows in the along-channel direction (x-direction) only, with the along-flow strain rate given by $\epsilon = \partial u/\partial x$. The channel is of width w and has a width-averaged thickness H. Despite the potential for complex ice-shelf geometry and flow upstream, flow is close to unidirectional in the region close to the calving front, which is the area of interest in this work.

The derivation of this scaling law can be summarized briefly as follows. (For a more detailed derivation see Hindmarsh (2012).)

The force balance equation for the along-channel flow is given by

$$4\frac{\partial}{\partial x}\left(\mu H\frac{\partial u}{\partial x}\right)+\frac{\partial}{\partial y}\left(\mu H\frac{\partial u}{\partial y}\right)=\rho g' H\frac{\partial H}{\partial x}, \tag{4.2}$$

where $g'=g(\rho_w-\rho)/\rho_w$ is the reduced gravity. Here ρ is the density of ice, ρ_w is the density of sea water and g the acceleration due to gravity. The effective viscosity μ is given by

$$\mu = B'\, e_{II}^{(1-n)/n}, \tag{4.3}$$

$$e_{II} = \left(e_{xx}^2+e_{xy}^2\right)^{1/2}, \tag{4.4}$$

with B' the consistency index (related to the flow law parameter B, where $B'=B/2$), e_{II} the second invariant of the strain-rate tensor and n the exponent from Glen's Flow Law. The second invariant is given in reduced form as there is no vertical shear within the floating shelf and flow is in the along-channel (x-direction) only.

Assuming that in the zone close to the calving front, of aspect ratio 1, the magnitude of the transverse-shear stress is equal to the magnitude of the extensional stress (Hindmarsh, 2012), then the force balance equation (4.2) implies that the characteristic length scale in the along-flow direction (L) scales linearly with characteristic length scale in the transverse-to-flow direction (Y)

$$L\sim 2Y\sim w. \tag{4.5}$$

Here the characteristic length scale transverse-to-flow is equal to half the channel width. At the calving front, $x=x_f$, the extensional stress in the shelf balances the hydrostatic pressure of the ocean

$$\mu\left.\frac{\partial u}{\partial x}\right|_{x=x_f}=\frac{\rho g'}{8}H, \tag{4.6}$$

If equation (4.6) is evaluated along the centre line of the ice shelf, where $\partial u/\partial y=0$, it becomes

$$\left(\frac{\partial u_c}{\partial x}\right)^{1/n}=\frac{\rho g'}{4B}H, \tag{4.7}$$

with u_c being the centre line velocity. Furthermore, by combining this with the scaling from the force balance equation (4.5), we can derive a scaling for the velocity at the front

$$u_c\sim w\left(\frac{\rho g'}{4B'}\right)^{n/(n+1)}\left(H\frac{\partial u}{\partial x}\right)^{n/(n+1)}. \tag{4.8}$$

Model	A	B	C	Fit:R^2
$u \propto (w\epsilon H)^A$	0.87 $\pm$0.13	-	-	0.93
$u \propto w^A (\epsilon H)^B$	0.83 $\pm$0.13	0.75 $\pm$0.19	-	0.94
$u \propto w^A \epsilon^B H^C$	0.79 $\pm$0.25	0.89 $\pm$0.26	0.64 $\pm$0.68	0.95
$u \propto w (\epsilon H)^A$	0.98 $\pm$0.08	-	-	0.98

Table 4.1: Adapted from Hindmarsh (2012): Multiple regression models applied to dataset from Alley et al. (2008).

This is for the case of a general Glen's Flow Law rheology with flow exponent n and flow law parameter B'. Assuming a constant B' between ice shelves and approximating the Glen's Flow Law exponent as $n = 3$, gives the proportionality

$$u_c \propto w(\epsilon H)^{3/4}. \tag{4.9}$$

Hindmarsh (2012) attempted to confirm this relationship using the dataset from Alley et al. (2008). Numerous multiple regression models were applied to the data. The four models with the highest R^2 values are presented in Table 4.1. From these results it is clear there is some ambiguity as to which model represents the data most accurately. Each model in the table has a large R^2 value but there is little agreement between the regression parameters (when the range is disregarded). For example, the highest R^2 value (0.98) is achieved using the regression model $u \propto w(\epsilon H)^A$ (with $A = 0.98$). Similar regression-model values could be obtained using the other regression models, such as the first model $u \propto (w\epsilon H)^A$, however the resulting regression parameter for this model ($A = 0.87$) is substantially different.

This ambiguity may be due to the relatively small number of shelves used in the analysis (18 data points from 10 ice shelves), or the fact that some data points were from locations away from centre lines. In addition, the data points corresponding to Jakobshavn and Pine Island Glacier have very high speed values in comparison to the other ice shelves in the dataset. It is reasonable to suggest that these shelves have experienced large scale damage, leading to a reduced effective ice viscosity and therefore a decrease in the resistance provided to the ice-shelf flow. Consequently they achieve much greater flow speeds.

In order to clarify the previous work (Alley et al. (2008) and Hindmarsh (2012)) and determine a relationship for the flow at the calving front, it is necessary to compile a large dataset using a systematic method to determine values for shelf width, thickness, speed and strain rate. The details of this process are given in the following section, where data

is collected from 22 Antarctic ice shelves ranging in size, aspect ratio and not limited to shelves with near-stationary calving front positions. Values are sampled systematically at points corresponding to central calving-front locations. The newly compiled dataset is then analysed to determine a relationship for ice-flow speed at the calving front. I initially assess the data using a Robust Regression procedure applied iteratively to the dataset (see Data Analysis section for details) before the ice shelves are classified depending on their geophysical characteristics in order to establish a suitable regression for the dataset.

4.2 Data Collection/Compilation

Data was complied for 22 Antarctic ice shelves, ranging in size from the large Ross and Ronne ice shelves to the smaller Cook and Dolleman (Las Heras) Glacier ice shelves. Data for ice-shelf thickness was obtained from the Bedmap2 dataset (Fretwell et al., 2013), which provides ice-thickness measurements on a 1 km grid. The widths of the ice shelves were taken from the MODIS Mosaic of Antarctica (MOA) Image Map (Haran et al., 2005), with values measured using the computer software ArcGIS. Here the shelf width is defined as the straight-line distance between the final two lateral pinning points, which are identified from the MOA grounding line and coastline outlines. This shelf-width definition is used for all shelves even when the shelf protrudes past the final pinning points.

4.2.1 Ice-Shelf Speed and Strain Rate

Measurements of the ice speed and the strain rate at the calving front were obtained using the 450 m resolution ice surface velocity dataset from Rignot et al. (2011b). As described in the previous chapter the surface velocity was smoothed using a low-pass Gaussian filter. From this velocity field the along-flow strain rate was calculated, $\hat{\mathbf{u}}.\mathbf{e}.\hat{\mathbf{u}}$, again as detailed in the previous chapter. It is assumed that the flow at the calving front is perpendicular to the calving face, and therefore the strain-rate in the direction of flow should be equivalent to the strain-rate normal to the calving-front. After visual assessment of the angle at which the streamlines meet the calving front, it is clear that this assumption is broadly true. An artefact resulting from this filtering process is the presence of large negative values of strain at the boundary with the ocean. These values are not representative of strain rates close to the calving front, with valid strain rates

beginning 9 km back from the original calving front.

4.2.2 Representative Values for Strain Rate, Speed and Thickness

For each ice shelf, a series of 20 flow lines spaced about the approximate centre of the shelf, trace the path taken by ice as it flows from the main body of the shelf towards the calving front. Along these flow lines, values of thickness, speed and strain rate can be sampled. In the scaling analysis of Hindmarsh (2012), equations were evaluated along the centre line of the ice shelf. In order to extract comparative values from the data, the flow line with maximum speed at the calving front is determined and then values are sampled along this. Theoretically, the maximum speed should be achieved on the centre line at the calving front.

The strain-rate field for Getz Ice Shelf along with the flow line of maximum velocity can be seen in Figure 4.2a. Strain-rate values extracted along the maximum speed flow-line are shown in Figures 4.2b and 4.2c. From these plots it is clear that despite the smoothing effect of the Gaussian filter there is still a large range of strain-rate values as the ice approaches the calving front. This range in strain rate can also be observed in the plan-view plot of strain rate (Fig 4.2a), where there is spatial variability in the strain-rate value. This may be a feature of the ice flow or the result of ice damage (crevassing), which may lead to a reduced effective viscosity of the ice and corresponding high strain values. Alternatively the high spatial variability may be due to errors in the velocity field.

To determine a representative strain rate systematically for the range of ice shelves used in this study, the mean strain rate over the final 20 km of the maximum-speed flow-line is used (exceptions; McMurdo: mean calculated over final 10 km due to gap in data and Publications: mean calculated over final 15 km as it is a small shelf). For all shelves, apart from Robert Glacier Ice Shelf and Venable Ice Shelf, 20 km is less than half the width of the shelf (see Table C.1 in Appendix for shelf-width details). Therefore, this suggests that this mean strain rate may be representative of the strain rate in the frontal region of the shelf. Here we are aiming to clarify the large scale dynamics and test the scaling argument of Hindmarsh (2012), therefore it is necessary to use values which are representative of the large-scale dynamics.

This 20 km section begins 9 km back along the flow-line from the original calving front, to account for the 9 km range of the Gaussian filter. Values of ice thickness and speed

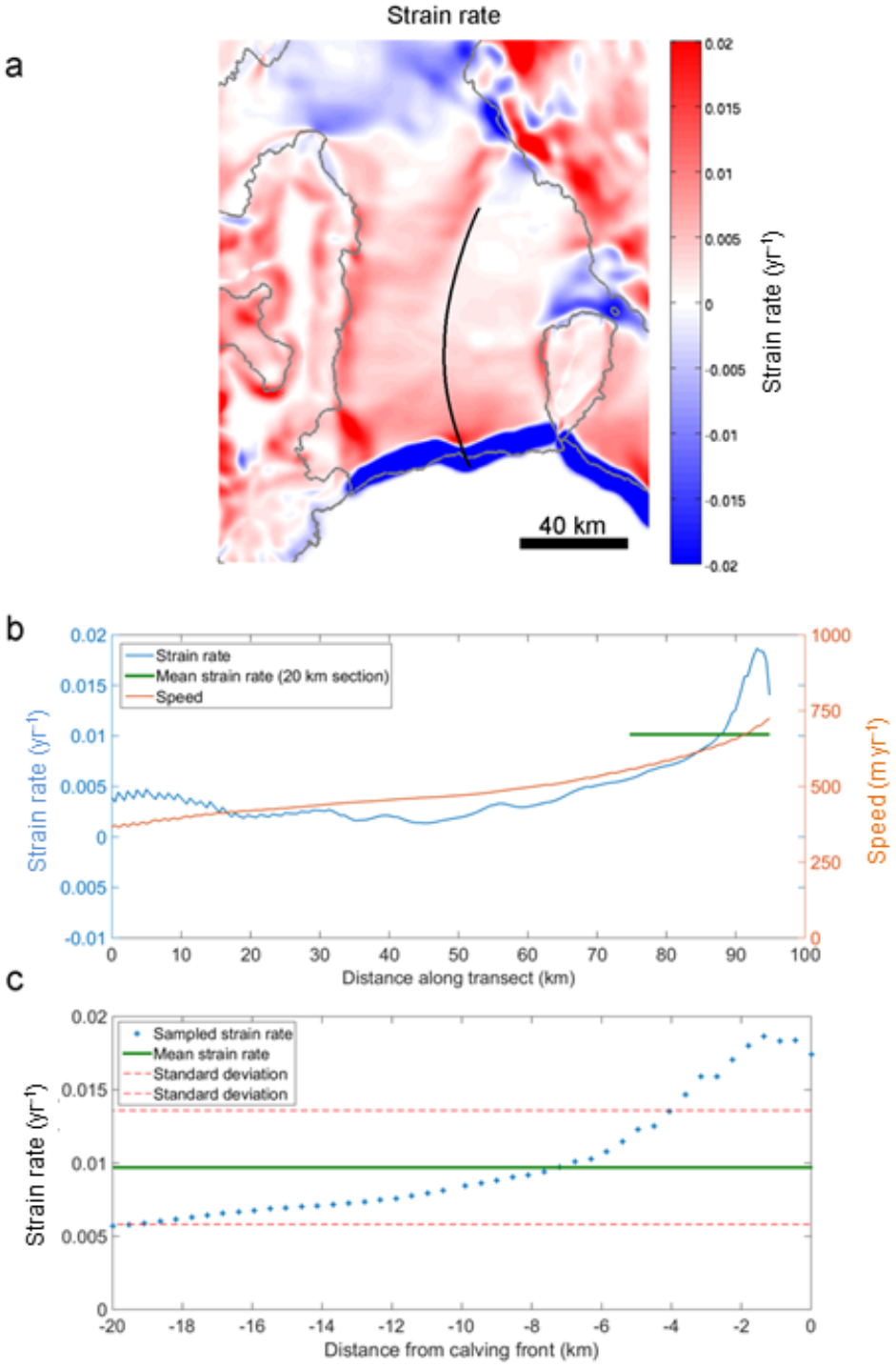

Figure 4.2: The process of calculating strain rate at calving front, Getz Ice Shelf: a) Along-flow strain-rate (yr^{-1}), with flow line of maximum velocity along which values of strain rate, speed and thickness are sampled. The large negative values at the calving front are an artefact of applying the low-pass filter to the velocity field; valid strain rate values begin 9 km back from the original calving front; b) Values of strain rate (yr^{-1}) (blue) and speed ($m\,yr^{-1}$) (orange) along flow line of maximum velocity. Bold green line indicates mean strain rate over final 20 km; c) Values of strain rate (yr^{-1}) (blue crosses) sampled along final 20 km of maximum-velocity flow line, with mean strain rate (bold green) and standard deviation (dashed red).

are also collected on the maximum-speed flow line at this newly defined calving-front position. The process of calculating the mean strain rate is shown in Figures 4.2a, 4.2b and 4.2c for the case of Getz Ice Shelf. The mean strain-rate value (bold green line) is shown in Figure 4.2b in relation to the values along the maximum-velocity flow line, while in Figure 4.2c the final 20 km section is shown in detail. The mean strain rate for Getz ice shelf is calculated to be 0.01 yr^{-1}, with a standard deviation of 0.005 yr^{-1}; most strain values along this 20 km transect are included within one standard deviation of the mean, with the exception being some higher values at the downstream end of the section.

The process of sampling ice thickness, speed and strain rate at the centre of the ice-shelf calving front is repeated for 22 Antarctic ice shelves and paired with data for the ice-shelf width. A table listing all data compiled can be found in the Appendix, Table C.1. Plots for all 22 ice shelves used to compile the dataset set, such as those from Getz Ice Shelf in Figure 4.2, can be found in the Appendix C and is also available at www.repository.cam.ac.uk/handle/1810/247061.

4.3 Data Analysis

From the work of Alley et al. (2008) and Hindmarsh (2012), we expect a relationship of the form $u = Aw\,(\epsilon H)^B$ (with $B = 1$ in the case of Alley et al. (2008) and $B = 3/4$ in the case of Hindmarsh (2012)), to relate the variables at the ice-shelf calving front. A relationship of either form should produce a linear trend in log-log space. Data from the 22 Antarctic ice shelves is plotted in log-log space in Figure 4.3. From this plot we can see that there is a broadly positive correlation between the variables, u/w and ϵH. However, there is a large degree of scatter in the data. Visual assessment suggests that Pine Island Glacier, Fimbul and Dolleman Ice Shelves may be outliers.

Figure 4.3 also shows error values associated with the data points, with u/w plotted against ϵH in log-log space. Mean values of strain rate are calculated over the final 20 km of the shelf, while point measurements of speed are used. Horizontal error bars indicate the standard deviation (σ) in the strain rate (strain rate calculated from filtered velocity field) over the final 20 km of each shelf ($\log((\epsilon-\sigma)H)$ to $\log((\epsilon+\sigma)H)$). Vertical error bars give the standard deviation in speed over the same 20 km transect, away from the mean speed value. This mean speed value is calculated and given in Table C.1 in the Appendix, but not shown in the figure. However when plotted the mean values are located very close to the point measurement values. From the plot in Figure 4.3 it is evident that the standard deviation in speed is relatively small, which suggests confidence

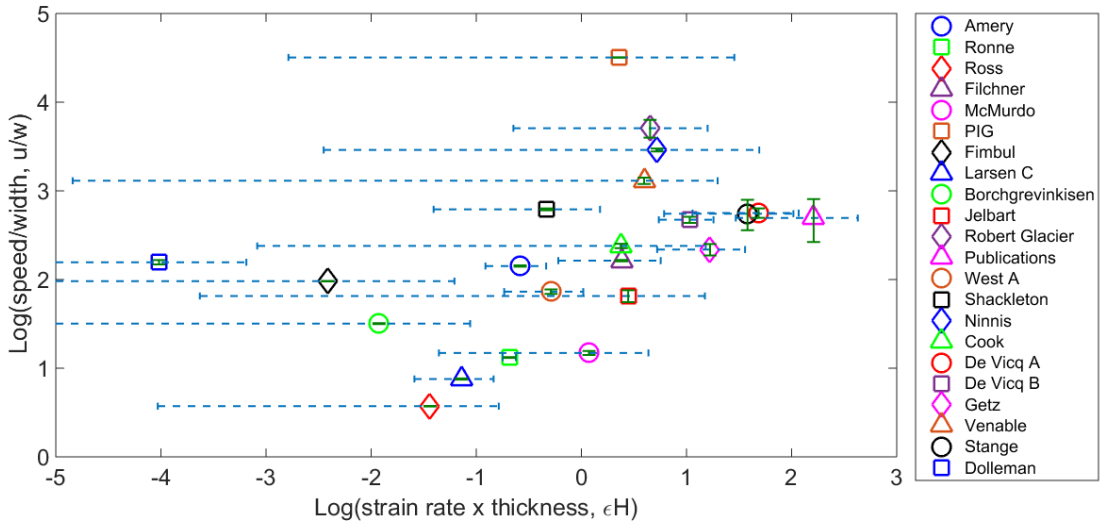

Figure 4.3: Full dataset of 22 Antarctic ice shelves, plotting speed divided by shelf width (u/w) against strain rate multiplied by shelf thickness (ϵH) in log-log space. Vertical error-bars (green) denote standard deviation in speed from mean speed, plotted about point measurement of speed. Horizontal error-bars (dashed blue) denote standard deviation in strain rate.

in the accuracy of the speed values. When comparing the standard deviation in speed calculated here, with the error in flow speed provided as part of the original data product (Rignot et al., 2011a), (see Table C.1 for details) we see that the standard deviation is of the same order of magnitude or higher, indicating that the original errors in the velocity field are not very significant for this analysis.

The standard deviation in strain rate is much larger, which is expected given the high spatial variability in strain rate observed in the previous data-compilation section. Values with large strain rate appear to have smaller standard deviations, but this may be because data points with low strain rate values have large relative standard deviations. From Figure 4.3 it is clear that there is a large degree of scatter to the data and some uncertainty in the horizontal position of data points.

As part of an initial assessment we apply a Robust Regression procedure iteratively to the full dataset, with the aim of identifying a linear trend in log-log space. A Robust Regression is similar to a Least-Squares regression but with data points re-weighted depending on the size of their residual until an optimum regression model is achieved. Here we use the MATLAB robust fitting option for a linear regression model with a bisquare weight function. The Robust Regression procedure is outlined in Holland and Welsch (1977). Using the Robust Regression method the most outlying data point can be identified, and removed from the dataset. If this process is then repeated, more outlying data points can be identified and removed until a threshold R^2 value is achieved indicating that a

regression model has been obtained with a good fit to the remaining data. I choose a threshold R^2 value of 0.8, which is exceeded for this dataset once 9 ice-shelf data points have been removed. This regression model takes the form $\log(u/w) = A + B\log(\epsilon H)$, with slope $B = 0.64$ and $R^2 = 0.83$ (see Figure C.1 in Appendix). Here all outliers are positioned above the regression line, suggesting a fundamental difference between the outlying and included shelves. Although this procedure allows outliers to be removed and a linear trend to be identified in log-log space, it assumes an underlying linear trend is present in the majority of the data and there is no physical premise or understanding used to determine which shelves are removed.

In the scaling analysis of Hindmarsh (2012), two assumptions were made in order to obtain the scaling relationship. First it was assumed that the shelf was laterally confined between pinning points. Secondly, the ice shelf was assumed to be modelled using a Glen's Flow Law rheology, with constant flow law parameters B and n. This ensures comparable rheology in the ice-shelf margins and along the centre line of the shelf. Preliminary assessment of the ice shelves in this dataset shows that some are not laterally confined at the calving front and there are some which may have non-uniform ice-rheology. I therefore look to make a classification of the geophysical characteristics of the shelves in relation to their confinement and rheology.

4.3.1 Classification of the geophysical characteristics of ice shelves

Assessment of ice-shelf confinement is undertaken using visual MODIS data and maps of the surface velocity field to identify whether the calving front is laterally confined. I define the calving front to be laterally confined if a section of the ice shelf less than half the shelf width protrudes past the final pinning point into the open ocean. The MODIS data is used to identify the extent of the shelf, while the velocity field can be utilized to locate pinning points and stationary ice along the ice-shelf margins.

The second assumption, concerning uniform ice-shelf rheology, is addressed through analysis of MODIS imagery to identify the presence of ice damage in the form of fractures and crevasses, which may lead to a reduction in the effective ice viscosity. In addition to this, the transverse-shear field ($\hat{\mathbf{n}}.\mathbf{e}.\hat{\mathbf{u}}$, with $\hat{\mathbf{n}}$ the unit vector normal to flow direction) is calculated to determine whether a threshold transverse-shear value is exceeded in the margins of the shelf. I use a threshold value of 0.05 yr^{-1}.

This threshold strain-rate value corresponds to a shear stress of 130 kPa; assuming

a Glen's Flow Law rheology as in equation (4.3), with $n = 3$ and $B = 1.42 \times 10^8$ $s^{1/3}$ Pa (B value at -10°C from Cuffey and Paterson (2010)), and approximating the second invariant of the strain-rate tensor with the transverse-shear value divided by two ($e_{II} \approx (\hat{\mathbf{n}}.\mathbf{e}.\hat{\mathbf{u}})/2$). This shear stress is greater than the 70 kPa critical stress value used by Albrecht and Levermann (2012) when simulating the evolution of fractures on the Ronne and Filchner ice shelves. However, it sits within the estimates for maximum stress derived from field measurements, which give values of 90 - 320 kPa (Vaughan, 1993). Comparisons can also be made with values of basal shear stresses for grounded ice, which rarely exceed 70 kPa over large areas (Joughin et al., 2004).

Where regions of high shear rate are identified using this 0.05 yr^{-1} threshold, there are often places of higher shear rate contained within these regions. Therefore this critical shear stress represents a minimum stress in these areas and it is likely that there are locations where the shear stress is higher. Including the other two components of the strain-rate tensor, the along-flow and perpendicular-to-flow strain, in the calculation of the second invariant will also contribute to increasing the value of shear stress. This suggests that these areas of high shear rate, greater than 0.05 yr^{-1}, correspond to regions where fractures and crevasses form. Once this damage has occurred the ice can no longer be described using constant flow law parameters (B and n in Glen's Flow Law), and therefore the Hindmarsh (2012) scaling relation breaks down.

The links between weak ice, damage (crevasses and fractures) and areas of high shear were considered in the work of Sandhäger (2003) and Vieli et al. (2006) when reconstructing the flow field for the pre-collapse Larsen B Ice Shelf. Sandhäger (2003) compared an ice-shelf model with uniform rheological parameters to one adjusted to account for weak viscosity in areas of high shear stress and areas with ice advected from areas of high shear. In doing so, it was observed that the adjusted model more accurately reproduced the flow field. This mechanical effect was attributed to ice damage in the form of fractures and crevasses sustained after undergoing high shear. High shear areas were identified by determining whether the modelled shear stress had exceeded a critical value. Vieli et al. (2006) hypothesized that high shear could lead to heating and weakening of the ice, while the formation of crevasses would allow surface melt to penetrate more deeply and warm the ice in these regions, leading to further softening. Vieli et al. (2006) identified weak ice margins as playing a dominant role in controlling the flow of the Larsen B Ice Shelf, and were able to locate weak ice zones by inverting for the flow law parameter B. This technique provided a better fit to observations than a model with uniform B.

Using the criteria for lateral confinement and weak ice margins, each shelf is allocated to one of three groups: YES - ice shelves which conform to the assumptions of the scaling

analysis being laterally confined with uniform rheology; NO - ice shelves that are not laterally confined and/or they have non-uniform rheology; MAYBE - shelves where it is unclear whether the assumptions are valid.

4.3.2 Examples of geophysical characteristics and classification

Here I show two examples of the geophysical classification of ice shelves, depending on their lateral confinement and rheology. (Plots used for the geophysical classification of all shelves can be found in the Appendix C and are also available at www.repository.cam.ac.uk/handle/1810/247061.)

Plots for Fimbul Ice Shelf are shown in Figures 4.4a (MODIS imagery), 4.4b (velocity field), 4.4c (strain-rate field) and 4.4d (shear-rate field). From visual assessment of the MODIS image, Figure 4.4a, it is clear that the calving front is not laterally confined with a large section of the shelf, approximately one shelf-width long, protruding out past pinning points. The velocity field, Figure 4.4b, shows high speed values of approximately 700 $\mathrm{m\,yr^{-1}}$ in the main body of the ice shelf, but slow-moving sections of ice (possibly grounded) are observed further upstream prior to the unconfined section. It is clear that the calving front has moved past these pinning points to form an ice tongue. The MODIS image shows some fracturing along the left margin of the shelf, which appears to correspond with high positive along-flow strain (Fig. 4.4c), rather than high transverse shear (Fig. 4.4d). This ice shelf should therefore be included in the NO group.

Figures 4.5a, 4.5b, 4.5c and 4.5d, show MODIS imagery, velocity field, strain-rate field and shear-rate field for Pine Island Glacier (PIG) Ice Shelf. From the MODIS (Fig. 4.5a) and velocity-field (Fig. 4.5b) plots it is clear that the ice shelf is confined laterally between sections of slow moving ice. However, in the MODIS data it is evident that there is a large amount of crevassing and fracturing in the ice shelf. Assessment of the velocity field indicates a large gradient in speed between the main body of the ice shelf, flowing at over $3500\,\mathrm{m\,yr^{-1}}$, and the near stationary margins. This feature is clearly evident in the plot of transverse shear-rate, Figure 4.5d, where high values of shear are observed in the shelf margins, saturating the colourscale, which is limited by the 0.05 $\mathrm{yr^{-1}}$ threshold criterion for uniform rheology. It is also clear that the margins and grounding line of the shelf are areas of high positive strain rate, Figure 4.5c. Based on the presence of numerous fractures and the high shear values in the shelf margins, we classify Pine Island Glacier Ice Shelf as having weak margins.

Table 4.2 lists all 22 ice shelves, their geophysical characteristics and their classification.

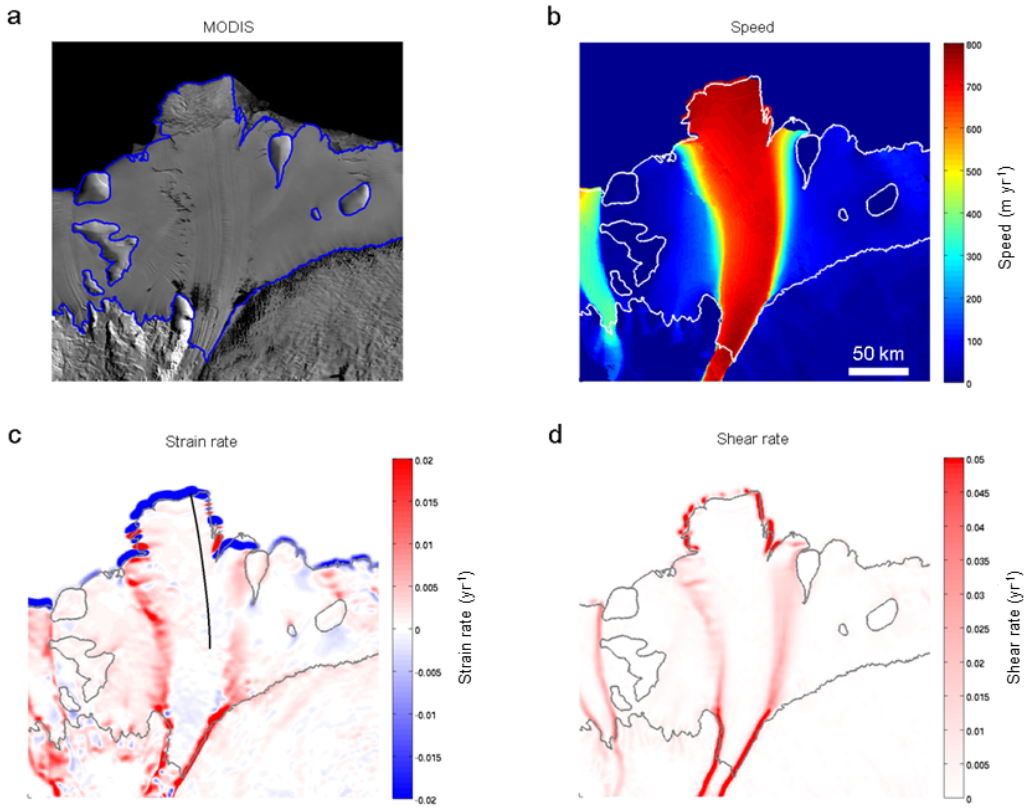

Figure 4.4: Plots for Fimbul Ice Shelf: a) MODIS image; b) Velocity field ($\mathrm{m\,yr^{-1}}$); c) Along-flow strain rate field ($\mathrm{yr^{-1}}$), with maximum-velocity flow line; d) Transverse-shear rate ($\mathrm{yr^{-1}}$). Note: artefacts due to the filtering of the velocity field are present near the ice-ocean boundary for the along-flow strain and transverse shear rates. All plots include grounding line, islands and coast outline. This is an example of a NO ice shelf as the calving front has past the lateral pinning points.

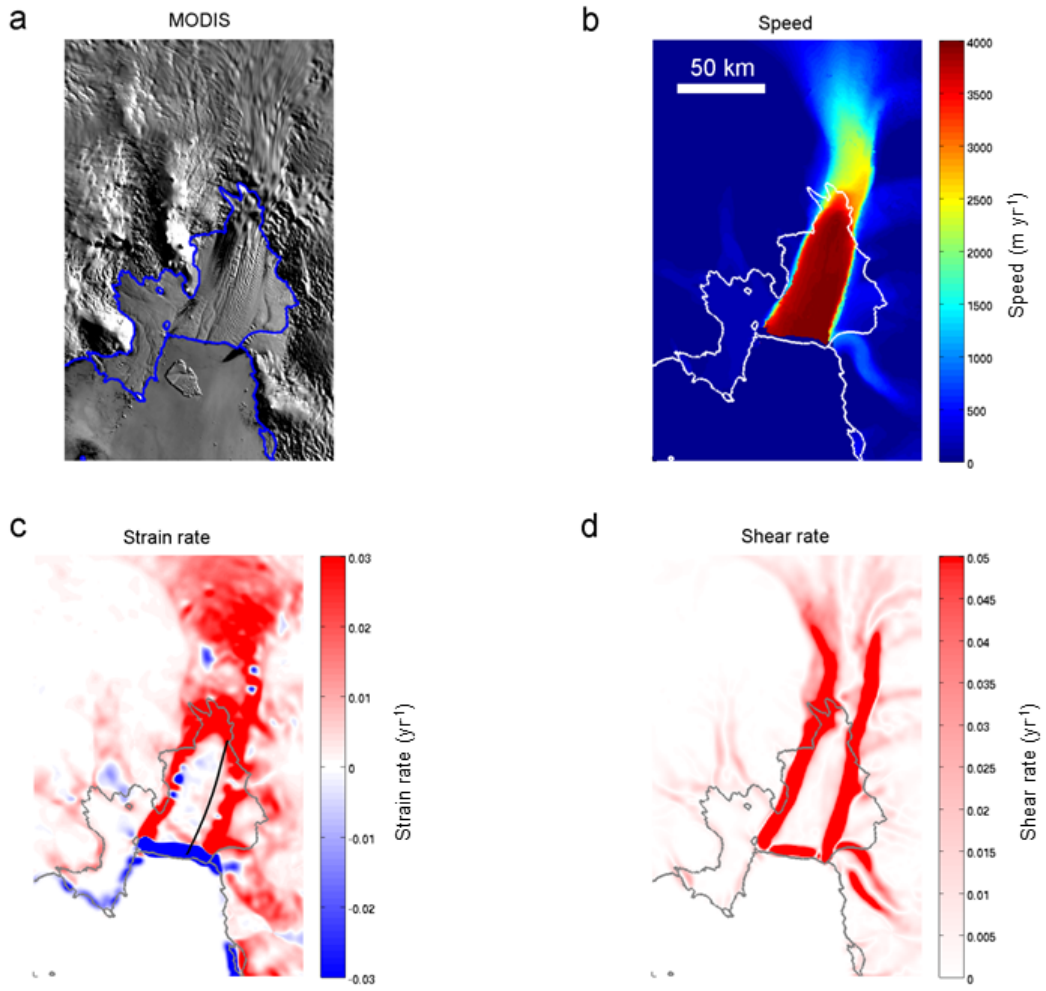

Figure 4.5: Plots for Pine Island Glacier (PIG) Ice Shelf: a) MODIS image; b) Velocity field (m yr^{-1}); c) Along-flow strain rate field (yr^{-1}), with maximum-velocity flow line; d) Transverse-shear rate (yr^{-1}). Note: artefacts due to the filtering of the velocity field are present near the ice-ocean boundary for the along-flow strain and transverse shear rates. All plots include grounding line, islands and coast outline. This is an example of a NO ice shelf due to the high shear values exceeding 0.05 yr^{-1} in the shelf margins.

Shelf	Not laterally confined? (MODIS)	Not laterally confined? (Speed field)	Damage?	High shear?	Comment	Assumptions Apply?
Amery	?	?	×	×	Possible non-confined	MAYBE
Borchgrevinkisen	?	?	?	×	Possible non-confined/some damage	MAYBE
Cook	?	?	✓	×	Possible non-confined/some damage	MAYBE
De Vicq A	×	×	×	×	-	YES
De Vicq B	×	×	×	×	-	YES
Dolleman	×	?	✓	?	Possible non-confined/some damage	MAYBE
Filchner	×	×	×	×		YES
Fimbul	✓	✓	?	×	Non-confined	NO
Getz	×	×	×	×	-	YES
Jelbart	×	×	?	×	-	YES
Larsen C	×	×	×	×	-	YES
McMurdo	×	×	×	×	-	YES
Ninnis	✓	✓	✓	✓	Non-confined with damage	NO
PIG	×	×	✓	✓	Damage	NO
Publications	?	✓	✓	✓	Non-confined with damage	NO
Ronne	×	×	×	×	-	YES
Robert Glacier	✓	✓	✓	✓	Non-confined with damage	NO
Ross	×	×	×	×	-	YES
Shackleton	✓	✓	✓	✓	Non-confined with damage	NO
Stange	×	×	×	×	-	YES
Venable	×	×	?	?	Possible damage	MAYBE
West A	?	?	✓	×	Possible non-confined/some damage	MAYBE

Table 4.2: Table showing classification of ice shelves in terms of the lateral confinement of the calving front and the presence of damage in ice shelf margins or high shear values ($\geq 0.05\,\mathrm{yr}^{-1}$) in margins.

4.3.3 Analysis of Laterally Confined and Uniform Rheology Shelves

Using the geophysical classification, I now investigate relationships between the variables for the YES category of ice shelves; those that are laterally confined and have uniform rheological parameters. Data from this subgroup of 10 ice shelves are plotted in log-log space in Figure 4.6. A Least-Squares linear regression is then applied to the data, which produces a model of the form, $\log(u/w) = 1.60 + 0.72\log(\epsilon H)$, with an R^2 value of 0.92. The linear fit can be seen in Figure 4.6, which includes the 95% confidence interval for the regression along with the excluded data points from the full dataset. This linear regression suggests the proportionality $u \propto w(\epsilon H)^{0.72}$ which is close to the relationship Hindmarsh derived from the scaling analysis ($u \propto w(\epsilon H)^{0.75}$).

This regression model can also be plotted in linear space, as seen in Figure 4.7. Here we observe that the regression model provides a good fit to the data. A number of points are clustered close to the origin, but using a regression in log-log space enables the non-linear trend through these points to be clearly identified. Again the data points for the excluded ice shelves are included in this plot and it is clear that they mostly lie above the curve, indicating that the speed at the calving front for the excluded shelves is greater than expected for the laterally-confined shelves. This is probably a consequence of the reduced resistance to flow due to the absence of lateral pinning points, or the presence of weak/damaged margins.

4.4 Discussion and Conclusions

In this chapter I have aimed to build on and clarify the work of Alley et al. (2008) and Hindmarsh (2012) concerning the ice-flow dynamics in the zone close to the ice-shelf calving front, primarily by compiling a larger dataset to compare with a relationship derived from a scaling analysis. From this dataset of 22 Antarctic ice shelves, I have observed that there is a positive correlation between the speed of ice at the calving front and the product of shelf width, strain rate and ice thickness. However, there is a large degree of scatter to the data when looking for trends.

In the process of analysing the data I have identified a subgroup containing those ice shelves that are laterally confined and have close to uniform rheological parameters. Applying a Least-Squares regression model to this data gives the proportionality $u \propto w(\epsilon H)^{0.72}$, with an R^2 value of 0.92. This is close to the scaling analysis relationship derived by Hindmarsh (2012), $u \propto w(\epsilon H)^{3/4}$. Possible explanations for this variance

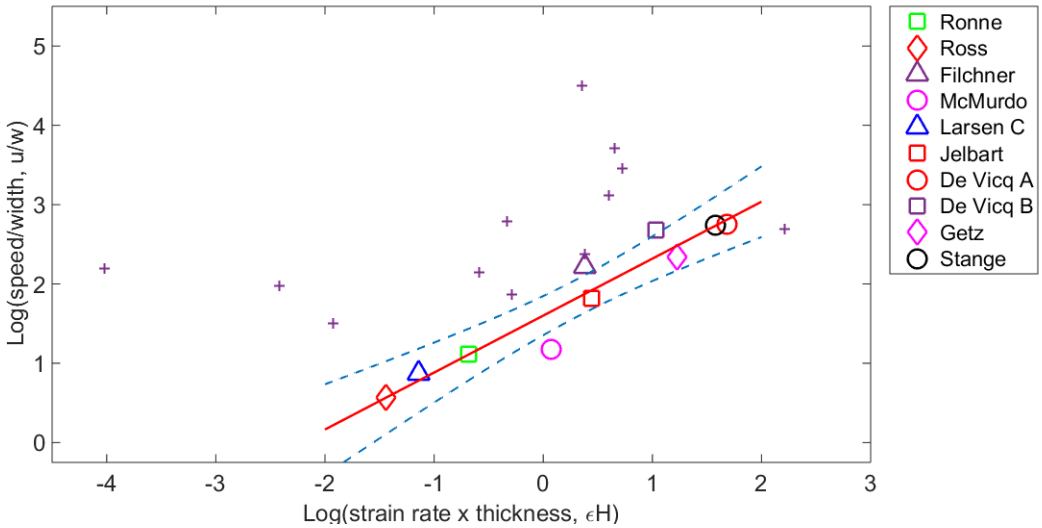

Figure 4.6: Scatter plot of u/w against ϵH in log-log space. Shelves that are laterally-confined and have close to uniform rheological parameters are identified in the key, with a Least-Squares linear regression applied to the data, shown by the red line. The blue dashed curves bound the 95% confidence interval for this regression model. Data points from the full dataset that are not included in the regression are denoted by purple crosses.

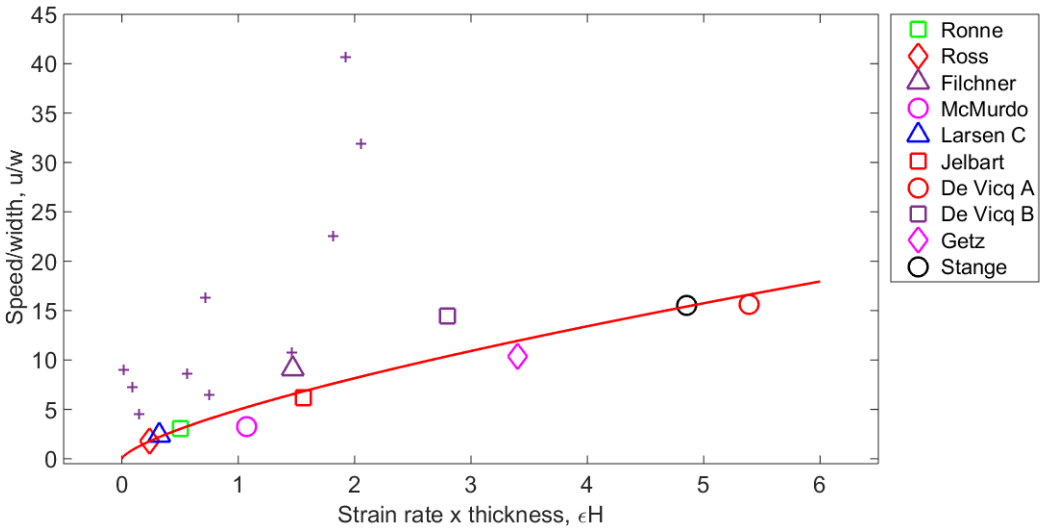

Figure 4.7: Scatter plot of u/w against ϵH. Least-Squares regression model calculated in log-log space, but plotted here in linear space, shown by red curve. Data points excluded from the regression model due to non-lateral confinement and/or weak margins are denoted by purple crosses. Two excluded data points are outside field of view: PIG at (1.45, 90.4) and Publications (9.1, 14.8).

away from the theoretical value are: small spatial variations in rheological parameters (B and n) not considered in the scaling analysis; the Glen's Flow Law exponent n may differ slightly from 3; non-parallel lateral boundaries at the calving front, allowing extension laterally; asymmetric or varying ice flux from upstream; effects of submarine melting or freeze-on; errors in the data and data compilation.

When comparing laterally-confined and non-damaged ice shelves, with the remaining shelves in the dataset, it is clear that the remaining shelves have greater ice-flow speeds at the calving front. This may be explained by the reduced resistance to flow these shelves experience due to the absence of lateral pinning-points, or weak rheology in the shelf margins.

It is clear that the spatial variation in flow law parameters plays an important role in controlling the flow dynamics of the ice shelf. Additional features pertaining to ice rheology that could be considered in future theoretical assessments of ice flow at the calving front could include: spatially varying rheological parameters such as the flow law parameter, B, and the Glen's Flow Law exponent, n; spatially varying ice-temperature field; or considering the ice deformation history (strain and shear history).

A more thorough assessment of the spatial variation in ice-shelf rheological parameters could be undertaken by inverting for the flow law parameter B. This would allow a quantitative measure of weakening in the ice-shelf margins to be used when making a geophysical classification of the ice shelves.

For some shelves in the NO and MAYBE groups, the effective ice rheology appears to be close to uniform (undamaged), however data from these shelves can not be compared to the scaling relation because the calving front is located on ice which protrudes past the final lateral pinning points. Additional data could be included from these shelves by taking values of speed, strain rate, ice thickness and width at the final pinning point of the shelf. This would only be valid for shelves where the final pinning points form a parallel section of the channel. Once ice flows past this final pinning point the ice tongue section of the shelf theoretically exerts little buttressing on the confined shelf. However, if the unconfined section is large there may be significant hoop stresses. Therefore the dynamics at the pinning point should remain fairly unchanged regardless of the presence of the ice tongue. This location could be determined by constructing a straight line between the two final lateral pinning points and finding where this line intersects the flow-line of maximum velocity. Alternatively, the Principal Axes of Strain could be calculated. The 2$^{\text{nd}}$ Principal Axes of Strain could then be used to determine where there is a transition from negative (upstream and confined) to positive (downstream and

unconfined) strain-rate values. This transition from negative 2nd Principal Strain Rate to positive 2nd Principal Strain Rate should define where the ice has started to spread laterally as it leaves the confines of pinning points.

When the dataset presented here is compared to the dataset of Alley et al. (2008), we see that for most of the ice shelves included in both datasets (Amery, Filchner, Ronne and Ross) the data is mostly consistent (exceptions McMurdo and PIG). If the ice-shelf data points from Alley et al. (2008) are plotted alongside this new dataset they can be found on or above the regression line we determine after geophysical interpretation.

The empirical law derived by Alley et al. (2008) was designed to be descriptive of calving. Although the work presented here is not informative of calving, the newly compiled dataset gives values of strain rate close to the calving front and could suggest a criteria for critical strain rates that can be sustained for ice shelves with a certain flow speed, thickness and width. By inverting the plots of u/w against ϵH, it is clear that the regression curve provides an upper bound on the product of strain rate and thickness for the range of shelves. This bounding curve was found using the mean strain rate over the final 20km of the shelves, so it is expected that higher strain rates would be plotted if the maximum strain rate along the flow line were considered, and therefore increasing the values of this bounding curve. For the non-confined shelves, values of shear and transverse strain, in addition to along-flow strain, may be informative of the deformation occurring at the calving front. These values may be useful in determining the material properties of ice at the calving front and helpful for predicting calving events.

From this investigation we have determined that the scaling analysis of Hindmarsh (2012) agrees well with the data collected for ice shelves that are laterally confined and have close to uniform rheological parameters. However, this scaling breaks down when the shelves are no longer confined and are able to spread in both the along-flow and transverse-to-flow directions, or when weak ice in the shelf margins results in reduced resistance to flow.

Chapter 5

Idealized Models for Laterally Confined Ice Shelves

5.1 Introduction

From analysis of the flow fields of Antarctic ice shelves in the previous two chapters, it is clear that most ice shelves are confined in an embayment, a channel or between lateral pinning-points that act to channel the main flow of the shelf. Therefore, in this chapter I develop some simple idealized models focused on understanding the flow of ice shelves confined laterally within a channel. Using idealized models allows a range of physical processes to be investigated. Parameters can be tested systematically without the complexities that arise from attempting to model a geophysical situation, where there are large numbers of variables and physical processes occurring, which are often not fully understood.

These idealized models can then be compared with geophysical data, with the aim of elucidating the large-scale flow dynamics and buttressing of ice shelves. I focus on comparisons with Amery Ice Shelf, which has a long thin channel geometry and is slightly diverging.

Initially I consider the flow of shelves in parallel and slowly diverging channels of infinite length. Using this geometry, similarity solutions can be formed for the shelf thickness profiles. Although direct comparisons can not be made with the geophysical data, some qualitative comparisons can be made and the solutions provide mathematical completeness for the development of later models.

Sections 4 and 5 form the main focus of this chapter, in which steady-state solutions for shelves in finite-length channels are developed. First, shear-dominated dynamics are

assumed throughout the shelf, allowing an analytical steady-state to be obtained for the thickness profile. The effects of varying parameters, such as viscosity, can be investigated using these solutions by assessing the impact on the shelf thickness and dynamics. Further comparisons can be made directly to the geophysical data. Secondly, a numerical model is developed and used to assess the impact of including both shear and extensional dynamics in the shelf. Comparisons are then made with the shear-only case and the geophysical example.

Within this Chapter I produce analytical solutions for Newtonian shelves in parallel channels. These solutions match those of Pegler (2012), however I have developed the theoretical work further to include general power-law rheologies and diverging channels.

5.2 Considering Shear-Dominated Dynamics

As observed in the previous two chapters many ice shelves are confined within a channel geometry. While confined within a channel, and especially far from the channel exit, the flow dynamics within the shelf are dominated by the shear stresses between the lateral side-walls (Pegler, 2012; Kowal et al., 2016).

When an ice shelf is confined in a channel, the dominant flow is in the along-channel direction, as seen in the analysis of the ice-surface velocity data in Chapter 3. This flow is induced by gradients in shelf thickness in the along-channel direction as detailed in Chapter 2. Any lateral flow must be due to gradients in thickness that are transverse to the channel direction. Observations suggest this lateral flow is much less than the along-channel flow and flow is unable to penetrate the side-walls of the channel. Therefore, I assume a uniform cross-channel thickness that produces no cross-channel flow.

5.3 Similarity Solution

The horizontal force-balance equation for a two-dimensional ice shelf with no vertical shear is given by

$$\nabla \mu H \left(\nabla . \mathbf{u}\right) + \nabla . \left(\mu H \mathbf{e}\right) = \frac{\rho g'}{2} H \nabla H. \tag{5.1}$$

For the case of an ice shelf confined to a narrow channel with the shear stress between the two no-slip side walls providing the dominant stress and controlling the dynamics of the shelf, this force balance equation reduces to

$$\frac{\partial}{\partial y}\left(\mu H \frac{\partial u}{\partial y}\right) = \rho g' H \frac{\partial H}{\partial x}, \tag{5.2}$$

where the channel is aligned in the x-direction and the y-coordinate designates the transverse position. This equation is subject to boundary conditions along the channel walls. Here I assume a no-slip condition at the channel walls, such that $u = 0$ at $y = 0$ and $y = w$.

5.3.1 Parallel Channel

In the case of a parallel channel of fixed width w, the force-balance equation (5.2) can be integrated and the no-slip side wall boundary conditions imposed to give an equation for the along-channel velocity of the shelf. The shelf thickness H is assumed to be uniform across the width of the channel, and is given as a function of x and time t, $H \equiv H(x,t)$. The velocity can be integrated horizontally across the channel width and vertically through the thickness of the shelf to give an equation for the flux q. For a shelf with Newtonian rheology, with constant dynamic viscosity μ, the kinematic viscosity is denoted by $\nu = \mu/\rho$ and the velocity and flux are

$$u(x,y) = \frac{g'}{2\nu}\frac{\partial H}{\partial x}(y^2 - wy), \tag{5.3}$$

$$q = -\frac{g'}{12\nu}w^3 H\frac{\partial H}{\partial x}. \tag{5.4}$$

For a power-law rheology the effective viscosity is given by

$$\mu_{eff} = B' e_{II}^{(1-n)/n}. \tag{5.5}$$

Here e_{II} is the second invariant of the strain-rate tensor and B' is the consistency index, determined by the rate factor B, such that $B' = B/2$. In this case, where the flow dynamics are controlled by the shear between the channel walls, the effective viscosity takes the form

$$\mu_{eff} = \frac{B'}{2^{(1-n)/n}}\left|\frac{\partial u}{\partial y}\right|^{(1-n)/n}. \tag{5.6}$$

Therefore, the velocity of the shelf and the flux are given by

$$u = (-w)^{n+1}\frac{2^{-2n}}{n+1}\left(\frac{\rho g'}{B'}\right)^n\left(\frac{\partial H}{\partial x}\right)^n\left[\left(\left|1 - \frac{2y}{w}\right|\right)^{n+1} - 1\right], \tag{5.7}$$

$$q = (-w)^{n+2}\frac{2^{-2n}}{n+2}\left(\frac{\rho g'}{B'}\right)^n H\left(\frac{\partial H}{\partial x}\right)^n. \tag{5.8}$$

I continue by considering the generic case with a general power-law rheology. The value of n can be chosen later to consider different fluid rheologies, be that Newtonian ($n = 1$) or Glen's Flow Law ($n = 3$).

The continuity equation is then given by

$$w\frac{\partial H}{\partial t} + \frac{2^{-2n}}{n+2}\left(\frac{\rho g'}{B'}\right)^n \frac{\partial}{\partial x}\left[H\left(\frac{\partial H}{\partial x}\right)^n (-w)^{n+2}\right] = 0, \tag{5.9}$$

where the effects of accumulation and ablation have been neglected, so that $a = 0$. From equations (5.8) and (5.9), scaling relationships for this system can determined. We have two length-scales, along-channel length $[x]$ and shelf thickness $[H]$, and one time scale $[T]$. There are two equations linking these three scales, which means it is possible to determine a similarity solution for the ice-shelf thickness profile. The equations for the shelf flux and evolution of the shelf thickness give

$$q_0 \sim (-w)^{n+2}\frac{2^{-2n}}{n+2}\left(\frac{\rho g'}{B'}\right)^n \frac{[H]^{n+1}}{[x^n]}, \tag{5.10}$$

$$\frac{[H]}{[T]} \sim w^{n+1}\frac{2^{-2n}}{(n+2)}\left(\frac{\rho g'}{B'}\right)^n \frac{[H]^{n+1}}{[x]^{n+1}}, \tag{5.11}$$

$$\tag{5.12}$$

where I have assumed a constant input flux $q = q_0$. From this

$$[x]^n \sim \frac{w^{n+2}}{q_0}\gamma[H]^{n+1} \quad \text{and} \quad [H]^n \sim -\gamma^{-1}w^{-(n+1)}\frac{[x]^{n+1}}{[T]}, \tag{5.13}$$

$$\text{where} \quad \gamma = (-1)^n\frac{2^{-2n}}{(n+2)}\left(\frac{\rho g'}{B'}\right)^n. \tag{5.14}$$

This can be rearranged further to give

$$\Rightarrow [x] \sim \left(w\gamma q_0^n[T]^{n+1}\right)^{\frac{1}{2n+1}}, \tag{5.15}$$

$$\Rightarrow [H] \sim -\left(\frac{q_0^{n+1}[T]^n}{\gamma w^{2n+2}}\right)^{\frac{1}{2n+1}}. \tag{5.16}$$

Here we can see that the front of the shelf propagates at a rate proportional to $t^{(n+1)/(2n+1)}$, which in the case of $n = 1$ gives $t^{2/3}$ and in the case of $n = 3$ gives $t^{4/7}$. The thickness of the shelf increases like $t^{n/(2n+1)}$. From this scaling relationship it is clear that there is a similarity solution of the form,

$$x = \left(\gamma w q_0^n t^{n+1}\right)^{\frac{1}{2n+1}}\eta, \tag{5.17}$$

$$H = \eta_N^{\frac{n+1}{n}}\left(\frac{q_0^{n+1}t^n}{\gamma w^{2n+2}}\right)^{\frac{1}{2n+1}}\Phi\left(\frac{\eta}{\eta_N}\right). \tag{5.18}$$

with $\chi = \eta/\eta_N$. Substituting the similarity solution variables into the continuity equation gives an ODE for the function $\Phi(\chi)$.

$$\frac{\partial H}{\partial t} = -\gamma w^{n+1} \frac{\partial}{\partial x}\left[H\left(\frac{\partial H}{\partial x}\right)^n\right], \tag{5.19}$$

$$\Rightarrow \frac{n}{2n+1}\Phi(\chi) - \frac{n+1}{2n+1}\chi\frac{\partial \Phi}{\partial \chi} = -\frac{\partial}{\partial \chi}\left[\Phi(\chi)\left(\frac{\partial \Phi}{\partial \chi}\right)^n\right]. \tag{5.20}$$

This ODE is subject to boundary conditions at the source and at the nose of the current. At the source I impose a constant input flux into the shelf, while at the nose the thickness of the shelf goes to zero and the advance of the front is equal to the mean speed at the front. These boundary conditions take the following form

$$w^{n+2}\gamma H\left(\frac{\partial H}{\partial x}\right)^n = q_0 \qquad \text{at } x = 0, \tag{5.21}$$

$$\Rightarrow \eta_N^{\frac{2n+1}{n}}\Phi(\chi)\frac{\partial \Phi}{\partial \chi} = 1 \qquad \text{at } \chi = 0. \tag{5.22}$$

$$H = 0 \qquad \text{at } x = x_N, \tag{5.23}$$

$$\Rightarrow \Phi(\chi) = 0 \qquad \text{at } \chi = 1. \tag{5.24}$$

$$\frac{\partial x}{\partial t} = \frac{q}{H} = w^{n+1}\gamma\left(\frac{\partial H}{\partial x}\right)^n \qquad \text{at } x = x_N, \tag{5.25}$$

$$\Rightarrow \left(\frac{\partial \Phi}{\partial \chi}\right)^n = \frac{n+1}{2n+1} \qquad \text{at } \chi = 1 \quad . \tag{5.26}$$

The ODE can be solved numerically using these boundary conditions for various values of the flow exponent n.

For a Newtonian shelf, with power-law flow exponent $n = 1$ the ODE and boundary conditions become

$$\frac{1}{3}\Phi(\chi) - \frac{2}{3}\chi\frac{\partial \Phi}{\partial \chi} = -\left(\frac{\partial \Phi}{\partial \chi}\right)^2 - \Phi(\chi)\frac{\partial^2 \Phi}{\partial \chi^2}, \tag{5.27}$$

$$\eta_N^3\Phi(\chi)\frac{\partial \Phi}{\partial \chi} = 1, \qquad \text{at } \chi = 0, \tag{5.28}$$

$$\Phi(\chi) = 0, \qquad \text{at } \chi = 1, \tag{5.29}$$

$$\frac{\partial \Phi}{\partial \chi} = \frac{2}{3}, \qquad \text{at } \chi = 1. \tag{5.30}$$

This can be solved numerically to determine a thickness profile for the shelf, as shown in Figure 5.1. This is the solution for a laterally-confined Newtonian gravity current (such

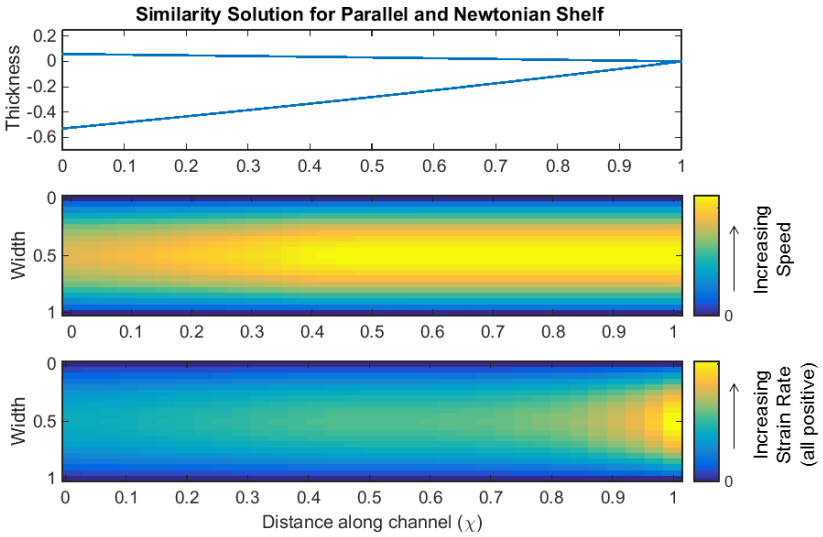

Figure 5.1: Similarity solution for a Newtonian shelf in a parallel channel. From top to bottom: thickness profile; speed plot; along-channel strain rate. Along-channel distance is given in terms of similarity variable χ. Values of speed and strain rate are not shown as these plots should be assessed qualitatively, rather than quantitatively.

as in a vertical Hele-Shaw cell) as determined previous by Huppert (1986) and Pegler et al. (2013). From Figure 5.1 it is clear that the thickness profile is almost linear, with a slight increase in thinning in the downstream direction. Here the speed and strain-rate maps do not show numerical values as I am concerned with the qualitative features rather than making direct quantitative comparisons with geophysical examples. The speed plot has a parabolic profile across the width of the channel, with no-slip along the channel walls and a peak in velocity at the centre of the channel. There is acceleration and positive along-channel strain rate throughout the shelf, with the greatest strain rate at the centre of the front of the shelf.

This process can be repeated for a power-law shelf, with flow exponent $n = 3$ as shown in Figure 5.2. Here the similarity solution again gives an approximately linear thickness profile, with even less curvature than the Newtonian case. It is also clear that there are significant differences in the structure of the velocity plot, with a central section of fast flow and margins with high shear and reduced effective viscosity. There is little acceleration of this central section along the length of the channel as can be seen in the along-flow strain rate plot, although there are some higher values towards the end of the shelf.

Comparison with Geophysical Data

Simple comparisons can be made between the thickness profiles, speed plots and strain-rate plot obtained from these similarity solutions and the corresponding geophysical data

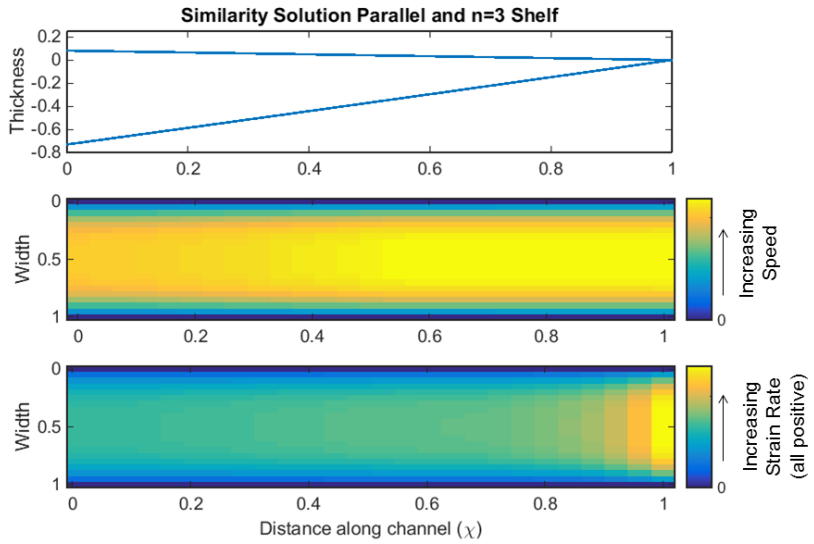

Figure 5.2: Similarity solution for a power-law $n = 3$ shelf in a parallel channel. From top to bottom: thickness profile; speed plot; along-channel strain rate. Along channel distance is given in terms of similarity variable χ.

for Amery Ice Shelf, which can be seen in Figure 5.3. Here it is clear that away from the upstream end (approximately 150 km downstream from the grounding line) the thickness profile is approximately linear, which agrees with the structure of the thickness profiles determined from the similarity solutions in both the Newtonian and $n = 3$ case. When comparisons are made between the speed plots, it is evident that in the middle part of Amery Ice Shelf there is 'plug like' flow across the width of the channel with narrow shear margins, which agrees qualitatively with the $n = 3$ speed plot. As Amery approaches the channel exit, the flow reaches the maximum speed of the confined section of the shelf, forming a maximum in the centre of the channel. Peaks of this nature are not found at the front of the shelf in the similarity solutions, but are instead stretched out over half the length of the shelf. Therefore, this must be due to the finite length of the channel and the boundary condition at the channel exit.

From the strain-rate plot for Amery it is clear that there is negative strain rate upstream and positive downstream, but in the similarity solutions for parallel channels, positive strain rates are observed throughout. However, Amery Ice Shelf is confined within a diverging channel.

5.3.2 Diverging Channel

Now consider the flow of a power-law fluid ice shelf in a narrow diverging channel, with width varying like $w = \alpha x$. In a similar manner to the previous section, the velocity and

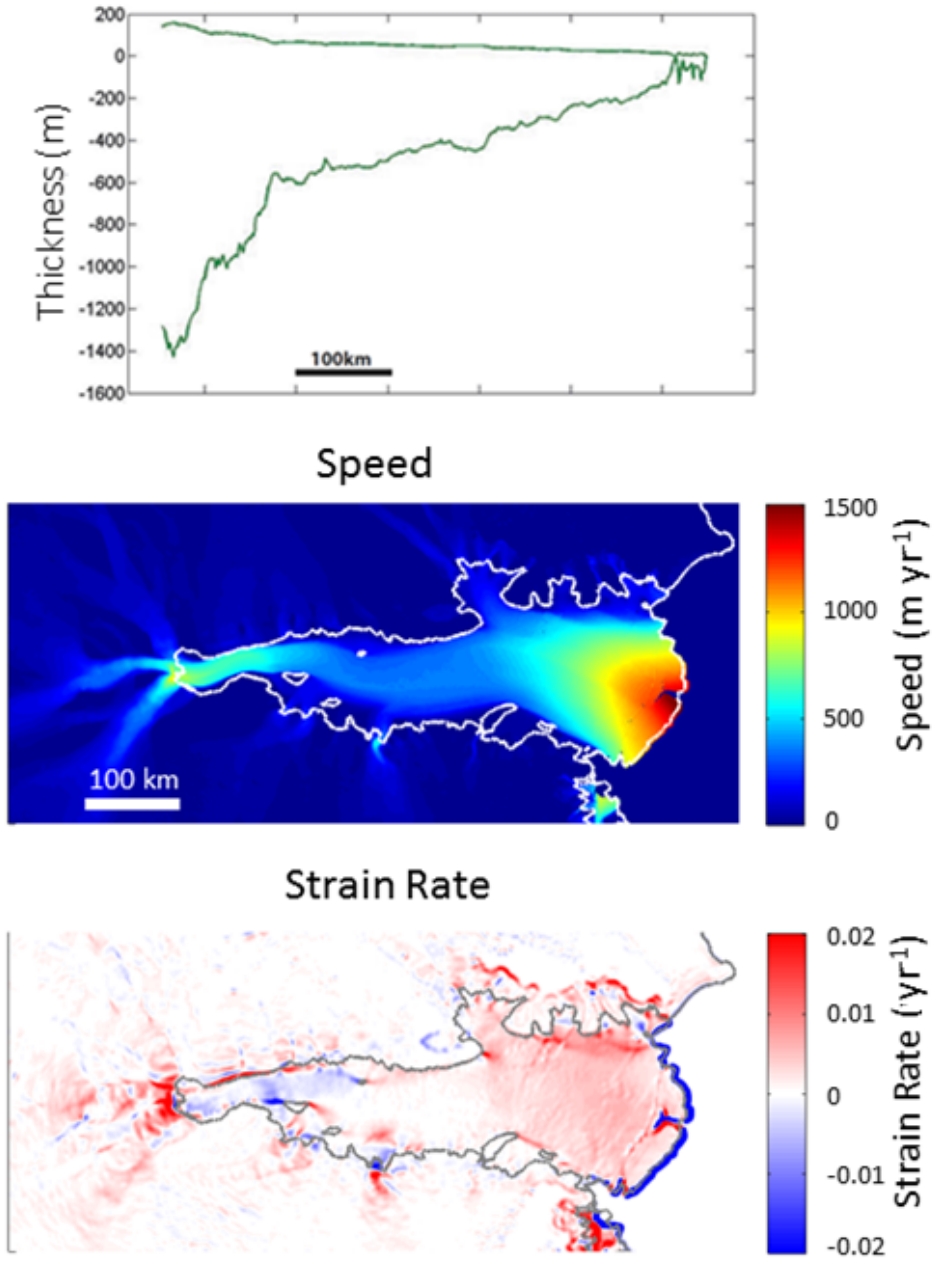

Figure 5.3: Plots for Amery Ice Shelf to be compared with model results. From top to bottom: width-averaged thickness profile; speed plot; along-channel strain rate. For Amery Ice Shelf the shelf thickness varies by less than 100 m across the width of the shelf.

flux take the form

$$u = (-\alpha x)^{n+1} \frac{2^{-2n}}{n+1} \left(\frac{\rho g'}{B}\right)^n \left(\frac{\partial H}{\partial x}\right)^n \left[\left(\left|1 - \frac{2y}{\alpha x}\right|\right)^{n+1} - 1\right], \tag{5.31}$$

$$q = (-\alpha x)^{n+2} \gamma' H \left(\frac{\partial H}{\partial x}\right)^n, \tag{5.32}$$

$$\text{where} \quad \gamma' = \frac{2^{-2n}}{n+2} \left(\frac{\rho g'}{B}\right)^n. \tag{5.33}$$

The continuity equation becomes

$$\frac{\partial H}{\partial t} = -\gamma' \frac{1}{\alpha x} \frac{\partial}{\partial x} \left[H \left(\frac{\partial H}{\partial x}\right)^n (-\alpha x)^{n+2}\right]. \tag{5.34}$$

From this we are able to obtain scaling relationships, which indicate the existence of similarity solutions with

$$x = \left(-\alpha \gamma' q_0^n t^{n+1}\right)^{\frac{1}{2n}} \eta, \tag{5.35}$$

$$H = \left(\frac{1}{(-\alpha)^{n+1} \gamma' t}\right)^{\frac{1}{n}} \Phi(\chi). \tag{5.36}$$

The propagation of the shelf front is therefore proportional to $t^{(n+1)/2n}$. This is in contrast to the parallel channel case, where the rate of propagation for the shelf front was $t^{(n+1)/(2n+1)}$. In the case of a Newtonian shelf we see that the front now propagates linearly in time, compared with $t^{2/3}$ in the parallel channel case. For an $n = 3$ shelf, the front advances like $t^{2/3}$ and hence slows as it advances. However, the deceleration is not as large as the parallel channel case, which propagates like $t^{4/7}$.

This can be explained by considering the relationship between the shelf thickness and the total shear stress produced in each case. For a parallel channel the shelf thins in the along-channel direction. There is a balance between the hydrostatic pressure generated by the thickness gradient and the shear stress with the side walls. As the front of the shelf advances and the shelf becomes thicker the total shear stress increases, slowing the rate of advance of the shelf front. For a diverging shelf, there is a balance between the driving hydrostatic pressure due to the thickness gradient, the shear stress against the side walls and lateral spreading of the shelf as the channel becomes wider. This lateral spreading is constant in a wedge-shaped diverging channel with fixed angle of divergence and acts to thin the shelf. Therefore, as the shelf advances the shelf thickens at a slower rate than the parallel case, due to the lateral spreading and associated thinning that also occurs. The increase in total shear stress is therefore reduced in comparison to the parallel case, and the rate of advance of the shelf front therefore decreases at a reduced

rate in comparison to the parallel case.

Substituting the similarity variables into the continuity equation gives

$$-\frac{1}{n}\Phi(\chi) - \left(\frac{n+1}{2n}\right)\chi\frac{\partial\Phi}{\partial\chi} = \frac{1}{\chi}\frac{\partial}{\partial\chi}\left[\chi^{n+2}\Phi(\chi)\left(\frac{\partial\Phi}{\partial\chi}\right)^n\right], \tag{5.37}$$

which determines the thickness profile of the shelf. As before the boundary conditions take the form

$$(-\alpha x)^{n+2}\gamma' H\left(\frac{\partial H}{\partial x}\right)^n = q_0 \qquad \text{at } x = 0, \tag{5.38}$$

$$\Rightarrow \chi^{n+2}\Phi(\chi)\left[\frac{\partial\Phi}{\partial\chi}\right]^n = \eta_N^2 \qquad \text{at } \chi = 0, \tag{5.39}$$

$$H = 0 \qquad \text{at } x = x_N, \tag{5.40}$$

$$\Rightarrow \Phi(\chi) = 0 \qquad \text{at } \chi = 1, \tag{5.41}$$

$$\frac{\partial x}{\partial t} = (-\alpha x)^{n+1}\gamma'\left(\frac{\partial H}{\partial x}\right)^n \qquad \text{at } x = x_N, \tag{5.42}$$

$$\Rightarrow \frac{n+1}{2n} = \chi^n\left[\frac{\partial\Phi}{\partial\chi}\right]^n \qquad \text{at } \chi = 1. \tag{5.43}$$

The ice-shelf thickness profile, speed and strain-rate plot for Newtonian rheology can be seen in Figure 5.4. It is clear that for this diverging geometry there is initially rapid thinning of the shelf as the shelf flows away from the point source. The point source forms a singularity at $x = 0$ with the thickness profile having the form $1/x$ near the source. The rate of thinning decreases in the along-channel direction leading to a concave profile. In the downstream half of the shelf the thinning is very gradual. From the speed plot there is little variation in the speed along the length of the channel. However, from the negative strain rates in Figure 5.4, it is evident that there is a reduction in the flow speed along the length of the channel. This is due to the widening geometry of the channel, which forces the shelf to slow as it fills the wider section of channel downstream. Figure 5.5 shows the same data, but includes only the region downstream of $\chi = 0.3$ away from the point-source, which is more relevant geophysically. This highlights that the concave thickness profile persists along the whole length of the shelf. It also shows the negative strain rates, which form a minimum at approximately $\chi = 0.45$ and then increase in value as the shelf spreads and thins in the downstream direction. This minimum may be because there is a peak in resistance from shear stress at this point in the shelf, where the channel is relatively narrow, the shelf is thick, but the thickness gradient has reduced from that further upstream. As the shelf flows downstream, the channel widens, while

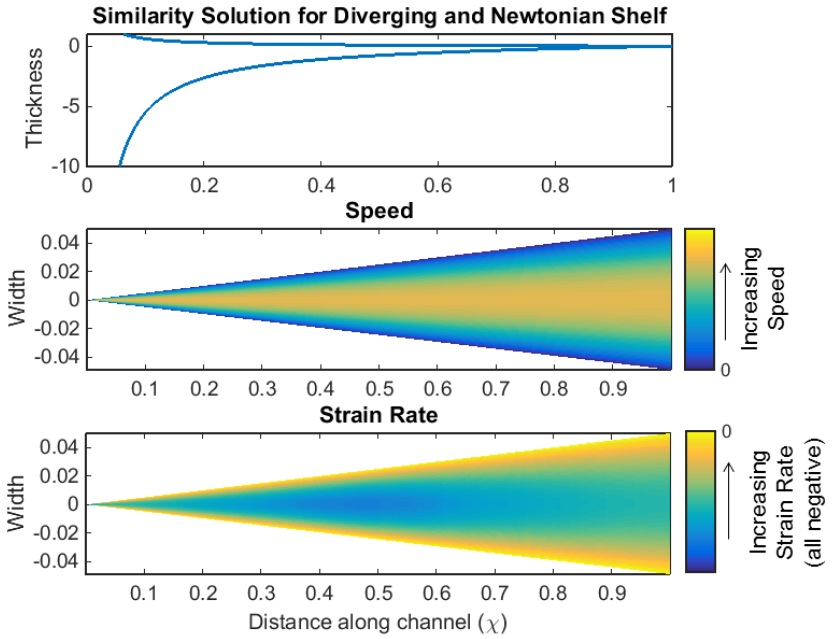

Figure 5.4: Similarity solution for a Newtonian shelf in a diverging channel. From top to bottom: thickness profile; speed plot; along-channel strain rate. Along-channel distance is given in terms of similarity variable χ.

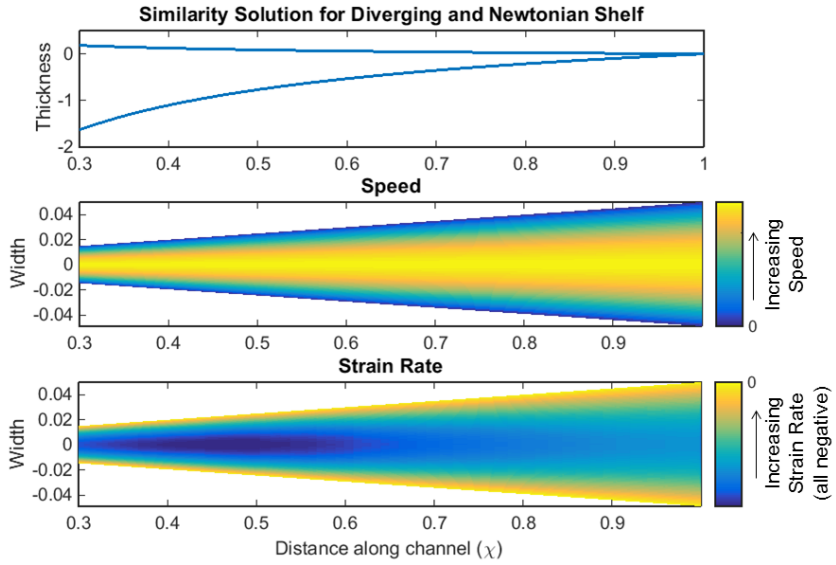

Figure 5.5: Similarity solution for a Newtonian shelf in a diverging channel. From top to bottom: thickness profile; speed plot; along-channel strain rate. Along-channel distance is given in terms of similarity variable χ. Plot shows area downstream of $\chi = 0.3$, allowing comparison with widening channel geometry such as Amery Ice Shelf.

the thickness and thickness gradient decrease, leading to reducing shear stress.

Similar features to the Newtonian case are observed in the thickness profile for the shear-thinning case with an $n = 3$ power-law rheology in Figure 5.6. However, here there is more rapid thinning in the upstream section of the shelf. Again the source forms a singularity but the thickness profile now takes the form $1/x^2$, near $x = 0$. This leads to a pronounced along-channel gradient in speed, which can be clearly seen in the speed and strain-rate plots, with high speed near the source and large negative strain rates as the shelf decelerates downstream. A major difference from the Newtonian example is that there is a transition to positive strain rate at $\chi = 0.5$. The value of the positive strain rate increases in the downstream direction towards the front of the shelf. Here the shear-thinning rheology may lead to a reduced effective viscosity and therefore less resistance to flow is generated by shear stresses and the lateral spreasding of the shelf, so the shelf can accelerate towards the front as in the parallel channel case.

A separate plot showing the features downstream of $\chi = 0.3$ is shown in Figure 5.7. The thickness plot in this figure has similar profile to that for Amery Ice Shelf with an almost linear slope, but here the thickness profile for the similarity solution thins to zero thickness at the front of the shelf, whereas the front of Amery retains a substantial ice thickness. The strain-rate plot also shows similar characteristics to the geophysical example with negative strain rate in the upstream section that transitions to positive strain rate in the downstream direction. Near the shelf front there is also a large region of large positive strain rate, which is similar to the region of high positive strain rate observed in the final third of Amery.

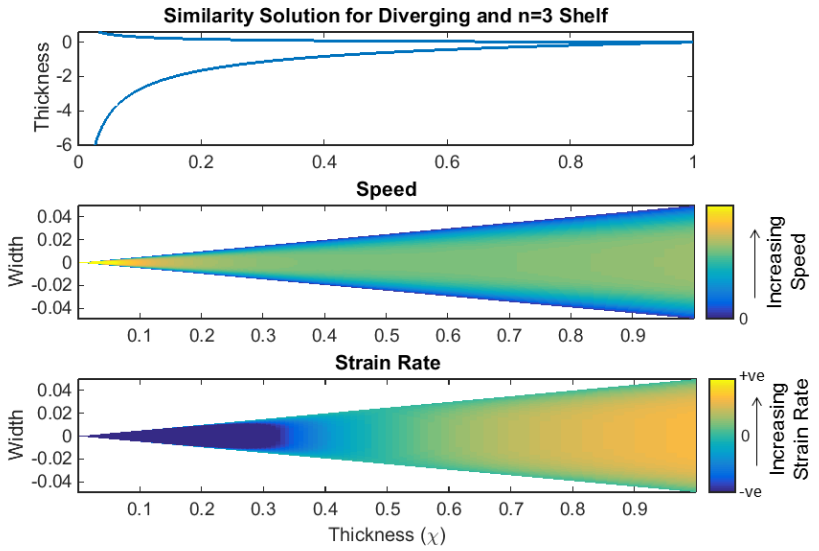

Figure 5.6: Similarity solution for a $n = 3$ power-law shelf in a diverging channel. From top to bottom: thickness profile; speed plot; along-channel strain rate. Along-channel distance is given in terms of similarity variable χ.

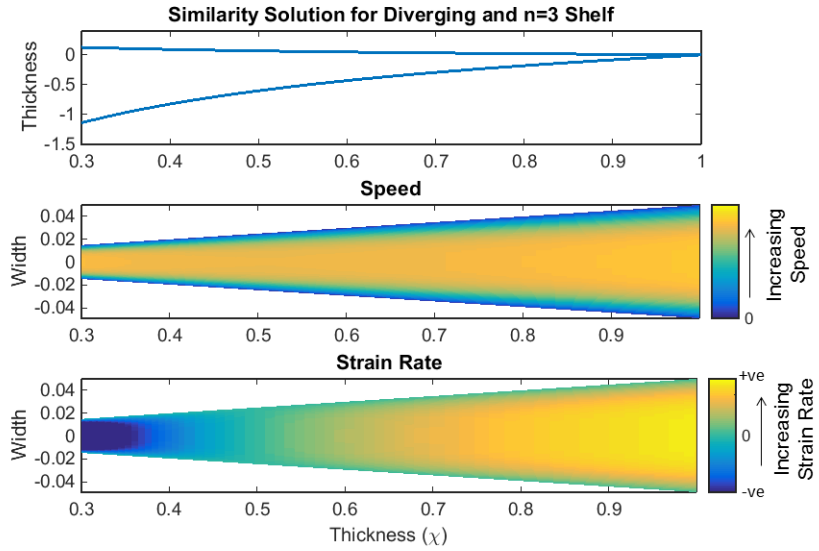

Figure 5.7: Similarity solution for a $n = 3$ power-law shelf in a diverging channel. From top to bottom: thickness profile; speed plot; along-channel strain rate. Along-channel distance is given in terms of similarity variable χ, where the section of the channel presented here begins at 0.3.

5.4 Steady-State Solutions - Finite Length Channel

In the previous two sections, ice-shelf thickness profiles and velocity fields were determined for the case of infinitely long channels. Similarity solutions could be obtained in these cases as the increasing shear stress generated as the shelf propagates along the channel is balanced by the increasing pressure gradient produced as the ice shelf becomes thicker. However, this is not the case in geophysical examples, where channel geometries and the locations of pinning points create confined shelves of finite length. Therefore I now consider the case of a finite channel, with a source of fluid/ice at one end, $x = 0$, and an open ocean at the other, $x = x_c$. Once the shelf leaves the confines of the channel, there is no longer any lateral resistance acting on the unconfined shelf and I assume that this section of the shelf provides no resistance to the flow further upstream. Therefore, a steady-state can be achieved where the total lateral resistance in the confined section of shelf balances the driving pressure gradient from the hydrostatic pressure at the source.

5.4.1 Parallel Channel

From the previous sections in this chapter we know that for the shear-dominated flow of a general power-law fluid shelf in a parallel channel of width w, we have

$$u = (-w)^{n+1}\frac{2^{-2n}}{n+1}\left(\frac{\rho g'}{B'}\right)^n\left(\frac{\partial H}{\partial x}\right)^n\left[\left(\left|1-\frac{2y}{w}\right|\right)^{n+1}-1\right], \tag{5.44}$$

$$q = (-w)^{n+2}\frac{2^{-2n}}{n+2}\left(\frac{\rho g'}{B'}\right)^n H\left(\frac{\partial H}{\partial x}\right)^n, \tag{5.45}$$

$$\bar{u} = (-1)^n w^{n+1}\frac{2^{-2n}}{n+2}\left(\frac{\rho g'}{B'}\right)^n\left(\frac{\partial H}{\partial x}\right)^n, \tag{5.46}$$

$$\frac{\partial H}{\partial t} = -\frac{1}{w}\frac{2^{-2n}}{n+2}\left(\frac{\rho g'}{B'}\right)^n\frac{\partial}{\partial x}\left[H\left(\frac{\partial H}{\partial x}\right)^n(-w)^{n+2}\right], \tag{5.47}$$

which represents the shelf velocity (given by equation (5.7)), shelf flux (given by equation (5.8)), width-averaged velocity ($\bar{u}$) and the continuity equation respectively.

Following the work of Pegler (2012) and Kowal et al. (2016), consider a steady-state shelf in a narrow parallel channel of finite length. The channel ends and the shelf flows into an open ocean at $x = x_c$, where there is no additional resistance to flow generated by the shelf once it has left the channel. Using the width-averaged velocity, $\bar{u}$, in the steady form of the continuity equation we have

$$\frac{\partial}{\partial x}(H\bar{u}) = 0 \quad \Rightarrow \quad H\bar{u} = \frac{q_0}{w}, \tag{5.48}$$

where q_0 is the input flux. The flux remains constant throughout the shelf to ensure a steady state, $wH\bar{u} = q_0$. Therefore, equation (5.46) gives

$$\frac{q_0}{Hw} = (-1)^{n+2} w^{n+1} \frac{2^{-2n}}{n+2} \left(\frac{\rho g'}{B'}\right)^n \left(\frac{\partial H}{\partial x}\right)^n, \tag{5.49}$$

$$\Rightarrow H = \left[-\left(\frac{n+1}{n}\right) \frac{4(n+2)^{\frac{1}{n}} q_0^{\frac{1}{n}}}{w^{\frac{n+2}{n}}} \left(\frac{B'}{\rho g'}\right) x + A \right]^{\frac{n}{n+1}}, \tag{5.50}$$

gives an equation for the steady-state thickness profile, where A is a constant of integration. A can be determined by imposing a boundary condition at either the upstream source ($x = 0$) or the exit of the channel $x = x_c$. Mathematically, I could impose a constant input thickness at $x = 0$, however this artificially imposes a grounding-line depth and location. It is more likely that the grounding-line depth and hence location is due to the condition at the channel exit and the dynamics within the floating shelf (Pegler, 2012; Kowal et al., 2016). I therefore choose to impose a boundary condition at the channel exit, balancing the width-averaged extensional stress with the hydrostatic pressure of the ocean. This is under the assumption that any section of the shelf downstream of the channel exit exerts no resistance to flow on the confined section. Therefore, this boundary condition along with the buttressing within the shelf of length x_c, determines the thickness of the shelf at the grounding line.

The boundary condition takes the form

$$\frac{\partial \bar{u}}{\partial x} = \frac{\rho g'}{8\bar{\mu}} H, \tag{5.51}$$

where $\bar{\mu}$ is the width-averaged viscosity given by

$$\bar{\mu} = \tilde{\mu} \left(\frac{1}{2} \overline{\left| \frac{\partial u}{\partial y} \right|} \right)^{(1-n)/n} \quad \text{and} \tag{5.52}$$

$$\overline{\left| \frac{\partial u}{\partial y} \right|} = (-1)^n w^n 2^{-2n} \left(\frac{\rho g'}{\tilde{\mu}}\right)^n \left(\frac{\partial H}{\partial x}\right)^n. \tag{5.53}$$

Therefore the constant of integration A can be calculated to be

$$A = \left(\frac{n+1}{n}\right) \frac{4(n+2)^{1/n} q_0^{1/n}}{w^{(n+2)/n}} \left(\frac{B'}{\rho g'}\right) \left[x_c + \frac{\sqrt{2} w n}{(n+2)^{1/2} (n+1)^{(n+1)/(2n)}} \right]. \tag{5.54}$$

Given this constant of integration the equation for the thickness profile becomes,

$$H = \left[-\left(\frac{n+1}{n}\right) \frac{4(n+2)^{1/n} q_0^{1/n}}{w^{(n+2)/n}} \left(\frac{B'}{\rho g'}\right) \left(x - x_c - \left(\frac{2}{n+2}\right)^{1/2} \frac{nw}{(n+1)^{(n+1)/(2n)}} \right) \right]^{n/(n+1)} \tag{5.55}$$

Steady-State Newtonian Shelf ($n = 1$)

For a Newtonian ($n = 1$) shelf the steady-state thickness profile takes the form

$$H_{n=1} = \left[-\frac{24 q_0 B'}{w^3 \rho g'} \left(x - x_c - \frac{w}{\sqrt{6}} \right) \right]^{1/2}, \tag{5.56}$$

as determined previously by Pegler (2012). This analytical solution can be used to estimate the thickness profile and speed map for the final two thirds of Amery Ice Shelf, which forms a near-parallel channel. Appropriate values for Amery Ice Shelf are: a channel length of 280 km; a width of 100 km; an ice thickness of 600 m; and a width-averaged velocity of 200 m yr^{-1}. The latter three are used to prescribe the input flux. This steady-state thickness profile has been plotted in Figure 5.8 along with the corresponding speed and strain-rate plot. Here it is clear that the rate of thinning increases downstream to produce a convex profile. Whereas, the similarity solution (Fig. 5.1) and steady-state shelves have a similar profiles in the upstream half of the shelf, in the case of the steady shelf in a finite channel, the slope increases as the shelf approaches the channel exit. This is due to the extensional-stress boundary condition at the channel exit, which acts to thin the shelf at the exit.

From the speed and strain-rate plots in Figure 5.8 we see that the dynamics are broadly similar to those in the similarity solution. However, the peak in speed does not extend as far upstream. This is a result of the extensional-stress boundary condition at the channel exit, which produces high strain rates and fast flow as the shelf exits the channel. This also leads to the increased thinning at the downstream end of the shelf.

This shear-dominated analytical solution captures many of the structural features observed in Amery Ice Shelf, such as the slightly convex thickness profile, and increase in velocity as the shelf approaches the calving front. Quantitatively there is fairly good agreement, with the shelf thinning from approximately 700 m to 200 m over the length of the channel, and a maximum flow speed of 600 m yr^{-1} is achieved at the exit. For Amery Ice Shelf the upstream thickness is 600 m, while flow speed at the exit is approximately 900 m yr^{-1}. However, the area of large positive strain rate does not extend as far upstream as the geophysical example and forms a central peak rather than spanning the width of the channel.

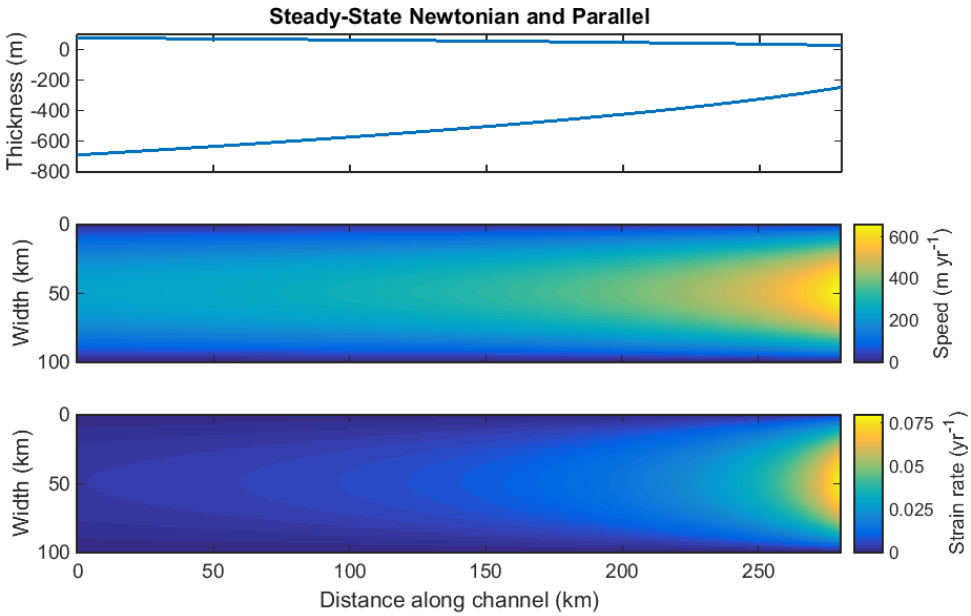

Figure 5.8: Thickness profile, speed plot and strain-rate plot for a steady-state Newtonian shelf in a parallel channel. Parameter values are chosen to approximate the roughly-parallel final two thirds of Amery Ice Shelf.

Steady-State $n = 3$ Power-Law Shelf

The steady-state thickness profile for a power-law fluid with $n = 3$ is

$$H_{n=3} = \left[-\frac{16}{3} \left(\frac{5q_0}{w^5} \right)^{1/3} \frac{B'}{\rho g'} \left(x - x_c - 4^{-2/3} \left(\frac{18}{5} \right)^{1/2} w \right) \right]^{3/4}. \tag{5.57}$$

I use the approximate geometry and characteristics of Amery Ice Shelf in Figure 5.9, with the same variables as in the Newtonian case, and the additional rate factor for a power-law rheology appropriate for ice at 0°C, $B = 7.47 \times 10^7$ Pa s$^{1/3}$.

The qualitative features are broadly similar to those of the similarity solution but there is an isolated peak in speed and strain rate in the final section of the shelf. This acts to modify the thickness profile near the exit, causing it to thin more rapidly, but this difference is not as distinctive as in the Newtonian example.

The thickness profile plot in Figure 5.9 shows a thinner shelf than in the Newtonian case for the same input flux. At the source the shelf is approximately 500 m thick, which is approximately 100 m thinner than Amery Ice Shelf. At the channel exit a maximum speed of approximately 800 m yr^{-1} is achieved, while strain rates increase in the down-stream direction. In the final 100 km of the shelf there is a large area where values range between 1 and 4 $\times 10^{-2}$ yr^{-1} reaching a maximum value of 8×10^{-2} yr^{-1} at the

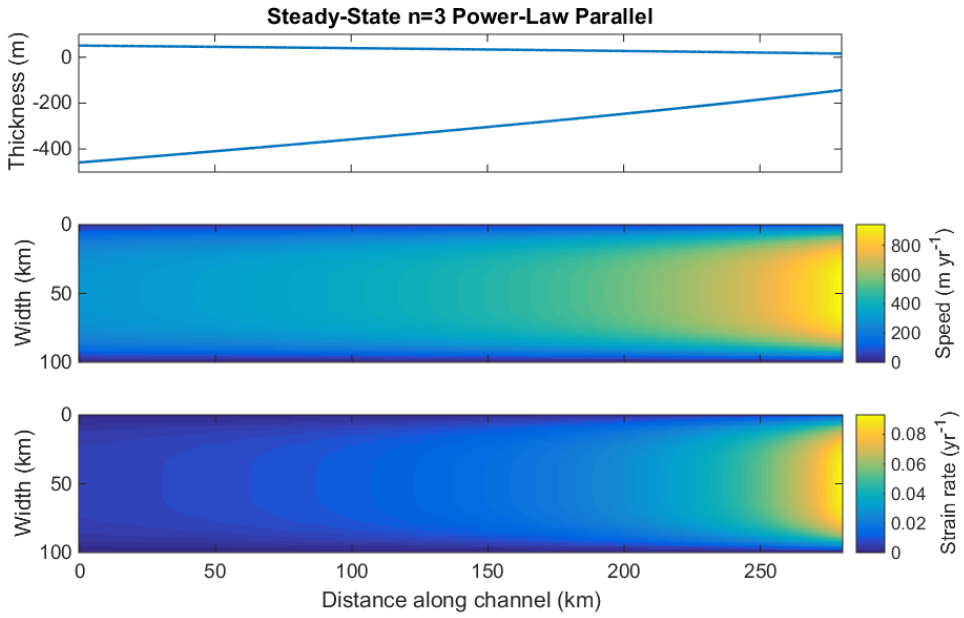

Figure 5.9: Thickness profile, speed plot and strain-rate plot for a steady-state $n = 3$ power-law shelf in a parallel channel. Parameter values are chosen to approximate the roughly-parallel final two thirds of Amery Ice Shelf.

channel exit. These values are similar to those found for Amery Ice Shelf, where there is a maximum speed of approximately 900 m yr^{-1} at the channel exit and strain rates of between 0.5 and 2 $\times 10^{-2}$ yr^{-1} in the final third of the channel.

5.4.2 Diverging Channel

In the case of a narrow diverging channel of width $w = \alpha x$, the width-averaged velocity for a general power-law ice shelf is

$$\bar{u} = (-1)^{n+2}(\alpha x)^{n+1}\frac{2^{-2n}}{n+2}\left(\frac{\rho g'}{B'}\right)^n\left(\frac{\partial H}{\partial x}\right)^n. \tag{5.58}$$

The steady-state continuity equation and the condition of constant flux can be used to determine the steady-state thickness profile

$$H = \left[\frac{2(n+1)(n+2)^{1/n}}{\alpha^{(n+2)/n}}q_0^{1/n}\left(\frac{B'}{\rho g'}\right)x^{-2/n} + A\right]^{n/(n+1)}, \tag{5.59}$$

where A is determined by imposing the extensional-stress boundary condition at the channel exit. In this case the width-averaged viscosity $\bar{\mu}$ is

$$\overline{\left|\frac{\partial u}{\partial y}\right|} = \frac{(-\alpha x)^n 2^{(1-2n)}}{(n+1)} \left(\frac{\rho g'}{B'}\right)^n \left(\frac{\partial H}{\partial x}\right)^n, \tag{5.60}$$

$$\Rightarrow \bar{\mu} = B' \left(\frac{-\alpha x}{4(n+1)^n} \frac{\rho g'}{B'} \frac{\partial H}{\partial x}\right)^{1-n}. \tag{5.61}$$

Therefore the boundary condition becomes

$$-\frac{2(\alpha x_c)^2 n}{(n+2)(n+1)^{(1-n)/n}} \frac{\partial^2 H}{\partial x^2} = H. \tag{5.62}$$

Here I assume that the angle of divergence α is small and the shelf flows out from the channel exit as a parallel current of width αx_c. In order to make the notation less cumbersome I write the equation for the shelf thickness profile in the form

$$H = \left[Cx^{-2/n} + A\right]^{n/(n+1)}, \tag{5.63}$$

in this notation the partial derivatives of H are,

$$\frac{\partial H}{\partial x} = -\frac{2}{n+1} C x^{-(2+n)/n} \left[Cx^{-2/n} + A\right]^{-1/(n+1)}, \tag{5.64}$$

$$\frac{\partial^2 H}{\partial x^2} = \frac{2(2+n)}{n(n+1)} C x^{-2(1+n)} n \left[Cx^{-2/n} + A\right]^{-1/(n+1)} \tag{5.65}$$

$$- \frac{4}{n(n+1)^2} C^2 x^{-2(2+n)/n} \left[Cx^{-2/n} + A\right]^{-(n+2)/(n+1)}. \tag{5.66}$$

These partial derivative are then used in equation (5.62) to determine the constant of integration A. This produces a quadratic equation with coefficients

$$D_1 A^2 + D_2 A + D_3 = 0, \tag{5.67}$$

$$D_1 = 1, \tag{5.68}$$

$$D_2 = 2C x_c^{-2/n} \left[1 + \frac{2\alpha^2}{(n+1)^{1/n}}\right], \tag{5.69}$$

$$D_3 = C x_c^{-4/n} \left[C + \frac{4\alpha^2}{(n+1)^{1/n}} C - \frac{8\alpha^2}{(n+2)(n+1)^{(1+n)/n}}\right]. \tag{5.70}$$

Therefore A can be determined using the quadratic formula,

$$A = \frac{-D_2 \pm \sqrt{D_2^2 - 4 D_1 D_3}}{2 D_1}. \tag{5.71}$$

Steady-State Newtonian Shelf

Using this solution for a general power-law shelf, solutions can be obtained for specific values of the flow exponent n. I initially consider the Newtonian case with $n = 1$ and divergence angle $\alpha = 0.1$. The geometry of the channel is chosen so that the downstream section of the channel approximates that of Amery Ice Shelf. From the point source, the channel is 1000 km long, widening to 100 km at the channel exit, similar to the parallel channel examples in the previous section and appropriate for the exit of Amery Ice Shelf. The input flux is chosen to be similar flux of ice in Amery Ice Shelf, and is calculated based on a shelf width of 50 km, with thickness 600 m and width-averaged speed 200 m yr^{-1}. These values are similar to those found approximated 150 km downstream of the grounding line for Amery Ice Shelf. Initially I impose a viscosity of $\mu = 2 \times 10^{14}$ Pa s, which is an appropriate Newtonian approximation for the viscosity of an ice shelf. The corresponding solution is plotted in Figure 5.10.

The top plot in Figure 5.10 shows the shelf thickness profile along the length of the channel, with the shelf fluid entering the channel at a point source at $x = 0$. In contrast to the steady-state, parallel-channel case, here the shelf takes a concave profile. In the upstream section of the shelf this is qualitatively similar to the similarity solution. However, the rate of thinning reduces significantly downstream and in the second half of the channel there is almost no change in thickness. This implies that in this final section there must be slow flow, as for shear-dominated flow the velocity is dependent on the thickness gradient. As the shelf widens but maintains a near constant thickness, there is a reduction in speed that can be seen in the speed map in Figure 5.10.

As with the similarity solution, negative strain rate is observed throughout the shelf (Fig. 5.10). In contrast to the steady-state, parallel-channel cases, there is no positive strain rate observed at the channel exit resulting from the extensional-stress boundary condition. This is because the extensional strain-rate is partially dependent on the ratio of the shelf thickness and the viscosity at the exit. For this shelf this ratio is not large enough to induce positive strain in comparison to the resistance from the shear between the channel walls and the deceleration (negative strain rate) as the shelf reduces in speed to fill the widening channel.

Comparing the results from these plots with Amery Ice Shelf, it is clear that the analytical shelf is much thicker; approximately an order of magnitude too thick. As a consequence the flow speed of the shelf is much less than the geophysical example. This may be due to the high resistance generated by shear stress in the upstream section of the channel, where the shelf is very narrow. I expect the magnitude of the resistance to

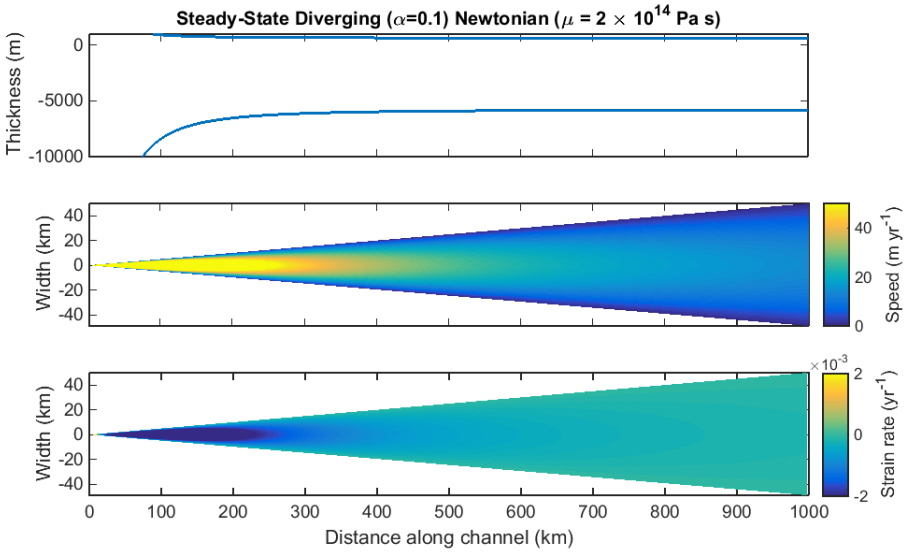

Figure 5.10: Thickness profile, speed plot and strain-rate plot for a steady-state Newtonian shelf in a diverging channel with $\alpha = 0.1$ and viscosity $\mu = 2 \times 10^{14}$ Pa s.

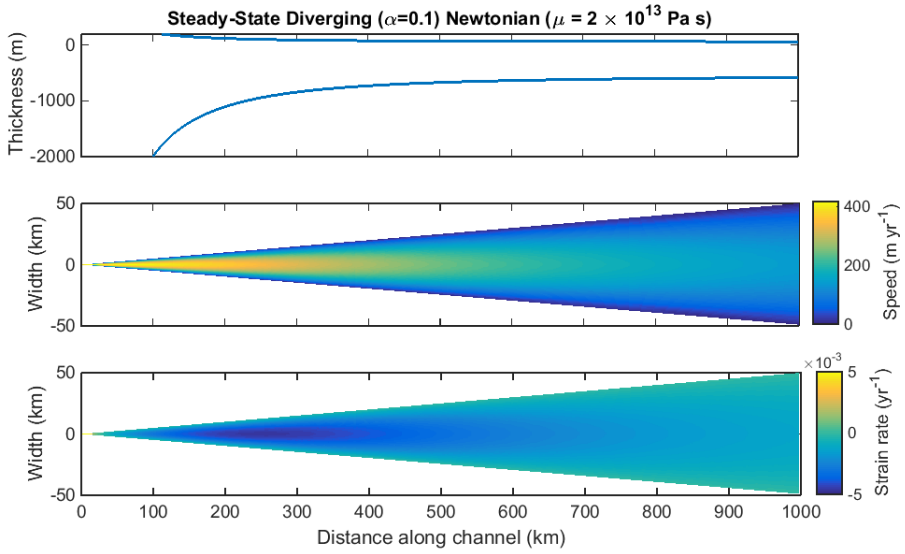

Figure 5.11: Thickness profile, speed plot and strain-rate plot for a steady-state Newtonian shelf in a diverging channel with $\alpha = 0.1$ and viscosity $\mu = 2 \times 10^{13}$ Pa s.

be dependent on the viscosity of the shelf. In order to investigate this and the consequences for the shelf thickness profile and flow dynamics I reduced the viscosity by an order of magnitude.

Figure 5.11 presents the results for a steady-state shelf in a diverging channel with Newtonian viscosity, $\mu = 2 \times 10^{13}$ Pa s. This reduction in viscosity has led to a decrease in the shelf thickness and an increase in the flow speed. Qualitatively the features are broadly the same as the previous case. However, the strain-rate map has a minimum that is separate from the point source, implying the greatest resistance to flow from shear stress is generated away from the source, where the second derivative of the shelf thickness, which is proportional to the strain rate for a shear-dominated flow, has reached a maximum and the channel remains relatively narrow.

The shelf viscosity is reduced further in Figure 5.12 to $\mu = 2 \times 10^{12}$ Pa s. From Figure 5.12a it is clear that there are distinctive changes to the speed and strain-rate maps. The thickness profile has become much thinner and the shelf continues to thin towards the exit. From the speed map it is evident that there is a central region of fast flow along the entire length of the shelf, which was not observed in earlier cases. The strain-rate map shows that there is positive strain rate throughout the shelf, with a peak in strain rate observed at the channel exit. These dynamics at the exit are similar to those observed in the parallel channel case and are due to the extensional-stress boundary condition and the decrease in negative strain rates as the shelf spreads laterally. As this shelf has reduced viscosity, there is less resistance generated as the shelf spreads laterally, and therefore the shelf behaves like it is confined in a parallel channel. The reduction in viscosity also means that the shear stress has reduced and there is no longer the requirement to have a very thick shelf to provide a large hydrostatic driving pressure to overcome the large shear stress. The thickness of the shelf has reduced, leading to a decrease in the area of shelf in contact with the channel wall and in turn a further reduction in shear stress allowing faster flow speeds to be achieved. The reduced viscosity and shear stress also leads to high extensional strain rates at the channel exit, where the channel-exit boundary condition strongly influences the flow.

In this case, speed and thickness values are obtained that are of the same order of magnitude as the geophysical example. I therefore modify the plots in Figure 5.12b, to include the last 500 km of the channel, so a direct comparison can be made between the dynamics observed here and those of Amery Ice Shelf. Here we observe that the structure of the shelf thickness profile is similar, but is much thinner than the geophysical example. Fast flow is observed at the exit, as in the geophysical case, but this extents further upstream than is observed geophysically.

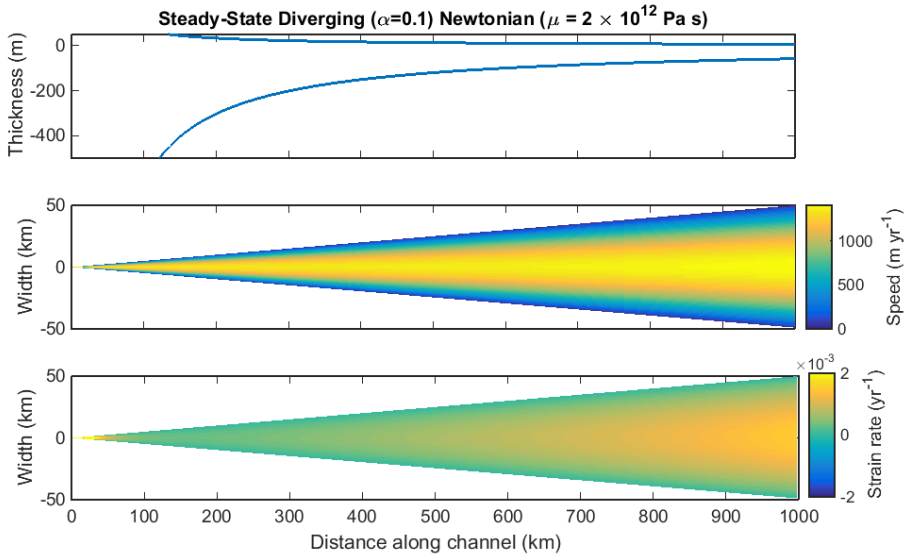

(a)

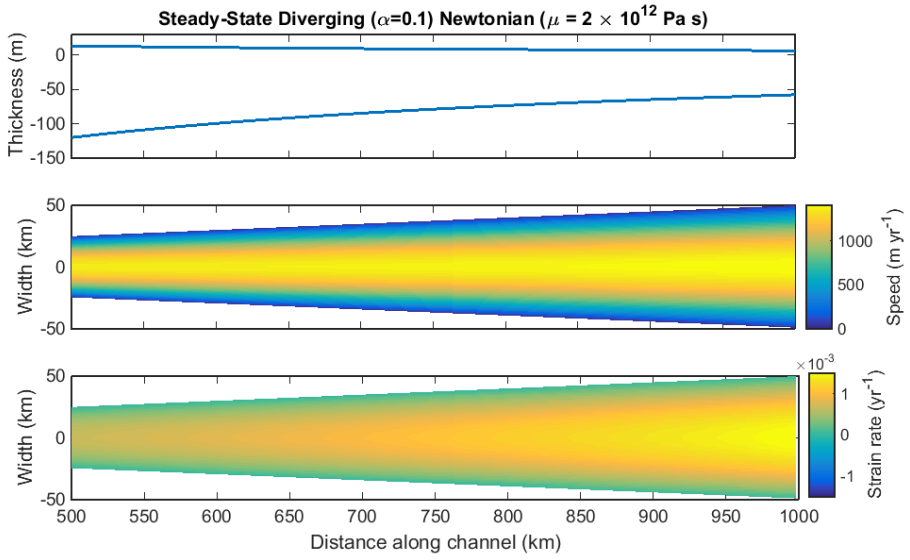

(b)

Figure 5.12: (a) Thickness profile, speed plot and strain-rate plot for a steady-state Newtonian shelf in a diverging channel with $\alpha = 0.1$ and viscosity $\mu = 2 \times 10^{12}$ Pa s. (b) Thickness profile, speed plot and strain-rate plots beginning 500 km from the point source.

From these plots and the comparison with the geophysical data, it is clear that although there are similarities in the structure of the thickness profiles, speed and strain-rate maps, the values are very sensitive to viscosity. This suggests that the quantitative features observed geophysically can not be captured in this model using Newtonian rheology. In the next section I consider a shear-thinning power-law rheology.

Steady-State $n = 3$ Shelf

Figure 5.13 shows the thickness profile, speed and strain-rate maps for an $n = 3$ power-law shelf, with rate factor appropriate for ice at 0°C ($B = 7.47 \times 10^7$ Pa $s^{1/3}$). Here the thickness profile is very similar to the most viscous Newtonian example, but thins more rapidly at the source, as was observed when comparing the Newtonian and shear-thinning similarity solutions. After the initial thinning, the shelf is much thicker than anything that would be expected geophysically, at least by an order of magnitude. This may be because initially there is a relatively high flux in a very narrow channel. Therefore, the shelf must be thick in order to provide a large enough hydrostatic pressure to overcome the large shear stresses that act on the shelf.

From the speed map in Figure 5.13 it is clear that near the source there is fast flow, which reduces in the along-channel direction to approximately 25 m yr^{-1} at the channel exit. This reduction in speed is also identified in the strain-rate map, where there are negative strain rates throughout the shelf. These values are much smaller than those observed geophysically.

The rate factor is reduced to a fifth of its former value in Figure 5.14, to $B = 1.49 \times 10^6$ Pa $s^{1/3}$. This leads to a reduction in the effective viscosity of the fluid and more geophysically appropriate values for the shelf thickness. On this occasion the shelf continues to thin as it approaches the channel exit. The flow dynamics have a similar structure to the previous example but the values of the flow speed have increased.

More comprehensive changes to the flow dynamics are evident when the rate factor is reduced further to $B = 7.47 \times 10^6$ Pa $s^{1/3}$ (an order of magnitude smaller than the original value). In Figure 5.15a the most striking difference is that now there are both negative and positive strain rates, with negative strain rates filling the upstream section of the shelf and positive strain rate in the region near to the channel exit. This is similar to the results for the shear-thinning and diverging similarity solution, while acceleration in the downstream region was also observed in the Newtonian case, when the viscosity was reduced substantially. Reducing the rate factor or viscosity leads to a reduction in resistance-to-extension at the channel exit (resistance from shear stress and lateral spreading), where the extensional-stress boundary condition is applied.

Figure 5.15b presents the final 500 km of the channel. In this interval, the width of the shelf increases from 50 km to 100 km. In the upstream section there are negative strain rates, which agrees with the negative strain observed in the narrow upstream section of Amery Ice Shelf. The magnitude of the strain rate decreases in the downstream direction

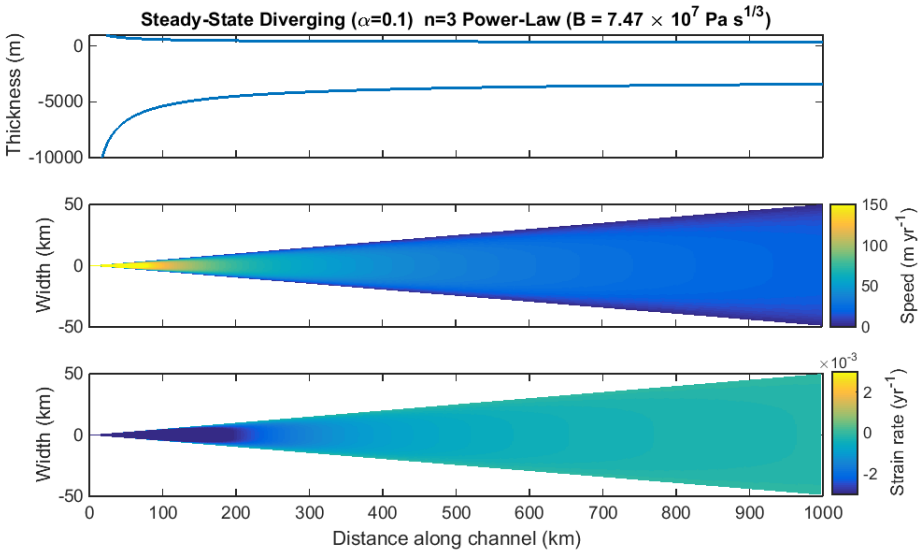

Figure 5.13: Thickness profile, speed plot and strain-rate plot for a steady-state $n = 3$ power-law shelf in a diverging channel with $\alpha = 0.1$ and rate factor $B = 7.47 \times 10^7$ Pa $\mathrm{s}^{1/3}$.

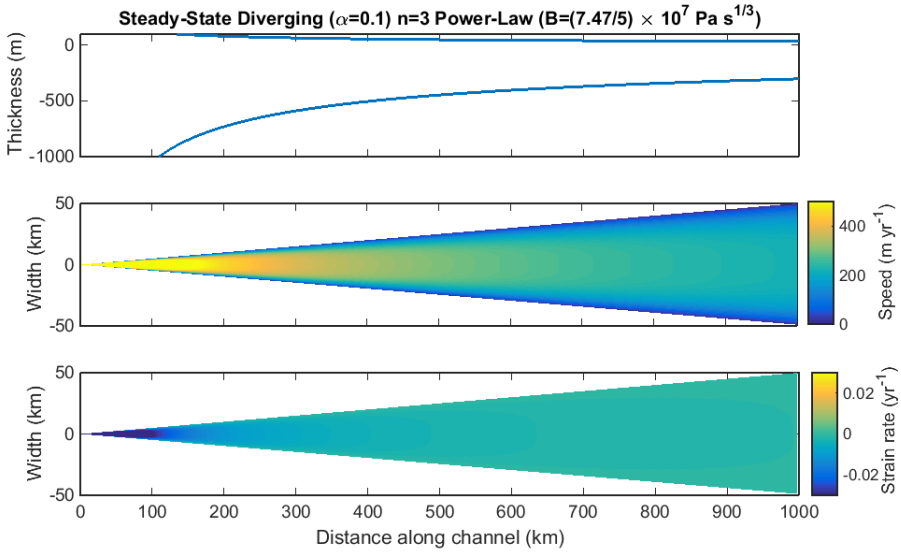

Figure 5.14: Thickness profile, speed plot and strain-rate plot for a steady-state $n = 3$ power-law shelf in a diverging channel with $\alpha = 0.1$ and rate factor $B = (1/5) \times 7.47 \times 10^7$ Pa $\mathrm{s}^{1/3}$.

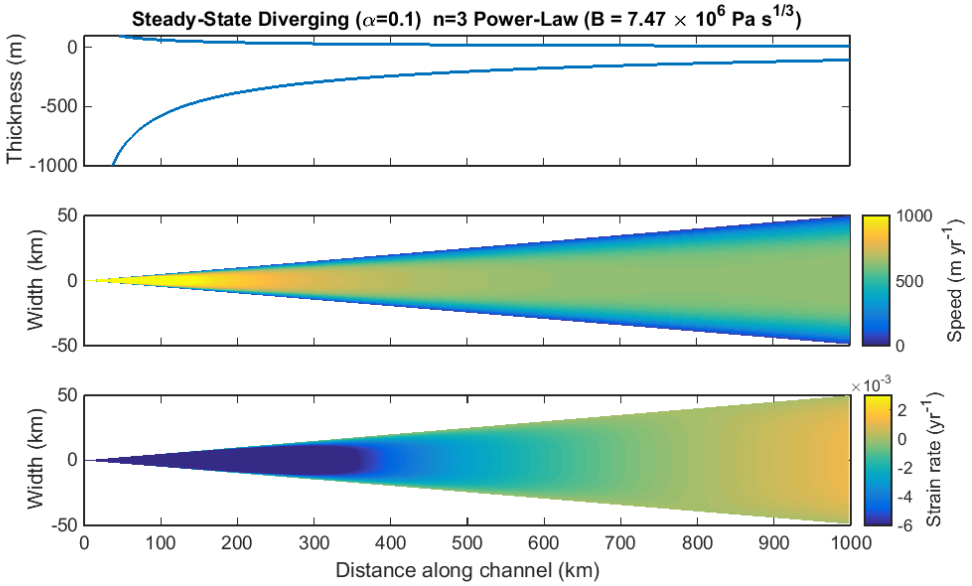

(a)

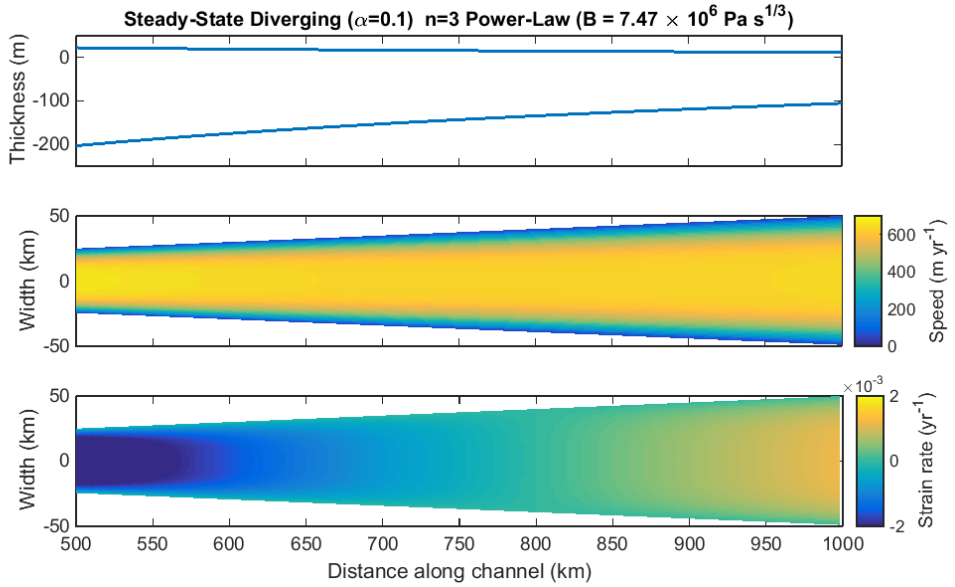

(b)

Figure 5.15: (a) Thickness profile, speed plot and strain-rate plot for a steady-state $n = 3$ power-law shelf, with reduced rate factor $B = 7.47 \times 10^6$ Pa s$^{1/3}$, in a diverging channel with $\alpha = 0.1$. (b) Thickness profile, speed plot and strain-rate plots beginning 500 km from the point source.

until there is a transition to positive strain rate approximately 175 km upstream from the channel exit. A similar transition is observed for Amery Ice Shelf and indicates a reduction in resistance from shear stress and lateral spreading. The flow in the final section is similar to that in the parallel channel cases, suggesting that the transition is mainly due to the reduction in resistance to flow from lateral spreading.

5.4.3 Summary: Steady-State Shear-Dominated Shelves

As with the similarity solutions, stark differences in the thickness profiles for parallel and diverging channels are found for the steady-state shear-dominated shelves. The shear-dominated parallel channel approximations provide a good estimate for the flow dynamics and thickness profile for the final two thirds of Amery Ice Shelf. Slight improvements in the agreement are observed when the $n = 3$ power-law rheology is used. One exception to this good agreement is near the channel exit, where the peak in positive strain rates is slightly larger than observed geophysically.

For the diverging shelves, high shear in the upstream section, where the channel is narrow, leads to thick and slow-flowing shelves. This thickness is needed to provide the hydrostatic pressure to drive against the high shear stress. For realistic viscosities and rate factors the downstream shelf is much thicker, by an order of magnitude, than Amery Ice Shelf. However, in these models the dynamics and thickness downstream (in the area with appropriate geometry for comparison with Amery) are often determined in the narrow upstream section of the channel, where there is large resistance to flow from high shear stress. These narrow sections are not representative of geometries seen geophysically, but are a mathematical tool for exploring the dynamics in these types of geometry. By reducing the viscosity or rate factor this leads to thinner shelves that flow faster, giving more geophysically realistic values.

The influence of the extensional-stress channel-exit boundary condition is dependent on the viscosity and thickness at the channel exit. For diverging shelves hydrostatic pressure balances shear stress and lateral spreading, hence strain rates are almost always negative upstream. As the shelf thins, a transition to positive strain rates may occur if the viscosity is low enough, as shown in Figure 5.15. If the effective viscosity is reduced, the negative extensional stress due to lateral spreading decreases and the shelf begins to behave like a shelf in a parallel channel, such that there are positive strain rates.

From theses examples, it is clear that, on the whole, the parallel-channel models provide the best estimate for shelf thickness and flow in the final two thirds of Amery Ice Shelf. However, when positive strain rates are observed in the diverging channel cases, there is

a large area of high positive strain rate that extends upstream, in a similar manner to the strain rate of Amery Ice Shelf.

5.5 Shear and Extensional Dynamics

In previous sections I have considered the flow of an ice shelf confined to a channel of finite length, where the dynamics of the flow are dominated by the shear stresses between the lateral no-slip boundary walls. I now include the extensional stress terms in the force balance equation derived in Chapter 2 and given by equation (2.27). I assume the shelf has uniform thickness across the channel width, and there is flow in the along-channel, x-direction only. The shear-only dynamics are expected to be a good approximation far from the source and channel exit. Therefore, when extensional terms are included, I expect additional dynamics to arise in regions close to the input and exit. Numerical calculations will allow an investigation of whether the inclusion of extensional terms has an influence on the dynamics and the thickness profile throughout the shelf or only at the ends of the shelf. In the case of a non-Newtonian ice rheology, the inclusion of extensional stresses may lead to interesting feedbacks. For example, increased extension within the shelf would lead to reduced effective viscosity, which in turn would reduce the resistance to flow and allow further extension. In the equation for the power-law ice rheology, I now include both the shear and extensional components of the strain-rate tensor, leading to additional variations in effective viscosity, different from those observed in the shear-only case.

5.5.1 Equations

Consider the same parallel geometry as considered in the previous sections: a parallel channel of width w and length x_c. The ice shelf flows in the along-channel (x) direction only, with no-slip side walls at $y = 0$ and $y = w$. At the upstream boundary I impose a constant input flux, as in the shear-only case. When extensional terms are included, it is required to impose a further condition at the source. This additional boundary condition is a constant input thickness, $H = H_0$ at $x = 0$. This implies that the input velocity is also kept constant. At the channel exit, where the shelf leaves the confines of the channel, the extensional stress within the shelf balances the hydrostatic pressure of the ocean.

The x-component of the full force-balance equation, with a uniform cross-channel thickness, $H \equiv H(x,t)$,

$$4\frac{\partial}{\partial x}\left(\mu H\frac{\partial u}{\partial x}\right)+\frac{\partial}{\partial y}\left(\mu H\frac{\partial u}{\partial y}\right)=\rho g' H\frac{\partial H}{\partial x}, \tag{5.72}$$

was solved to determine the along-channel velocity. In the case of a power-law rheology, the effective viscosity is given by

$$\mu = B' e_{II}^{(1-n)/2n} \quad \text{with} \quad e_{II} = \left(e_{xx}^2 + e_{xy}^2\right) = \left[\left(\frac{\partial u}{\partial x}\right)^2 + \frac{1}{4}\left(\frac{\partial u}{\partial y}\right)^2\right], \tag{5.73}$$

with consistency index $B' = B/2$ (B the rate factor), and e_{II} the second invariant of the strain-rate tensor.

Using the force-balance equation, I determine the velocity field for a given thickness profile. This velocity field can then be used to calculate a width-averaged velocity $\bar{u}$ for the current thickness profile. This is then used in the continuity equation,

$$\frac{\partial H}{\partial t} + \frac{\partial}{\partial x}\left(H\bar{u}\right) = 0. \tag{5.74}$$

to evolve the thickness profile forward in time, where I am again assuming there is zero net accumulation or ablation. As in the previous idealized models in this chapter, the continuity equation assumes no interaction with the ocean or atmosphere in the form of melting or accumulation. The shelf thickness profile was then evolved in time, with the velocity field and width-averaged velocity updated for each iteration of the thickness profile. Equations (5.72) and (5.74) were solved iteratively until a steady-state thickness profile was achieved.

5.5.2 Numerical Model

Discretization of equations

The reduced force-balance equation (5.72) can be discretized in terms of derivatives in the velocity to give

$$\begin{aligned} &4\left(\frac{\partial \mu}{\partial x}H + \mu\frac{\partial H}{\partial x}\right)\left(\frac{u_{m+1,n} - u_{m-1,n}}{2d}\right) + 4\mu H\left(\frac{u_{m+1,n} - 2u_{m,n} + u_{m-1,n}}{d^2}\right) \\ &+ \left(\frac{\partial \mu}{\partial y}H + \mu\frac{\partial H}{\partial y}\right)\left(\frac{u_{m,n+1} - u_{m,n-1}}{2d}\right) + \mu H\left(\frac{u_{m,n+1} - 2u_{m,n} + u_{m,n-1}}{d^2}\right) = \rho g' H\frac{\partial H}{\partial x}. \end{aligned} \tag{5.75}$$

Here partial derivatives in μ and H represent the partial derivatives at node points (m, n) and are determined using central differences of the μ and H fields

$$\frac{\partial H}{\partial x} = \frac{\partial H}{\partial x}_{m,n} = \frac{H_{m+1,n} - H_{m-1,n}}{2d} \quad \text{and} \quad \frac{\partial H}{\partial y} = \frac{\partial H}{\partial y}_{m,n} = \frac{H_{m,n+1} - H_{m,n-1}}{2d}, \tag{5.76}$$

$$\frac{\partial \mu}{\partial x} = \frac{\partial \mu}{\partial x}_{m,n} = \frac{\mu_{m+1,n} - \mu_{m-1,n}}{2d} \quad \text{and} \quad \frac{\partial \mu}{\partial y} = \frac{\partial \mu}{\partial y}_{m,n} = \frac{\mu_{m,n+1} - \mu_{m,n-1}}{2d}. \tag{5.77}$$

The variable d denotes the spacing between nodes, which is an equal distance in the x and y directions. Here as before, I assume that the shelf has a uniform thickness across the width of the channel ($H_{m,n} = H_m \ \forall\, n = 1...N$) and hence $\partial H/\partial y \equiv 0$. Successive Over Relaxation (SOR) is used to determine the velocity field for a given thickness profile, H. At each iteration (iterations denoted by superscript i) of the velocity field the updated velocity field is given by

$$\begin{aligned} u^{i+1}_{m,n} =&(1-r)u^i_{m,n} + \frac{r}{10\mu H}\Bigg[\left[2d\left(\frac{\partial \mu}{\partial x}H + \mu\frac{\partial H}{\partial x}\right) + 4\mu H\right]u^i_{m+1,n} \\ &+ \left[\frac{d}{2}\left(\frac{\partial \mu}{\partial y}H + \mu\frac{\partial H}{\partial y}\right) + \mu H\right]u^i_{m,n+1} + \left[4\mu H - \frac{2}{d}\left(\frac{\partial \mu}{\partial x}H + \mu\frac{\partial H}{\partial x}\right)\right]u^i_{m-1,n} \\ &+ \left[\mu H - \frac{d}{2}\left(\frac{\partial \mu}{\partial y}H + \mu\frac{\partial H}{\partial y}\right)\right]u^i_{m,n-1} - d^2\rho g' H\frac{\partial H}{\partial x}\Bigg]. \end{aligned} \tag{5.78}$$

Here the value of r can be varied depending on the style of relaxation required;

$$0 < r < 1 \quad \text{under-relaxation,} \tag{5.79}$$

$$r = 1 \quad \text{Gauss-Seidel,} \tag{5.80}$$

$$1 < r < 2 \quad \text{over-relaxation,} \tag{5.81}$$

$$r > 2 \quad \text{unstable.} \tag{5.82}$$

The Successive Over Relaxation (SOR) part of the my code was tested to ensure the scheme converges to a steady velocity field. Different values of r were chosen to test for the rates of convergence. Convergence was measured by the maximum absolute difference between the velocity at grid points on consecutive iterations. Results from the SOR code used to calculate the velocity field (from a field of zeros to the final velocity field) for the shear-only steady-state thickness profile, with both shear and extensional stresses considered in the dynamics, is given in Table 5.1 below. Convergence was said to occur once the difference at each grid point between consecutive iterations was less than 0.05 m yr^{-1}. For the Newtonian case with shear and extensional stresses considered, the average velocity value was approximately 110 m yr^{-1}, and therefore in this case the absolute error was equivalent to a relative error of 4.5×10^{-4}.

The main purpose of this SOR scheme was to determine the velocity field corresponding to the updated thickness profile at each timestep. It was expected that the changes in thickness profile between timesteps would be relatively small, and therefore changes in the velocity field would be small too. The most computationally expensive use of the SOR code was to determine the initial velocity field, corresponding to the initial thickness profile. After this, the previous velocity field was used as a starting point to calculate the

r value	i
0.5	5955
1	3134
1.5	1430

Table 5.1: Rates of convergence for Successive Over Relaxation using different values of r to obtain velocity field for the shear-only steady-state thickness profile.

velocity field for the evolved thickness profile. I found that just one iteration of SOR was needed to determine an accurate velocity field, and therefore chose to use $r = 1$. Despite this being slightly more computationally expensive for the first iterations of the velocity field, once the shelf thickness was evolving slowly it was expected that the velocity field would evolve slowly too, and therefore there was no need to employ an r value greater than 1.

The velocity field was solved on an M by N grid. Boundary conditions were imposed on the velocity field along the four boundaries: two lateral walls; source edge; and channel-exit edge. At the upstream boundary there was a constant input flux (Q_0) and input thickness (H_0). Therefore, I imposed a constant input velocity, given by the analytical solution for shear dominated flow of a Newtonian shelf

$$u(0, y) = -\frac{Q_0}{H_0}\frac{6}{w^2}\left(y^2 - wy\right), \tag{5.83}$$

$$\Rightarrow u^i_{1,n} = -\frac{Q_0}{H_0}\frac{6}{w^2}\left((nd)^2 - wnd\right). \tag{5.84}$$

This form of the input condition was chosen as it provides a simple structure to the input flow with no flow at the boundary walls and the maximum flow in the centre of the channel.

Flow along the side-walls was set to zero

$$u(x, 0) = u(x, w) = 0, \quad \Rightarrow \quad u^i_{m,1} = u^i_{m,N} = 0. \tag{5.85}$$

At the channel exit the extensional stress balances the hydrostatic pressure of the ocean

$$\frac{\partial u}{\partial x} = \frac{\rho g'}{8\mu}H \quad \Rightarrow \quad u^i_{M+1,n} = u^i_{M-1,n} + 2d\frac{\rho g'}{8\mu}H^t_M. \tag{5.86}$$

Here I invoked an imaginary row of grid points in the velocity field beyond the channel exit, denoted by subscript $M + 1$. I used these imaginary points to impose the channel exit boundary condition. The corresponding imaginary point in the width-averaged velocity was then used in the central differencing scheme to determine the evolution of the

thickness at the M node point.

For a given thickness profile, once the velocity field had converged, the width-averaged velocity ($\bar{u}^t$, where superscript t denotes timestep in evolution of thickness profile) was determined and used to evolve the thickness profile. At each time-step the thickness profile was calculated explicitly

$$H_m^{t+1} = H_m^t - \Delta t \left(\frac{H_{m+1}^t \bar{u}_{m+1}^t - H_{m-1}^t \bar{u}_{m-1}^t}{2d} \right). \tag{5.87}$$

During this evolution of the thickness profile the input-thickness boundary condition was maintained, with $H = H_0$ at $x = 0$.

Central-differencing was used to evolve the thickness profile, as can be seen in equation (5.87). This method provides second-order accuracy. At the upstream boundary the thickness is imposed, and hence an (previous) imaginary node (H_{-1}) is not needed at the upstream boundary. However, at the channel exit an imaginary node was needed and the shelf thickness at the imaginary node ($M + 1$) was determined by extrapolating the thickness gradient linearly by one grid spacing: i.e. $H_{M+1}^t = 2H_M^t - H_{M-1}^t$.

Model details

The model domain was chosen to have an aspect ratio appropriate for the final two thirds of Amery Ice Shelf, which forms an approximately parallel section and is about 100 km wide and about 280 km long. The domain has 140 nodes in the along-channel direction and 50 across the channel. The spacing between the nodes is equal in both the x and y direction and was chosen to be 2 km.

The time step for evolving the thickness profile was chosen so that the process of evolving the profile was stable, but also so that it made efficient use of computational time. The continuity equation given in equation (5.74) is solved explicitly for a given width-averaged velocity. This equation is hyperbolic and, to ensure stability in the numerical scheme, I controlled the Courant number $\mathcal{C}$. This prevents a fluid particle moving more than one grid-spacing in a timestep. For this 1D explicit scheme, stability should be achieved with a Courant number of 1 or less

$$\mathcal{C} = \frac{\hat{u}\Delta t}{d} \leq 1, \tag{5.88}$$

$$\Rightarrow \Delta t \leq \frac{d}{\hat{u}}, \tag{5.89}$$

$$\Delta t \leq \frac{2000\text{m}}{1000\text{m yr}^{-1}} = 2\text{yr}. \tag{5.90}$$

Here $\hat{u}$ is the maximum expected velocity of the shelf, which I have chosen to be 1000 m yr^{-1}. Therefore, the timestep was set to be less than 2 years. In the model runs given below the timestep is $\Delta t = 0.1$ yr. This ensures stability in the evolution of the thickness profile as it is less than 2 years, but also ensures the stable evolution of the flow and effective viscosity fields, which rely on effective viscosity fields from the previous timestep.

Initial conditions

Each run of the model was initiated from a uniform thickness profile with the thickness equal to the input thickness imposed at the upstream end of the channel.

Accounting for the Non-Newtonian Rheology

When a power-law rheology is used, the effective viscosity is dependent on the values of along-flow strain rate and shear rate. This was addressed by calculating the effective-viscosity field from the previous velocity field. This effective viscosity was then used in the next set of iterations of the Successive Over Relaxation scheme, using the updated thickness profile. Gradients in the effective viscosity field were also updated so that the correct partial derivatives could be used to calculate the velocity field.

5.5.3 Model runs

I performed a number of runs of the model, primarily with variations in the ice-shelf rheology. The first set of runs used a Newtonian approximation for ice rheology with a constant effective viscosity $\mu = 2 \times 10^{14}$ Pa s (as in earlier sections). Comparisons were then made between the steady-state results and those obtained from the shear-only model, in addition to comparisons with geophysical data from Amery Ice Shelf.

Secondly, a power-law rheology was used, with a rate factor (consistency index) corresponding to ice at 0°C. Again the results from this numerical calculation were compared to the analytical results of the shear-only case and the geophysical data. It should be noted here that the formulation of the second invariant of the strain-rate tensor (used in the equation for the power-law rheology) varies between the shear-only case and that with extension; when extensional stresses are included in the dynamics, the extensional strain component was also included in the second invariant. This differs from the shear-only case, where only the shear component was included.

5.5.4 Steady States

Newtonian - $n = 1$

Input Thickness Corresponding to Shear-Only Flow

Figure 5.16 presents the results for a Newtonian shelf with shear-and-extensional dynamics in steady-state calculated using the numerical code detailed in the previous section. Here the input flux and input thickness have been fixed to equal those in the analytical shear-only case approximating Amery Ice Shelf. From the thickness plot in Figure 5.16, it is evident that the profiles produced in the shear-only and shear-and-extension cases are very similar, with the shear-only profile denoted by a solid blue curve and the shear-and-extension shelf by a dotted red curve. However, the shear-and-extension shelf is slightly thinner than the shear-only shelf. This difference can be seen more clearly in Figure 5.17, which shows the difference in thickness between the shear-only and shear-and-extension shelves for this case. There is a maximum thinning of approximately 35 m or approximately 7% of the shear-only thickness at that point.

The shelf is thinner in the shear-and-extension case because the effect of the extensional stress boundary condition at the channel exit propagates further upstream when extensional dynamics are considered. The influence of the extensional dynamics acts to stiffen the shelf and effectively pull the shelf towards the exit, which results in thinning. This increase in strain rate upstream from the channel exit can also be detected in the strain-rate plot in Figure 5.16, which compares the value of the along-channel strain rate along the shelf centreline in the shear-only (red) and shear-and-extension (blue) cases. It is clear that throughout the shelf, with the exception of at the exit, the strain rate is larger in the shear-and-extension case. This is because the inclusion of extensional dynamics in the calculation allows extensional stresses to be transferred through the shelf, propagating the effect of the extensional strain at the exit. The strain rate is greater at the channel exit in the shear-only case because the shelf is thicker than the shear-and-extension case.

The speed map in Figure 5.16 has a similar structure to the shear-only case. However, here the speed contours are stretched in the along-channel direction due to the influence of the extensional stresses. This leads to a slightly increased speed at the channel exit. The effect of the extensional dynamics is also evident in the strain-rate plot. At the upstream end of the channel there is an increase in strain rate as the shear-and-extensional shelf thins after leaving the source, resulting in increased flow speed and strain rate in comparison to the shear-only case. At the channel exit, the area of high strain rate spans the width of the channel rather than just the central section as in the shear-only case.

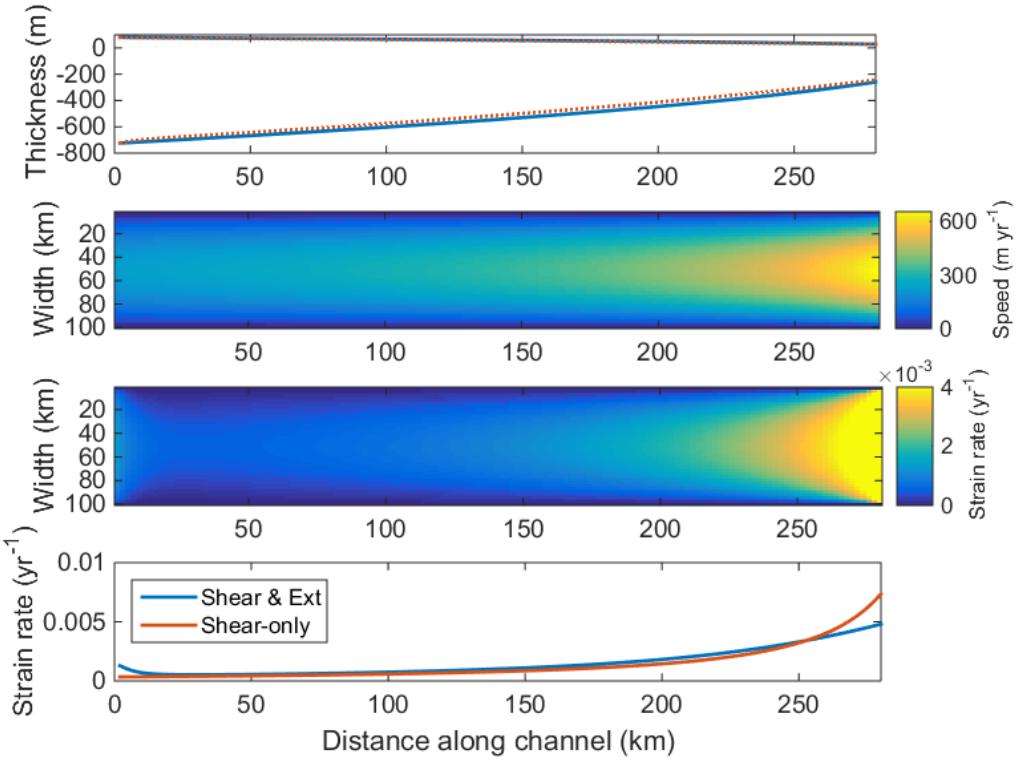

Figure 5.16: Thickness profile, speed map, strain-rate map and centreline strain rate for a steady-state Newtonian shelf, with dynamics controlled by shear and extension. For thickness plot: solid blue curve represents shear-only steady state; dashed red curve represents shear-and-extension steady state. Here the channel geometry and input flux have been set to approximate the final two thirds of the Amery Ice Shelf, which forms an approximately parallel channel. The input thickness is set to equal that of the input thickness of the equivalent shear-only shelf.

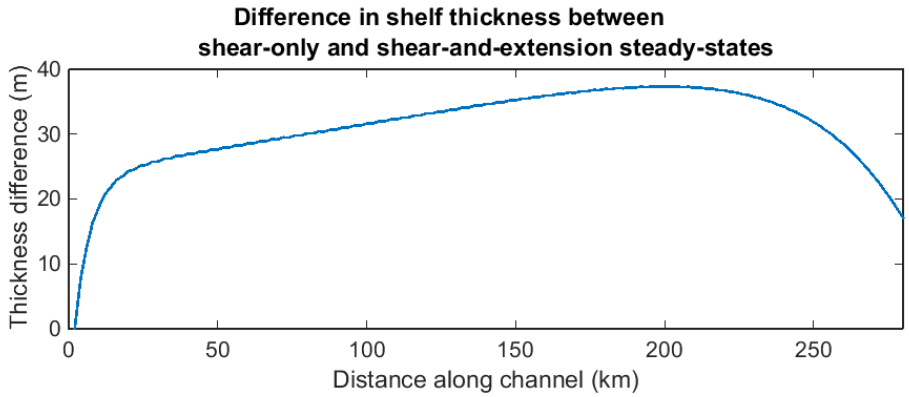

Figure 5.17: Plot showing difference in thickness between shear-only and shear-and-extension steady-state thickness profiles. Difference equals shear-only minus shear-and-extension. Therefore it is clear that the shear-and-extension shelf is thinner throughout the length of the channel.

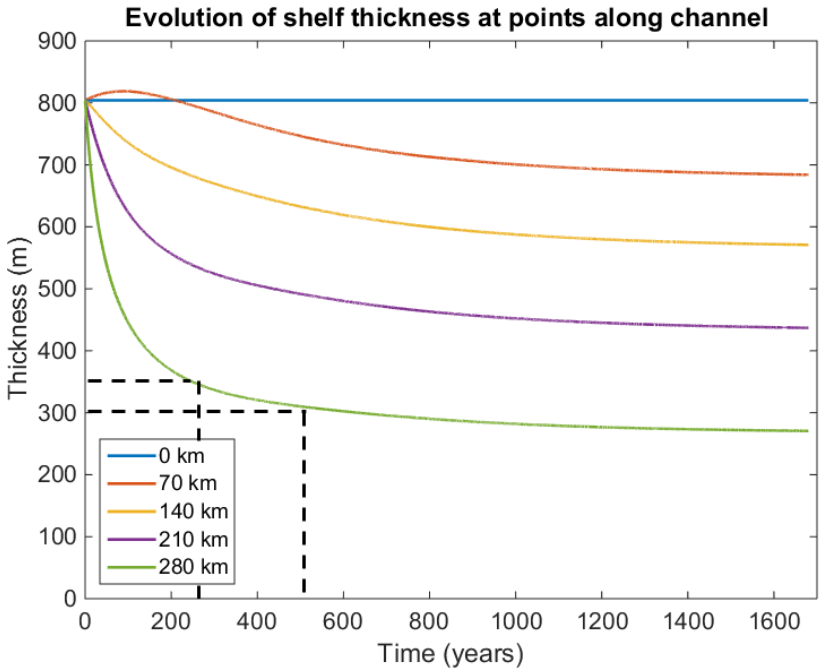

Figure 5.18: Plot showing the evolution of the shelf thickness at equally spaced points along the shelf. The Newtonian shelf evolves from a uniform thickness towards a steady-state. Dashed lines provide estimate of the time taken to adjust to a thickening of 50 m at the calving front, motivated by the retreat of the calving front following a large calving event - approximately 200 years.

When comparing the shear-and-extension steady-state thickness profile, speed and strain-rate maps with those of Amery Ice Shelf we see that the main characteristics are broadly similar. However, one of the clear differences is that Amery is approximately 200 m thinner and the flow is faster, with flow at the channel exit approximately 400 m yr^{-1} faster. These features are linked as the flux through the shelf must be conserved. This may be the result of the shear-thinning properties of ice, which are not captured in this model. For a shear-thinning rheology we might expect a region of faster flow in the centre of the shelf, with narrow margins of high shear along the channel walls. Faster flow would then result in a thinner shelf. Additional thinning may be caused by basal melting. From the work in Chapter 3 this melting could amount to 2 - 5 m yr^{-1} in the upstream section of the shelf with less melting further downstream, but this could significantly affect the shelf profile. The effects of a shear-thinning rheology are investigated in the next section.

The evolution of the shelf thickness at five points along the shelf is shown in Figure 5.18. This shows the evolution of the thickness from a uniform slab, with thickness equal to the input thickness of the shear-only steady-state shelf, to the steady-state shear-and-extension shelf profile. From this it is clear that the most pronounced changes occur at the channel exit, at 280 km. It is also apparent that at 70 km there is initially a thickening of the shelf for the first 200 years. This is because the shelf downstream from

this point is much thicker than in the final steady-state configuration. Therefore, there is more shear stress acting to resist the flow, which causes the upstream section of the shelf to thicken. It is evident that at the channel exit 90% of the adjustment occurs within the first 300 year. However, this adjustment time is longer at locations further upstream; at 70 km from the source it takes approximated 1000 years to adjust to 90 % of the steady-state value. This model captures the evolution of the shelf from a slab of uniform thickness. Geophysically it is likely that any adjustments in thickness, such as following a calving event, would involve much smaller changes in shelf thickness. From Figure 5.18 we can estimate that if a large calving event increased the thickness of the calving front by 50 m (from approximately 300 m in steady state to 350 m) for a shelf of approximately characteristics of Amery, it would take approximately 200 years for a new steady-state to be achieved.

Varying Input Thickness

From the previous example it is clear that the input thickness determined by the analytical solution for the shear-only shelf is larger than that observed geophysically for Amery Ice Shelf. It is also observed from the geophysical data that the shelf thins substantially upstream before entering the roughly parallel section that is considered in this model. From the model thickness plots it was clear that for the shear-and-extension shelf, there is an area of substantial thinning as the shelf leaves the source. I investigate the impact of varying the input thickness, on the steady-state thickness profile and the shelf flow dynamics by adjusting the input thickness of the shelf while retaining the same input flux; firstly by increasing the input thickness by 200 m and secondly by reducing the input thickness by 200 m. The numerical scheme was then run to steady-state, to determine the final thickness profile in each case.

Figure 5.19 shows the resulting plots for a shelf with input thickness 200 m greater than the analytical shear-only steady-state. When compared with the plots for the original shelf (Fig. 5.16) it is apparent that for the majority of the shelf the thickness profile and dynamics remain unchanged. However, near to the upstream boundary there are substantial differences. Within the first 20 km of the shelf there is a rapid adjustment of the shelf thickness, which thins by 200 m, resulting in rapid acceleration of the shelf flow and high positive strain rates. These strain rates reach a maximum of 0.0075 yr^{-1}, which is larger than the maximum strain rate at the channel exit in the shear-and-extension case. Downstream of this adjustment region the shelf remains unchanged, highlighting how the steady state is mainly determined by the channel-exit boundary condition and the shear dynamics throughout the majority of the shelf. At the upstream boundary there is then a extensionally controlled adjustment region as the shelf adapts to the shear-dominated dynamics from the imposed input thickness.

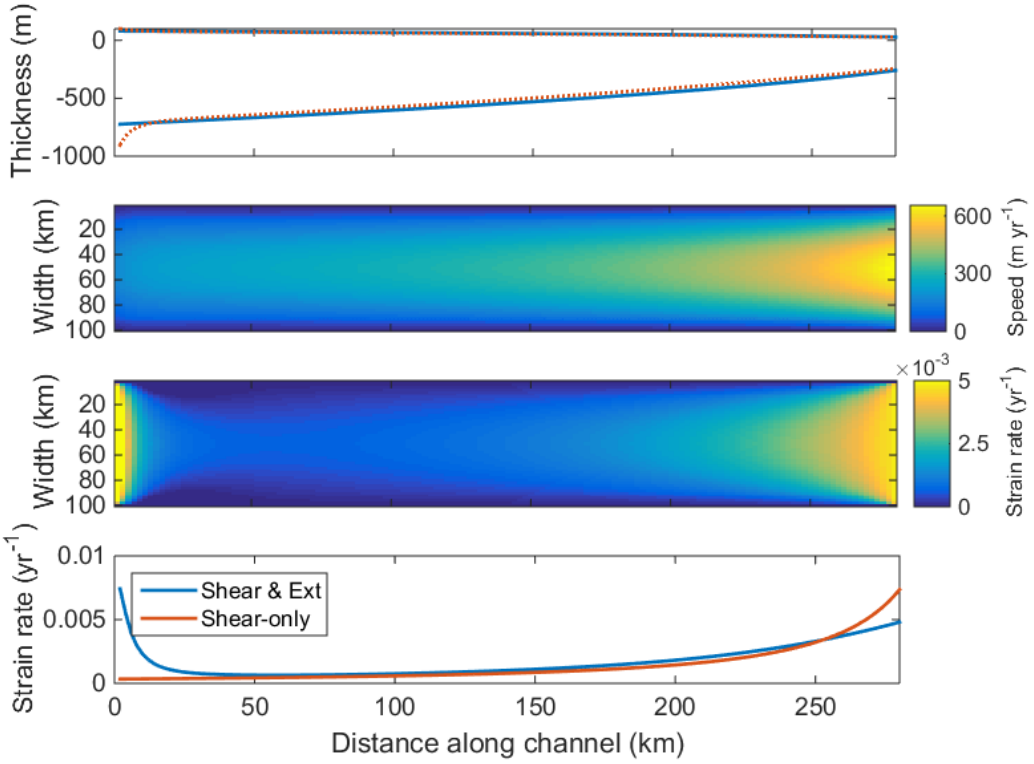

Figure 5.19: Thickness profile, speed map, strain-rate map and centreline strain rate for a steady-state Newtonian shelf, with dynamics controlled by shear and extension. For thickness plot: solid blue curve represents shear-only steady state; dashed red curve represents shear-and-extension steady state. The input thickness is set to be 200 m thicker than the input thickness of the equivalent shear-only shelf.

The input thickness is reduced by 200 m from the shear-only input thickness in Figure 5.20. As in the previous case with an increased input thickness, the only changes here are in a small region just downstream of the source. On this occasion the shelf slows as it leaves the source as the shelf must thicken in order to flow against the resistance from shear stresses that are present throughout the shelf. This leads to negative strain rates for the first 25 km of the shelf. Again, the dynamics in the shelf are controlled by the extensional boundary condition at the channel exit and the shear stresses throughout the majority of the shelf, leaving a small adjustment region at the upstream end of the shelf, where extensional dynamics control the adjustment.

Summary: Newtonian Shelves with Shear and Extensional Dynamics

When comparisons are made between the shear-only and shear-and-extension steady-states, the main features of the flow and thickness profile remain the same. There is a small difference in the thickness profiles between the shear-only and shear-and-extension shelves that can be seen in Figure 5.21. When the same input thickness is used, the shear-

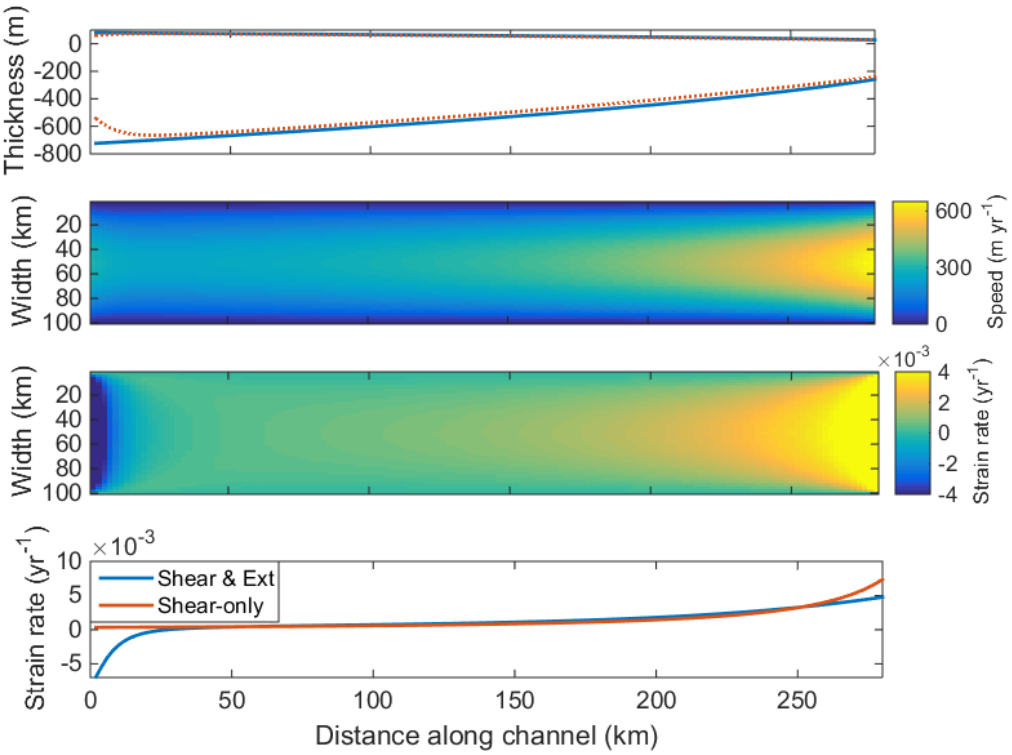

Figure 5.20: Thickness profile, speed map, strain-rate map and centreline strain rate for a steady-state Newtonian shelf, with dynamics controlled by shear and extension. For thickness plot: solid blue curve represents shear-only steady state; dashed red curve represents shear-and-extension steady state. The input thickness is set to be 200 m thinner than the input thickness of the equivalent shear-only shelf.

and-extension shelf initially thins after leaving the source. This is due to the presence of a thinner shelf downstream that provides less resistance to flow from shear stresses due to the reduced contact area with the lateral walls. The reduced thickness of the shelf is due to the inclusion of extensional stresses in the calculation, which act stiffen the shelf and propagate the effects of the extensional boundary condition upstream, acting to pull the shelf towards the exit. This feature can be seen in the centreline plots of strain rate, where there is increased positive strain rate throughout the shelf when extensional dynamics are included, with the exception of the final 20 - 30 km. In this final section of the shear-only shelf, the shelf is relatively thick at the exit, which induces higher strain rates. This leads to thinning at the exit and a large gradient in thickness, as seen in Figure 5.21, which drives relatively fast shear-flow and hence leads to high strain rates near the exit. The extensional effect of this boundary condition can propagate upstream in the shear-and-extension case.

Varying the input thickness had the effect of creating an extensional adjustment zone near the upstream boundary, where the thickness of the shelf adjusted to the mainly shear-dominated dynamics in the downstream part of the shelf and the extensional stress

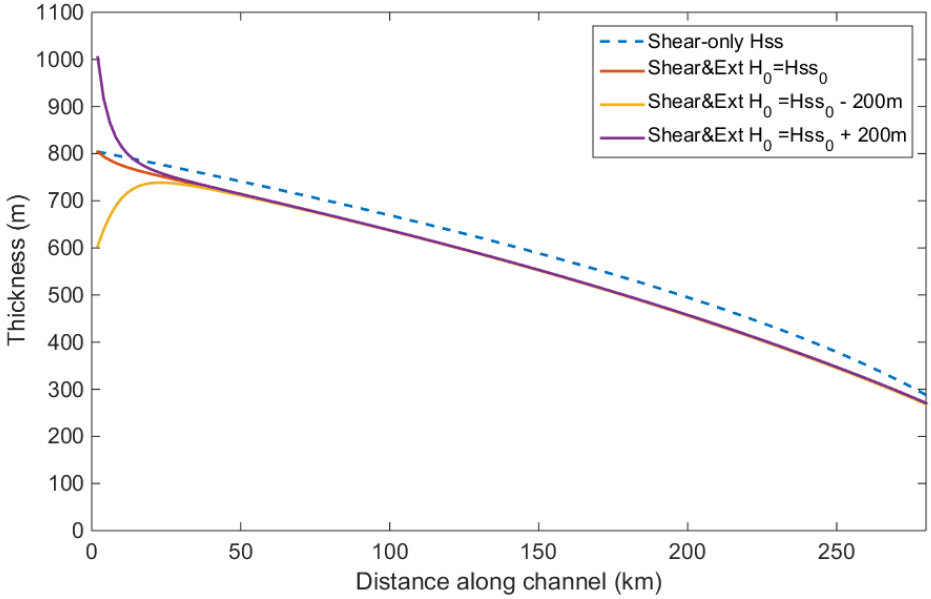

Figure 5.21: Plot comparing the steady-state shelf thickness for shear-only (blue dashed) and shear-and-extension dynamics. A range of different input thickness are used in the shear-and-extension cases: (i) same input thickness as shear-only steady-state - red curve; (ii) 200 m less that shear-only input thickness - yellow curve; (iii) 200 m greater than shear-only input thickness - purple curve.

boundary condition at the channel exit. This adjustment region can be seen for the two examples in Figure 5.21 and occurs within 30 km of the source, which is much less than the channel width (100 km).

When comparisons are sought between the geophysical example of Amery Ice Shelf and the Newtonian steady-states produced here the basic structure of the flow and thickness profiles are similar. However, there are some quantitative discrepancies, which may be expected given the shear-thinning properties of ice and the effects of basal melting that are not accounted for in this assessment. From this Newtonian approximation, is it possible to identify that the inclusion of extensional dynamics leads to increased positive strain rate upstream of the channel exit as observed geophysically. In addition, we have observed that there may be adjustment regions just downstream of the source where the shelf adapts to the thickness determine by the shelf dynamics downstream. For Amery Ice Shelf there is a clear change in thickness gradient approximately 120 - 150 km downstream of the grounding line. If this was associated with an adjustment to the dynamics further downstream I would expect this to be associated with positive strain rate, as observed in Figure 5.19. However, in the geophysical case the strain is negative, suggesting that this change in slope is not descriptive of an adjustment region, but is due to the widening of the channel and/or the effects of melting. Negative strain due to a widening channel was observed for the diverging channel cases considered earlier.

Power-Law - $n = 3$

I now investigate the changing dynamics that arise with the inclusion of extensional terms for power-law rheology shelves. In comparison with the shear-only case, here additional differences arise as the extensional component of the strain-rate tensor is included in the second invariant of the strain-rate tensor, which is used to calculate the effective viscosity.

Input Thickness Corresponding to Shear-Only Flow

The results for a steady-state, $n = 3$ power-law shelf with shear-and-extensional dynamics considered are shown in Figure 5.22. The thickness profile has changed very little from the shear-only case. The difference in the thickness can be seen in Figure 5.23, where it is clear that the change is small, with a maximum difference of 7 m. This is in contrast to the Newtonian case, where the inclusion of extensional terms in the force-balance equation led to a decrease in thickness throughout the shelf, with a maximum decrease of 37 m. For the power-law case, we observe that there is both thinning and thickening of the shelf when extensional terms are included, in comparison to the shear-only case: in the first 50 km of the shelf, the shelf with extension is thinner than the shear-only shelf; throughout the middle section of the shelf the shear-only case is thinner; while in the final 60 km the shear-and-extension shelf is thinner. These differences contrast to those in the Newtonian case, where there was significant thinning throughout.

From the speed map in Figure 5.22 there is a slight difference in the along-channel structure of the flow, with contours stretched further along the channel with the inclusion of extension. This may be expected as the inclusion of extensional terms acts to stiffen the shelf. In comparison with the shear-only case, there is a change in the structure of the strain-rate field, as can be seen in Figure 5.22. Upstream there is an area of adjustment, where the flow adjusts from that imposed by the input condition, to that further downstream. From 100 km downstream there is an increase in strain rate in a similar manner to the shear-only case, with speed map contours stretched in the along-channel direction. At the channel exit there are peaks in strain rate in the channel margins. This is very different from the shear-only case, where there was a central maximum. These peaks in the margins are located where there is high shear between the channel walls and the fast flow in the centre of the shelf. There is also high extensional strain rate as the channel exit boundary condition is imposed here. This leads to a large second invariant of the strain-rate tensor and in turn a relatively low viscosity. Low viscosities may then lead to a feedback with increased shear and strain rates. Features of this nature are not prominent in the strain-rate plot for Amery Ice Shelf in Figure 5.24. However, this style of dynamics may explain the high positive strain-rate features found: along the

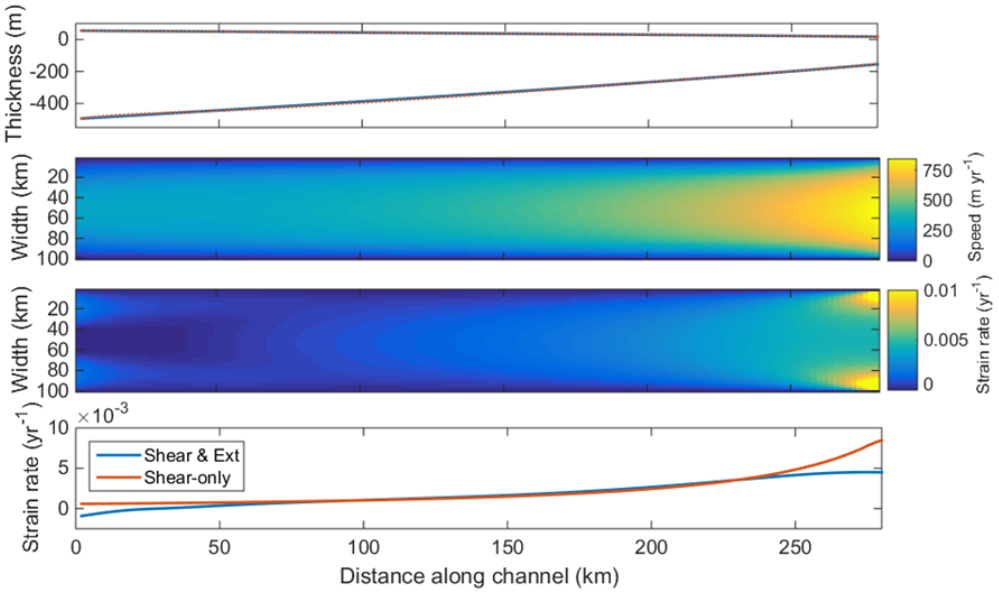

Figure 5.22: Thickness profile, speed map, strain-rate map and centreline strain rate for a steady-state $n = 3$ power-law shelf, with dynamics controlled by shear and extension. For thickness plot: solid blue curve represents shear-only steady state; dashed red curve represents shear-and-extension steady state.

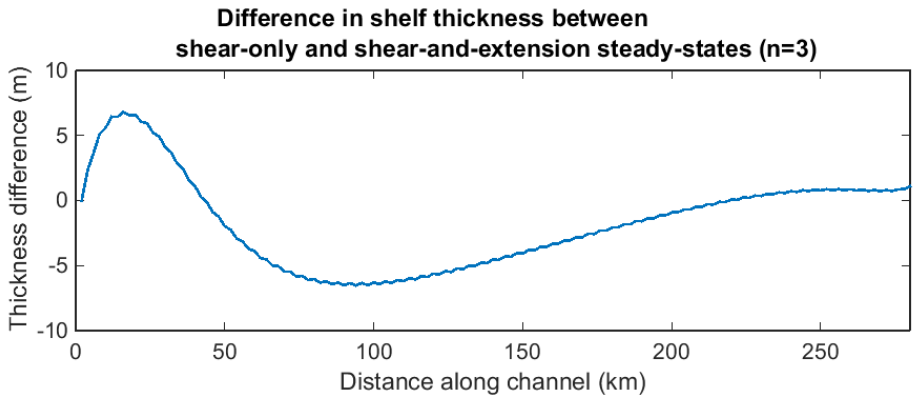

Figure 5.23: Plot showing difference in thickness between shear-only and shear-and-extension steady-state thickness profiles. Difference equals shear-only minus shear-and-extension.

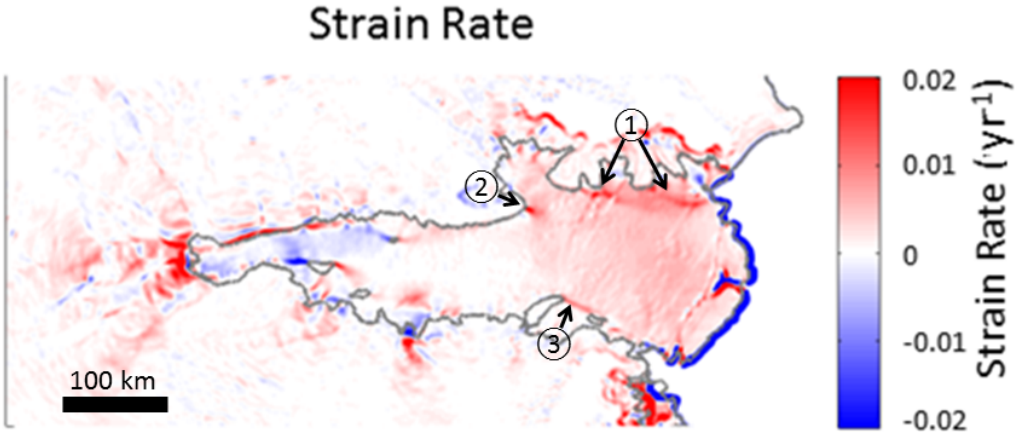

Figure 5.24: Strain-rate plot for Amery Ice Shelf. Numbers mark locations of high strain rate, which may be explained by the feedback between high shear and strain rates leading to weak viscosity that allows further high shear and strain rates. (1) Western shear margin of main flow. (2) Shear margin following inflow from Charybdis Ice Stream. (3) Shear margin past island protruding into main flow.

western boundary (upper boundary in Fig. 5.24) of Amery Ice Shelf in the final third of the channel; in the margin of the flow where the tributary ice shelf from the Charybdis ice stream merges with the main flow; and on the eastern boundary (lower boundary in plot) where an island protrudes into the main section of the flow. These features are labelled in Figure 5.24.

From the centreline strain rate (Fig. 5.22) it is clear that there is an area of negative strain rate in the upstream part of the shelf as the flow adjusts from the imposed input flow (parabolic across the channel) to the flow downstream. Throughout the majority of the shelf, from 60 km to 230 km, the centreline strain rates for the shear-only and shear-and-extension shelves are very similar, with slightly larger values in the shear-and-extension case, due to the channel exit boundary condition being able to propagate further upstream, although this is felt to a lesser extent than in the Newtonian case. As observed in the strain-rate map, the largest strain rates are found in the margins at the channel exit, and in comparison to the shear-only case the strain rate is much reduced along the centreline at the channel exit. This suggests that the viscosity is relatively large in the centre of the channel.

The evolution of the shelf thickness at points along the shelf can be seen in Figure 5.25. From this figure it is clear that the most rapid change occurs at the channel exit. Initially there is a large hydrostatic pressure gradient at the exit, which leads to a large and positive extensional stress that acts to thin the shelf rapidly. Meanwhile, at 70 km along the channel (red curve) there is little change in thickness over the first 100 years

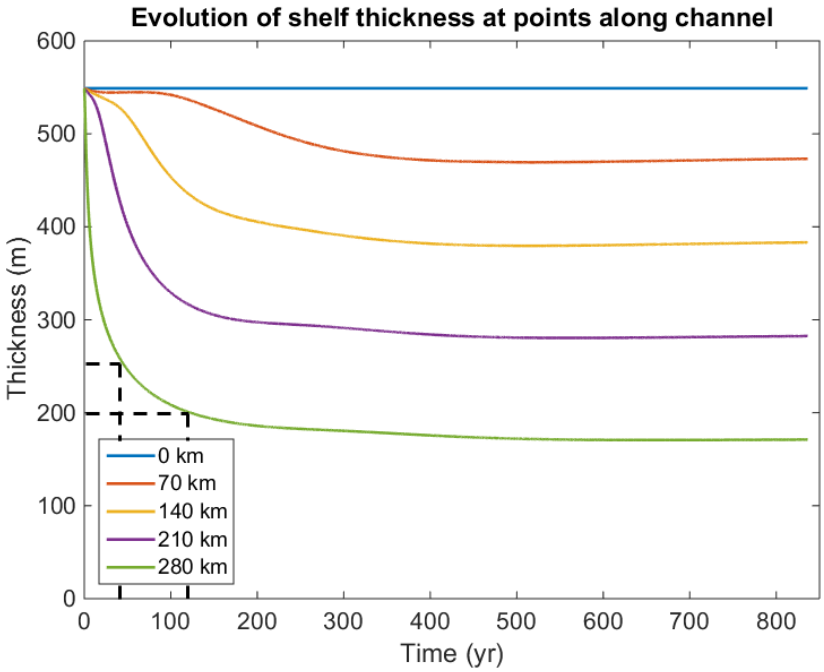

Figure 5.25: Plot showing the evolution of the shelf thickness at equally spaced points along the shelf. The $n = 3$ power-law shelf evolves from a uniform thickness towards a steady-state. Dashed lines provide estimate of the time taken to adjust to a thickening of 50 m at the calving front, motivated by the retreat of the calving front following a large calving event - approximately 100 years.

as the thick shelf downstream provides resistance to flow. At the channel exit 90% of the adjustment to steady state is achieved within 150 years, this is much shorter than in the Newtonian case (300 years). Further upstream, at 70 km from the source, after 400 years the shelf is very close to its steady-state thickness profile. This can be compared with the time taken to reach an equivalent stage for the Newtonian case (Fig. 5.18) which was 1000 years. These long adjustment times may be due to the relatively high viscosity of the Newtonian shelf, which remains unchanged throughout the evolution. However, in the shear-and-extension power-law case, as the shelf evolves from the initial state, it is likely that high strain rates and shear rates are generated. This then leads to reduced viscosities, which produce a feedback to generate higher strain and shear rates, and higher velocities. This enables the power-law shelf to evolve more quickly towards its steady state.

For a calving event increasing the shelf thickness at the calving front from approximately 200 m (in steady state) to 250 m, it will take approximately 100 years for the shelf to re-adjust to steady-state, as shown in Figure 5.25. This is half the time required for a Newtonian shelf.

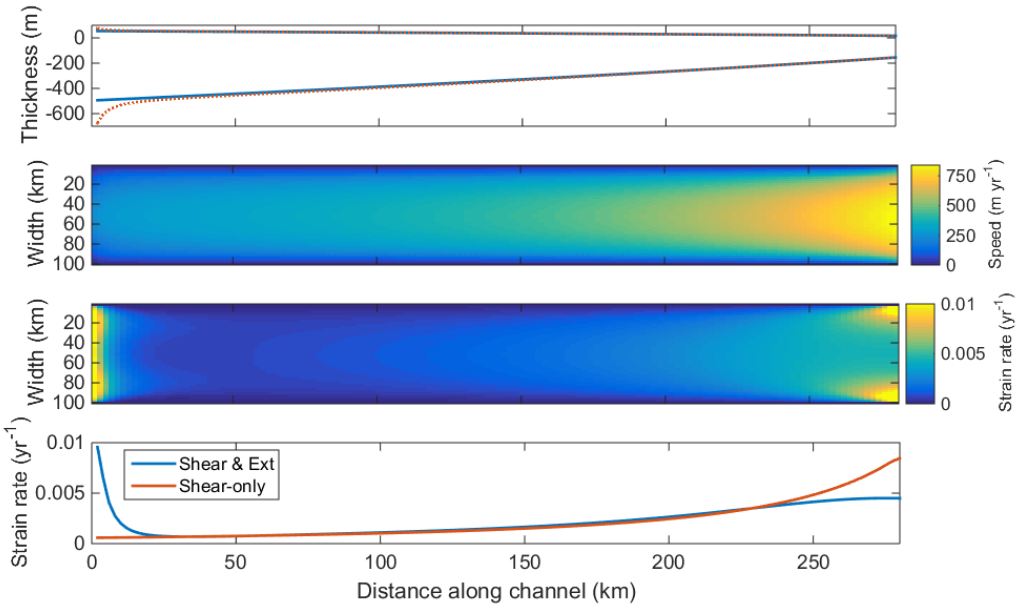

Figure 5.26: Thickness profile, speed map, strain-rate map and centreline strain rate for a steady-state $n = 3$ power-law shelf, with dynamics controlled by shear and extension. For thickness plot: solid blue curve represents shear-only steady state; dashed red curve represents shear-and-extension steady state. The input thickness is set to be 200 m thicker than the input thickness of the equivalent shear-only shelf.

Varying Input Thickness

As with the Newtonian shelves, I examined the impact of varying the input thickness of the shelf.

In Figure 5.26 the input thickness imposed is 200 m greater than the input thickness for the steady-state shear-only shelf, while the input thickness is reduced in Figure 5.27. Qualitatively the dynamics are the same as those observed in the Newtonian case only affecting the flow and thickness profile within the first part of the channel. This similarity with the Newtonian case suggests that there is little impact from the feedback between strain/shear rates and effective viscosity in this region.

Summary: $n = 3$ Power-Law Shelves with Shear and Extensional Dynamics

In the case of the Newtonian shelf, the inclusion of extensional terms led to a thinning of the shelf along its entire length in comparison to the shear-only case. This can be explained by considering the stiffening of the shelf when extensional terms are included. The stiffening leads to the influence of the channel-exit boundary condition propagating upstream, acting to pull the fluid downstream and thin the shelf. In contrast, when extensional terms are included in the power-law case, there was both thinning and thickening of the shelf, although the magnitude of the change was reduced from the Newtonian

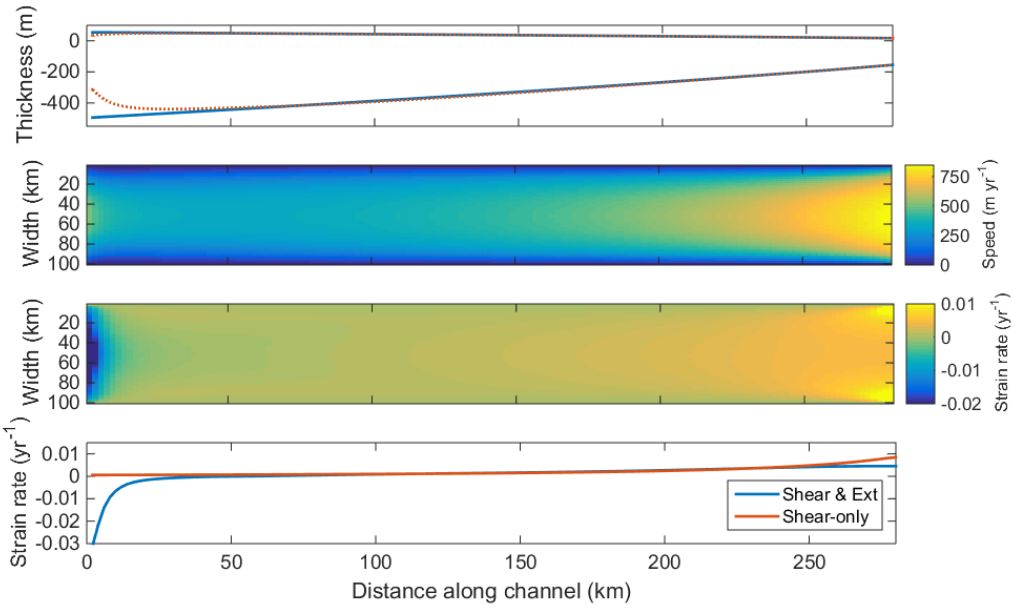

Figure 5.27: Thickness profile, speed map, strain-rate map and centreline strain rate for a steady-state $n = 3$ power-law shelf, with dynamics controlled by shear and extension. For thickness plot: solid blue curve represents shear-only steady state; dashed red curve represents shear-and-extension steady state. The input thickness is set to be 200 m thinner than the input thickness of the equivalent shear-only shelf.

case. As with the Newtonian case, the inclusion of extensional terms in the force balance should act to stiffen and thin the shear-and-extension shelf. However, there must also be a consequence of including the extensional term in the definition of the power-law rheology. This would act to reduce the effective viscosity of the shelf, reducing stiffness of the shelf and the effectiveness to propagate the exit boundary condition upstream. On the other hand a reduction in effective viscosity may lead to reduced resistance to flow from shear stresses, which would influence the thickness profile. There are also likely to be spatial variations in the effective viscosity that will impact the flow dynamics and thickness profile. In the following section I address the influence of these two components on determining the steady-state shelf for a shear-and-extension power-law shelf.

5.5.5 Investigating Changes Between Shear-Only and Shear-and-Extension with Power-Law Rheology

In the previous section the two types of steady-state power-law ice shelf were compared: shelves with shear-only dynamics and shelves with shear-and-extensional dynamics. In doing so two features of the problem were changed. Extensional stresses were included in the force-balance equation, and in addition the extensional strain rate was included within the rheological model. As two features were varied it is difficult to determine the influence of each on the subsequent dynamics and thickness profile. Therefore, I devel-

oped a model that allows the influence of the extensional terms to be varied separately in the force-balance equation and in the rheological model. I used the variables C_1 and C_2 to change the importance of the extensional terms in the force-balance equation and rheological model respectively. Their values can range between 0 and 1. A value of 0 means the extensional terms have no influence and 1 that these terms have full influence. The equations for the force balance and effective viscosity become

$$4C_1\frac{\partial}{\partial x}\left(\mu H\frac{\partial u}{\partial x}\right)+\frac{\partial}{\partial y}\left(\mu H\frac{\partial u}{\partial y}\right)=\rho g' H\frac{\partial H}{\partial x}, \tag{5.91}$$

$$\mu = B\left(C_2\left(\frac{\partial u}{\partial x}\right)^2+\frac{1}{4}\left(\frac{\partial u}{\partial y}\right)^2\right)^{(1-n)/2n}. \tag{5.92}$$

Flow Dynamics for Fixed Thickness Profile

To determine the influence of each term I initially chose to keep the thickness profile constant, as the shear-only steady-state profile and then performed a Successive Over Relaxation (SOR) calculation to determine the corresponding velocity field, for a range of C_1 and C_2 values. To test this methodology I first performed the SOR with small values of C_1 and C_2, as this should replicate the shear-only case for which I have an analytical solution.

Figure 5.28 shows plots for C values of $C_1 = 0.001$ and $C_2 = 0.001$. The top right plot in Figure 5.28 shows the difference between the speed for the analytical steady-state solution and the solution obtained using SOR with $C_1 = 0.001$ and $C_2 = 0.001$ (speed from analytical shear-only steady-state minus speed from SOR). We see that there is very little difference in the velocity field, with maximum differences of approximately $\pm$ 0.25 m yr^{-1} in areas where the flow speed is approximately 800 m yr^{-1}, implying a relative error of less than 0.05 %. These slight differences are at the channel exit, but this may be due to the implementation of the channel exit boundary condition, which is imposed on the width-averaged thickness and velocity in the analytical case, but here is imposed directly on the velocity field. Differences that emerge along the centreline are due to the low shear-rates that occur here. In the analytical case these shear rates are zero and lead to an area of infinite viscosity, however when a numerical method is used in this situation it is not possible to obtain an infinite viscosity.

In Figure 5.29 $C_1 = 0.1$ and $C_2 = 1$, these values imply that the extensional stresses in the force-balance equation have been set to have a small influence, while the extensional component of the strain-rate tensor has been included in the power-law rheological model. We observe that for the new speed field (with $C_1 = 0.1$ and $C_2 = 1$) there is a region of faster flow in the centre of the channel bounded by regions of slower flow, as

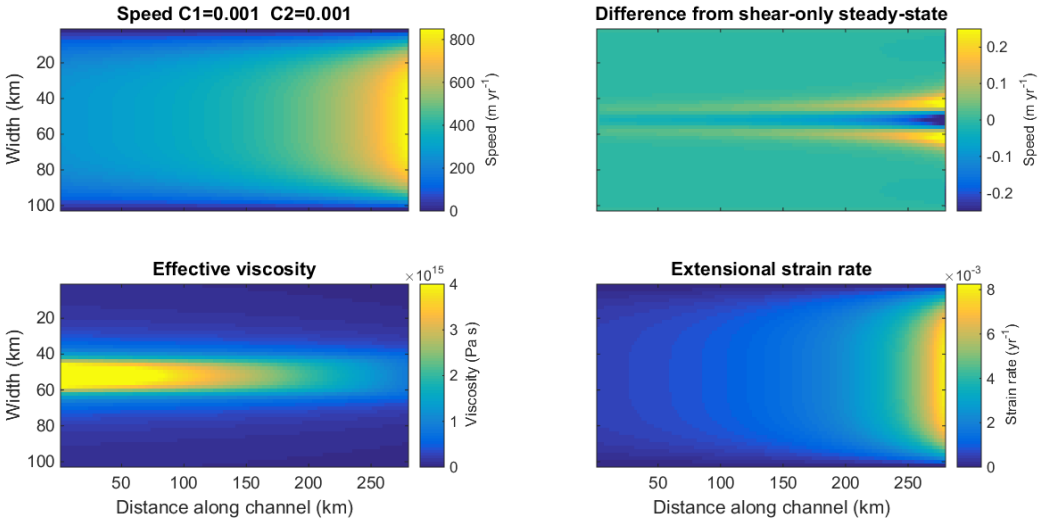

Figure 5.28: Speed, difference in speed from steady-state shear-only (shear-only minus new), effective viscosity and strain rate for $C_1 = 0.001$ and $C_2 = 0.001$, for shear-only steady-state thickness profile. Extensional terms have a minimal influence in both the force-balance and rheological model.

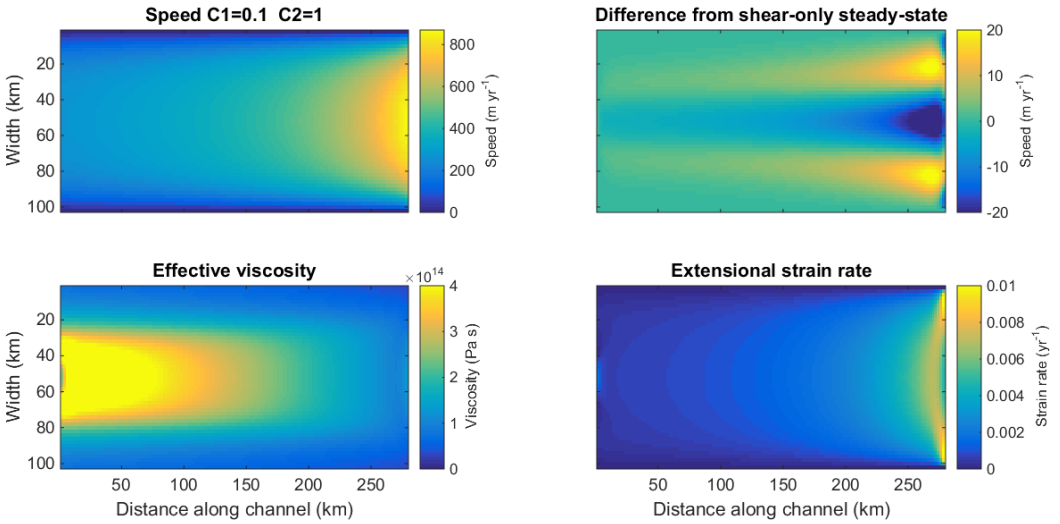

Figure 5.29: Speed, difference in speed from steady-state shear-only (shear-only minus new), effective viscosity and strain rate for $C_1 = 0.1$ and $C_2 = 1$, for shear-only steady-state thickness profile. Extensional terms only fully influence the rheological model.

shown in the difference plot in Figure 5.29. This suggests that there is a considerable change to the cross-channel velocity profile, moving from a 'plug-flow' like structure in the shear-only case to a more parabolic profile when extension is included in the power-law rheology. This is because the shear components of the strain-rate tensor have a less dominant role controlling the spatial structure of the effective viscosity. This also leads to a marked change in the effective viscosity field, where the viscosity has decreased by nearly an order of magnitude throughout the shelf. There is a change in the structure of the strain-rate field near the channel exit. The strain rate has increased in the margins of the shelf at the channel exit. This is due to the inclusion of extensional terms in the rheological model, which act to reduce the effective viscosity, leading to peaks in strain rate forming in these areas. There is also an arch of high strain rate that connects these two regions across the channel that was not evident in previous cases. Despite this, the strain rate in the centre of the shelf at the exit remains fairly unchanged from the shear-only case.

The influence of the extensional strain rate on the effective viscosity is reduced in Figure 5.30 with the full force-balance equation used, such that $C_1 = 1$ and $C_2 = 0.1$. We now observe that the shelf velocity at the channel exit has been reduced by approximately 50 m yr^{-1}. In contrast to the previous choice of C values, there is now a reduction in velocity in the centre of the channel at the exit, while in the margins the flow is faster. Here there is a spatial structure to the effective viscosity field across the width of the shelf at the channel exit due to the variation in shearing across the channel width. This leads to a central region of high effective viscosity bounded by weaker viscosities. At the channel exit the flow is determined by the extensional stress boundary condition, which is implemented pointwise along the boundary in this model. The model assumes a uniform shelf thickness across the channel width. Therefore in areas with weak viscosity (margins), the resulting strain rates are high, leading to fast flow. Whereas, in the centre of the shelf the effective viscosity is high and therefore the flow is slower. The analytical shear-only solution, implements the channel-exit boundary condition on the width-averaged speed using the width-averaged effective viscosity. This leads to the spatial variation in speed between the two models. The inclusion of extensional terms in the force-balance equation allows these effects at the boundary to propagate further upstream than in the shear-only case, leading to a slight increase in flow speed upstream from the exit. The high strain rates in the margins can be seen in the strain-rate plot in Figure 5.30. These areas appear to be linked by an arch of high strain rates that traverses the channel within the final 40 km of the channel.

Figure 5.31 shows the case where the extensional terms have full influence in both the force-balance and rheology ($C_1 = 1$ and $C_2 = 1$). Here we observe that the speed at

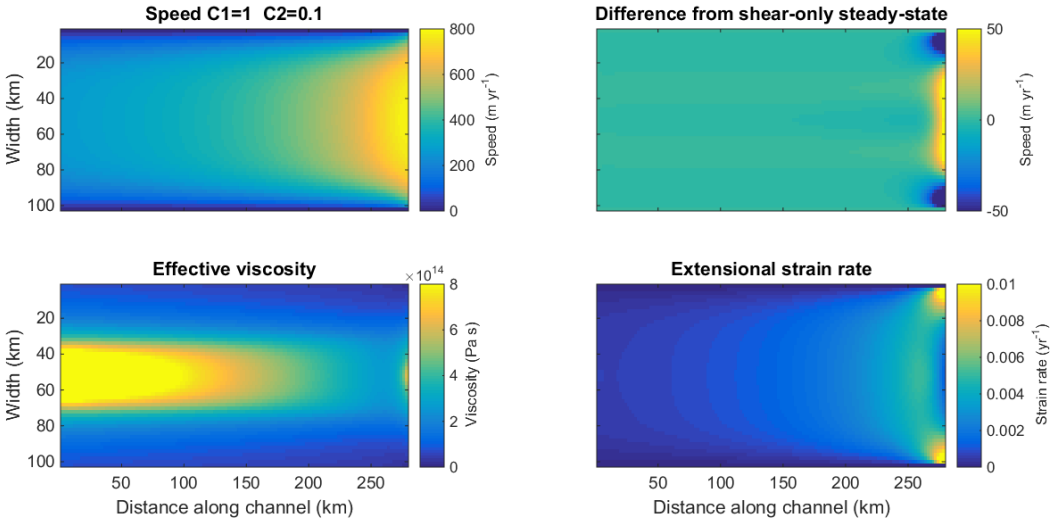

Figure 5.30: Speed, difference in speed from steady-state shear-only (shear-only minus new), effective viscosity and strain rate for $C_1 = 1$ and $C_2 = 0.1$, for shear-only steady-state thickness profile. Extensional terms only full influence force-balance.

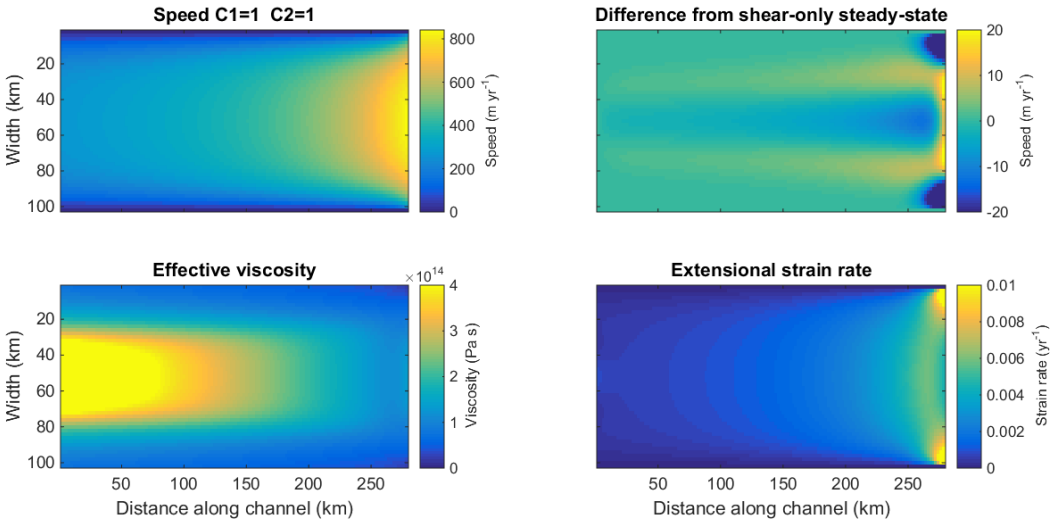

Figure 5.31: Speed, difference in speed from steady-state shear-only (shear-only minus new), effective viscosity and strain rate for $C_1 = 1$ and $C_2 = 1$, for shear-only steady-state thickness profile. Extensional terms are included fully in both rheological model and force-balance.

the channel exit is slightly reduced from the shear-only case, a result of the inclusion of the extensional term in the force-balance equation. The cross-channel contours in speed are slightly flattened in the centre of the channel and are stretched a little in the along-channel direction. This is due to the inclusion of extension in both terms. In the force-balance equation the extensional term acts to stiffen the shelf pulling the fluid towards the channel exit. On the other hand, the inclusion of the extensional term in the rheological model means the value of the effective viscosity is not solely dependent on the shear rate. Therefore, as strain rates tend to be greater in the centre of the shelf the variation in effective viscosity across the channel width becomes less pronounced, reducing the prominence of the narrow shear margins and preventing the formation of a central plug-flow region.

When considering the difference in speeds between the shear-only case and this case, with shear-and-extension in all terms (Fig. 5.31b), it is clear that there are two different effects. Firstly, at the immediate channel exit the difference in speed takes the same form as when extensional terms are included in the force balance equation. There is a reduction in speed in the centre of the shelf and an increase in the margins. Secondly, back from the exit there is an increase in speed along the centre of the channel and a decrease to either side. This is similar to what is observed when extension is included in the rheological model. The effective viscosity map (Fig. 5.31c) has a similar structure and magnitude to the case when extension is included in the rheological model as would be expected, while the strain-rate field (Fig. 5.31d) has a similar structure to the case when extensional stresses are considered in the force-balance equation.

Evolving the shelf thickness profile for a range of different models

Following the approach in the previous section, I used the same model to determine the velocity field and then evolved the ice-shelf thickness profile towards a steady-state, iterating for a new velocity field at each time step in the evolution of the shelf thickness.

Figures 5.32a and 5.32b show the steady-state thickness profile and dynamics respectively for C parameter values of $C_1 = 0.1$ and $C_2 = 0.1$. Here we see that the shelf has thickened slightly in comparison to the shear-only case. This thickening is almost uniform along the entire length of the shelf. In response to this thickening and in order to maintain a constant flux through the shelf, the flow speed is reduced, reaching a peak of over 600 m yr^{-1} at the exit of the channel. The reduction in speed can be seen in the speed-difference plot in Figure 5.32b. As both C values are reduced we would expect the results to be similar to the shear-only case, but there are some differences. One substantial difference are the peaks in strain rate found in the margins of the shelf at the exit. These features are not found in the shear-only cases, where there is a central

maximum. This may be due to the different methods used to implement the boundary condition in the two cases: using the width-averaged effective viscosity and strain rate for the analytical solution for the shear-only shelf; but implementing the condition point-wise for this numerical model. The broad scale changes to the shelf thickness and speed suggest that C values of 0.1 are not small enough to completely reduce the influence of the extensional terms. However, varying the values of the C parameters does provide a useful method for determining the different influences from inclusion of the extensional terms in the force-balance and rheological model separately.

The influence of the extension in the force-balance equation is reduced in Figures 5.33a and 5.33b, where $C_1 = 0.1$ and $C_2 = 1$. From Figure 5.33a we see that the inclusion of the extensional component of the strain rate in the power-law-rheology model leads to a slight decrease in shelf thickness in comparison to the shear-only case. The difference in speed is given in Figure 5.33b. Here it is clear that at the channel exit there is a central region where the shelf is flowing faster (approximately 100 m yr^{-1} faster) than the shear-only case. In the channel margins there is a slight reduction in flow speed. This central region of faster flow extends back from the channel exit, along the centre of the shelf. This increase in centreline velocity is due to the reduction in the effective viscosity, which can be seen in the effective viscosity plot (Fig. 5.33b) showing an approximate halving in viscosity from the shear-only case. The decrease in effective viscosity in the centre of the shelf allows shear to increase in this region and the central plug region found in the shear-only case is no longer present. As identified in the early example with a fixed thickness profile (Fig. 5.29) the strain-rate plot has peaks in the margins of the shelf at the exit, where there is weak effective viscosity. These regions are then connected by an arc of high strain rates that spans the width of the shelf.

In contrast to the previous example ($C_1 = 0.1$ and $C_2 = 1$, Fig. 5.33a and 5.33b), when extensional terms are included to their full extent in the force-balance equation but reduced in the rheological model, with $C_1 = 1$ and $C_2 = 0.1$, (in Fig. 5.34a and 5.34b) we observe that there is a slow down in the flow in the centre of the channel at the exit. This is associated with a thickening of the shelf, from 50 km downstream to the exit. With the inclusion of the extensional term in the force-balance equation, this leads to a stiffening of the shelf, particularly along the centre of the shelf where there is relatively high effective viscosity. An exception to this is in the margins of the shelf at the exit, where there is again high strain due to the weak effective viscosity in this area of high shear. The spatial distribution of the effective viscosity can be seen in Figure 5.34b and contrasted with that in the previous example (Fig. 5.33b) and the case where both C values are small (Fig. 5.32b). From these plots it is clear that the inclusion of extension in the force-balance equation leads to stiffening and in areas of high viscosity

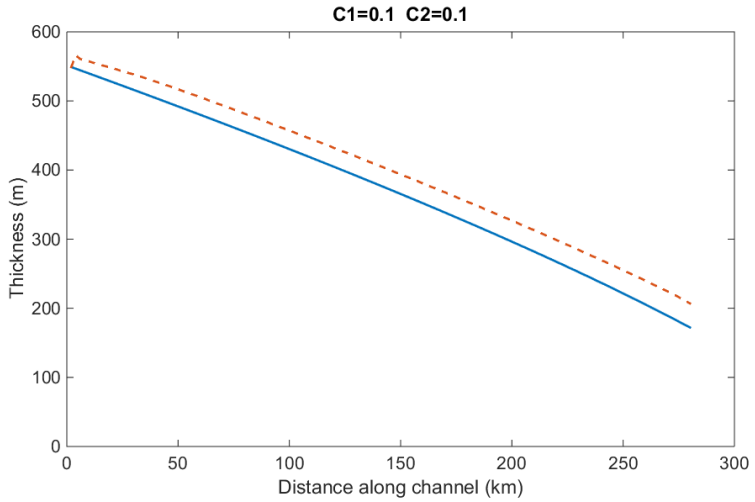

(a)

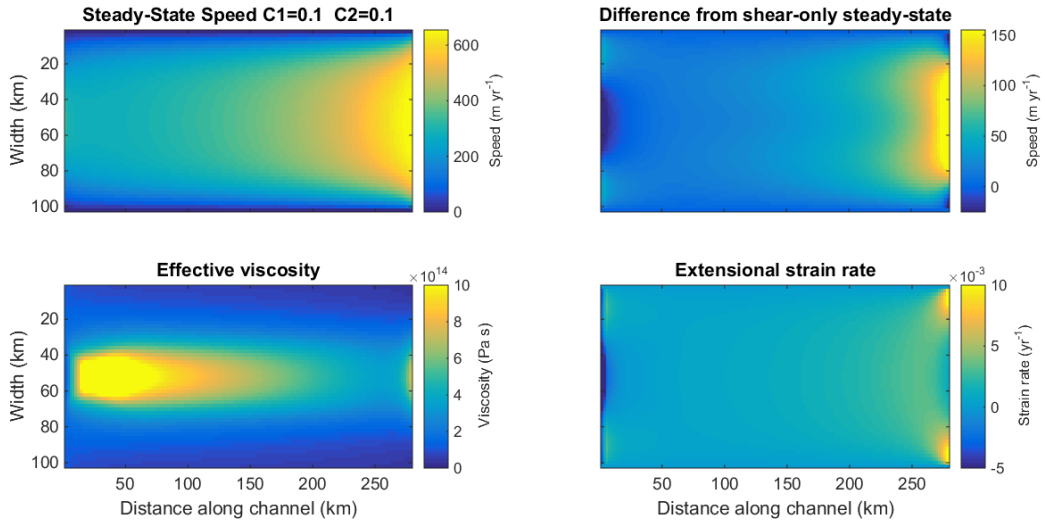

(b)

Figure 5.32: (a) Steady-state thickness profile for shelf with extensional parameter values $C_1 = 0.1$ and $C_2 = 0.1$ (red dashed curve) and shear-only shelf (blue solid curve). (b) Corresponding plots for C value thickness profile: Speed; Shear-only speed minus C value speed; effective viscosity; and strain rate.

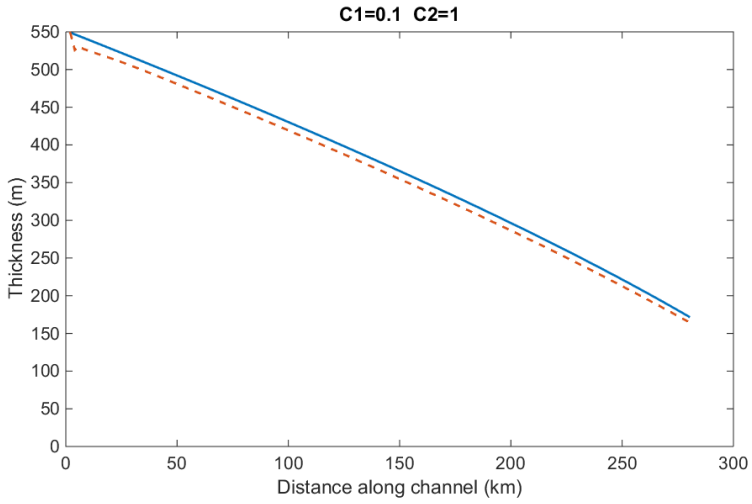

(a)

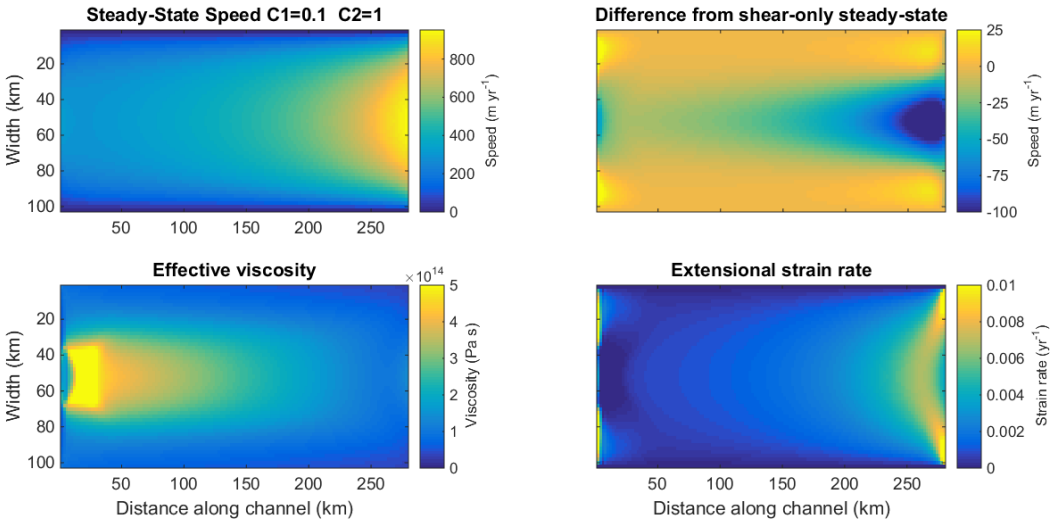

(b)

Figure 5.33: (a) Steady-state thickness profile for shelf with extensional parameter values $C_1 = 0.1$ and $C_2 = 1$ (red dashed curve) and shear-only shelf (blue solid curve). (b) Corresponding plots for C value thickness profile: Speed; Shear-only speed minus C value speed; effective viscosity; and strain rate.

a reduction in the strain rates (and shear rate). This leads to an increase in the effective viscosity, forming a high viscosity area near the channel exit that is not observed in previous examples. High effective viscosity at the channel exit suggests reduced shear in this region, which is clear from the speed map. This high effective viscosity reduces the magnitude of the strain rate generated due to the imposed channel-exit boundary condition. As the strain rate at the channel exit is reduced so is the speed of the flow, which leads to a thickening of the shelf.

Both extensional terms in the force-balance equation and rheological model are included in Figures 5.35a and 5.35b, with $C_1 = 1$ and $C_2 = 1$. From the thickness profile plot in Figure 5.35a there is a slight thinning of the shelf in comparison to the shear-only case. This thinning is similar to the change observed in the Newtonian case, when extensional terms are considered. The shelf dynamics and effective viscosity are shown in Figure 5.35b. From the speed-difference plot, comparing the shear-only and shear-and-extension speed maps, it is clear that in the centre of the channel at the channel exit the shear-only shelf has faster flow in a 10 - 15 km region back from the exit, while in the margins the flow is slower for the shear-only case. This may be due to the implementation of the boundary condition in the shear-only analytical calculation. At the channel exit there is a large spatial gradient in the effective viscosity across the width of the shelf because in the centre of the shelf there are relatively low shear rates, but high shear in the margins. Therefore, there is a spatial variation in the effect of the channel-exit boundary condition, which uses a uniform shelf thickness across the width of the channel. Where effective viscosity is low (margins) the induced strain rate will be larger than in areas with high effective viscosity (centre). This is observed in the strain rate map, with peaks in the margins and relatively low strain rates in the centre of the shelf at the exit.

The inclusion of extensional terms in the force-balance equation also has an impact on the flow speed at the channel exit, as observed in Figure 5.34b with $C_1 = 1$ and $C_2 = 0.1$. This acts to stiffen the shelf and allows the effects of the channel-exit boundary condition to propagate further upstream. However, as the shelf is stiffer there is additional resistance to the flow, as the section of shelf at the channel exit must pull on the shelf further upstream, which acts to slow the flow at the exit. Upstream from the channel exit, we observe an increase in flow speed in the central section of the flow for the shear-and-extension case. Again this is due to the stiffening of the shelf with the inclusion of extensional terms in the force-balance equation. The stiffening acts to slow the flow at the exit, but in turn pulls the upstream section of the shelf towards the channel exit. In the shear-only case the effect of the extensional stress boundary condition is only felt in a small region close to the channel exit. However, with the inclusion of

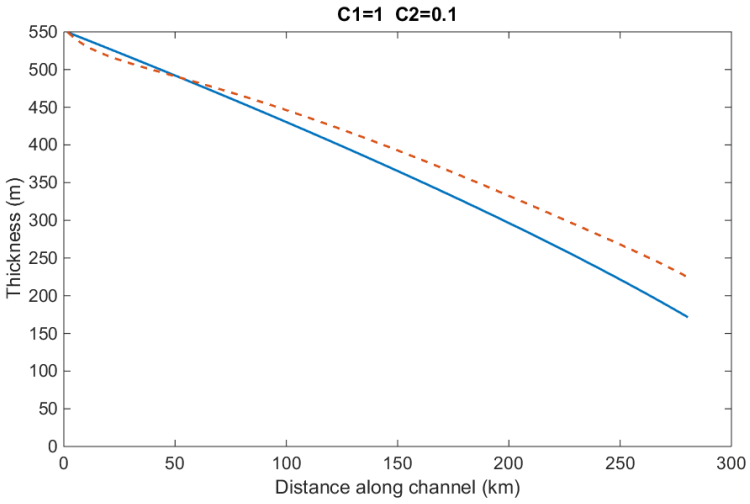

(a)

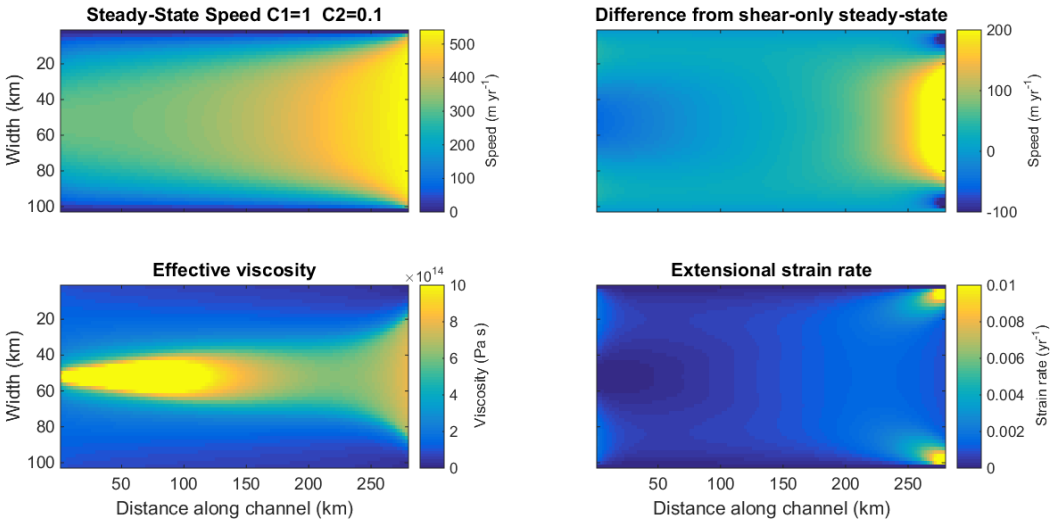

(b)

Figure 5.34: (a) Steady-state thickness profile for shelf with extensional parameter values $C_1 = 1$ and $C_2 = 0.1$ (red dashed curve) and shear-only shelf (blue solid curve). (b) Corresponding plots for C value thickness profile: Speed; Shear-only speed minus C value speed; effective viscosity; and strain rate.

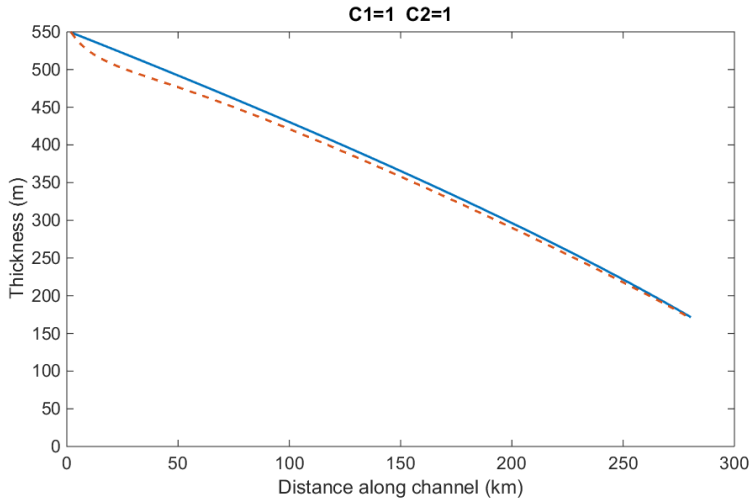

(a)

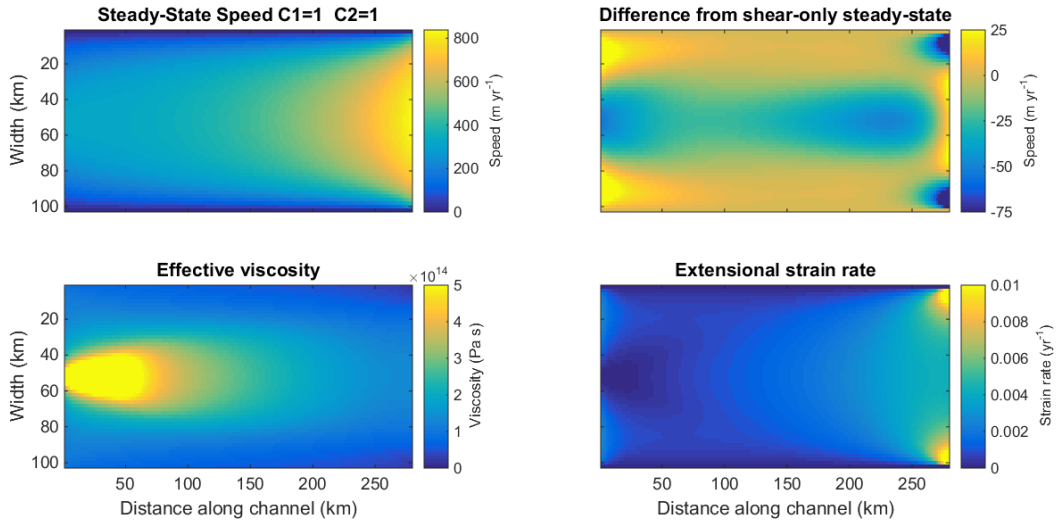

(b)

Figure 5.35: (a) Steady-state thickness profile for shelf with extensional parameter values $C_1 = 1$ and $C_2 = 1$ (red dashed curve) and shear-only shelf (blue solid curve). (b) Corresponding plots for C value thickness profile: Speed; Shear-only speed minus C value speed; effective viscosity; and strain rate.

extensional terms in the force balance the effect of the channel-exit boundary condition can propagate further upstream. From the speed-difference plot I can infer that, in the shear-only case, the information from the channel-exit boundary condition influences the flow in the final 10 - 15 km of the channel. However, in the shear-and-extension case, this information propagates further upstream leading to an increase in speed of approximately 25 - 50 m yr^{-1}. Consequently there is a thinning of the shelf in comparison to the shear-only case.

Including extensional terms in the rheological model prevents the formation of a prominent central plug-flow as the effective viscosity along the centre of the shelf has been reduced. This leads to a more parabolic-like cross-channel speed profile and contributes to the increase in speed in the centre of the shelf as observed in Figure 5.35b. As in the early strain-rate plots, here there are peaks in strain rate in the margins at the exit and an area of relatively high strain rate that spans the width of the channel at the exit.

Summary

From the set of model runs in the previous section, where the influence of the extensional terms in the force-balance equation and rheological model are varied, it is evident that the effects of adjusting these two components are complex. One key difference between the two appears to be the effect at the downstream end of the channel versus further upstream. When extension is included in the force-balance equation, this leads to a slow down in speed in the centre of the shelf at the channel exit. This is because including extension acts to stiffen the shelf and there is therefore more resistance to flow at the exit due to the slower flow upstream, which resists some of the extension at the front. When extension is included in the rheological model there is a decrease in the effective viscosity throughout the shelf by approximately 50%. The effect is most prominent along the centreline of the shelf, as there is no longer a central plug-flow region, but a fast flowing central peak that flows faster than the same region in the shear-only steady state.

In both cases, there are differing effects between the central region of the shelf and the margins. Throughout most of the length of the shelf margins there is little change as the influence of extensional terms is varied. However, there are some prominent changes at the channel exit. When extension is included in the rheological model, the cross-channel velocity profile is changed from plug flow to a more even near-parabolic profile. Therefore, there are no longer areas of such high shear in the margins at the exit, which increases the effective viscosity it those regions, reduces the strain rate at the exit and in turn the flow speed. In contrast, when extension is included in the force-balance equation,

there is an increase in speed in the margins. This is partly due to the pointwise implementation of the channel-exit boundary condition. However, there is also an increase in shear in the margins as there is a wide central region of fast flow due to the increased stiffness in the shelf which resists deformation in the central section of the shelf. This increase shear in the margins leads to reduced effective viscosity and therefore faster flow.

The individual effects of the inclusion of extensional terms can be seen when both are included in Figure 5.35b, with decreased flow in the centre of the shelf at the channel exit, but increased flow in the centre further back from the exit. The magnitude of these differences is partly dependent on the rate factor, which determines the magnitude of the effective viscosity and therefore the stiffness of the shelf when extensional terms are included in the force-balance equation.

5.6 Conclusion

5.6.1 Thickness profile

For an ice shelf in a parallel-channel, with dynamics dominated by the lateral shear between the channel walls, a similarity solution for the shelf thickness produces an almost linear profile, which is slightly convex. This profile becomes more convex at the downstream boundary for the steady-state shear-only shelf. In the steady-state case, an extensional-stress boundary condition is imposed at the exit, which balances the extensional stress in the shelf with the hydrostatic pressure of the ocean. The shelf thickness profile is determined by the boundary condition at the channel exit and the shear dynamics in the shelf, which balance the imposed input flux.

Including extensional dynamics in the shelf model allows different input thicknesses to be imposed upstream. However, the majority of the thickness profile remains unchanged, with a small extensionally controlled region near the source, where the shelf thins or thickens rapidly, to adjust to the downstream thickness profile. The inclusion of extensional dynamics acts to stiffen the shelf. This can lead to thinning of the shelf as the extensional stress from the channel-exit boundary condition can propagate upstream. If the shelf has a large viscosity the resistance to extension is increased and the shelf thickens.

For shelves in a diverging channel, the thickness profile takes a concave profile, with rapid thinning near the source. The similarity solution implies the shelf thins like $1/x$ in the Newtonian case and more rapidly, like $1/x^2$, in the case of an $n = 3$ power-law. The thickness profile is dependent on balancing the hydrostatic pressure, with the resistance

from shear stresses and the lateral spreading of the shelf. In the upstream section, where the shelf is narrow, there are high shear stresses which can lead to the formation of a very thick shelf.

5.6.2 Shelf Flow Dynamics: Speed and Strain Rate

For a diverging shelf, there is a large gradient in thickness at the upstream end of the channel as the shelf leaves the source, and as shear-dominated flow is dependent on the thickness gradient ($\partial H/\partial x$) this results in fast flow. Upstream the shelf is narrow and thick, generating resistance from shear stresses and the lateral spreading of the shelf. As the shelf leaves the source it slows, leading to negative strain rates. The dynamics are dependent on the effective viscosity, with low effective viscosities leading to positive strain rates in the downstream regions as the resistance to flow is reduced. For low effective viscosities, the resistance to flow from lateral spreading is reduced and the flow dynamics appear similar to those in the parallel channel case.

For the parallel cases the shelf thins in the downstream direction and, in order to maintain constant flux, there must be acceleration of the flow. The similarity solution and shear-only steady-state shelves produce parabolic ($n = 1$) or plug-flow ($n = 3$) cross-channel profiles. However, these are modified with the inclusion of extensional dynamics. The consideration of extensional dynamics acts to stiffen the shelf so that flow is reduced at the channel exit, due to the resistance from slower flow upstream. However, this stiffening also acts to increase the flow speed in the upstream sections of the shelf. The magnitude of this effect is dependent on the value of the effective viscosity.

When the extensional component is included in the rheological model it acts to decrease the effective viscosity throughout the shelf, but the most pronounced change is along the centre of the shelf where there are the highest strain rates. Therefore, this leads to an increase in flow speed along the centre of the shelf. When the extensional-stress boundary condition is implemented pointwise along the channel exit, there is an increase in the strain rate in the margins of the shelf. Here there is high shear and therefore weak viscosity, which enables high strain rates to be obtained in these regions. With the inclusion of extensional terms, there are peaks in strain rate at the channel exit in the margins and high strain rate across the channel width, similar to that observed for Amery Ice Shelf.

5.6.3 Comparison to Amery Ice Shelf

The steady-state shear-only shelves confined to parallel channels produce shelf thickness profiles and speed fields that are broadly similar to those in the final two thirds of Amery

Ice Shelf. The Newtonian case provides a good estimate, but the structure of the velocity field is much improved when a shear-thinning rheology is used. Quantitatively, the steady-state $n = 3$ power-law shelf, with shear-dominated dynamics, provides a good fit to Amery. The shelf thins from approximately 550 m to 200 m over the 280 km length of the shelf, achieving a speed of 800 m yr^{-1} at the channel exit.

These shear-only, parallel-channel models produce isolated peaks in strain rate at the centre of the channel exit. When a diverging channel model is used, with a low effective viscosity, there is often a large area of high positive strain rates near the channel exit. Qualitatively, this region looks like the region of high positive strain observed in the final third of Amery Ice Shelf.

With the inclusion of extensional dynamics, slight improvements are made to the model fit to Amery Ice Shelf, particularly with regard to the strain-rate field, which no longer has a central peak at the channel exit, but rather a central region with strain-rate values of approximately 0.005 yr^{-1}, with larger values in the margins, where there is high shear and weak effective viscosity.

Chapter 6

Fluid-Mechanical Experiments Simulating the Flow of an Ice Shelf

6.1 Introduction

I performed a series of experiments designed to simulate the flow of an ice shelf in a parallel channel. For each experiment the rheology of the fluid used to simulate the ice shelf was varied. A Newtonian rheology was used along with two shear-thinning power-law fluids consisting of different concentrations of Xanthan gum. This collection of fluids had power-law flow exponent values of $n = 1$, $n \approx 6$ and $n > 6$. Comparisons can then be made with idealized models and geophysical data. Here there is also potential to vary many parameters systematically such as: shelf rheology; input flux; channel geometry, to assess the impact on the shelf thickness profile and flow dynamics.

6.2 Experimental Set Up

A set of experiments were performed simulating the flow of an ice shelf confined within a parallel channel. From these experiments, surface velocities and the evolution of the shelf-thickness profiles were measured to make comparisons with idealized models and geophysical data. A side-view and plan-view schematic of the experimental set up is shown in Figure 6.1.

The viscous fluid representing the ice shelf was confined to flow within a parallel channel formed from two wall sections each 1 m long and 6 cm tall. One channel wall was opaque, while the other was transparent so that images of the current profile could be taken through the channel wall with an SLR camera, thereby capturing the evolution of the shelf thickness during the experiment. These channel walls were placed within a large shallow tank (width 1 m, length 2 m and depth 5 cm), and were positioned at

the centre of the shorter (1 m) wall, so that they were placed against the end of the tank. The channel therefore occupied half the length of the tank. An end-plate was placed between the walls to form a sealed end and to keep the channel width fixed. An additional bracket was placed across the top of the two side-walls mid-way along the channel, which ensured a fixed channel width. (This bracket did not interfere with the internal geometry of the channel.) For the set of experiments presented here the channel width was held constant at 10 cm.

The large tank was filled to a depth of 2-3 cm (depth set specifically for each experiment) with a dense salt solution that represents the ocean. For the Xanthan gum solutions, which have a density of 1×10^3 kg m^{-3}, the ocean consisted of a brine solution of sodium chloride, with a density of 1.1×10^3 kg m^{-3}. In contrast, for the denser Golden Syrup currents (density 1.44×10^3 kg m^{-3}) the ocean was a potassium carbonate solution, with density 1.54×10^3 kg m^{-3}. This density ratio of shelf current to ocean was set to be approximately 0.9, which matches the geophysical case.

Above the closed end of the channel was placed a reservoir of viscous fluid, which was kept at a constant depth by the immersion of a plastic block that displaces the equivalent volume of fluid that has left the reservoir. The position of the plastic block was controlled manually while the experiment was running. The fluid flowed from the reservoir into a vertical cylindrical pipe and was deposited in the centre of the channel, next to the end-plate, onto the surface of the dense salt solution. This arrangement acted as a gravity-feeding system for the supply of fluid at a constant rate into the channel. The flow of fluid from the reservoir was initiated by the removal of a rubber bung from the end of the delivery pipe. The viscous fluid was then free to spread on the surface of the salt solution within the channel and flow towards the exit. Once the fluid shelf leaves the confines of the channel there was no further confinement until it met the end of the large tank.

The flow of the ice shelf within the final 40 cm of the channel was filmed from above by a video camera that captured 5 frames per second. White tracer particles of 1-2 mm diameter were deposited randomly on the surface of the ice shelf current (dyed dark blue) close to the input pipe. The particles were dropped from a chute onto a sieve, which distributed the particles randomly across the surface of the shelf. The flow rate of the particles from the chute was adjusted so that there were approximately 3-4 particles per square centimetre.

The evolution of the flow was also monitored from a side viewing camera, which captured the evolution of the shelf thickness profile, through the transparent wall.

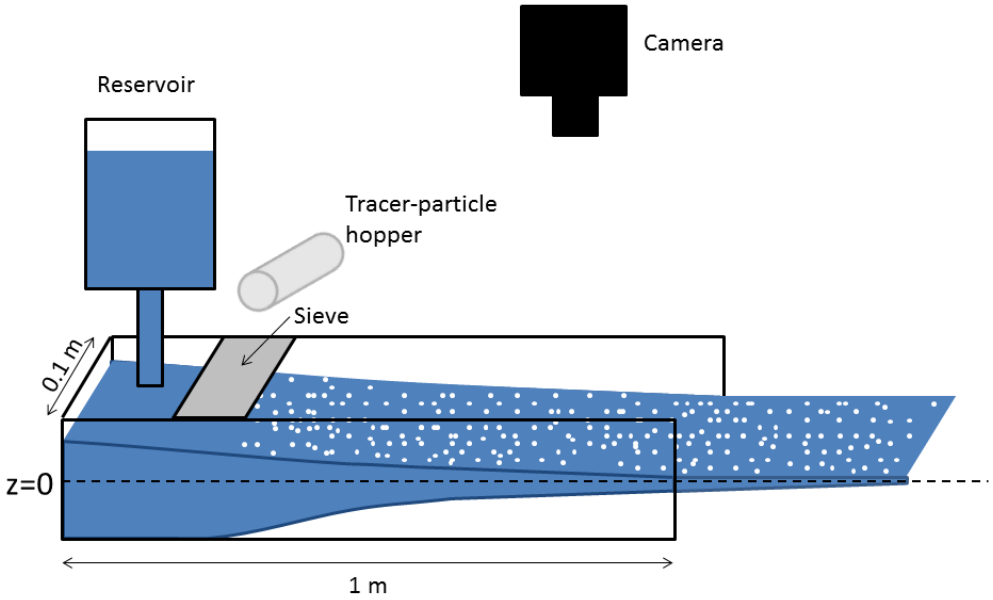

(a)

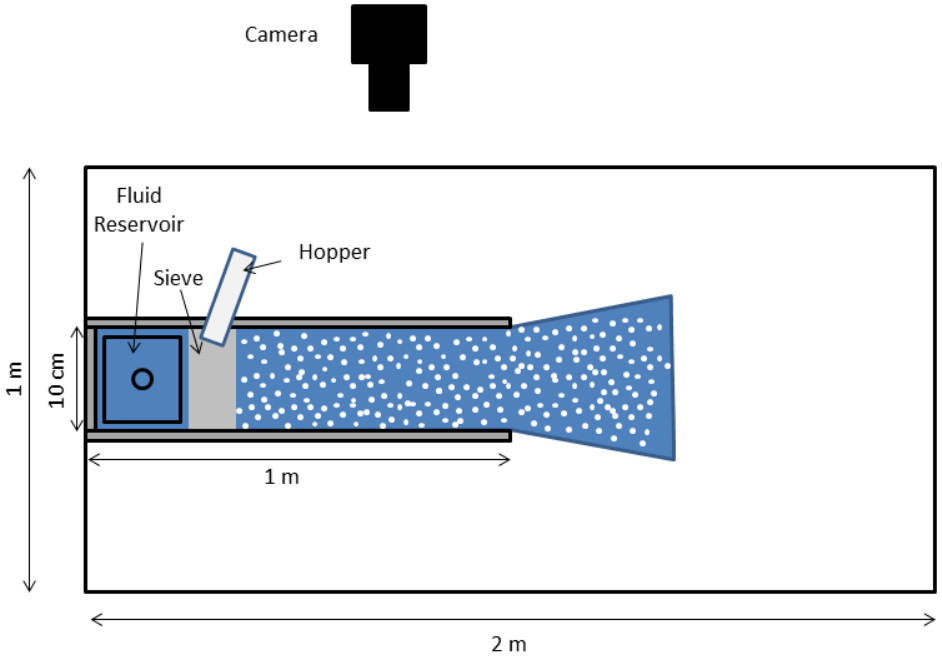

(b)

Figure 6.1: Schematic depicting the experimental set up used to simulate the flow of an ice shelf in a parallel channel. Side view (a) and plan view (b). The large shallow tank in which the parallel channel is situated is filled to a set depth with a dense salt solution, the surface of this salt solution is denoted by $z = 0$. Less dense viscous fluid flows from a reservoir at a constant rate to the sealed end of a parallel channel. This fluid is then able to spread under gravity. Tracer particles are deposited on the surface of the current from a hopper through a sieve to distribute the particles. These particles and the current is filmed from above so that a surface velocity field can be inferred. Images of the profile of the current are captured from a side viewing camera while the current is confined in the channel.

All the experiments where undertaken in the same basement laboratory, with an approximately constant temperature of 20 °C. The mixing of the Xanthan solutions and running of the corresponding experiment was performed within 8 hours in all cases, in order to minimize any degrading of the Xanthan solution. Once the large tank was filled with salt solution (representing the ocean), it was left for at least an hour before the experiment was run to ensure the salt solution was at room temperature. The Golden Syrup and Xanthan solutions were also stored at room temperature prior to the experiment.

6.3 Data Processing

6.3.1 Processing Thickness Profile Data

Side-view images of the sheet-shelf system were captured every 4 seconds during the experiment through the clear channel wall with an SLR camera. These images were then processed with MATLAB to determine the elevation of the current above the dense salt solution. An example image from the SLR camera is shown in Figure 6.2. The image was first cropped to include only the length of sheet/shelf confined within the channel above the water line and approximately 50 cm upstream from the exit. Image processing in MATLAB was used to identify the extent of the current above the water line by identifying the change in colour between the cross-section of the current against the transparent wall and the surface of the current, which is covered in tracer particles. This boundary can be seen clearly in Figure 6.2. The vertical extent of the current at each pixel point along the length of the channel was then used to determine the elevation of the current above the water line. This point-wise elevation was smoothed using a low-pass Gaussian filter, and converted to elevation measurements in millimetres and along-channel distance in centimetres. The elevation of the current above the ocean level is calculated for each experiment and shown in the sections below. The location of the grounding line can be determined by the point at which there is a change in the slope of the upper surface, with the grounded section being much steeper than the floating shelf. For both the Newtonian and shear-thinning shelves, a steady-state is not achieved within the time frame of the experiment and the thickness profiles continue to evolve, with the grounding line advancing along the channel.

6.3.2 Processing PIV data

Images of the surface of the current were captured every fifth of a second from a camera mounted above the experiment. Particle Image Velocimetry (PIV) was calculated from the deformation and translation of tracer particles distributed on the current surface

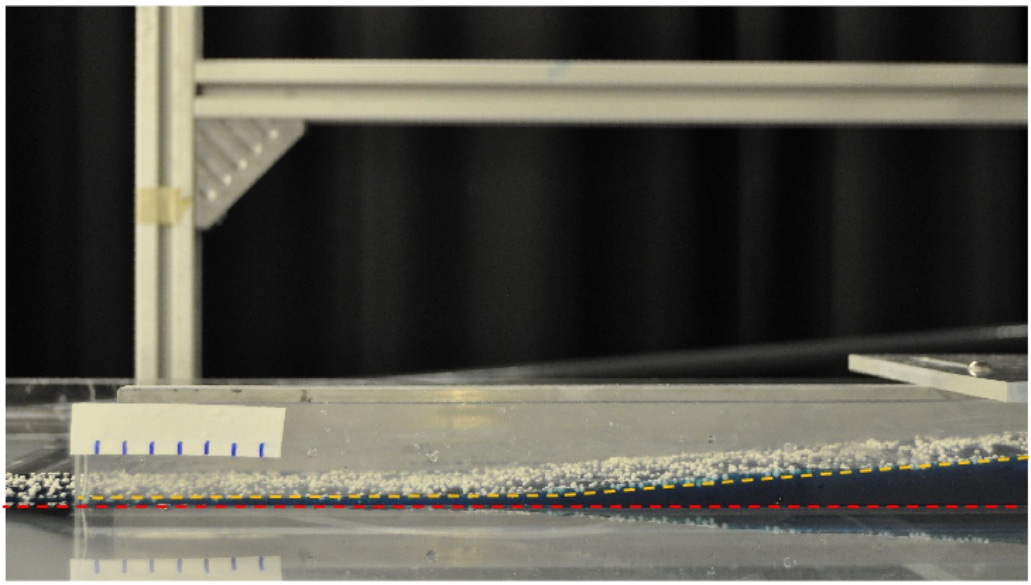

Figure 6.2: Image used to calculate the elevation of the current above the water line for a 1.5% Xanthan current. The blue fluid, representing the sheet-shelf, flows in the channel from the source on the right towards the channel exit on the left. The dense salt solution can be seen in the foreground and forms a line along the length of the channel above which I calculate the elevation of the sheet-shelf. Each mark on the scale bar at the left end of the channel indicates one centimetre. The red dashed line added to the original image identifies the level of the dense salt solution representing the ocean, while the yellow dashed line indicates the surface of the sheet-shelf current.

using the computer software DIGIFLOW. Velocity vectors were calculated on a grid with a 4 mm spacing, with velocities calculated from the deformation and translation of sets of particles between consecutive frames within an 8 mm square centred on the grid point. The velocity was then interpolated onto a 0.5 mm grid. This PIV processing was performed for a number of short intervals for all the experiments run.

As part of the analysis of this surface-velocity data, some further processing was made to the PIV data in MATLAB. Firstly, the velocity field was averaged over a 4 second interval, with the aim of removing small scale noise. Typical velocities for these flows were between 2 and 5 mm s^{-1} and therefore it was expected that there would be very few changes to the flow in the four seconds over which the average was calculated. In addition to this, a low-pass Gaussian filter was applied to each velocity field, in a similar manner to the spatial filtering (smoothing) of the geophysical data in Chapter 3. Here again, the aim was to reduce noise in the data, but also to smooth the velocity field between areas where there are differing distributions of tracer particles, leading to errors in the velocity field where there were insufficient particles. This low-pass Gaussian filter had a standard deviation of 4 mm and a range of 10 mm. The filtering was performed for individual time steps during the experiment, these were then used to calculate a time-averaged velocity field, over a four-second interval, which could be directly compared to the time averaging of the original PIV velocity field.

6.3.3 Assessing Experimental Data

In the following sections, results from the fluid-mechanical experiments simulating the flow of an ice shelf within a parallel channel are given. I chose to perform experiments with Golden Syrup, as this is a Newtonian fluid with constant viscosity (at fixed temperatures), and also two shear-thinning fluids of differing Xanthan concentrations. Here I choose 1% and 1.5% concentrations. Work by Sayag and Worster (2013b), using a 1% Xanthan solution, mixed in a similar manner to the method used here, found the flow exponent to be $n \approx 6$, with a consistency index $\tilde{\mu} \approx 10$ Pa $s^{1/n}$ ($\tilde{\mu} = B/2$). Lower concentrations of Xanthan would produce a flow exponent closer to $n = 3$, as would be appropriate for ice, but the consistency index would not be large enough for the fluid to be considered viscous in this situation. The main aim of using these fluids was to identify the differing dynamics between Newtonian and shear-thinning fluids in this set up, and to determine whether the increase in Xanthan concentration makes an appreciable difference.

A plot showing the evolution of the shelf-elevation profile in each case is given, which is derived from side-view images. In addition to this, surface velocity data is presented

for a number of time intervals for each experiment. Two different plots of along-channel velocity are presented:

- The first is the initial PIV data, inferred from the deformation and translation of groups of particles between frames and calculated using the computer software DIGIFLOW.
- Secondly, a low-pass Gaussian filter was applied to the PIV data, in a similar manner to that applied to the geophysical data in earlier sections.

For each method a snapshot velocity-field is given, calculated from the displacements between two consecutive frames, along with an average velocity-field, calculated over a 4-second (20 frame) interval. From this an average velocity field and a strain-rate plot are given along with a transect of velocities along the sheet-shelf centreline. None of the currents shown here reach a steady-state during the experimental run and therefore the thickness profiles and velocity fields shown here represent transient states.

6.4 Results

6.4.1 Newtonian: Golden Syrup

Elevation Profile

Figure 6.3 shows a plot of the evolution of the elevation profile for a Golden Syrup ice sheet-shelf system above a 2 cm deep salt solution. The system is flowing from right to left. In Figure D.2 in the Appendix an example of the image processing and subsequent smoothing of the profile can be seen. From this it is clear that the maximum variation of the smoothed profile away from the smoothed profile is 0.5 mm. These variations are mainly due to the varying presence and absence of tracer particles on the surface of the current leading to errors in determining the position of the surface. The smoothing of the profile reduces the significance of these errors.

From Figure 6.3 we see that the early-time profile in this plot has a sloping sheet to the right that transitions into a long shelf. For this first profile it is difficult to determine the exact location of the grounding line from the processed data, as there isn't a sharp change in the slope of the sheet-shelf surface, but it appears to be between 21 and 35 cm back from the channel exit. Here the most likely location of the grounding line is approximately 33 cm back from the channel exit, at the base of the linear sloping grounded section. This inaccuracy is partly due to the presence of a surface bulge between 15 and 20 cm, which is present at the same location throughout the experiment. This surface undulation is identified in the original images that can be seen in Figure D.1 in the

Appendix, where it is evident that the bulge is found midway along the channel between 15 and 20 cm back from the channel exit. I hypothesise that the presence of this bulge is due to flow in the initial stages of the experiment, where a thick section of shelf formed at the nose of the current, following the initiation of the input flux from the gravity feeder with the removal of the rubber bung. This thick nose may have made contact with the channel wall at this location, leaving a residual mark on the wall. At early times, before the grounding line has entered the field of view this bulge is present in an otherwise thin shelf, as shown in Figure D.1a. As this undulation is present throughout the experiment it is clear that it is not a dynamic feature, but instead masks the true location of the current surface. I therefore use dashed lines in Figure 6.3 to indicate the approximate location of the true surface, from visual assessment and comparison with the original images (Fig. D.1).

As the system evolves in time, the grounded section of the current thickens and the grounding line advances from 33 cm to approximately 19 cm back from the channel exit, over the final five intervals shown here; covering a period of 10 minutes and 40 seconds. There is a distinctive difference between the slope of the current when grounded, which is close to linear, and the slope once the current is floating. For the floating shelf, there is at first an almost-flat section near the grounding line before the shelf thins towards the channel exit. The elevation of the shelf at the exit appears to increase with the evolution of the system. This is expected as the shelf evolves and may be due to the advance of the grounding line and the corresponding evolution of the flow within the shelf as lateral shear increases for a thicker shelf.

From this set of profiles, characteristic features of the system can be identified, from right to left: a steep and linearly sloping grounded sheet, which thins to the grounding line and thickens in time; downstream of the grounding line there is a gently sloping, almost flat region of floating shelf with dynamics controlled mainly by shear stresses; and in the final 10 cm (one channel-width) of the channel the shelf thins rapidly with a nonlinear convex slope, where extensional dynamics become important.

When comparisons are made with the thickness profiles for ice shelves determined in the earlier theoretical work (Chapter 5), a distinctive difference between Newtonian and shear-thinning shelves was the more convex profile for Newtonian shelves, while shear-thinning shelves thinned in a more linear manner. From this experiment it is clear, for this Newtonian shelf, that the rate of thinning does increase towards the exit leading to a convex profile.

There are some small-scale undulations present in the elevation profiles, which appear

fixed in position. This is most likely due to the presence of tracer particles that have become stuck to the channel walls and remain fixed in position for extended periods of time. These particles therefore give the impression that there is an undulation in the sheet-shelf surface when the image is processed. Many of these undulations have an amplitude smaller than 0.5 mm.

It is observed visually during the experiment, that there is little variation in the elevation of the shelf across the width of the channel, implying that the along-channel elevation profile derived from the elevation along the side wall is representative of the elevation across the entire channel width. The presence of only small variations in the current elevation across the channel width is confirmed by the cross-channel velocity field, an example of which can be seen in Figure D.3 in the Appendix, for this Golden Syrup experiment. It is evident that there are only small cross-channel velocity values along the length of the channel, except near the channel exit, where there is slow flow away from the walls and towards the centre of the current as the shelf nears the exit of the channel. It is expected that variations in the shelf elevation/thickness across the width of the channel will induce lateral flow, as variations in thickness lead to varying hydrostatic driving pressures.

Interval 1

For the first interval of this experiment, 130 seconds after the first tracer particles leave the channel exit, there is a large section of floating shelf with the grounding line found approximately 35 cm from the channel exit. This is shown in the velocity field plots in Figures 6.4 and 6.5. Within the channel, there is a parabolic cross-channel profile in

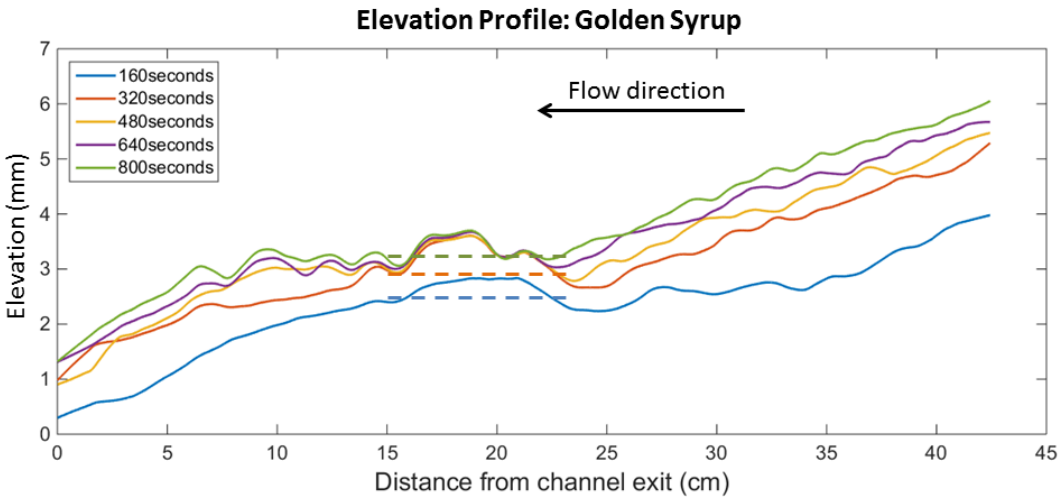

Figure 6.3: Elevation profile for the second Golden Syrup current in a parallel channel. Different coloured curves represent profiles at a series of times corresponding to the time after the first tracer particles left the channel exit.

velocity, which is suggested by the velocity fields in Figures 6.4a, 6.4b, 6.5a and 6.5b, and confirmed by the cross-channel velocity profiles, in Figure 6.6, where quadratic curves have been fitted to the data. In the channel margins of the speed plots there is a noisy signal, where I would expect a smooth transition to the no-slip boundary condition, as shown in the initial velocity field in Figure 6.4a. However, this is improved when a time average is taken (Fig. 6.4b) and improved further when the Gaussian low-pass filter and time averaging are applied (Fig. 6.5b). This noise is likely to be due to the insufficient density of particles in these margins, where there is relatively slow flow and also the proximity of the channel walls, which limit the size of the window that can be used in the PIV processing to determine a velocity for these areas. This noisy velocity signal within the margins leads to falsely high strain-rate values, as can be seen in Figures 6.4c and 6.5c.

From the cross-channel profiles in Figure 6.6, it can be inferred clearly that while the shelf is confined there are no-slip boundary conditions along the channel walls, which results in a parabolic cross-channel profile for this Newtonian fluid. This parabolic profile is also consistent with a uniform cross-channel thickness, as assumed in the theoretical work in Chapter 5. In contrast to the profiles within the channel, once the shelf has left the channel there is an almost uniform cross-shelf velocity profile, as shown by the cross-channel profile at 400 mm in Figure 6.6. This indicates a clear distinction between the dominant dynamics controlling the flow in the channel, where there is lateral resistance from the channel walls resulting in shear flow, and once the shelf leaves the channel this lateral resistance is removed (no shear) and the flow is controlled by extensional dynamics only.

At the upstream end of the the strain-rate plots (Figs. 6.4c and 6.5c) there is a band of negative strain rate followed by a band of positive strain rate that both transverse the width of the channel. These are positioned close to the location of the grounding line, however are difficult to interpret fully as they are found at the edge of the image used to calculate the velocity field. These features will be addressed more directly at the next time interval for this flow, when the grounding line has advanced further into the field of view.

In the upstream section of the shelf, there is a gradual acceleration of the flow in the downstream direction, corresponding to an along-flow strain rate of approximately 0.0025 s^{-1}. At 10 cm back from the channel exit there is a prominent acceleration in the current, which continues to the channel exit. Here, the along-flow strain rate has increased to approximately 0.01 s^{-1}. This zone is of aspect ratio 1, as the channel width is also 10 cm. This area of acceleration can clearly be identified in the along-channel strain-rate plots, Figures 6.4c and 6.5c, and the centreline transects Figures 6.4d and 6.5d. This

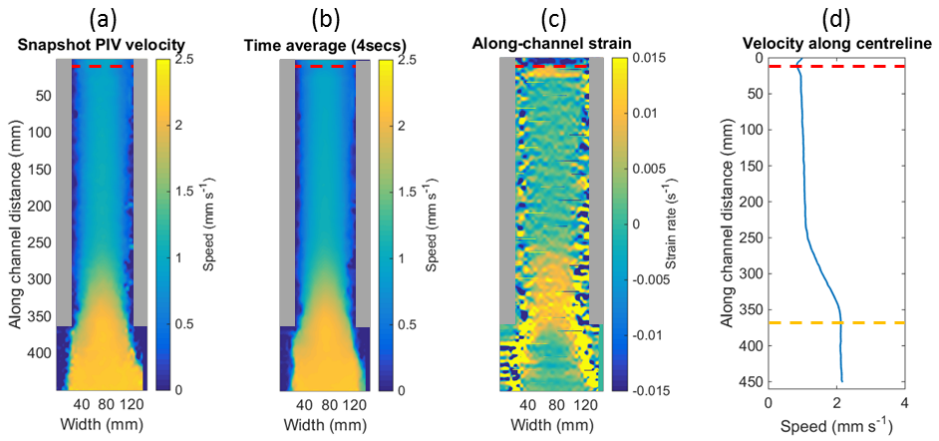

Figure 6.4: Original PIV data: Golden Syrup, Interval 1. From right to left: speed plot calculated from displacement between two consecutive frames; time-averaged speed calculated over 4 seconds; along-channel strain rate field; centreline transect of time-averaged velocity. Red dashed lines indicate location of grounding line and yellow dashed line channel exit.

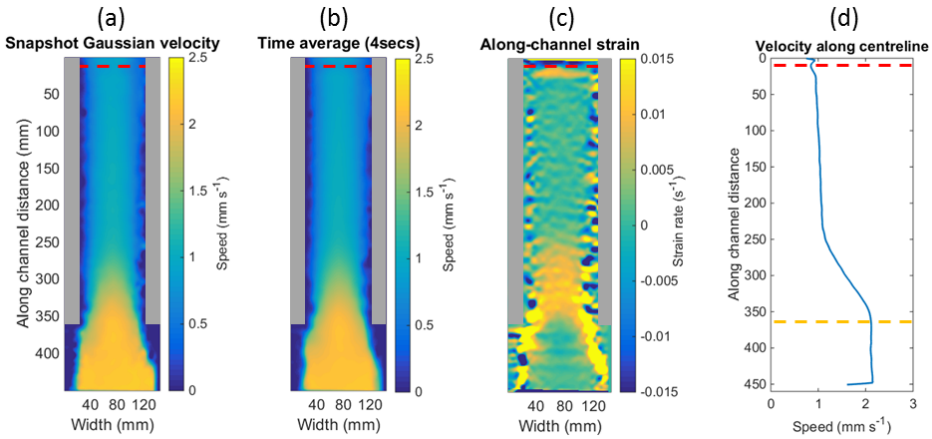

Figure 6.5: Gaussian filtering of PIV data: Golden Syrup, Interval 1. From right to left: speed plot calculated from displacement between two consecutive frames, with low-pass Gaussian filter applied; time-averaged filtered-speed calculated over 4 seconds; along-channel strain rate field; centreline transect of time-averaged velocity. Red dashed lines indicate location of grounding line and yellow dashed line channel exit.

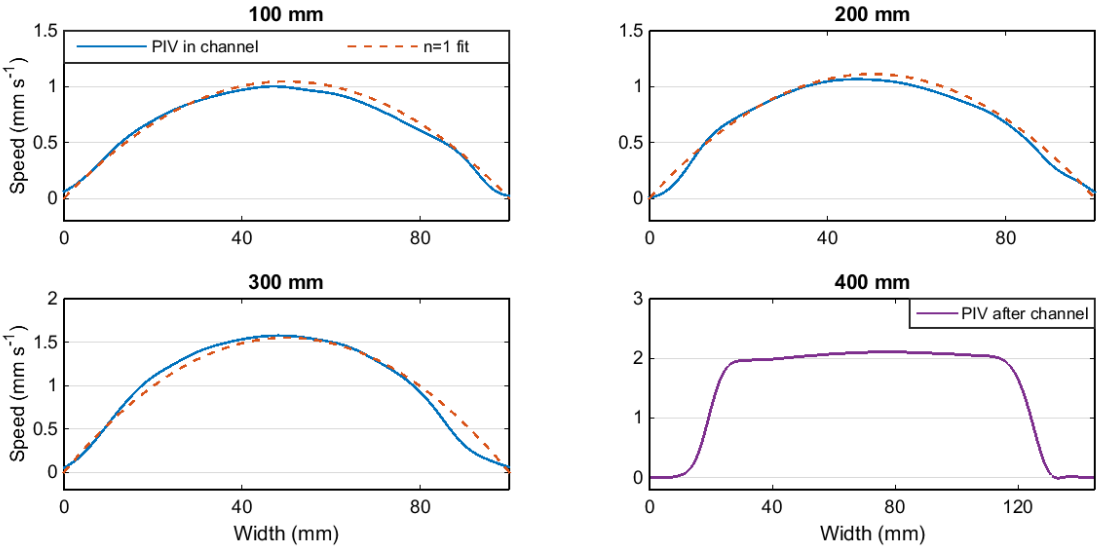

Figure 6.6: Cross-channel profile of along channel velocity at a three points in the channel (100 mm, 200 mm, 300 mm) and one point outside the channel (400 mm), during the first time interval of the Golden Syrup Experiment. Blue curve indicates Gaussian low-pass filtered and time-averaged PIV data. Dashed red curve indicates fitted parabolic profile for those sections within the channel. Purple curve denotes PIV data outside the channel and spanning the field of view.

transition from gradual acceleration to increased acceleration in the final section of the channel, corresponds to the rapid thinning of the shelf observed in the final 10 cm of the channel, following the gradual thinning further upstream, as shown in the elevation profile in Figure 6.3.

The flow reaches its maximum velocity at the centre of the channel exit. After this point, the shelf is no longer laterally confined, which means that there is no longer any resistance to flow provided by the side walls, but also that the shelf can now spread laterally in addition to the along-channel direction. This lateral spreading of the shelf and the increase in the transverse velocity causes the along-channel component of the velocity to be reduced after it leaves the channel. The hydrostatic driving pressure induces flow in both directions once the shelf is unconfined.

Interval 2

The second interval of velocity data for this Golden Syrup experiment is 11 minutes after the first and corresponds to the 800-seconds (after tracer particles first leave channel exit) elevation profile shown in Figure 6.3. The grounding line has advanced by approximately 14 cm in this time and is now found midway along the section of channel, shown in Figures 6.7 and 6.8, approximately 19 cm from the exit. In both the grounded and floating sections of the current there appears to be a parabolic cross-channel profile, until

the shelf leaves the confines of the channel, as confirmed by the cross-channel profiles in Figure 6.9.

Upstream of the grounding line there is a band of negative strain rate, which spans the width of the channel. This can be seen in the strain-rate plots in Figures 6.7c and 6.8c. This deceleration is also apparent in the centreline velocity transects. From these transects we observe that upstream of the grounding line there is little variation in velocity along-flow, but at the grounding line there is a sudden dip in the velocity. This is followed by a uniform acceleration of the floating shelf towards the channel exit. This is different from the along-channel acceleration at the previous interval, where there was an area of gentle positive strain rate downstream of the grounding line, followed by prominent positive strain rate in an aspect ratio 1 area at the exit. In this case there is prominent strain rate (approximately 0.075 s^{-1}) throughout the whole shelf. This may be because there is a steeper thickness profile in comparison to the earlier interval (see Fig. 6.3), which would result in faster flow for a shear-dominated flow. The shelf is also thicker in the downstream region near the exit when compared with the previous time interval considered. This would produce greater hydrostatic driving pressure and in turn increased extensional stress.

Once the shelf leaves the channel, it is no longer confined and begins to spread laterally. This spreading leads to a reduction in the along-channel component of the velocity as is evident in all the velocity plots.

From the cross-channel velocity profiles in Figure 6.9, it is clear that while the sheet-shelf is confined there is a close-to parabolic cross-channel profile. This supports the assumption of no-slip lateral boundaries and suggests that in this geometry the grounded current is thick enough that the shear stress from the lateral boundaries has a strong control on the dynamics. Here, the grounded current is approximately 2.6 cm thick (0.6 cm elevation in a 2 cm salt solution, 45 cm back from the channel exit) so we would expect this lateral shear to influence the flow approximately 2.6 cm in from each side wall of the 10 cm wide channel. This may not be true at earlier times when the grounded section of the flow is less thick and therefore the dynamics may be dominated by the vertical shear. Once the shelf leaves the channel, there is no longer any transverse shearing of the flow, as is clear in the transect at 400 mm in Figure 6.9, which shows an almost uniform velocity across the width of the shelf.

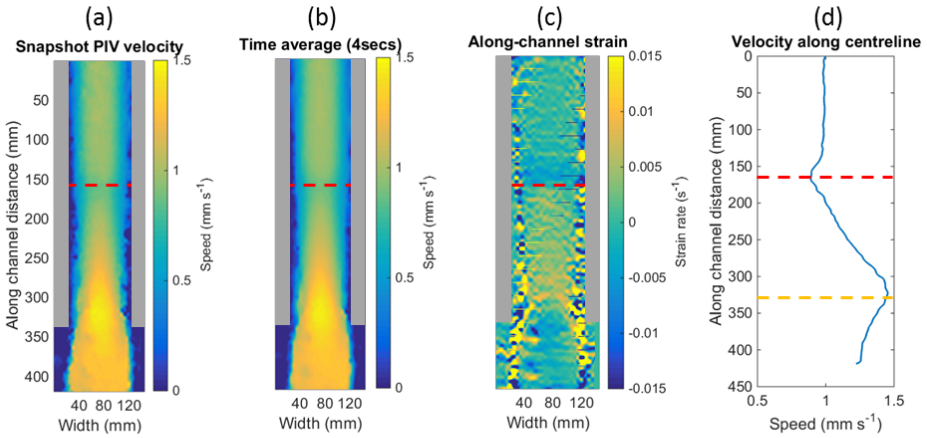

Figure 6.7: Original PIV data: Golden Syrup, Interval 2. From right to left: speed plot calculated from displacement between two consecutive frames; time-averaged speed calculated over 4 seconds; along-channel strain rate field; centreline transect of time-averaged velocity. Red dashed lines indicate location of grounding line and yellow dashed line channel exit.

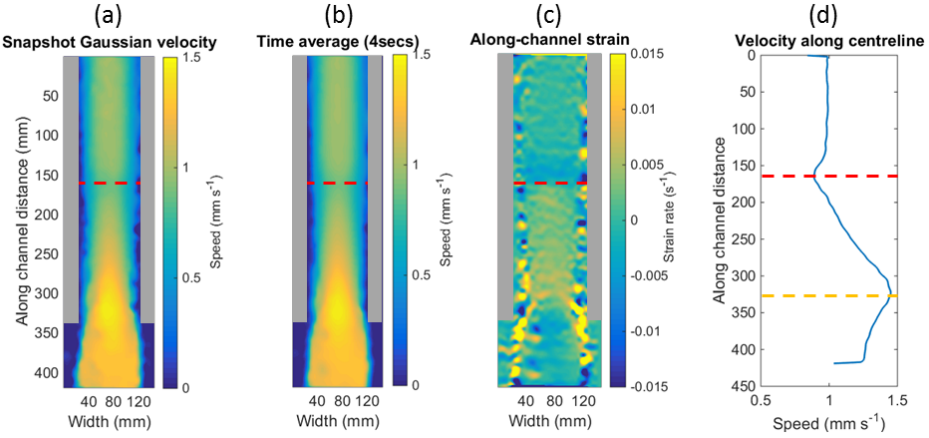

Figure 6.8: Gaussian filtering of PIV data: Golden Syrup, Interval 2. From right to left: speed plot calculated from displacement between two consecutive frames, with low-pass Gaussian filter applied; time-averaged filtered-speed calculated over 4 seconds; along-channel strain rate field; centreline transect of time-averaged velocity. Red dashed lines indicate location of grounding line and yellow dashed line channel exit.

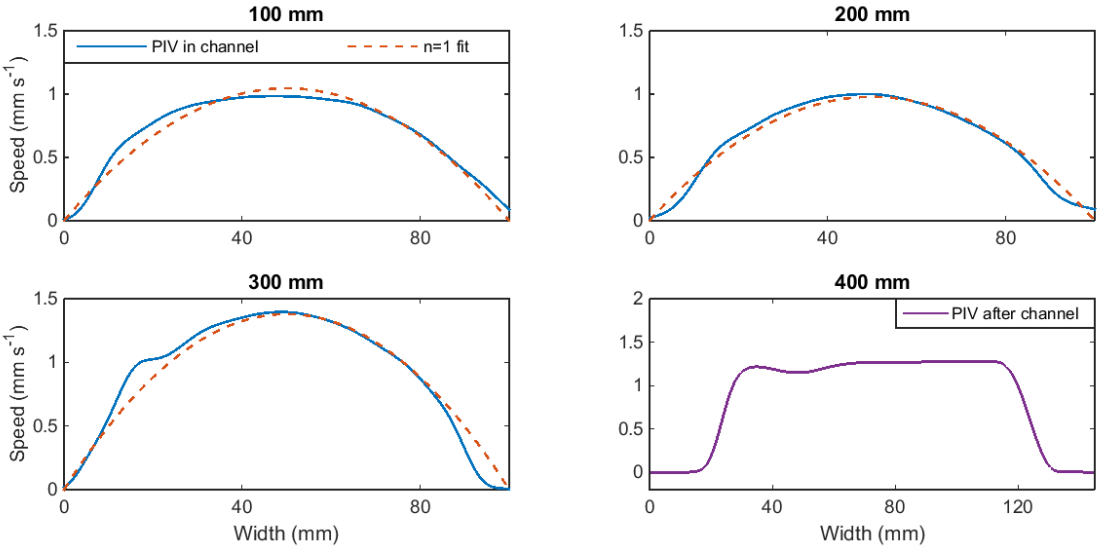

Figure 6.9: Cross-channel profile of along channel velocity at a three points in the channel (100 mm, 200 mm, 300 mm) and one point outside the channel (400 mm), during the second interval of the Golden Syrup Experiment. Blue curve indicates Gaussian low-pass filtered and time-averaged PIV data. Dashed red curve indicates fitted parabolic profile for those sections within the channel. Purple curve denotes PIV data outside the channel and spanning the field of view.

Fitted profiles

It is clear from the cross-channel profiles in velocity, shown in Figures 6.6 and 6.9, that while the shelf is confined in the channel a shear-dominated (parabolic) cross-channel profile provides a good fit to the PIV data. I now apply this idea to the full PIV dataset with the aim of smoothing the data and attempting to resolve the flow field within the narrow boundary layer, where poorly resolved velocity data leads to erroneous high strain rates in the shelf margins.

In the earlier theoretical modelling chapter (Chapter 5) I derived the cross-channel velocity profile for a laterally confined shelf with shear dominated dynamics. For a general power-law rheology this takes the form

$$u = (-w)^{n+1} \frac{2^{-2n}}{n+1} \left(\frac{\rho g'}{\tilde{\mu}}\right)^n \left(\frac{\partial H}{\partial x}\right)^n \left[\left(\left|1 - \frac{2y}{w}\right|\right)^{n+1} - 1\right]. \tag{6.1}$$

Here x is the along-channel coordinate and y the cross-channel coordinate. Using the PIV data I fit a cross-channel profile of this form to each cross-channel profile of observations using a nonlinear regression. The nonlinear regression takes the form

$$u = A\left[\left(\left|1 - \frac{2y}{w}\right|\right)^{n+1} - 1\right], \tag{6.2}$$

where A is dependent on the along-channel position and w is the known channel width. If this technique provides a good fit to the data then the inferred value of A could be used to determine the thickness gradient of the shelf at each point along the channel (compare equations 6.1 and 6.2). For this Golden Syrup experiment with a Newtonian rheology I use $n = 1$. The regression to each cross-channel profile uses the weighted observations from neighbouring cross-channel profiles. For this a Gaussian weighting is given to the neighbouring cross-channel profiles; four profiles upstream and four downstream, in addition to the data from the profile being considered.

This method is only valid for the floating and confined section of the shelf in these experiments. However, in the figures below the whole dataset is considered, with the grounded and unconfined sections identified by a transparent mask. This approach also provides a test of whether it is possible to identify areas where the shear-dominated assumption may break down, such as near the exit of the channel where the extensional stresses become important. There is also potential for extension to become important near the grounding line, where there may be an extensional adjustment region with a relatively thick sheet adjusting to a thinner shelf.

The fitted velocity field for the first interval of the Golden Syrup experiment is given in Figure 6.10a, along with the strain rate field and centreline velocity transect. The velocity plot provides a smooth field with well resolved flow in the margins. The relative difference between the original PIV data and fitted model is given in Figure 6.10b. Here it is clear that throughout the central section of the confined shelf there is good agreement and a small relative difference. In the shelf margins the relative difference changes sign intermittently, suggesting that this is due to the uneven distribution of particles in the margin, which leads to poorly resolved velocities in some locations, rather than a consistent under or over estimation. From the strain-rate plot in Figure 6.10)a)iii) it is now clear that the large strain-rate values are found in a region of aspect ratio one at the end of the channel and the margins of the channel are areas of relatively low strain rate. It is evident from the relative difference plot, Figure 6.10b that there is a change in the dynamics once the shelf leaves the confines of the channel (masked region in plot), as this shear dominated profile now provides a bad fit to the PIV data as expected.

Similar results are found for the fitted velocity field for the second interval, in Figure 6.11. Again a smooth velocity field is produced, which agrees well with the original PIV data in the central regions of the shelf. The velocities within the margins of the shelf appear to be overestimated in the fitted model. However, when compared with the original velocity field in Figure 6.7a it is clear that the PIV data is patchy in the margins

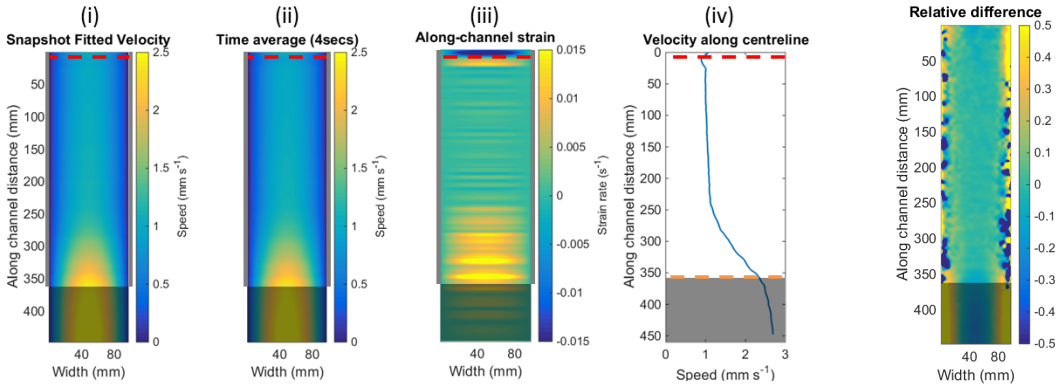

(a) (b)

Figure 6.10: Results of fitting shear-dominated velocity field to PIV observations for Golden Syrup experiment, Interval 1: (a) shear-dominated profile fitted to PIV data, with along-channel strain rate and centreline transect; (b) relative difference plot, original minus fitted velocity.

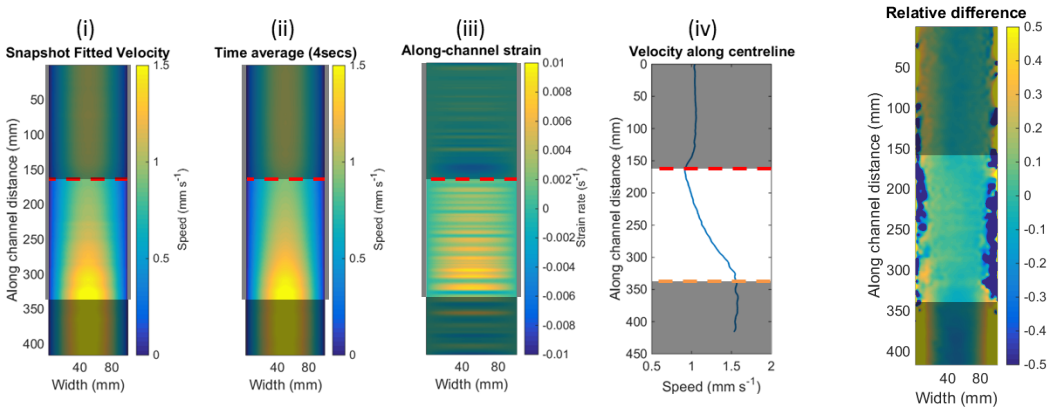

(a) (b)

Figure 6.11: Results of fitting shear-dominated velocity field to PIV observations for Golden Syrup experiment, Interval 2: (a) shear-dominated profile fitted to PIV data, with along-channel strain rate and centreline transect; (b) relative difference plot, original minus fitted velocity.

and does not produce a smooth profile. These features in the margins of the original PIV are smoothed when a time average is taken (Figure 6.7b), suggesting that this patchiness is due to insufficient distribution of tracer particles in the margins. When the relative difference plot is analysed without the masking of the grounded and unconfined regions (Figure D.4 in Appendix), it is clear that in both regions the parabolic cross-channel profile underestimates the velocity in the margins and overestimates in the centre of the current. This implies that in those regions there is a more uniform cross-channel profile of velocity, and that cross-channel shear is not the dominant mechanism controlling the flow. While grounded the vertical shear plays a dominant role and once unconfined the dynamics are controlled by extensional stresses.

6.4.2 1% Xanthan

Thickness Profile

The second experiment, presented here, uses a 1% Xanthan solution to simulate the ice sheet and shelf. The elevation profile of the sheet-shelf above a 2 cm deep ocean is given in Figure 6.12, with profiles displayed at 40 second intervals. As with the Golden Syrup current, an example of the image processing and plots of the elevation profile before smoothing can be seen in the Appendix; Figure D.5. Again there are mainly small differences between original and smoothed elevation profiles, but in this case there are some points with larger differences at the upstream end of the channel. This may be because there is a variation in the distribution and density of tracer particles along the length of the current.

From Figure 6.12 we observe the thickening of the grounded current and the advance of the grounding line, from 40 cm to 5 cm back from the calving front in a 160 second time period. The slope of the grounded current remains fairly constant as it thickens. However, the slope of the shelf is almost zero and it is difficult to resolve given that there are changes in thickness of less than a millimetre over the length of the shelf. This lack of thickness change along the length of the shelf suggests there is little deformation of the shelf section of the flow.

As with the previous experiment using Golden Syrup, there are some undulations in the surface of the sheet and shelf resulting from the presence of tracer particles on the surface of the current. In contrast to the Golden Syrup experiment here the grounding line advances much quicker and the grounded section of the current has a steeper slope, with a gradient of -0.038, in comparison to the -0.015 slope in the Golden Syrup case.

Interval 1

In Figures 6.13 - 6.14 the grounding line is approximately 16 cm from the channel exit, and corresponds to 160 seconds after the first tracer particles exited the channel. As the fluid crosses the grounding line there is a sharp increase in the along-channel velocity. There is then a further more gradual acceleration as the shelf moves along the channel. This can be seen in the velocity plots in Figures 6.13a, 6.13b, 6.14a and 6.14b and also in the centreline velocity transects, in Figures 6.13d and 6.14d.

As in the previous case, the grounding line is highlighted by consecutive bands of large negative and positive strain rate. In this case the bands appear to be arched/curved across the channel, suggesting that the grounding line forms an arc across the channel width, rather than forming a linear feature across the channel width. This feature is most clear in the strain-rate field calculated from the Gaussian low-pass filtered velocity as the surrounding small-scale noise has been smoothed out (Fig 6.14c). This zone of high positive strain rate downstream of the grounding line suggests an adjustment region between the grounded sheet and shelf in which extensional dynamics are important. This may be similar to the areas identified in the numerical modelling in Chapter 5, where there is an extensionally-controlled adjustment zone for a relatively thick sheet joining a shear-dominated shelf downstream, where the thickness is controlled by the balance between shear dynamics and the input flux rather than the input thickness.

Once the flow has advanced past the grounding line there is a constant acceleration of the flow, which continues past the channel exit rather than slowing as is observed in the Newtonian case. This similarity in dynamics between the confined and unconfined

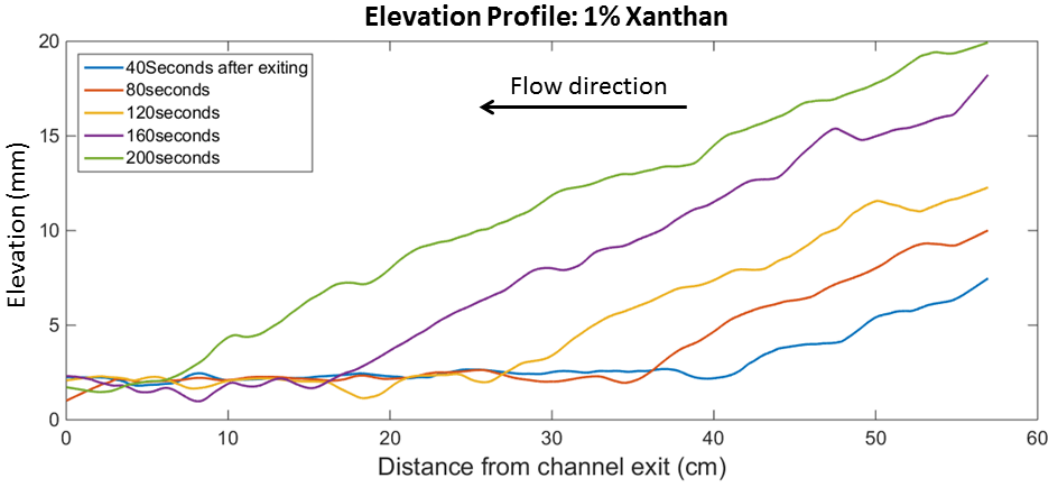

Figure 6.12: Elevation profile for the 1% Xanthan current in a parallel channel. Different coloured curves represent profiles at a series of times after tracer particles first leave the channel exit.

shelf suggests that there is little lateral resistance to the flow while confined in the channel and therefore the shelf must slip along the side walls. However, it is clear from the original PIV data in Figure 6.13 that the narrow boundary layers along the channel walls are poorly resolved.

Cross-channel profiles of along-channel velocity are shown in Figures 6.15 and 6.16, at intervals along the channel (100, 200, 275 and 350 mm). Here the profiles represent the Gaussian low-pass filtered and time-averaged version of the velocity field. For the profiles in Figure 6.15 a velocity profile for the flow of a shear-dominated shelf with an $n = 5$ power-law rheology has been fitted to the data. Here it is clear that the data is matched well in the centre of the channel, but there is a mismatch in the margins, where there is a sharp gradient in the profiles. This sharp gradient from fast flow in the centre to stationary flow on the wall has been smoothed by the filtering, suggesting that the original PIV data did not resolve a boundary layer of slow flow if one is present. Figure 6.16 shows the same velocity data, however in this case a $n = 7$ power-law rheology is used. Here it is evident that there is only a slight improvement in the fit, and again the margins are poorly resolved. This suggests that the mismatch is due to the slip of the fluid along the side walls, rather than the inability of the model to simulate the power-law rheology correctly. It is also clear that the cross-shelf profiles within the channel (100, 200, 275 mm) have the same features as the profile for the section of unconfined shelf (350 mm). This implies that the sheet and shelf experience little lateral resistance while confined in the channel and slip along the channel walls.

Figure D.6 in the Appendix, shows the original velocity data for the experimental currents determined by the PIV software and calculated from the displacement of particles within 8 mm squares, before any further interpolation, Gaussian filtering or time averaging is performed. Here the entire image from the video camera is analysed with the PIV software, including the channel walls and ocean bordering the shelf once it is unconfined. In these areas there are no tracer particles, and therefore should be zero velocities. It is clear that in the case of the 1% Xanthan current, shown in Figure D.6 c and d, there is little change in the cross-shelf velocity profile from the confined to unconfined section of the shelf. There is a drop-off in flow speed at the edges of the current in a 5 - 10 mm interval, the exact location of which varies along the length of the shelf. This profile can be contrasted to the data from the Golden Syrup experiments (Figure D.6 a and b), where there is a smooth transition to zero velocity at the channel walls while the current is confined. However, there is a distinctive difference once the shelf is unconfined, with a sharp reduction in speed at the edge of the flow, in a similar 5 - 10 mm interval at the edge of the current.

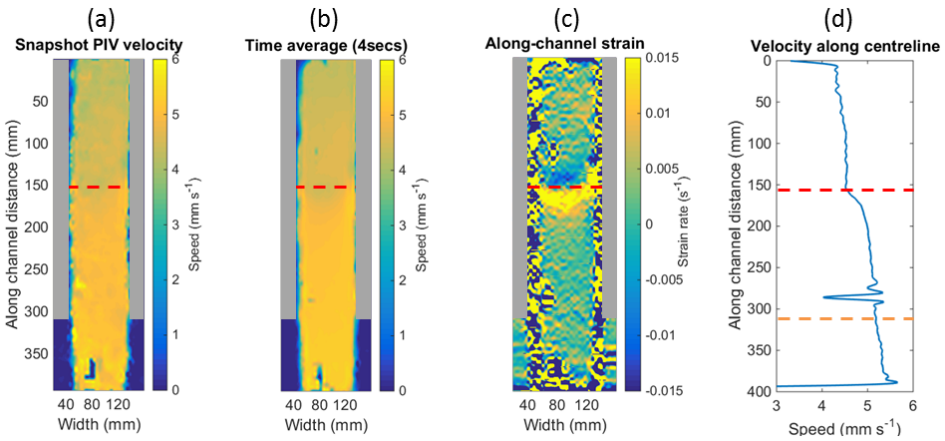

Figure 6.13: Original PIV data: 1% Xanthan, Interval 1. From right to left: speed plot calculated from displacement between two consecutive frames; time-averaged speed calculated over 4 seconds; along-channel strain rate field; centreline transect of time-averaged velocity. Red dashed lines indicate location of grounding line and yellow dashed line channel exit.

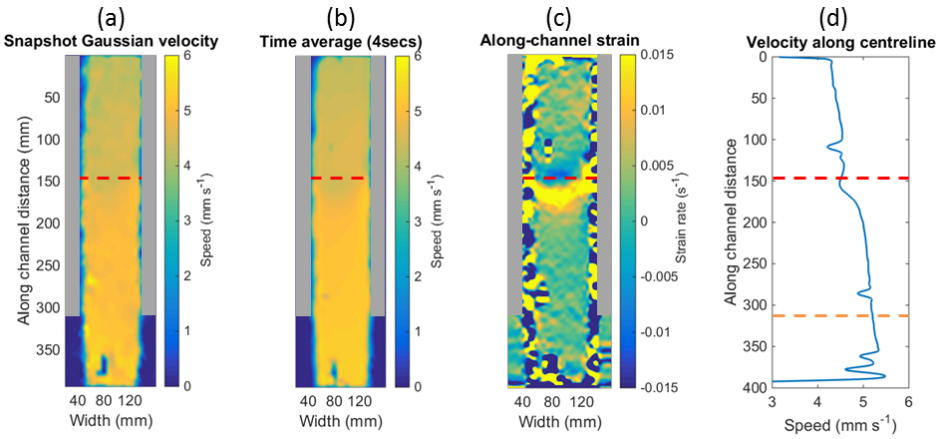

Figure 6.14: Gaussian filtering of PIV data: 1% Xanthan, Interval 1. From right to left: speed plot calculated from displacement between two consecutive frames, with low-pass Gaussian filter applied; time-averaged filtered-speed calculated over 4 seconds; along-channel strain rate field; centreline transect of time-averaged velocity. Red dashed lines indicate location of grounding line and yellow dashed line channel exit.

Interval 2

Between the first and second interval there is a 34 second gap, with the second interval occurring 195 seconds after the first tracer particles leave the channel. Plots for this interval can be seen in Figures 6.17 and 6.18. Here the grounding line has advanced further down the channel and is approximately 70 mm from the exit. Again the grounding line is associated with bands of negative followed by positive strain rate, which form curved structures across the channel width. It is difficult to discern any further features from the velocity-field and strain-rate maps. However, the centreline transects shown in Figures 6.17d and 6.18d, show constant low acceleration in the grounded sheet, followed by an area of rapid adjustment at the grounding line, with deceleration and then high acceleration. This high acceleration suggests an area of rapid extension of the flow as it thins and adjusts to the dynamics in the shelf. Following this, there is then again uniform acceleration in the floating shelf at a similar rate to the acceleration in the grounded sheet. There is no change in acceleration as the shelf leaves the channel, supporting the idea that the walls exert no resistance on the shelf.

As in the previous time interval, there is also little or no cross-channel gradient in velocity, especially in the shelf, implying that there is slip along the channel walls or the velocity is not resolved sufficiently in the margins of the shelf. From the theoretical modelling in the previous chapter, for a power-law rheology with shear-dominated dynamics away from the ends of the channel I expect margins with high shear and close to uniform flow in the centre of the channel. However, here there appear to be no shear margins, or they are too narrow to be resolved.

Once the shelf leaves the confines of the channel, there is no evidence of lateral spreading of the shelf, from the widening of the current, as was observed in the Golden Syrup experiment. This suggests that the lateral hydrostatic driving pressure is not large enough to induce significant lateral flow. However, if this is the case, there should also be insufficient along-channel hydrostatic driving pressure, to drive flow and cause deformation. We would therefore expect the flow in the unconfined section to be due to deformation upstream that is transferred through the shelf and acts to push it along. However, low along-channel acceleration is observed from the grounding line all the way along the floating shelf, from the centreline transect plots Figures 6.17d and 6.18d. From the plot of the transverse velocity component and the cross-channel strain rate in Figure D.7 in the Appendix, there is no appreciable change in the magnitude of the cross-channel strain rate between the confined section of the shelf and the unconfined section. This implies that there is little lateral spreading of the shelf once it leaves the

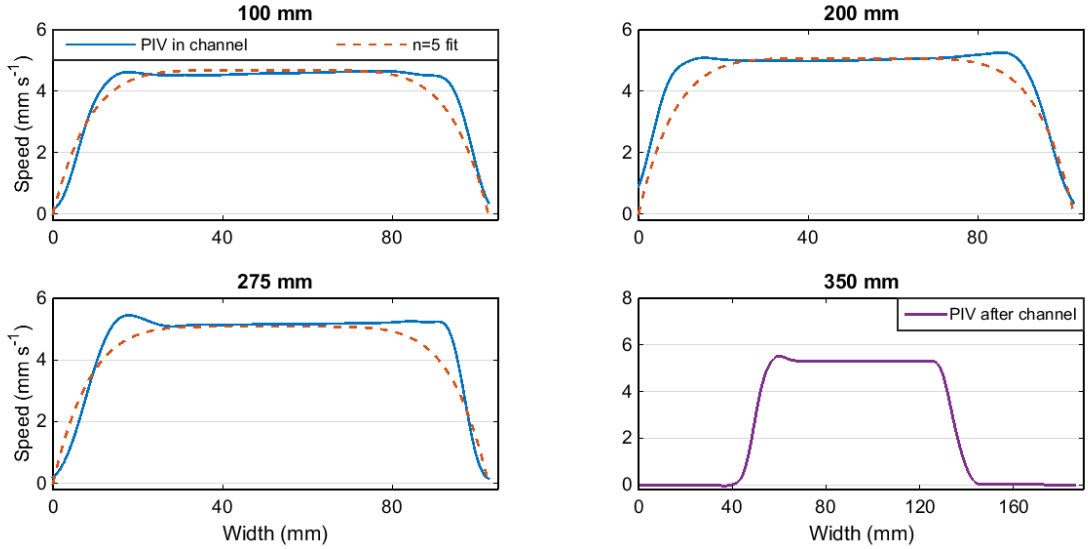

Figure 6.15: Cross-channel profile of along channel velocity at a three points in the channel (100 mm, 200 mm, 275 mm) and one point outside the channel (350 mm), during the first interval of the 1% Xanthan Experiment. Blue curve indicates Gaussian low-pass filtered and time-averaged PIV data. Dashed red curve indicates fitted cross-channel profile for shear-dominated flow with $n = 5$ power-law rheology for those sections within the channel. Purple curve denotes PIV data outside the channel and spanning the field of view.

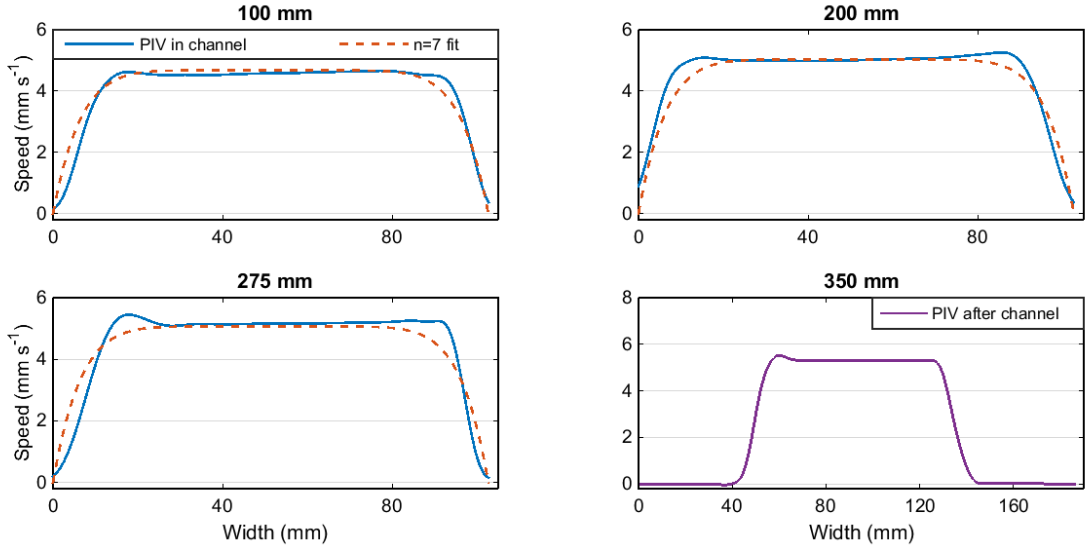

Figure 6.16: Cross-channel profile of along channel velocity at a three points in the channel (100 mm, 200 mm, 275 mm) and one point outside the channel (350 mm), during the first interval of the 1% Xanthan Experiment. Blue curve indicates Gaussian low-pass filtered and time-averaged PIV data. Dashed red curve indicates fitted cross-channel profile for shear-dominated flow with $n = 7$ power-law rheology for those sections within the channel. Purple curve denotes PIV data outside the channel and spanning the field of view.

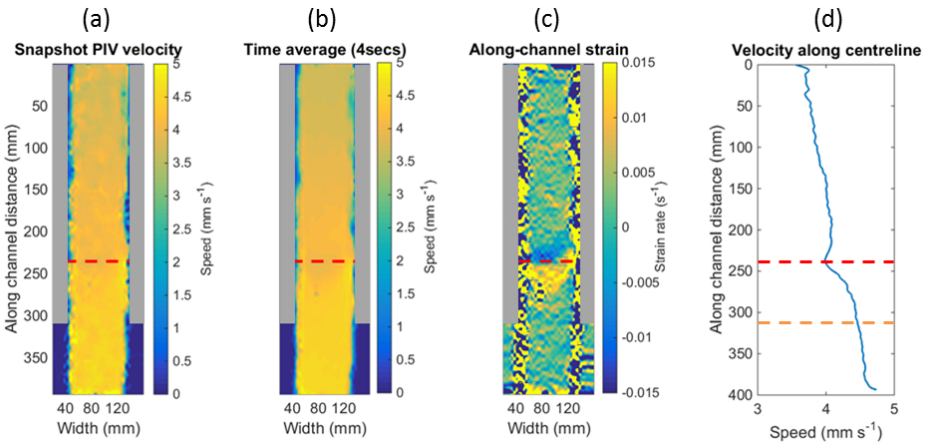

Figure 6.17: Original PIV data: 1% Xanthan, Interval 2. From right to left: speed plot calculated from displacement between two consecutive frames; time-averaged speed calculated over 4 seconds; along-channel strain rate field; centreline transect of time-averaged velocity. Red dashed lines indicate location of grounding line and yellow dashed line channel exit.

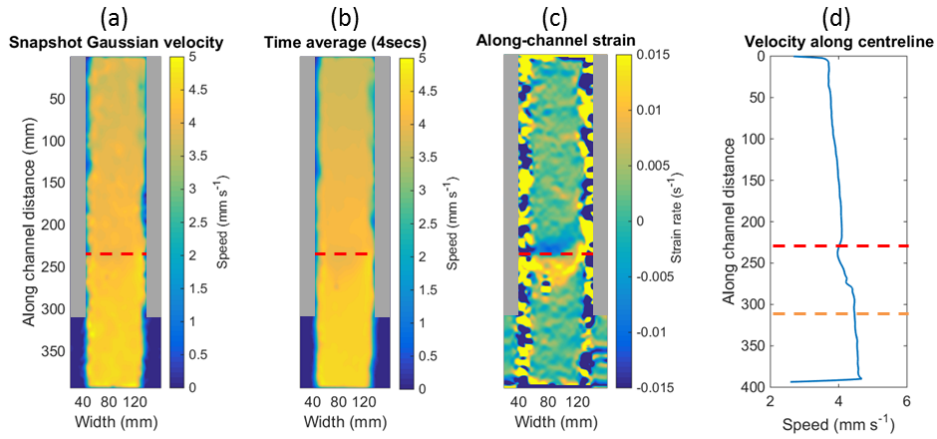

Figure 6.18: Gaussian filtering of PIV data: 1% Xanthan, Interval 2. From right to left: speed plot calculated from displacement between two consecutive frames, with low-pass Gaussian filter applied; time-averaged filtered-speed calculated over 4 seconds; along-channel strain rate field; centreline transect of time-averaged velocity. Red dashed lines indicate location of grounding line and yellow dashed line channel exit.

channel. This suggests that the rheology of the Xanthan solution is allowing some along-flow deformation, but not lateral deformation once the shelf leaves the confines of the channel. This may be due to the deformation history of the fluid, which is constrained to deform in the along-channel direction only while in the channel, deforming significantly in the proximity of the grounding line, and leads to preferential weakening in the along-channel direction. It may also be true that as the deformation in this case is occurring on such small scales, then this may not be accurately captured by the PIV technique.

6.4.3 1.5% Xanthan

Thickness Profile

Figure 6.19 shows the evolution of the elevation profile for a 1.5% Xanthan sheet-shelf confined to a parallel channel of width 10 cm. The salt solution representing the ocean is set to a depth of 2.5 cm. In Figure 6.19, elevation profiles are given every 64 seconds (the non-smoothed thickness profiles can be seen in Figure D.8). Initially there is no grounded section within the field of view, (at 64 seconds) but rather a long shelf, which appears to have close to uniform thickness along the length of the channel, thinning marginally with a change in elevation of approximately 1.5 mm over 35 cm. A grounded sheet then forms at the upstream end of the channel (right end in plot). As the system evolves, the grounding line advances downstream and the grounded sheet thickens, retaining a linear thickness profile as observed in the two previous experiments. Here the slope of the grounded current is approximately -0.065, which is steeper than both the 1% Xanthan solution (-0.038) and the Golden Syrup sheet (-0.015).

After 160 seconds the grounding line has advanced to approximately 13 cm back from the channel exit. Downstream of this a floating shelf is found with an elevation of approximately 4 mm at the grounding line, thinning to approximately 2 mm at the exit. Here it is assumed that the rapid thinning in the final centimetre of the channel is an error from the processing of the side-view images. Within the shelf the thinning is almost linear, with the possibility of some increased thinning near the channel exit.

Interval 1

Figures for the velocity field from the first interval using the 1.5% Xanthan solution can be seen in Figures 6.20 - 6.21. Here the grounding line is positioned close to the edge of the frame of view at the top of the channel, and corresponds to an elevation profile 160 seconds after the first tracer particles exit the channel. After passing the grounding line, there is a band of high positive strain rates and the shelf accelerates rapidly downstream before the rate of acceleration is reduced, as can be seen in the centreline transect in Figures 6.20d and 6.21d. There is a slight reduction in flow speed between the snapshot

velocity fields in Figures 6.20a and 6.21a, and the time average velocity fields in Figures 6.20b and 6.21b. This suggests that there is a reduction in the velocity in the 4 second interval over which the time average velocity field is calculated.

From the centreline transects, Figures 6.20d and 6.21d, it is evident that there is significant acceleration just downstream of the grounding line. This suggests the presence of an extensionally dominated adjustment region, which in this case is approximately 5 cm long (half a channel width). Throughout the length of the channel there is a decrease in the acceleration along the centreline, which continues into the unconfined section of the shelf. This slow decrease in acceleration may be due to the gradual decrease in the shelf thickness downstream and therefore a decrease in the hydrostatic driving pressure. Despite there being evidence for an extensional adjustment region near the grounding line, there is no evidence of a similar region near the exit, where we would expect a transition from shear dominated flow in the confined shelf to extensional flow in the unconfined shelf. This suggests that there is little or no shearing within the channel and the shelf is sliding along the lateral walls with the flow controlled by deformation upstream and the local extensional dynamics. This is confirmed by the original PIV data, as shown in Figure D.6 e, where again there is little change in the cross-shelf profile as the current transitions from confined to unconfined. The only change is the magnitude of the central peak.

As with the previous 1% Xanthan current, here there is little evidence of lateral spreading of the shelf once it leaves the confines of the channel, as can be seen in Figures 6.20 and 6.21. Here the shelf appears to widen slightly but this is mainly due to the absence

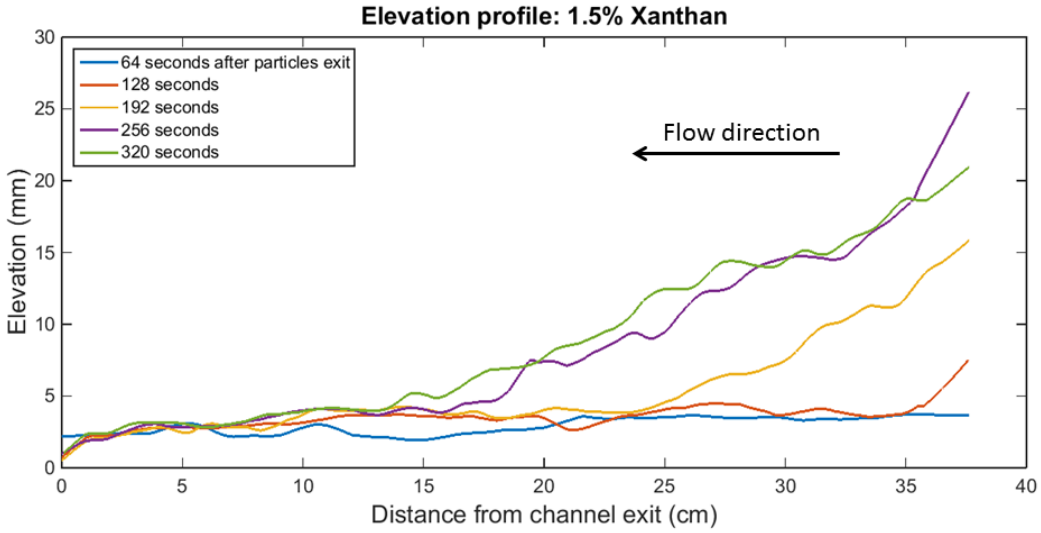

Figure 6.19: Elevation profile for the 1.5% Xanthan current in a parallel channel. Different coloured curves represent profiles at a series of times.

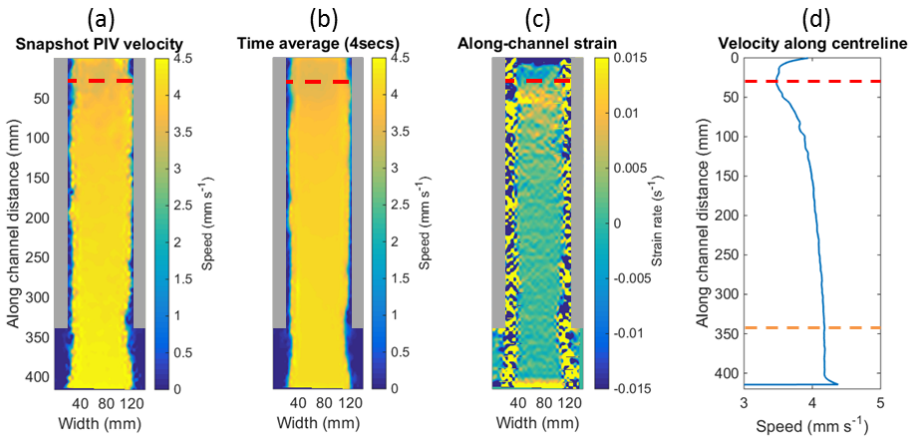

Figure 6.20: Original PIV data: 1.5% Xanthan, Interval 1. From right to left: speed plot calculated from displacement between two consecutive frames; time-averaged speed calculated over 4 seconds; along-channel strain rate field; centreline transect of time-averaged velocity. Red dashed lines indicate location of grounding line and yellow dashed line channel exit.

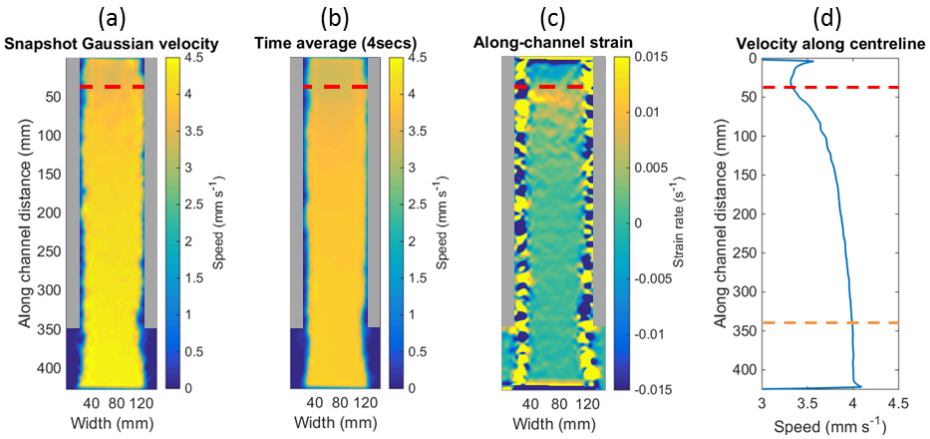

Figure 6.21: Gaussian filtering of PIV data: 1.5% Xanthan, Interval 1. From right to left: speed plot calculated from displacement between two consecutive frames, with low-pass Gaussian filter applied; time-averaged filtered-speed calculated over 4 seconds; along-channel strain rate field; centreline transect of time-averaged velocity. Red dashed lines indicate location of grounding line and yellow dashed line channel exit.

of tracer particles in the margins of the confined shelf near the channel exit, which gives the impression of lateral spreading.

Interval 2

In the 58 second period between the first and second interval, the grounding line has advanced further down the channel, so that it is now positioned approximately 21 cm back from the channel exit, corresponding to an elevation profile at 218 seconds. Similar dynamics to the previous case are present throughout the majority of the sheet-shelf system, but there has been a reduction in the average velocity of roughly 1 mm s^{-1}. This is because the current has thickened in this time interval potentially leading to increased lateral shear-stress against the channel walls. A similar flux can also be maintained due to the increased thickness of the current. One feature that is particularly different is the constant acceleration of the flow throughout the entire length of the floating shelf after the adjustment region near the grounding line. This can be observed in the strain-rate field inferred from the filtered velocity, Figure 6.23c, and in the centreline transect plots, Figures 6.22d and 6.23d. This difference can be related to the evolution of the shelf elevation profile, Figure 6.19, where at early times there is very little variation in thickness along the length of the shelf. However, as the shelf evolves and the grounding line advances, there is an increased thickness gradient within the shelf, which would drive flow and deformation within the floating section of the current.

6.5 Summary/Analysis

6.5.1 Newtonian vs Power-Law

From the experiments presented here it is clear that there are differences between the dynamics associated with the Newtonian and power-law fluids. While the currents are grounded, both fluids produce an approximately linear sloping sheet. However, this slope is increased for the power-law fluids in comparison to the Golden Syrup case, and there is a further increase for the higher concentration of Xanthan, corresponding to a larger value of n. For both fluids, the location of the grounding line can clearly be identified from the elevation plots due to the sharp change in slope between the sheet and shelf.

For the Newtonian shelf, we see that there is a convex thickness profile. The upstream section of the shelf has a fairly flat profile, but the shelf thins more rapidly as it approaches the channel exit, in a region one channel-width back from the exit. This thinning at the channel exit was identified in the theoretical work in the previous chapter and is associated with the extensional stresses that become important near the channel exit. Similar features are not observed for the Xanthan elevation profiles, where

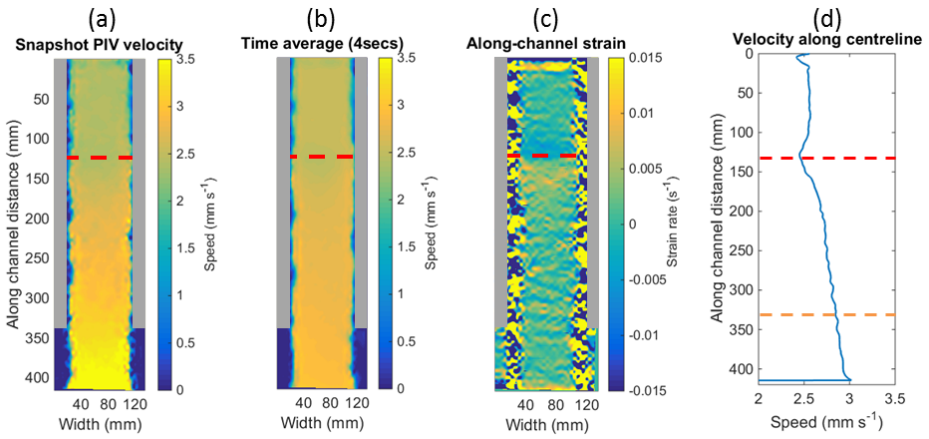

Figure 6.22: Original PIV data: 1.5% Xanthan, Interval 2. From right to left: speed plot calculated from displacement between two consecutive frames; time-averaged speed calculated over 4 seconds; along-channel strain rate field; centreline transect of time-averaged velocity. Red dashed lines indicate location of grounding line and yellow dashed line channel exit.

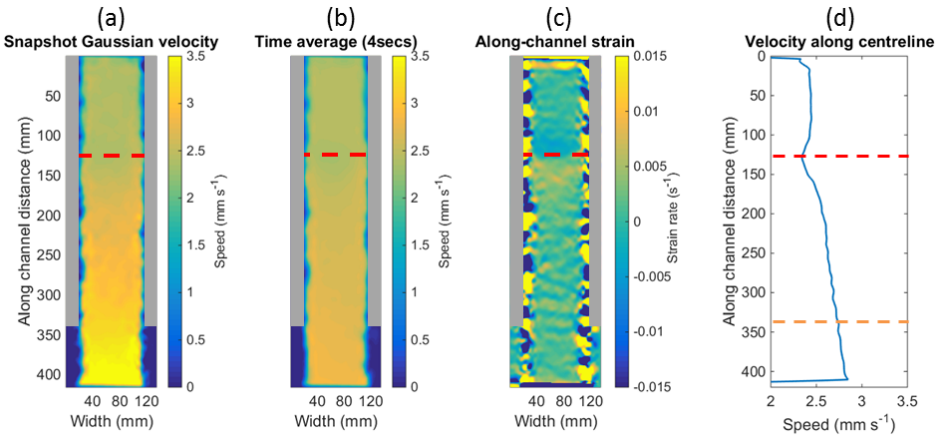

Figure 6.23: Gaussian filtering of PIV data: 1.5% Xanthan, Interval 2. From right to left: speed plot calculated from displacement between two consecutive frames, with low-pass Gaussian filter applied; time-averaged filtered-speed calculated over 4 seconds; along-channel strain rate field; centreline transect of time-averaged velocity. Red dashed lines indicate location of grounding line and yellow dashed line channel exit.

there is little thinning of the shelf along its length and the thinning that is present is approximately linear. This suggests that for the Xanthan case there is not a transition to extensional dynamics at the mouth of the channel, as in the Newtonian experiment and the theoretical models.

From the velocity field data for the Newtonian experiments it is clear that a parabolic cross-channel profile can be fitted to the data, such that there is no-slip along the channel walls and the peak velocity is found in the centre of the channel. This style of dynamics breaks down once the Golden Syrup shelf leaves the confines of the channel, where there is then uniform flow across the width of the shelf, due to the stress-free lateral boundary conditions.

For both of the power-law fluids considered here, the velocity data indicates that there is roughly uniform flow across the width of the channel, and little variation between the confined and unconfined velocity profiles. The uniform velocity across the channel width can be seen clearly in the cross-channel profiles in Figure 6.15, where the smoothing of the Gaussian filter gives the impression of narrow boundary layers. These boundary layers are poorly resolved by the PIV processing. However, it is clear from this data and the centreline transects of along-shelf velocity that there is little change in the shelf dynamics between the confined and unconfined sections, which implies that the shelf must slip along the channel walls.

From the centreline transects of along-channel velocity and the strain-rate plots it is clear that there are compressional and extensional features associated with the grounding line, in both Newtonian and power-law sheet-shelf systems. In all cases negative strain rates are found upstream of the grounding line and are followed by extensional strain once the shelf has formed. These features traverse the width of the channel and are each 25 - 50 mm long in all cases. For the 1% Xanthan experiment it was observed that these features formed arched shapes across the channel width, suggesting that the grounding line was not a linear feature in this case and furthermore that lateral shear may partly govern the dynamics of the grounded sheet.

In the Newtonian case, extensional regions were found at the channel exit, where the extensional stresses become important as identified in the theoretical work. However, this is not the case for the power-law currents, which implies that these shelves do not transition from shear dominated dynamics to extensional dynamics, but rather are only governed by extensional stresses along the length of the channel. These power-law shelves experience no lateral resistance from friction with the side walls and do not satisfy the no-slip condition assumed in the theoretical work.

A measure of the deformation within the shelf can be taken from the along-flow strain-rate plots, which show that away from the grounding line for the Golden Syrup shelf the highest strain rates are between 0.01 and 0.015 s^{-1}, while for the Xanthan shelves along-flow strain rates are less than 0.005 s^{-1}. This indicates that there is much more deformation in the Newtonian shelves, arising due to the no-slip conditions along the channel walls and the thinning of the shelf in the along-channel direction.

Once the shelf leaves the channel it is expected that the shelf will spread laterally due to the hydrostatic pressure difference between the shelf and the salt solution on which it is floating. This occurs in the Golden Syrup current and can be identified by the widening of the current as it leaves the channel. However, in the case of the 1% and 1.5% Xanthan solutions this spreading does not appear to occur. This indicates that the effective viscosity of the power-law fluid is high and acts to resist extension due to the driving hydrostatic pressure. For these power-law shelves there are low levels of deformation, which leads to high effective viscosity and in turn resistance to further deformation.

6.5.2 Gradient of grounded current

During this set of experiments it was observed that the thickness gradient of the grounded section of the current is increased as the flow exponent n was increased, with a slope of approximately 0.015 in the Newtonian case increasing to 0.065 for the 1.5% Xanthan case. This increase in slope with increasing n agrees with the numerical results of Longo et al. (2015), where they considered the flow of a grounded non-Newtonian power-law viscous gravity current in a channel. A plot from this work demonstrating the increasing slope of the current with increasing n can be seen in Figure D.9 the Appendix. It is found that away from the front of the gravity current (the area applicable for the sheet in this case) the slope is increased for larger values of the power-law flow exponent n.

6.5.3 Shelf thickness profile

Newtonian

Based on the idealized models developed in Chapter 5 and the parabolic fit to the cross-channel profile in velocity for the Golden Syrup experiment, I would expect to see a mainly shear-dominated thickness profile, with an adjustment zone within one channel-width of the exit. This adjustment region signifies where the extensional stresses become important to the dynamics. Figure 6.24, shows the shelf thickness profile (red curve) inferred from the elevation profile for the floating shelf section of the system, corresponding to the 320 second elevation profile shown in Figure 6.3. Figure 6.24 also presents

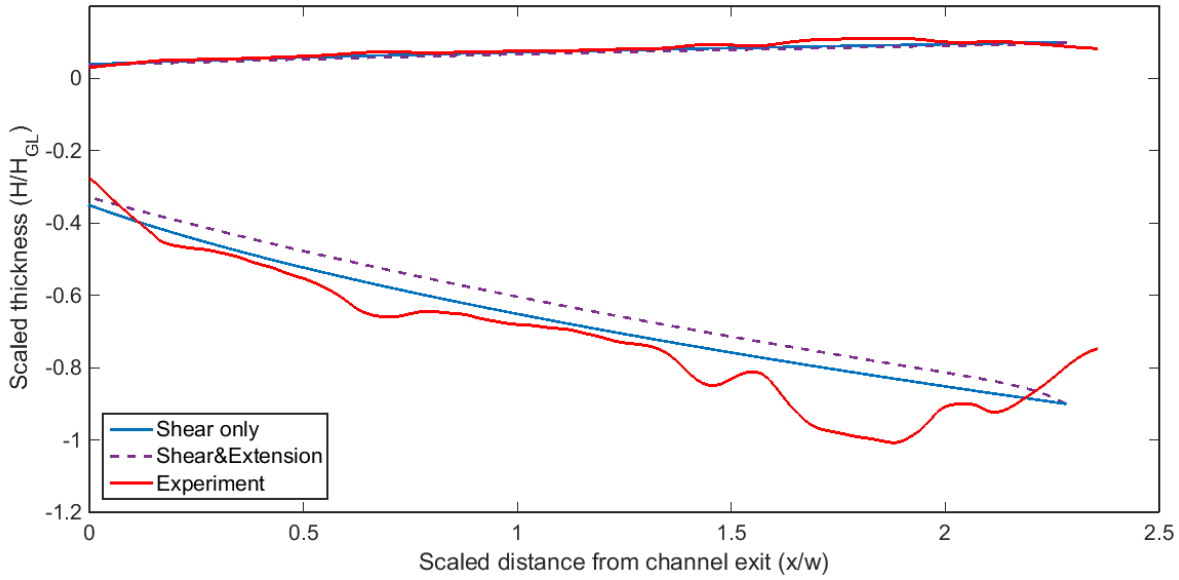

Figure 6.24: Shelf thickness profiles for a Golden Syrup shelf: red curve represents the extent of the shelf inferred from the image analysis of the current at 320 seconds; blue and purple curves represent numerical calculations for steady-state shelf thickness profiles with shear-only dynamics (solid blue curve) and shear-and-extensional dynamics (purple dashed curve). Here each curve represents the surface and base of the shelf, as calculated from Archimedes Principle, given the densities of the Golden Syrup shelf and Potassium Carbonate solution ocean. This plot gives the shelf thickness divided by the grounding line thickness on the vertical axis against the distance back from the channel exit in terms of channel-widths.

the theoretical thickness profile for a steady-state Newtonian shelf, as developed in the previous chapter for both a shear-only shelf (blue curve) and shelf with shear and extension (purple dashed curve). Here we see that all profiles have a similar shape despite the experiment not reaching a steady state. It is clear that they have a convex thickness profile and thin to approximately 0.4 times the grounding line thickness at the exit. This indicates that for the Golden Syrup shelf the flow of the shelf is governed by the shear stresses throughout the majority of the shelf.

For the majority of the sheet and shelf, it was observed that there was very little variation in the cross-channel thickness, implying that the assumption of uniform cross-channel thickness (as assumed in the theoretical modelling) is applicable for this geometry. However, in the region immediately upstream of the channel exit, there was found to be a relatively small cross-channel flow, with fluid flowing towards the centre of the channel (Fig. D.3). This flow must be induced by variations in the cross-channel thickness. In this region extensional dynamics are important as the shelf approaches the exit. However, extensional stresses will be felt most strongly in the centre of the channel away from the resistance at the side walls (see strain-rate plots in Figure 6.28) and therefore

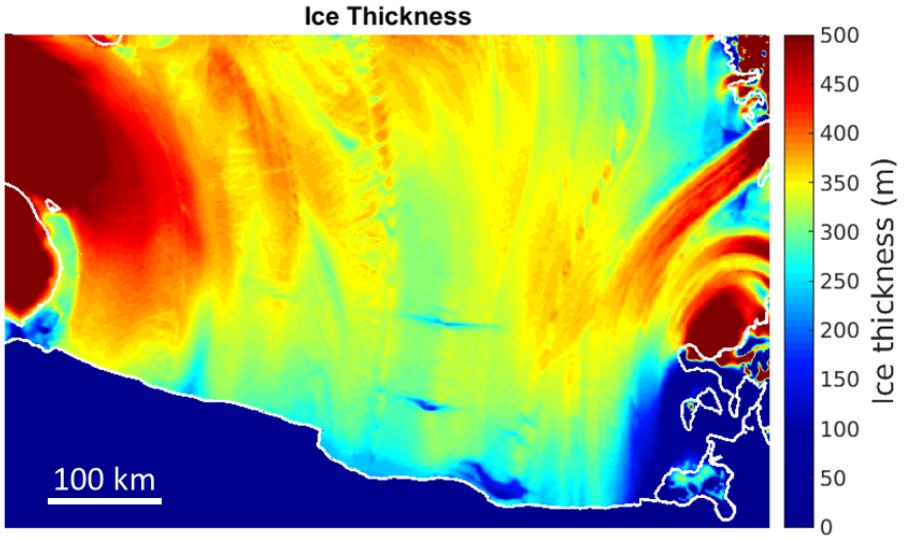

Figure 6.25: Ice thickness for the Ross Ice Shelf in the region close to the calving front. The calving front is indicated by the white outline running along the bottom of the plot, with the outline of islands shown on the left and right of the plot. An area of relative thin ice can be seen at the centre of the ice front extending back into the shelf.

lead to the most pronounced thinning in the centre of the shelf. As a consequence of this, a gradient in thickness is produced transverse to the main flow (and main component of extension), which induces flow towards the centre of the channel. Once the shelf leaves the channel, there is no longer the shear resistance and the extensional dynamics lead to the spreading of the shelf in the along-channel and transverse directions. A geophysical example with similar characteristics is Ross Ice Shelf, where relatively thin ice is found at the centre of the calving front, relative to the thicker ice found in the margins, this area forms a concave region across the front of the shelf at the exit of the embayment as shown in Figure 6.25. This indicates how a significant cross-channel component of the ice-shelf flow can develop near the end of a confinement, due to high strain and thinning in the centre of the shelf.

Power-Law: Xanthan

From the experiments using Xanthan solutions, it is evident that the shelf slips along the side walls of the channel. Therefore, I would not expect a thickness profile calculated for a shear-dominated shelf to match well or have the same features as the thickness profile from the experimental data. However, the thickness profile from the experiment may have similar characteristics to a profile for an extensionally dominated shelf. I therefore calculate the shelf thickness profile for purely extensional dynamics. In this case, the

power-law rheology is determined by the along-shelf strain rate and takes the form

$$\mu = B' \left| \frac{\partial u}{\partial x} \right|^{(1-n)/n}. \tag{6.3}$$

As in the earlier modelling work, I consider a uniform cross-shelf thickness, such that the force balance and continuity equations are

$$\frac{\partial}{\partial x}\left(\mu H \frac{\partial u}{\partial x}\right) = \frac{\rho g'}{4} H \frac{\partial H}{\partial x}, \tag{6.4}$$

$$\frac{\partial H}{\partial t} + \frac{\partial}{\partial x}(Hu) = 0. \tag{6.5}$$

I solve for the steady-state thickness profile ($H \equiv H(x)$), for a given constant input flux Q_0 and fixed input thickness H_0. Although the shelf in the experiment may not be in steady state, considering a steady-state shelf enables the identification of key characteristics of the shelf-thickness profile and velocity field, and allows for direct comparison with the steady-state shear-dominated dynamics considered in the modelling work in Chapter 5.

If we assume that the along-flow strain rate in the shelf is always positive, given that the hydrostatic driving pressure induces flow in one direction only, then the rheological model can be incorporated into the force-balance equation to give

$$\frac{\partial}{\partial x}\left(B' H \left(\frac{\partial u}{\partial x}\right)^{1/n}\right) = \frac{\rho g'}{4} H \frac{\partial H}{\partial x}, \tag{6.6}$$

$$\Rightarrow \frac{\partial u}{\partial x} = \left(\frac{\rho g'}{8B'} H\right)^n. \tag{6.7}$$

This equation along with the constant flux throughout the shelf in steady state, $Q_0 = UH$, can be used in the steady-state continuity equation to determine the shelf thickness profile,

$$\frac{\partial H}{\partial x} u + H \frac{\partial u}{\partial x} = 0, \tag{6.8}$$

$$\frac{\partial H}{\partial x} \frac{Q_0}{H} + H \left(\frac{\rho g'}{8B'} H\right)^n = 0, \tag{6.9}$$

$$\Rightarrow H = \left(\frac{n+1}{Q_0}\left(\frac{\rho g'}{8B'}\right)^n x + A\right)^{-1/(n+1)}, \tag{6.10}$$

where A is a constant of integration. This is determined by considering the shelf-thickness boundary condition at the upstream boundary; $H = H_0$ at $x = 0$. Therefore

$$H = \left(\frac{n+1}{Q_0} \left(\frac{\rho g'}{8B'} \right)^n x + H_0^{-(n+1)} \right)^{-1/(n+1)}, \tag{6.11}$$

$$u = \left(Q_0^n (n+1) \left(\frac{\rho g'}{8B'} \right)^n x + H_0^{-(n+1)} Q_0^{n+1} \right)^{1/(n+1)}. \tag{6.12}$$

Figure 6.26 shows the shelf-thickness profile, speed and strain-rate plots for a purely extensional shelf with the model parameters chosen to be appropriate for the fluids used in the 1% Xanthan experiment, with $n = 6$, $\tilde{\mu} = 10$ Pa s$^{1/3}$, input thickness $H_0 = 27.5$ mm and input speed $u_0 = 5$ mm s^{-1}. Here it is evident that there is little thinning of the shelf along the length of the channel. There is some acceleration of the flow within the 160 mm channel, from 5 mm s^{-1} at the grounding line to approximately 5.15 mm s^{-1} at the channel exit. The strain rate decreases slightly along the length of the shelf from 5×10^{-4} s^{-1} to 4.25×10^{-4} s^{-1}. This style of thinning and flow is similar to that observed in the experimental data, as shown in comparative plots in Figure 6.27. In these plots from the experimental data it is clear that small undulations in the surface of the shelf, due to errors determining the position of the surface, correspond to larger variations in the total thickness of the shelf. It is also apparent that there is an adjustment region just downstream of the grounding line, where there is high along-flow strain, within the first 40 mm of the shelf. These dynamics are not captured in the analytical model, but the flow within the final 120 mm of the shelf shows good agreement with the theoretical solutions, both qualitatively and quantitatively. The adjustment region is addressed in a later section.

If the power-law exponent is decreased, this analytical solution provides a profile that thins more rapidly in the along-channel direction compared with the $n = 6$ case shown here. Consequently, the flow in the shelf is increased along with the strain rate. Plots for purely extensional Newtonian ($n = 1$) and $n = 3$ power-law shelves can be found in Figures D.10 and D.11 in the Appendix.

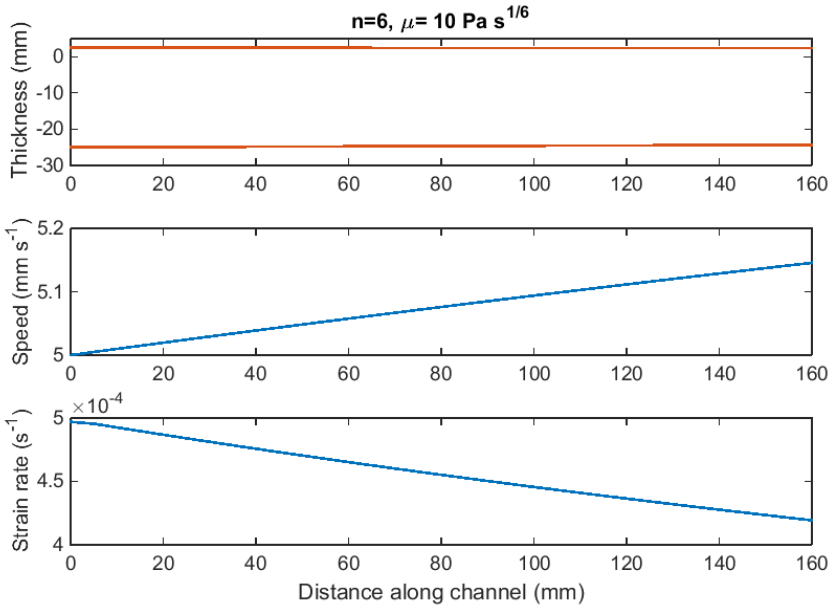

Figure 6.26: Shelf thickness, speed and strain rate (top to bottom) for a purely extensional shelf, with $n = 6$ power-law rheology and consistency index $\tilde{\mu} = 10$ Pa s$^{1/6}$.

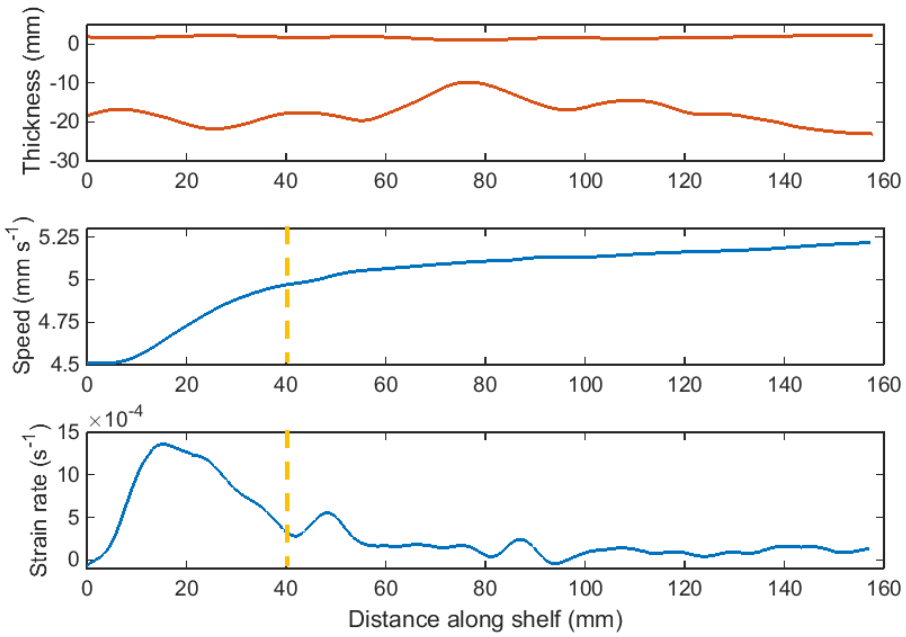

Figure 6.27: Shelf thickness, speed and strain rate (top to bottom) for the first interval of the 1% Xanthan shelf section of the current. Here the fluid flows from left to right, with an adjustment region near the grounding line, which can be identified by a sharp increase in speed and high strain rates in the first 40 mm of the shelf and is indicated by a dashed orange line.

6.5.4 Extensive adjustment regions

At the channel exit of the Newtonian experiments, there was found to be an area of high extensive strain rate approximately one channel-width long and spanning the width of the channel. In this region I expect there to be a transition from the shear dominated dynamics upstream far from the channel exit, to the extensional dynamics that control the flow of the shelf once it leaves the channel. From the idealized models presented in Chapter 5, it was observed that the along-flow strain rate increased in the region near the channel exit. Figure 6.28 presents the strain-rate field for the steady-state shelf considered in the idealized model, where both shear and extensional dynamics are considered throughout the shelf, alongside the strain rate from the first interval of the Golden Syrup experiment. A completely direct comparison with the experimental data is not possible, as the experimental systems do not reach a steady-state. However, from comparison between these two plots it is clear that high strain rate is found at the channel exit in a region of aspect ratio one. The highest strain rates are found in the centre of the channel and are associated with the thinning of the shelf in the centre and the induced flow from the channel walls, as suggested in the previous section. From Figure 6.28 it is clear that strain rates in this area immediately upstream of the channel exit are the largest throughout the whole shelf.

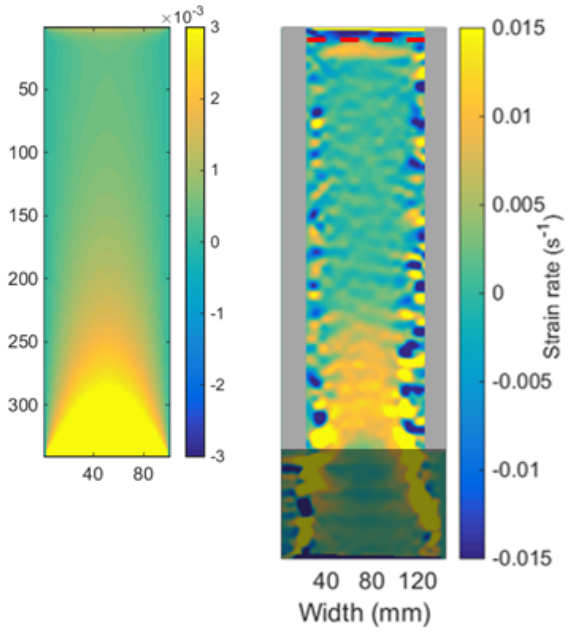

Figure 6.28: Strain-rate maps for: a modelled Newtonian ice shelf with shear and extensional dynamics in steady state (region shown is confined within the channel), shown on the left; and on the right the first interval of the Golden Syrup experiment, where both the confined and unconfined sections of the shelf are shown, with the unconfined section masked. In both cases high strain rates are found in a region of aspect ratio one in the mouth of the channel.

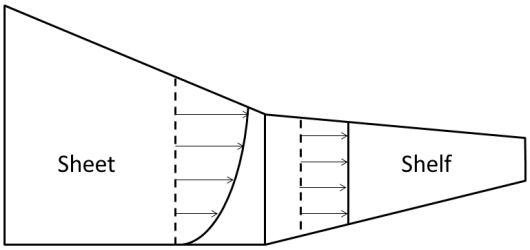

Figure 6.29: Diagram showing the transition across the grounding line from vertical shear flow in the grounded sheet to vertical plug flow in the shelf. There is a decrease in the surface speed but an increase at depth.

6.5.5 Compressive and extensive dynamics at grounding line

For both the Newtonian and power-law experiments, prominent strain-rate features are found at the grounding line that span the width of the channel. Upstream of the grounding line is found an area of compression or deceleration. This may be due to the transition from vertically sheared flow in the grounded section, to uniform flow in the vertical in the shelf once the basal resistance is removed, as shown in the diagram in Figure 6.29. From the PIV data, we have a measure of the surface velocity, however there are likely to be complex vertical variations in velocity at this point. If we consider the grounding line to be temporarily fixed, then the volume flux must be conserved across the grounding line, but the vertical profile of the velocity must change from a vertical-shear profile to plug flow in the shelf (Fig. 6.29). Therefore we should expect a reduction in the surface velocity, which will be represented by negative along-flow strain rates in this PIV data.

The positive along-flow strain rate found downstream of the grounding line may partly be due to the removal of basal resistance from the current as it begins to float. This reduction in resistance leads to increased extension. In addition to this, there may be an adjustment of the fluid to the thickness of the shelf downstream. Features of this kind were found in the development of numerical models for an idealized shelf in a parallel channel in Chapter 5. There was found to be an area of extension and rapid thinning of the shelf as it adjusts to the dynamics within the shelf, which can be seen in Figure 6.30. Figure 6.30 presents a confined Newtonian shelf in steady state, with parameters chosen to approximate a geophysical ice shelf. In this example the thickness of the current at the grounding line is much larger than that in the shelf, where the thickness is determined by the shear and extensional dynamics in the downstream section of the shelf. Therefore thinning and extension occur downstream of the grounding line as this adjustment is made. This is indicated by high strain rate at the upstream boundary.

Similar regions of high extension near the grounding line are found for purely exten-

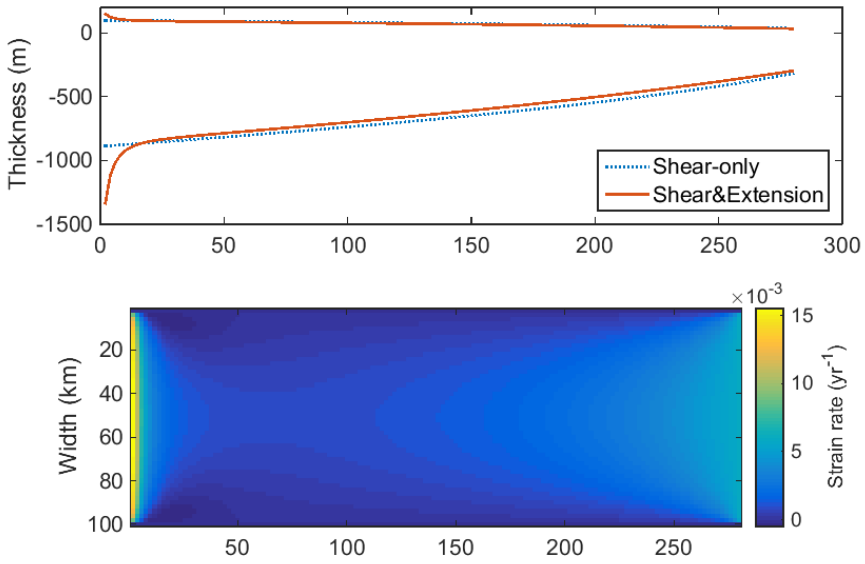

Figure 6.30: Upper plot shows thickness profile for a steady-state Newtonian shelf confined within a parallel channel, with shear and extensional dynamics (solid red curve), where the thickness of the shelf at the grounding line is much greater than the thickness of the shelf which is governed by the shear and extensional dynamics within the confined shelf. There is therefore rapid thinning downstream of the grounding line. The dashed blue curve indicates the shear-only shelf profile. The lower plot shows the along-flow strain rate corresponding to the shear-and-extension shelf. High positive strain is found at the upstream end of the shelf, where the shelf thins rapidly. This strain is even larger than the strain rate found at the channel exit.

sional shelves when the input thickness exceeds the thickness of the shelf downstream. This can be seen in Figure 6.31 for a power-law ($n = 6$, $\tilde{\mu} = 10$ Pa s$^{1/6}$) shelf, where the input thickness is 55 mm, however there is little thinning in the majority of the shelf and the thickness at the exit is approximately 30 mm. This leads to rapid thinning and high strain in a region close to the grounding line. The difference in dynamics resulting from this thicker fluid at the grounding line can be identified by comparing Figures 6.26 and 6.31, which have the same rheology and same input flux but different input thicknesses. Clearly there is increased strain upstream, by approximately two orders of magnitude when the input thickness is increased.

6.5.6 Lateral spreading

From the Golden Syrup PIV plots (Figs. 6.4 - 6.8) it was clear that after the shelf left the confines of the channel there was some lateral spreading of the current. For the first interval the along-flow velocity component remained constant after leaving the channel, while there was a decrease in velocity for the second interval, this suggests there was little spreading of the shelf in the along-channel direction once it left the channel. The

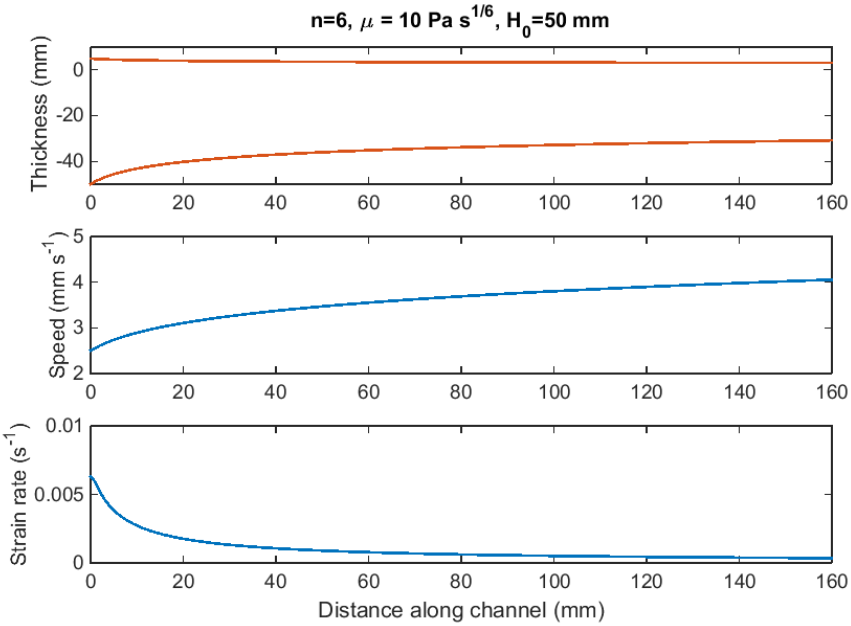

Figure 6.31: Shelf thickness, speed and strain rate for a purely extension shelf, with $n = 6$ power-law rheology and consistency index $\tilde{\mu} = 10$ Pa s$^{1/6}$. For comparison with Figure 6.26, here the input flux has been held constant but the input thickness has been doubled to 50 mm, leading to rapid thinning and high strain near the upstream boundary.

lateral spreading once the shelf leaves the confinement is due to the lateral hydrostatic driving pressure, which induces a flow. This flow is prohibited while the shelf is confined by the presence of the channel walls. This lateral spreading is not observed in the case of the power-law fluids. In Figure 6.32 I present cross-channel profiles in along-channel velocity, taken 40 mm downstream of the channel exit, with the approximate location of the edge of the shelf marked by red dashed lines. From these plots it is evident that there is considerable lateral spreading of approximately 22 mm (over the 40 mm interval) in the case of the Golden Syrup shelf, but no evidence for spreading in the two power-law cases.

The spreading of viscous power-law fluids on a dense inviscid layer has been studied analytically by Pegler et al. (2012). For a 2D geometry with the viscous power-law fluid spreading in one dimension perpendicular to the vertical layer thickness H, the rate of change of the layer thickness is given by

$$\left.\frac{DH}{Dt}\right|_{2D} = -H\left(\frac{\rho g' H}{8\tilde{\mu}}\right)^n. \tag{6.13}$$

However, if a 3D geometry is considered in which the layer can spread in the plane perpendicular to the vertical, then the rate of change of the layer thickness is

$$\left.\frac{DH}{Dt}\right|_{3D} = -2H\left(\frac{\rho g' H}{12\tilde{\mu}}\right)^n. \tag{6.14}$$

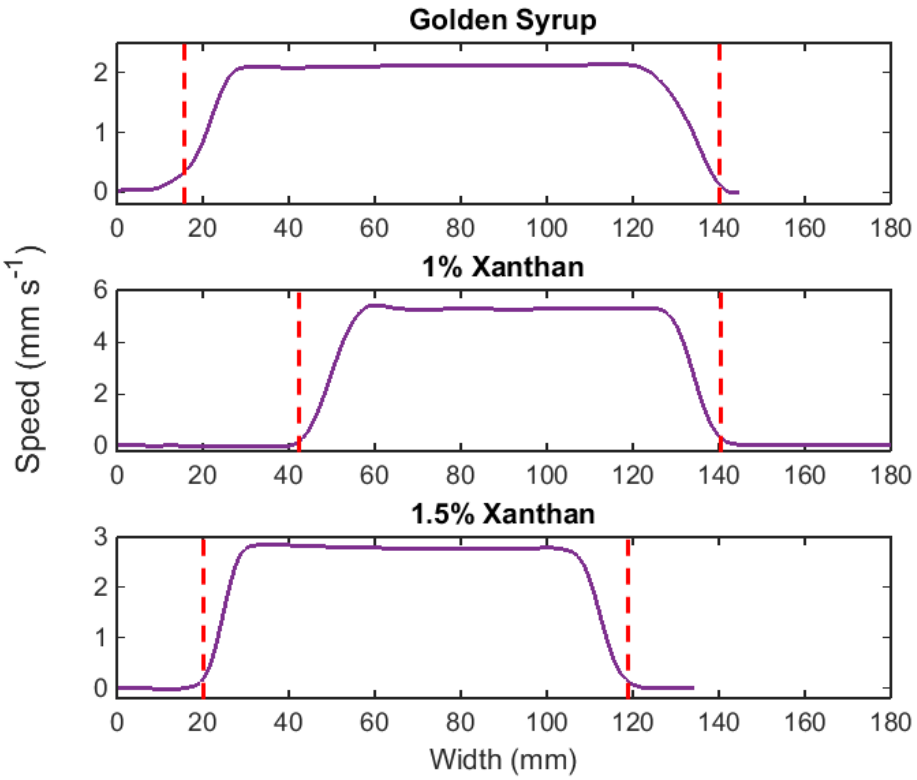

Figure 6.32: Cross-shelf profiles for along-channel velocity, for Golden Syrup, 1% and 1.5% Xanthan solutions. Profiles are taken 40 mm from the channel exit (of width 100 mm), with red vertical dashed lines marking the approximate location of the edge of the shelf.

Both of these equations come from the work of Pegler et al. (2012). From the experimental data we have observed that there is little along-channel deformation of the shelf once it leaves the channel and therefore it is reasonable to approximate the lateral deformation as 2D spreading.

The rate of thickness change of the Golden Syrup shelf once it leaves the channel during the first interval can be determined from the 2D lateral spreading of the shelf as the along-channel velocity remains constant throughout the floating shelf, implying little along-channel spreading/deformation (see Fig. 6.5d). It is therefore suitable to consider a vertical cross-section through the unconfined shelf, perpendicular to the flow, which has a constant area as the shelf flows away from the channel exit, as shown in Figure 6.33. The thickness of the shelf is known as it leaves the channel (H_1), from the confined-shelf elevation profile and the channel has a set width of 100 mm. Therefore, assuming a constant cross-sectional area and uniform cross-shelf thickness, the shelf thickness can be calculated at any point downstream, given the width of the shelf at that point from the PIV data. Using the shelf width at 40 mm from the channel exit, (W_2) as shown in

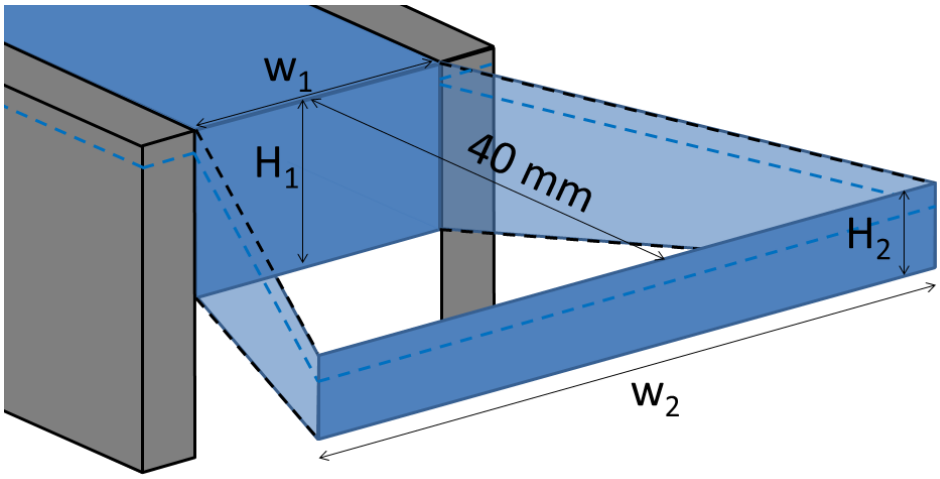

Figure 6.33: Diagram depicting the idealized spreading of a shelf as it leaves the confinement of a channel, with two cross-sections identified at the channel exit (H_1, w_1) and 40 mm downstream of the channel exit (H_2, w_2). Under the assumption that there is no further along-flow extension (as observed in the first interval of the Golden Syrup experiment) the cross-sectional area is constant between cross sections. Approximating the shelf to have a uniform cross-channel thickness, it is possible to estimate the rate of thinning and lateral spreading.

Figure 6.32, the shelf thickness at the exit and 40 mm downstream are,

$$H_1 = \left(\frac{\rho_w}{\rho_w - \rho}\right) h_1 = 15.2 \times 0.5 = 7.6 \text{ mm}, \tag{6.15}$$

$$H_2 = \frac{H_1 \times 100}{W_2} = \frac{7.6 \times 100}{122} = 4.23 \text{ mm}. \tag{6.16}$$

Here we have $\rho_w = 1.54{\times}10^3$ kg m^{-3} the density of the inviscid dense ocean, $\rho = 1.44{\times}10^3$ kg m^{-3} the density of the Golden Syrup shelf, h_1 the elevation of the shelf at the channel exit. This can then be used to estimate the rate of thickness change of the unconfined shelf due to lateral spreading

$$\frac{DH}{Dt}_{\text{exp}} \approx \frac{H_2 - H_1}{T_2 - T_1}, \tag{6.17}$$

where $T_2 - T_1$ is determined by calculating the travel time of the fluid from the channel exit to the cross-section 40 mm downstream. The speed is given by the along-channel velocity u, which in this case is $u = 2.1$ mm s^{-1}, so $T_2 - T_1 = 19.05$ s. Therefore, in this case

$$\frac{DH}{Dt}_{\text{exp}} \approx -0.0719 \text{ mm s}^{-1}. \tag{6.18}$$

If we assume 2D spreading and use equation (6.13) above, the rate of thickness change is

$$\frac{DH}{Dt}_{2D} = -H_1 \left(\frac{\rho g' H_1}{8\tilde{\mu}} \right), \tag{6.19}$$

$$= -\left(7.6 \times 10^{-3}\right) \times \frac{1.44 \times 0.65 \times 7.6}{8 \times 77} \tag{6.20}$$

$$= -8.78 \times 10^{-5} \text{ m s}^{-1} = -0.088 \text{ mm s}^{-1}. \tag{6.21}$$

With $g' = g(\rho_w - \rho)/\rho_w = 0.65$ the reduced gravity, n the power-law exponent for this Newtonian fluid ($n = 1$) and the consistency index B', which is equal to the dynamic viscosity; $B' = \mu = 77$ Pa s. This value of the shelf thinning is only slightly greater than that estimated from the data and lies within the bounds of experimental error.

This theoretical assessment can be improved slightly by considering the average thickness of the unconfined section of the shelf, which can be estimated as earlier from the rate of spreading observed in the experimental data. This approach leads to a thinning rate of -0.0728 mm s^{-1}, which provides even better agreement with the estimate derived from the experimental data, with a difference of less than 2%.

If the shelf was considered to be spreading in both the along flow and transverse directions, as might be expected theoretically due to the presence of a hydrostatic driving pressure in the along-flow and lateral directions, then the 3D analytical solution would be more appropriate, for this experiment

$$\overline{\frac{DH}{Dt}}_{3D} = -2\bar{H} \left(\frac{\rho g' \bar{H}}{12\tilde{\mu}} \right)^n = -0.097 \text{ mm s}^{-1}, \tag{6.22}$$

which exceeds the rate of thinning observed in the experimental data. This result is some what expected, as from the experimental data it is apparent that there is no change in the along-flow velocity once the shelf leaves the confines of the channel, indicating there is no extension in this direction and the only extension occurs laterally.

For the case of the two Xanthan experiments no measurable lateral spreading of the unconfined shelf was observed. From the analytical assessment of Pegler et al. (2012), for the 1% Xanthan solution (interval 1), with $n = 6$ and $\tilde{\mu} = 10$ Pa s$^{1/n}$ (taken from Sayag and Worster (2013b)) we would expect rates of thinning of

$$\frac{DH}{Dt}_{2D} = 0.026 \text{ mm s}^{-1}, \tag{6.23}$$

and

$$\frac{DH}{Dt}_{3D} = 0.0045 \text{ mm s}^{-1}, \tag{6.24}$$

in the 2D and 3D spreading cases respectively. Here there is considerably reduced thinning in the case of 3D spreading due to the resistance to spreading generated by hoop stresses. The rates of thinning calculated here would correspond to lateral spreading of 0.73 mm over the 40 mm section downstream of the exit in the 2D case for this experiment, while extension in all directions in the horizontal plane would result in spreading of approximately 0.13 mm. It is therefore clear that in the 1% Xanthan case using this experimental set up it is difficult to detect spreading over the 40 mm section. However, spreading may be evident if a longer section of unconfined shelf was considered. For the 1.5% Xanthan solution, the fluid is likely to have a larger value of n and a larger consistency index $\tilde{\mu}$, this will therefore lead to lower rates of thinning and consequently less lateral spreading.

From this assessment of the lateral spreading it is clear that there are distinctive differences between the Golden Syrup and 1% Xanthan shelves once they leave the confinement of the channel, which is seen both in the experimental data and the theoretical model. For the Golden Syrup shelf, the deformation is mainly lateral after exiting the channel, and a 2-dimensional model approximation of this gives good agreement. From the theoretical model for the 1% Xanthan shelf, it is clear that lateral spreading of <0.73 mm is expected over the 40 mm section of unconfined shelf, which is in stark contrast to the 22 mm of spreading in the Newtonian case. This small-scale spreading of the Xanthan shelf can not be accurately measured from this experimental set up.

6.5.7 Comparison with geophysical examples

Scaling relationship at channel exit

In a similar manner to the geophysical cases considered earlier in this thesis, in Chapter 4, I now use the data from the fluid-mechanical experiments to test whether the scaling relationship for the flow speed at the centre of the shelf front, as developed by Hindmarsh (2012), holds for these laboratory scale models. For a general power-law fluid with flow exponent n, this relationship takes the form $u_c \propto w(\epsilon H)^{n/(n+1)}$.

To assess the experimental data, I sampled the flow speed, along-flow strain rate, and shelf thickness at the channel exit, which is kept at a constant width of 100 mm for all experiments. As with the geophysical data, the data gathered from the experiments contains some noise, I therefore applied a Gaussian low-pass filter to the PIV data and time average over a four second interval, as detailed in the previous sections in this chapter.

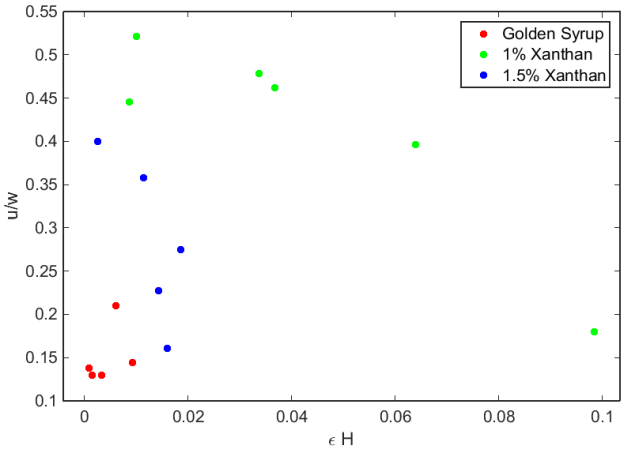

Figure 6.34: Data points from all experiments, plotting speed at exit divided by channel width, against strain rate at exit multiplied by shelf thickness at exit. The key denotes the shelf fluid.

As the fastest speeds are expected in the centre of the channel at the channel exit, the flow speed is sampled on the centreline of the shelf, at the point of fastest along-channel flow before the shelf leaves the confines of the channel. From inspection of the data, this falls within the final 2 cm of the channel in all cases. The strain rate is then calculated as an average over a 5 cm interval along the centreline back from the point at which the speed is sampled. This average is therefore calculated over half the region with high strain-rate that has aspect ratio one, as identified earlier. The thickness is determined by the elevation profiles from the side-viewing camera, and sampled in the same location as the speed. Data is gathered from the experiments presented earlier in this chapter along with additional data from other PIV intervals for the same experiments and some repeat experiments.

Data collected in this manner is presented in Figure 6.34 (and in Table D.1 in the Appendix), with each of the different fluids identified by a different coloured marker. In the lower left corner there is a cluster of data points corresponding to the Golden Syrup Experiments. Here these currents have a low speed at the channel exit, and the product of the strain rate and shelf thickness is also low. On the other hand, there is a much more expansive scatter for the Xanthan solution data points, with the 1% solutions spanning a wide range of ϵH values. From the earlier analysis it was clear that the Xanthan shelves slip along the side walls and therefore the theoretical scaling relationship should not provide a fit to the data, as it assumes no slip at the lateral boundaries.

However, there is evidence to suggest that the no-slip lateral boundary condition holds in the case of the Golden Syrup shelves. In Figure 6.35 I present the results from the Golden Syrup experiments plotted in log-log space. A linear fit to the data is expected

of the form

$$\log_{10}(u_c) = \log_{10}(Cw) + \frac{n}{n+1}\log_{10}(\epsilon H). \tag{6.25}$$

with C a constant and n the flow exponent, to be calculated from the slope of the linear regression to the data. For this data the linear regression provides a fit with a slope of 0.1, implying a flow exponent of $n = 1/9$, which is significantly different from the true value. Here the data points are collected at a range of time intervals during two experiments with the same parameter values. If more data points were used as part of this assessment, from a wider range of parameter values, such as varying the width of the shelf and the input flux, then this may lead to a linear regression with a more suitable slope.

In addition to the linear regression to the data points, Figure 6.35 also features the plot of the full scaling relationship

$$u \sim w\left(\frac{\rho g'}{4B}\right)^{n/(n+1)} (H\epsilon)^{n/(n+1)}, \tag{6.26}$$

with these parameters values allocated to be suitable for this experiment (and $\epsilon = \partial u/\partial x$). Here we observe that the data points lie above the line of the scaling relationship implying that the flow at the centre of the channel exit is faster than expected. In the geophysical analysis in Chapter 4, behaviour of this kind was explained by the reduced lateral resistance due to weak ice or absence of lateral pinning points. It may be the case here that there is some slip along the channel walls, possibly only in the region near the channel exit, where the shelf is thin. Furthermore, it was observed earlier in this section that there was a transverse component in velocity immediately upstream of the channel exit, which was induced by lateral variations in thickness, as a result of thinning and high values of extension in the centre of the channel. These dynamics may further act to increase the rate of fluid flow at the channel exit and are not considered in the development of this scaling relationship.

Figure 6.36 shows the data points for the Xanthan shelves, plotted in log-log space with the scaling relationship evaluated appropriately for the 1% Xanthan shelf. Here, as expected, we see that the data points are all above the line for the scaling relationship, confirming that the shelves experience little resistance from the channel walls.

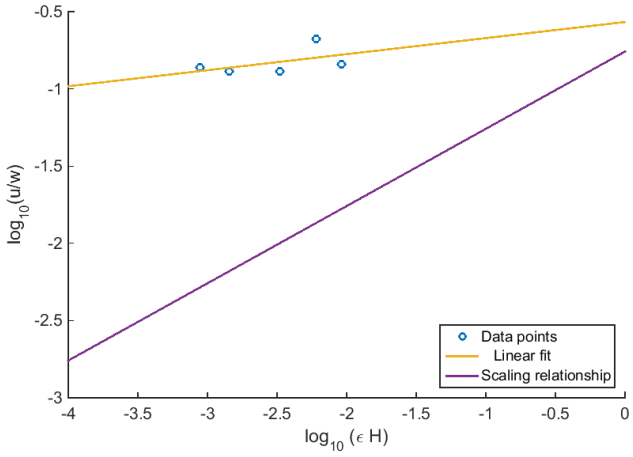

Figure 6.35: Data points for Golden Syrup experiments, plotting speed at exit divided by channel width, against strain rate at exit multiplied by shelf thickness at exit in log-log space. A linear regression to the data points is given by the yellow line. In addition the theoretical scaling relationship amended for to the experimental parameters ($u = w(\rho g'/4B)^{n/(n+1)}(H\epsilon)^{n/(n+1)}$) is given by the purple line.

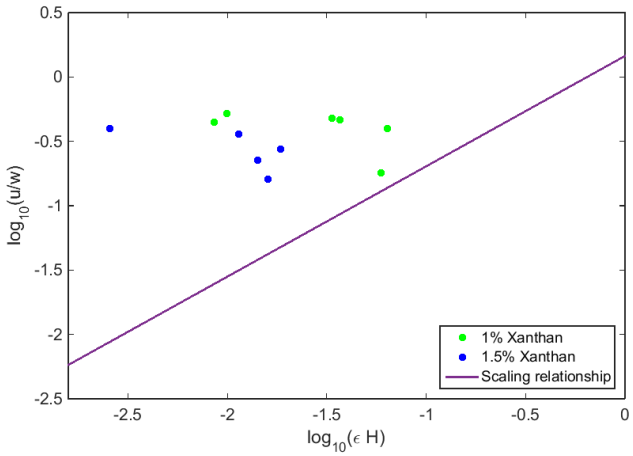

Figure 6.36: Data points for Xanthan experiments, plotting speed at exit divided by channel width, against strain rate at exit multiplied by shelf thickness at exit in log-log space. The theoretical scaling relationship with values appropriate for the 1% Xanthan fluid ($u = w(\rho g'/4B)^{n/(n+1)}(H\epsilon)^{n/(n+1)}$) is given by the purple line.

6.5.8 Principal Strain Rates and Principal Strain Axes for Experimental Velocity Fields

I now use the Principal Strain Rates and Principal Strain Axes to analyse the velocity fields for a selection of the experiments. The Principal Strain Rates and Axes are calculated using the time-averaged and Gaussian-filtered velocity fields as displayed in the previous sections. The complete Principal Strain Rate field is given, but only a sample of the Principal Strain Axes are shown, with axes sampled every 50 pixels (approximately 1.5 cm).

Golden Syrup: Interval 1

For the first interval of the Golden Syrup experiment there is a large section of floating shelf confined within the channel. Here there are low values of the 1st Principal Strain Rate in the upstream sections of the shelf, as shown in Figure 6.37 a) i). As the current nears the exit, there is an area one channel-width upstream from the exit where there is an increase in the value of the 1st Principal Strain Rate, representing increased extension of the shelf as it nears the exit and extensional dynamics become important in governing the flow. These values decrease again as the shelf leaves the confinement of the channel. On the other hand, the 2nd Principal Strain Rate (Fig. 6.37 a) i)) is negative throughout the final 10 cm of the channel, except at the centre of the shelf near the channel exit where there is an area of positive 2nd Principal Strain Rate. The boundary of this region forms an arced curve across the exit of the channel. From this point forward, into the unconfined section of the shelf, the 1st and 2nd Principal Strain Rates are positive, implying that the shelf is spreading in all directions. This feature is similar to the positive 1st and 2nd Principal Strain Rates found in the geophysical examples as a shelf leaves an area of lateral confinement, such as for Amery Ice Shelf.

There is a clear distinctive pattern made by the 1st Principal Strain Axes in the final confined section of the shelf, as shown in Figure 6.37 b) i) (location (1)). As the shelf accelerates towards the channel exit there is shearing with the lateral boundaries, as indicated by the orientation of the 1st Principal Strain Axes; at approximately 45° to the channel walls in the margins of the shelf, pointing downstream. This corresponds with negative 2nd Principal Strain Rates, with the 2nd Principal Strain Axes aligned at 45° upstream. This suggests that there is resistance to flow generated in this area due to the shearing with the side walls in addition to the extensional stresses induced by the hydrostatic driving pressure. As identified earlier, in the region close to the channel exit there may also be a component of the velocity flowing in towards the centre of the channel from the margins, which may act to enhance the lateral extension.

In the centre of the channel in this end region, the 1st Principal Strain Axes are aligned in the flow-direction. At the channel exit, there is a change in the orientation of the 1st Principal Strain Axes, which are now aligned perpendicular to the channel; location (2). This continues for the remaining unconfined shelf. There is a corresponding change in the orientation of the 2nd Principal Strain Axes in this area. Before exiting the channel, the 2nd Principal Strain Rate is negative (implying some resistance to flow is being generated) and the 2nd Principal Strain Axes are aligned perpendicular to the flow along the centre of the channel; location (3). From the channel exit downstream, the 2nd Principal Strain Rate becomes positive, and the 2nd Principal Strain Axes are aligned in the flow direction. This is evidence that once the shelf leaves the confines of the channel it is spreading in both directions, with the lateral spreading being most dominant.

1% Xanthan: Interval 1

Figure 6.38a shows plots of the 1st and 2nd Principal Strain Rates for the 1% Xanthan solution experiment during the first interval. As previously identified by the along-flow strain rate plot in the previous section, there are bands of negative and positive strain rate at the grounding line. In the 1st Principal Strain Rate plot there are no other clear features of the flow, with the margins producing large strain rates that switch sign intermittently along the length of the channel. Similar features are found in the margins of the current in the plot of the 2nd Principal Strain Rate. This is a result of the poorly resolved velocity field in the margins of the shelf. In the 2nd Principal Strain Rate plot, there are negative strain-rate values either side of the grounding line, with a noisy signal throughout most of the sheet and shelf.

From the Principal Strain Axes, shown in Figure 6.38b, the plot is dominated by the noisy signal from the margins of the shelf. However, just upstream of the grounding line, downstream of location (1), the negative 1st Principal Strain Rate Axes are aligned transverse to the flow, while the positive 1st Principal Strain Rate Axes, downstream of the grounding line, are aligned with the flow for approximately 5 cm. This lateral orientation of the negative 1st Principal Strain Rate Axes upstream of the grounding line may be due to the curved shape of the grounding line, which can be inferred from the curved strain-rate features at the grounding line.

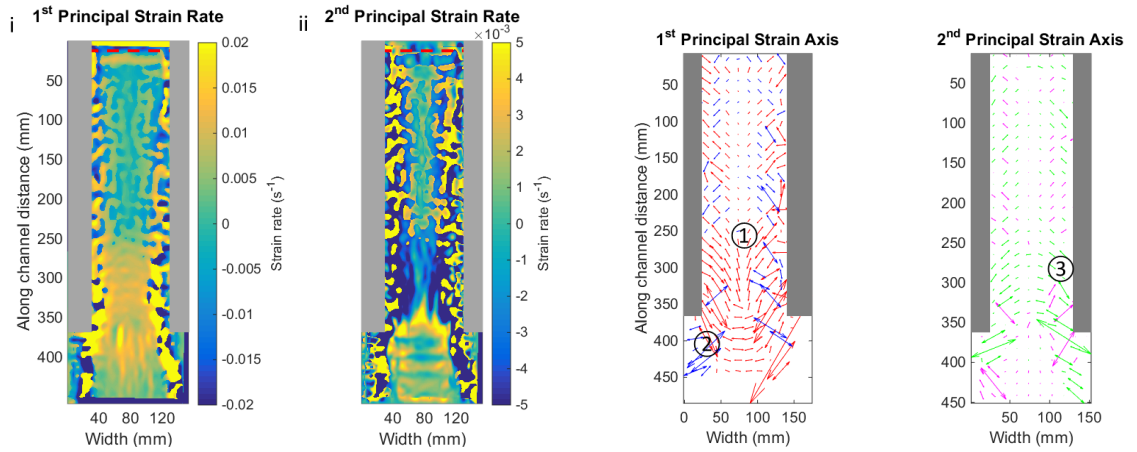

(a) (b)

Figure 6.37: Principal Strain Rates (a) and Principal Strain Axes (b) for the first interval of the Golden Syrup experiment. For Principal Strain Axes; red and magenta represent positive strains, blue and green represent negative strains. Location (1) identifies the start of the extension region as the shelf approaches the channel exit, with axes aligned at 45° in the margins and with the flow in the centre of the chanel. Location (2) marks the unconfined section of the shelf where there is predominantly lateral spreading of the shelf. Location (3) highlights the changing orientation of the 2nd Principal Strain Axes while the shelf is confined, with diagonal axes in the margins and axes aligned perpendicular to the flow in the centre of the channel.

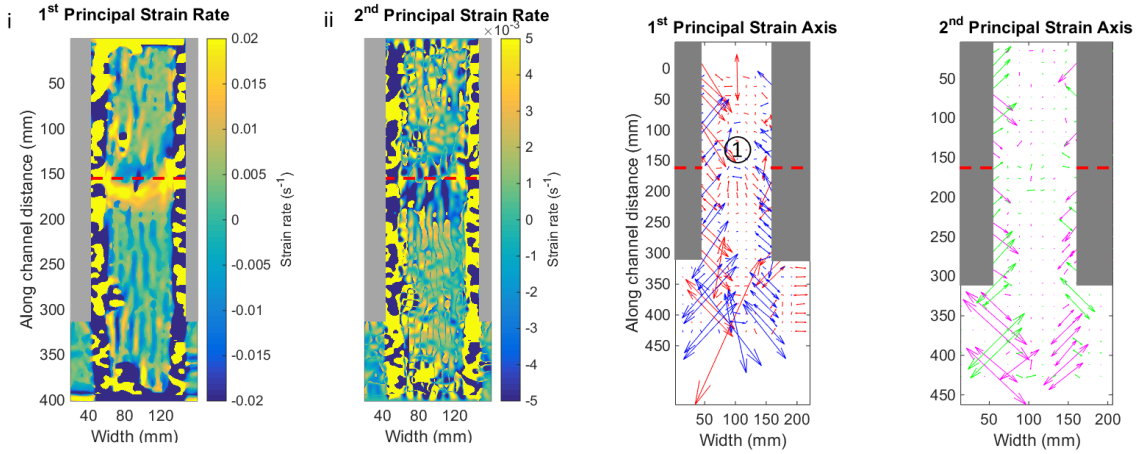

(a) (b)

Figure 6.38: Principal Strain Rates (a) and Principal Strain Axes (b) for the second interval of the 1% Xanthan experiment. For Principal Strain Axes; red and magenta represent positive strains, blue and green represent negative strains.

Summary: Principal Strain Rates and Axes for Experimental Velocity Fields

From the assessment of the experimental data using the Principal Strain Rates and Axes, there is a clear difference between the dynamics observed for the Golden Syrup and Xanthan currents. Very few features can be inferred from the Principal Strain Rates and Axes plots for the Xanthan systems, indicating that there is very little deformation of the current. However, there are clear dynamical features at the grounding line, where there is a transition from vertically shear dominated flow to extension flow in the shelf. These features are identified in the 1st Principal Strain Rate plot, and the 1st Principal Strain Axes plot where upstream of the grounding line there is predominantly compression aligned perpendicular to the flow, which is followed by positive strain rates downstream of the grounding line that are orientated with the flow, suggesting extension of the shelf as it adjusts to the dynamics downstream.

The plots for the Golden Syrup experiment provide features which are comparable with those observed in the geophysical data. Shear margins are clearly identified with Principal Strain Axes aligned at 45° to the channel walls, and negative 2nd Principal Strain Rates imply resistance to shelf flow is being generated here. At the centre of the channel exit, both the 1st and 2nd Principal Strain Rates become positive, which provides evidence that the shelf is spreading in all directions. The Principal Strain Rates continue to be positive throughout the unconfined shelf, indicating that this spreading continues. In the unconfined section of the shelf, the 1st Principal Strain Axes are aligned perpendicular to the main flow of the shelf and illustrate that the lateral spreading of the shelf is dominant. These features are similar to those found on Amery Ice Shelf as the shelf leaves the confinement of pinning points.

6.6 Conclusion

In this Chapter, I have presented results from fluid-mechanical laboratory experiments designed to simulate the flow of an ice shelf in a parallel channel. The main aim of this work was to make comparisons between the dynamics arising from the use of Newtonian and power-law fluids. Analysis was undertaken of the surface-velocity field inferred from PIV tracking of tracer particles distributed on the current surface, along with current thickness profiles captured by a side-viewing camera.

From the experimental results it was clear that the grounded-sheet section of the current has a nearly linear thickness gradient, which remains constant as the grounding advances and the current thickens. This is true for both the Newtonian and power-law currents. Comparing experiments with different fluids we observe that the slope of the grounded

section is increased for increasing values of the power-law flow exponent n. This result agrees with the numerical modelling of Longo et al. (2015) who considered power-law gravity currents that were grounded and confined to a channel. This comparison was made for the section of the grounded gravity current upstream from the nose, which is relevant to the upstream section of the flow being considered in this case.

For all experiments the location of the grounding line was associated with bands of negative followed by positive along-flow strain rate or 1st Principal Strain Rate, which span the width of the channel. This negative strain rate is due to the adjustment of the flow from vertically shear-dominated flow while grounded, to vertical plug flow when the current is floating. As a consequence there is a reduction in the surface velocity, which is observed from the PIV data. The vertically integrated velocity should be constant across the grounding line, however there will be depth dependent changes. The positive strain-rate bands may be due to the removal of basal resistance once the current begins to float. This reduction in resistance will lead to faster flow. In addition, from the theoretical work in Chapter 5, I have identified the potential for extensional adjustment regions at the grounding line, where a thick sheet meets a relatively thin shelf. The thickness of the shelf is determined by the flow dynamics within the confined section of the shelf and potentially further downstream into an unconfined section if hoop stresses are influential. This provides a further explanation for the high positive strain observed downstream of the grounding line.

For the floating sections of the current, there are clear differences between the dynamics observed in the Golden Syrup and Xanthan cases. Evidence from experiments suggests that the Xanthan shelves slip along the channel walls. The velocity field derived from PIV is not resolved well enough to properly determine the dynamics in the narrow boundary layer next to the channel walls. However, cross channel profiles and fits for shear dominated profiles suggest there is slip. In the case of the 1% Xanthan shelf a shear-dominated cross-channel profile with $n = 7$ power-law rheology appears to provide the best fit to the data, but there is considerable mismatch at the boundaries where the velocity is poorly resolved. Once the shelf is unconfined there are low levels of deformation of the shelf and low strain rates, with the dynamics changing little from the confined shelf section. While the shelf is confined, it is clear from the elevation profiles that there is little or no thinning of the shelf. This similarity between the dynamics of the confined and unconfined sections of shelf suggests that the channel walls provide little to no resistance to flow. Comparisons with a purely extensional shelf, suggest that extensional dynamics control the flow. Similar dynamics are observed for both 1% and 1.5% Xanthan shelves.

In contrast, the Golden Syrup shelves appear to conform to the no-slip lateral boundary condition throughout most of the channel, which is shown by the cross-channel profiles in along-channel velocity and the good agreement between the velocity field from the PIV data and the shear-dominated model. There is some mismatch in the margins, which is most likely a result of poorly resolved PIV data, due to an absence of tracer particles in some locations. In comparison to the Xanthan cases, there is also a substantial change in the dynamics of the Golden Syrup shelves as they approach the channel exit. For the Golden Syrup shelves there is a zone of high extension in a region of unit aspect ratio immediately upstream of the exit. In this region the extensional stresses play an important role in governing the flow along with the shear stresses, which are dominant further upstream and provide resistance to the flow. These dynamics were observed in the modelling work in Chapter 5. From the experimental results, it is also apparent that a small cross-channel flow is induced near to the channel exit because of the increase in extension near the channel exit, which acts to thin the shelf, predominantly in the centre of the shelf where extension is largest. The thinning of the shelf in the centre leads to a cross-channel thickness gradient and the resulting flow. Thinning at the centre of the shelf near the opening of a confinement is also observed geophysically for the Ross Ice Shelf.

From the experiments, this extensional zone is followed by lateral spreading of the current as it leaves the channel and a uniform cross-shelf profile in velocity for the unconfined shelf, which can be contrasted to the parabolic profile in the channel. From analysis of the along-shelf velocity, there is little change in the along-shelf flow once the shelf leaves the channel and the lateral spreading of the shelf can be well estimated by a 2D approximation considering a laterally spreading perpendicular cross-section.

It is clear that the Golden Syrup shelf shows similar characteristics to the geophysical examples of confined shelves, with shear margins and lateral spreading as the shelf leaves a lateral confinement. However, fewer direct comparisons can be made with the Xanthan shelves, apart from possible considering the dynamics of ice tongues.

It was observed for both the Golden Syrup and Xanthan shelves that the flow speed at the channel exit exceeded that expected by the scaling relationship considered in Chapter 4. This suggests that the no-slip condition is not met along the channel side walls. For the Xanthan shelves there is evidence to suggest that this is the case. However, for the Golden Syrup it is expected that the no-slip condition holds. This might break down close to the channel exit, or the presence of a cross-channel flow may be influential and is not considered in the scaling analysis.

For future experiments of this nature, a more thoroughly resolved velocity field would be required, so that variations in velocity and boundary conditions can be more accurately measured. This could be achieved with smaller tracer particles that are uniformly distributed across the whole current surface, but would also require a camera with a greater resolution or to reduce the field of view with the same camera. Direct comparisons with geophysical examples may be achieved with a power-law fluid with flow exponent $n \approx 3$. However, this can not be obtained with a low concentration Xanthan solution, as the fluid viscosity (consistency index) reduces with decreasing Xanthan concentration. It would also be necessary to ensure that the no-slip condition is met along the side walls, possibly by using rough walls to increase resistance. Improvements could also be made to the measurements of the shelf-thickness profile by using a laser scanner to produce a 2D altimetry map of the current surface, repeat scans would allow the evolution of the sheet-shelf system to be captured. There is also potential to investigate the flow regime and grounding line evolution systematically by varying parameters such as the input flux, channel width and ocean depth.

Chapter 7

Conclusion

In this thesis I have used geophysical data analysis, idealized models and fluid-mechanical laboratory experiments to understand the flow dynamics and buttressing of ice shelves confined to a channel.

Immediately downstream of the grounding line, where the ice shelf is first formed, we often see convergent flow and negative strain rates in Antarctic ice shelves. This is partly linked to the melting of the ice at depth. From analysis of ice-surface velocity and ice-shelf thickness data, I have estimated rates of thickening and thinning of shelves due to surface and basal processes such as: surface accumulation; surface and basal melting; and basal freeze-on. For Amery Ice Shelf, I estimated rates of thinning of up to 5 m yr^{-1} in the upstream sections of the shelf, which agree with values of basal melting from other studies (Wen et al., 2010; Rignot et al., 2013). This may significantly affect the flow and lead to negative strain rates. Negative strain rates will also be obtained as the shelf decelerates as it spreads to fill a widening channel.

In the laboratory experiments I presented, the grounding line is associated with consecutive bands of negative and positive strain rate that span the width of the channel. In this case, the negative strain rate is due to the transition from vertical shear flow in the grounded part of the current to uniform flow in the vertical when the current is floating. While flux is conserved across the grounding line, there is an adjustment in the vertical structure of the flow, which leads to a deceleration of the surface velocity. The following positive strain-rate band may form as the basal resistance is removed and the shear stress is reduced as the shelf thins. From the idealized modelling, it is apparent that at the upstream boundary of the shelf there can be an extensionally-controlled adjustment region, in which the thickness of the shelf changes rapidly to match the thickness of the shelf downstream.

The shelf thickness is determined principally by the shear dynamics of the confined

shelf. The adjustment region at the grounding line is less than a channel width long, and for a thick sheet adjusting to a thin shelf, this would produce a region of positive strain rate. Therefore, in the case of the experiments, which do not reach steady state, this suggests that there is a thinning of the shelf in an extensionally-controlled adjustment region downstream of the grounding line. In the idealized model, I showed that it is also possible for the shelf to thicken downstream of the grounding line, which may be relevant geophysically if a grounding line was positioned on top of a bedrock cliff, or to an ice shelf downstream of an ice rise.

For a shelf confined within a diverging channel, negative strain rates were found in the upstream section of shelf due to the lateral spreading of the flow and the shear stress from the lateral boundaries. In these geometries, there must be a balance between the hydrostatic pressure from the imposed input flux, the shear stress generated by flow along stationary lateral boundaries and the lateral spreading of the shelf as the channel widens. The magnitude of the resistance generated by shearing and lateral spreading is dependent on the effective viscosity of the shelf, the input flux and the angle of divergence of the channel. In the idealized models, the diverging channel geometry was used as a tool to explore the dynamics of shelves that diverge slowly, such as Amery Ice Shelf. However, from these models it was clear that the dynamics near the point source have a significant effect on the thickness profile throughout the length of the channel.

The final two thirds of Amery Ice Shelf forms an approximately parallel channel. Here the shelf thins almost linearly in the downstream direction. This leads to a mainly positive strain-rate field throughout the shelf, with maximum speed and strain rate (for the confined section of the shelf) achieved at the centre of the channel exit. For this parallel geometry, there is a balance between the imposed input flux at the grounding line and the shear dynamics within the shelf. For a steady-state, shear-only shelf, the thickness profile is determined by the boundary condition at the channel exit, which balances the extensional stress with the hydrostatic pressure of the ocean, and the resistance from shear stresses within the shelf. This leads to a convex profile, with the magnitude of the thickness gradient increasing near to the channel exit, due to the thinning induced by the extensional-stress boundary condition.

When extensional stresses are included in the dynamics, there is only a slight change to the thickness profile. The extensional terms act to stiffen the shelf, such that the channel-exit boundary condition can propagate further upstream. This leads to a reduction in the strain rate at the channel exit, due to the resistance from slower-flowing fluid upstream, but leads to an increase in strain rate upstream as the downstream shelf pulls on the upstream section. Therefore, because the strain rate has increased, there

is less resistance to flow and the shelf becomes thinner. The magnitude of this effect is dependent on the effective viscosity. For a power-law shelf, the inclusion of extensional terms in the rheological model leads to a reduction in effective viscosity throughout the shelf of approximately 50%. The effect is most pronounced along the shelf centre line and towards the shelf front, where the strain rates are high.

In the idealized models presented here, it was assumed that there were no-slip boundary conditions along the channel walls. For the case of a Newtonian ice shelf, this leads to a parabolic cross-channel profile in velocity. In the case of a power-law fluid, shear margins form where the effective viscosity is reduced due to high shear, while the central section of the shelf has an almost uniform profile. This is often the case geophysically, upstream from the channel exit. When extensional dynamics are included in the rheological model, the cross-channel gradient in effective viscosity is reduced and the shear margins become less prominent, with the exception of at the channel exit. Here the shear margins are enhanced, where there are both high shear and high strain rates, which leads to low effective viscosity and in turn further higher strain and shear rates.

From the fluid-mechanical experiments, there was a clear difference in the flow dynamics for Newtonian and power-law shelves. The Golden Syrup (Newtonian) shelves conformed to the assumption of no-slip along the channel walls and produced a parabolic cross-channel profile as expected. However, for the two Xanthan shelves, with $n \approx 6$ and $n > 6$, the data from the experiments suggests that the no-slip condition was not met. These Xanthan currents appear to behave like purely extensional flows, with the dynamics changing very little, if at all, between the confined and unconfined sections of the shelf. For the Golden Syrup shelves, there is good agreement between the idealized models and the experimental results. A convex thickness profile is observed experimentally with an area of increased thinning and strain rate in an aspect ratio 1 area upstream of the channel exit, which agrees with the idealized model.

From the experimental results, it is clear that properties in the margins of the shelf are crucial for determining the shelf flow dynamics and thickness profile. In the geophysical data it is apparent that the margins of ice shelves are often areas with high levels of deformation, with high values of shear and strain rate. These properties of the flow field are linked to the presence and formation of fractures and crevasses, which are observed in the MODIS data. Comparing these crevasse features in ice-shelf margins with the Principal Strain Rates and Axes indicates that the 1^{st} Principal Strain Axes are aligned at 45° to the margin and correspond to positive 1^{st} Principal Strain Rates angled towards the central section of the flow. These features are associated with negative 2^{nd} Principal Strain Rates, with the 1^{st} and 2^{nd} Principal Strain Axes aligned at 90°. This

is due to the shear flow between the stationary, grounded-ice or bedrock and the fast flowing ice shelf. These areas of damaged ice, in the shelf margins, with weak effective viscosity allow high levels of deformation to be achieved. The negative component of the Principal Strain Rates is indicative of shear flow and implies that these areas generate resistance to flow, thereby making a positive contribution to buttressing.

The important role that shear margins play was highlighted with an assessment of the flow speed at ice-shelf calving fronts. It was shown that for ice shelves with intact shear margins (with comparable rheology in the margins and the centre of the shelf) and that are laterally confined by pinning points at the calving front, then the flow at the centre of the calving front conforms to the scaling relationship $u \propto w(\epsilon H)^{3/4}$, proposed by Hindmarsh (2012). For those shelves with weak or damaged margins or those that are not laterally confined at the calving front, the flow speed at the calving front is greater. This is because they are subject to reduced resistance from the lateral boundaries.

This scaling relationship did not hold for the experimental results, which suggests that even the Golden-Syrup shelf may slip along the channel walls in the final part of the channel. However, this may also be explained by the lateral flow observed near the channel exit. This is due to the presence of a lateral gradient in shelf thickness, which is induced by enhanced extension in the centre of the shelf, in comparison to extension in the margins.

For Amery Ice Shelf, the final third of the shelf is a region of high positive strain rate, as the channel becomes wider and the shelf approaches the exit of the channel. This large strain-rate feature is not observed in the parallel-channel models, but is observed for diverging channel models when the effective viscosity is sufficiently low that the resistance from lateral spreading has a reduced impact on the dynamics.

In the final part of Amery Ice Shelf both Principal Strain Rates become positive, indicating that there is spreading of the shelf in all directions. While the shelf is confined, the 1st Principal Strain Axes are mainly aligned in the flow direction, with the 2nd Principal Strain Axes aligned perpendicular to the flow. At the channel exit the 1st Principal Strain Axes becomes aligned perpendicular to the flow, indicating the main component of extension is lateral.

Once the shelf leaves the confines of the channel, it is expected that there will be some lateral spreading of the shelf. In the case of the Newtonian shelves in the experiments, a 2D approximation of the spreading of the shelf after it leaves the channel exit provides a good fit to the data from experiments. For power-law shelves the rate of lateral spreading

is reduced, and for the Xanthan shelves lateral spreading was too slow to be observed in these experiments.

While the shelf is confined, the majority of the shelf contributes to positive buttressing via compression and shear stress. When both Principal Strain Rates are positive this implies that there is no longer a positive contribution to buttressing from compression or shearing. The upstream boundary of this region was defined to be the compressive arch, and Doake et al. (1998) hypothesised that this compressive arch would be stable to calving events downstream of the arch. However, I have proposed that there are additional positive contributions to buttressing downstream of the compressive arch due to hoop stresses. Therefore, if a section of ice were removed downstream of the arch, this may result in a reduction in total buttressing generated by the ice shelf.

Hoop stresses make a positive contribution to buttressing if the rate of lateral (azimuthal) extension is greater than the along-flow (radial) extension. From the surface-velocity data it is possible to determine pointwise the areas of the shelf that make a positive contribution to buttressing via hoop stresses. If these regions are connected to other, positively buttressing regions linked to the grounding line, then they will contribute to buttressing of the grounded ice. This technique allows areas that make no contribution to buttressing, or provide a negative contribution to buttressing, to be identified. These areas could be removed from the shelf causing no increase in the rate of ice discharge from the grounded ice. The non-positive-buttressing regions identified by this method usually form concave regions at the calving front of ice shelves and are smaller than the regions that would be identified using only the upstream boundary of the positive Principal Strain Rates.

In this thesis, I have shown how idealized modelling and fluid mechanical experiments can be combined to inform interpretations of field data and used to elucidate the flow dynamics and buttressing of ice shelves.

Bibliography

Albrecht, T. and Levermann, A. (2012). Fracture field for large-scale ice dynamics. *J. Glaciol.*, 58(207):165–176.

Alley, R. B., Horgan, H. J., Joughin, I., Cuffey, K. M., Dupont, T. K., Parizek, B. R., Anandakrishnan, S., and Bassis, J. (2008). A simple law for ice-shelf calving. *Science*, 322(5906):1344.

Anandakrishnan, S. and Alley, R. B. (1997). Tidal forcing of basal seismicity of ice stream C, West Antarctica, observed far inland. *Journal of Geophysical Research: Solid Earth*, 102(B7):15183–15196.

Bamber, J. L., Vaughan, D. G., and Joughin, I. (2000). Widespread complex flow in the interior of the Antarctic Ice Sheet. *Science*, 287(February):16–19.

Bartholomew, I., Nienow, P., Mair, D., Hubbard, A., King, M. A., and Sole, A. (2010). Seasonal evolution of subglacial drainage and acceleration in a Greenland outlet glacier. *Nature Geoscience*, 3(6):408–411.

Bassis, J. N. and Jacobs, S. (2013). Diverse calving patterns linked to glacier geometry. *Nat. Geosci.*, 6(10):833–836.

Benn, D. I., Warren, C. R., and Mottram, R. H. (2007). Calving processes and the dynamics of calving glaciers. *Earth-Science Rev.*, 82(3-4):143–179.

Berger, S., Favier, L., Drews, R., Derwael, J.-J., and Pattyn, F. (2016). The control of an uncharted pinning point on the flow of an Antarctic ice shelf. *Journal of Glaciology*, pages 1–9.

Blankenship, D. D., Bentley, C. R., Rooney, S. T., and Alley, R. B. (1986). Seismic measurements reveal a saturated porous layer beneath an active Antarctic ice stream. *Nature*, 322(6074):54–57.

Budd, W. F. (1966). The dynamics of the Amery Ice Shelf. *Journal of Glaciology*, 6(45):335–358.

Church, J., Clark, P., Cazenave, A., Gregory, J., Jevrejeva, S., Levermann, A., Merrifield, M., Milne, G., Nerem, R., Nunn, P., Payne, A., Pfeffer, W., Stammer, D., and Unnikrishnan, A. (2013). Sea level change. *Climate Change 2013: The Physical Science Basis. Contribution of Working Group I to the Fifth Assessment Report of the Intergovernmental Panel on Climate Change*, pages 1137–1216.

Cuffey, K. and Paterson, W. (2010). *The Physics of Glaciers*. Butterworth-Heinemann. 4th Edition.

Di Pietro, N. D. and Cox, R. G. (1979). The Spreading of a Very Viscous Liquid on a Quiescent Water Surface. *The Quarterly Journal of Mechanics and Applied Mathematics*, 32(4):355–381.

Doake, C., Corr, H., Rott, H., Skvarca, P., and Young, N. (1998). Breakup and conditions for stability of the northern Larsen Ice Shelf, Antarctica. *Nature*, 391(6669):778–780.

Fretwell, P., Pritchard, H. D., Vaughan, D. G., Bamber, J. L., Barrand, N. E., Bell, R., Bianchi, C., Bingham, R. G., Blankenship, D. D., Casassa, G., Catania, G., Callens, D., Conway, H., Cook, A. J., Corr, H. F. J., Damaske, D., Damm, V., Ferraccioli, F., Forsberg, R., Fujita, S., Gim, Y., Gogineni, P., Griggs, J. A., Hindmarsh, R. C. A., Holmlund, P., Holt, J. W., Jacobel, R. W., Jenkins, A., Jokat, W., Jordan, T., King, E. C., Kohler, J., Krabill, W., Riger-Kusk, M., Langley, K. A., Leitchenkov, G., Leuschen, C., Luyendyk, B. P., Matsuoka, K., Mouginot, J., Nitsche, F. O., Nogi, Y., Nost, O. A., Popov, S. V., Rignot, E., Rippin, D. M., Rivera, A., Roberts, J., Ross, N., Siegert, M. J., Smith, A. M., Steinhage, D., Studinger, M., Sun, B., Tinto, B. K., Welch, B. C., Wilson, D., Young, D. A., Xiangbin, C., and Zirizzotti, A. (2013). Bedmap2: Improved ice bed, surface and thickness datasets for Antarctica. *Cryosphere*, 7(1):375–393.

Fricker, H. A. (2005). Multi-year monitoring of rift propagation on the Amery Ice Shelf, East Antarctica. *Geophysical Research Letters*, 32(2):L02502.

Fricker, H. A., Young, N. W., Allison, I., and Coleman, R. (2002). Iceberg calving from the Amery Ice Shelf, East Antarctica. *Annals of Glaciology*, 34:241–246.

Fürst, J. J., Durand, G., Gillet-Chaulet, F., Merino, N., Tavard, L., Mouginot, J., Gourmelen, N., and Gagliardini, O. (2015). Assimilation of Antarctic velocity observations provides evidence for uncharted pinning points. *Cryosphere*, 9(4):1427–1443.

Fürst, J. J., Durand, G., Gillet-chaulet, F., Tavard, L., Rankl, M., Braun, M., and Gagliardini, O. (2016). The safety band of Antarctic ice shelves. *Nature Clim. Change*, (February):2014–2017.

Gudmundsson, G. H. (2011). The Cryosphere Ice-stream response to ocean tides and the form of the basal sliding. pages 259–270.

Gudmundsson, G. H. (2013). Ice-shelf buttressing and the stability of marine ice sheets. *The Cryosphere*, 7(2):647–655.

Haran, T., Bohlander, J., Scambos, T., Painter, T., and Fahnestock, M. (2005). MODIS Mosaic of Antarctica 2003-2004 (MOA2004) Image Map.

Hewitt, I. J. (2011). Modelling distributed and channelized subglacial drainage: The spacing of channels. *Journal of Glaciology*, 57(202):302–314.

Hewitt, I. J. (2013). Seasonal changes in ice sheet motion due to melt water lubrication. *Earth and Planetary Science Letters*, 371-372:16–25.

Hindmarsh, R. C. A. (2012). An observationally validated theory of viscous flow dynamics at the ice-shelf calving front. *J. Glaciol.*, 58(208):375–387.

Holland, P. R., Brisbourne, A., Corr, H. F. J., McGrath, D., Purdon, K., Paden, J., Fricker, H. A., Paolo, F. S., and Fleming, A. H. (2015). Oceanic and atmospheric forcing of Larsen C Ice-Shelf thinning. *Cryosphere*, 9(3):1005–1024.

Holland, P. W. and Welsch, R. E. (1977). Robust regression using iteratively reweighted least-squares. *Communications in Statistics -Theory and Methods*, 6:9:813–827.

Huppert, H. E. (1986). The intrusion of fluid mechanics into geology. *Journal of Fluid Mechanics*, 173(-1):557.

Jacobs, S. S., Jenkins, A., Giulivi, C. F., and Dutrieux, P. (2011). Stronger ocean circulation and increased melting under Pine Island Glacier ice shelf. *Nature Geoscience*, 4(8):519–523.

Jenkins, A., Dutrieux, P., Jacobs, S. S., McPhail, S. D., Perrett, J. R., Webb, A. T., and White, D. (2010). Observations beneath Pine Island Glacier in West Antarctica and implications for its retreat. *Nature Geoscience*, 3(7):468–472.

Joughin, I., MacAyeal, D. R., and Tulaczyk, S. (2004). Basal shear stress of the Ross ice streams from control method inversions. *J. Geophys. Res. B Solid Earth*, 109(9):1–20.

Joughin, I. and Padman, L. (2003). Melting and freezing beneath Filchner-Ronne Ice Shelf, Antarctica. *Geophysical Research Letters*, 30(9):0–3.

Joughin, I., Rignot, E., Rosanova, C. E., Lucchitta, B. K., and Bohlander, J. (2003). Timing of Recent Accelerations of Pine Island Glacier, Antarctica. *Geophysical Research Letters*, 30(13):n/a–n/a.

Joughin, I., Smith, B. E., and Holland, D. M. (2010). Sensitivity of 21st century sea level to ocean-induced thinning of Pine Island Glacier, Antarctica. *Geophysical Research Letters*, 37(20):1–5.

Kowal, K. N., Pegler, S. S., and Worster, M. G. (2016). Dynamics of laterally confined marine ice sheets. *Journal of Fluid Mechanics*, 790:R2.

Longo, S., Di Federico, V., and Chiapponi, L. (2015). Non-Newtonian power-law gravity currents propagating in confining boundaries. *Environmental Fluid Mechanics*, 15(3):515–535.

MacAyeal, D. R. (1989). Large-scale ice flow over a viscous basal sediment: Theory and application to ice stream B, Antarctica. *Journal of Geophysical Research: Solid Earth*, 94(B4):4071–4087.

Ng, F. S. L. (2015). Spatial complexity of ice flow across the Antarctic Ice Sheet. *Nature Geoscience*, 8(11):847–850.

Oerlemans, J. and van der Veen, C. J. (1984). *Ice Sheets and Climate*. Springer Netherlands, Dordrecht.

Pegler, S. S. (2012). *The fluid mechanics of ice-shelf buttressing*. PhD thesis, St Catherine's College, University of Cambridge.

Pegler, S. S., Kowal, K. N., Hasenclever, L. Q., and Worster, M. G. (2013). Lateral controls on grounding-line dynamics. *Journal of Fluid Mechanics*, 722:R1.

Pegler, S. S., Lister, J. R., and Worster, M. G. (2012). Release of a viscous power-law fluid over an inviscid ocean. *Journal of Fluid Mechanics*, 700(April):63–76.

Pegler, S. S. and Worster, M. G. (2012). Dynamics of a viscous layer flowing radially over an inviscid ocean. *Journal of Fluid Mechanics*, 696(March):152–174.

Pritchard, H., Ligtenberg, S., Fricker, H., Vaughan, D., van den Broeke, M., and Padman, L. (2012). Antarctic ice-sheet loss driven by basal melting of ice shelves. *Nature*, 484(7395):502–505.

Reeh, N., Christensen, E. L., Mayer, C., and Olesen, O. B. (2003). Tidal bending of glaciers : a linear viscoelastic approach.

Riahi, K., Rao, S., Krey, V., Cho, C., Chirkov, V., Fischer, G., Kindermann, G., Nakicenovic, N., and Rafaj, P. (2011). RCP 8.5 - A scenario of comparatively high greenhouse gas emissions. *Climatic Change*, 109(1):33–57.

Rignot, E. (2008). Changes in West Antarctic ice stream dynamics observed with ALOS PALSAR data. *Geophysical Research Letters*, 35(12):1–5.

Rignot, E., Casassa, G., Gogineni, P., Krabill, W., Rivera, A., and Thomas, R. (2004). Accelerated ice discharge from the Antarctic Peninsula following the collapse of Larsen B ice shelf. *Geophysical Research Letters*, 31(18):L18401.

Rignot, E., Jacobs, S., Mouginot, J., and Scheuchl, B. (2013). Ice-shelf melting around Antarctica. *Science*, 341(6143):266–70.

Rignot, E., Mouginot, J., and Scheuchl, B. (2011a). Ice flow of the Antarctic ice sheet. *Science (New York, N.Y.)*, 333(6048):1427–1430.

Rignot, E., Mouginot, J., and Scheuchl, B. (2011b). MEaSUREs InSAR-Based Antarctica Ice Velocity Map [450m]. Boulder, Colorado USA: NASA DAAC at the National Snow and Ice Data Center.

Robin, G. d. Q. (1979). Formation, flow, and disintegration of ice shelves. *Journal of Glaciology*, 24(90):259–271.

Rott, H., Rack, W., Skvarca, P., and De Angelis, H. (2002). Northern Larsen Ice Shelf, Antarctica: Further retreat after collapse. *Ann. Glaciol.*, 34:277–282.

Sandhäger, H. (2003). Numerical study on the influence of fractures and zones of weakness on the flow regime of Larsen Ice Shelf. *FRISP Rep.*, 14(14).

Sayag, R. and Worster, M. G. (2013a). Axisymmetric gravity currents of power-law fluids over a rigid horizontal surface. *Journal of Fluid Mechanics*, 716:R5.

Sayag, R. and Worster, M. G. (2013b). Elastic dynamics and tidal migration of grounding lines modify subglacial lubrication and melting. *Geophysical Research Letters*, 40(22):5877–5881.

Scambos, T., Hulbe, C., and Fahnestock, M. (2003). Climate-induced ice shelf disintegration in the Antarctic Peninsula. volume 79, pages 79–92.

Scambos, T. A., Bohlander, J. A., Shuman, C. A., and Skvarca, P. (2004). Glacier acceleration and thinning after ice shelf collapse in the Larsen B embayment, Antarctica. *Geophysical Research Letters*, 31(18):2001–2004.

Schoof, C. (2007). Marine ice-sheet dynamics. Part 1. The case of rapid sliding. *Journal of Fluid Mechanics*, 573:27.

Shepherd, A., Ivins, E. R., A, G., Barletta, V. R., Bentley, M. J., Bettadpur, S., Briggs, K. H., Bromwich, D. H., Forsberg, R., Galin, N., Horwath, M., Jacobs, S., Joughin, I.,

King, M. a., Lenaerts, J. T. M., Li, J., Ligtenberg, S. R. M., Luckman, A., Luthcke, S. B., McMillan, M., Meister, R., Milne, G., Mouginot, J., Muir, A., Nicolas, J. P., Paden, J., Payne, A. J., Pritchard, H., Rignot, E., Rott, H., Sørensen, L. S., Scambos, T. A., Scheuchl, B., Schrama, E. J. O., Smith, B., Sundal, A. V., van Angelen, J. H., van de Berg, W. J., van den Broeke, M. R., Vaughan, D. G., Velicogna, I., Wahr, J., Whitehouse, P. L., Wingham, D. J., Yi, D., Young, D., and Zwally, H. J. (2012). A reconciled estimate of ice-sheet mass balance. *Science (New York, N.Y.)*, 338(6111):1183–9.

Shepherd, A., Wingham, D., and Rignot, E. (2004). Warm ocean is eroding West Antarctic Ice Sheet. *Geophysical Research Letters*, 31(23):1–4.

Thompson, J., Simons, M., and Tsai, V. C. (2014). Modeling the elastic transmission of tidal stresses to great distances inland in channelized ice streams. pages 2007–2029.

van den Broeke, M. (2005). Strong surface melting preceded collapse of Antarctic Peninsula ice shelf. *Geophysical Research Letters*, 32(12):1–4.

Vaughan, D. G. (1993). Relating the occurrence of crevasses to surface strain rates.

Vaughan, D. G. and Doake, C. S. M. (1996). Recent atmospheric warming and retreat of ice shelves on the Antarctic Peninsula.

Vaughan, D. G., Marshall, G. J., Connolley, W. M., Parkinson, C., Mulvaney, R., Hodgson, D. A., King, J. C., Pudsey, C. J., and Turner, J. (2003). Recent Rapid Regional Climate Warming on the Antarctic Peninsula. *Climatic Change*, 60(3):243–274.

Vieli, A., Payne, A. J., Du, Z., and Shepherd, A. (2006). Numerical modelling and data assimilation of the Larsen B ice shelf, Antarctic Peninsula. *Philos. Trans. A. Math. Phys. Eng. Sci.*, 364(1844):1815–1839.

Walker, C. C., Bassis, J. N., Fricker, H. A., and Czerwinski, R. J. (2015). Observations of interannual and spatial variability in rift propagation in the Amery Ice Shelf, Antarctica, 200214. *Journal of Glaciology*, 61(226):243–252.

Weertman, J. (1974). Stability of the junction of an ice sheet and an ice shelf. *Journal of Glaciology*, 13(67):3–11.

Wen, J., Wang, Y., Wang, W., Jezek, K. C., Liu, H., and Allison, I. (2010). Basal melting and freezing under the Amery Ice Shelf, East Antarctica. *Journal of Glaciology*, 56(195):81–90.

Appendix A

Appendix: Fundamental Equations for the Flow of Ice Shelves: Viscoelastic Rheology for Tidal Flexure

The viscoelastic rheological model for ice shelves subject to tidal forcing proposed by Reeh et al. (2003) includes an instantaneous elastic response, delayed elastic response and viscous response. These three responses correspond with three components of the strain in this model: ε_I, ε_D and ε_V. The model gives an equation for the total strain ε of the form

$$\varepsilon = \varepsilon_I + \varepsilon_D + \varepsilon_V, \tag{A.1}$$

$$= \frac{3\sigma'}{3E_I} + \frac{3\sigma'}{2E_D}\left[1 - \exp -\frac{E_D}{3\mu_D}t\right] + \frac{\sigma'}{2\mu_V}t, \tag{A.2}$$

where: σ' is the deviatoric stress; E_I is the Young's modulus; E_D is the elastic modulus and μ_D is the elastic viscosity associated with the delayed elastic response; and μ_V is the viscosity related to slow viscous deformation. From the article by Reeh et al. (2003), these parameters have the following typical values

$$\mu_V = 25000 \text{ GPas}, \tag{A.3}$$

$$E_I = 9.3 \text{ GPa}, \tag{A.4}$$

$$E_D = 10 \text{ GPa}, \tag{A.5}$$

$$\mu_D = 600 \text{ GPas}. \tag{A.6}$$

I use these values along with a typical maximum deviatoric stress at the grounding line during the tidal cycle ($\sigma' = 10^4$ Pa (Thompson et al., 2014)) to calculate the evolution

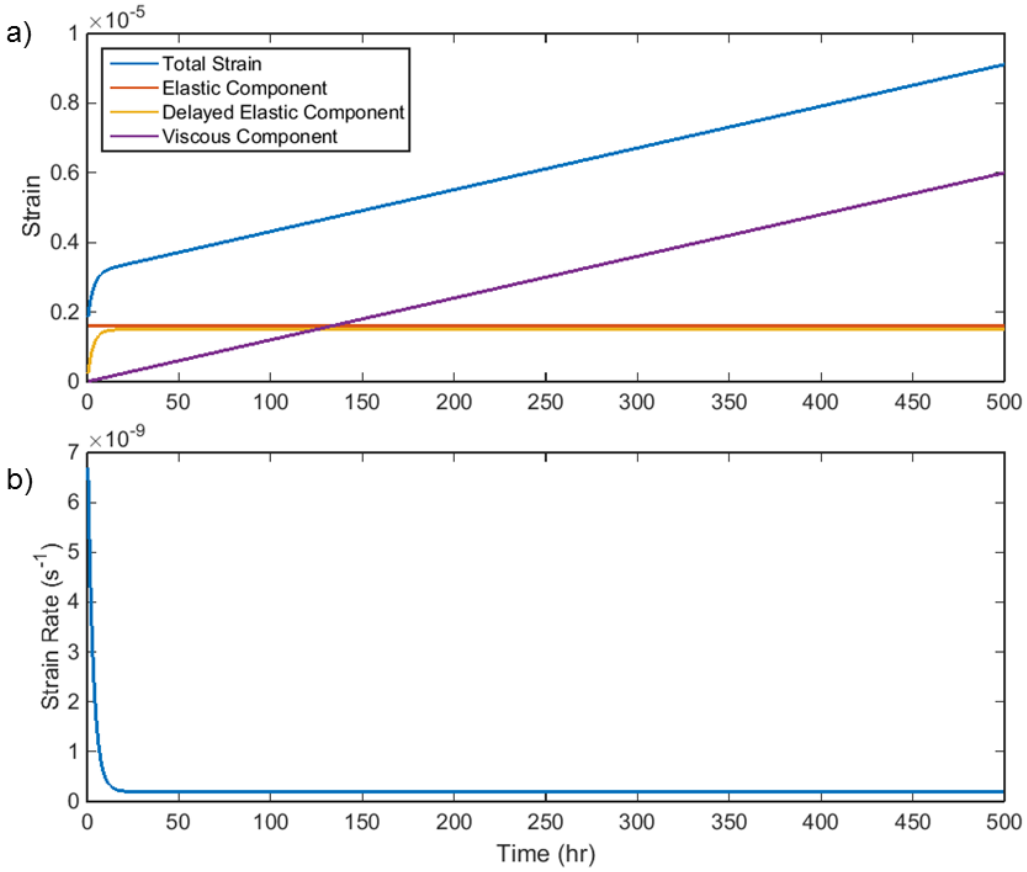

Figure A.1: Strain (a) and strain rate (b) evolution for a viscoelastic ice-shelf rheology (Reeh et al., 2003), where a constant loading of 10^4 Pa has been applied. In the upper panel (a) the three components of the strain: instantaneous elastic; delayed elastic; and viscous, are shown, together with the total strain. The lower panel (b) shown the strain rate (total) against time.

of the strain and strain rate for a constantly imposed loading of this magnitude. The results can be seen in Figure A.1. It is clear in Figure A.1a that from the outset there is a significant elastic response, which is maintained for the length of the loading. Within approximately 10 hours the strain value from the delayed elastic response is of a similar value. After approximately 6 days of loading the viscous strain reaches a value comparable with the instantaneous elastic response. After a further 6 days the viscous response is greater than the combined response from the instantaneous and delayed elastic response. Therefore, for timescales of interest in this thesis (1 - 1000+ years) the viscous dynamics dominate. From the strain-rate plot in Figure A.1b it is evident that there are initially high strain rates within the first few hours of the stress being applied. However, there is then a decrease to the strain rate associated with the viscous deformation after 20 hours.

Appendix B

Appendix: Ice-Surface Velocity Data for Antarctic Ice Shelves: Basal Melt and Freeze-on Rates

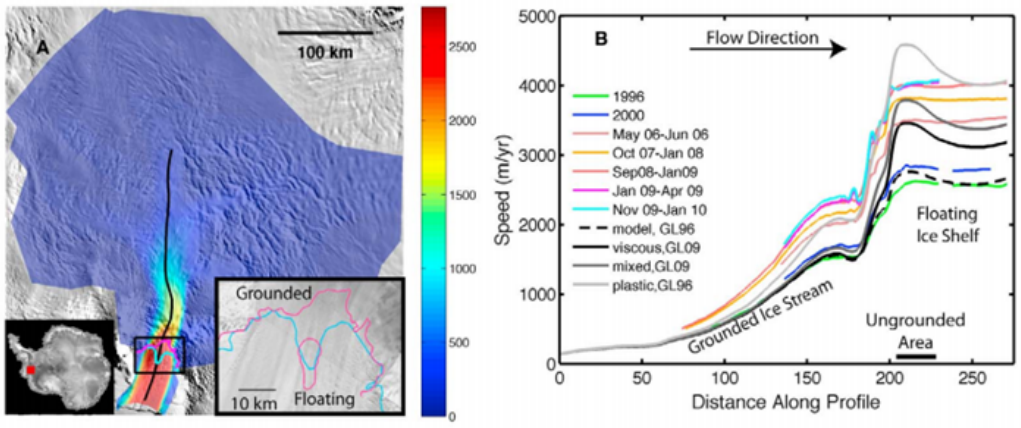

Figure B.1: Figure taken from Joughin et al. (2010). Showing acceleration of Pine Island Glacier and Ice Shelf between 1996 and Jan 2010. The ice shelf appears to have approximately a uniform speed along the length of the shelf, but accelerates from 2500 m yr^{-1} to 4000 m yr^{-1}, between 1996 and 2010.

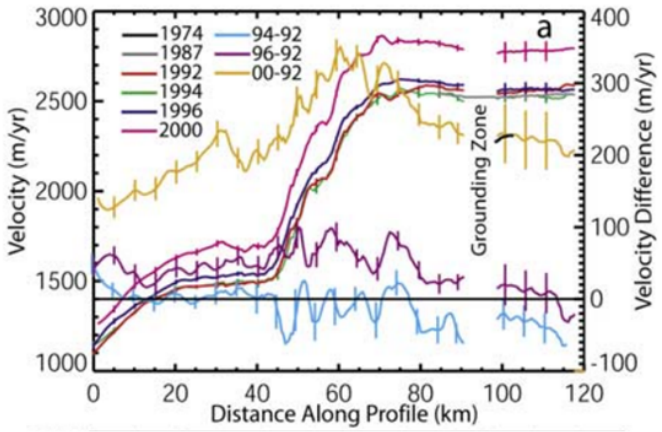

Figure B.2: Figure taken from Joughin et al. (2003). Shows the change in flow speed of PIG from 1974 to 2000. Between 1987 and 1996 the flow speed is almost constant, but there is then a substantial acceleration between 1996 and 2000.

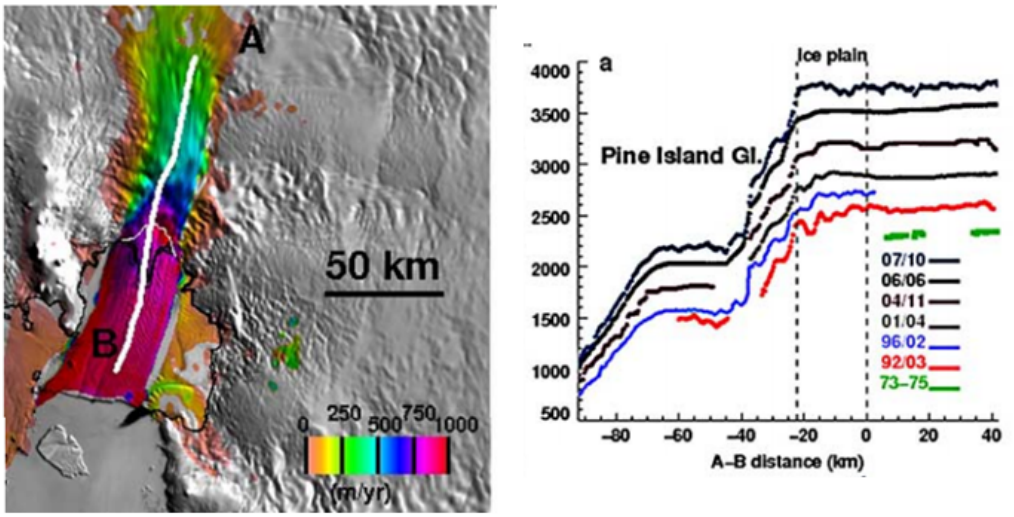

Figure B.3: Figure taken from Rignot (2008). Showing the acceleration of PIG between 1992 and 2007.

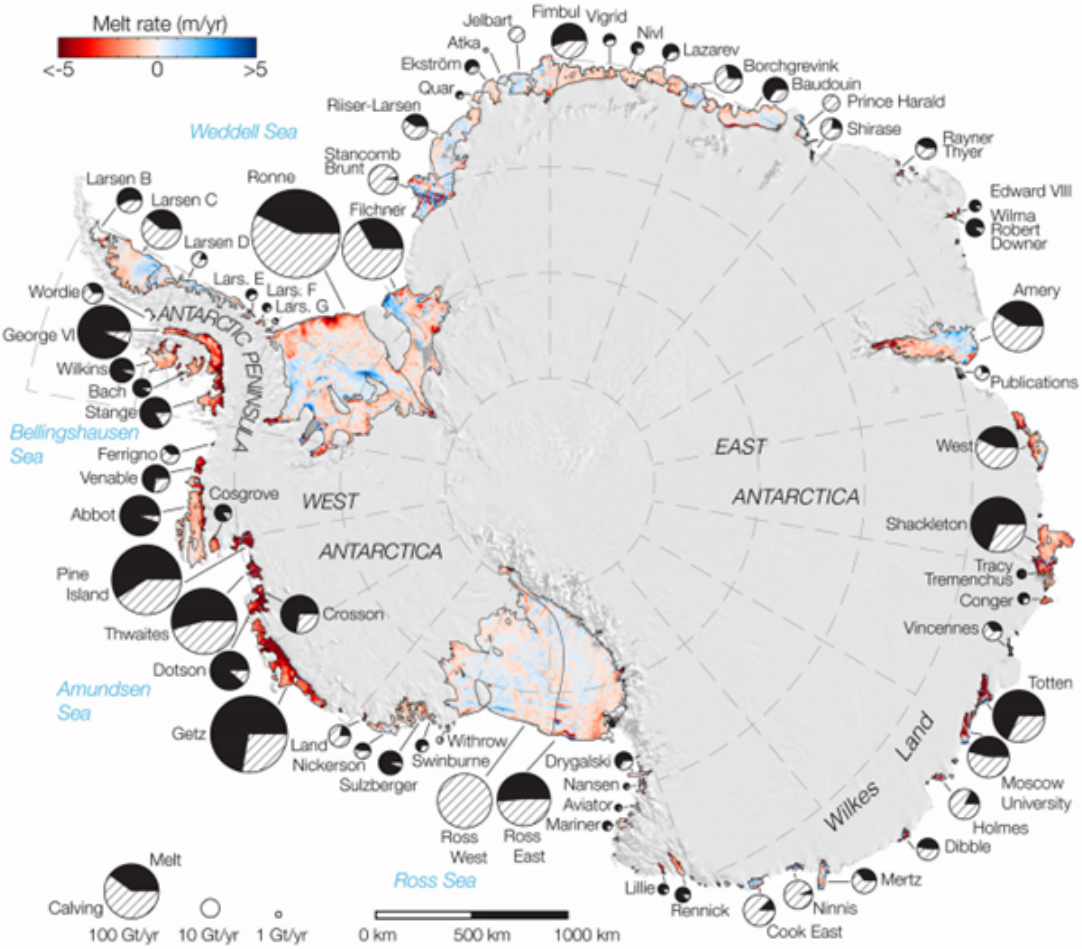

Figure B.4: Figure taken from Rignot et al. (2013). Basal melt rates and freeze-on for Antarctic Ice Shelves. Area of circles represents mass loss from those shelves, with hatched fill corresponding to iceberg calving and black fill to basal melting.

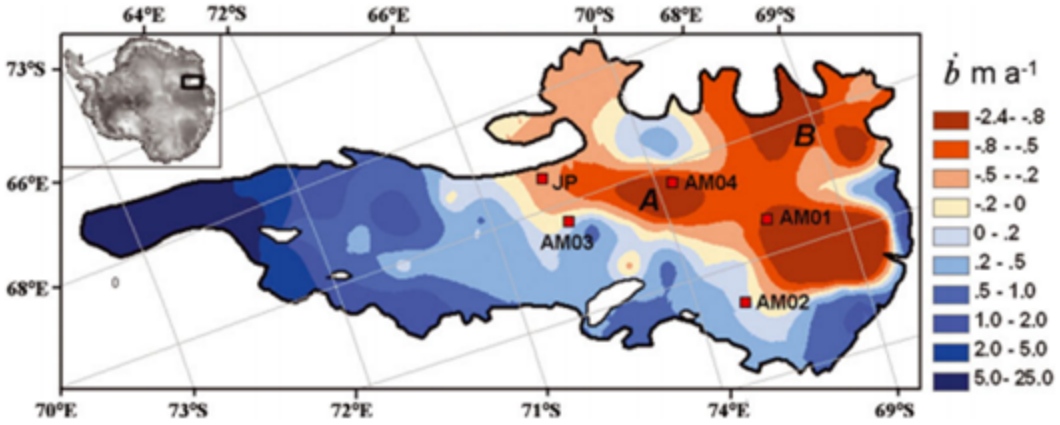

Figure B.5: Figure taken from Wen et al. (2010). Basal melt rates and freeze-on for Amery Ice Shelf. Red/negative areas represent freeze-on, and blue/positive areas represent melt.

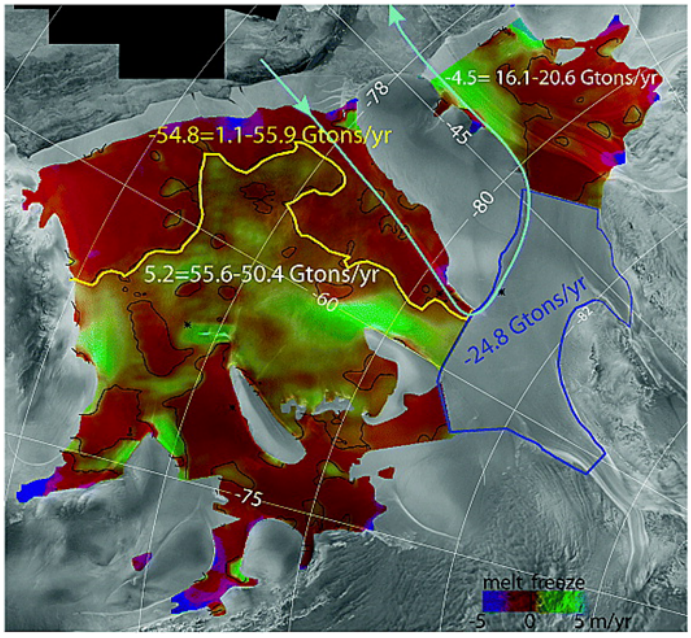

Figure B.6: Figure taken from Joughin and Padman (2003). Basal melt rates and freeze-on for Ronne Ice Shelf. Green/positive areas represent freeze-on, and blue/purple/negative areas represent melt.

Appendix C

Appendix: Assessment of Ice Flow Dynamics in the Zone Close to the Calving Front

The results of the Robust Regression procedure applied iteratively to the full dataset can be seen in Figure C.1. Here an R^2 value of 0.83 is achieved once 9 ice shelves have been removed from the initial dataset. The resulting regression model takes the form $\log(u/w) = A + B\log(\epsilon H)$, with intercept $A = 1.67$ and slope $B = 0.64$.

The full dataset used in this work is given in Table C.1, with values for: shelf width, shelf thickness, flow speed, strain rate, mean speed over final 20 km section, standard deviation in strain rate and speed, and error in velocity field from Rignot et al. (2011a).

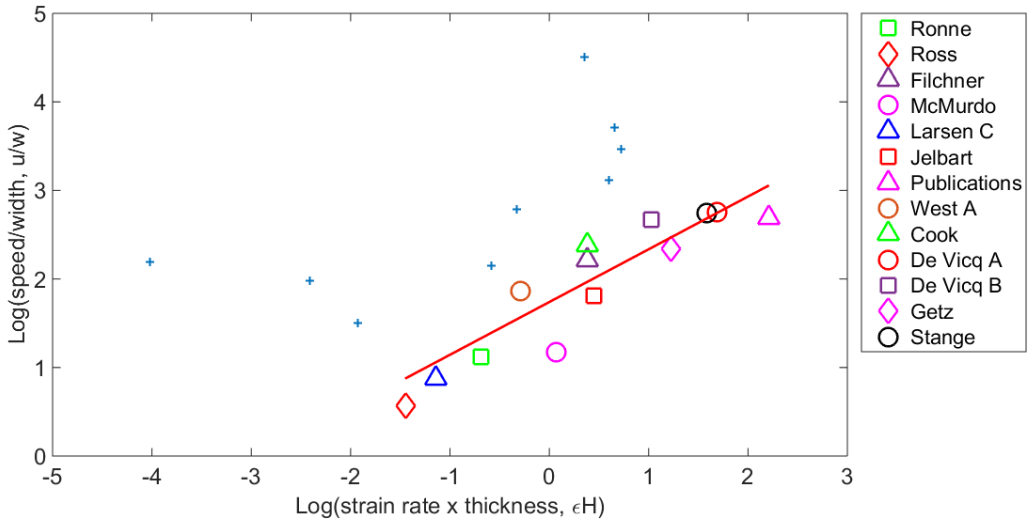

Figure C.1: Linear regression achieved after removing 9 outlying data points using an iterative Robust Regression process. Removed points shown as blue crosses.

Shelf	Width (km)	C.F. Thick-ness (m)	C.F. Speed (m yr^{-1})	Strain rate (yr^{-1})	Mean speed (m yr^{-1})	Strain rate S.D.	Speed S.D.	Rignot - Speed Error
Amery	165	233	1419	0.0024	1407	0.00067	10. 7	$\sim$ 9
Borchgrevinkisen	105	240	472	0.0006	469	0.00084	2.4	$\sim$ 4 - 16
Cook	75	360	809	0.0041	772	0.0050	20.1	$\sim$ 4-12
De Vicq A	55	452	860	0.0119	760	0.0056	45.6	$\sim$ 4
De Vicq B	80	258	1160	0.0099	1101	0.0025	39.8	$\sim$ 4
Dolleman	65	5	584	0.0036	574	0.0047	14.4	$\sim$ 5
Filchner	170	432	1554	0.0034	1533	0.0015	11.9	$\sim$ 7
Fimbul	105	288	762	0.0003	758	0.00073	1.9	$\sim$ 8 - 12
Getz	70	335	725	0.0102	624	0.0040	46.5	$\sim$ 4
Jelbart	95	260	583	0.006	551	0.0065	39.3	$\sim$ 8 - 16
Larsen C	290	307	698	0.0010	690	0.00037	4.3	$\sim$ 4
McMurdo	130	327	420	0.0033	404	0.0025	9.4	$\sim$ 7
Ninnis	40	584	1274	0.0035	1259	0.0058	21.5	$\sim$ 8 - 14
PIG	45	500	4067	0.0029	4030	0.0057	10.9	$\sim$ 3
Publications	55	234	813	0.0389	582	0.0204	193.4	$\sim$ 5
Ronne	460	353	1410	0.0014	1398	0.00001	6.7	$\sim$ 9
Robert Glacier	16	137	651	0.0140	512	0.0102	65.0	$\sim$ 10 - 14
Ross	621	242	1100	0.0010	1090	0.0009	4.0	$\sim$ 4
Shackleton	110	231	1793	0.0031	1772	0.0021	19.4	$\sim$ 9 - 12
Stange	45	231	699	0.0210	560	0.0115	118.7	$\sim$ 7
Venable	30	383	675	0.0047	631	0.0048	24.1	$\sim$ 5
West A	120	187	773	0.0040	747	0.0014	19.3	$\sim$ 8 - 12

Table C.1: Table showing full dataset for 22 Antarctic ice shelves.

Supplementary Material: Assessment of Flow Dynamics in the Zone Close to the Calving Front of Antarctic Ice Shelves

Martin G. Wearing[1,2], Richard C. A. Hindmarsh[1], M. Grae Worster[2]

[1]British Antarctic Survey, Cambridge, CB3 0ET, UK
[2]Department of Applied Mathematics and Theoretical Physics, University of Cambridge, Cambridge, CB3 0WA

This supplementary material contains plots for 22 Antarctic ice shelves with each ice shelf assigned a separate page.

The top four plots show:

- the MODIS imagery used in the geophysical classification (Haran and others (2005)).
- the non-filtered ice-surface velocity field (450m resolution) for each ice shelf (using velocity dataset from Rignot and others (2011)).
- the along-flow strain rate calculated from the filtered velocity field (see below for filtering details). Additional black line indicates the flow line of maximum speed.
- the absolute transverse shear rate calculated from the filtered velocity field. This is displayed with a colour bar ranging from 0 - 0.05yr^{-1}, with saturated regions indicating values greater than 0.05yr^{-1}.

Each of these plots also includes a grounding line and coastline outline from MODIS (Haran and others (2005)).

The filtered velocity field used to calculate the along-flow strain rate and transverse shear rate is generated by applying a low-pass Gaussian filter to the original velocity field from Rignot and others (2011). We use the MATLAB *imfilter* function, with a Gaussian filter of size 9km (20 grid cells) and standard deviation 1.8km (4 grid cells). As a result of this filtering there are some artefacts in the along-flow strain rate and transverse shear rate plots. Valid values can be found 9km from the ice-ocean boundary.

Values of along-flow strain rate and speed sampled along the flow line of maximum velocity are displayed in the lower two plots. The upper of the two plots gives values of strain rate (blue) and speed (orange) along the full flow line transect, with the mean strain-rate calculated over the final 20km shown as a thick green line. The lower plot displays the strain rate values from the final 20km section of the shelf (blue crosses), with the mean strain rate (bold green) and standard deviation in strain rate (dashed red). The methodology for calculating these quantities is given in the main text.

Acknowledgements
This work was supported by a British Antarctic Survey studentship funded by the Natural Environment Research Council (NERC), grant number NE/K50094X/1.

References

Haran, T., J. Bohlander, T. Scambos, T. Painter and M. Fahnestock, 2005. MODIS Mosaic of Antarctica 2003-2004 (MOA2004) Image Map

Rignot, E., J. Mouginot, and B. Scheuchl, 2011. MEaSUREs InSAR-Based Antarctica Ice Velocity Map [450m]. Boulder, Colorado, USA: NASA DAAC at the National Snow and Ice Data Center.

Amery Ice Shelf

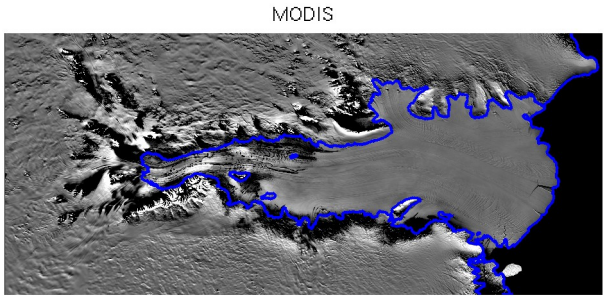

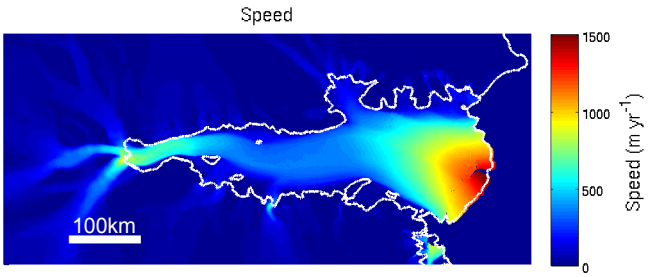

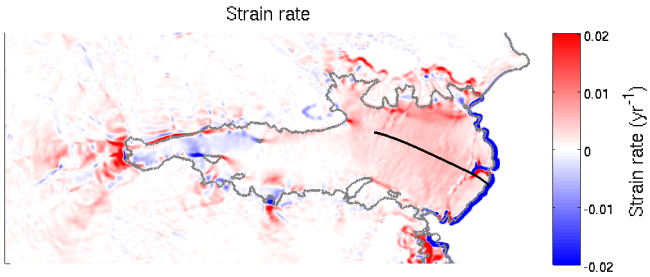

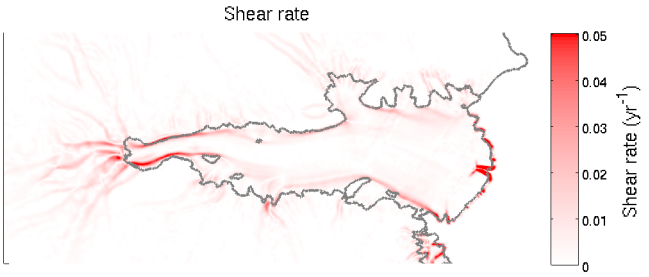

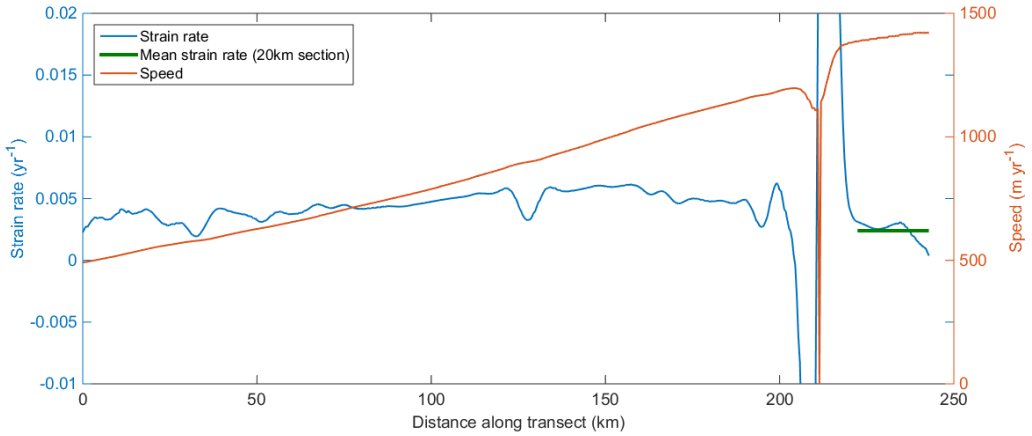

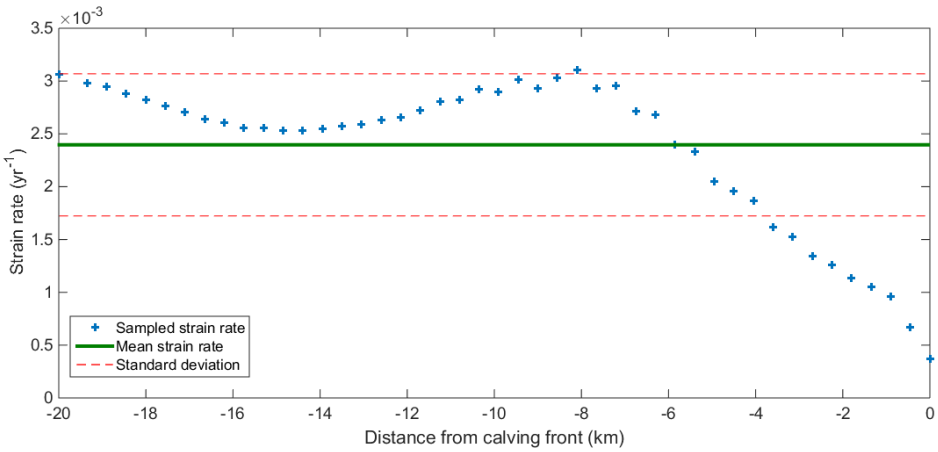

Borchgrevinkisen Ice Shelf

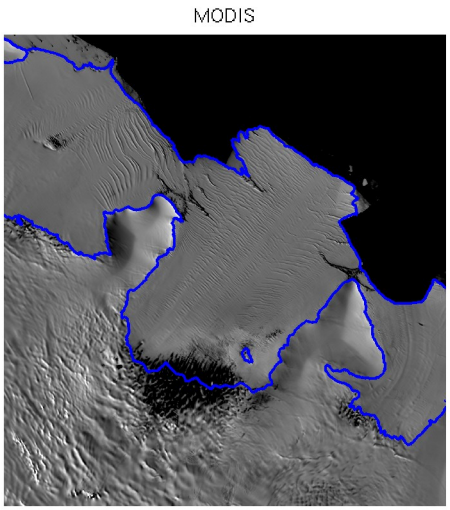

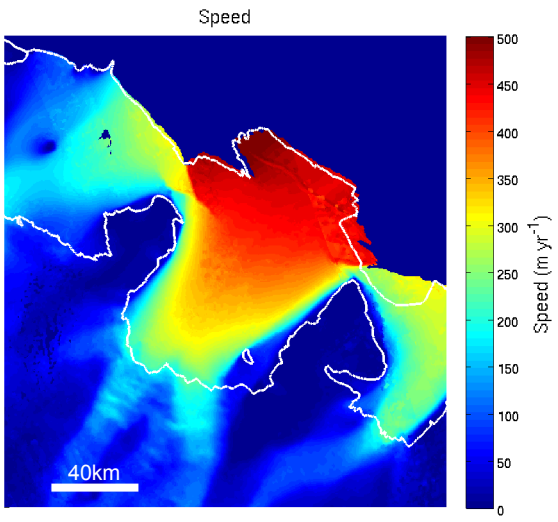

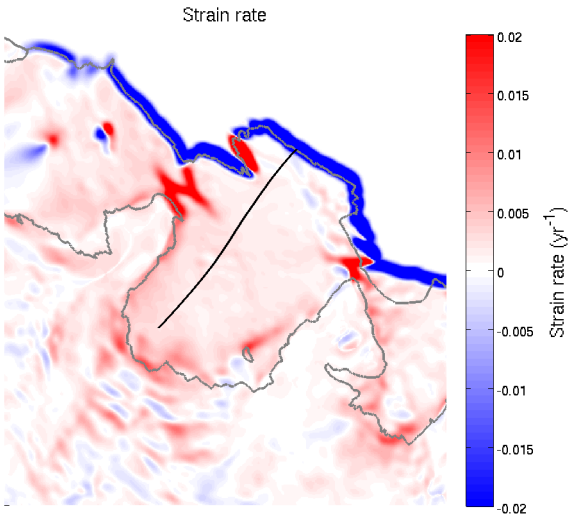

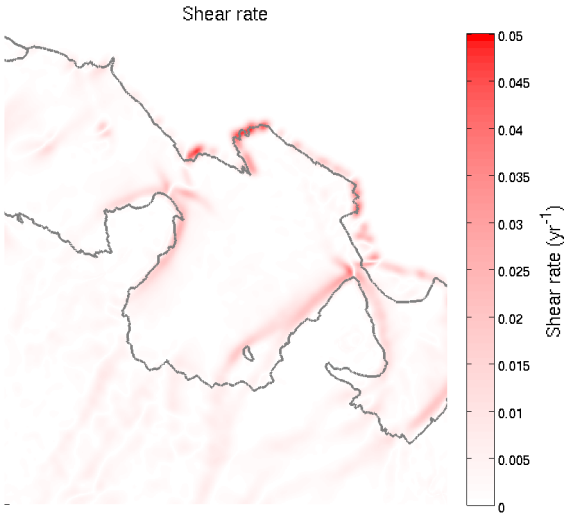

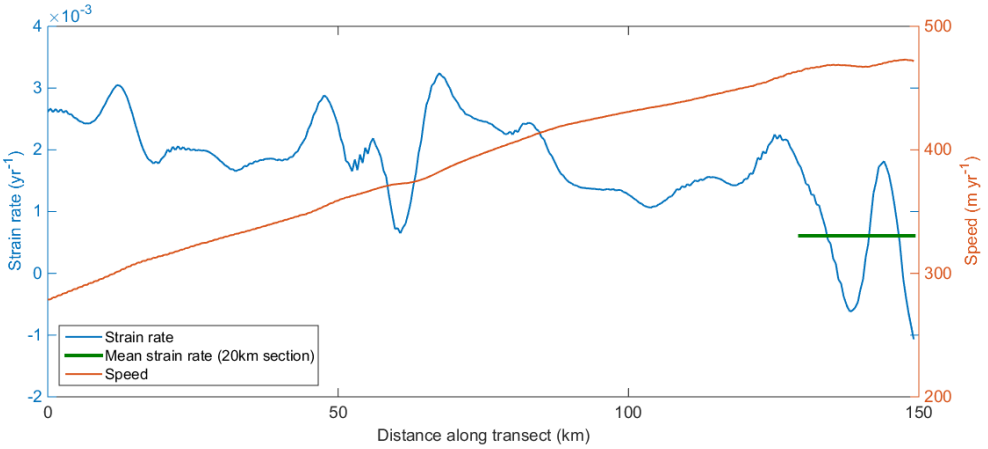

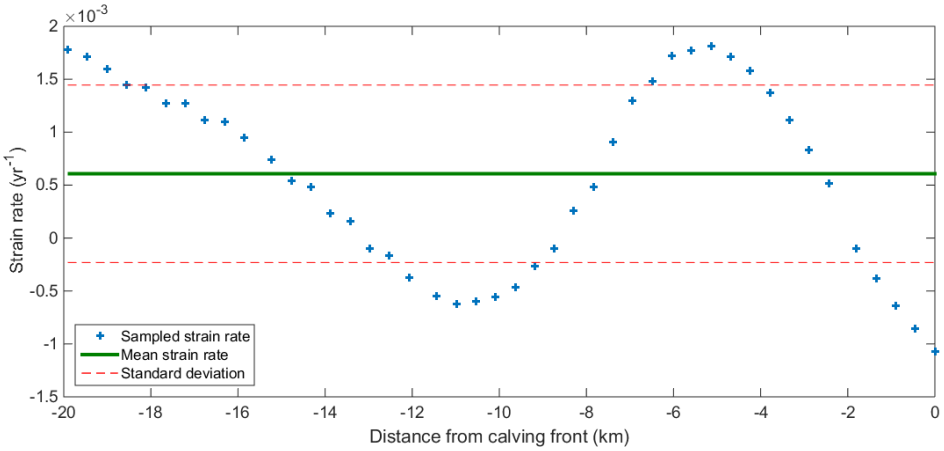

Cook Ice Shelf

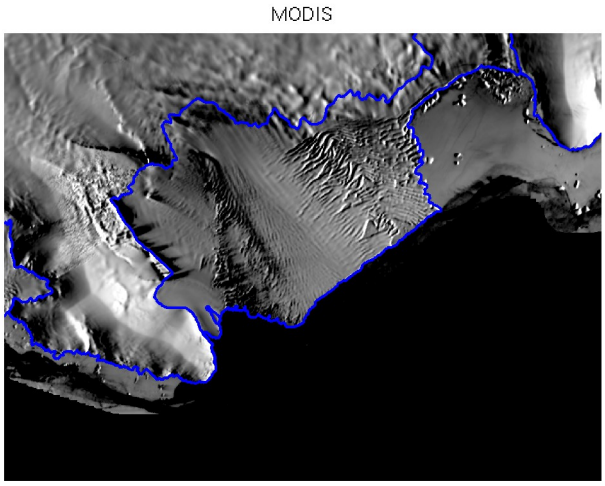

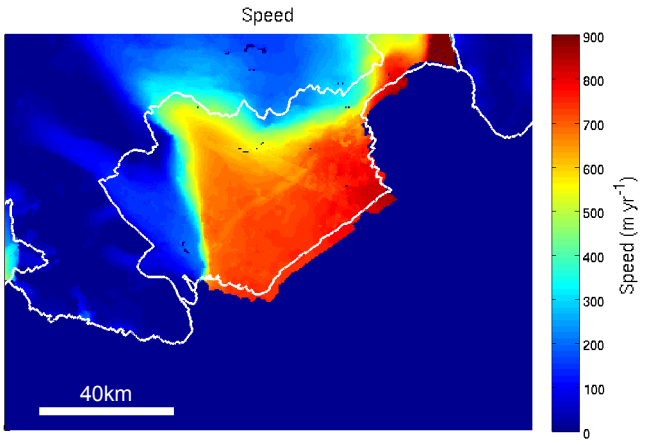

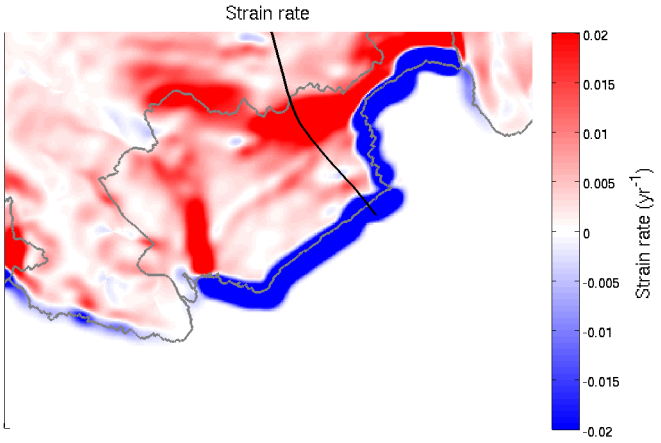

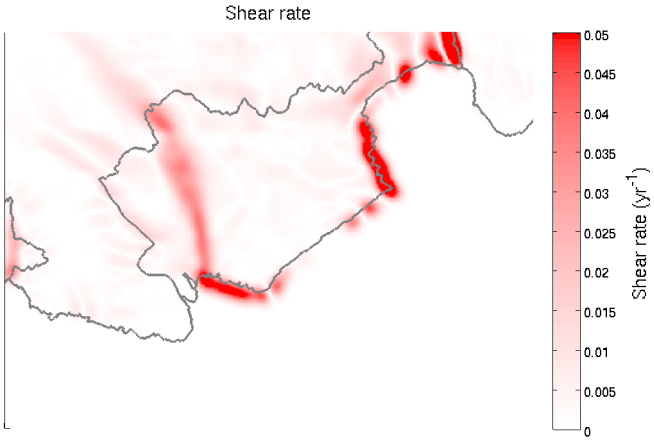

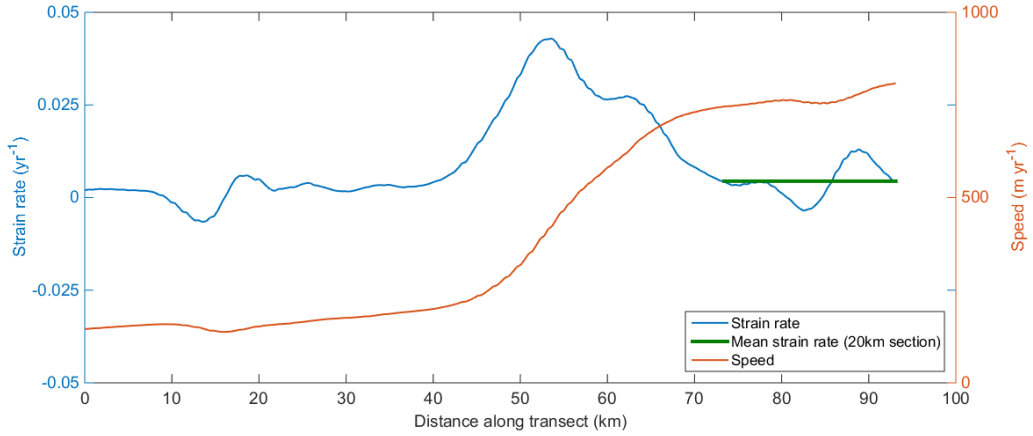

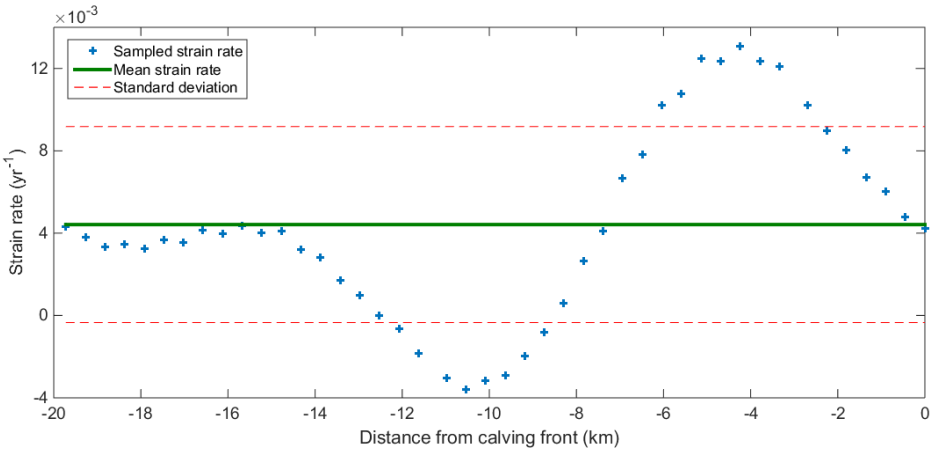

De Vicq A Ice Shelf

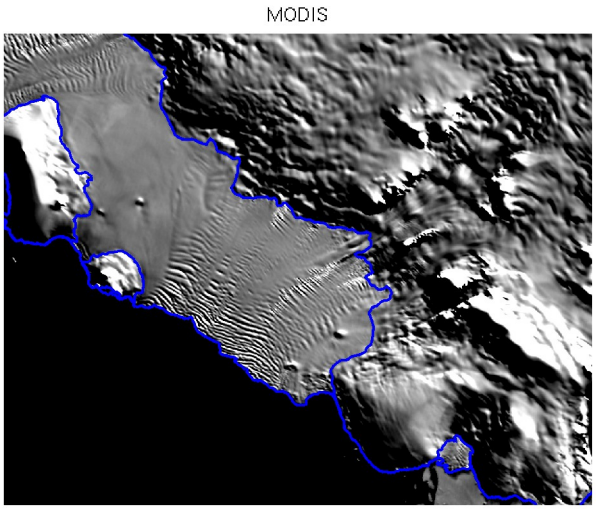

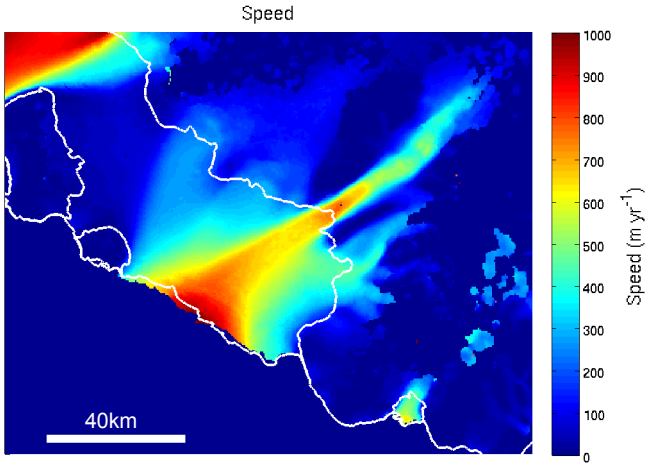

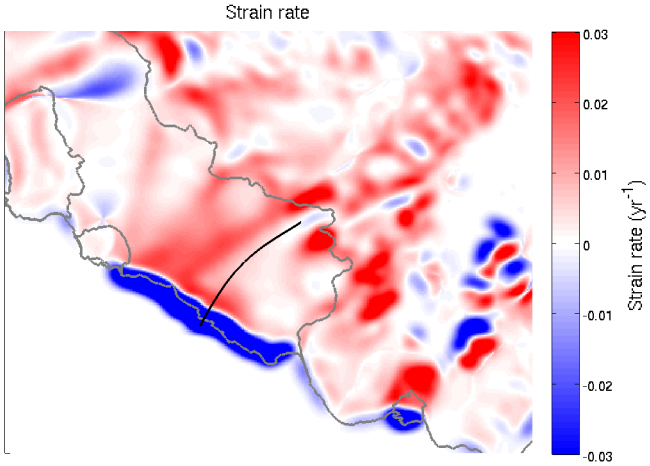

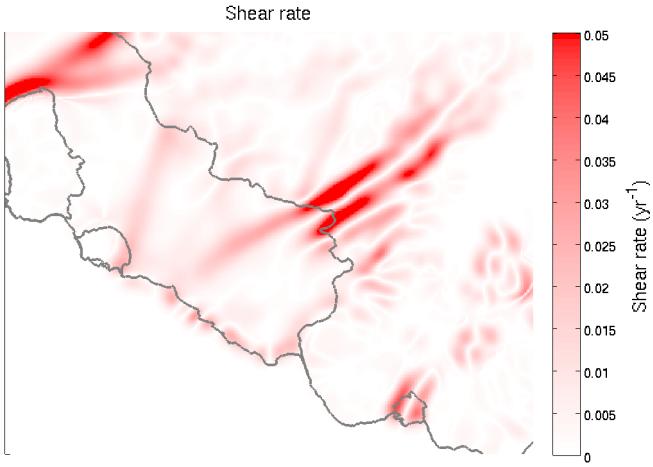

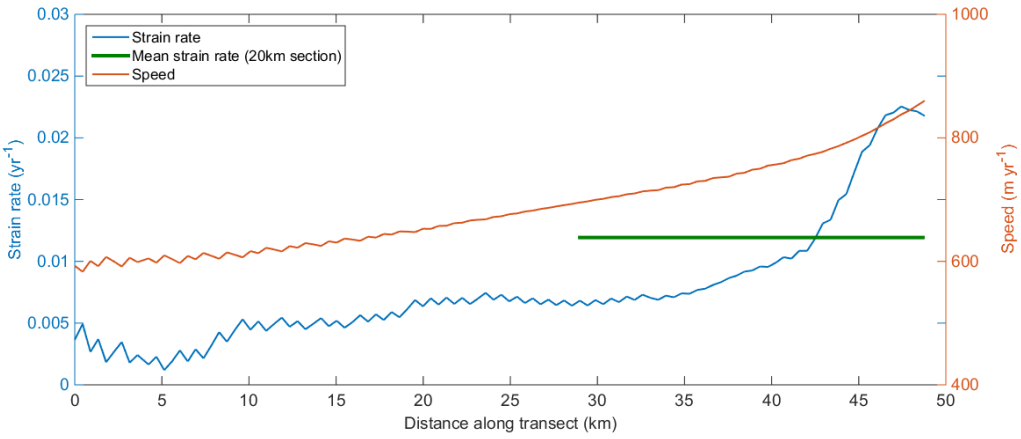

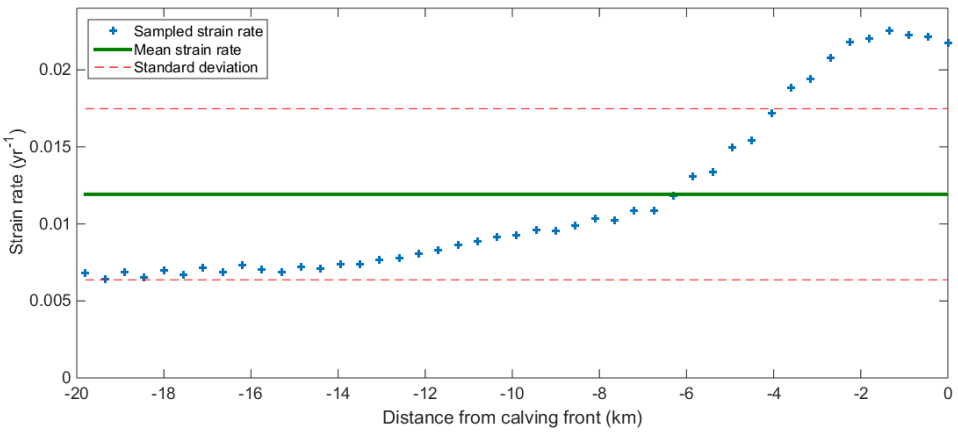

De Vicq B Ice Shelf

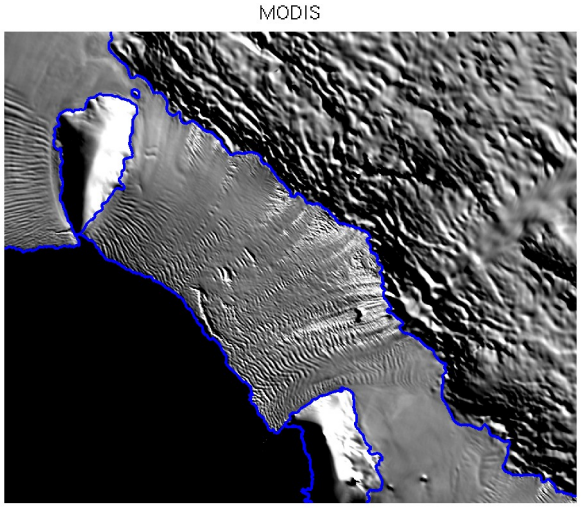

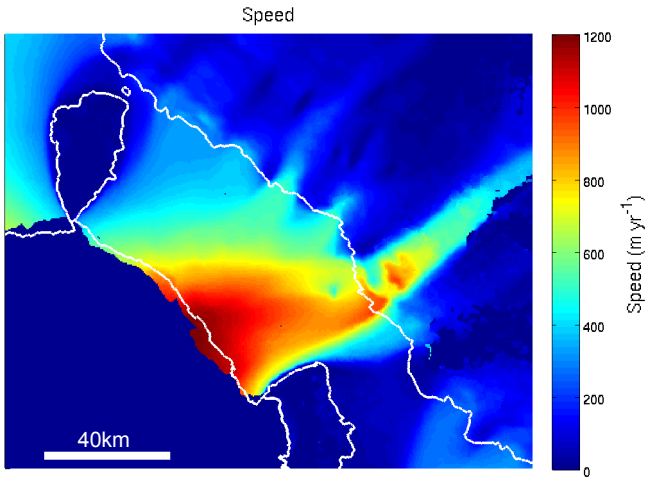

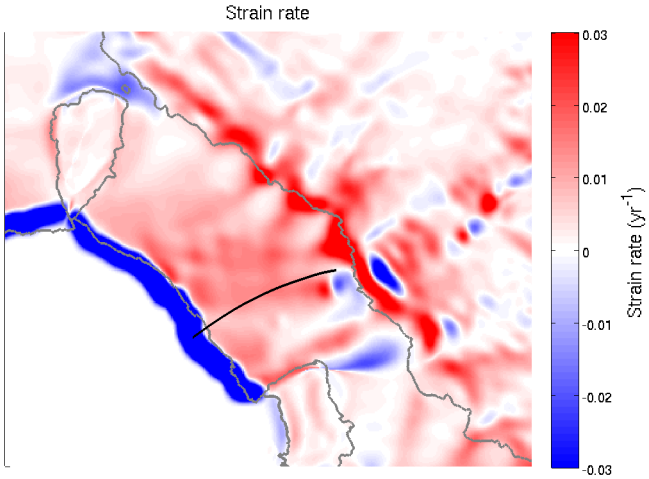

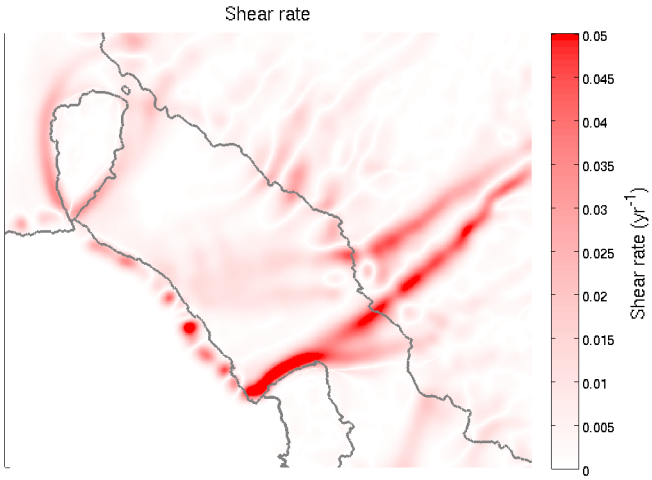

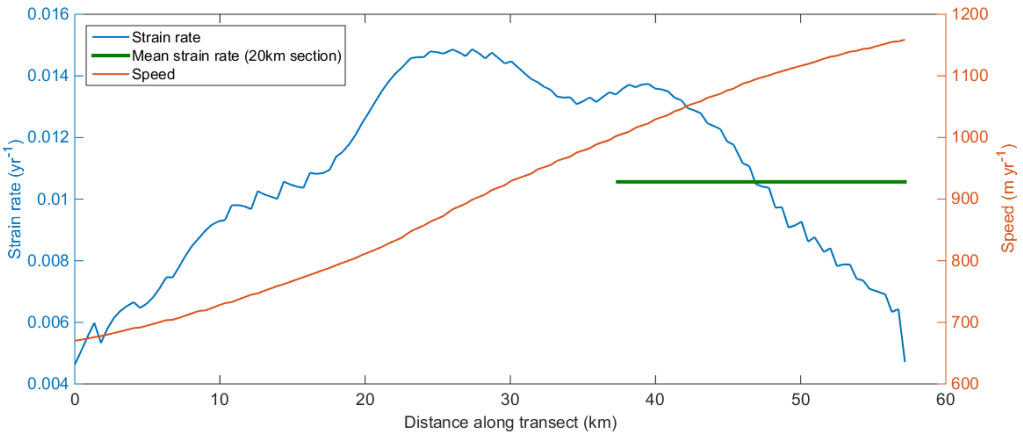

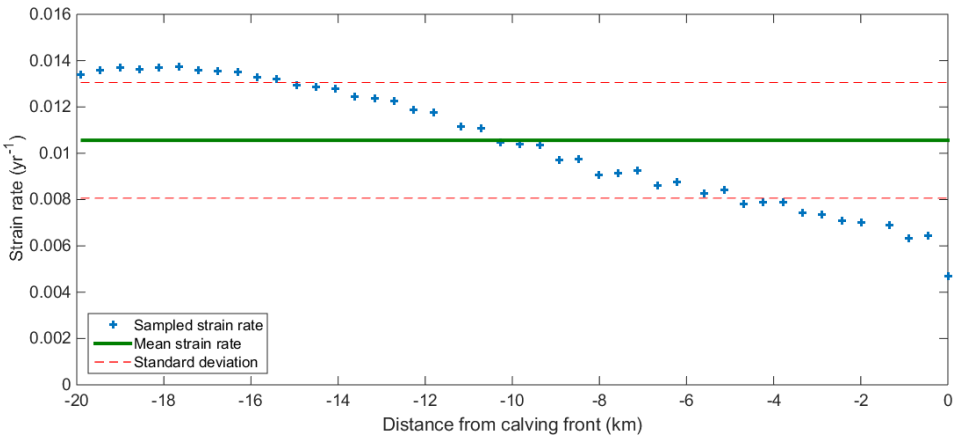

Dolleman Ice Shelf

MODIS

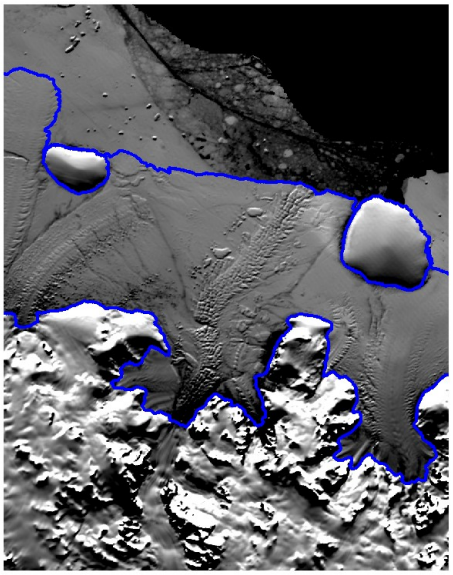

Speed

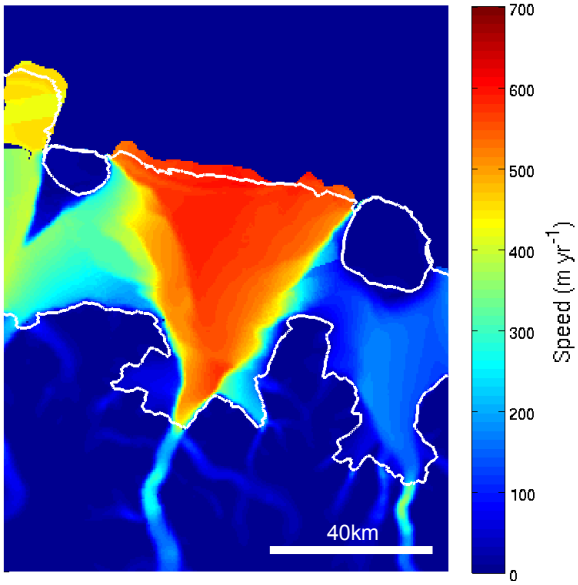

Strain rate

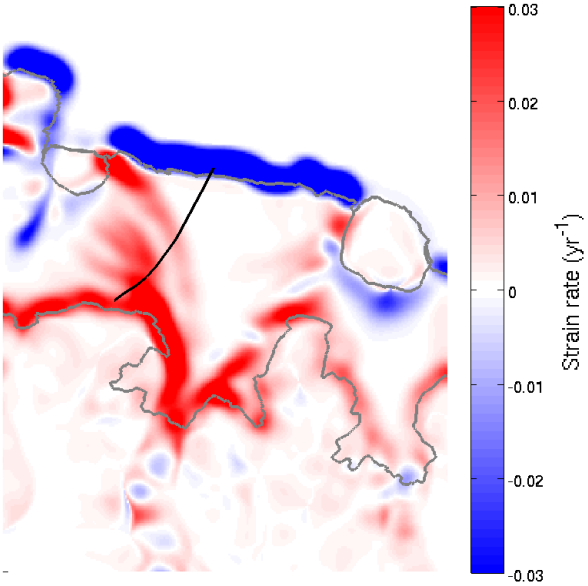

Shear rate

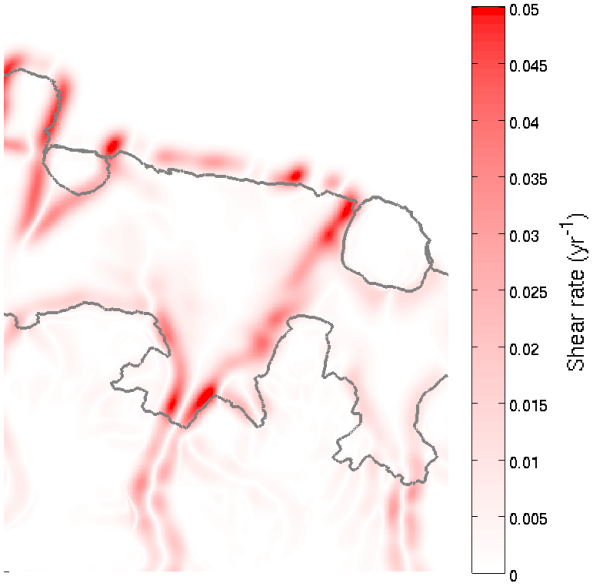

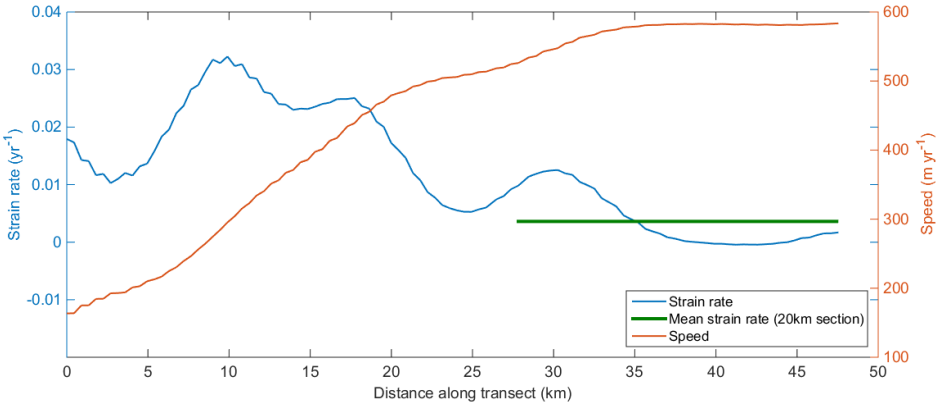

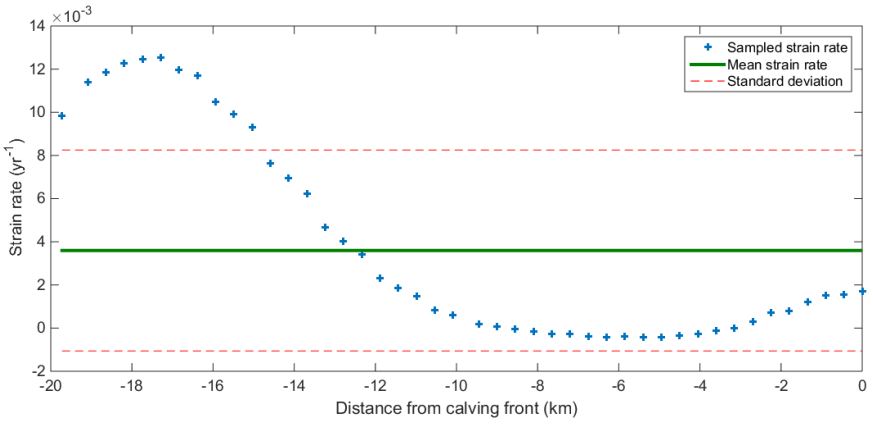

Filchner Ice Shelf

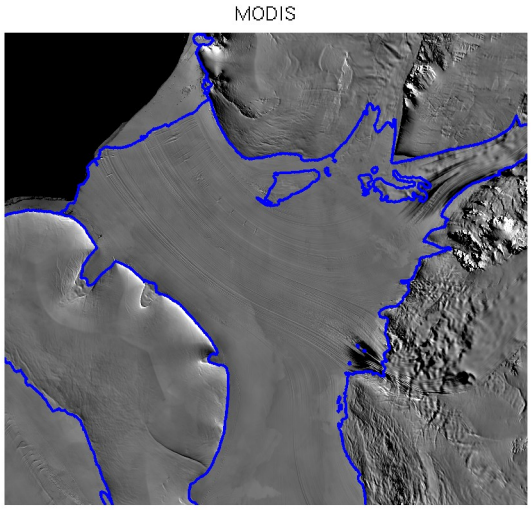

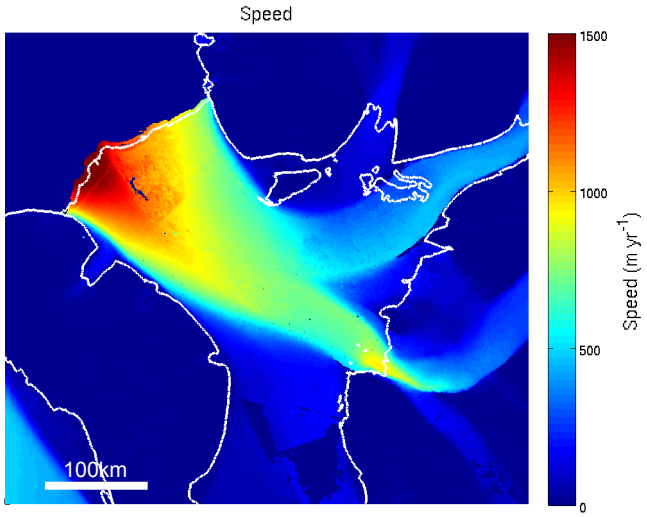

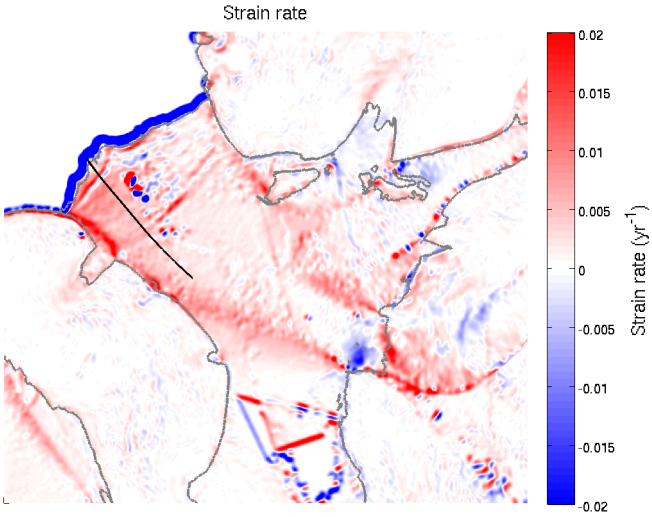

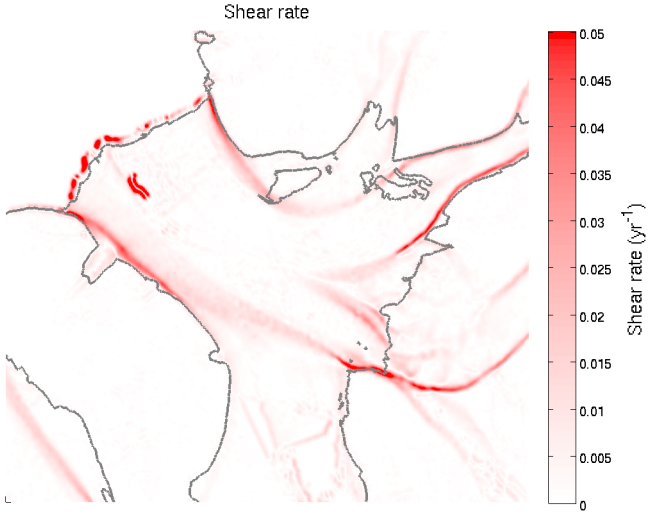

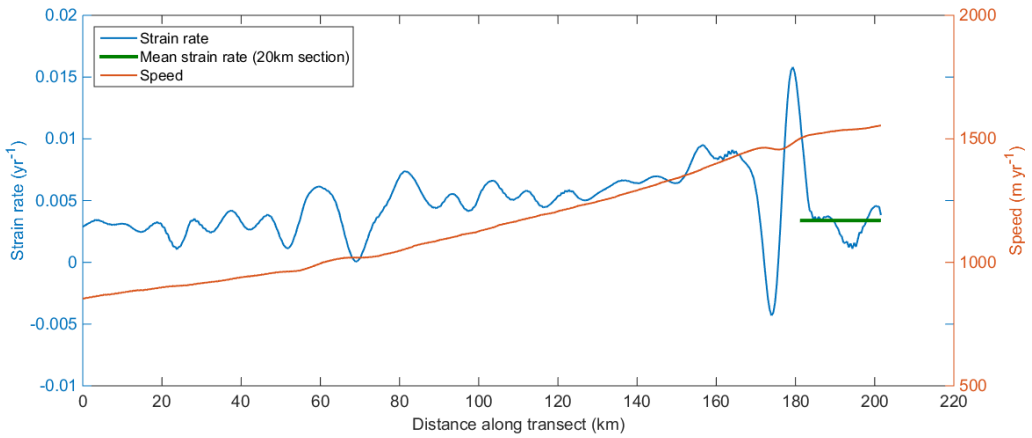

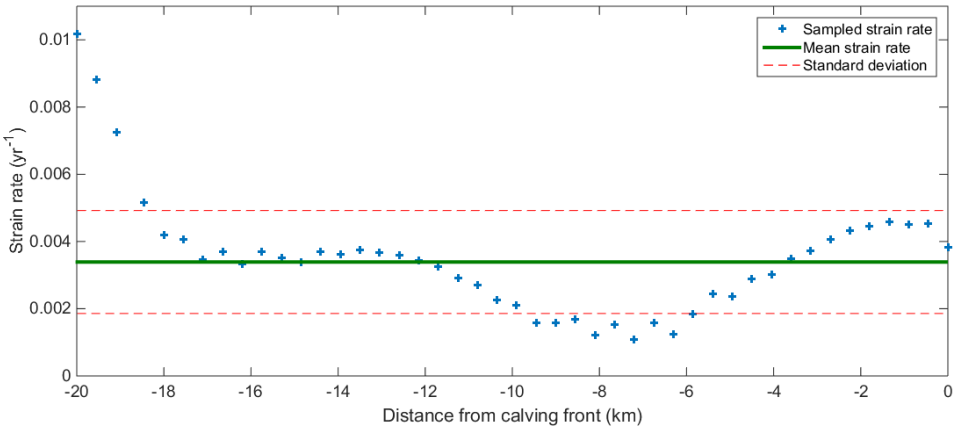

Fimbul Ice Shelf

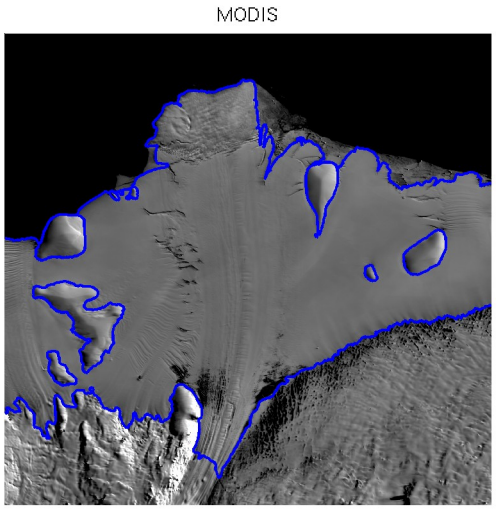

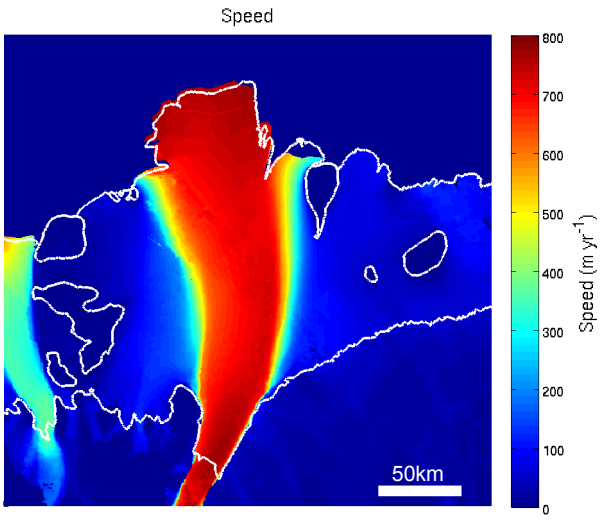

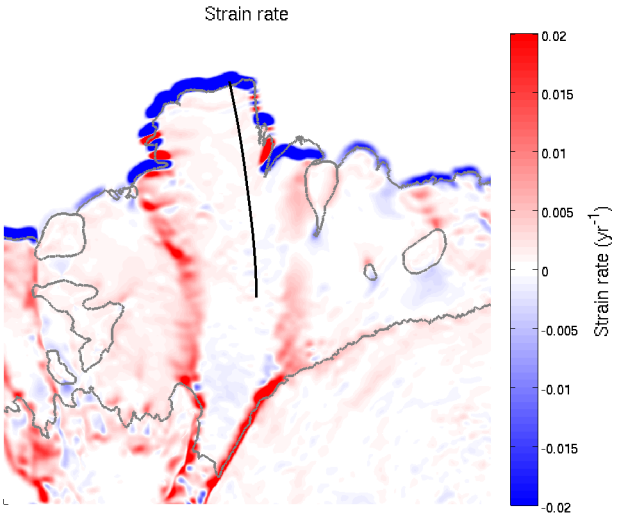

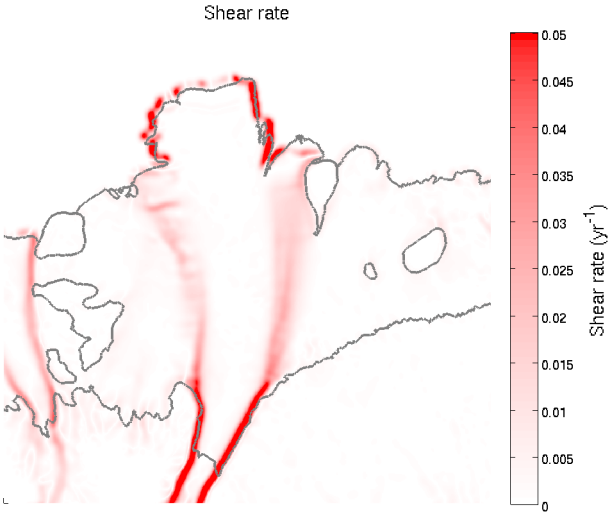

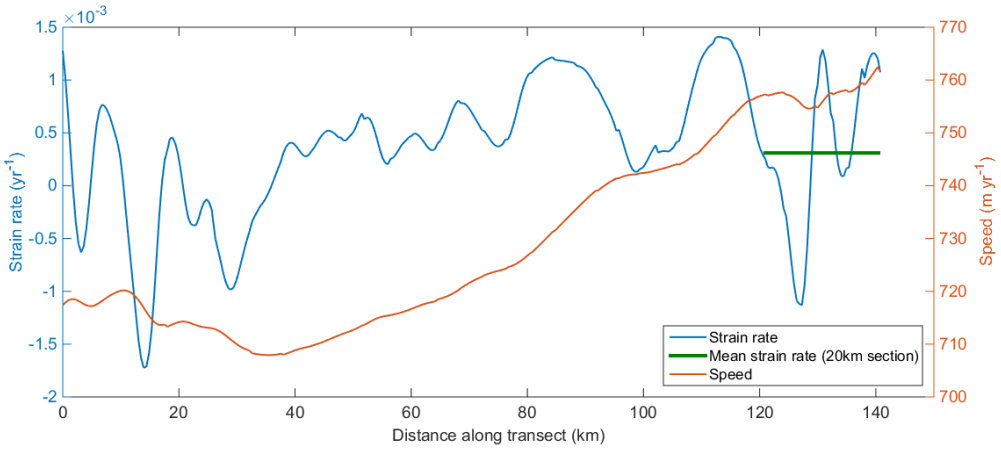

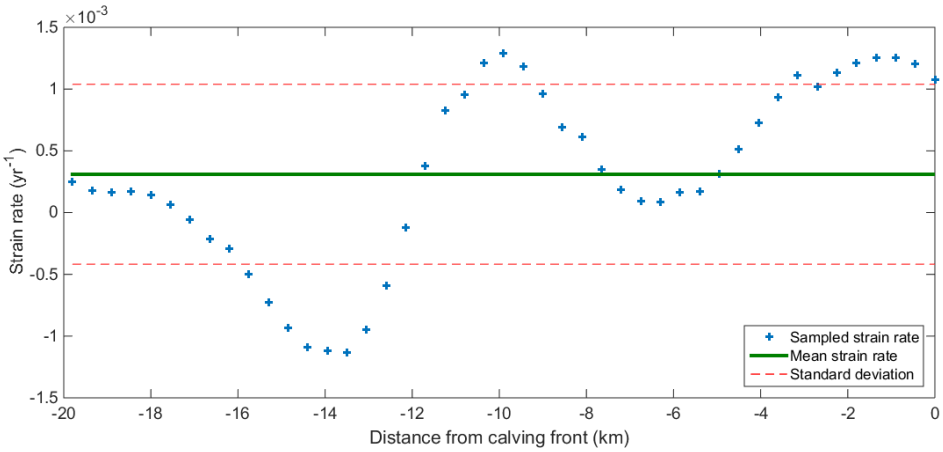

Getz Ice Shelf

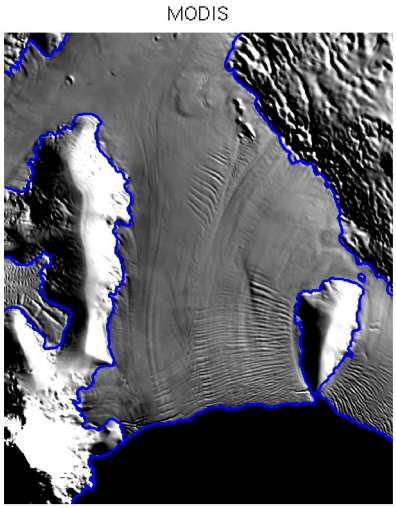

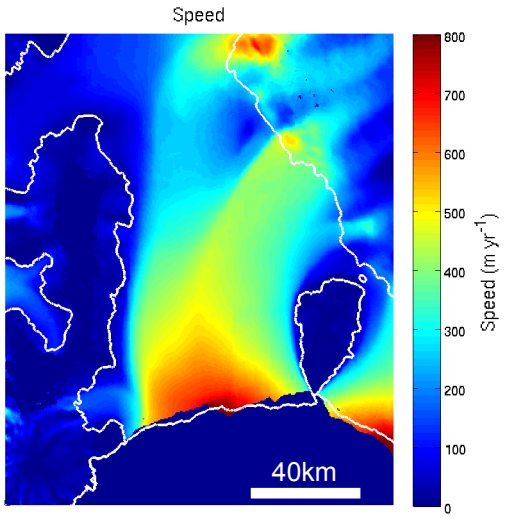

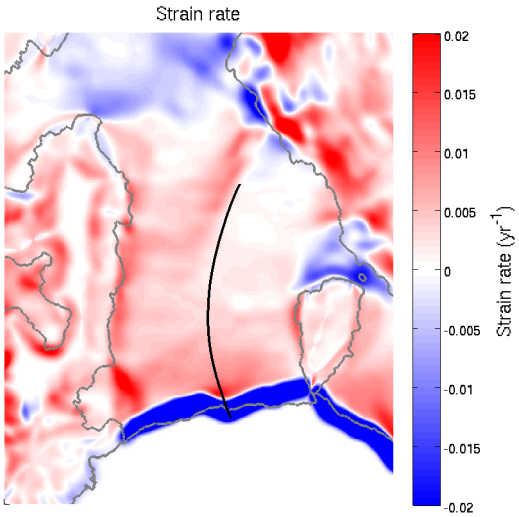

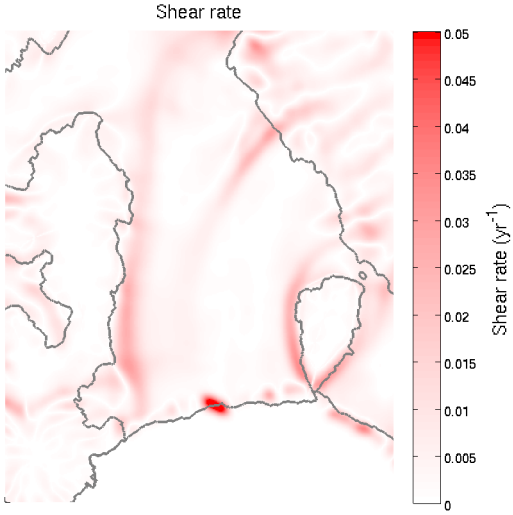

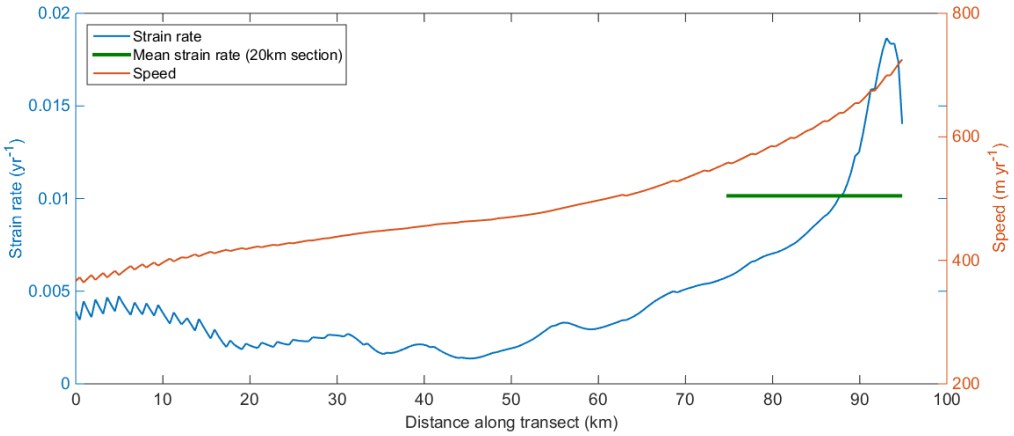

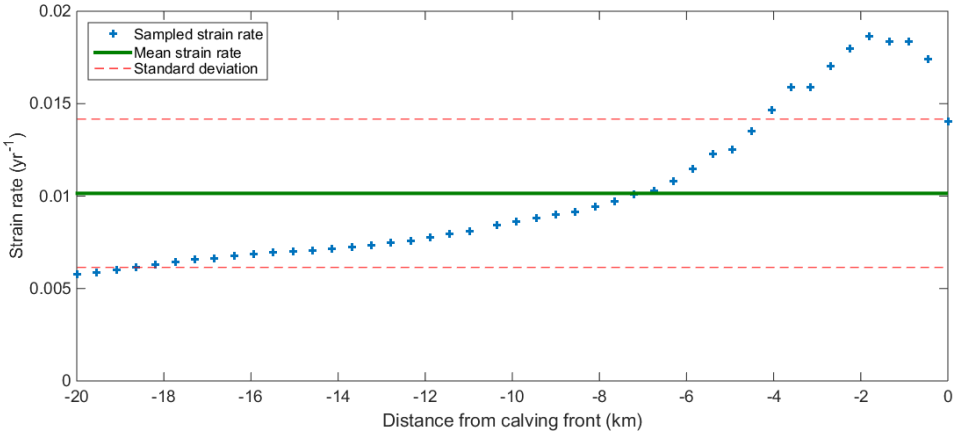

Jelbart Ice Shelf

MODIS

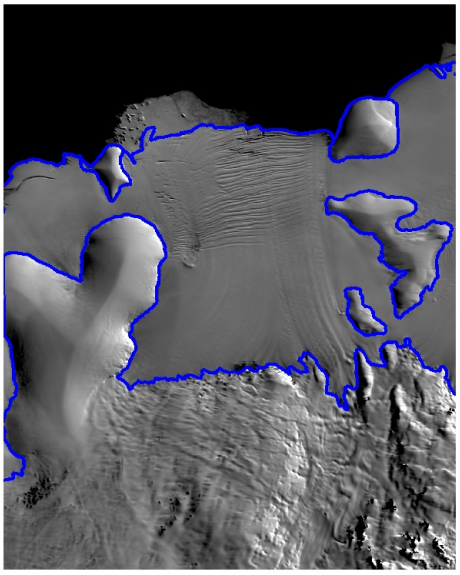

Speed

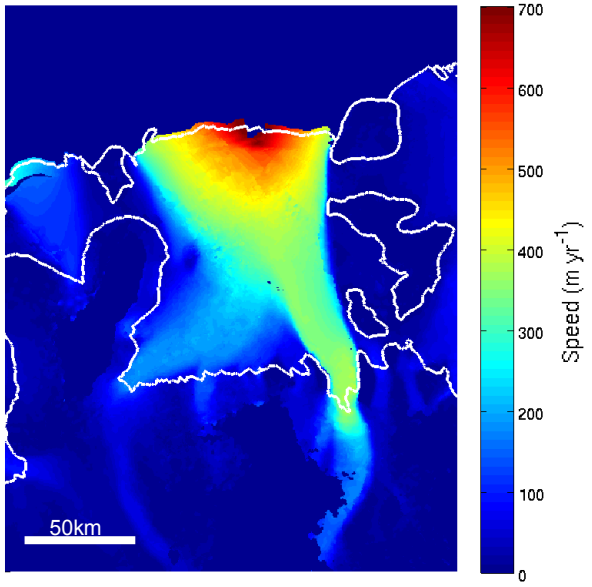

Strain rate

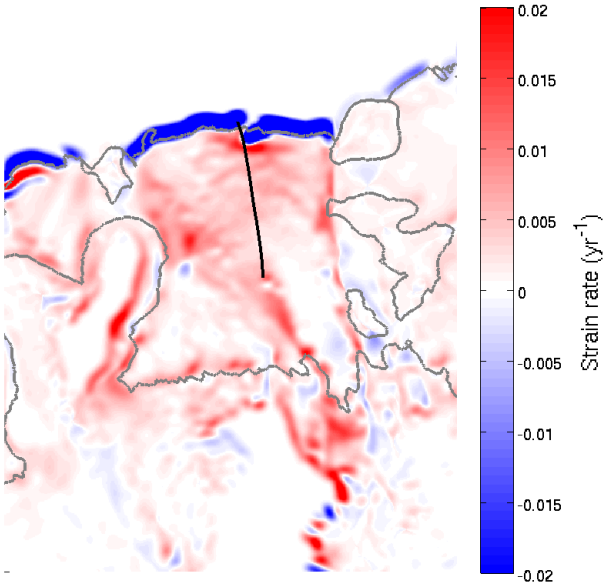

Shear rate

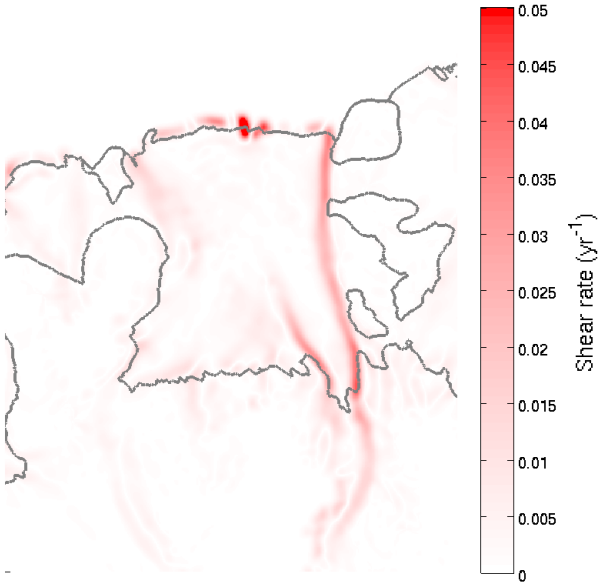

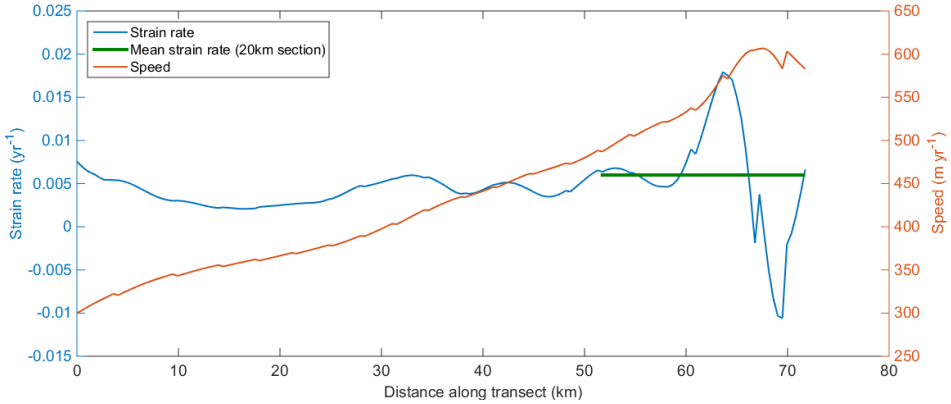

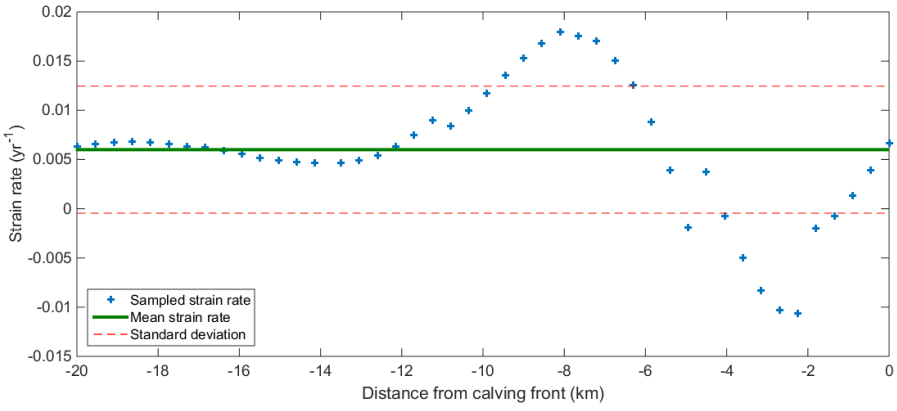

Larsen C Ice Shelf

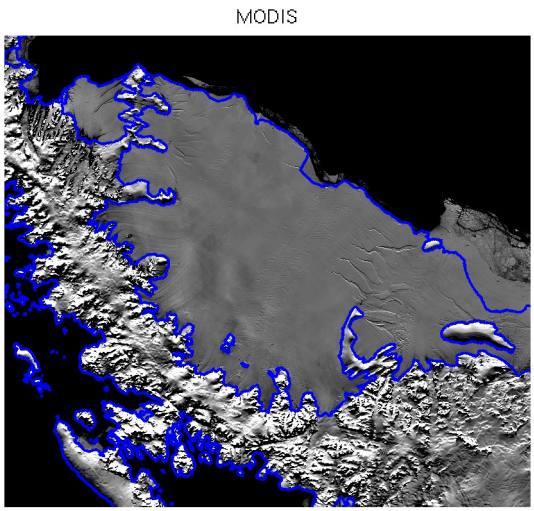

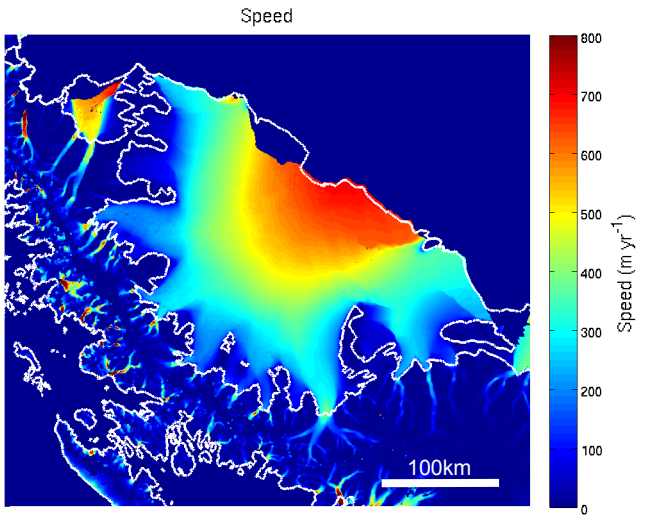

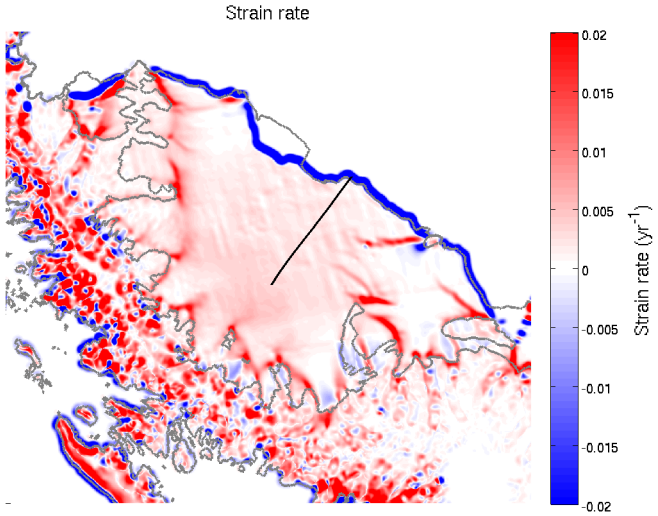

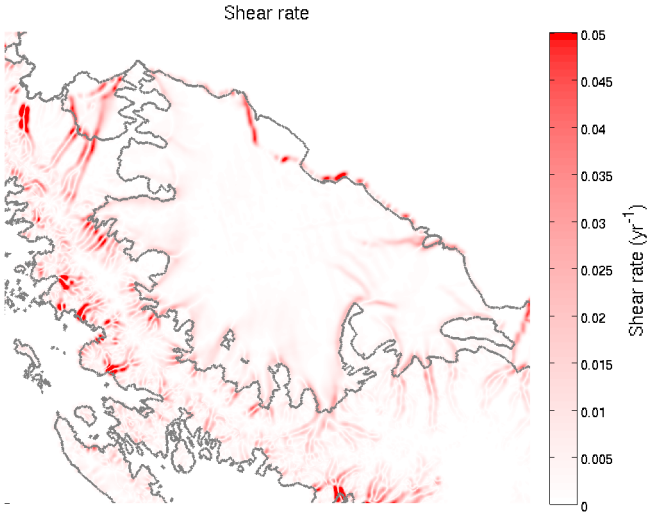

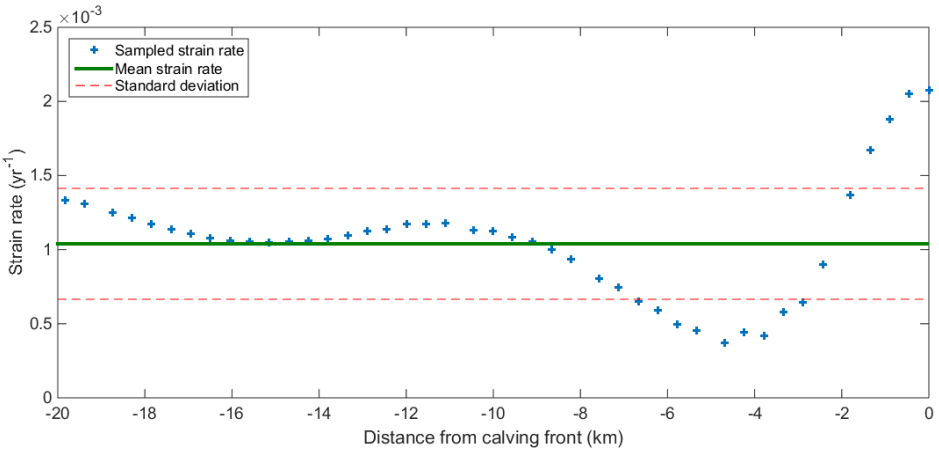

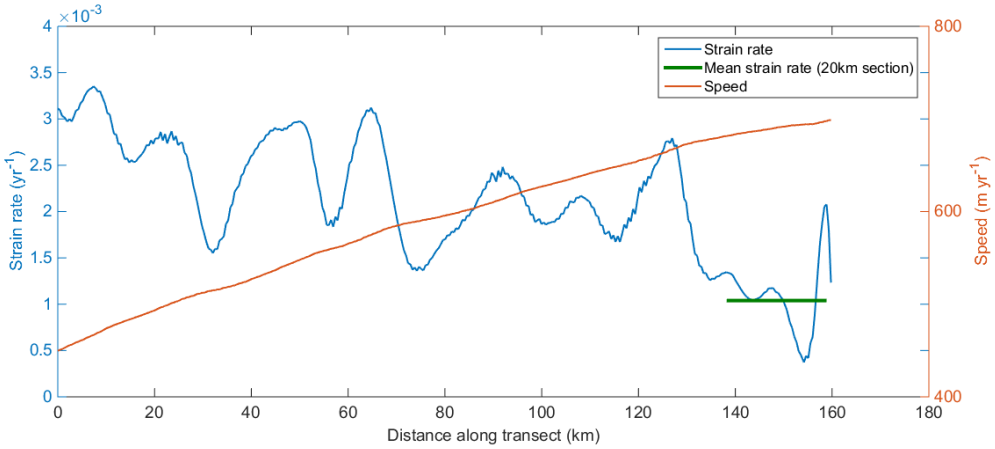

McMurdo Ice Shelf

MODIS

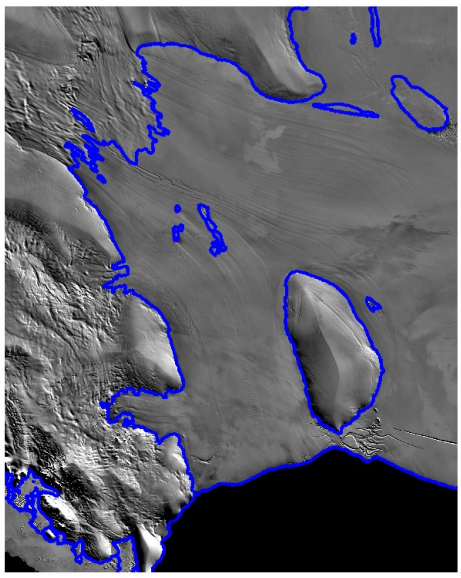

Speed

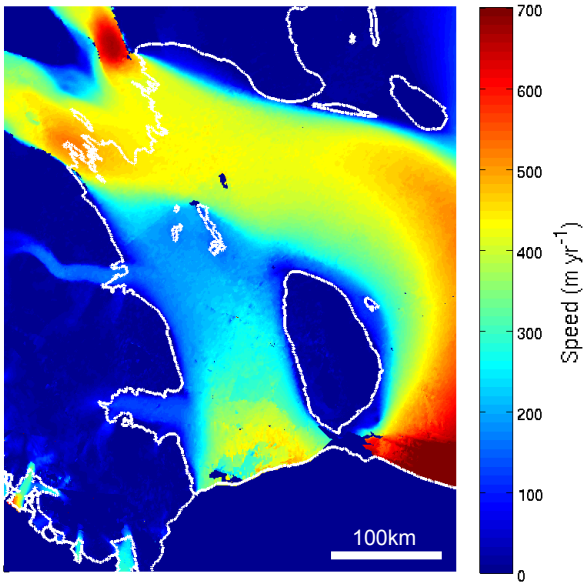

Strain rate

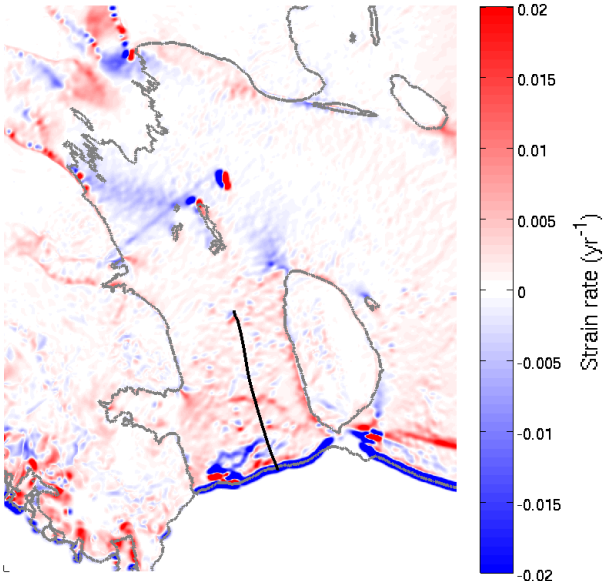

Shear rate

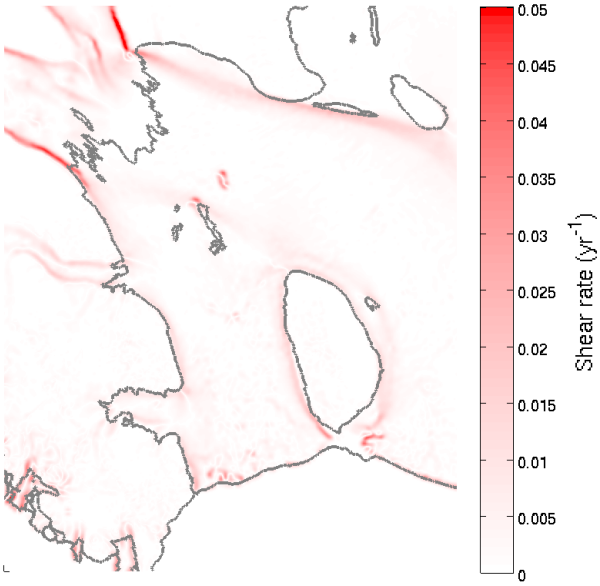

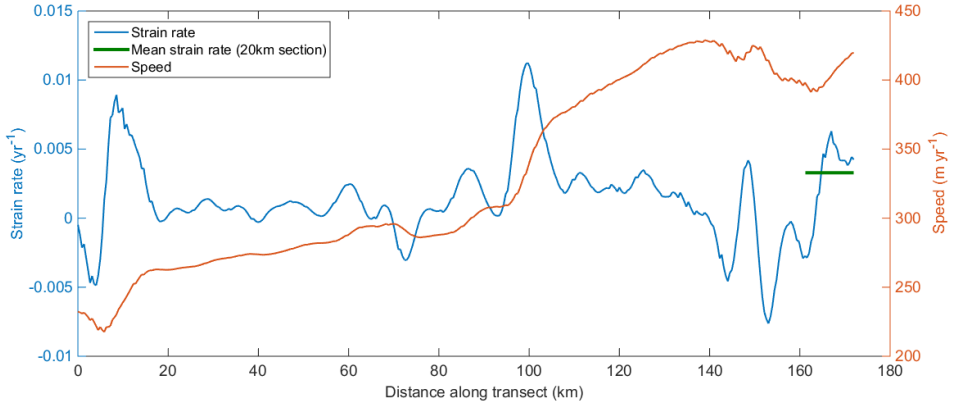

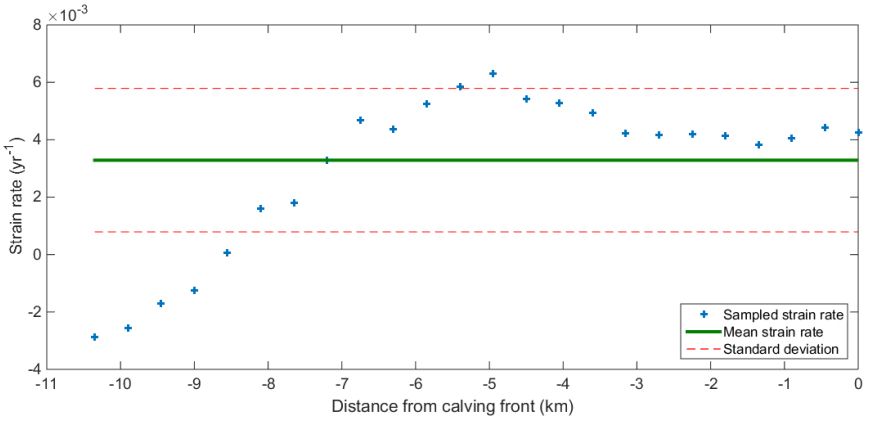

Ninnis Ice Shelf

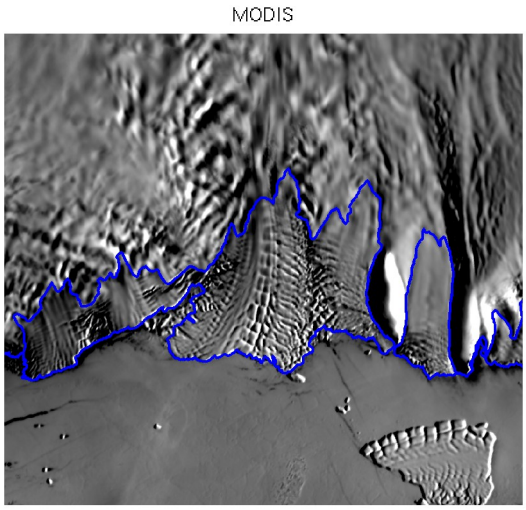

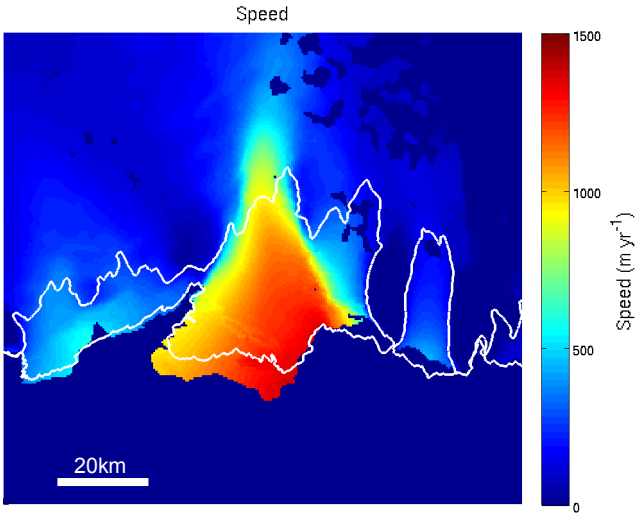

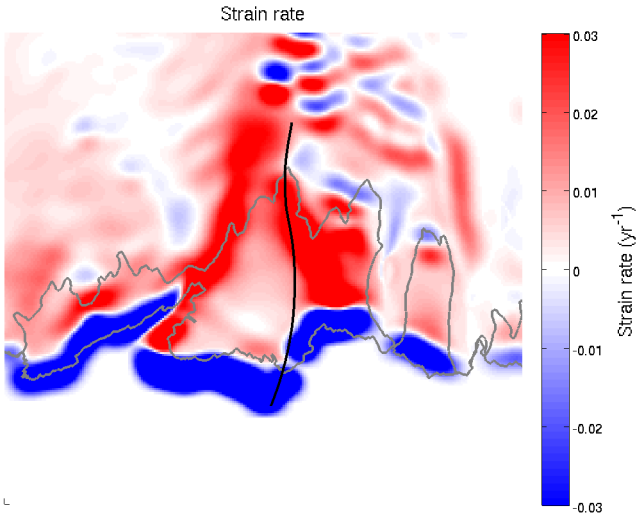

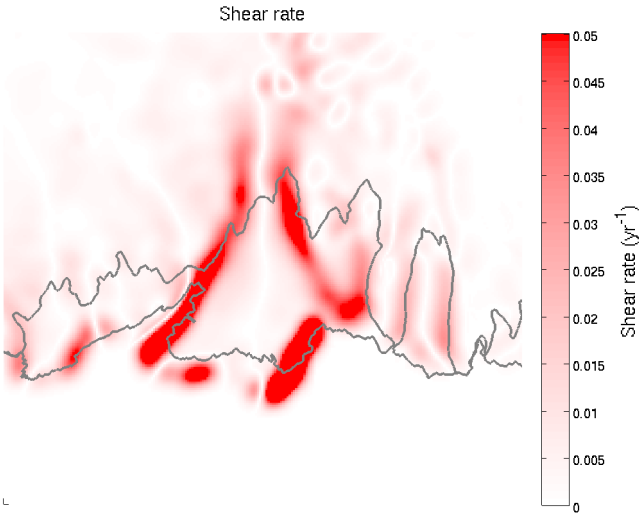

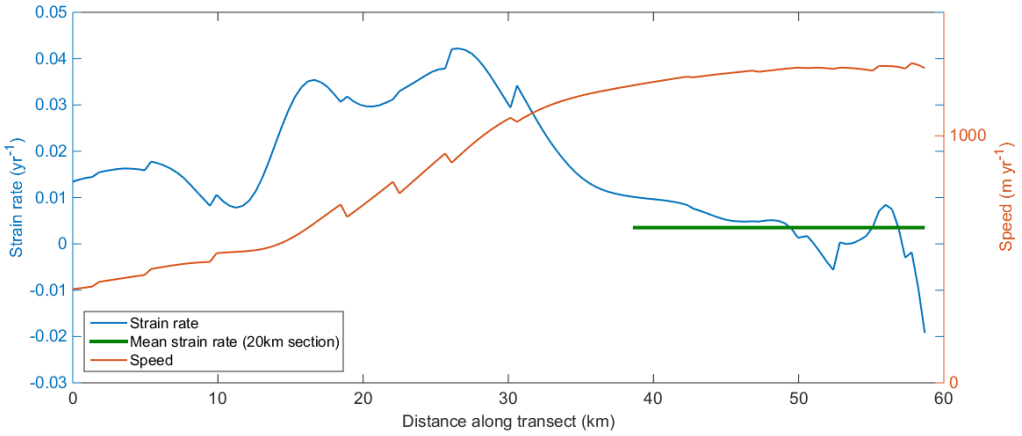

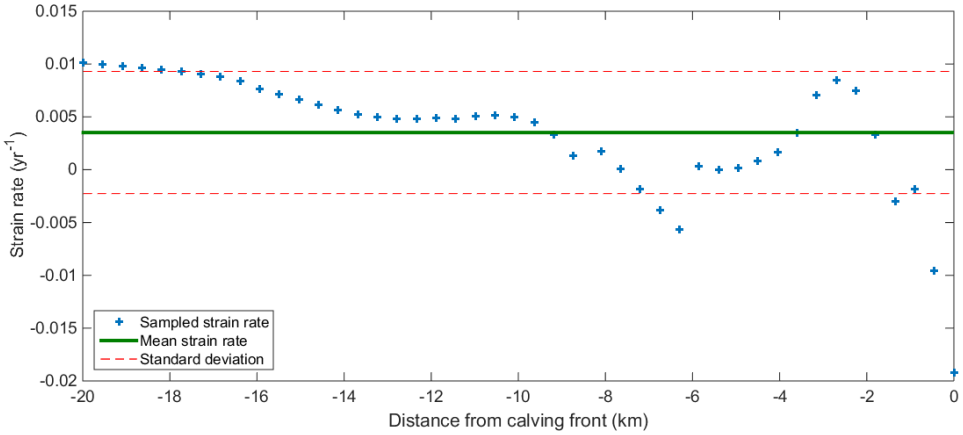

PIG Ice Shelf

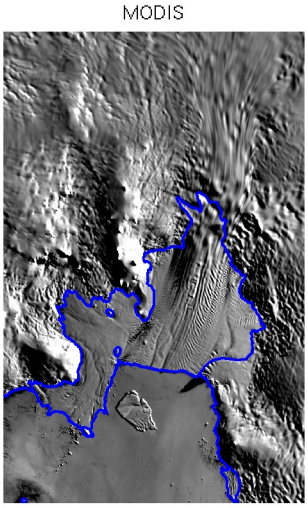

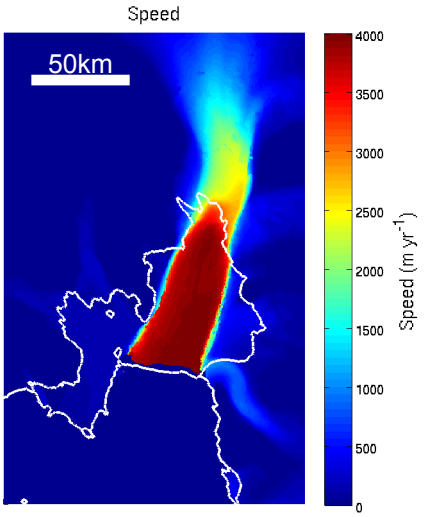

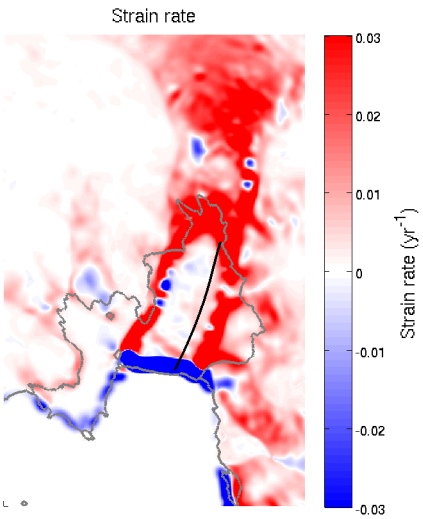

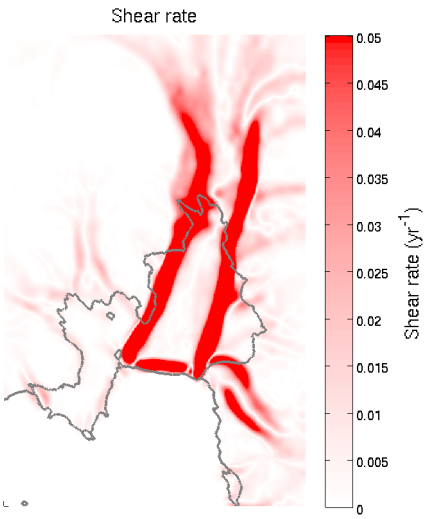

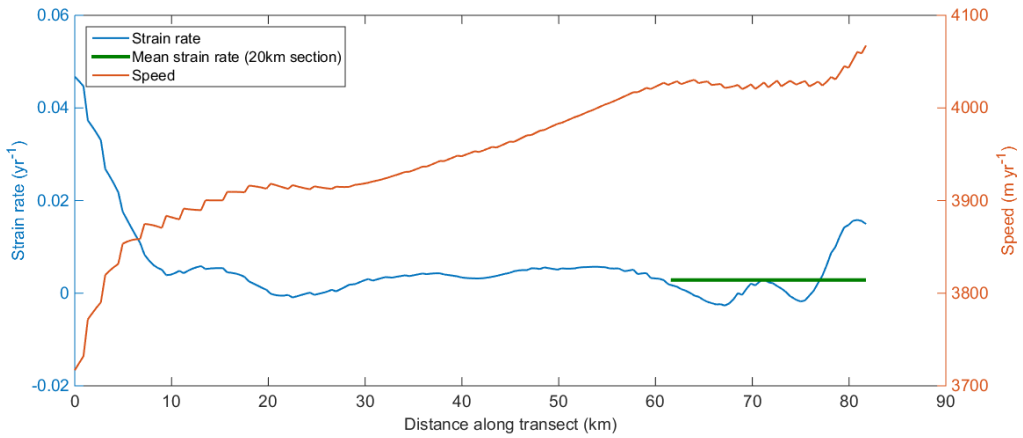

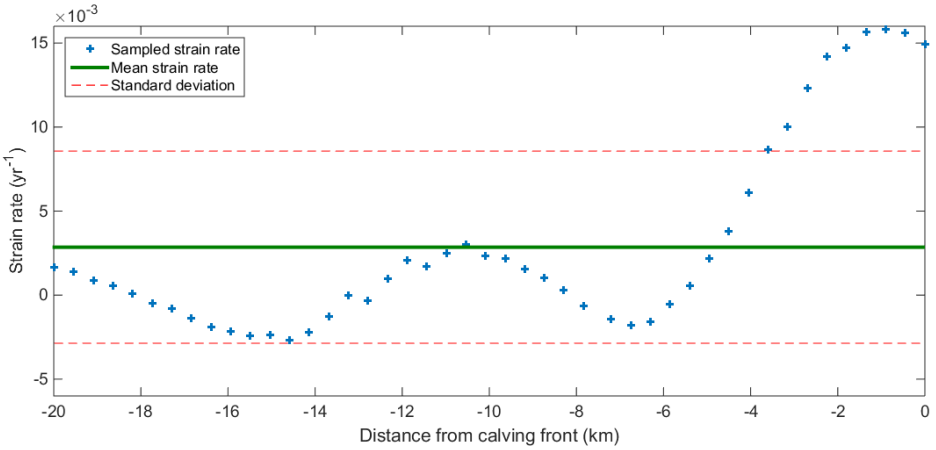

Publications Ice Shelf

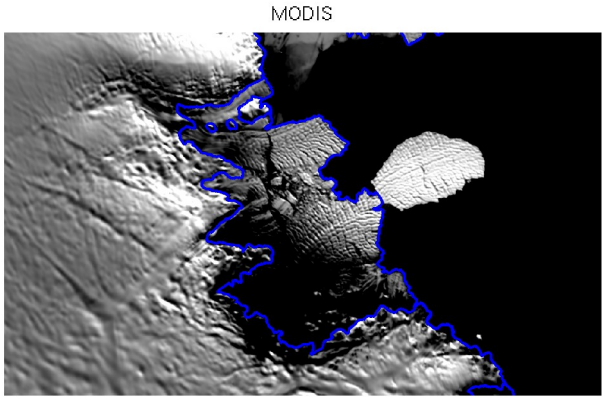

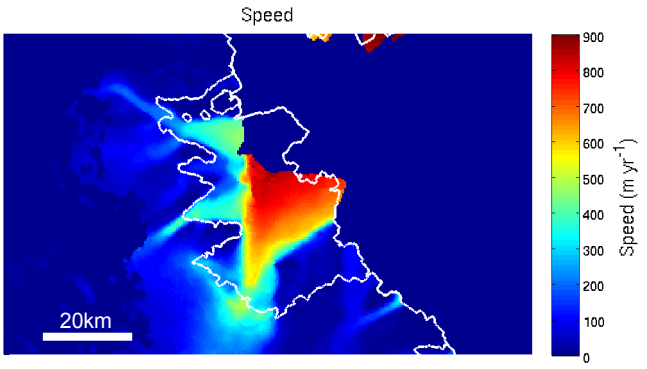

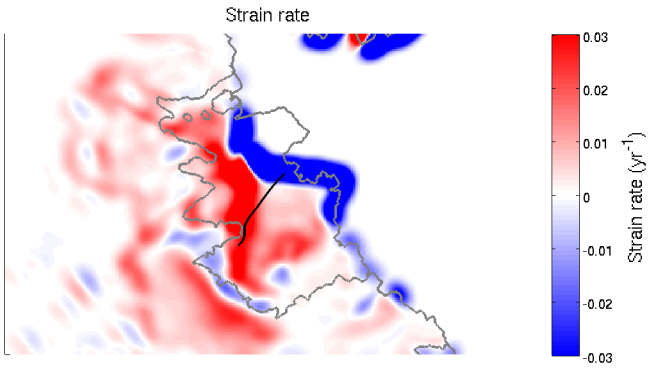

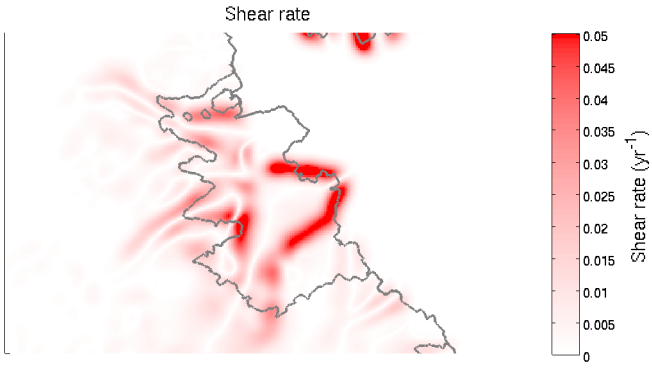

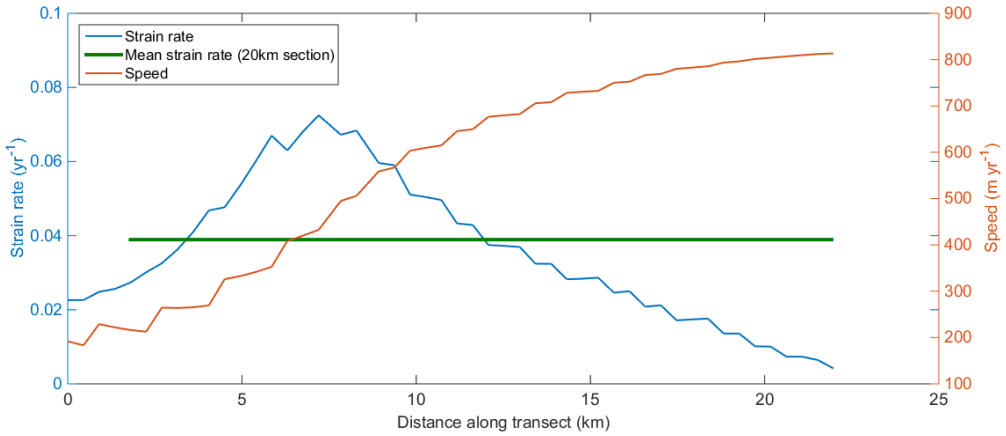

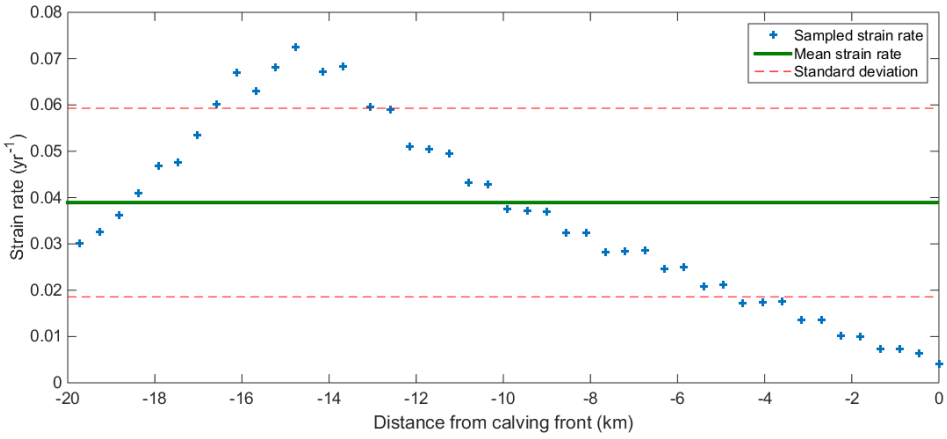

Ronne Ice Shelf

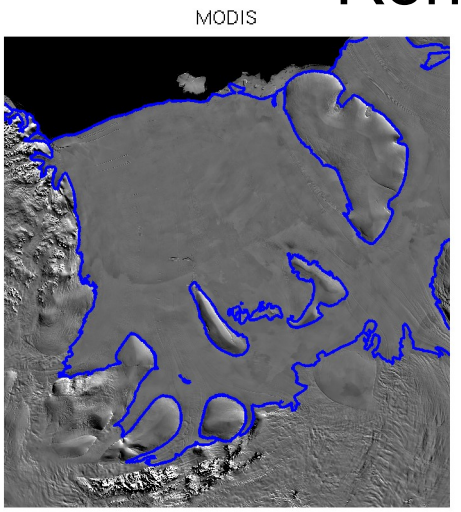

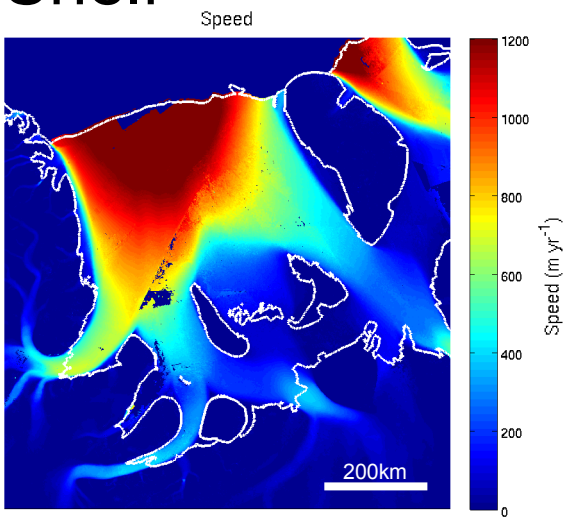

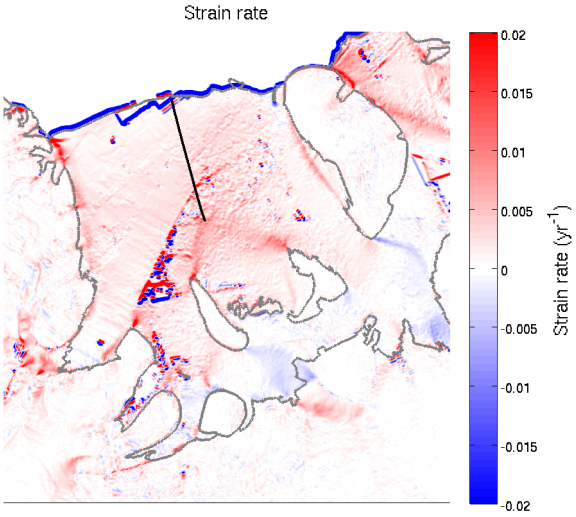

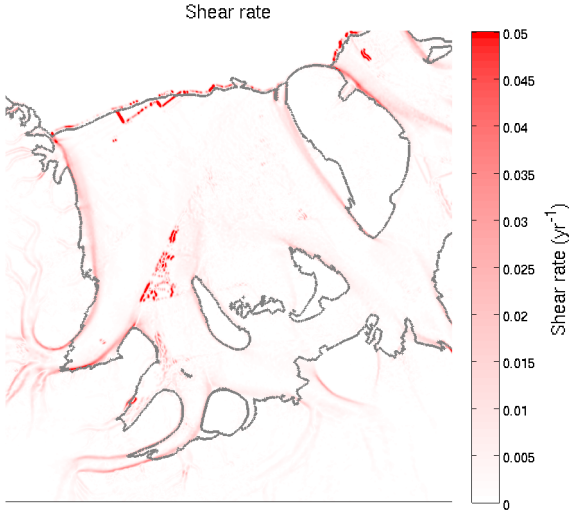

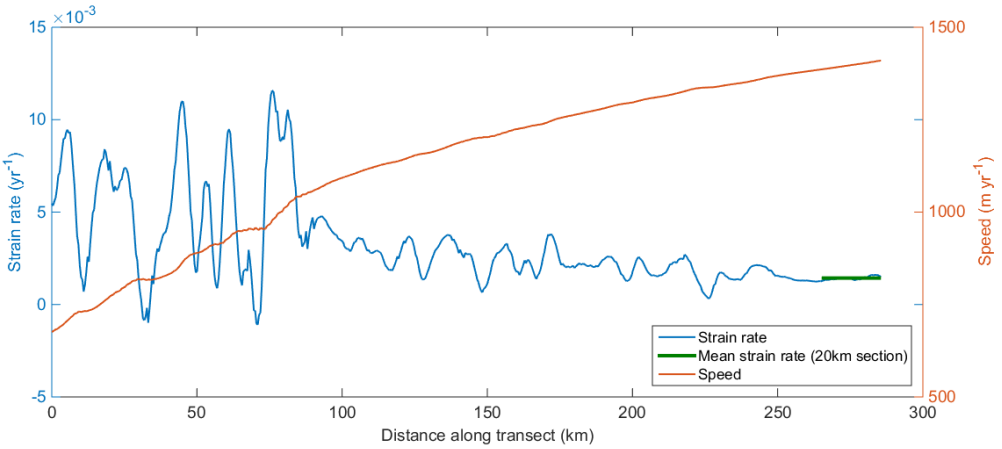

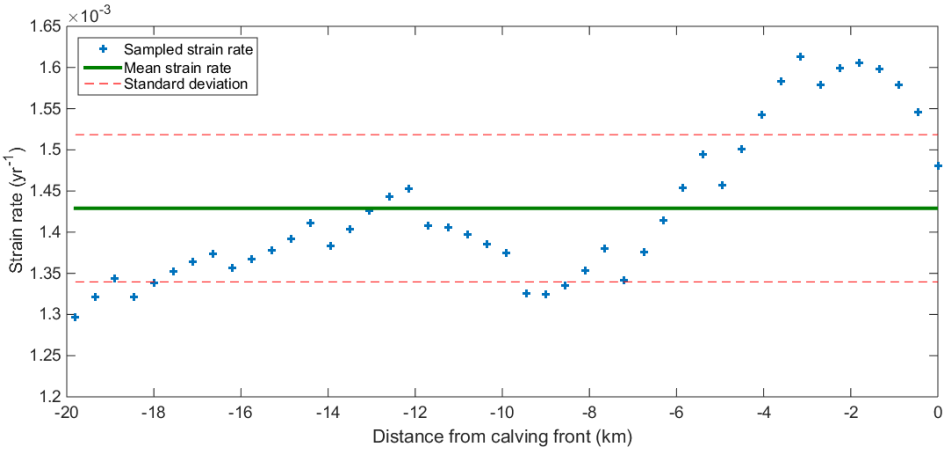

Robert Glacier Ice Shelf

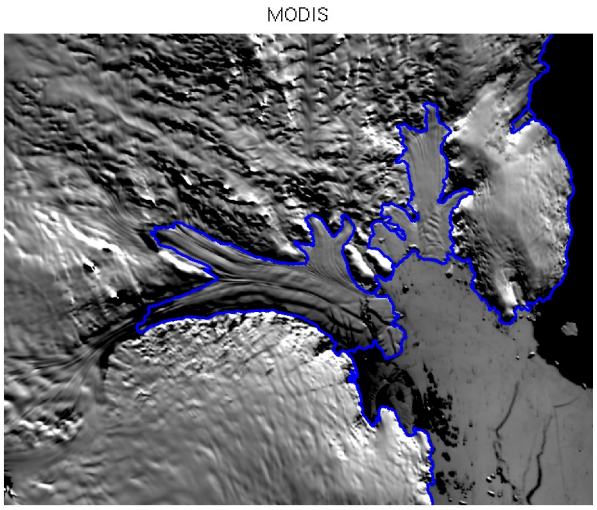

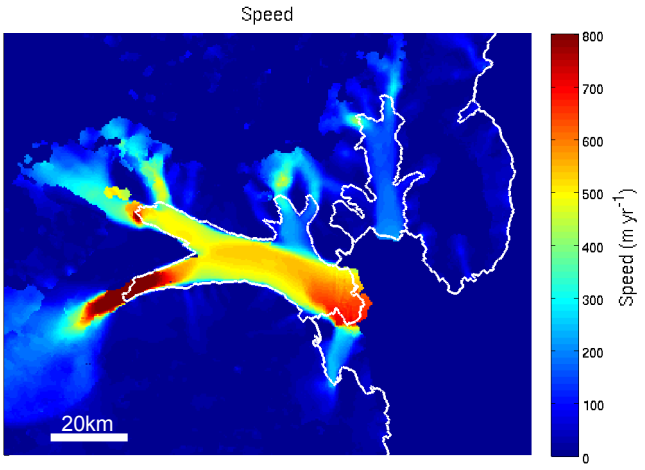

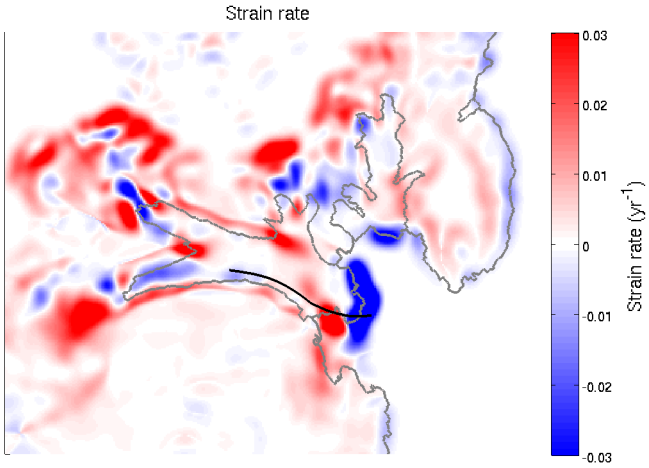

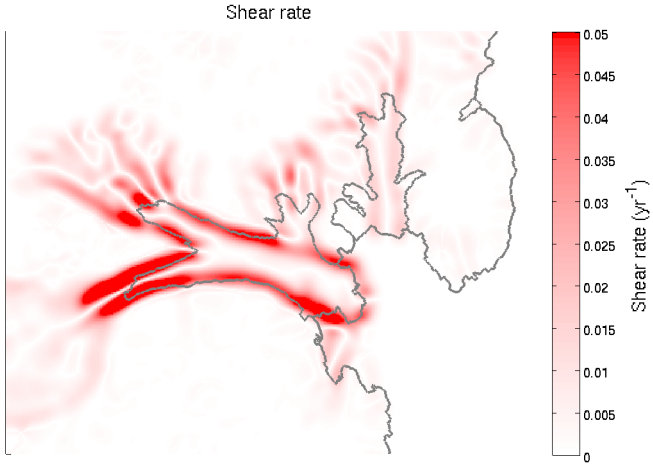

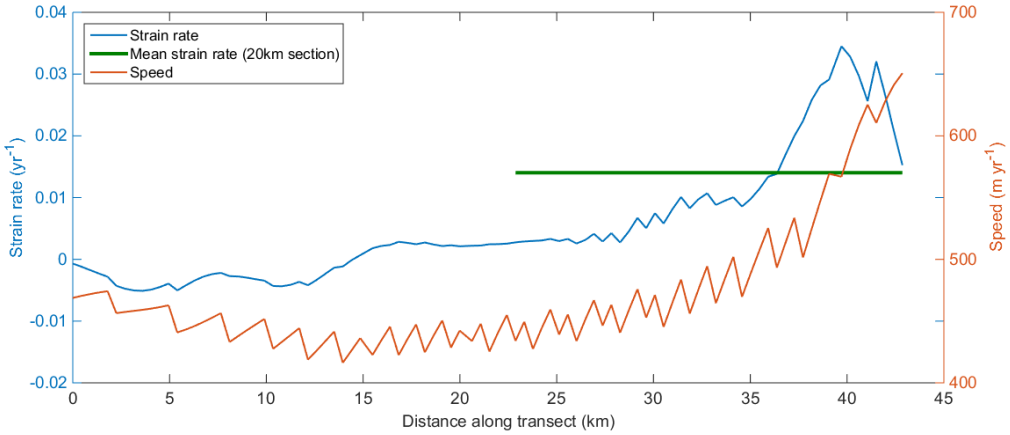

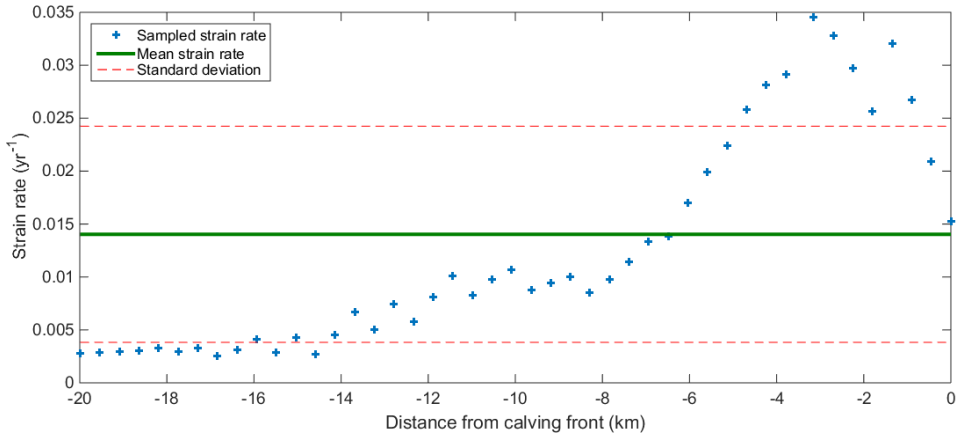

Ross Ice Shelf

MODIS

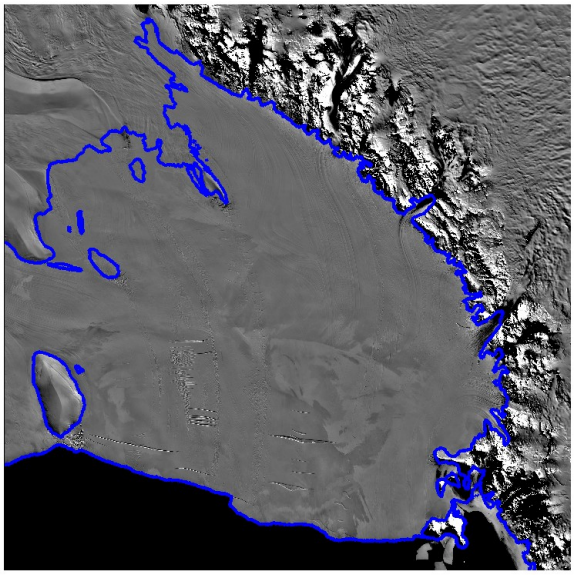

Speed

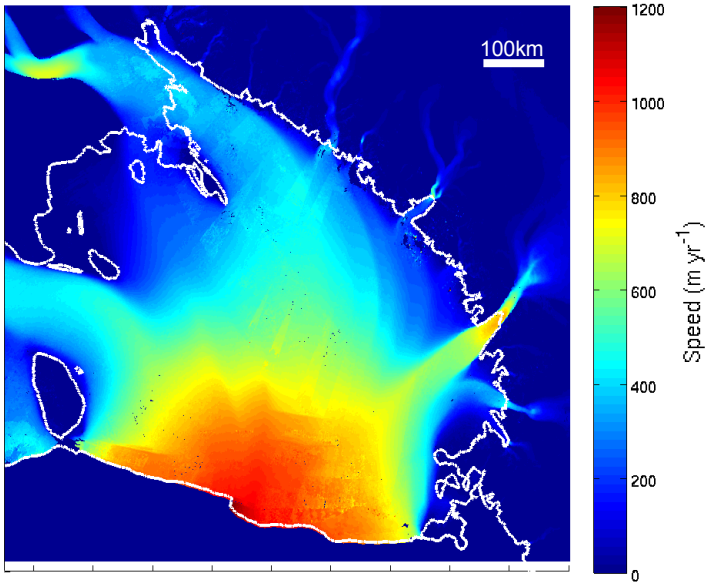

Strain rate

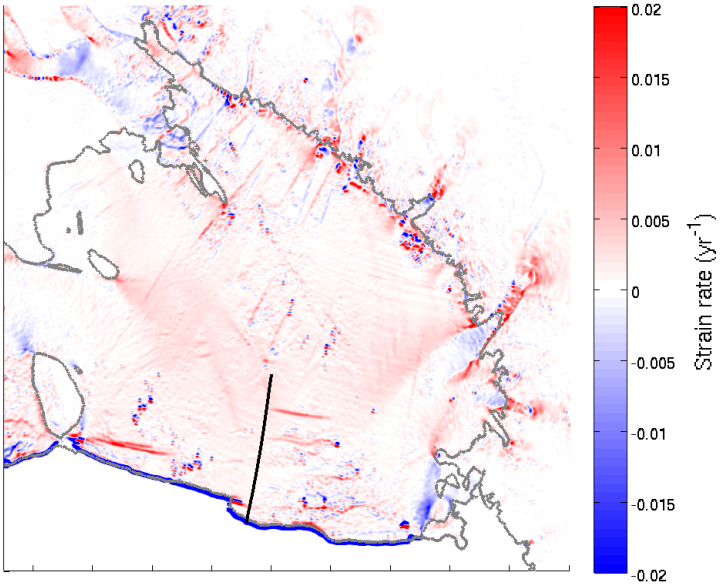

Shear rate

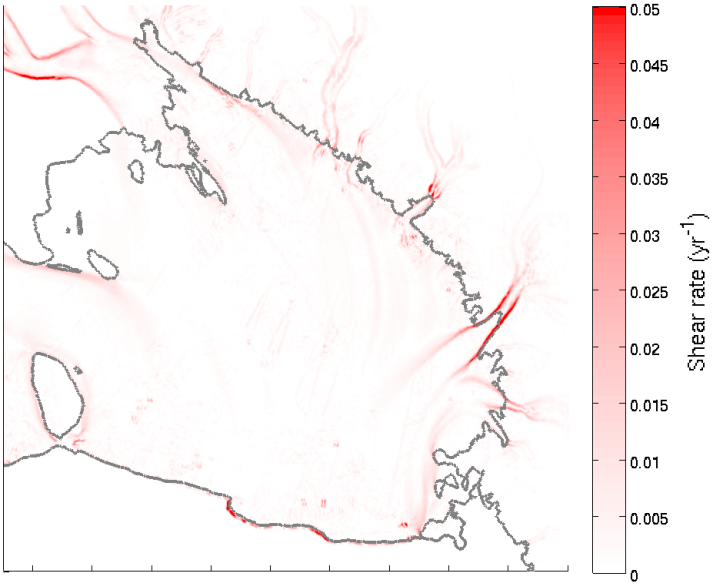

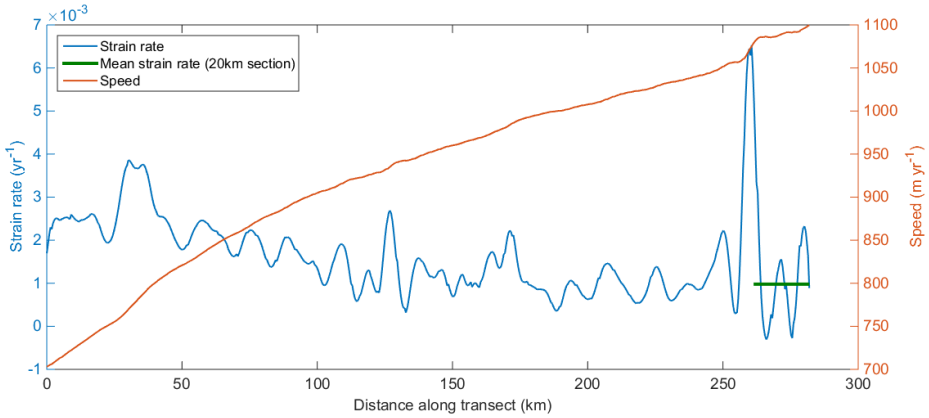

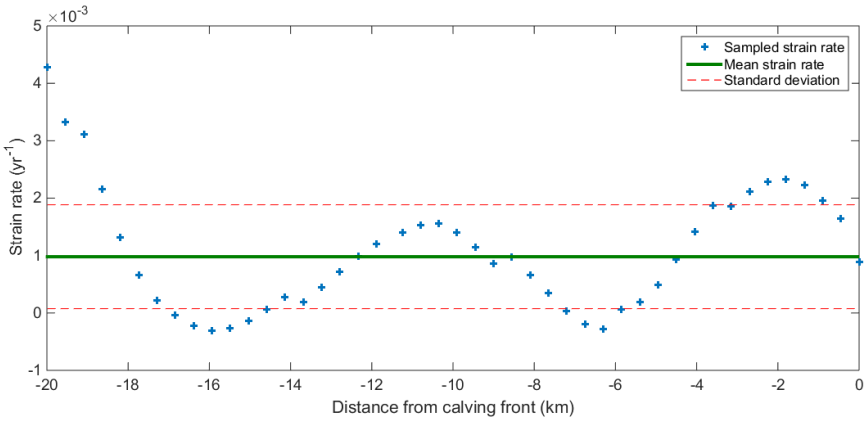

Shackleton Ice Shelf

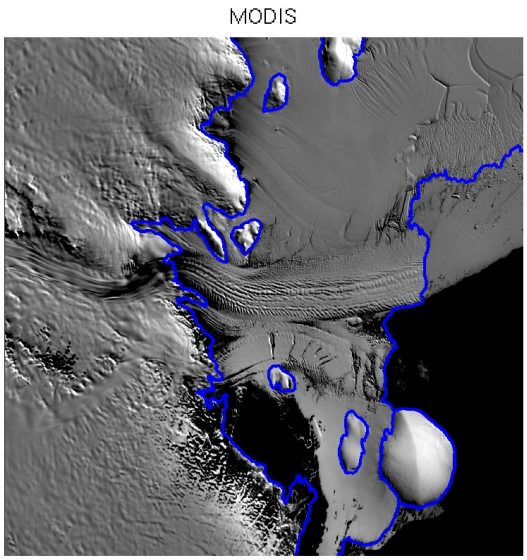

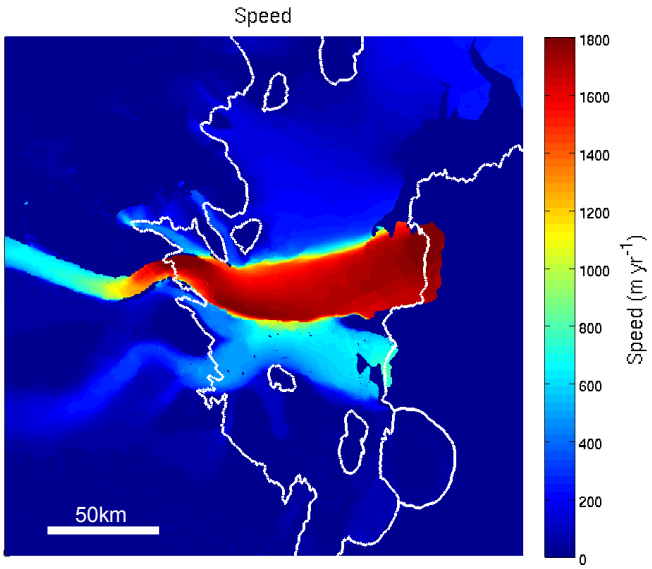

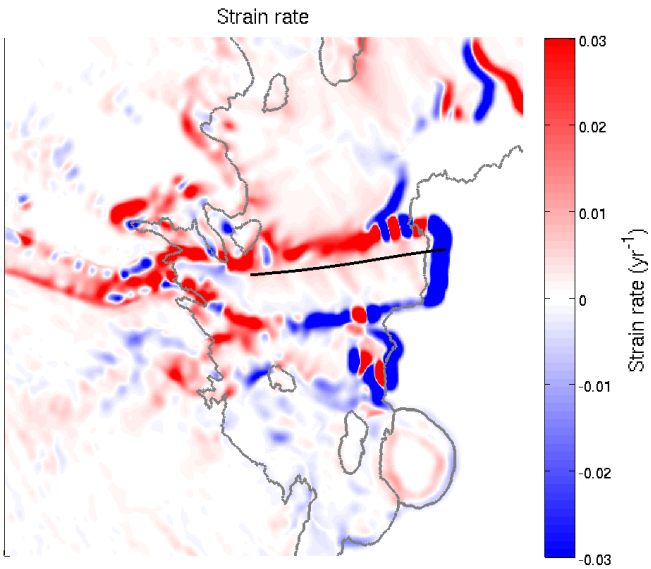

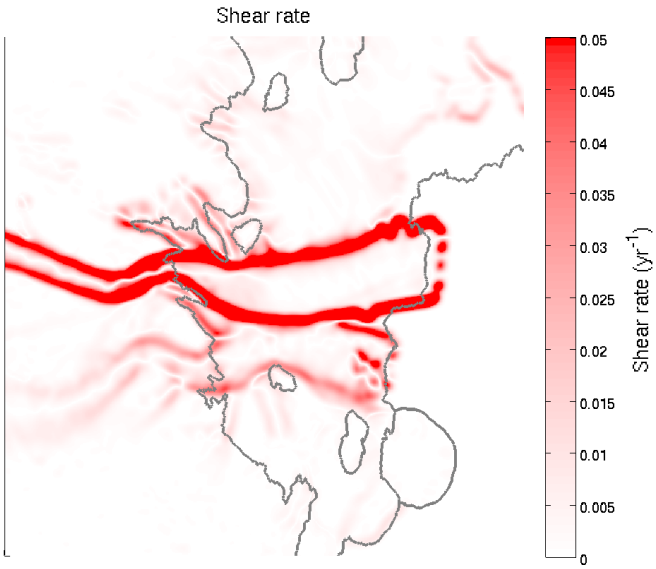

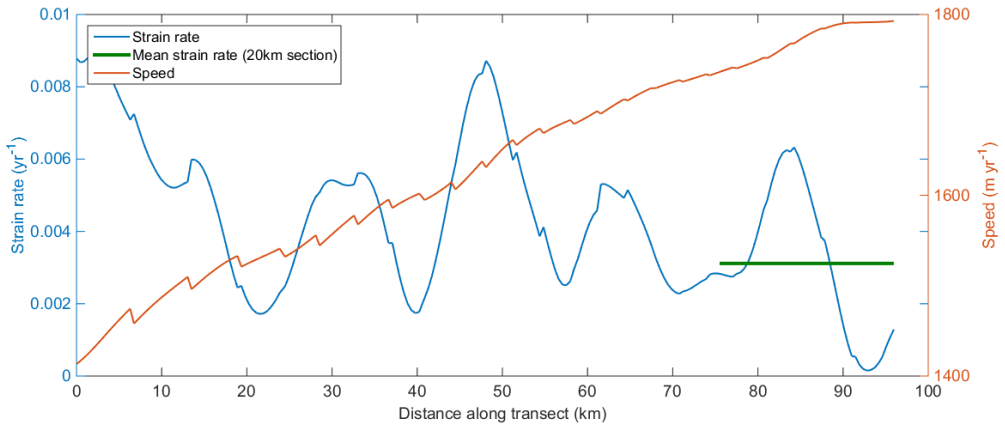

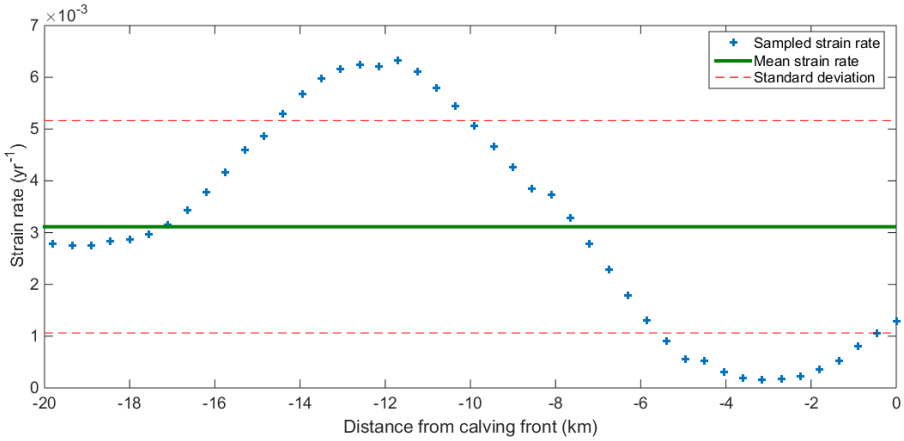

Stange Ice Shelf

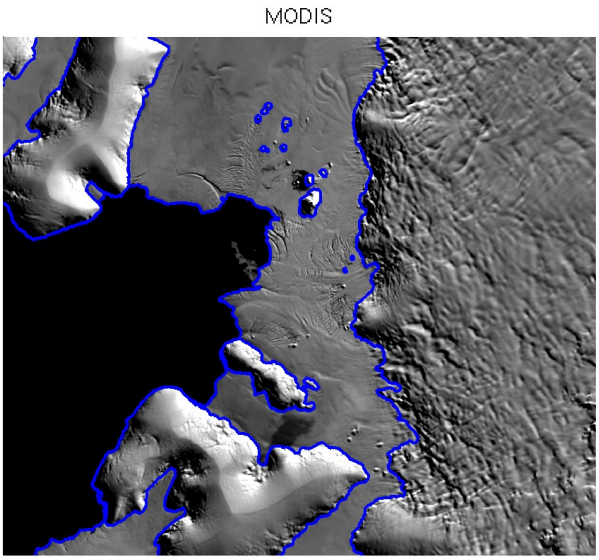

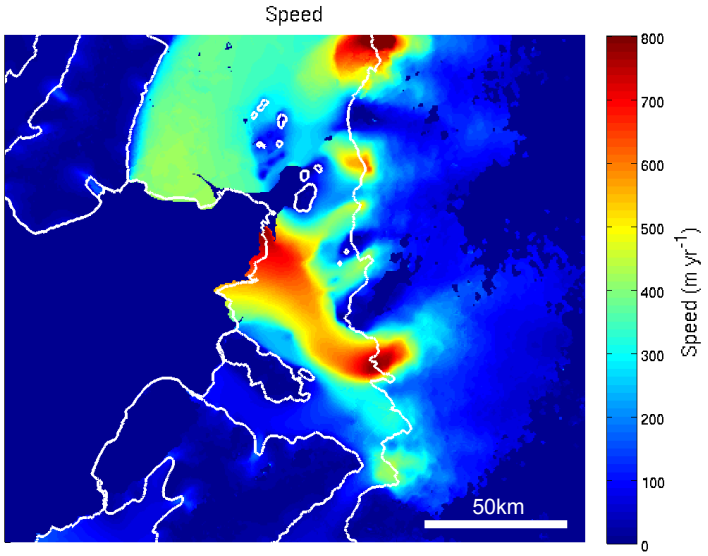

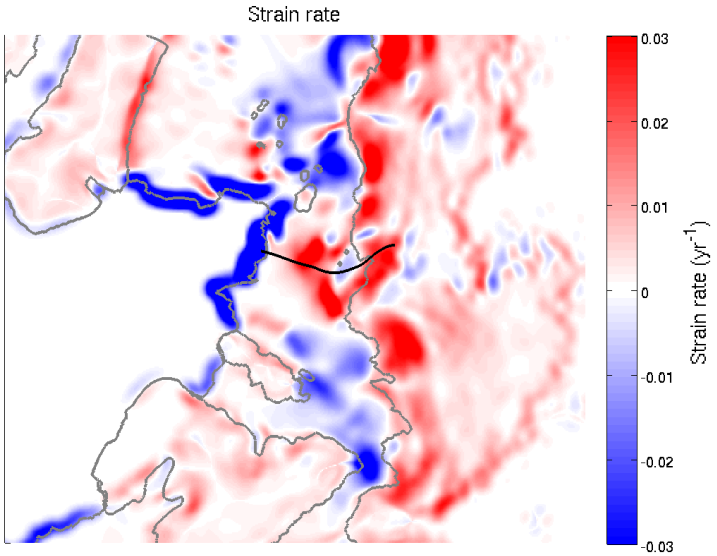

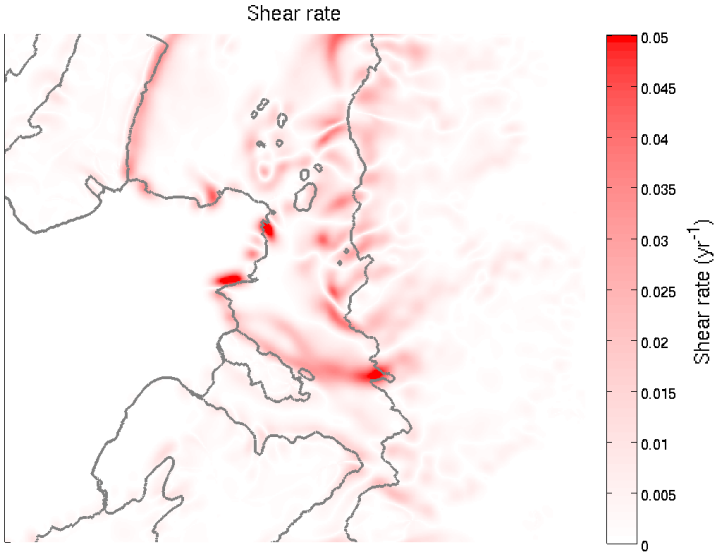

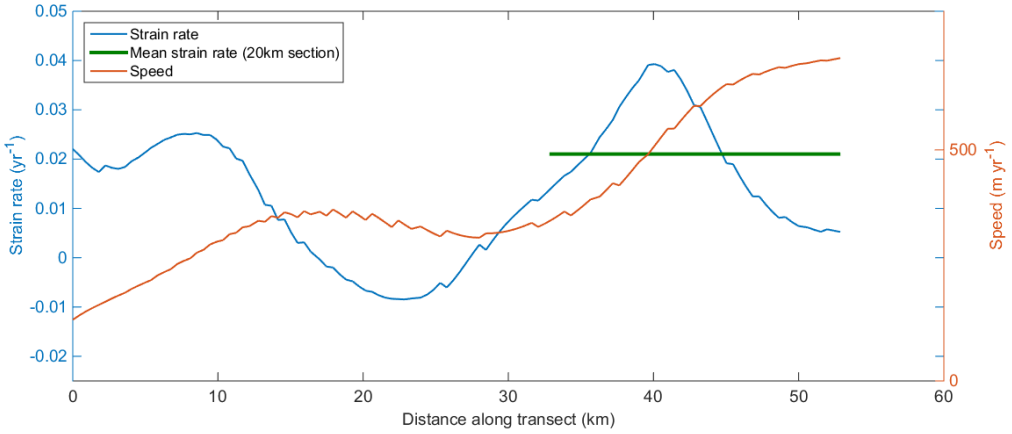

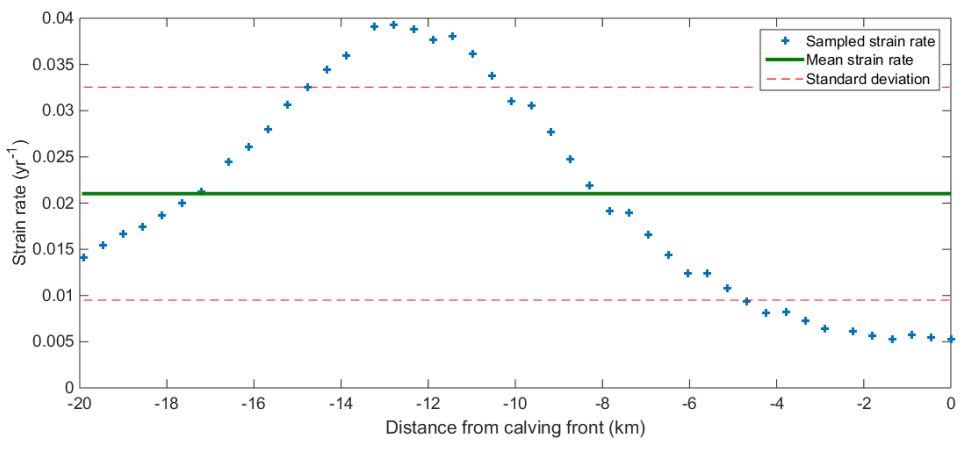

Venable Ice Shelf

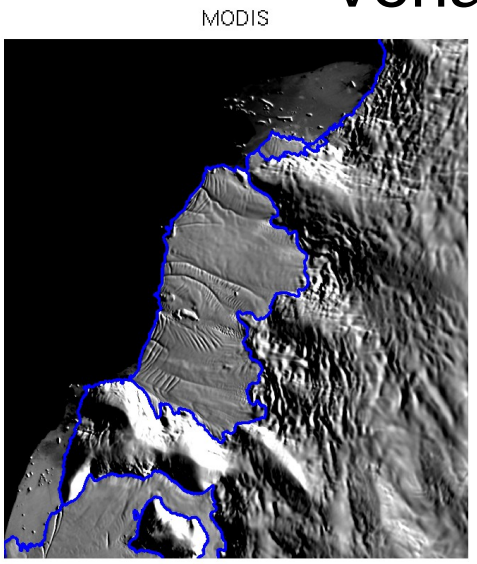

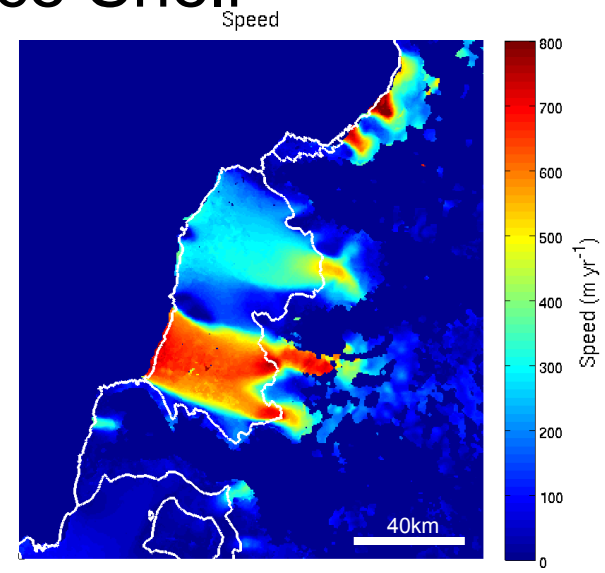

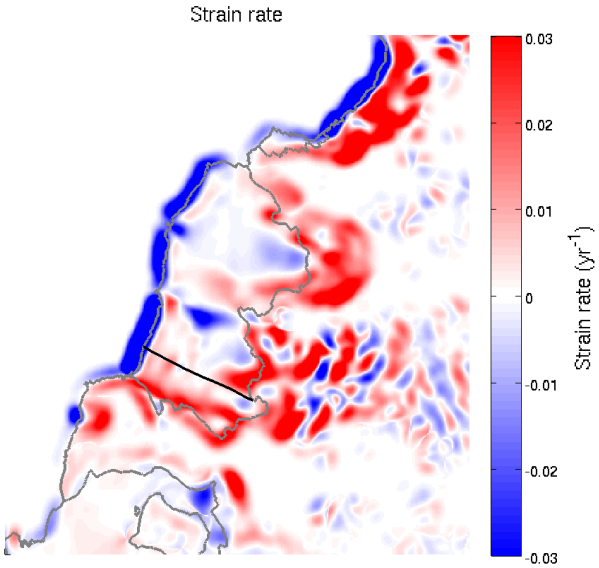

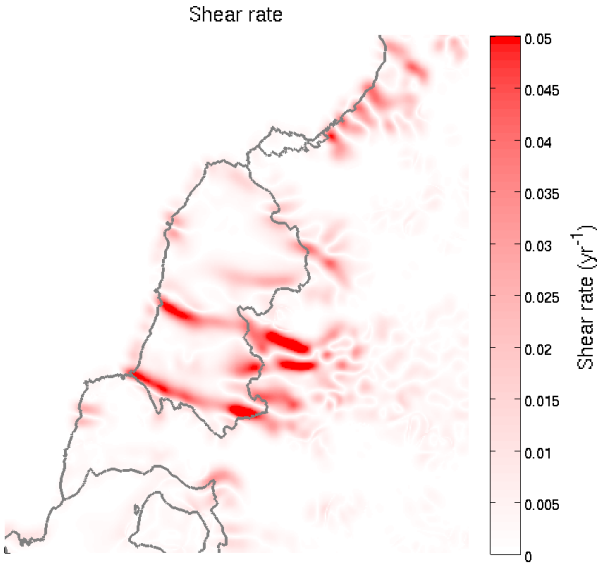

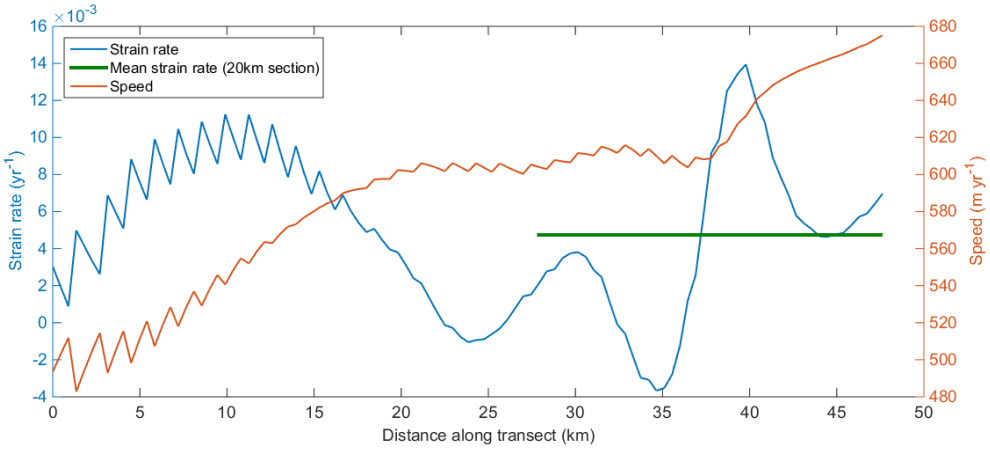

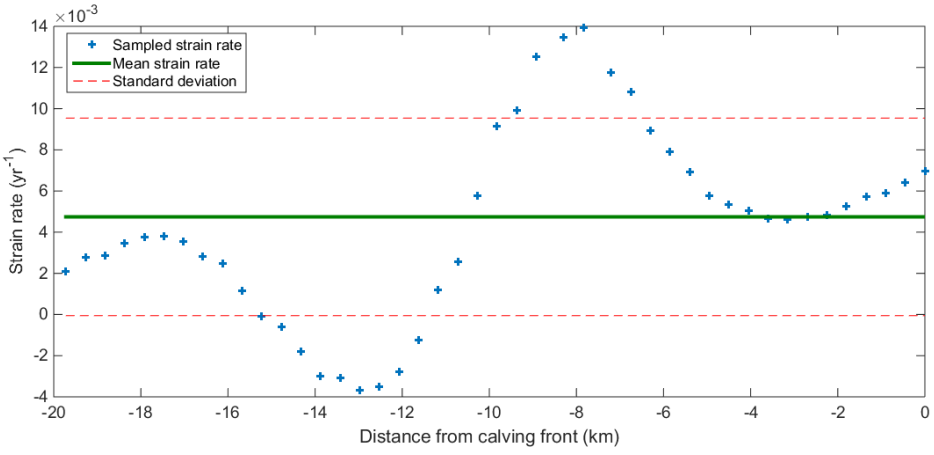

West A Ice Shelf

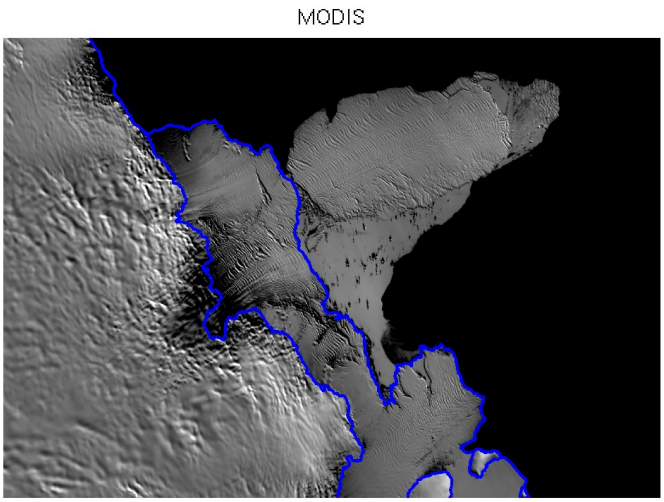

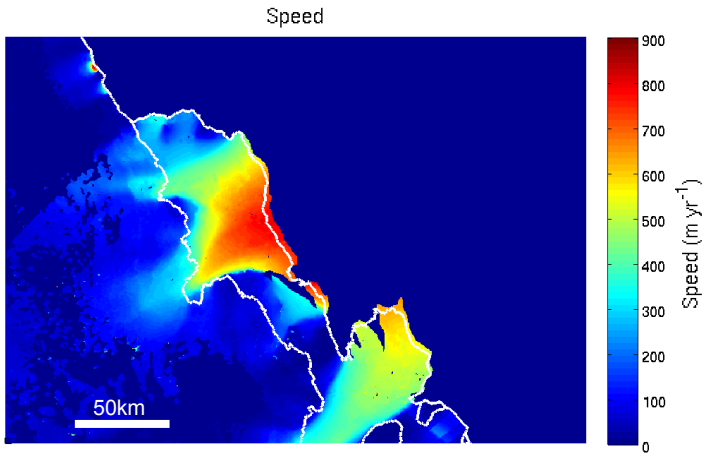

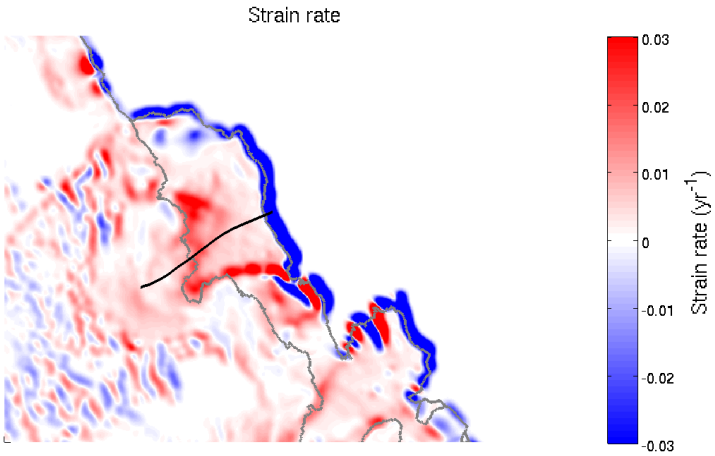

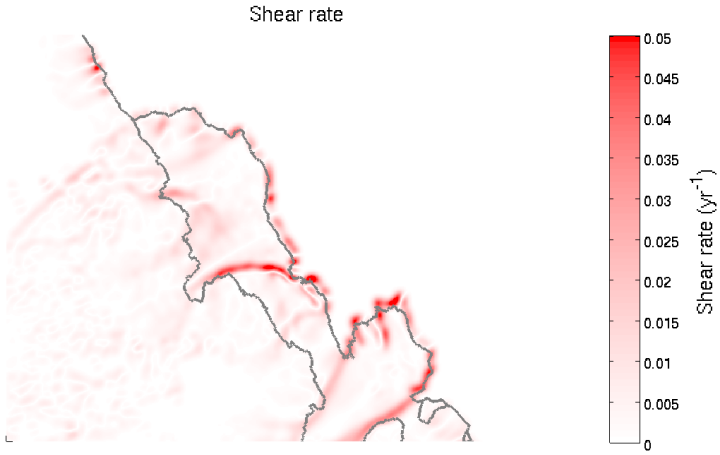

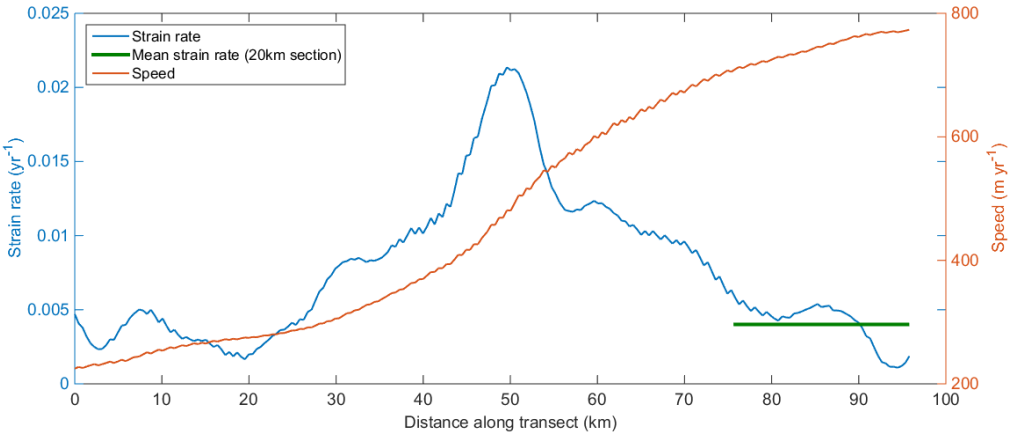

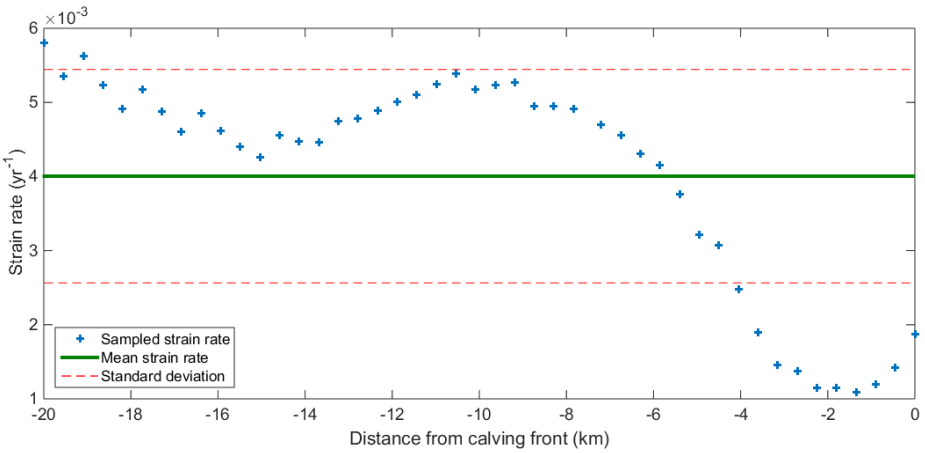

Appendix D

Appendix: Fluid-Mechanical Experiments Simulating the Flow of an Ice Shelf

Fluid	Thickness (mm)	Speed (mm s^{-1})	Strain Rate (s^{-1})
Golden Syrup	30.8	1.30	0.0001
	30.8	1.30	0.0001
	7.7	2.10	0.0008
	15.4	1.38	0.0001
	23.1	1.45	0.0004
1% Xanthan	33.0	4.62	0.0011
	33.0	1.80	0.0018
	27.5	4.79	0.0012
	27.5	4.45	0.0003
	27.5	3.96	0.0023
	27.5	5.22	0.0004
1.5% Xanthan	22.0	3.58	0.0005
	33.0	1.60	0.0005
	11.0	4.00	0.0002
	22.0	2.75	0.0008
	22.0	2.27	0.0006

Table D.1: Details of shelf thickness, flow speed and along-flow strain rate at the centre of the channel exit, used to analyse the scaling relationship for flow at the channel exit and plotted in Figure 6.34, for the range of experiments presented in the text.

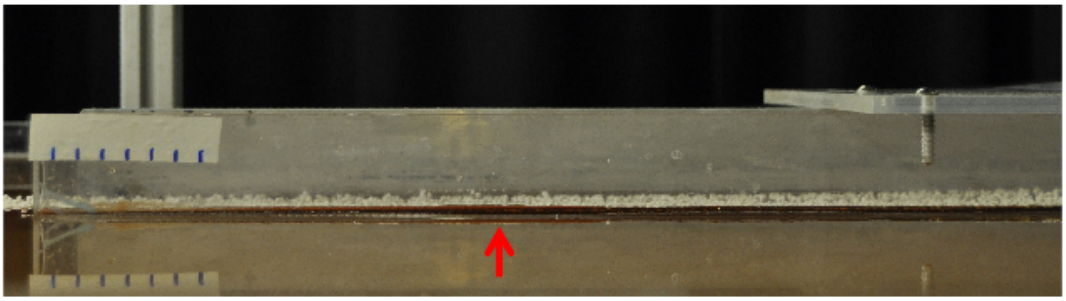

(a)

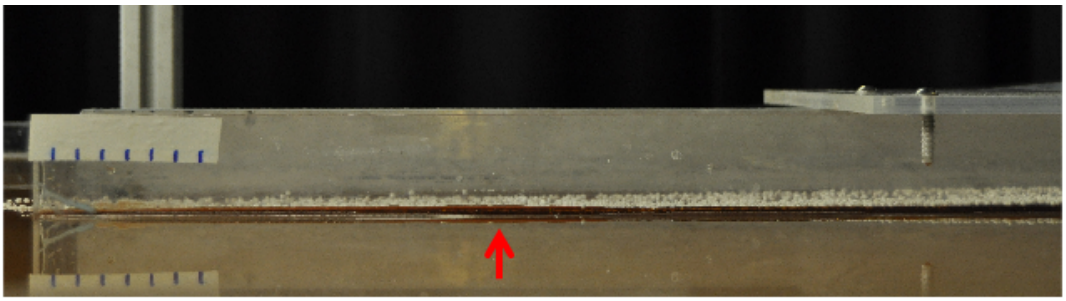

(b)

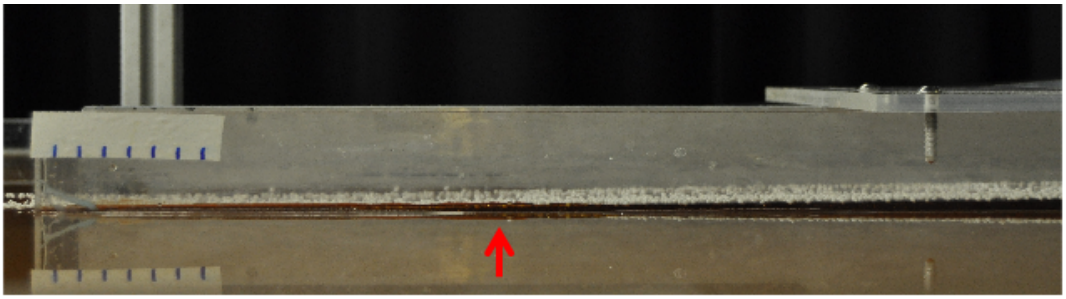

(c)

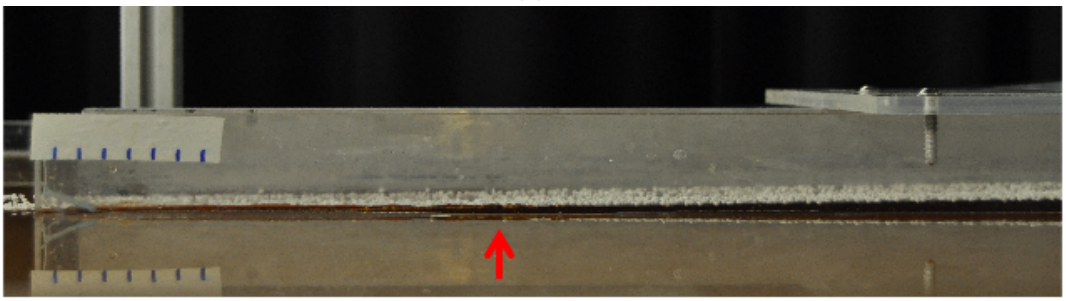

(d)

Figure D.1: Original images used to determine thickness profile of Golden Syrup Sheet-Shelf System, each taken at different time intervals: (a) early time before grounding line enters field of view; (b) 160 seconds; (c) 480 seconds; (d) 800 seconds after first particles leave channel exit. Corresponding to profiles given in Figure 6.3. It is possible to see a small undulation on the surface of the current, identified by an arrow, which is found in the same location at each time interval and becomes incorporated into the grounded section by the final interval.

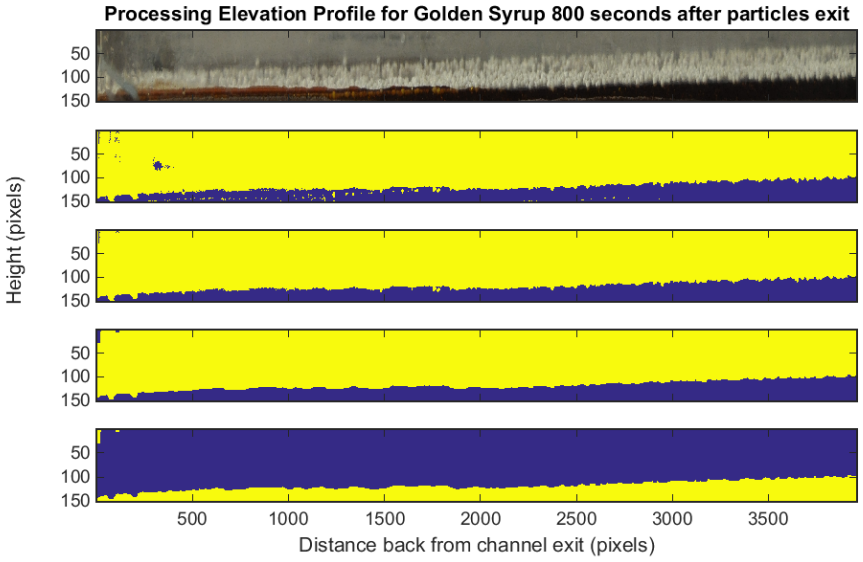

(a)

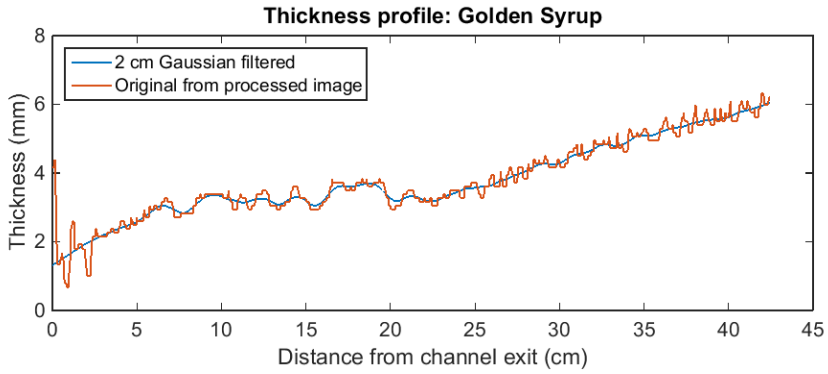

(b)

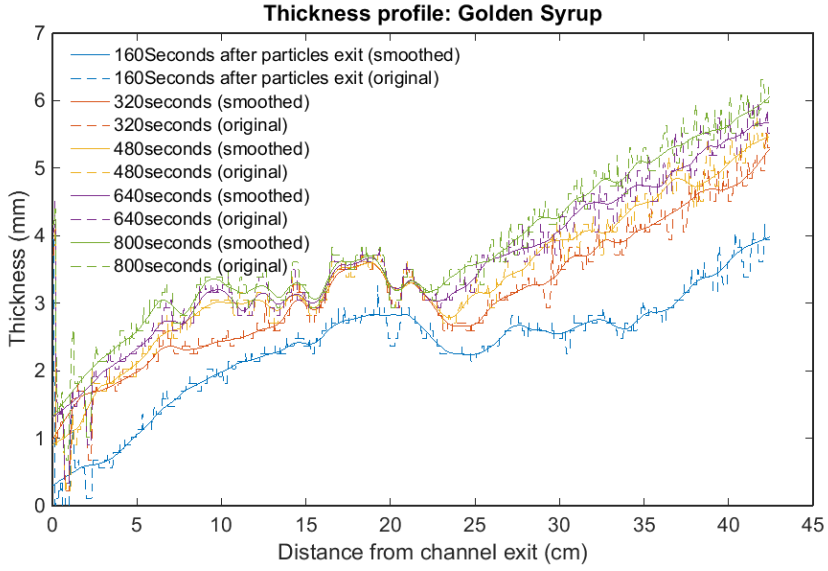

(c)

Figure D.2: Plots for elevation profile of Golden Syrup current: (a) Image processing for the elevation profile 800 seconds after the first particles leave exit (first step applies threshold filter to convert to binary image, subsequent steps attempt to improve fit - filling in holes and removing false values); (b) Elevation profile at 800 seconds determined from image processing and smoothed profile, using 2 cm Gaussian filtering; (c) Elevation profile evolution during the experiment, showing both elevation profile from image processing and smoothed profile.

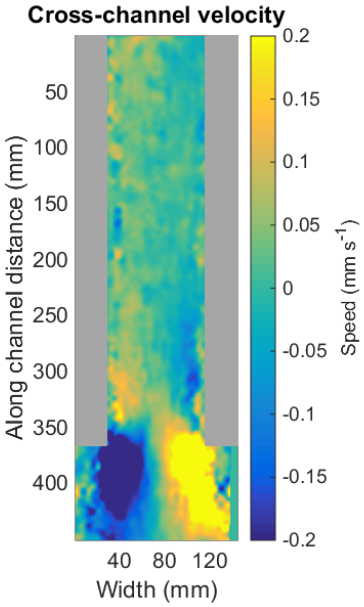

Figure D.3: Cross-channel velocity component for the first interval of the Golden Syrup experiment. Here it is clear that there is little cross-channel flow in the upstream section. However, in the final 5 cm of the channel there tends to be flow away from the side walls into the centre of the channel. Once the shelf leaves the confines of the channel there is considerable lateral flow.

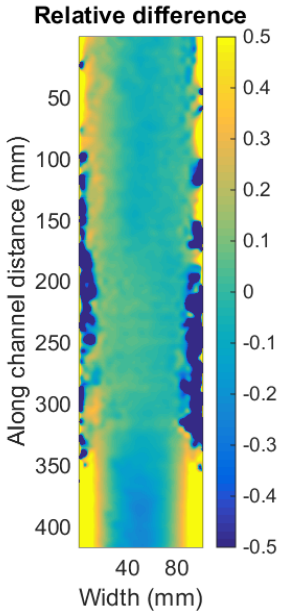

Figure D.4: Relative difference plot between original PIV along-channel velocity field and fitted model speed, with negative values indicating an over estimation by the model. Upstream of the grounding line the fitted model overestimates the

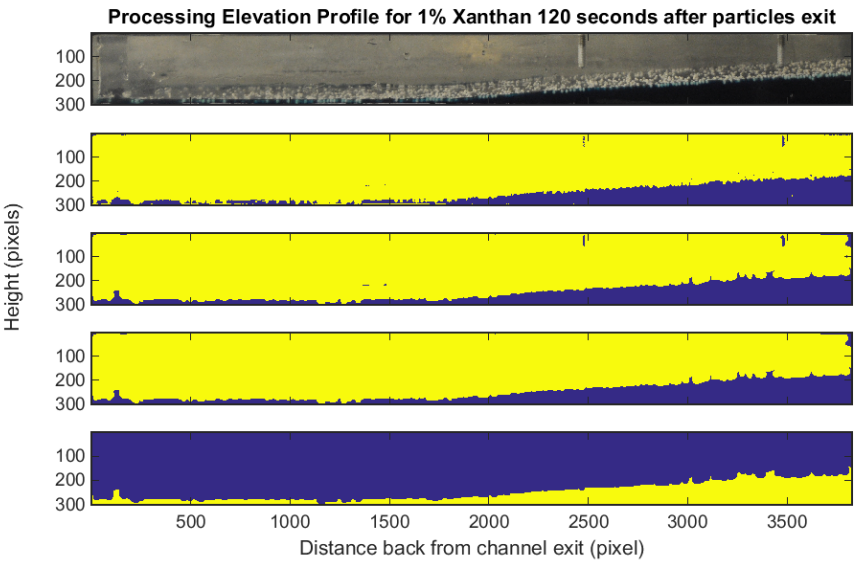

(a)

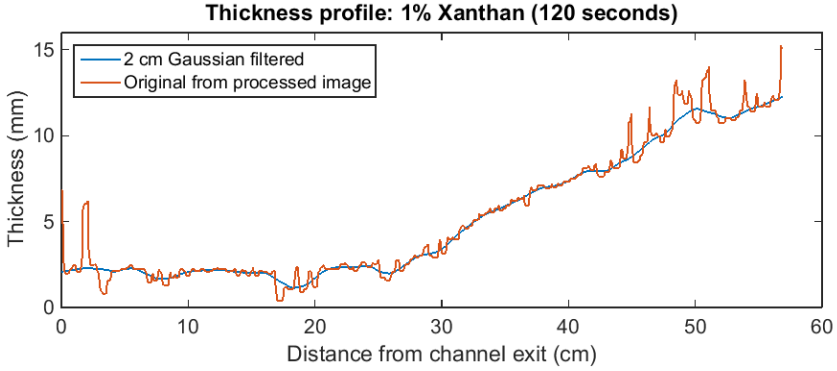

(b)

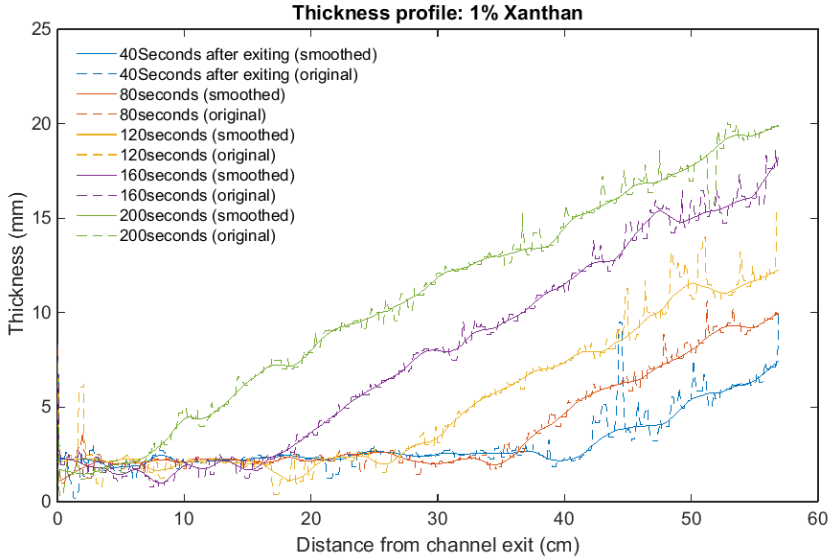

(c)

Figure D.5: Plots for elevation profile of 1% Xanthan current: (a) Image processing for the elevation profile 120 seconds after the first particles leave exit (first step applies threshold filter to convert to binary image, subsequent steps attempt to improve fit - filling in holes and removing false values); (b) Elevation profile at 120 seconds determined from image processing and smoothed profile, using 2 cm Gaussian filtering; (c) Elevation profile evolution during the experiment, showing both elevation profile from image processing and smoothed profile.

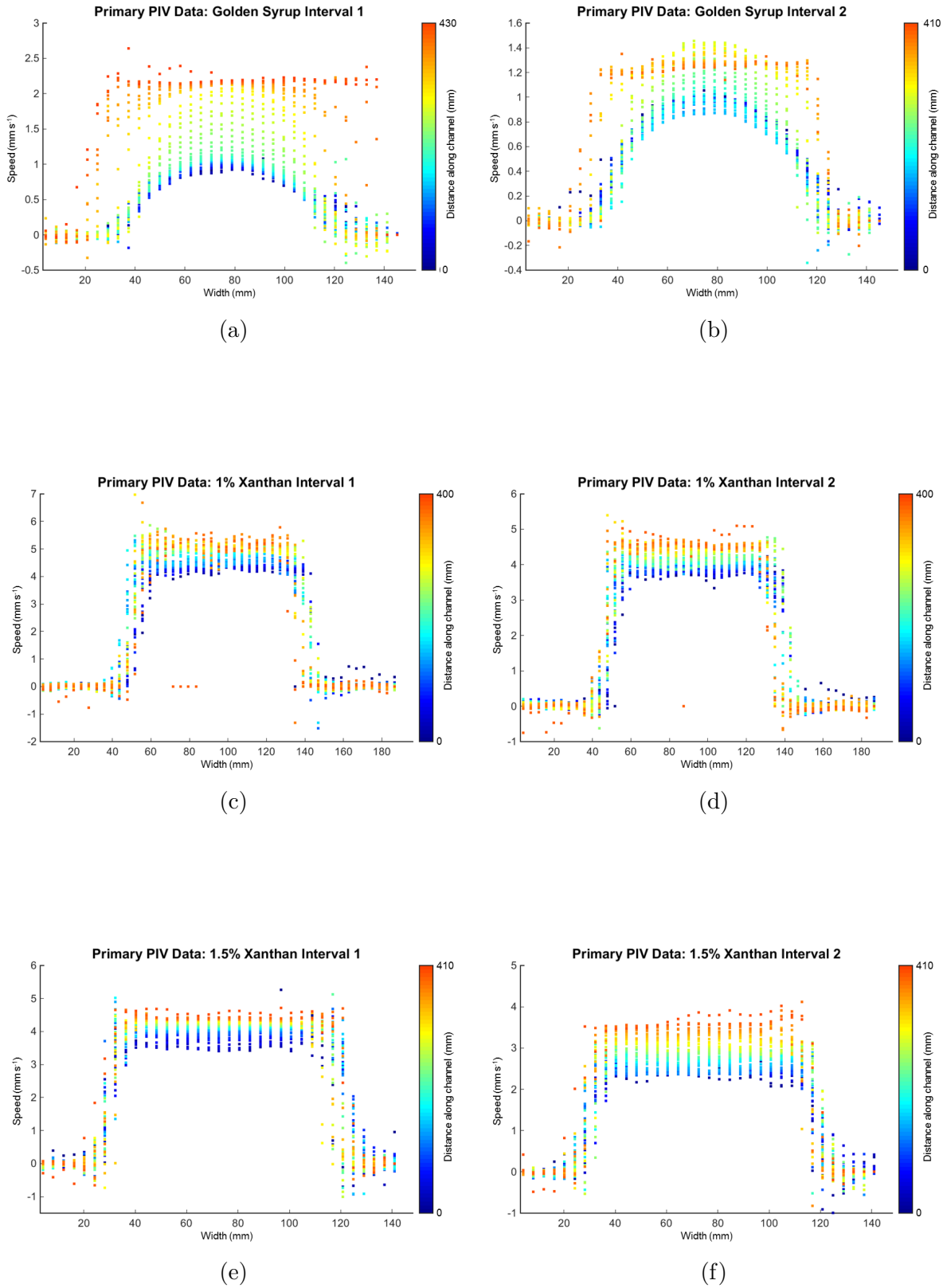

Figure D.6: Along-channel flow speeds across the width of the current at intervals along the length of the current while confined and unconfined. This data is the original PIV data as determined by the PIV software from the displacement of 8 mm squares of particles calculated on a 4 mm grid, prior to any interpolation or filtering. (a) and (b) show the velocity profile from the Golden Syrup experiment, intervals 1 and 2 respectively. (c) and (d) give velocities for the 1% Xanthan experiments, intervals 1 and 2. (e) and (f) give velocities for the 1.5% Xanthan experiments, intervals 1 and 2.

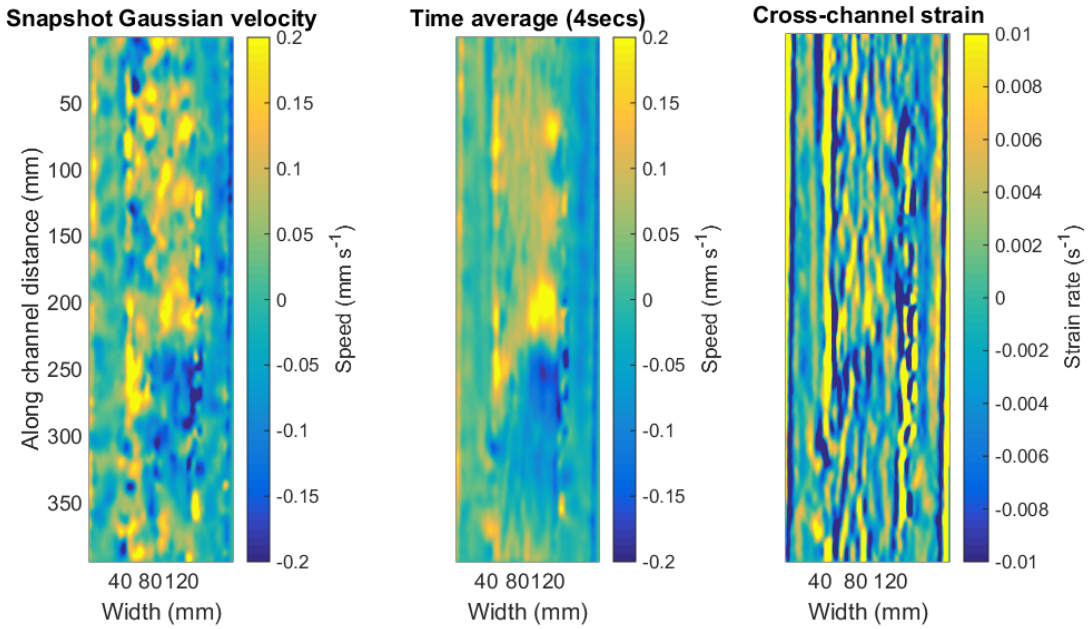

Figure D.7: Cross-channel velocity component for the second interval of the 1% Xanthan current. (a) Snapshot of Gaussian filtered velocity. (b) Time-averaged and Gaussian filtered velocity. (c) Cross-channel strain rate.

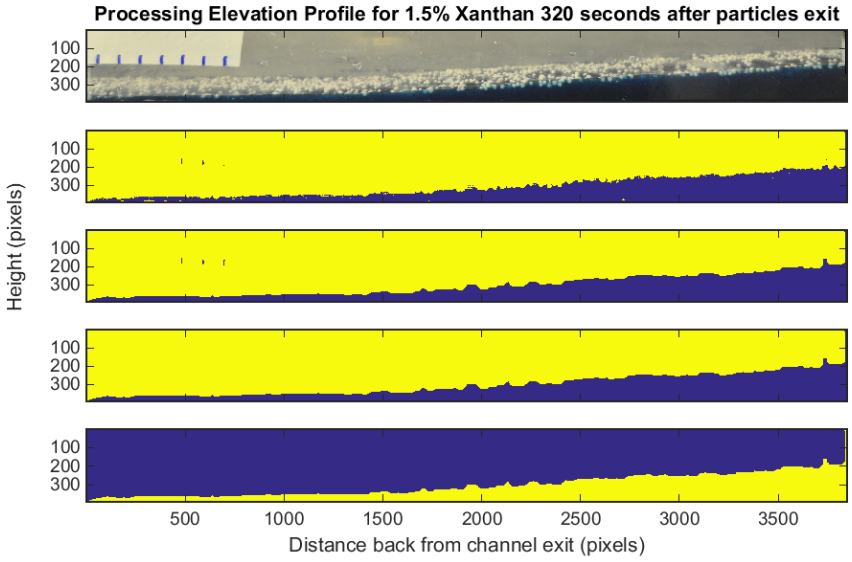

(a)

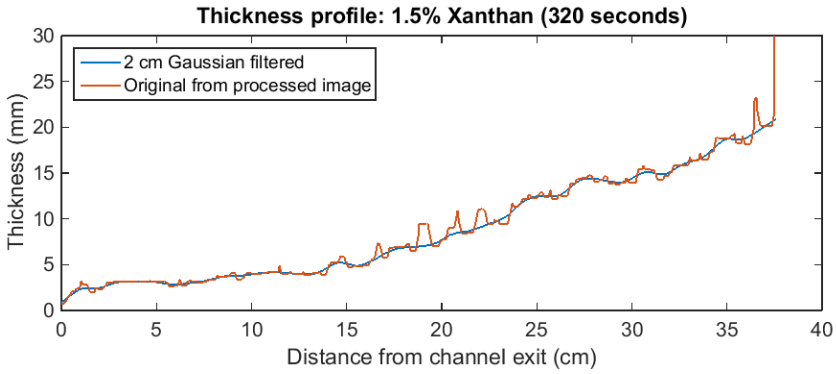

(b)

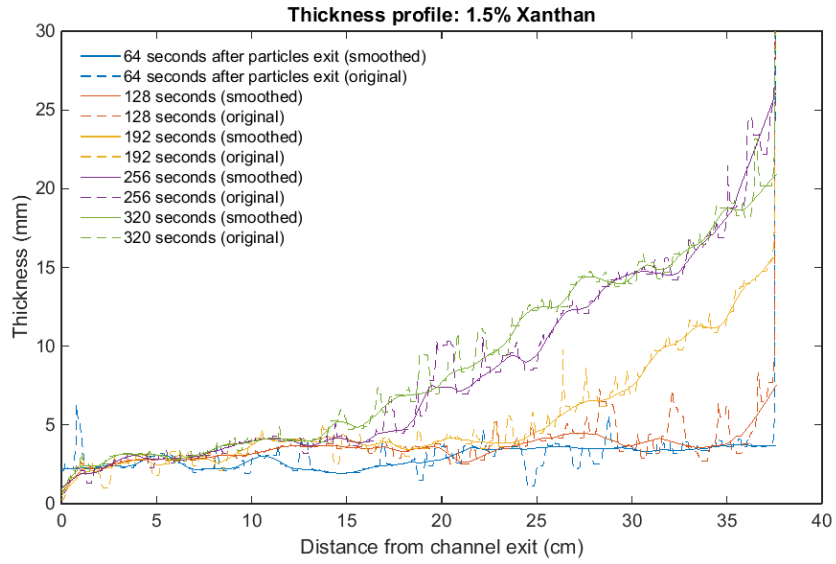

(c)

Figure D.8: Plots for elevation profile of 1.5% Xanthan current: (a) Image processing for the elevation profile 320 seconds after the first particles leave exit (first step applies threshold filter to convert to binary image, subsequent steps attempt to improve fit - filling in holes and removing false values); (b) Elevation profile at 320 seconds determined from image processing and smoothed profile, using 2 cm Gaussian filtering; (c) Elevation profile evolution during the experiment, showing both elevation profile from image processing and smoothed profile.

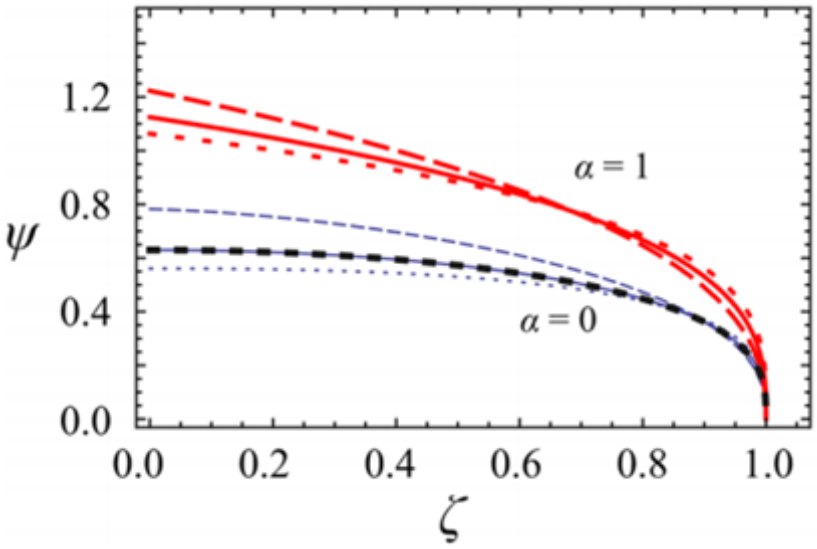

Figure D.9: Figure adapted from Longo et al. (2015). Plot of shape function ψ for power-law viscous gravity current confined in a horizontal channel, with a semi-circular base, against along-channel similarity variable η. Red curves represent constant flux release. Blue curves represent fixed volume release. Solid curves for $n = 1$. Dashed curves $n = 2$ and dotted curves $n = 2/3$. It is clear that away from the nose of the current the slope increases for larger values of the power-law flow exponent n.

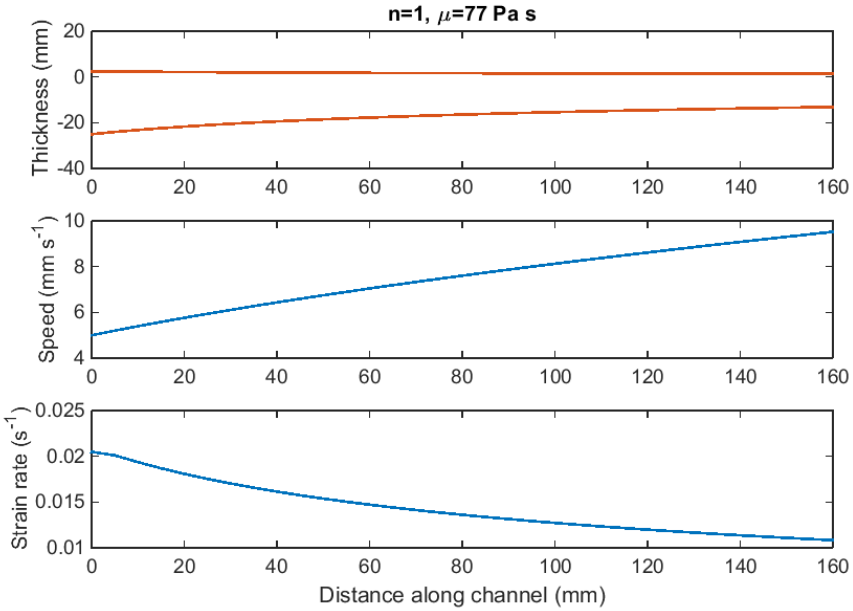

Figure D.10: Shelf thickness, speed and strain rate for a purely extension shelf, with Newtonian rheology and viscosity $\mu = 77$ Pa s.

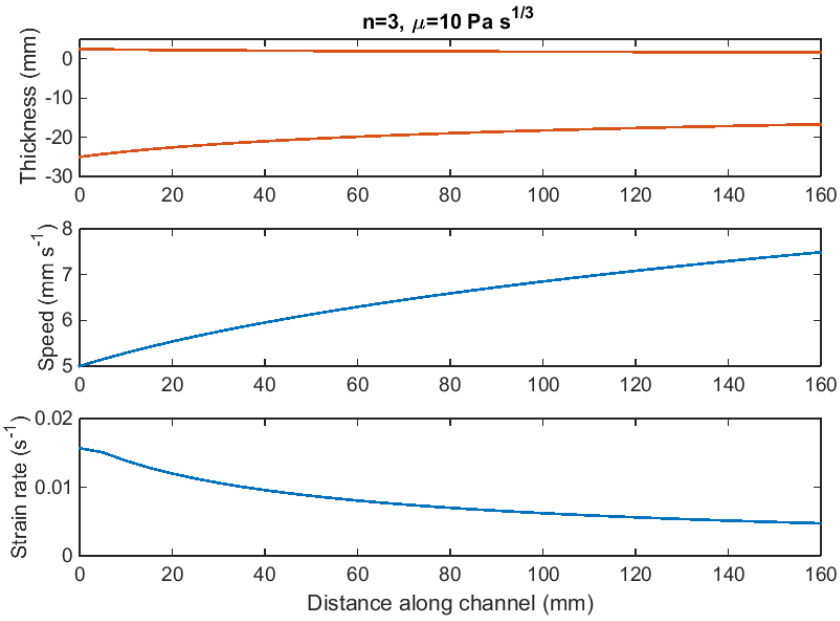

Figure D.11: Shelf thickness, speed and strain rate for a purely extension shelf, with $n = 3$ power-law rheology and consistency index $\tilde{\mu} = 10$ Pa s$^{1/3}$.